Arrestins: multifunctional regulators of signaling pathways

By

Nicole Anna Perry-Hauser

Dissertation

Submitted to the Faculty of the

Graduate School of Vanderbilt University

in partial fulfillment of the requirements

for the degree of

DOCTOR OF PHILOSOPHY

in

Pharmacology

May 10, 2019

Nashville, Tennessee

Approved:

Dr. Benjamin Spiller (Chair)

Dr. Raymond Blind

Dr. Annette Beck-Sickinger

Dr. Tina M. Iverson

Dr. Vsevolod V. Gurevich

To my father, who always believed I was extraordinary.

ACKNOWLEDGEMENTS

The journey to any doctoral degree is by no means a minor task. However, perhaps more daunting is finding the right words to convey thanks for everyone involved in the accomplishment.

None of this would be possible without the tremendous love and care of my mother, Debra Perry, who has always been and will always be my biggest supporter. You held me when I needed comfort, heartened me when I was discouraged, and celebrated me for even the smallest accomplishments. Together we made it through the loss of your husband and my father, David Perry, who I know looks upon us both with pride.

To Eric, my husband, my best friend, my rock: What can I say that hasn't been said? Thank you for leaving the comforts of Cincinnati for Nashville and all the other sacrifices you've made so that I can pursue my crazy dreams. While not home, this city will always be the place where we made our vows and I personally cannot wait for the adventures to come.

To Seva: You agreed to let me work in the lab when I was a twenty-two-year-old inexperienced scientist and took the time to teach me at the bench, a characteristic I had never experienced in a mentor. You exposed me to the world of GPCR and arrestin biology and gave me opportunities to engage in the community by sending me to conferences both internationally and nationally. I am incredibly grateful for your insight – working for you has been a privilege and a delight.

To Tina: Thank you, thank you for showing me what it means to be a woman in science. You taught me how to believe in my abilities and navigate the difficult world of academia. I am a better scientist for having worked with you.

To the entire Gurevich/Iverson team, who all played a hand in my scientific career: Deepak Balasubramanian, Sandra Berndt, Qiuyan Chen, Jeff Dunning, Nathan Gilbert, Eugenia Gurevich,

Ali Kaya, Lioudamila Loukachevitch, Kathryn McCulloch, Srimal Samaranayake, Pankaj Sharma, Prashant Singh, Chrystal Starbird, Haley Stubbs, Kimberley Thibeault, Sergey Vishnivetskiy, Izumi Yamakawa, and Chen Zhang. And, of course, all the students I have mentored: Mariana Lopes, Andrew Magnus, Kevin Fialkowski, Luwi Shamambo, Nicole Kendrick, Bridget Collins, Jonas Tholen, and Susanne Prokop.

To the Vanderbilt Department of Pharmacology, which provided a scholarly environment to grow and develop friendships: Joey Barnett (Acting Chair), Christine Konradi (DGS), Sean Davies (Associate DGS), Karen Gieg, and the entirety of the Pharmacology Graduate Student Association.

To my Thesis Committee, thank you for reading through the whole dissertation: Ben Spiller (Chair), Ray Blind, Annette Beck-Sickinger, Tina Iverson, and Seva Gurevich.

To my friends, who give me guidance when I need it, and have learned to cope with my ever-constant anxiety: Megan Gamm, Lauren Hall, Samantha Stulen, Hilary Weismantel, and Aimee Wilde. You are the sisters I never had.

To my family, both blood and acquired, who will likely never know the exact nature of my work: Grey and Nancy Perry along with the Perry and Stephens clan, the Jouberts, my in-laws Michele Wainscott and Lynn Henry, and the Hauser family.

And lastly, to my father, who always believed I was extraordinary.

TABLE OF CONTENTS

Page

LIST OF TABLES

Page

LIST OF FIGURES

Page

SECTION A: ARRESTIN INTERACTION WITH INTRACELLULAR EFFECTORS

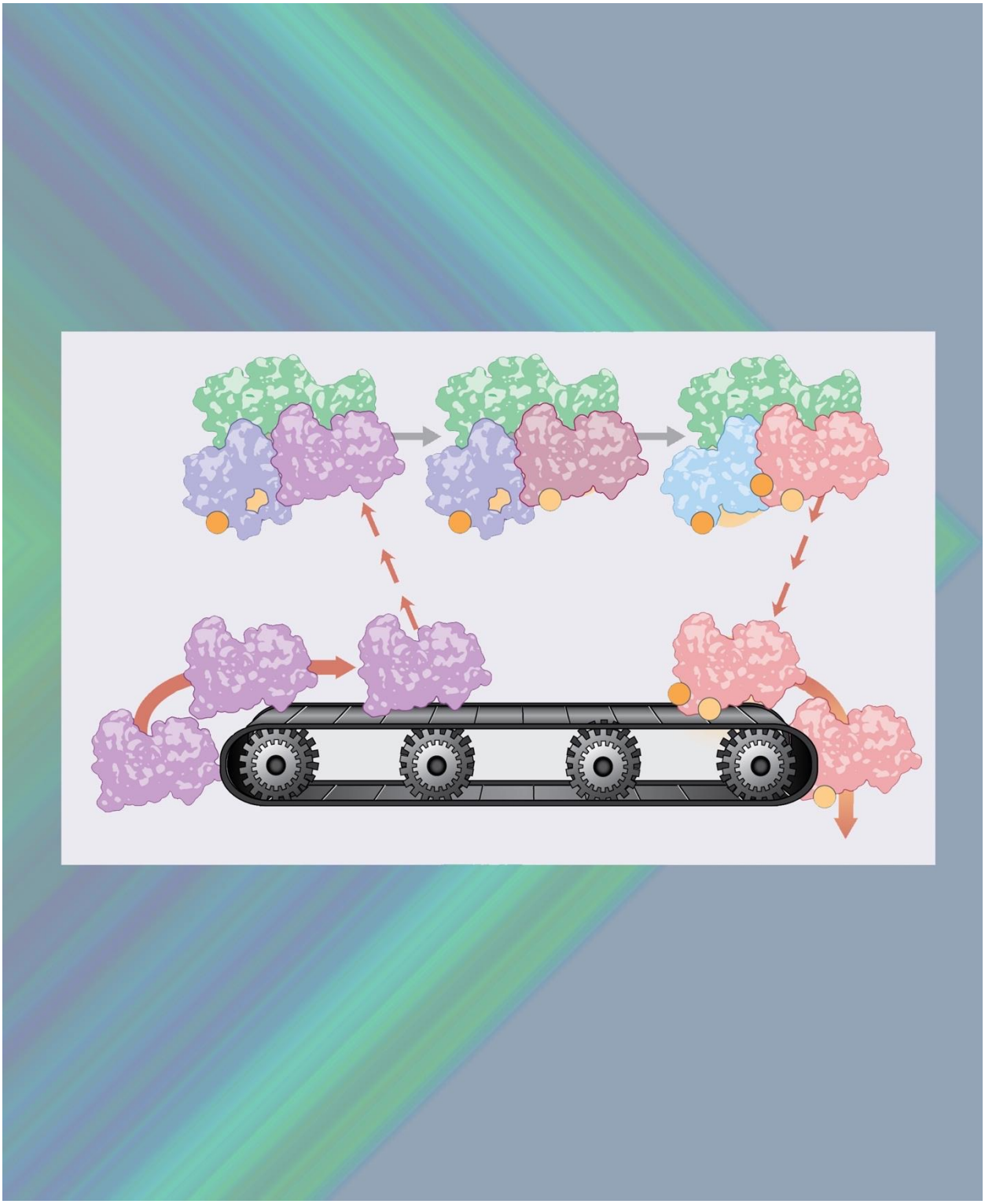

CHAPTER 1

INTRODUCTION

1.1 Thesis Overview

Mammalian cells respond to environmental cues using a process called receptor signaling, which transmits information from the extracellular environment to the inside of a cell. An important aspect of receptor signaling is easy activation, i.e. when a signaling molecule like a neurotransmitter or hormone is sensed, the body must quickly respond. Receptor signaling is heavily regulated in order to ensure a correct biological response. Proper regulation is key; for example, if a signaling process turns on cellular growth incorrectly, it could result in the formation of cancerous tumors. Finally, receptor signaling must also be deactivated, otherwise your heart rate would never slow down after a fright!

I study a protein that is a master regulator of signaling and the key player in the deactivation of the largest group of receptors, G protein-coupled receptors, which are targeted by more than a third of clinically used drugs. This protein is called arrestin, and my research focuses on how arrestins make the choice between different cellular outcomes (**Figure 1.1**). For example, arrestin signaling can promote the activation of cellular pathways involved in cell proliferation in response to extracellular mitogens. Mitogens signal through receptors to cause cell division through activation of mitogen-activated protein kinase (MAPK) cascades, a process that results in cell growth. Recent work has shown that arrestins act as scaffolds for MAPK cascades. Scaffold proteins promote signaling by bringing all molecular components together and localizing them to a specific part of the cell. Arrestins bind all members of MAPK cascades and localize them within

the cell; however, the mechanism of arrestin scaffolding is poorly understood. My thesis research aims to characterize the arrestin-MAPK interactions in order to better understand how arrestin dictates signaling through MAPK cascades and controls cellular outcomes.

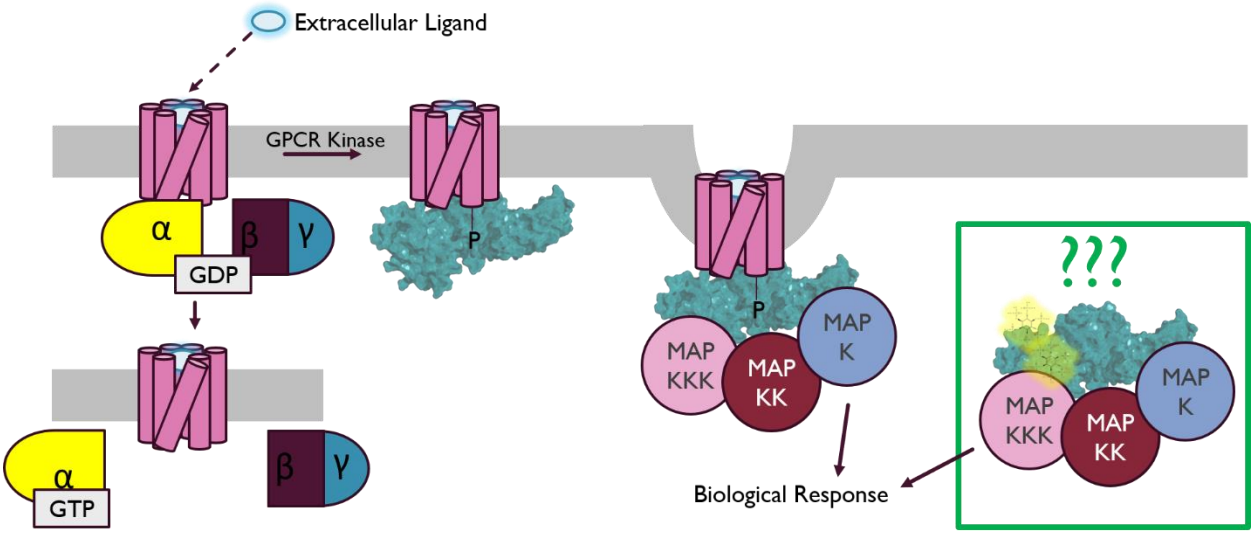

Figure 1.1. Arrestin scaffolding of MAPK cascades. G protein-coupled receptors (GPCRs; pink) are seven-transmembrane proteins that transmit information from the extracellular environment to the inside of a cell. The GPCR acts as a guanine-nucleotide exchange factor (GEF) for heterotrimeric G proteins (yellow, purple, and teal), which then dissociate from the receptor to initiate signaling events. To deactivate receptor signaling, GPCR kinase (GRK) phosphorylates the receptor to recruit arrestin (green), which desensitizes the receptor and leads to receptor internalization. In addition to this function, arrestins can act as signal transducers for intracellular effectors. One example is the ability of arrestins to scaffold mitogen-activated protein kinase (MAPK) cascades. My thesis aims to characterize the interaction between arrestins and MAPK cascades in order to better understand how arrestin dictates cellular outcomes.

1.2 Thesis Aim I: Arrestin interaction with MAP kinase cascades

While the interaction between various MAPK cascades and arrestin is widely accepted in the signaling field, the mechanism through which arrestin binds MAPKs and directs their signaling is poorly understood. The first aim of my thesis project was to characterize the arrestin/MAPK interface. Initially, I tested the affinity of each respective kinase for arrestin using microscale thermophoresis (MST), surface plasmon resonance (SPR), and NMR spectroscopy (in the case of fully annotated ERK2). To map the binding site(s) of MAP kinases on arrestin-3, I used a

combination of pull-down assays with purified proteins, peptide array analysis, and NMR spectroscopy. This work led to several publications, which are highlighted throughout the first section of my thesis work, *Arrestin Interaction with Intracellular Effectors.*

1.3 Thesis Aim II: The molecular basis for signal amplification

Research has shown that response amplitude of MAPK signaling is determined by scaffolding of specific modules to allow for sequential physical interaction between the kinases (1); however, the mechanistic basis for this interaction has not been clearly elucidated. The second aim of my thesis work was to assess how the interaction of active and inactive MAPKs with arrestin controlled signal amplification. For example, MAP kinases undergo large conformational changes in response to phosphorylation of their activation loop. It is likely that these changes influence the ability of the kinase to interact with arrestin-3. To study the effect of kinase activation on binding, I first determined the affinities of the kinases in the ASK1-MKK4/7-JNK3 cascade for arrestin-3 in the presence of physiological ATP and $MgCl_2$. In general, I found that inactive kinases (kinases that have not been phosphorylated) have a higher affinity for arrestin-3 than their activated forms. This allowed the development of the first plausible mechanism for signaling amplification by arrestins, which I call the "conveyor belt model" ((2); Chapter 6).

1.4 Thesis Aim III: The molecular basis for signal bias

A long-standing mystery in the signaling field is how arrestin "chooses" between the activation of closely related molecules (like JNK3 and ERK2, which are >40% identical); this is called signal bias. My work contributed to the development of a model for signal bias by arrestin-3 ((3); Chapter 4). This model proposes that arrestin changes conformation when it is signaling,

but adopts slightly different active conformations, depending on the activator. This, in turn creates different binding sites for effectors. As of yet, there are no available experimental structures for arrestin-3 with any effector (signaling) molecule.

For the third aim of my thesis, I focused on obtaining a co-structure of arrestin-3 and JNK3 as a model system for other arrestin/MAPK interactions. In addition, I worked on crystallizing ERK2 and p38α with arrestin-3 peptides that I had identified in my binding studies. While I was unsuccessful in obtaining a crystal co-structure of arrestin-3/JNK3 or MAPK/peptide, I did develop expression and purification conditions for several recombinant protein constructs I designed using a previously crystallized bovine arrestin-3 sequence (residues M1-R393) and one of three MAPKs: JNK3, p38α, or ERK2. I collected SAXS data on all three constructs and have been using the fusions to study multiple kinase interactions with arrestin-3 *in vitro*. This work is in preparation for submission (Chapter 7).

While the biochemical methods outlined in my previous aims have provided an in-depth picture of kinase interaction with arrestin-3 *in vitro*, I also worked to validate my findings in a cellular context using arrestin-2/3 knockout HEK cells. Initially, I tested the ability of several arrestin-3 peptides to facilitate JNK3 activation in cells ((4); Chapter 5). During this study, I found that one peptide of arrestin-3, T1A15, inhibited JNK3 activation in cells. We are currently using this peptide as a negative regulator of JNK3 activation in a mouse model of Parkinson's disease. While we have data showing that arrestin-3 mutant V343T, defective in JNK3 activation, prevents L-DOPA-induced rotations in hemiparkinsonian mice (a model of L-DOPA-induced dyskinesia), the data with short peptides are still inconclusive.

1.5 Project Significance

Identifying how a signaling process results in a specific outcome could provide guidance for future drug discovery efforts that help to control diseases such as neurodegenerative disorders and cancer. For example, "kinase inhibitors" are drugs that target the MAPKs I study and are currently used in some cancer treatments. However, resistance to kinase inhibitors can come from the body's ability to boost signaling pathways even in the presence of the inhibitor allowing the tumor to resume its uncontrolled growth. A better understanding of kinase activation could pave the way to the development of novel therapeutics to modify this signaling that would use a different mechanism than kinase inhibitors available today. Besides, MAPKs play a variety of roles in perfectly healthy cells, so global inhibition of any MAPK results in unwanted side effects. Thus, we need to target our therapeutic intervention to the cells we want, rather than affecting signaling indiscriminately in all cells.

1.6 Additional Notes

The focus of my thesis work was to elucidate the interaction between the nonvisual arrestins and MAPKs (see Section A); however, in addition to this effort, I was also fortunate enough to work on several other projects. Most of this work was still related to the arrestin proteins (see Sections B and C), but two studies were off-topic (see Section D). I have included the additional published works for completeness.

CHAPTER 2

MONO-FUNCTIONAL ELEMENTS OF MULTI-FUNCTIONAL PROTEINS

This review was published as Chapter 18 in The Structural Basis of Arrestin Functions (5). **Nicole A. Perry** was first author, and Xuanzhi Zhan, T.M. Iverson, Eugenia V. Gurevich, and Vsevolod V. Gurevich contributed to this work.

2.1 Introduction

The nonvisual arrestins, arrestin-2 and arrestin-3 (see footnote 1)[1], are multi-functional proteins. The arrestin proteins were initially discovered for their interaction with active, phosphorylated G protein-coupled receptors (GPCRs), which blocks further G protein activation. In addition to their role in receptor desensitization, the arrestins modulate receptor endocytosis via clathrin and its adaptor protein AP2 (6,7), and mediate G protein-independent signaling (8). For example, LC tandem mass spectrometry experiments of nonvisual arrestin activated by the angiotensin II type 1a receptor identified over 100 interacting proteins involved in cellular signaling, organization, and nucleic acid binding (9). Due to the emerging role of the arrestin proteins in the control of major signaling pathways, both identifying additional arrestin interaction partners and increasing understanding of arrestin-facilitated effector activation could lead to the development of new therapeutic approaches targeting these pathways.

Recent evidence suggests that arrestins can be divided into mono-functional elements that

[1] This chapter uses the systematic names of the arrestin proteins: arrestin-1 (historic name *S*-antigen, visual or rod arrestin), arrestin-2 (β-arrestin or β-arrestin1), arrestin-3 (β-arrestin2), and arrestin-4 (cone or X-arrestin).

perform only one of the functions of the intact protein. Mono-functional elements can range in size from a single domain (10,11) to a peptide (12), and have many pragmatic advantages over the conventional methods used to study the function of multifunctional proteins like arrestin. For example, over-expression, knockout, and knockdown is anticipated to result in pleiotropic effects in cells, making it difficult to examine a single cellular process (13). In order to isolate the biological importance of individual functions of an arrestin, it is necessary to engineer variant arrestins where only one function is disabled. Alternatively, one can 'knock in' a single function of arrestin through the expression of a mono-functional element (13).

Ideally, a mono-functional element performs only a single function of arrestin. In order to engineer a mono-functional element, the molecular mechanisms and folding of the protein must be well understood; for example, mechanistic information regarding protein kinases permits the design of kinase-dead mutants where only the kinase activity is impaired (13). It is important to note that not all peptides are truly mono-functional. Instead, some of these peptide elements simply reduce or eliminate the unwanted cellular effects that may be encountered with more conventional techniques that study protein function. Here we examine arrestin functions that can be localized to specific peptide elements. These include the interaction of arrestins with receptors, clathrin, AP2, and various effectors.

2.2 Arrestin-receptor interactions

One of the first applications of mono-functional elements of arrestin was in unraveling the interactions with cognate GPCRs. GPCRs constitute the largest family of proteins in the human proteome, comprising over 800 members. GPCRs recognize a variety of extracellular stimuli including photons, ions, small molecules, peptides, and proteins (14). Upon agonist activation,

GPCRs transmit signals across the membrane (~30Å) and elicit an intracellular response by coupling to cognate heterotrimeric G proteins, which activate downstream effectors to initiate signaling cascades. Following phosphorylation of the receptor by specific G protein-coupled receptor kinase(s) (GRK) (15), arrestin binds to the receptor. This interaction blocks further G protein binding (16-18), which terminates G protein signaling. The arrestin-receptor interaction then initiates receptor internalization by interacting with clathrin (6) and clathrin adaptor AP2 (7) to recruit GPCRs to coated pits for endocytosis. GPCR sequestration is necessary both to attenuate the signaling response and to allow for resensitization of the receptor. In addition to these roles, arrestin also functions as an adaptor by recruiting signaling proteins to the agonist-activated GPCRs (19).

The best-characterized arrestin-receptor interaction is between arrestin-1 and rhodopsin (**Figure 2.1**). Visual arrestin-1 terminates rhodopsin signaling in rod photoreceptors by binding to light-activated, phosphorylated rhodopsin and physically blocking the interaction between the heterotrimeric G protein (transducin) and the receptor (18,20). The use of mono-functional elements in binding studies was one of several key experiments that revealed how rhodopsin and transducin interacted. For example, peptides corresponding to the second, third, and fourth cytoplasmic loop of rhodopsin bind to transducin (21), while peptides Glu311-Val328 and Ile340-Phe350 in the C-terminal region of transducin bind rhodopsin (22). A peptide modified from this C-terminus of transducin was also used in crystallographic studies, and was the first to demonstrate structural aspects of the rhodopsin-transducin interaction. The identity of the binding pocket on receptor for this C-terminal peptide on G protein was confirmed by structures of the β2AR with G_s and the $A_{2A}R$ with mini-G_s (23,24).

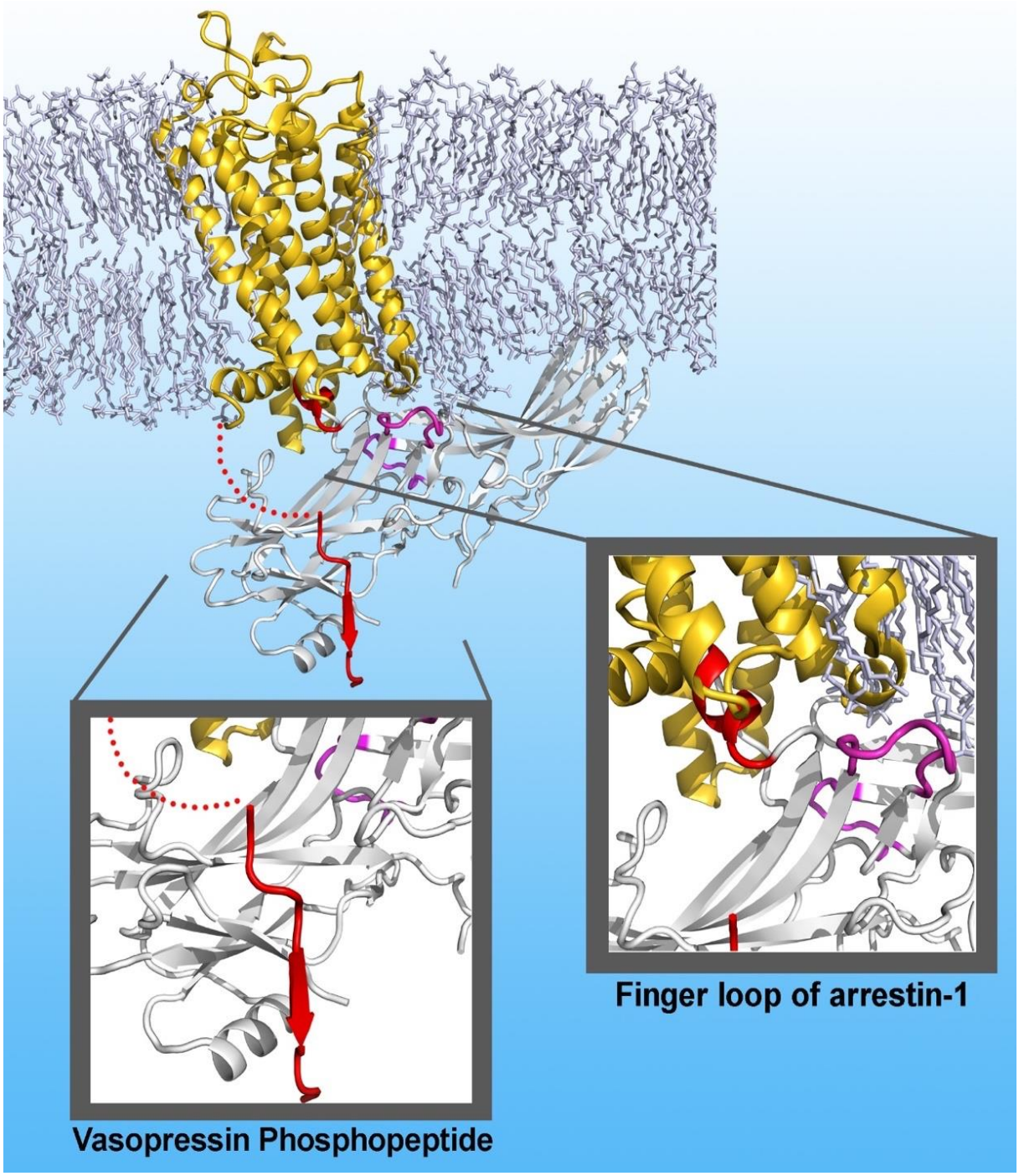

Figure 2.1. Arrestin-rhodopsin interface. The crystal structure of arrestin in complex with rhodopsin was determined using femtosecond X-ray laser crystallography (PDB 4ZWJ) (25). Left inset. The vasopressin receptor phosphopeptide (red) is shown over top of active arrestin-1 (white) in complex with rhodopsin (gold). This 29-residue phosphopeptide is derived from the carboxy-terminus of the vasopressin receptor (26). Right inset. The finger loop of arrestin (red) is shown inserting into the hydrophobic core of the receptor. The middle loop and C-loop (magenta) also form part of the arrestin-rhodopsin interface (25). The unstructured region of rhodopsin is depicted using a dashed line (red).

Similar approaches have been instrumental in assessing the rhodopsin-arrestin interaction, which ultimately suggested the presence of a multi-site interaction between arrestin and the intracellular loops of rhodopsin (20). For example, synthetic peptides of the four cytoplasmic loops of bovine rhodopsin were used to inhibit the rhodopsin-arrestin interaction. It was determined that the first and third cytoplasmic loops of rhodopsin were involved in arrestin binding, which is similar to the interface for both transducin and rhodopsin kinase (systematic name GRK1) (20). These studies demonstrated that the rhodopsin-arrestin interaction can be successfully recapitulated with receptor peptide elements, although it should be noted that the reconstituted individual interactions had significantly lower affinity than the multi-site interaction of the two native proteins.

As observed with the receptor-G protein interaction, the interacting surface of arrestin with receptor can also be divided into mono-functional elements. Early biochemical studies suggesting the presence of mono-functional elements of arrestin included the identification of both an activation and phosphorylation sensor, with each sensor recognizing one state of the activated receptor (27). When engaged by the receptor simultaneously, these sensors allow arrestin to transition into an active, receptor-binding conformation (27-29). The first evidence for the activation and phosphorylation sensor came from experiments testing the binding of visual arrestin-1 to different states of rhodopsin (inactive, phosphorylated, light-activated, or light-activated and phosphorylated) (27). Arrestin binding to light-activated, phosphorylated rhodopsin was significantly greater than even the sum of the other conditions, suggesting a multi-site interaction that allows arrestin to “probe” the state of the receptor. Collectively, experiments assessing the rhodopsin/arrestin interface have implicated a large portion of the arrestin surface, including most of the concave surface for both domains, in the interaction (20,27,30-34).

The use of mono-functional elements was instrumental in gaining structural insights into the interface between arrestin and receptor. For example, a fully phosphorylated carboxy-terminal peptide derived from human V2 vasopressin receptor was used in conjunction with an antibody to induce the active arrestin-2 conformation for crystallization (26). The phosphopeptide-bound arrestin-2 exhibited a number of structural differences compared to the basal state, including a ~20° domain rotation that is now proposed to be a hallmark of active arrestin (35,36) and is also observed in a C-terminally truncated arrestin-1 (37) and arrestin bound to rhodopsin (25). A complementary structural study examined the interaction of receptor with a peptide analog of the finger loop of arrestin-1. The arrestin peptide bound to the conserved E(D)RY motif of the cytoplasmic crevice of activated rhodopsin, in addition to TM7/H8 (38).

The utility of these mono-functional elements in identifying the structural basis for the receptor-arrestin interaction was recently confirmed with the structure of constitutively active human rhodopsin with intact pre-activated mouse visual arrestin-1, as determined using serial femtosecond X-ray crystallography (25) (**Figure 2.1**). The rhodopsin-arrestin structure revealed that only four discrete interfaces mediate the interaction between the receptor and arrestin. Examination of the interfaces identifies peptide-like regions that are involved in the interaction. These regions include the finger loop of arrestin (residues Q70-L78 of arrestin) (35), which inserts in the hydrophobic pocket between helices that opens upon GPCR activation (39) through interactions with the C-terminus of transmembrane 7 (TM7), the N-terminus of rhodopsin helix 8, which is necessary for high-affinity binding, and intracellular loop 1 (ICL1) of rhodopsin (25). The second interface consists of the middle loop (26) (also called 139 loop in arrestin-1 (40,41)) and C-loop of arrestin, which make contact with intracellular loop 2 (ICL2) of rhodopsin, in addition to the back loop of arrestin that interacts with transmembrane helix 5 (TM5). The third

interface visible in the crystal structure shows the β-strand (residues 79-86) interacting with TM5, TM6, and ICL3. The final rhodopsin-arrestin interface, which consists of the N-domain of arrestin and the phosphorylated C-terminus of rhodopsin, is not present in this crystal structure because the C-terminus of rhodopsin was not phosphorylated in this study (25)). However, modeling this interaction based upon the arrestin-2-phosphopeptide structure (42) confirms that this region acts as a direct interacting site between arrestin and the receptor.

2.3 Arrestin-clathrin interactions

Following agonist activation, many GPCRs are internalized via clathrin-mediated endocytosis (11), and the arrestins have been shown to bind clathrin and the clathrin adaptor protein AP-2 with comparable affinity (K_d ~ 10-60 nM) (43) (**Figure 2.2**). In this process, the non-visual arrestins can act as scaffolds that bridge clathrin and receptor, and experiments to identify the clathrin binding site on arrestins took advantage of the observation that non-visual arrestins bind to clathrin with greater affinity than the visual arrestins. Here, arrestin-1/arrestin-2 chimeras were used to scan for the clathrin binding site, which was identified as a peptide element located within the C-terminus of non-visual arrestins (6). A chimera containing residues 1-345 of visual arrestin and 341-418 of arrestin-2 was able to bind clathrin cages with similar affinity as arrestin-2. Moreover, expression of the separated arrestin-2 C-terminus, which contains both clathrin and AP2 binding sites, inhibits arrestin-dependent GPCR internalization in cells. This observation is consistent with the C-terminal peptide binding to clathrin/AP2 cages and successfully outcompeting the arrestin-receptor complexes (44). Together these findings suggested that the C-terminal 77 amino acids contained the major site for the arrestin-clathrin interaction and could be used as a mono-functional element. The location of this binding site is distal to the arrestin-receptor

interface and allows a model where arrestin can bind both receptor and clathrin simultaneously.

In complementary studies to locate the binding site for arrestin on clathrin, a proteolysis approach was used. Positive results were found for the terminal domain (TD) of clathrin, which is an approximately 50 kDa amino-terminal region located on the distal portion of the triskelion leg, a motif comprised of three heavy chains and three light chains (11). In these experiments, the TD was isolated by subjecting clathrin cages to limited tryptic digestion and assessed for arrestin binding using pull-down assays. The arrestin binding site within clathrin was further localized using truncated constructs of the TD, specifically a construct containing heavy chain residues 1-85 that did not bind arrestin, which directed investigators to residues 86-100. This peptide was later reduced to the region between residues 89-100 via similar techniques (11). The clathrin-derived segment has been validated as important for arrestin binding using deletion and alanine scanning mutagenesis (11). Interestingly, the strong interaction between the non-visual arrestins and clathrin does not function in the lattice assembly process (11,45).

Crystallographic studies of the TD of clathrin in complex either with an arrestin-3 peptide (46) or with full-length arrestin-2 (47) revealed the architectural details for how the arrestin C-terminus interacts with this binding site. The binding pocket on clathrin (**Figure 2.2**) is located in the N-terminal domain of the clathrin heavy chain and the Lϕxϕ[D/E] motif on the carboxyl terminal region of arrestin (ϕ represents a hydrophobic residue and x represents a polar residue). While the arrestin-2-clathrin interaction appeared to be dominated by this peptide-based binding mode, the structure with full-length arrestin-2 additionally identified a previously uncharacterized eight-amino acid loop ~68Å away

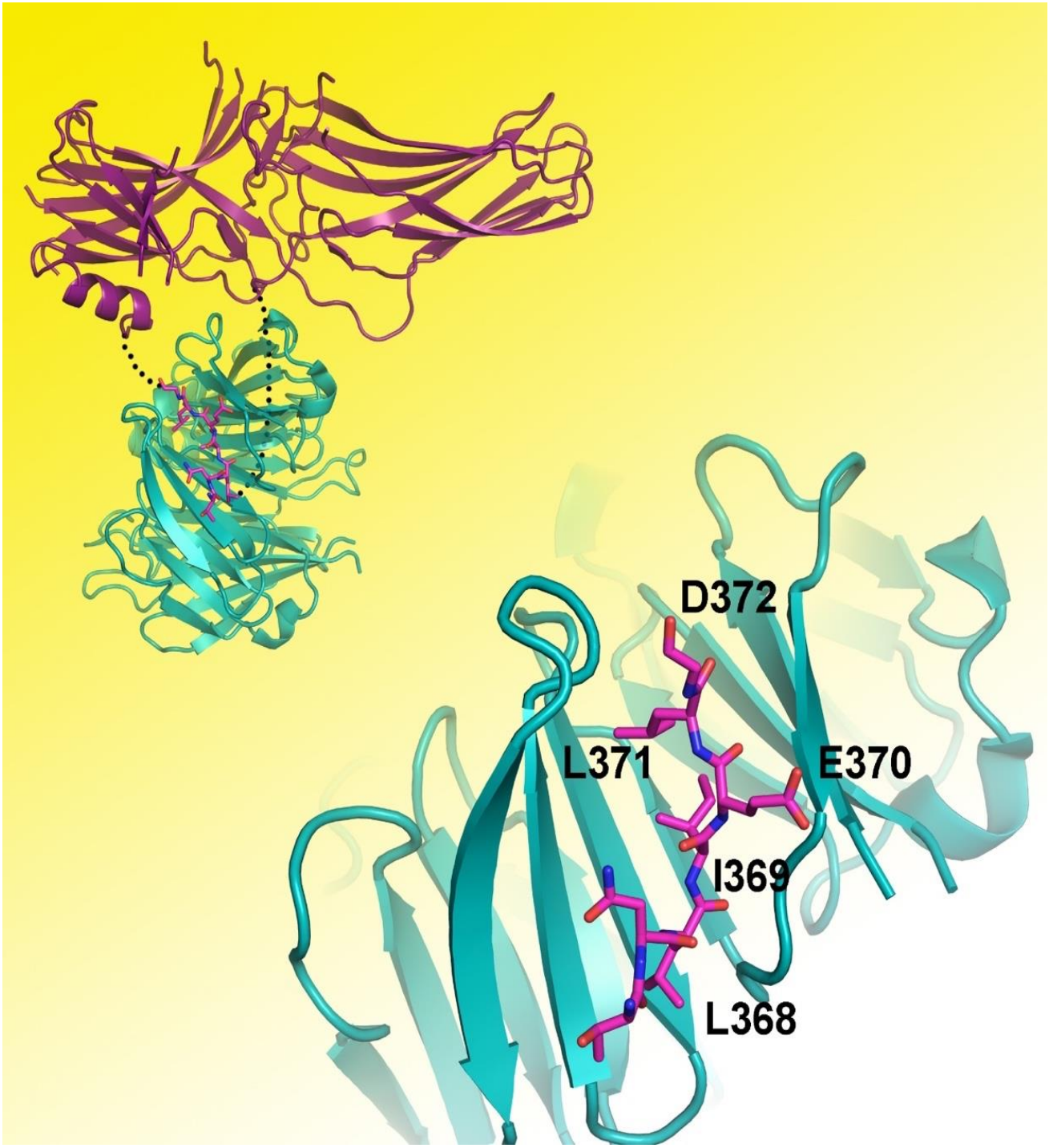

Figure 2.2. Arrestin-clathrin interaction. The crystal structure of arrestin-2 (deep purple) with clathrin (teal) was determined using X-ray crystallography to 2.2Å resolution (PDB 3GC3) (47). The LϕXϕ(D/E) motif (pink) from arrestin-2 interacts with the clathrin binding box (unstructured regions of arrestin-2 are depicted as a black dotted line in the cartoon).

from the Lϕxϕ[D/E] motif (47). This sequence is not present in arrestin-3, but is present in the two visual arrestins, arrestin-1 and -4, which suggests an additional mechanism through which the visual arrestins can bind clathrin.

Validation of the interaction of arrestin-1 peptides with clathrin adaptor AP2 used not only in vitro binding, but was expanded to investigate the role in an organism using a transgenic mouse model (48). Interestingly, despite the peptide having a much lower affinity for AP2 than that of the corresponding arrestin-2 element, disruption of the arrestin-1/AP2 interaction using the peptide was detrimental for photoreceptor survival (48). This can likely be explained by the high concentration of arrestin-1 in rod cells (49,50). Together, these results demonstrate that arrestin-clathrin interactions are based upon peptide elements, and that these can recapitulate function in both in vitro and in vivo analyses.

2.4 Arrestin-effector interactions

The role of arrestins in signal transduction was first described in 1999 (51); however, it is becoming increasingly apparent that arrestins play a critical role in a variety of signal transduction pathways. A global proteomics analysis was used to determine the scope of functions performed by arrestin-2 and -3, and identified 337 non-redundant interacting proteins, 102 of which interacted with both non-visual arrestins (9). This study found a wide distribution for subcellular localization of the interacting proteins, which displayed a range of functions in signal transduction, cellular organization, metabolism, and nucleic acid binding. As anticipated, the screen also detected well-known binding partners, including the extracellular signal-regulated kinase 1 (ERK1), clathrin and AP2, and phosphodiesterase 4. Of the identified signaling proteins that interact with arrestins, the best studied are Src and mitogen activated protein (MAP) family kinases.

2.3.1 Src family kinases

The Src (short for sarcoma, as the *c*-Src kinase was discovered for its role as an oncogene) family kinases play a key role in signal transduction from a number of cell surface receptors, most notably the receptor tyrosine kinases. Src family kinases are therefore critical for a variety of cellular processes, including cell proliferation, differentiation, and migration, which explains why many members of this kinase family are implicated in cancer (52). The Src family of kinases includes nine characterized members - Src, Yes, Fyn, Fgr, Lck, Hck, Blk, Lyn, and Frk. These kinases contain SH2 and SH3 domains that are necessary for phospho-tyrosine recognition of activated receptor tyrosine kinases. Of these members, Src, Fyn, and Yes are the most widely expressed. Src family kinases are also known to play a role in GPCR signaling, both through interaction with GPCRs and through receptor-associated transactivation of receptor tyrosine kinases (53). Arrestins 1, 2, and 3 have been shown to bind Src family kinases and recruit them to activated GPCRs.

The prototypic non-receptor tyrosine kinase, *c*-Src, was the first identified downstream signaling interaction partner of arrestin (51). Upon activation of receptor tyrosine kinases, *c*-Src is recruited to the plasma membrane where it catalyzes the phosphorylation of tyrosine residues. Confocal microscopy demonstrated that this redistribution could also be induced by agonist activation of the β_2-adrenergic receptor through the assembly of a protein complex that contained receptor, arrestin, and c-Src (51). This complex could also be isolated using co-immunoprecipitation after exposure to a β_2-adrenergic receptor agonist and covalent crosslinking. These results suggest that the arrestin/*c*-Src interaction is important for the localization of *c*-Src to the membrane and trans-activation (54).

The interaction site for *c*-Src on arrestin was identified by co-expressing Flag-tagged

deletion or truncation arrestin mutants in COS-7 cells with wild-type *c*-Src. Co-immunoprecipitation revealed that deleting amino acids 1-185 resulted in a complete loss of binding to *c*-Src, and that a fragment of arrestin containing amino acids 1-163 was able to bind *c*-Src similar to the full-length arrestin (51). Site-directed mutagenesis of hydrophobic residues in the P-X-X-P motif in arrestin, which is the minimal consensus sequence for binding to the SH3 domain (55), reduced *c*-Src binding, indicating that *c*-Src interacts with the N-terminal domain of arrestin. Although the *c*-Src binding sites have not been precisely mapped on arrestin, the use of mutational studies to distinguish a specific domain suggest that the binding site can be localized to specific arrestin elements.

In addition to *c*-Src, the Src family kinases Fyn and Yes have been reported to interact with arrestins. Activation of luteinizing hormone receptor involves several signaling cascades that can lead to Fyn activation, including the formation of a ternary complex between luteinizing hormone receptor, a non-visual arrestin, and Fyn (56). In a similar manner, Yes is recruited to the endothelin type A receptor via an interaction with arrestin-2 (57). The exact location of the interaction sites for these proteins on arrestins is unknown; however, it is probable that the kinases bind in a similar manner to *c*-Src, with single element interactions.

2.3.2 MAP kinases

Arrestin has also been shown to act as a scaffold protein for mitogen activated protein kinase (MAPK) cascades, and, in particular can activate the subfamilies c-Jun N-terminal kinase (JNK), extracellular signal-regulated kinases (ERK), and p38. Activating these terminal kinases involves sequential action of three upstream kinases (MAPK kinase kinase, MAPK kinase, and MAPK) and arrestins are proposed to simultaneously bind and orient all kinases in the cascade

(58-60) (**Figure 2.3**). It is widely accepted that scaffold proteins are important elements in regulating signaling specificity of MAPK cascades (61,62). Identification of specific binding sites for MAPKs and their upstream activators on arrestin would offer insight into the signaling process and enable the development of designer arrestins with controlled signaling outputs (63).

The mechanism for arrestin-dependent assembly of MAPK signaling complexes is not completely understood; however, it has been shown that effector interaction with arrestin is not exclusively dependent on the arrestin-receptor complex formation (64). For example, receptor-independent arrestin-3 is able to effectively scaffold the ASK1-MKK4/7-JNK3 kinase cascade (64-66), while ERK2 binding to arrestin-2/3 occurs independent of receptor binding, but is significantly enhanced in the receptor-bound state (64,67). It has also been established that effector recruitment to arrestin is not necessarily indicative of effector activation (64,65). This is evidenced most clearly by the activation of JNK3 only via arrestin-3 recruitment (58,64,65), despite JNK3 binding to all isoforms of arrestin (68,69). It is therefore necessary to elucidate which regions of arrestin are able to both bind and activate effectors when designing peptides for therapeutics.

Mono-functional elements of arrestin act as binding regions for the ASK1-MKK4/7-JNK3 cascade. This binding was determined using in vitro analysis, such as scanning peptide arrays and binding assays with purified proteins, as well as in cell analysis with mutant arrestin constructs (4,67,70,71). Binding does not necessarily cause activation, yet in the case of JNK3, a mono-functional arrestin element can enhance activation to the same level as intact arrestin-3 (72). Next, investigators will move toward more targeted identification of binding sites for other MAP kinases.

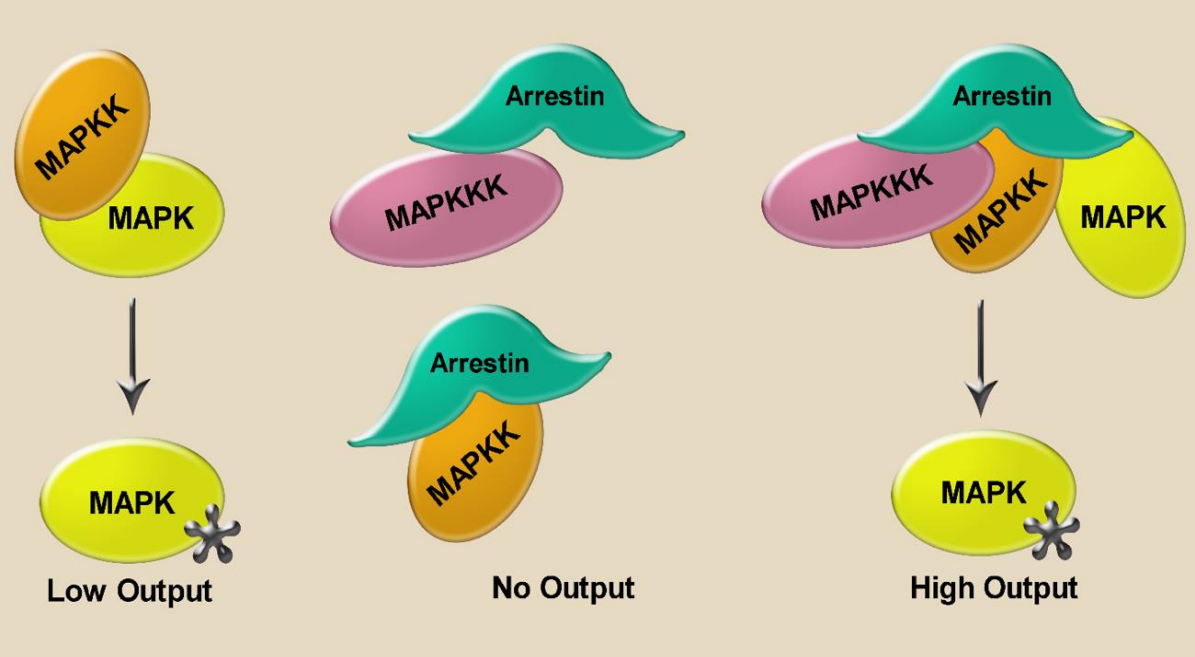

Figure 2.3. Arrestin acts as a molecular scaffold for mitogen-activated protein kinase cascades. Scaffold proteins promote signaling by localizing molecular components to a specific area of the cell. Arrestin is known to scaffold numerous effectors, most notably the mitogen-activated protein kinase (MAPK) cascades. Cartoon representation of effector binding to the non-receptor bound surface of arrestin is shown. In the absence of arrestin, components of the MAPK cascade (MAPKKK – MAPKK – MAPK) are diffusion limited and exhibit a low output of activated MAPK (phosphorylation indicated by black star). When only one component of a MAPK cascade is bound to arrestin, there is no signaling output. In contrast, when arrestin scaffolds the complete MAPK cascade there is robust activation of the final effector kinase.

2.3.3 Miscellaneous effectors

Several mono-functional binding sites on arrestin for non-kinase effectors have been mapped to a similar extent. For example, spot-immobilized peptide array analysis was used to map the interaction site for cAMP-specific phosphodiesterases (PDE4D5, PDE4D3), which revealed a difference in localization of the binding site between the isoforms (12). Calmodulin, an intracellular calcium regulator, was identified as an arrestin-interacting partner in the presence of calcium with a binding site on the concave side of the C-domain and the finger loop of arrestin (73). This study was conducted using co-immunoprecipitation and site-directed spin labeling (SDSL) electron paramagnetic resonance (EPR) spectroscopy. The N-domain of arrestin-4 was

shown to re-localize Mdm2 from the nucleus to the cytoplasm using a nuclear exclusion assay, indicating that this was the site of high affinity binding of this E3 ubiquitin ligase (69). This list of studies, although not exhaustive for the number of identified interacting partners of arrestin, supports the notion that different regions of arrestin are specialized for binding specific effectors.

2.3.4 Manipulating arrestin-dependent signal transduction using mono-functional elements

The c-Jun NH_2-terminal protein kinase 3 (JNK3) is the final effector in the ASK1-MKK4/7-JNK3 signaling cascade, and is known for its role in neuronal apoptosis (74). Previous studies indicate that all components of the JNK3 signaling cascade interact with non-visual arrestins (58,64). These data suggested that the members of this MAPK cascade might interact with arrestin via peptide-like surface segments. This hypothesis was tested using *in vitro* pull-down assay with maltose binding protein (MBP)-fusion of intact wild-type arrestin-3 as a positive control, and MBP without a fusion peptide as a negative control. MBP fusions of the peptides representing the entire non-receptor binding surface of arrestin-3 (**Figure 2.4**) were tested for binding to the JNK3α2 isoform (72). This experiment successfully identified three arrestin-derived peptides that bind to JNK3α2. One of the peptides, termed T1 (amino acids M1-R52) demonstrated the greatest binding to JNK3α2. Therefore, it was further divided into three peptide regions T1A (M1-K25), T1B (R26-R52), and T1C (N16-D45), which allowed to identify the first twenty-five amino acids of arrestin-3 as a critical element for JNK3α2 binding (Figure 4). Interestingly, this region of arrestin-3 had previously been implicated in binding to the kinase domain of ASK1 (70). These data suggested that the T1A peptide could be used to recapitulate arrestin-3 scaffolding of the ASK1-MKK4/7-JNK3 signaling cascade.

To assess the functional capabilities of the T1A peptide, binding experiments with purified upstream kinases MKK4 and MKK7 were performed (75). A peptide corresponding to the first 25

amino acids of arrestin-2 was used as a "natural" negative control, because arrestin-2 does not promote JNK3 activation despite sharing 78% sequence identity with arrestin-3 (76). While both peptides bind MKK4 comparably, T1A exhibited more robust binding to JNK3 and MKK7. Both MKKs interacted with T1A in a comparable manner to full-length arrestin-3. Since purified ASK1 was not available for *in vitro* pull downs, HA-ASK1 binding was tested in COS7 cells. It effectively co-immunoprecipitated with YFP-T1A. This demonstrated that the T1A peptide was able to bind all upstream kinases of the JNK3 activation cascade: ASK1, MKK4, and MKK7.

To test whether T1A facilitates JNK3 phosphorylation like full-length arrestin-3, it was co-expressed with HA-ASK1 and HA-JNK3 in COS7 cells and found to be active (75). In contrast to T1A, B1A did not facilitate the phosphorylation of JNK3 in cells, which suggests that the specific sequence of the peptide determines its functional capabilities. Thus, the first twenty-five residues of arrestin-3 are largely responsible for scaffolding the JNK3 cascade. This makes T1A the smallest known MAPK scaffold reported.

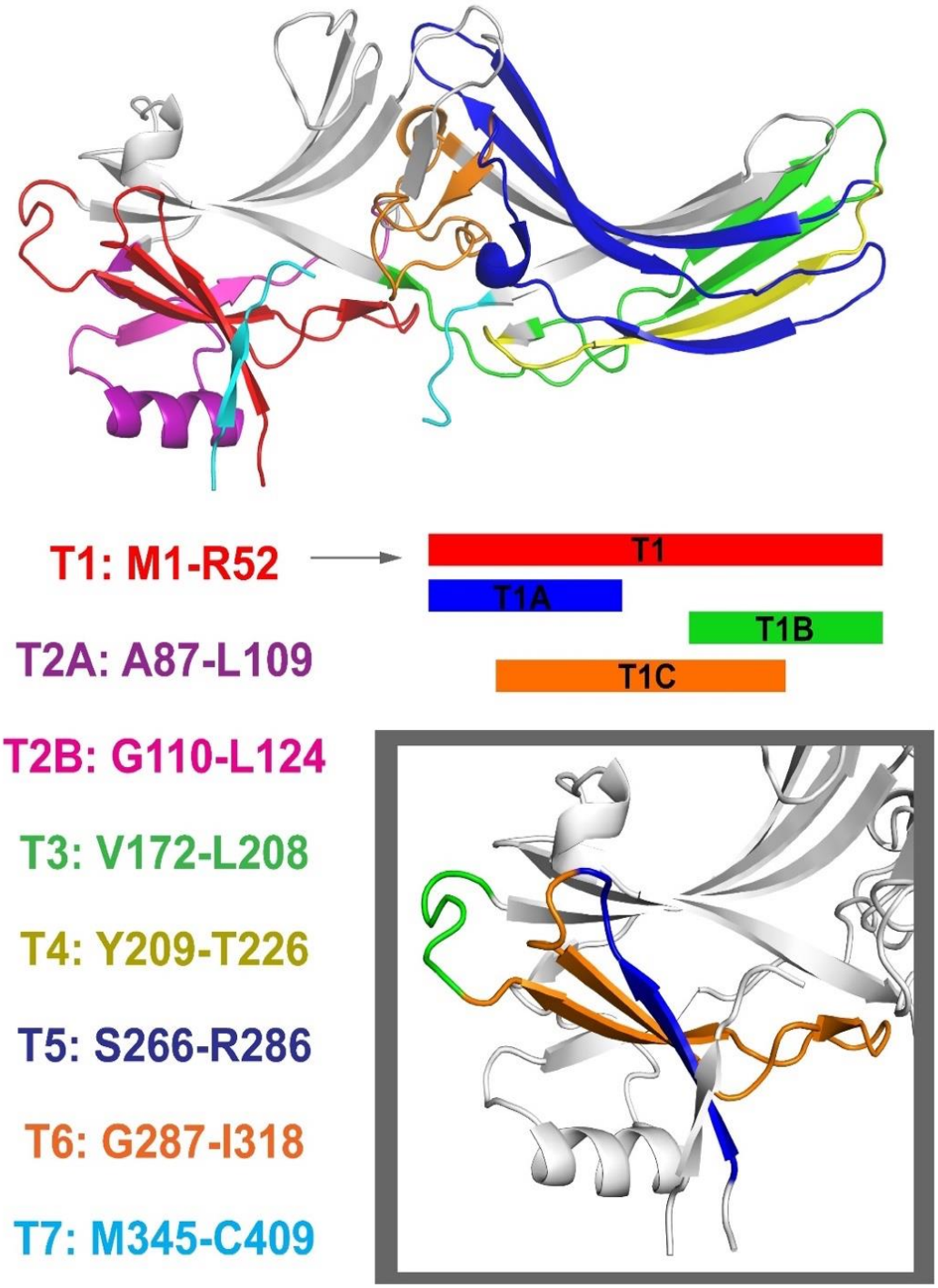

Figure 2.4. Peptides of the non-receptor-binding surface of arrestin-3. The non-receptor-binding surface of arrestin-3 was divided into peptide fragments to assess the binding of JNK3 to different regions of arrestin-3 (PDB 3P2D) (72). Each segment is color-coded, with the corresponding residues listed. T1 bound with high affinity to arrestin-3, and was further divided into smaller segments to isolate a twenty-five residue peptide, T1A, that not only binds JNK3 with high affinity (72), but can scaffold the complete ASK1-MKK4/7-JNK3 cascade in cell, facilitating JNK3 activation (4).

A reciprocal study used 25-mer peptides spanning the complete sequence of JNK3 to probe the interaction between the non-visual arrestins and JNK3 (70). This analysis isolated the N-terminus of JNK3 (amino acids 6-45) as critical for the arrestin binding, which was in accordance with previous site-directed mutagenesis studies (77). Alanine substitution further localized the interaction site to residues F^{5} and C^{21}-F^{24}. Similar analysis was conducted with ASK1 and MKK4, identifying two regions on the non-visual arrestins that support ASK1 binding, and one region that supports MKK4 binding.

2.4 Conclusions

The use of mono-functional elements has isolated regions of arrestin necessary to interact with receptors and certain downstream effectors. Multiple studies of arrestins have used peptides or domains to localize protein interaction sites and have been vital for our current understanding of these multifunctional proteins. As the field moves toward the interactions of arrestins with effectors, tools that allow investigators the ability to assess single functions of arrestin are critical for furthering our understanding of arrestin-mediated signaling.

CHAPTER 3

USING IN VITRO PULL-DOWN AND IN-CELL EXPRESSION ASSAYS TO STUDY PROTEIN INTERACTIONS WITH ARRESTIN

This review was accepted for publication in Methods in Molecular Biology. **Nicole A. Perry** was first-author, and Xuanzhi Zhan, T.M. Iverson, Eugenia V. Gurevich, and Vsevolod V. Gurevich contributed to this work.

3.1 Introduction

Mammals have only two non-visual arrestins (arrestin-2 and -3, a.k.a. β-arrestin1 and 2) (78), both of which demonstrate an amazing versatility: they interact with hundreds of GPCR subtypes and also numerous non-receptor signaling proteins (79). The rich multi-functionality of these ~45 kDa proteins raises questions as to where these different partners bind and how many proteins can be brought together by a single arrestin molecule simultaneously. It also creates practical problems in studying biological functions of arrestins; for example, conventional protein over-expression or knockdown in the case of arrestins affects numerous cellular processes, resulting in pleiotropic effects (13). One could envision an alternative approach using comprehensive mutagenesis of every residue in a ~400 amino acid protein to identify binding sites for interacting partners (80), but it is hardly practical to test dozens of distinct functions of hundreds of mutants. In addition, protein-protein interactions are often mediated by groups of residues, and mutation in any single residue might not affect an interaction significantly. There are a few known exceptions in arrestins, where one or two point mutations significantly changed

receptor preference (81,82), the binding of MEK1 (83), or c-Raf1 (84), but as a rule, greater perturbations are necessary.

If protein binding is mediated primarily through peptide-based interactions, one possible approach in the identification of elements involved in binding a partner is via separation of the protein in question into a series of peptides and identification of those elements that still bind a partner. This approach was used successfully to identify three arrestin-3-derived peptides that can interact with JNK3 (72); however, this is not to suggest that other secondary elements in the intact structure do not play a role in the interaction. Interestingly, a 25-residue peptide termed T1A was found to bind JNK3 and each of the upstream kinases in the ASK1-MKK4/7-JNK3 cascade and facilitate JNK3 activation in cells, making it the smallest MAPK scaffold identified so far (4). Here we describe two critical methods used in these studies: an *in vitro* pull-down with purified proteins that unambiguously shows that an interaction is direct, and a cell-based functional assay, demonstrating the biological relevance of the interactions detected *in vitro*. Together, these techniques provide a powerful depiction of how arrestin interacts with downstream effectors.

3.2 *In vitro* pull-down

The *in vitro* pull-down described here can be used to verify any protein-protein interaction when the proteins in question can be isolated with relatively high purity. The simplest way to perform this experiment is to have usable tags on both proteins (maltose binding protein/MBP, glutathione S-transferase/GST, His, etc.), so that the pull-down can be performed both ways. If a protein can be expressed as a fusion with one of these tags, it is amenable to this technique and can provide convincing evidence for a direct interaction.

The main advantage of an *in vitro* pull-down with purified proteins is that any interaction

detected by this method is direct, meaning that it does not require helpers and/or intermediaries. The limitations are mostly related to the affinity of the interaction: only relatively high-affinity interactions survive several washes necessary to remove non-specifically bound proteins. This affinity could also be impacted by the addition of another partner protein or co-factor; for example, ATP interaction with a protein kinase could change the kinase's affinity for an interacting partner. Another drawback is that investigated proteins must be expressed and purified, and need tags suitable for pull-down. Lastly, as far as scaffolding proteins are involved, their expression level determines the binding outcome; at higher than optimal concentrations scaffolds suppress signaling in cells and *in vitro* (85,86). An overview of the *in vitro* pull-down method is provided (**Fig. 3.1**).

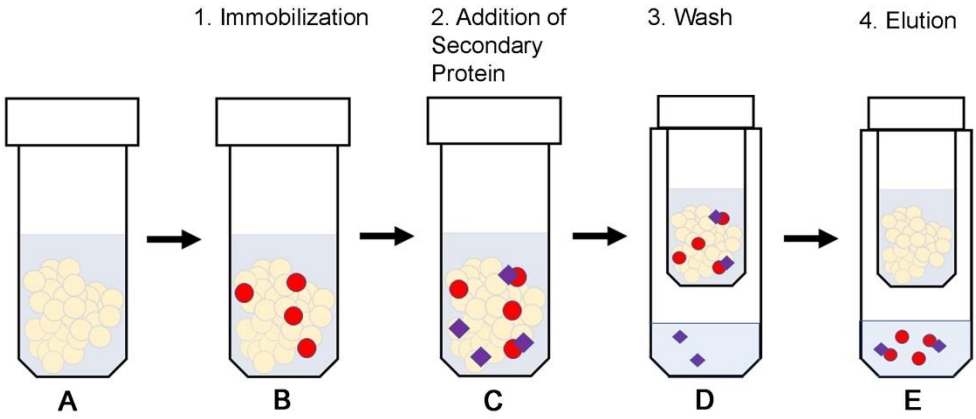

Fig. 3.1. Schematic overview of the *in vitro* pull-down assay. This is described as a pull-down for a protein with an MBP affinity tag, but the procedure can be easily modified for a protein with any type of affinity tag. **A.** Prepare MBP affinity resin (or an alternative resin appropriate for the tag) by washing the suspension in Wash Buffer A. **B.** Immobilize MBP-fused proteins on the resin by incubating for 1 h with gentle rotation at 4°C. **C.** Add the secondary protein (either tagged, or for which a validated commercial antibody is available) to the mixture and incubate for an additional 2 h with gentle rotation at 4°C. **D.** Wash each sample three times quickly with Wash Buffer B. This will remove any non-specific interactions. **E.** Elute the bound proteins using buffer containing 50 mM maltose, or an alternative appropriate elution buffer for proteins with other tags. The eluate is then analyzed by both coomassie (to control even bait protein loading) and western blot (to assess binding).

3.3 Cell-based activation

The cell-based activation or phosphorylation assay is suitable when the protein in question facilitates or suppresses the activation or phosphorylation of other proteins, which can be easily assessed experimentally. Here we present ASK1-dependent JNK3 phosphorylation as an example, but similar assays can show the effect of the protein of interest on other processes, such as MKK4- or MKK7-dependent JNK1/2/3 phosphorylation (87). When the interaction is studied in a cellular context, one can also use co-immunoprecipitation as an alternative approach (88).

The main advantage of cell-based assays is that they demonstrate how the process occurs in an intact living cell. The main disadvantage is that one can never be sure whether additional proteins and/or metabolites are involved. Below is a schematic of the cell-based assay for detection of phosphorylated JNK3 in the presence of HA-ASK1, HA-JNK3, and GFP-tagged arrestins (**Fig. 3.2**). Our laboratory is specifically interested in JNK3 for its interaction with arrestin-3 and its role in neuronal apoptosis; however, this set-up can be used to detect any arrestin-dependent activation, such as the other JNK isoforms, other MAP kinases, etc.

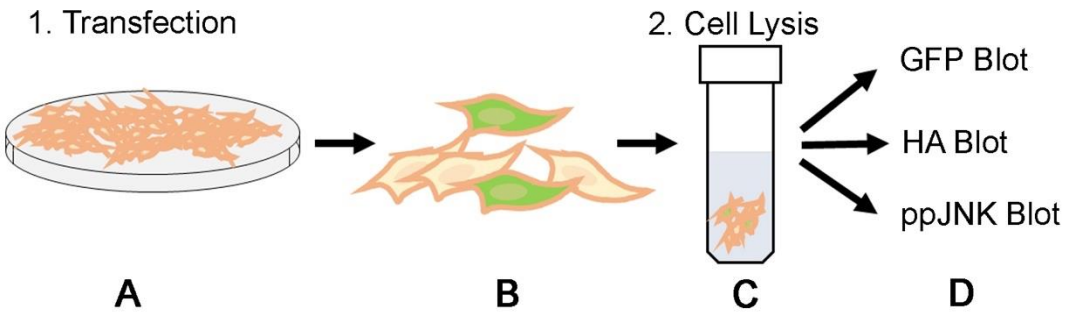

Fig. 3.2. Schematic overview of the in-cell assay. A. Transfect the cells at 90-100% confluency with HA-ASK1, HA-JNK3, and the appropriate Venus-arrestin construct. **B.** Allow 48 h for protein expression with serum starvation overnight before the assay. The cells can be monitored using a fluorescent microscope. Cells that have been transfected will glow green because of the Venus (GFP) transfection. **C.** Lyse the cells to release the protein using the lysis buffer described below. **D.** Run a western blot for arrestin expression (GFP), ASK1 and JNK3 expression (HA), and ppJNK.

3.4 Materials

3.4.1 *In vitro* pull-down assay

MBP-fusion protein expression

1. Lysis buffer: 50 mM Tris-HCl, pH 8.0, 5 mM EGTA, 2 mM benzamidine (BA), Protease Inhibitor Cocktail (Sigma-Aldrich, Product #P2714)
2. Equilibration buffer: 20 mM Tris-HCl, pH 7.5, 150 mM NaCl, 2 mM BA
3. Elution buffer: 20 mM Tris-HCl, pH 7.5, 150 mM NaCl, 2 mM BA and 50 mM Maltose
4. Sonicator, Fisher Scientific, Model 505
5. MBPTrap HP 5 mL column, GE Healthcare Life Sciences (Product code: 28918779)
6. PD-10 Desalting Column with Sephadex G-25 resin from GE Healthcare Life Sciences
7. AKTA protein purification chromatography systems, GE Healthcare Life Sciences

In vitro pull-down

1. Ultrafree®-MC-DV centrifugal filters, Durapore® - PVDF 0.65µm
2. Amylose resin: Stored in 20% ethanol, New England Biolabs Inc. (#E8021S, store at 4ºC)
3. Wash buffer A: 20 mM Tris-HCl, pH 7.5, and 150 mM NaCl
4. Wash buffer B: 50 mM HEPES, pH 7.3, and 150 mM NaCl
5. Elution buffer: 50 mM HEPES, pH 7.3, 150 mM NaCl, 50 mM maltose

SDS Polyacrylamide Gel

1. Resolving gel buffer: 1.5 M Tris-HCl buffer, pH 8.8
2. Stacking gel buffer: 0.5 M Tris-HCl buffer, pH 6.8
3. 30% acrylamide/bis solution 29:1: 3.3% crosslinker
4. Ammonium persulfate: 10% solution in water
5. *N,N,N,N'*-Tetramethyl-ethylenediamine (TEMED)

6. SDS Solution 10% (w/v)
7. SDS-PAGE running buffer: TG-SDS 10X concentrate
8. Sample buffer, Laemmli (2x) concentrate (store at -20ºC)
9. Bio-Safe Coomassie G-250 Stain

Immunoblotting

1. Transfer buffer: TG 10X concentrate with 15% methanol
2. Immobilion-P transfer membrane (Merck Millipore Ltd.)
3. Blocking solution: 5% milk (w/v) in Tris-buffered saline) and 0.05% Tween-20 (TBS-T) or 2% bovine serum albumin in TBS-T.
4. SuperSignal® West Pico Luminol/Enhancer Solution and Stable Peroxide Solution
5. Premium X-ray film

Antibodies

1. SAPK/JNK and phospho-JNK Rabbit (Cell Signaling, 1:1,000 dilution, #9252P, #9251).
2. HA Rabbit (Cell Signaling, 1:1,000 dilution, #3724)
3. GFP Mouse (Cell Signaling, 1:1,000 dilution, #2526) (used for Venus constructs)
4. Secondary antibodies: Peroxidase-conjugated AffiniPure Goat Anti-Mouse IgG and Anti-Rabbit (Jackson Immuno Research Laboratories Inc, 1:10,000 dilution, store at -20ºC).

3.4.2 In-cell assay

Cell Types

1. COS7 African green monkey cells (ATCC)
2. HEK 293 cells (ATCC)

Transfection

1. Transfection reagent: Trans-Hi™ Reagent (FormuMax, Lot 1029) or Lipofectamine® 2000 (Invitrogen by Life Technologies, Ref #11668-019).
2. Media: DMEM (1X) + GlutaMAX™-1, 4.5g/L D-Glucose, 110 mg/L Sodium Pyruvate, supplemented with 10% fetal bovine serum and 5% Penicillin/Streptomycin
3. 0.05% Trypsin-EDTA (1X)
4. Corning® 100mm x 20mm Style Dish, Cell Culture Treated
5. Disposable 6-well plate

Cell Lysis

1. Lysis buffer: 50 mM Tris-HCl, pH 7.5, 2 mM EDTA, 250 mM NaCl, 10% Glycerol, 0.5% NP-40, 20 mM NaF, 1 mM Na_3VO_4, 10 mM N-ethylmaleinaide, 1 mM PMSF, 2 mM Benzamide
2. Phosphate buffered saline (PBS)
3. Corning™ Falcon™ Cell Scrapers

3.5 Methods

3.5.1 *In vitro* pull-down assay

Expression and purification of arrestins

We recently described in detail methods used for the expression and purification of untagged arrestins in *E. coli* (89). Purification of MBP-tagged arrestin-3 and MBP fusions of arrestin-3-derived peptides was described in (72) and is detailed below.

Expression of MBP-fusion proteins

1. Express MBP-fusion proteins in *E. coli* (BL21-codon plus (DE3)-RIL). Inoculate cells in a 500 mL flask (100 mL LB) from a single colony or glycerol stock and grow overnight at 30°C at 205 rpm.
2. Use around 10-20 mL of the overnight culture to inoculate each of the four 1-L cultures (in 2 L flasks), and grow the cultures at 30°C at 205 rpm to an optical density between 0.6-0.7 (approximately 3 h post-inoculation). Remove the flasks from the shaker and chill in an ice-water bath for 20-30 min (*see* **Note 3.6.1.1**).
3. Induce the cultures with 1 mM isopropyl β-D-thiogalactoside for an additional 5-6 h at 30°C followed by centrifugation (15 min, 6,000 rpm). Freeze the pellets at -80°C *(see* **Note 3.6.1.2**).
4. Thaw protein pellets on ice and resuspend in lysis buffer (approximately 30 mL per 1 L culture). Add a small amount of lysozyme to the suspension and incubate on ice for 40 min.
5. Sonicate the suspension at 75% max amplitude for 2 min (5 sec on, 10 sec off) Incubate the lysate with 25 µL DNaseI and 2 mM $MgCl_2$ for 30 min (*see* **Note 3.6.1.3**).
6. Centrifuge the lysate for 1 h at 18,000 rpm (Sorvall SS-34 rotor in RC 5B plus centrifuge). Filter the supernatant through a 0.45 µM filter before loading on the MBP column.

7. Wash the MBP trap column with 5 column volumes of Equilibration buffer before loading the lysate. Filter the lysate and load on the column at 3 mL/min (check system pressure to ensure that the column is not over-pressurized). After the entire lysate enters the column, wash the system with Equilibration buffer until the UV absorption returns to baseline. Use a gradient elution (100% Elution buffer, 0-50 mM maltose, flow rate 2 mL/min, 25 min) to elute the MBP-fusion protein off the column. This should result in a symmetric peak. Collect the fractions and analyze the protein using SDS-PAGE (*see* **Note 3.6.1.4**).
8. Pool the fractions containing the correct MBP-fusion protein and concentrate to an appropriate volume for a PD-10 Desalting column (less than 2.5 mL) (*see* **Note 3.6.1.5**). Equilibrate the column by washing 4 times in equilibration buffer (approximately 25 mL buffer). This can be accomplished by gravity flow or by low-speed centrifugation (1,000 x g). Apply 2.5 mL of protein sample to the column (add buffer if the sample is less than 2.5 mL) and allow the sample to completely enter the column bed. Discard all flow through. Elute the sample with 3.5 mL of buffer solution and concentrate as necessary. This step removes maltose from the protein sample.

Immobilization of MBP-fusion proteins

1. Remove MBP-fusion proteins and the protein being assayed as a potential binding partner from the -80°C freezer. Allow the proteins to thaw on ice before proceeding to the next step (*see* **Note 3.6.1.6**).
2. Remove amylose resin from the 4°C fridge and shake at low speed for gentle resuspension. Allotting 25 µL resin per sample condition, cut the tip of a plastic pipette and remove enough resin for each sample condition plus one additional (*see* **Note 3.6.1.7**). Add 1 mL of Wash Buffer A to the microcentrifuge tube containing the resin and centrifuge at low

speed (around 3200 rpm) for 30 sec. Repeat three times. Remove the supernatant without disturbing the resin, leaving enough volume to distribute 25 µL of resin per sample. Using a cut plastic pipette tip, resuspend the resin and aliquot to microcentrifuge tubes.

3. To immobilize the MBP-fusion proteins on the amylose resin, distribute 5-10 µg of an individual MBP-fusion construct diluted to 25 µL in Wash Buffer A to one of the microcentrifuge tubes containing amylose resin. Incubate the proteins at 4°C for 1 h using gentle rotation (*see* **Notes 3.6.1.8-3.6.1.9**).

Addition of secondary protein

1. Add 5-10 µg of the prey protein to a total volume of 50 µL in Wash Buffer A. For consistency, calculate the volume of protein and buffer needed for one sample and multiply these values by the number of samples plus one additional to generate a master mix. From the master mix, distribute 50 µL to each microcentrifuge tube containing an immobilized MBP-fusion construct. Incubate for 2 h at 4°C with gentle rotation.

Elution

1. Prior to removing samples from the 4°C incubation, prepare a series of tubes for washing and elution. Label an Ultrafree centrifugal filter for each sample, in addition to a microcentrifuge tube with the cap removed, and a microcentrifuge tube labeled to hold the final eluted sample. Place the centrifugal filter and the microcentrifuge tube with the cap removed into a 4°C centrifuge to cool before adding the samples.
2. Remove the samples from the 4°C fridge and place on ice. Transfer each sample into a centrifugal filter using a cut plastic pipette tip. Centrifuge the samples at 3200 rpm for 20 sec.

3. Add 300 µL of Wash Buffer B directly to each sample and centrifuge at 3200 rpm for 20 sec. Quickly remove the centrifugal filter and place into the microcentrifuge tube with the cap removed (*see* **Note 3.6.1.10**). Proceed with two additional 300 µL washes in Wash Buffer B at 3200 rpm for 20 sec.
4. Move the centrifugal filters into the final microcentrifuge tube and add 100 µL Elution Buffer to each sample. Incubate at 4°C for 5 min with gentle rotation. Elute the samples by centrifugation at 4°C for 1 min at 3200 rpm.

Methanol Precipitation

1. Add 1 mL of 100% methanol to each microcentrifuge tube containing eluted sample. Centrifuge the samples at high speed (around 12,000-14,000 rpm) for 10 min. Discard the supernatant and let the samples air dry for 30 min or until droplets are no longer visible (*see* **Note 3.6.1.11**).
2. Resuspend in 30 µL SDS Loading Buffer with Dye. Make sure to wash the sides of the tube up to 1 mL. Vortex each sample and centrifuge the samples in preparation for SDS-PAGE.

SDS-PAGE and Western Analysis

1. Prepare two 10% SDS-PAGE gels (4% stacking). Run 12 µL of sample on a gel for Coomassie staining to verify equal loading of the MBP-fusion constructs on the amylose resin (**Fig. 3.3 top panel**). Run 8 µL of sample on another gel for western blotting to assess protein interaction (**Fig. 3.3 lower panel**).
2. Use a primary antibody against the prey protein when performing the western analysis. This will inform whether a protein interaction occurred.

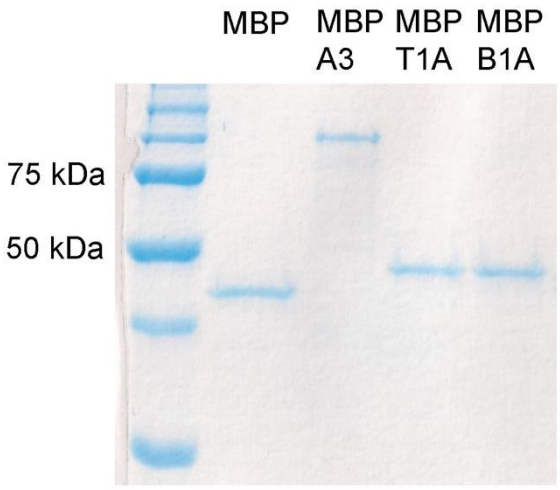

Fig. 3.3. **Representative Coomassie gel and western blot for an MBP pull-down using His-JNK3 as prey protein.** The Coomassie gel is used to assess even loading of the MBP fusion constructs, while the Western blot to show relative binding of His-JNK3 (A3, arrestin3; T1A, first 25 amino acids of arrestin-3; B1A, first 25 amino acids of arrestin-2).

3.5.2 In-cell activation assay

All cell culture experiments were performed in the class II laminar flow hood until the cell lysis step. Make sure to maintain lab etiquette when working with cells – clean all materials with 70% ethanol before entering the hood space, wear gloves and a lab coat.

Cell Seeding and Transfection

1. Grow COS7 African green monkey cells in DMEM solution containing 10% FBS and 5% penicillin/streptomycin at 37°C and 5% CO_2. Other cell lines can be used depending on the system being tested.
2. Remove cells from 10-cm plates using 2.5 mL 0.05% Trypsin (~3-5 mins) and seed into 6-well plates at a density that ensures 90-95% confluency within 24 hours (approximately 50,000 cells/mL) (*see* **Note 3.6.2.1**).

3. After 24 hours, replace the cell media with serum-free media and transfect the cells with pcDNA3-HA-ASK1 (0.4 µg), pcDNA3-HA-JNK3α2 (0.2 µg), and pcDNA3-Venus arrestin constructs (0.2-0.6 µg) at a 1:2 ratio of DNA:Lipofectamine 2000 (*see* **Note 3.6.2.2**). The µg amounts of pcDNA3-Venus arrestin constructs were previously optimized using western analysis of different transfected amounts (*see* **Note 3.6.2.3**). Equalize the DNA amounts using an empty pcDNA3 vector. After 5-6 hours, replace the serum-free media with DMEM solution containing 10% FBS and 5% penicillin/streptomycin.
4. The night before cell lysis (approximately 12 hr), replace the media with serum-free media to exclude any possible receptor stimulation from factors in the serum.

Cell Lysis

1. 48 hours post-transfection, remove the cells from incubation and wash 3X with 1 mL cold phosphate buffered saline (PBS). Place the cells on ice and incubate with 1 mL phosphatase inhibitors (20 mM NaF and 1 mM Na_3VO_4) in PBS for 15 minutes prior to complete lysis (*see* **Note 3.6.2.4**).
2. After treatment with phosphatase inhibitors, wash the cells twice with 1 mL cold PBS. Prepare lysis buffer and keep on ice. Add PMSF and BA to the lysis buffer immediately prior to adding the buffer to the cells (*see* **Note 3.6.2.5**). Add 100 µL of lysis buffer to each well and incubate the plate for 10 min on ice with gentle rotation.
3. Mechanically remove cells from the wells using a cell scraper and resuspend by pipetting (*see* **Note 3.6.2.6**). Remove the solutions from each well and transfer to a 1.5 mL centrifuge tube. Centrifuge the cells for 10 min (4°C, microcentrifuge at maximum speed) to pellet the debris and take the top 80% of the lysate for analysis.

4. Measure protein concentration using a Bradford Assay (or any alternative method). The yields typically range between 0.5-2 mg/mL (*see* **Note 3.6.2.7**).

Gel Electrophoresis

1. Prepare samples for gel electrophoresis by combining 10 µL of 2X Lammeli Buffer with the correct amount of protein for visualization by western- ppJNK3 blot (8.5µg), HA blot (5 µg), and Venus blot (1 µg) (*see* **Note 3.6.2.8**). Boil the samples for 2-3 min to ensure that the proteins will enter the gel.
2. Prepare a 10% SDS-PAGE gel (4% stacking) for each respective blot (ppJNK3 blot (**Fig. 3.4 upper panel**), HA blot (**Fig. 3.4 middle panel**), and Venus/GFP blot (**Fig. 3.4 lower panel**). Load samples into wells at 80 mV for 15 mins, and then run at 150 mV for another 45 min-1 h (until the dye front is close to the bottom of the gel).

Transfer and Visualization

1. Remove gels from their casing after electrophoresis and transfer to PDVF membrane for 45 mins (100V). After transfer, block the membranes with 5% milk (w/v) in TBS-T for 1 h (alternatively, you can use a 5% milk/2% BSA in TBS-T combination for enhanced blocking). Wash the membranes 5 times for 5 min in TBS-T before overnight incubation with the corresponding primary antibody (see **Note 3.6.2.9**).
2. The next morning, wash the membranes 5 times for 5 min in TBS-T and then incubate with HRP-conjugated secondary antibodies for 1 h. Detect bands by X-ray film using enhanced chemiluminescence (or an alternative method if you prefer). Perform densiometric quantification to assess the difference in ppJNK3 levels (*see* **Note 3.6.2.10**).

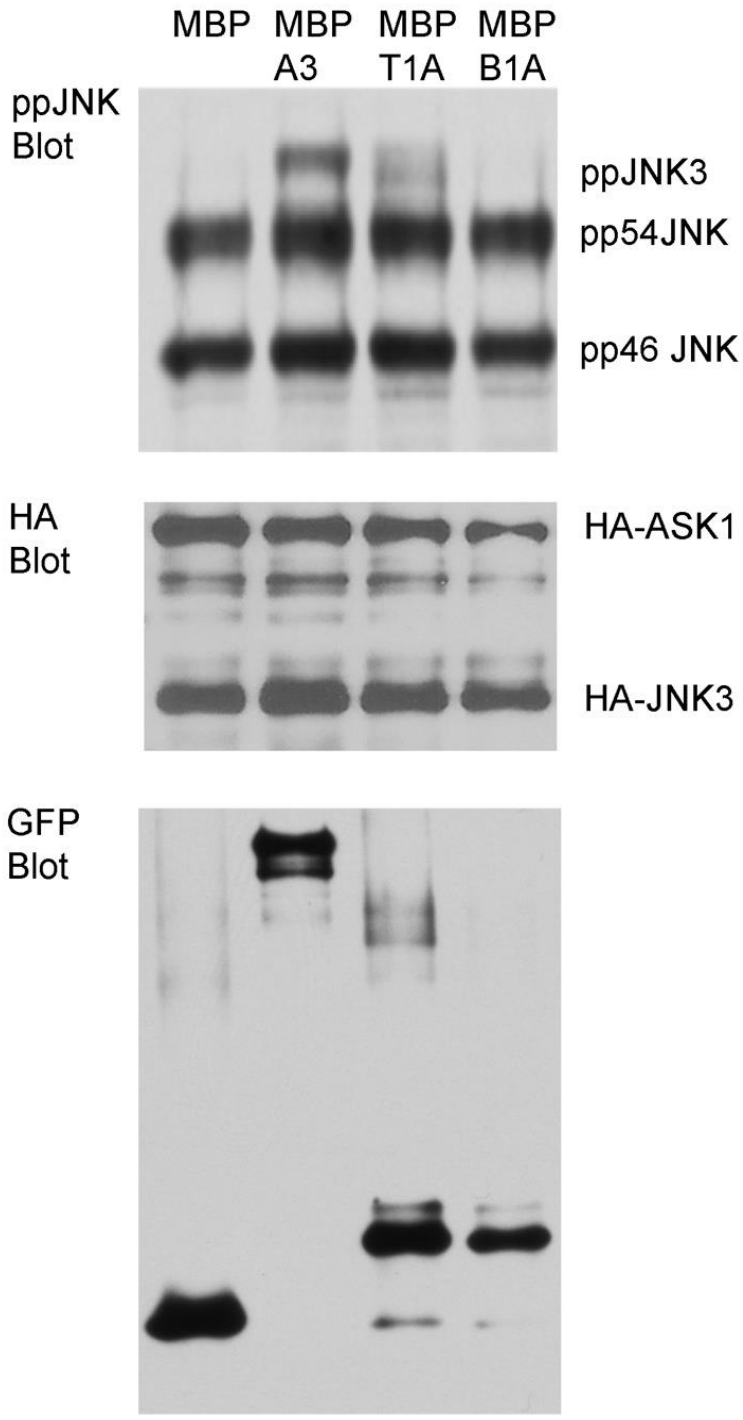

Fig. 3.4. Representative western blots for antibodies against ppJNK, HA, and GFP. The HA and GFP blots are used to confirm equal protein expression following transfection. The top band of the ppJNK blot represents ppJNK3, while the other bands are isoforms of ppJNK1/2 (pp54 JNK and pp46JNK). Quantification was performed on ppJNK3 bands and compared across Venus fusion constructs (not shown).

3.6 Notes

3.6.1 *In vitro* pull-down assay

1. Chilling the flasks slows down cell growth prior to lowering the temperature for induction. This promotes proper folding of the protein.
2. Can be stored at -80°C after this step for several weeks.
3. DNAse I treatment reduces the viscosity and helps with filtration of the lysate during later steps.
4. Boil the samples at 100°C for 5 min to make it easier for loading the gel. This helps if you have a lot of protein in the sample.
5. Alternatives to the PD-10 Desalting column include the HiTrap Desalting Column available from GE, or buffer exchange using a concentrator with the correct cut-off to retain your protein of interest.
6. Limit the number of times that you thaw a protein by freezing your samples in small aliquots.
7. Cutting the pipette tip ensures successful pipetting of the resin.
8. Be careful not to agitate the resin as it will stick to the walls of the tube and cannot be recovered.
9. Optimization may be required when loading the MBP-fusion proteins onto the amylose resin. This is because some protein samples are cleaner than others, and competing proteins might reduce the binding.
10. The washing step must be performed quickly to minimize change in equilibrium between the bound and unbound state. To assist in this, try not to process more than ten samples at a time.

11. Methanol will prevent dissolution of the sample proteins in SDS-PAGE buffer.

3.6.2 In-cell activation assay

1. A 12-well plate can also be used, as this will typically yield enough protein for measurement. The greater the confluency of your cells prior to transfection, the greater the chance of cell survival. Transfection reagent and DNA are toxic to the cells.
2. Lipofectamine 2000 is more effective for transfection with high DNA, while other transfection agents, such as Trans-Hi are more effective with lower DNA amounts.
3. Obtaining an even transfection of the pcDNA3-Venus arrestin constructs is one of the more difficult aspects of this assay. Perform a titration using different µg amounts of each construct prior to experimentation to balance the constructs.
4. This prevents the removal of phosphate groups from modified proteins in the cell lysate.
5. These reagents are not stable over a prolonged period. Make sure to add them directly prior to administering the lysis buffer to the cells.
6. Complete lysis is important for extraction of all the protein in the cell. Make sure to scrape the cells off so that you do not have any remaining on the dish.
7. Low yields may indicate high cell death. Revisit the transfection amounts and monitor your cell population over the 48 h, if you encounter this issue.
8. These values are experimentally determined. If there is no detectable signal, increase the amounts used for western analysis. Alternatively, if the signal is too high, decrease the amounts used for analysis.
9. It is important to wash the milk away completely if the primary antibody solution is to be frozen and reused).

10. Our preferred software package is QuantityOne 1-D Analysis Software from Bio-Rad.

CHAPTER 4

STRUCTURAL BASIS OF ARRESTIN-3 ACTIVATION AND SIGNALING

This article was published in Nature Communications (3). Qiuyan Chen was the first author, and **Nicole A. Perry**, Sergey A. Vishnivetskiy, Sandra Berndt, Nathaniel C. Gilbert, Ya Zhou, Prashant K. Singh, Jonas Tholen, Melanie D. Ohi, Eugenia V. Gurevich, Chad A Brautigam, Candice S. Klug, Vsevolod V. Gurevich, and T.M. Iverson contributed to this work.

4.1 Introduction

Arrestins modulate G protein-coupled receptor (GPCR) signaling in two ways. First, arrestins bind to activated, phosphorylated receptor and sterically block G protein coupling, terminating G protein activation (17). Second, receptor-bound non-visual arrestins (arrestin-2 and -3, a.k.a. β-arrestin-1 and -2) initiate G protein-independent signaling (90) via >100 proteins (9). This arrestin-mediated signaling regulates cell proliferation and apoptosis (90).

GPCR-dependent arrestin signaling occurs in the context of a complex between arrestin and phosphorylated, activated GPCR. In classic biochemical work on rhodopsin and arrestin-1, this arrestin–receptor interaction was found to rely on arrestin "sensors" that detect the phosphorylation and activation of the receptors. The phosphate sensor is formed by a group of positively charged side chains on the concave side of the N-domain that directly bind receptor-attached phosphates and is relatively unselective for the underlying sequence (91). The activation sensor distinguishes between active and inactive GPCRs. To our knowledge, neither the identity of the activation sensor nor how it recognizes >800 distinct GPCRs have

been proposed. These phosphate and activation sensors are believed to act synergistically, as the simultaneous triggering of both sensors elicits the highest-affinity receptor binding (27).

Structural studies in the context of biochemical work suggest that triggering the phosphate and activation sensors of arrestin promotes a conformational change. Structures of all four vertebrate arrestins in the basal state (35,91-93) showed that arrestin is a two-domain protein with limited interaction between domains. Two inter-domain interactions have been suggested as key for stabilizing the basal conformation. The first is a group of buried charged side chains known as the "polar core" (35). The second is a sequence in the C-terminus of arrestin termed the "C-tail" (residues 385–393 of arrestin-3) that binds to the N-domain in a way that both contributes a charge to the polar core and blocks access to the phosphate sensor (35). Perturbation of either the polar core or the C-tail shifts the arrestin equilibrium to favor activation, suggesting that the inter-domain arrangement changes during activation (94).

Recently, several strategies to stabilize active arrestin allowed structural characterization. These included the use of: (a) a more easily activated (termed "pre-activated") splice variant of visual arrestin-1 called p44 (37), which is truncated before the C-tail; (b) an antibody to stabilize arrestin-2 bound to a vasopressin receptor phosphopeptide (26); (c) the R175E mutant of arrestin-1 which has a destabilized polar core (95); and (d) arrestin-1 with activating mutations tethered to constitutively active rhodopsin (25). In the structures of p44, the phosphopeptide-bound arrestin-2, and the receptor-bound arrestin-1, a ~20° inter-domain rotation was observed, identifying inter-domain rotation as a hallmark of arrestin activation (25,26,37). In the R175E variant, a ~7.5° inter- domain rotation suggests that this structure represents an activation intermediate (95).

Despite these advances, many fundamental questions in arrestin-mediated

signaling remain unanswered. Non-visual arrestins bind >800 distinct GPCRs, yet it is not clear how this broad receptor specificity is achieved. It is also unclear how the phosphate and activation sensors elicit the inter-domain rotation that accompanies arrestin activation, or how the active arrestin conformation initiates signaling. Finally, the arrestin-3 isoform is uniquely able to signal independently of GPCRs (58,96-99). Previous studies identified that receptor-independent arrestin-3 activation biases signaling toward the activation of c-Jun N-terminal Kinase-3 (JNK3) (96,97). However, it is neither clear how arrestin-3 is activated in the absence of GPCRs nor are there compelling hypotheses for why receptor-independent arrestin-3 activation preferentially initiates the JNK3 signaling cascade. Indeed, it is not clear how arrestin activated by any input correctly directs signaling toward one out of >100 downstream effectors.

To address these questions, we determined the 2.4 Å resolution crystal structure of arrestin-3 in complex with the non-receptor activator inositol hexakisphosphate (IP_6). We demonstrate that the same sensors critical for detecting the phosphorylated and activated state of GPCRs are triggered during receptor-independent activation and reveal how the triggering of these sensors elicits inter-domain rearrangements. Moreover, we identify properties of the arrestin activation sensor that allow broad specificity for GPCRs. Finally, we propose a mechanism for arrestin-dependent signal initiation and bias. Collectively, these findings address many outstanding questions in the arrestin field.

4.2 Results

Structure of IP_6-activated arrestin-3. GPCR-independent arrestin-3 initiation of the JNK3 cascade is established in the literature (58,96-99). Although a physiological non-

receptor activator of arrestin-3 has not been unambiguously identified, inositol phos- phates and heparin have been suggested as possibilities (100). To test whether IP_6 could activate arrestin-3, we determined the structure to 2.4 Å resolution (**Fig. 4.1a**; Table 4.1), which shows that the IP_6-arrestin-3 complex is a trimer (**Fig. 4.1a**). In the structure, we identified electron density consistent with two bound IP_6 molecules per arrestin (**Fig. 4.2a, b**); each IP_6 molecule is located between the protomers of the arrestin trimer (**Fig. 4.1a**). The structure shows that IP_6 binds to arrestin-3 at the same location as C-tail in basal arrestin such that IP_6 displaces the C-tail (**Fig. 4.2c**). The IP_6-bound structure exhibits an inter-domain twist of 17.7° with respect to the basal con- formation (**Fig. 4.1b**). Moreover, the IP_6 binding sites in the N-domain overlap with the binding sites for phosphorylated receptor (**Fig. 4.1c,d**). These observations are consistent with this structure representing activated arrestin-3.

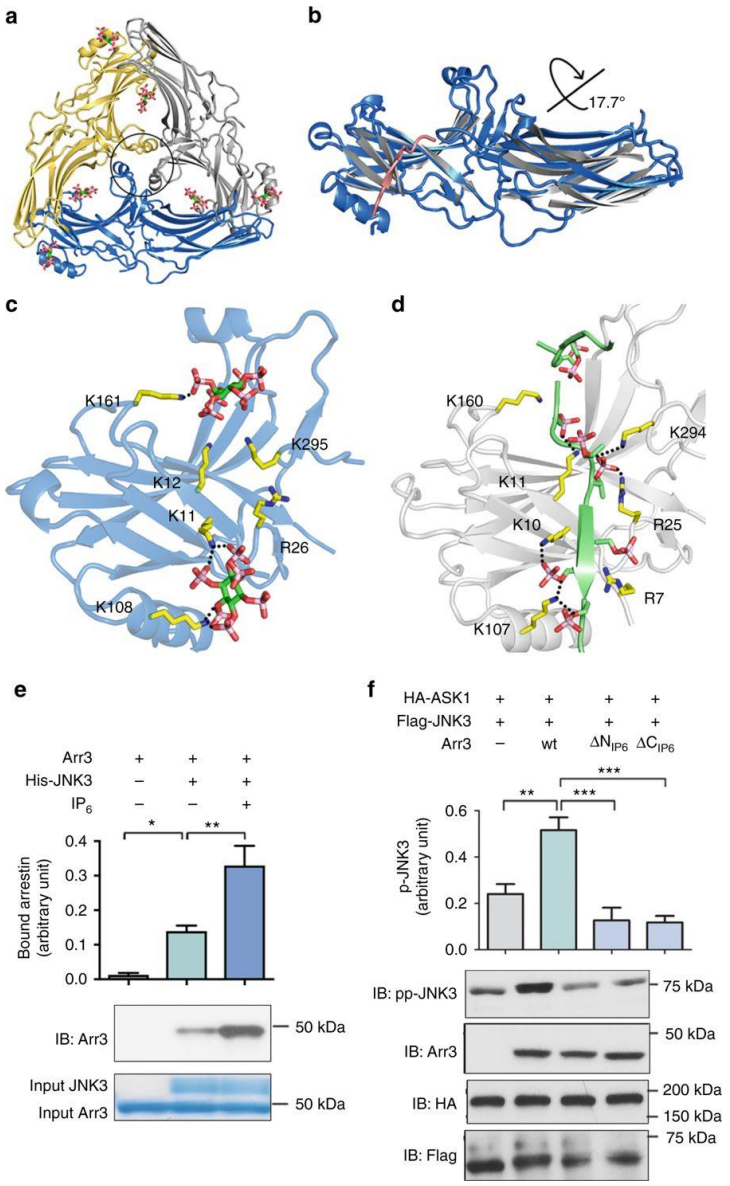

Fig. 4.1. The structure of IP_6-activated arrestin-3. (a) Ribbon diagram of the IP_6-activated arrestin-3 (Arr3) trimer. Each protomer is shown in a different color (gray, yellow, blue); IP_6 is shown as sticks. Finger loops are circled. **(b)** Overlay of the N-domain of IP_6-activated (blue) with basal arrestin-3 (gray with a pink C-tail, PDB 3P2D (92)) highlights the 17.7° inter-domain rotation. **(c)** IP_6 binding sites within the phosphate sensor on the arrestin-3 N-domain. **(d)** Phospho- peptide binding sites within the phosphate sensor on arrestin-2 N-domain (PDB entry 4JQI (101)). **(e)** Arrestin-3 binding to purified His_6-JNK3 immobilized on Ni-NTA resin in the presence or absence of 100 μM IP_6 ($n = 8$). The quantity of bound arrestin-3 was measured by densitometry (mean ± SEM) and compared using one-way ANOVA. $*p \leq 0.05$; $**p \leq 0.01$. **(f)** Measurement of JNK3 activation by arrestin-3 and mutants of the IP_6 binding sites. JNK3 activation (mean ± SEM) was assessed by measuring the phospho-JNK3 (ppJNK3) level in HEK293 cells co-transfected with HA-ASK1, Flag-JNK3 and either empty vector, arrestin-3, the ΔN_{IP6} arrestin-3 (R8Q, K11A, K12A, K108Q, K161Q, K295Q) or the ΔC_{IP6} arrestin-3 (K233Q, R237Q, K251Q, K325Q, K327Q). The assay was repeated three times and JNK3 phosphorylation was compared using one-way ANOVA. $**p \leq 0.01$, $***p \leq 0.001$

Table 4.1. Summary of crystallographic data collection and refinement statistics

Table 1 Summary of crystallographic data collection and refinement statistics[a]

Data collection	
Beamline	LS-CAT ID-D
Wavelength	1.7394 Å
Resolution (Å)	50.0–2.4
Space group	$P6_3$
Unit cell dimensions	$a = b = 97.575$ Å, $c = 76.938$ Å
R_{sym}	0.051 (0.546)
R_{pim}	0.031 (0.416)
$CC_{1/2}$[b]	0.865
I/σ	26.2 (2.00)
Completeness	97.5 (96.0)
Redundancy	3.4 (2.6)
Refinement	
R_{cryst}[c]	0.210
R_{free}	0.243
RMS deviation from ideal	
Bond lengths	0.004 Å
Bond angles	1.09°
Ramachandran statistics	
Most favored	95.0%
Additionally allowed	4.5%
Disallowed	0.6%

[a]Numbers in parenthesis are values for data in the outer resolution shell, corresponding to 2.44–2.40 Å resolution
[b]$CC_{1/2}$ is only reported for the outer resolution shell
[c]$R_{cryst} = \Sigma||F_{obs}| - |F_{calc}||/\Sigma F_{obs}$. R_{free} is the same as R_{cryst} for a set of data omitted from the refinement

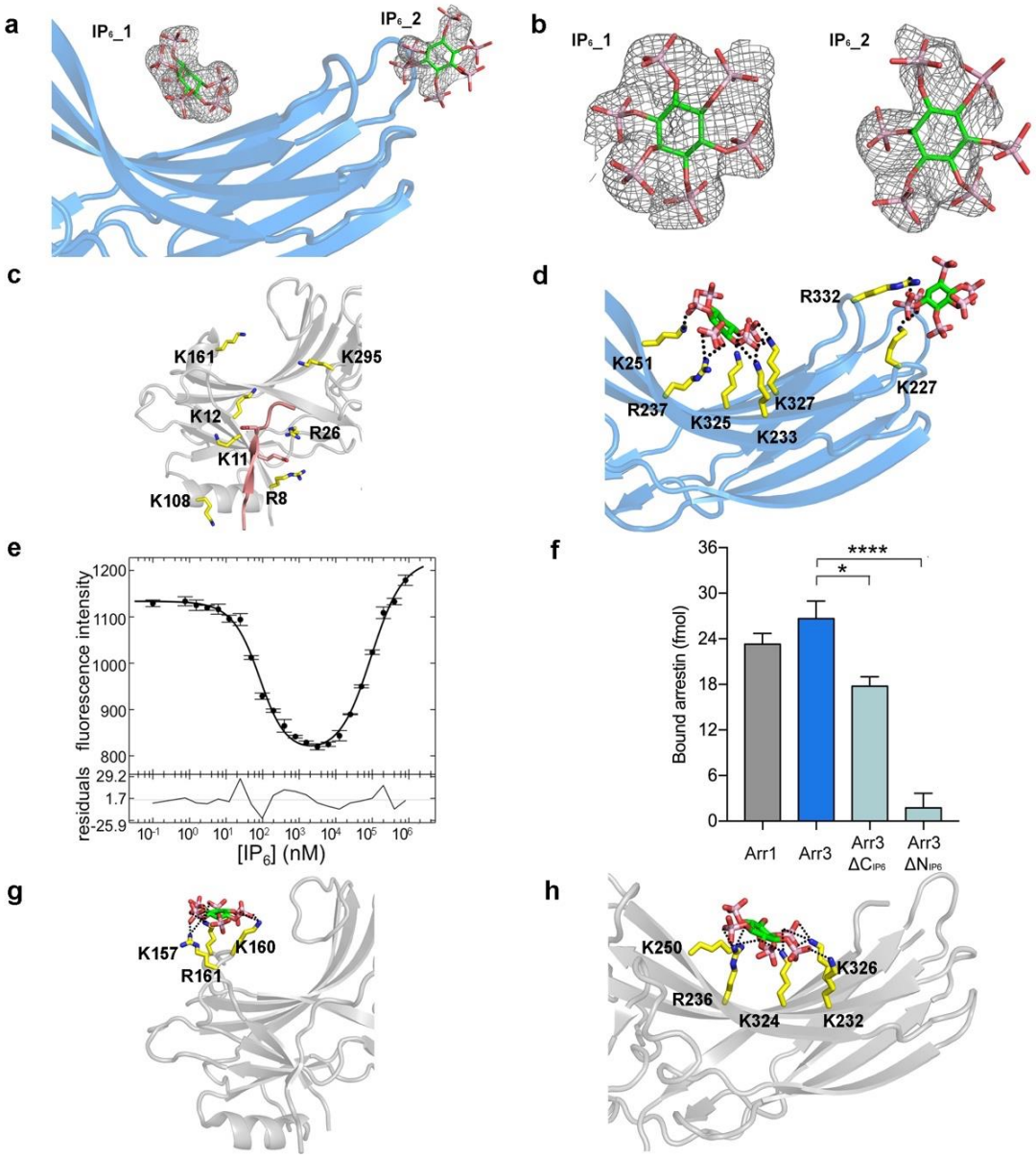

Fig. 4.2. IP_6 binding sites in arrestins. (**a**) – (**b**) Electron density for the IP_6 molecules bound to arrestin-3. IP_6 molecules are superimposed on a $2F_o - F_c$ composite omit map calculated after refinement in Phenix and contoured at 1.2σ. (**c**) The arrestin-3 C-tail binds to the N-domain in basal state (PDB entry 3P2D(102)), protecting the phosphate sensor. IP_6 or phosphopeptide binds at this same location, triggering the phosphate sensor and displacing the C-tail. (**d**) IP_6 binding sites in the arrestin-3 C-domain. (**e**) MST-measured fluorescence binding isotherm for IP_6 and arrestin-3. Circles in the upper panel represent the fluorescence-intensity average of three individual data acquisitions, error bars show S.D. The solid line is the fitted isotherm for the two-site model. The lower panel shows the residuals between the data and the fit. (**f**) Binding of the ΔN_{IP6} and ΔC_{IP6} arrestin-3 mutants to phosphorylated, active rhodopsin as compared to arrestin-1 and arrestin-3. The ΔC_{IP6} variant binds to phosphorylated, activated rhodopsin at a level similar to wild-type arrestin-1, consistent with correctly-folded protein. The ΔN_{IP6} variant alters receptor-binding residues and barely binds rhodopsin. (**g**) IP_6 binding sites on arrestin-2 N-domain (PDB entry 1ZSH(103)) (**h**) IP_6 binding sites on arrestin-2 C-domain (PDB entry 1ZSH(103)).

IP_6 binding supports GPCR-independent activation in cells. As IP_6-bound arrestin-3 adopts an active conformation, we tested whether IP_6 binding enhances effector binding in vitro and induces arrestin-3-dependent JNK3 activation (58,96-99) in cells. To identify whether IP_6 enhances JNK3 binding, we compared the capacity of column-immobilized His_6-JNK3 to bind arrestin-3 in the presence or absence of IP_6 (**Fig. 4.1e**). Even in the absence of IP_6, arrestin-3 binds to JNK3, as described in (98,104). This may reflect either low-affinity binding of JNK3 to the basal arrestin-3, or the ability of arrestin-3 to spontaneously sample the active conformation in the absence of activator. We observed an approximate doubling of the arrestin-3 binding to JNK3 in the presence of IP_6 (**Fig. 4.1e**). This is consistent with IP_6 shifting the conformational equilibrium of arrestin-3 to an active state that binds JNK3.

We next mutagenized the IP_6 binding residues in the N-domain (ΔN_{IP6}; **Fig. 4.1c**) or the C-domain (ΔC_{IP6}, **Fig. 4.2d**), then tested the impact on receptor-independent JNK3 activation in HEK293 cells (**Fig. 4.1f**). Co-expression of wild-type arrestin-3 with ASK1 (an upstream kinase in the JNK3 cascade (64)) and JNK3 resulted in robust JNK3 phosphorylation. This was significantly attenuated in cells expressing the ΔN_{IP6} or ΔC_{IP6} arrestin-3 variants, providing strong evidence that IP_6 activates arrestin-3 in cells, and facilitates arrestin-dependent JNK3 activation.

To rule out alternative interpretations for the loss of function in the arrestin-3 variants, we performed two types of assays. First, we tested whether the affinity of arrestin-3 for IP_6 would allow binding at physiological concentrations of IP_6. Second, we ensured that the ΔN_{IP6} and ΔC_{IP6} variants specifically reduced receptor-independent signaling and had no global signaling defect.

To determine whether arrestin-3 binds IP_6 at the concentrations found in cells, we used

microscale thermophoresis (MST) to measure binding affinity. We labeled wild-type arrestin-3 with AlexaFluor C5 maleimide dye, titrated IP_6 into fluorophore- labeled arrestin-3, activated with an infrared laser, and monitored the fluorescence intensity. MST allowed us to obtain binding curves and calculate equilibrium dissociation constants. Wild-type arrestin-3 exhibits two binding affinities for IP_6 (K_D = 57 nM and 90 μM; **Fig. 4.2e**). As intracellular IP_6 concentrations range between 35 and 105 μM (105,106), these affinities are consistent with IP_6 being able to occupy both binding sites in cells.

To ensure that the mutants had no global signaling deficit, we evaluated folding and rhodopsin binding of purified wild-type and mutant arrestin-3 in vitro. As the IP_6 binding sites in the arrestin-3 N-domain overlap with the binding sites for phos- phorylated receptor (**Fig. 4.1c, d**), we anticipated that the ΔN_{IP6} variant would exhibit dramatically reduced receptor binding. However, the binding sites in the C-domain are unique to IP_6, and if this variant is correctly folded and functional, the ΔC_{IP6} mutations should only have a minor impact on receptor association. As anticipated, the ΔC_{IP6} arrestin-3 variant retained significant receptor binding, while ΔN_{IP6} arrestin-3 mutant showed a substantial reduction (**Fig. 4.2f**) but was properly folded. Collectively, these experiments support the importance of the IP_6-binding sites in receptor-independent arrestin-3 signaling.

IP_6 triggers the arrestin-3 phosphate sensor. The IP_6 molecules make extensive contacts with arginine and lysine side chains on the arrestin-3 N-domain (**Fig. 4.1c**). Critically, phosphate binding recruits Lys295 of the lariat loop, which contains two out of five charged residues in the polar core (**Fig. 4.3a, b**). This interaction likely elicits a conformational change that disrupts the polar core and triggers the phosphate sensor (**Fig. 4.3a, b**). A comparison of the IP_6-bound structure to the reported structure of arrestin-2 with

a vasopressin receptor phosphopeptide shows that the positions of the IP_6 phosphates closely resemble those of the peptide-attached phosphates (**Fig. 4.1c, d**)(101). The structure of arrestin-3 in the basal conformation (92) shows that the C-tail binds to the N-domain, sterically occluding the phosphate binding sites (**Fig. 4.2c**) but does not recruit Lys295. As a result, the polar core remains intact (**Fig. 4.3b**). Thus, IP_6 and poly-phosphated receptors bind to the same arrestin elements and trigger the phosphate sensor via the same mechanism by: (a) recruiting phosphate-binding side chains, (b) altering the conformation of the lariat loop, and (c) disrupting the polar core (**Fig. 4.3a, b**). This helps explain how relatively disparate phosphorylated species promote arrestin activation and helps clarify how the C-tail stabilizes the basal conformation.

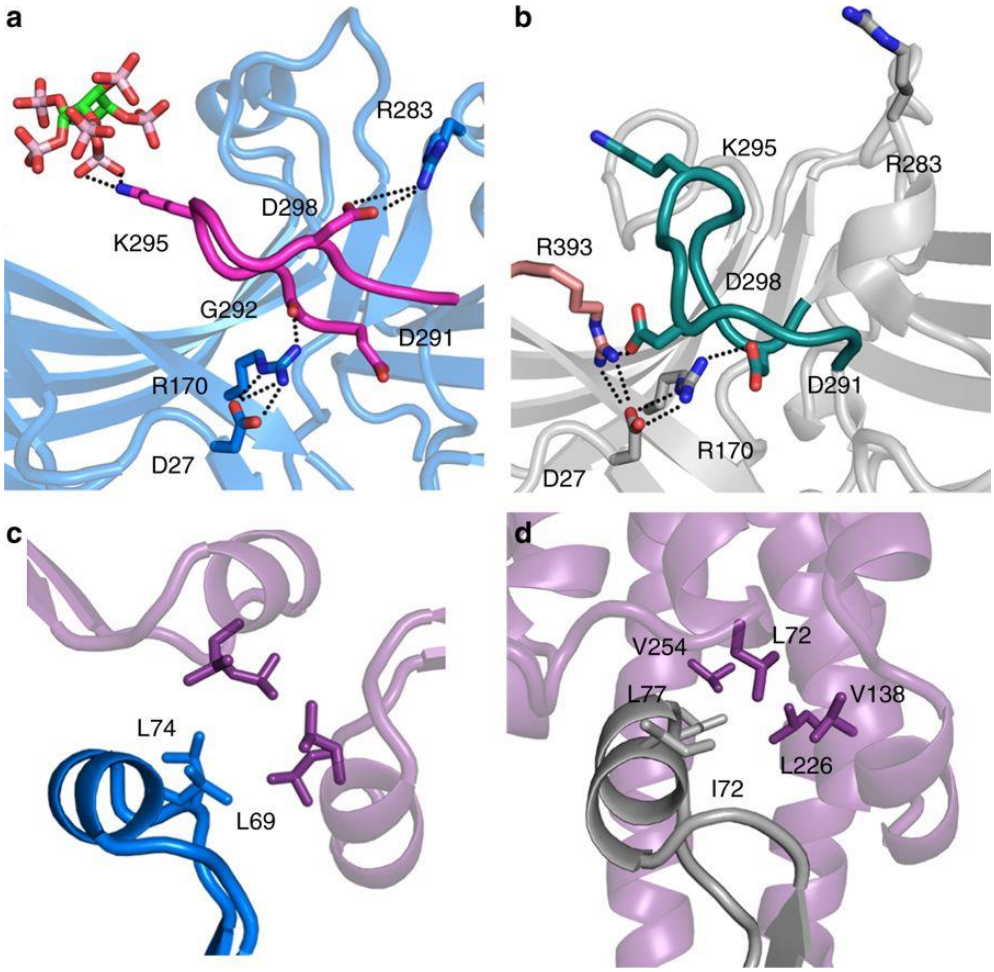

Fig. 4.3. The phosphate and activation sensors in IP_6-activated arrestin-3. **(a)** Conformation of the lariat loop in IP_6-activated arrestin-3 disrupts the polar core. **(b)** Conformation of the lariat loop in basal arrestin-3 (PDB 3P2D (92)) with an intact polar core. **(c)** Helical conformation of the finger loop stabilized by the active arrestin-3 trimer. **(d)** Similar hydrophobic contacts are observed in the arrestin-1-rhodopsin interaction (4ZWJ (25)) and have distances of 3.5–4 Å between hydrophobic side chains.

Intriguingly, the Benovic and Brenner groups showed that soaking crystals of arrestin-2 with IP_6 did not trigger the phosphate sensor (103). Comparing the binding locations of the IP_6 in arrestin-2 vs. arrestin-3 (103) shows that one of the IP_6 molecules binds arrestin-2 in a different location (**Fig. 4.1c, Fig. 4.2d, g, h**). As a result, IP_6 binding to the arrestin-2 does not recruit Lys294 (equivalent to arrestin-3 Lys295). This leaves the polar core intact despite strict conservation of phosphate binding residues. While it is not clear how IP_6 binding is directed differently in these isoforms, it is consistent with reports that arrestin-2 does not support receptor-independent signaling (58,97).

Engagement of the arrestin-3 activation sensor. We wanted to explore whether the activation sensor is also triggered in IP_6-activated arrestin-3. The activation sensor of arrestins is proposed to distinguish between active and inactive GPCRs (27), although its identity has not been suggested in the literature. To offer insight into the identity of the activation sensor, we analyzed differences between active and inactive receptors. The most striking structural difference is the accessibility of a hydrophobic pocket on the intracellular side of the protein unique to active GPCRs (39). This pocket represents a major site of interaction with both G proteins (23,107) and arrestins (25,108). In fact, it contributes 596 $Å^2$ out of a total of 1362 $Å^2$ of buried surface area in the rhodopsin-arrestin complex (58). Cocrystal structures of opsin with pre-activated arrestin-1 or an arrestin-derived peptide suggest that the hydrophobic pocket binds to an α-helical conformation of the finger loop (25,108). However, there is controversy on this because of the quality of the electron density for this helix in these structures (**Fig. 4.4a, b**). The α-helix of the finger loop contains an ED(I/L)D motif (residues 68–71 of arrestin-3) (25,108) that lacks secondary structure in basal arrestins (91,92,109,110)and is not altered in partially activated arrestin (111). Helix formation of the

finger loop presents several hydrophobic residues to the intracellular hydrophobic pocket of activated receptor (25,108).

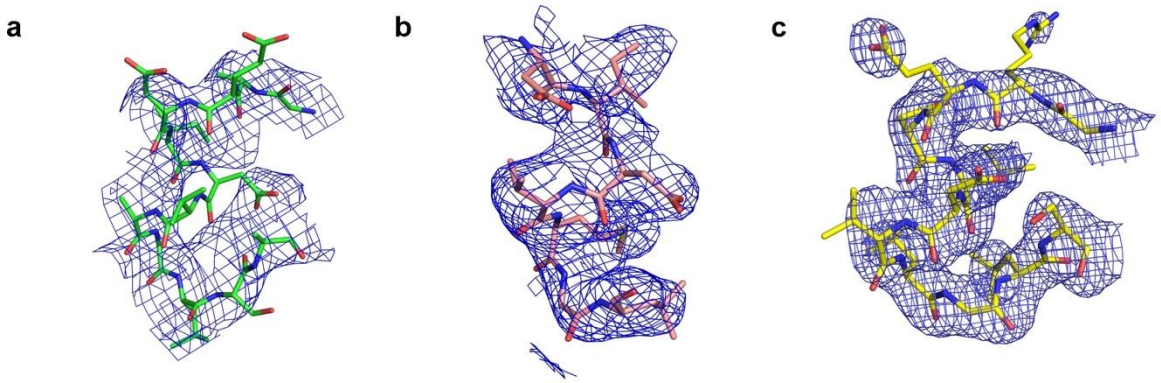

Fig. 4.4. Electron density for the receptor-associated finger loop of arrestin as compared to the IP_6-bound trimer. Composite omit electron density is contoured at 1σ for (**a**) the finger loop of arrestin-1 in the structure of opsin-arrestin1 (PDB 4ZWJ(112)); (**b**) a peptide corresponding to the arrestin finger loop cocrystallized with opsin (PDB 4PXF(108)); (**c**) the finger loop of arresin-3 in the IP_6-activated trimer. The quality of the electron density in panels (**a**) – (**c**) differs significantly, likely reflecting different mobility of the finger loop in each structure determination. The quality of the electron density in panels (**a**) and (**b**) led to some controversy as to whether the finger loops was correctly assigned as a helix in these prior publications(108,112).

Similarly, in the IP_6-mediated trimer the finger loop is presented as an α-helix (**Fig. 4.3c, d**). In contrast with the receptor-bound structure (25), this helix is associated with clear electron density (**Fig. 4.4c**). In this conformation, hydrophobic residues would be exposed to solvent if the IP_6-activated arrestin-3 were a monomer, but in the context of the trimer, these form Van der Waals (<4 Å) self-contacts around the molecular three-fold axis (**Fig. 4.3c**) and are shielded from solvent. This suggests that receptor-independent trimerization and the GPCR hydrophobic pocket stabilize the triggered activation sensor in the same way (**Fig. 4.3c, d**).

IP_6-mediated arrestin-3 trimerization and activation. If trimerization stabilizes the triggered activation sensor, then the trimer should be quite stable in the presence of IP_6. It

would also be critical for receptor-independent activation of arrestin-3. Importantly, the IP_6-bound arrestin-3 trimer buries 3053 $Å^2$ of surface area per protomer, a value indicative of a biologically relevant oligomer (113). The trimer does not appear to be influenced by crystal contacts (**Fig. 4.5a**); however, it does require the inter-domain twist of active arrestin. Indeed, modeling the basal conformation causes the misalignment of the IP_6 binding sites (**Fig. 4.5b**). This would be predicted to reduce IP_6 affinity and therefore disfavor trimerization. We therefore next explored the stability of the arrestin-3 trimer in solution.

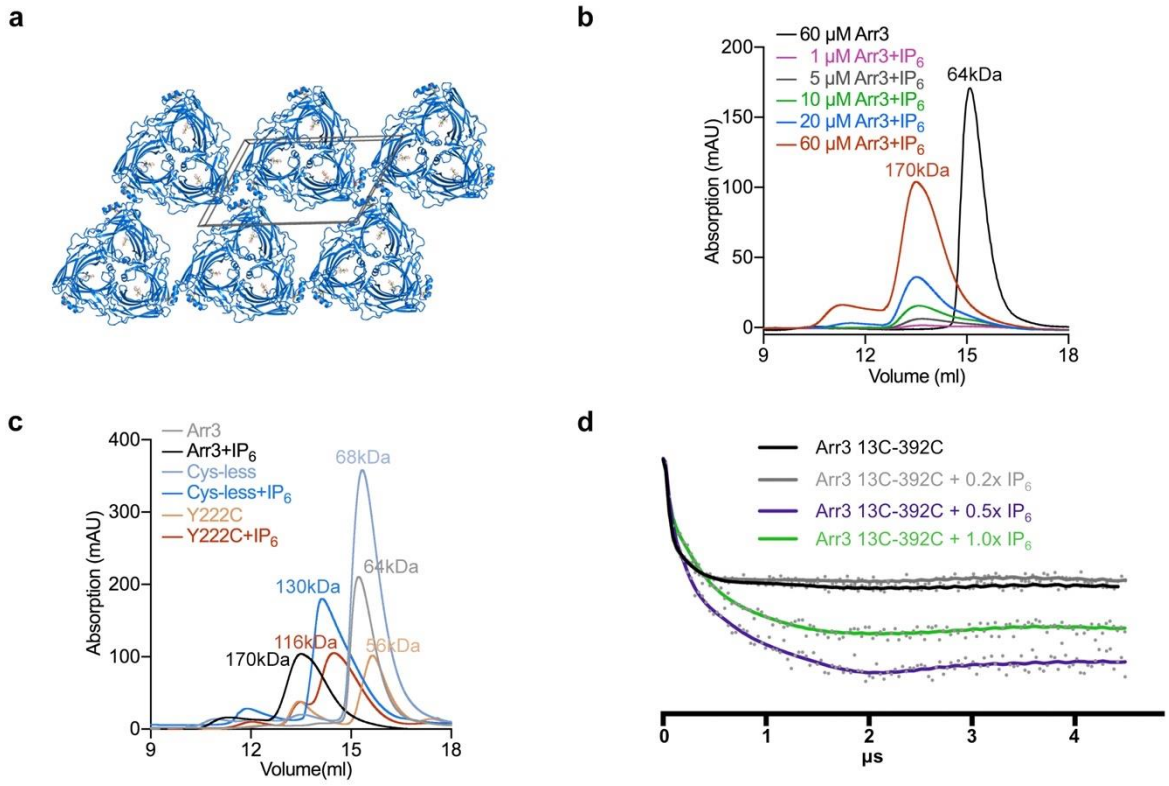

Fig. 4.5. Evaluation of trimerization upon IP_6 binding to arrestin-3. (**a**) Packing of the arrestin-3 trimer into the crystal lattice. The unit cell is delineated with black lines. The crystal contacts are at non-functional regions of arrestin-3. Moreover, there is limited surface area involved in the crystal contacts. Together, this suggests that crystal packing does not influence trimer formation. (**b**) SEC of wild-type arrestin-3 on a 24-mL Superdex S-200 increase column in buffer containing 100 μM IP_6 shows trimer formation in all arrestin-3 concentrations tested. The lowest concentration is 1μM arrestin-3, and is associated with a 2 mAu change in absorbance. (**c**) SEC of wild-type and Cys-less variants of arrestin-3 show that IP_6 addition to the Cys-less variants results in a loss of the high molecular weight peak that corresponds to the IP_6-dependent trimer. A shift is still observed, corresponding to a lower predicted molecular mass. (**d**) Background corrected dipolar evolution Q-band DEER data (dots) and the resulting fits (solid line) to the data using the LongDistances algorithms and software.

Using analytical ultracentrifugation, we found that the addition of IP_6 to purified arrestin-3 converts the observed molar mass from 43 ± 1 kD (monomer) to 134 ± 5 kD (trimer) (**Fig. 4.6a, b**). Size exclusion chromatography (Fig. 4.5c) is also consistent with IP_6-dependent trimerization of arrestin-3. We then explored the effect of arrestin-3 concentration on IP_6- dependent trimerization and found that the trimer is stable at the lowest arrestin-3 concentration detectable by our instruments (~1 μM).

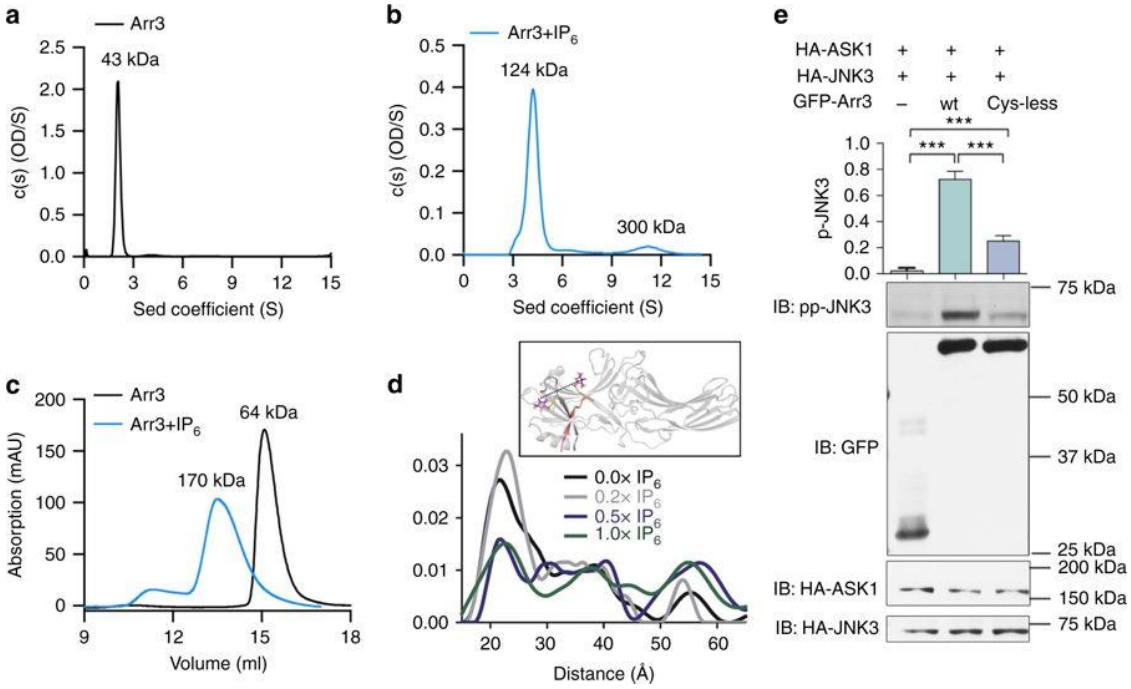

Fig. 4.6. IP_6 mediated trimerization and receptor-independent activation in cells. (a-b) Sedimentation velocity analytical ultracentrifugation (SVAUC) of arrestin-3. Measurements were performed in triplicate. a Representative SVAUC run in the absence of IP_6 predicts a molecular weight matching a monomer. **(b)** In the presence of 100 μM IP_6, the predicted molecular weight is consistent with a trimer. **(c)** Representative size exclusion chromatograms of arrestin-3 (Arr3) in the presence and absence of IP_6. In the absence of IP_6, 60 μM arrestin-3 (black) elutes at volume corresponding to the Stokes radius of a globular protein with a molecular mass of 64 ± 5.9 kDa. In the presence of 100 μM IP_6, the elution volume is consistent with a globular protein of molecular mass 169.6 ± 9.7 kDa. The ratio of these molecular weights is consistent with IP_6-dependent trimer formation. Measurements were performed in triplicate, errors are ± SEM. **(d)** Plot of the probability of the distances between spin labels at S13 and A392 for 100 μM arrestin-3 in the presence of the indicated molar ratios of IP_6; inset shows the location of the spin labeled sites in basal arrestin-3 (PDB entry 3P2D (92)). **(e)** Comparison of JNK3 activation by GFP-arrestin-3 and Cys-less mutant. GFP-tagged arrestin allowed comparison of the expression levels of wild-type and variant arrestin-3, as described (96,114). JNK3 activation (mean ± SEM) was assessed by measuring the pp-JNK3 levels in COS7 cells co-transfected with HA-ASK1, HA-JNK3 and GFP or Venus- tagged wild-type and Cys-less arrestin-3. Assay was repeated five times and JNK3 phosphorylation was compared by one-way ANOVA followed by Bonferroni post hoc test with correction for multiple comparisons. ***$p < 0.001$

We next assessed whether trimerization contributes to receptor-independent activation in cells using a trimerization deficient arrestin-3 variant. To design a trimerization deficient variant, we identified residues that are surface exposed in basal (monomeric) arrestin-3, buried in the trimer interface, and not associated with known biochemical functions of arrestin. This suggested Cys17 as a candidate side chain for targeting. We used a fully Cys-less variant of arrestin-3 because it has previously been shown to bind receptors normally (33). This indicates that the Cys-less variant is folded and rules out many alternative interpretations of any results.

We first assessed whether the Cys-less variant lost the ability to form trimers, using size exclusion chromatography. We found that the Cys-less variant does not form stable trimers in response to IP_6 but appears to shift to a molecular weight consistent with a dimer (**Fig. 4.5d**). Comparing the arrestin-3 trimer to the arrestin-2 oligomers suggests that while the trimer can stabilize the inter-domain twist (**Fig. 4.1a, b**), other arrestin oligomers cannot. This makes Cys-less arrestin-3 suitable for measuring how trimerization impacts receptor-independent signaling.

To quantify IP_6-dependent activation of Cys-less arrestin-3 in vitro, we employed double electron electron resonance (DEER) spectroscopy. One of the hallmarks of arrestin activation is the displacement of the C-tail from the N-domain upon the binding of phosphates to the phosphate sensor. We monitored this process via attached spin labels to cysteines replacing Ser13 in the N-domain and Ala392 in the C-tail. At these positions, the spin labels are separated by 22 Å in basal arrestin-3, when the C-tail is bound to the N-domain. Upon arrestin activation and C-tail release, these convert to a wide distribution of longer inter-spin distances. After titration with IP_6, we found that only ~ 30% of the 22 Å distance converted

to longer distances (**Fig. 4.6d, Fig. 4.5e**), a ~ 70% loss in IP_6-dependent activation. Cys-less arrestin-3 was reported to exhibit nearly 100% release of the C-tail in response to phosphorhodopsin in the same assay, which rules out the possibility that Cys-less arrestin-3 is signaling deficient.

We then compared the ability of wild-type and Cys-less arrestin-3 to mediate receptor-independent JNK3 activation in cells. We observed a 65% reduction in JNK3 activation in cells expressing the Cys-less mutant as compared to wild-type arrestin-3 (**Fig. 4.6e**). This correlates with the loss of IP_6-dependent activation measured by DEER.

Our observed trimer contrasts with reported multi angle laser light scattering (MALLS) of IP_6-bound arrestin-3, which were explained by a dimer (115). To investigate this discrepancy, we evaluated differences in the experimental design and identified that a protease inhibitor, benzamidine, used in the MALLS studies induces heterogeneous oligomerization, with oligomers having an average molecular weight consistent with a dimer. As benzamidine is not present in cells, it is likely that these oligomers are non-physiological.

The phosphate and activation sensors are intimately linked. With the phosphates of IP_6 apparently triggering the phosphate sensor and trimerization likely triggering the activation sensor, we wanted to explore the relationship between IP_6-binding and trimerization. Since IP_6 molecules mediate trimer formation, we propose that IP_6-binding and trimerization are intertwined. This would suggest that triggering the phosphate and activation sensors are linked during receptor-independent arrestin-3 activation.

To test this, we first evaluated the ability of the ΔN_{IP6} and ΔC_{IP6} variants of arrestin-3 to form IP_6-dependent trimers. As described above, the IP_6-binding sites are altered by mutagenesis in these variants, and receptor-independent JNK3 activation in cells is

compromised (**Fig. 4.1f**). Size exclusion chromatography showed that these variants no longer trimerize in the presence of IP_6, instead exhibiting mobility consistent with a monomer.

We next tested how loss of trimerization impacts IP_6 affinity using MST. The Cys-less variant is a valuable tool for this measurement because trimerization is disrupted; however, our experimental design used a maleamide-conjugated fluoro- phore, which interacts with cysteines. Thus, we re-introduced a cysteine residue to allow labeling. The T222C variant was considered suitable for this purpose because T222 is distal from all characterized functional regions. This mutant is also monodisperse, consistent with correct folding (**Fig. 4.5c**). When compared to wild-type arrestin-3 (K_D = 57 nM and 90 μM; **Fig. 4.2e**), the T222C-Cys-less variant shows substantially reduced IP_6 binding affinity (K_D = 1.1 μM and 1.2 mM, **Fig. 4.7b**), consistent with trimerization contributing to IP_6 affinity.

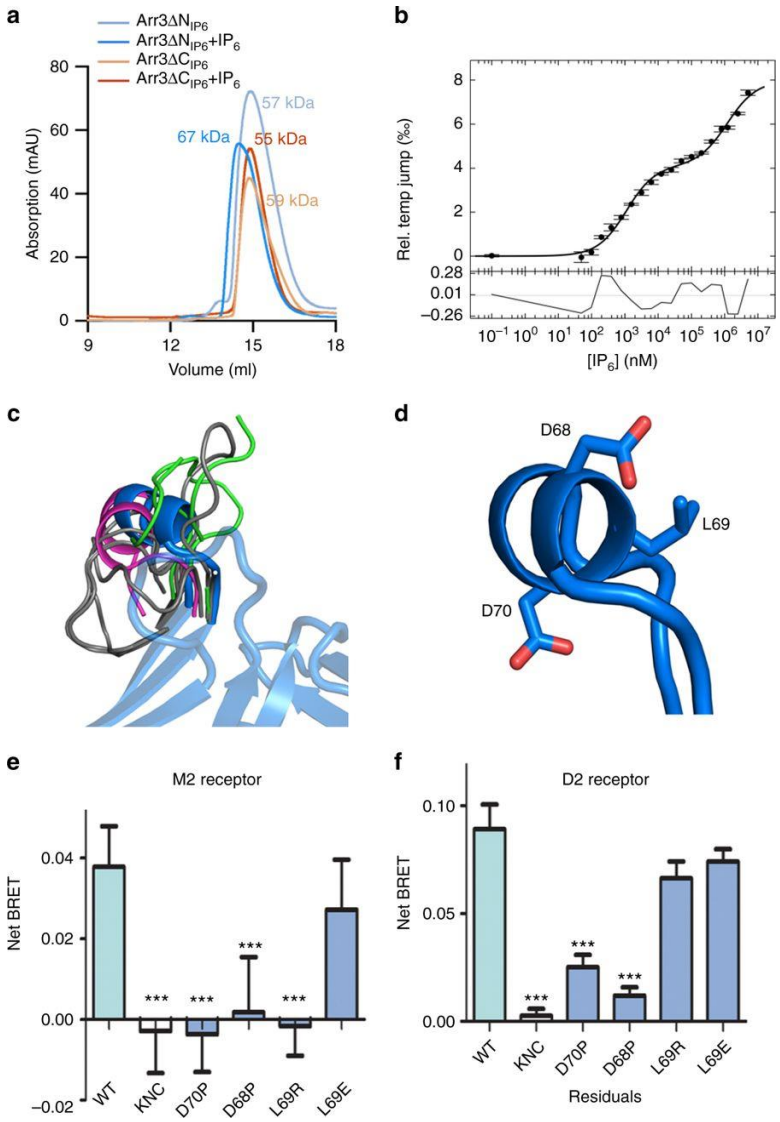

Fig. 4.7. The interplay between phosphate and activation sensors in receptor-independent and receptor-dependent signaling. (a) Size exclusion chromatography (SEC) of the ΔN_{IP6} and ΔC_{IP6} mutants measured on a Superdex S200 Increase 10/300 GL column (24 mL). Arrestin-3 (1–393) runs anomalously on size exclusion chromatography, but exhibits a characteristic shift in molecular weight upon the addition of IP_6. In the absence of IP_6, both the ΔN_{IP6} and the ΔC_{IP6} mutants are monodisperse and have a similar elution volume to wild-type, but in the presence of IP_6, no mobility shift is observed. **(b)** Temperature-jump binding curve for the Cys-less-T222C arrestin-3. **(c)** Overlay of finger loop of arrestin structures. Basal (gray): PDB entries 1CF1(109), 1JSY(116), 1ZSH(103), 3P2D(92), 1G4M(91); active (green): PDB entries 4ZRG(95), 4JQI(101), 4J2Q(37). Bound to receptor (magenta): 4ZWJ(25). Bound to IP_6 (blue) **(d)** The conserved motif EDL/(I)D folds into an α-helix. **(e,f)** Evaluation of mean binding ± SEM of wild-type and mutant Venus-arrestin-3 binding to the luciferase- tagged e M2 muscarinic or f D2 dopamine receptor by BRET. In arrestin-3-KNC (K11A, K12A, L49A, D51A, R52A, L69A, Y239A, D241A, C252A, P253A, D260A and Q262A), two key phosphate-binding lysines and 10 residues that bind other parts of the receptor were mutated to alanines. This precludes GPCR binding as described (105,117), making this an appropriate negative control. Data from three experiments were compared to wild-type by one-way ANOVA. ***$p \leq 0.001$

Collectively, these data strongly suggest IP_6-binding and trimerization work together to support receptor-independent arrestin-3 activation of JNK3. Because IP_6 appears to directly bind the phosphate sensor, and trimerization appears to stabilize a triggered activation sensor, we conclude that during receptor- independent activation, triggering of these sensors is intimately linked. This mirrors the observed synergy of these two sensors in receptor-dependent signaling (27).

Arrestin-3 sensors in broad receptor selectivity. There are >800 GPCRs, but only two non-visual arrestins (arrestin-2 and arrestin-3) that recognize the phosphorylated and activated forms of these receptors; arrestin-3 also recognizes non-receptor activators. Intuitively, the mechanism of broad receptor specificity of the phosphate sensor is straightforward, as the N-domain of arrestin can bind receptor-attached phosphates with the correct spacing. In contrast, it is less clear how the activation sensor might recognize this large number of receptors.

If our assignment of the finger loop as a part of the activation sensor is correct, this element must interact with the hydrophobic pocket on >800 GPCRs with limited sequence similarity. We therefore analyzed the finger loop to identify properties that could contribute to broad receptor recognition. An overlay of available arrestin structures suggests that the finger loop is on a flexible tether (**Fig. 4.7c**) and can be presented at many angles to an interaction partner. This could allow the finger loop to adapt to the different hydrophobic pockets on receptors. If so, the helicity, hydrophobicity, and flexibility of the finger loop would be predicted to contribute to the broad receptor specificity of the activation sensor. Hence, perturbation of these properties would reduce activation sensor-dependent receptor binding. We therefore designed mutations (**Fig. 4.7d**) that introduced (a) a helix- breaking

proline (D68P), (b) a flexibility-reducing proline terminating the helix (D70P), or (c) a charge within the hydrophobic region (L69E/R). Modeling based on available structures suggests that neither introduced proline should directly interact with the receptor.

We measured the binding of these variants to M2 muscarinic and D2 dopamine receptors, which we selected because they are more dependent upon the activation sensor than on receptor- attached phosphates for arrestin binding (114). We used a bioluminescence resonance energy transfer (BRET) assay in COS7 cells cotransfected with luciferase-tagged receptors and Venus-tagged arrestin-3 (96) (**Fig. 4.7e, f, Fig. 4.8a, b**). Wild-type arrestin-3 shows a robust increase in BRET signal upon agonist stimulation, whereas arrestin-3-KNC (a negative control with 12 substitutions of key receptor-binding residues that binds poorly to receptors (96)) does not (114,117). Mutants designed to perturb helix formation or flexibility had substantially reduced binding to both receptors (**Fig. 4.7e, f**). Interestingly, charged residues had different effects on binding to the M2 and D2 receptors. This variability may reflect the presence or absence of complementary charges in the inter-helical cavity of different GPCRs, or the strength of other interactions between receptor and arrestin-3.

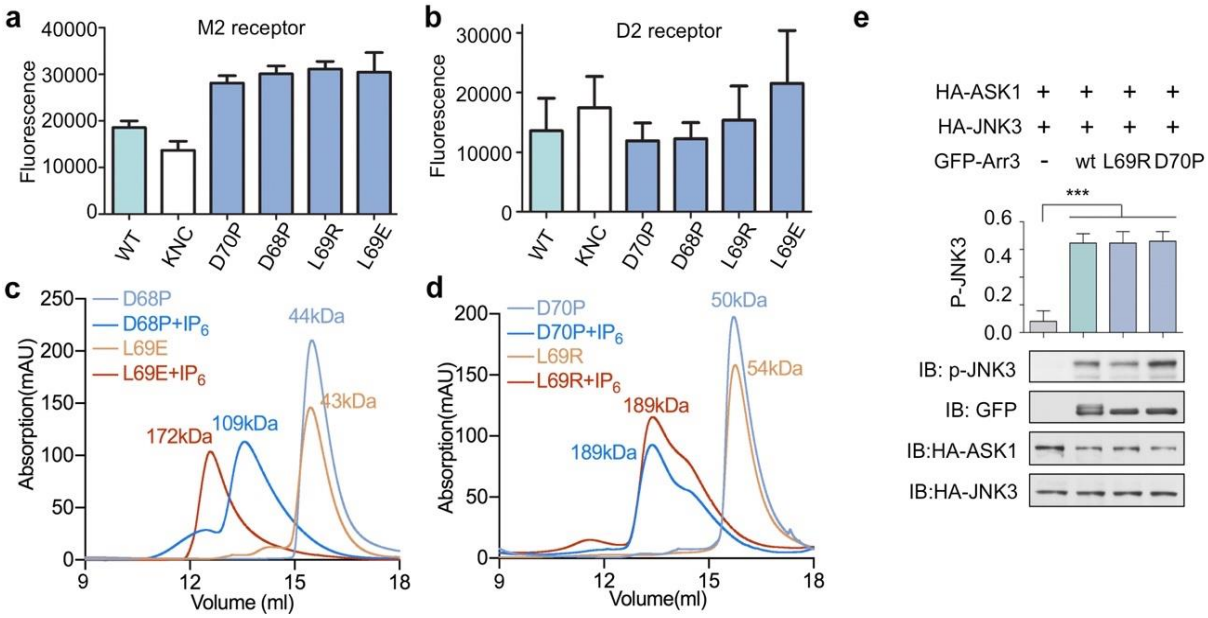

Fig. 4.8. Role of the finger loop in arrestin-3 activation. (**a**) – (**b**) Expression of Venus-arrestin-3 variants in the BRET assays measured by fluorescence before agonist addition (λ_{ex}=500 nm, λ_{em}=535 nm) (n=3). (**c**) – (**d**) Size exclusion chromatograms of arrestin-3 finger loop variants in the presence and absence of IP_6 show that L69E exhibits an IP_6-dependent conversion to a high molecular weight species similar in elution volume to the wild-type trimer, L69R and D70P can convert to a high molecular weight species, but this conversion is incomplete, and D68P still shifts in molecular weight, but the shift is not consistent with the molecular weight of a trimer and more similar to a dimer. (**e**) Comparison of JNK3 activation by wild type arrestin-3 and the L69R and D70P finger loop mutants. JNK3 activation was assessed by measuring the phospho-JNK3 level in COS7 cells co-transfected with HA-ASK1, HA-JNK3 and either GFP, Venus-tagged wild type arrestin-3, or the Venus-tagged arrestin-3 loop mutants. The data are from four independent experiments. The JNK3 phosphorylation was compared using one-way ANOVA followed by Bonferroni post hoc test with correction for multiple comparison. ***, $p<0.001$ to GFP. There were no significant differences between either of the mutants and wild-type arrestin-3.

As the finger loop is also a major contact for IP_6-dependent arrestin-3 trimerization, we tested if finger loop variants affect receptor-independent activation and signaling. Alteration of the finger loop prevented IP_6-dependent trimerization of the D68P variant, reduced trimerization of the L69R and D70P mutations, and had no detectable impact in the L69E variant (**Fig. 4.8c, d**). JNK3 activation in cells was not affected in the D69R and D70P mutations (**Fig. 4.8e**). One interpretation of this finding is that IP_6-induced arrestin-3 activation is more dependent upon the phosphate sensor than the activation sensor, a property shared with many GPCRs (114). However, given our data suggesting that triggering the phosphate and activation sensors during receptor-independent activation is closely linked, it is more likely that the finger loop of our variants is presented in a way that allows trimerization.

Switch regions in arrestin-mediated signaling. A major functional consequence of non-visual arrestin activation is the engagement of downstream effectors, yet how activated arrestin supports signaling has never been explained. In the IP_6-activated arrestin-3 structure we identified structural changes in known effector binding elements that may promote signal initiation. Activation-induced conformational changes in these regions have not been previously reported, although inspection of the coordinates for the active arrestin-1 and arrestin-2 indicates that similar changes accompany activation of other arrestins (25,37,101). We suggest that these conformational changes act as molecular switches functionally analogous to the switch regions of G proteins, and therefore term these “arrestin switch” regions. In conjunction with the inter-domain twist, these conformational changes would create effector-binding sites and turn on signaling when arrestin is activated.

Arrestin switch I (aSwI; residues 89–97; **Fig. 4.9a**) is strongly conserved in arrestin-3 homologs from other species, but not in the other three arrestin isoforms (**Fig. 4.9a, inset**). In arrestin-3, this nine amino acid segment contains seven prolines, including two PPXP motifs that may be recognized by SH3 domains (51,116). Comparison of the basal (92) and active conformations of aSwI reveals a maximal displacement of 5.8 Å and includes an unusual pair of tandem *cis* bonds (Pro94-Pro95 and Pro95-Arg96) in the best-fitting model. This rare structural feature is associated with conformational change (118,119). However, the electron density of this region is difficult to interpret, and not all residues could be modeled with confidence. The flexibility of this switch may be important for adapting to different effectors.

Arrestin switch II (aSwII; residues 176–191; **Fig. 4.9a**) contains two distinct parts: IIa (residues 176–183) and IIb (184–191). ASwIIa connects the N- and C-domain and has been proposed to act as a hinge between domains (120,121). ASwIIa also contains a polyproline motif (PQP residues 181–183) suggested as a non-canonical SH3 binding site in arrestin-2 (116). The aSwIIa shows a nearly identical conformation in all available active arrestin structures, but variable conformations in basal arrestins (**Fig. 4.9a, inset**).

ASwIIb includes the entirety of the first β-strand of the C-domain (residues 184–191) and superimposes in all active arrestin structures. As compared to most arrestins in the basal state, the β-strand of aSwII is register-shifted, which moves it one position in arrestin-2 and -3 and two positions in arrestin-1, although the active position of aSwIIb is observed in one crystal form of basal arrestin-2 (103,116). Register-shifted β-strands are unusual, but have proposed roles in regulating signaling (122,123)and forming protein binding sites (124).

Arrestin switch III (aSwIII, residues 307–316; **Fig. 4.9a**) is an extension of the lariat

loop (109), which is a part of the polar core that stabilizes the orientation of the two domains in the basal state. ASwIII becomes disordered in both activated arrestin-3 and arrestin-2 (101), a property commonly associated with the ability to mediate protein-protein interactions (125,126).

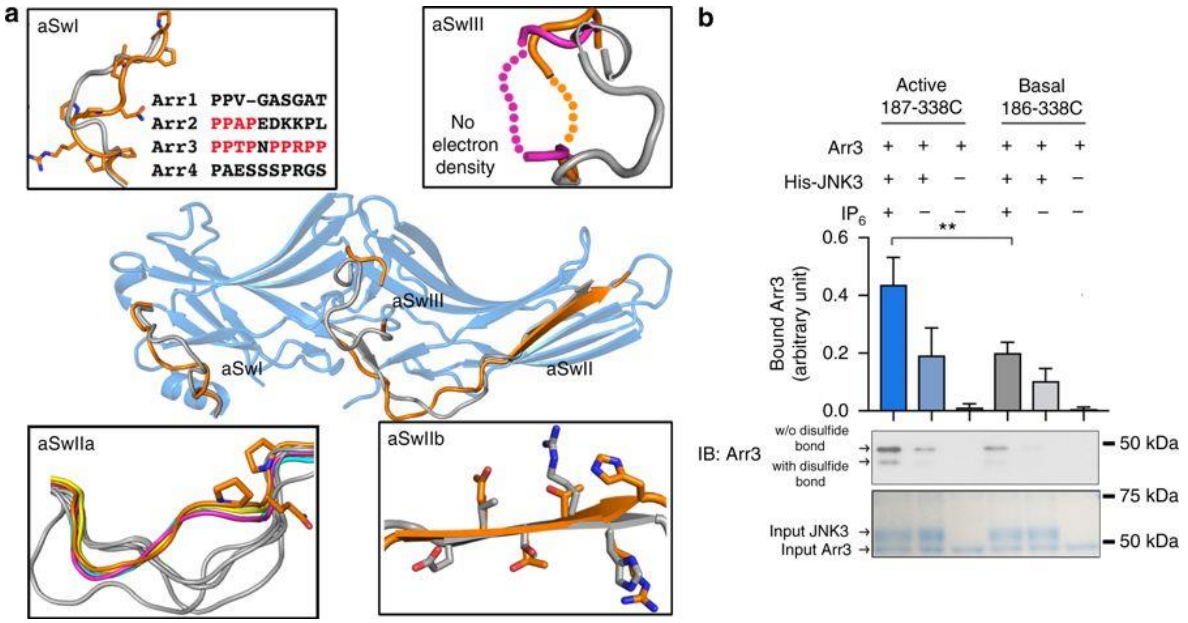

Fig. 4.9. Arrestin switch regions. (a) Conformations of the arrestin switch regions in the active form (orange (IP_6-activated arrestin-3 (Arr3)), magenta (phosphopeptide-activated arrestin-2; PDB 4JQI (101)), cyan (rhodopsin-activated arrestin-1; (PDB 4ZWJ (25))), yellow (p44; PDB 4J2Q (37)) differ from those in basal arrestin-3 (gray, PDB 3P2D (92)). Insets highlight switch regions. In the inset showing aSwI, the sequences in four bovine arrestin isoforms are shown. **(b)** Quantitation of arrestin-3 binding to His_6-JNK3 in the presence and absence of IP_6 (100 μM), monitored using an in vitro pull-down assay. JNK3 was immobilized on Ni^{2+} resin, exposed to arrestin-3 (with disulfides stabilizing active or basal aSwIIb), washed, then eluted in sample buffer and visualized by SDS-PAGE and Western. Disulfide trapped arrestin-3 (red box) was quantified separately by densitometry and the ratio was calculated (means ± SEM). $^{**}p \leq 0.01$. The overall amount was normalized by the ratio of disulfide trapped arrestin (**Fig. 4.8**).

Using the same terminology, the arrestin C-tail may be considered aSwIV. In basal arrestins, the C-tail is anchored to the N-domain (91,92,109,110,116). Receptor binding induces release of the C-tail, which becomes unstructured (30,33,127). The binding sites for clathrin (7) and clathrin adapter AP-2 (7) are localized in the C-tail of non-visual

arrestins, and both become fully accessible upon C-tail release (47).

To test the role of the switch regions, we focused on aSwIIb, and used disulfide trapping to stabilize the register-shifted β-strand. We used the Cys-less arrestin-3 as background to avoid unintended disulfide bonds with native cysteines. We introduced a cysteine at position 338 and either position 186 (stabilizing the basal conformation), or position 187 (stabilizing the active conformation). Electrophoretic mobility suggests that disulfides formed at statistically identical levels in these variants.

We then assessed the binding of each of these disulfide- stabilized versions of arrestin-3 to JNK3. In the presence of IP_6, column-immobilized JNK3 exhibits increased binding to arrestin- 3 with aSwII trapped in the active conformation (**Fig. 4.9b**). In the absence of IP_6, the binding is lower for both variants, suggesting that the disulfide-trapped aSwII does not fully shift the arrestin equilibrium to an active state in the absence of IP_6.

4.3 Discussion

We used IP_6-bound arrestin-3 to identify the structural requirements for receptor-independent arrestin activation, and to suggest how activation results in arrestin-mediated signaling. These data inform on several aspects of arrestin activation that have been enigmatic: how an arrestin can interact with many disparate receptor and non-receptor activators, adopt an active conformation, then initiate a variety of downstream signaling pathways.

Arrestin-3 is activated by >800 GPCRs plus non-receptor activators, including IP_6. When coupling to receptors, arrestin acts as a coincidence detector that binds with high affinity to phosphorylated and activated receptors, as mediated by two independent sensors. We show that the IP_6 triggers the same two sensors. Indeed, the binding site for IP_6 sterically

overlaps with the binding site for receptor-attached phosphates (**Fig. 4.1c, d**). Similarly, the surface of the finger loop that interacts with the hydrophobic pocket of receptor also interacts with sister protomers in the trimer (25,108) (**Fig. 4.3c, d**). Because the same surfaces support receptor-independent trimerization and receptor binding, receptor-dependent and receptor-independent arrestin-3 activation appear to be mutually exclusive, i.e., the trimer does not bind receptors. The use of the same sensors and surfaces for trimerization and receptor binding also suggests that receptor-dependent and receptor-independent arrestin activation occur via a similar mechanism.

Structurally, arrestin activation involves several conformational rearrangements. First, negatively charged phosphates bind to the N-domain, displacing the C-tail and disrupting the polar core (101). Our data and previous reports suggest the disruption of the polar core by phosphate binding is a hallmark of a triggered phosphate sensor (36,109,128). Second, a hydrophobic environment induces the external presentation of hydrophobic residues of the finger loop on the central crest of the arrestin molecule, which folds into a short α-helix (25,108). Our data suggest that this helical finger loop is a hallmark of the triggered activation sensor. Finally, both receptor-dependent and receptor-independent arrestin activation induce an inter-domain twist in IP_6-bound arrestin-3 (**Fig. 4.1b**) and all other activated arrestin structures (25,37,101,129).

Molecular mechanisms connecting the phosphate and activation sensors to the domain twist have not been proposed. Our data suggest that each sensor acts via a distinct pathway. Triggering the phosphate sensor likely facilitates the inter-domain rotation in two ways. First, IP_6 phosphates bind Lys295 on the lariat loop (**Fig. 4.3a**). This changes the loop position, removing two negative charges from the polar core (**Fig. 4.3a, b**). Second, IP_6 directly

displaces the C-tail, which contributes Arg393 to the polar core (**Fig. 4.3b**). Both changes break the polar core, making domain rotation possible.

Triggering the activation sensor likely promotes inter-domain rotation by a complementary mechanism. An interaction between the finger loop and a hydrophobic environment can induce helix formation. The finger loop is part of the N-domain, but in basal arrestin, the hydrophobic residues are shielded from solvent via an interaction with a loop in the C-domain (residues 243–247, **Fig. 4.10a, b**). Activation-associated rearrangement of the finger loop alters this hydrophobic core, so that the β-strands surrounding the finger loop in the basal state shift in a manner promoting the domain rotation (**Fig. 4.10a**).

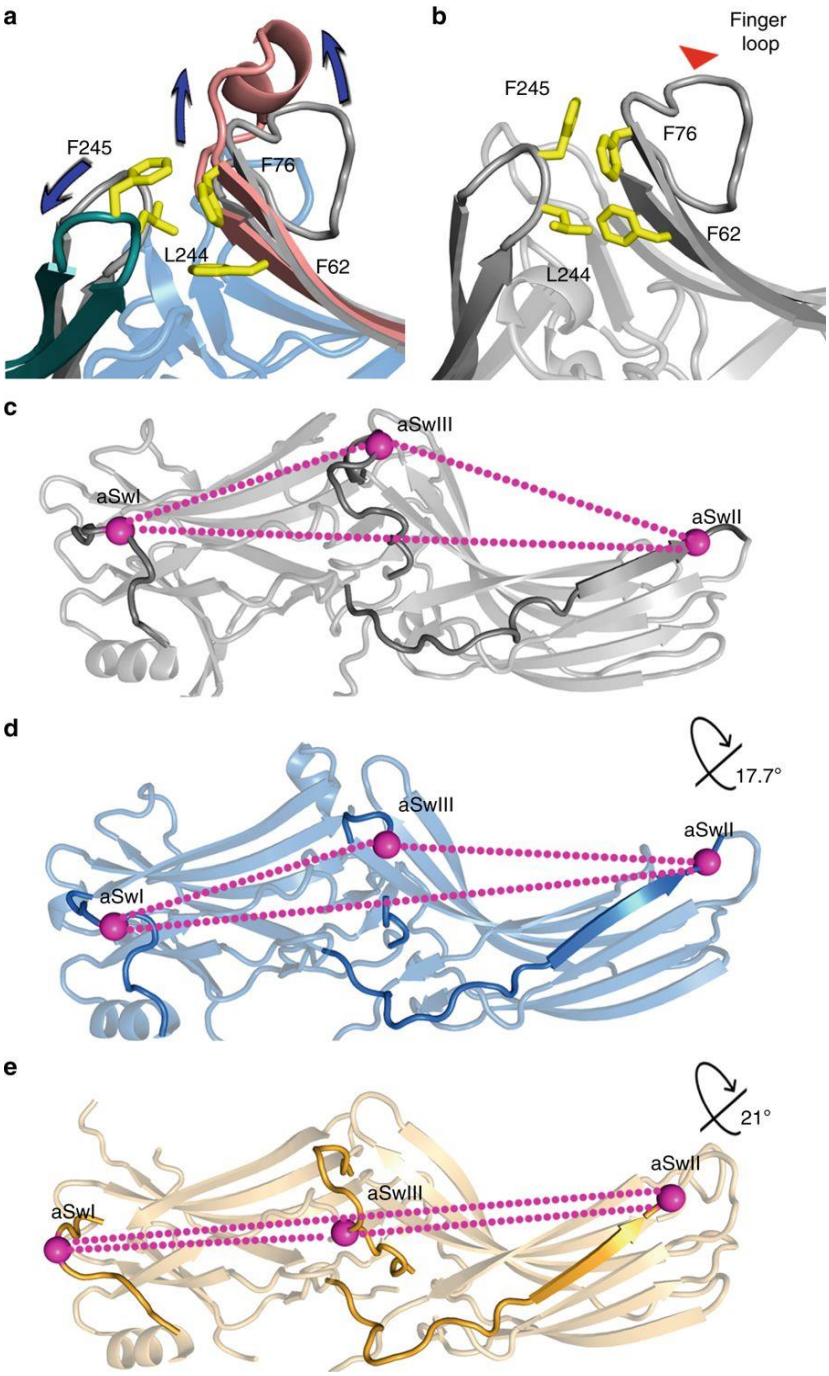

Fig. 4.10. Mechanisms of arrestin activation and domain rotation. (a) Overlay of the hydrophobic core between β-strands supporting the finger loop (pink) and the C-loop (green) in the active arrestin-3 and in the basal arrestin-3 (gray, PDB 3P2D (92)). **(b)** Conformation of hydrophobic core between β-strands surrounding the finger loop and the C-loop in the basal arrestin-3 (PDB 3P2D (92)). **(c-e)** The inter-domain twist realigns the arrestin switch regions. In each panel, the switch regions are darker elements; magenta balls mark equivalent residues. c Basal arrestin-3 (PDB 3P2D (92)). d IP_6-activated arrestin-3 with a 17.7° inter-domain rotation. e p44 arrestin-1 (PDB 4J2Q (37)) with a 21° inter-domain rotation

Based on this model, we propose how arrestins have achieved an inter-domain twist in reported structures. Our analysis suggests that in the IP_6-bound arrestin-3, a physiologically relevant activator triggers both sensors, which appear to be highly interdependent. During receptor-induced activation, the sensors may act more independently, with some GPCRs relying more heavily on one sensor (114). However, the two sensors likely act synergistically, as arrestins exhibit the highest binding when receptor is both activated and phosphorylated (27).

The comparison of IP_6-activated arrestin-3 and other active arrestin structures suggests a general model explaining how activated arrestins initiate and direct signaling. First, the inter-domain twist and the new positions of switches likely work in conjunction to form effector-binding sites. Because receptor- independent activation apparently biases signaling toward the JNK3 cascade (58,64,97-99), IP_6-activated arrestin-3 is the first case where the signaling bias can be correlated with the structure. The inspection of other active arrestin structures suggests an intriguing possible mechanism of signal bias. The inter-domain twist is of different magnitude in available active structures, consistent with the proposed ability of active arrestin to adopt a range of conformations (94,130,131). Moreover, conformations of the switch regions in our structure differ from those observed in other active arrestins. This ability to adopt a range of active conformations agrees with electron microscopy images of a chimeric β_2-adrenergic receptor with arrestin-2 (132), fluorescence quenching binding studies of rhodopsin-arrestin-1 (133) and NMR spectroscopy of rhodopsin-arrestin-1 (111), all of which suggest heterogeneity of the receptor-arrestin complex.

Conceivably, signaling toward different effectors can be directed by combining distinct conformations of the arrestin switch regions with different inter-domain rotation

angles (**Fig. 4.10c–e**). The magnitude of each conformational change likely depends on the identity of the activator. In case of GPCRs, the conformations may be further influenced by the phosphorylation pattern of the receptor (134,135). Structures of arrestin in complex with a range of activators, including receptors with different phosphorylation patterns, are required to test this idea.

4.4 Materials and Methods

Materials. DNA modifying enzymes were from New England Biolabs (Ipswich, MA). DNA purification kits were from Zymo Research (Irvine, CA). HEK293 and COS7 cells are from ATCC. Cell culture reagents and media were from Mediatech (Manassas, VA) or Invitrogen (Carlsbad, CA). The luciferase substrate coelenter- azine-*h* was from NanoLight (Pinetop, AZ). All other reagents were from Amresco (Solon, OH) or Sigma-Aldrich (St. Louis, MO).

Arrestin-3 expression and purification. Bovine arrestin-3 was cloned into the pTrcHisB vector (Invitrogen; Carlsbad, CA) with the codon for L394 mutagenized to a stop codon (TGA). This created a version of arrestin-3 truncated immediately after the C-tail attachment point (encoding residues 1–393 and deleting residues 394–408). This version of arrestin-3 has activation propensity indistinguishable from wild-type and was used to produce protein for the structure of the basal conformation of arrestin-3 (92). Because it has superior properties after purification, arrestin-3 (1–393) was used for the in vitro experiments in the manuscript, except for a subset of the replicates that tested the effects of benzamidine. Only for these benzamidine experiments, one of the replicates arrestin-3 with a stop codon introduced at position R393. This variant of arrestin (1–392) is more easily activated.

Experiments in cells used full-length arrestin-3 (1–408).

The pTrcHisB plasmid containing arrestin-3 (1–393) was transformed into E. coli BL21 Gold and grown in 1 L cultures in LB medium supplemented with 100 mg/L ampicillin. Cells were grown at 30 °C overnight with shaking at 250 r.p.m., then protein expression was induced with the addition of 35 μM IPTG for 4 h. Cells were collected by centrifugation and the pellet was stored at −80 °C.

Arrestin-3 was purified using a modification of a previously described protocol (136). Briefly, cell pellets were resuspended in buffer containing 50 mM MOPS, pH 7.2, 5 mM EGTA, 2 mM tris-(2-carboxyethyl) phosphine (TCEP), and two protease inhibitor cocktail tablets (Sigma). Cells were disrupted by sonication at 4 °C. The lysate was clarified by centrifugation at 20,800×g (SLA 3000 rotor, RC- 5B Plus centrifuge) for 60 min, and arrestin was precipitated by the addition of $(NH_4)_2SO_4$ to a final concentration 0.32 mg/mL. Precipitated arrestin-3 was collected by centrifugation at 20,800×g (SLA 3000 rotor, RC-5B Plus centrifuge) for 90 min, and dissolved in buffer containing 10 mM MOPS pH 7.2, 2 mM EGTA, and 1 mM TCEP, then centrifuged again at 20,800×g (SLA 3000 rotor, RC-5B Plus centrifuge) for 60 min to remove particulates. The supernatant containing soluble arrestin-3 was applied onto a heparin column and eluted with a linear NaCl gradient. Fractions containing arrestin-3 were identified by SDS-PAGE and Western and combined. The salt concentration of the pooled fractions was adjusted to 100 mM, and the solution was loaded onto a linked HiTrap Q HP (GE healthcare) and HiTrap SP HP (GE healthcare) column. At a NaCl concentration of 100 mM, arrestin-3 flows through the Q column (while most contaminants bind) but binds the SP column. The columns were uncoupled and a linear NaCl gradient was used to elute arrestin-3 from the SP column. The fractions containing arrestin-3

were identified by SDS-PAGE and combined, concentrated with a 30 kDa cutoff concentrator, then further purified using a Superdex 200 increase 10/ 300 GL column (GE healthcare) equilibrated with 20 mM MOPS pH 7.2, 150 mM NaCl, and 2 mM TCEP. Folding and trimerization were monitored by size exclusion chromatography.

Crystallography. Purified arrestin-3 (residues 1–393) was concentrated to 5 mg/ mL and incubated with IP_6 at 1:20 molar ratio for 30 min on ice. Crystals in the hexagonal space group $P6_3$ were grown using the sitting drop vapor diffusion method by combining 2 µl of arrestin-3-IP_6 and 2 µl of reservoir solution (100 mM Succinate/Phosphate/Glycine pH 8.5 and 25% PEG 1500). Microcrystals appeared within 24 h and were used for seeding. Crystals were harvested after 7 days, cryoprotected in 50% w/v glycerol and cryocooled by plunging into liquid nitrogen.

Diffraction data (Table 4.1) were collected at the Advanced Photon Source LS- CAT beamline 21-ID-D. Data were processed using HKL2000 (137). The structure was determined by molecular replacement in PHASER (138) using isolated domains of a pruned version of arrestin-2 (PDB entry 1G4M (91)) as the search model. The best solution was associated with an initial R/R_{free} of 0.34/0.37 and was improved by model building in COOT (139) and refinement in PHENIX (140). The myoD conformation of IP_6 was placed into difference electron density manually using the conformation found in PDB entry 4HNW. Figures were prepared in PYMOL.

JNK3 activation measurements in HEK293 and COS7 cells. HA-tagged ASK1 and Flag-tagged JNK3 were co-transfected with either: (1) empty vector; (2) wild- type arrestin-3 (residues 1–408); or the indicated arrestin-3 mutants (residues 1–408). Lipofectamine2000 (Thermo Fisher) was used for transfection. After 48- hours, cells were incubated with

phosphatase inhibitors (50 mM NaF and 10 mM Na_3VO_4) in PBS for 15 min at 37 °C and lysed with lysis buffer containing 50 mM Tris pH7.8, 2 mM EDTA, 250 mM NaCl, 10% glycerol, 0.5% NP-50, 20 mM NaF, 1 mM Na_3VO_4, 1 mM phenylmethanesulfonyl fluoride (PMSF) and 2 mM benzamidine. Sonication was used to further lyse the cells (60 Sonic Dismembrator, Fisher Scientific). The whole cell lysate was centrifuged at 10,000×*g* for 15 min and the supernatant was used for Western analysis. Activation of JNK3 was assessed using a phospho-JNK specific antibody (Cell Signaling #9251, 1:1000 dilution). The expression level of HA-ASK1, Flag-JNK3 and arrestin-3 were assessed by Western analysis using antibodies against the HA tag (Cell Signaling #C29F4, 1:1000 dilu- tion), the Flag tag (Sigma #F3165, 1:500 dilution), arrestin (F4C1)(141) or GFP (JL-8, Choltech #632381, 1:2000 dilution), respectively. The results were quantified using VersaDoc and QuantityOne software (Bio-Rad).

DEER distance measurements. Cysteine substitutions of Ser13 and Ala392 were introduced into otherwise Cys-less arrestin-3 (residues 1–393). This variant was purified and spin-labeled with MTSL, as described previously (142). Double electron electron resonance (DEER) spectroscopy data were collected using a Bruker E580 operating at Q-band and equipped with an EN5107D2 resonator. Samples contained 20% deuterated glycerol as a cryoprotectant and 100 μM protein with varying amounts of IP_6 were run at 80 K following flash freezing in a dry ice and acetone mixture. Acquired raw dipolar evolution data were phase and background corrected, plotted and analyzed for distance distributions in the same way for each data set using the algorithms included in the LongDistances software program (143) written by C. Altenbach (University of California-Los Angeles, CA). The upper reliable distance limit of 65 Å was determined based on the maximum data col- lection time (t = 4.5

μs) of the DEER experiments according to the equation $d \approx 5$ (t/2)1/3 (144) and is reflected in the *x*-axis of the distance distribution plot. The release of the C-tail causes the distances to spread out and possibly become longer than the observable range of our data.

Microscale thermophoresis. Microscale thermophoresis (MST) was conducted using a NT.115 MST instrument (NanoTemper Technologies GmbH) equipped with green and blue filter sets. All arrestin-3 variants (residues 1–393; 20 μM in MST buffer (20 mM 3-morpholinopropane-1-sulfonic acid (MOPS) pH 7.5, 150 mM NaCl, and 1 mM TCEP) were labeled by adding 200 μL of 20 μM arrestin-3 to 1 μL of 40 mM Alexa Fluor C5 maleimide dye (final dye concentration, 200 μM; Molecular Probes, Eugene, OR) in DMSO and incubating the mixture at room temperature in the dark for 30 min. Free dye was separated from the protein-dye conjugate using a PD10 G25 column (GE Healthcare Bio-Sciences, Piscataway, NJ) equilibrated in MST buffer. Lauryl maltose neopentyl glycol (MNG-3; Anatrace, Maumee, OH) at 1% (w/v) in all solutions prevented the adherence of protein to the plasticware. The labeling stoichiometry was 0.95–2.0 dye molecules per arrestin-3 as estimated by spectrophotometry.

Titrations were usually accomplished by preparing 15 samples of IP_6 in a 1:1 dilution scheme. A sixteenth sample with no IP_6 established the baseline fluorescence or temperature jump. Labeled arrestin-3 (50 nM) and the reaction mixtures were equilibrated for 45 min then loaded into premium coated capillary tubes (NanoTemper). Data were acquired using 40% MST and 50% LED settings. A 5 s pre-IR phase was recorded, followed by a 60 sec phase with the IR laser on and a 5 s post-IR phase. In the case of the wild-type arrestin-3 construct, the pre-IR fluorescence varied strongly (~ 30% difference between the maximum and minimum intensity values) as a function of IP_6 concentration, allowing this signal to be

analyzed directly. The temperature-jump methodology was used to analyze data from the ΔN_{IP6} or T222C variants (145). To prevent aggregation of the latter mutant, we included 0.5 mg/mL soybean trypsin inhibitor (Worthington Biochemical) in the MST buffer; this mutant also required an adjustment of the illumination protocol, featuring 75% LED power and an IR-on phase of only 30 s. Data were the average of at least two replicates. Data were analyzed in a version of PALMIST (145) modified to include two-site binding models (manuscript submitted). MST figures were rendered using GUSSI (146).

Analytical ultracentrifugation. Purified arrestin-3 (residues 1–393) with or without IP_6 (100 μM) was analyzed in an Optima XLI ultracentrifuge (Beckman Coulter, Brea, CA) equipped with a four-hole An-60 Ti rotor at 142,000×*g* at 4 °C. Samples were loaded into double-sector cells (path length of 1.2 cm) with charcoal- filled Epon centerpieces and sapphire windows. Sedfit (version 12.0) was used to analyze velocity scans using every scan from a total of between 250–300 scans (147). Approximate size distributions were determined for a confidence level of p = 0.95, a resolution of n = 300, and sedimentation coefficients between 0.1 and 15 S. The frictional ratio could float.

BRET measurements of arrestin-3 binding to receptors. Interactions between N-terminally Venus-tagged arrestin-3 (residues 1–408) and C-terminally RLuc8- tagged M2 muscarinic receptor or D2 dopamine receptor were determined by BRET, as described, using the highest (saturating) arrestin-3 concentrations (96). Absolute levels of luminescence were used as the measure of the expression levels of RLuc-tagged receptors, whereas direct fluorescence was used to determine the expression of Venus-tagged arrestins, as described (96). BRET was measured 15 min after the addition of 10 μM M2 agonist carbachol or 10 μM D2 agonist quinpirole, both of which were added along with 5 μM of the luciferase

substrate coelenterazine-h. Luminescence and fluorescence were measured using Infinite F500 multimode plate reader (Tecan). Net BRET was calculated as the difference between BRET signal in the presence and absence of agonist to determine the expression of Venus-tagged arrestins, as described (96). BRET was measured 15 min after the addition of 10 μM M2 agonist carbachol or 10 μM D2 agonist quinpirole, both of which were added in conjunction with 5 μM of the luciferase substrate coelenterazine-h. Luminescence and fluorescence were measured using Infinite F500 multimode plate reader (Tecan). Net BRET was calculated as the difference between BRET signal in the presence and absence of agonist.

JNK3 binding of arrestin-3 variants. His tagged JNK3α2 (10 μg) was incubated with Ni-NTA resin for 2 h and wild-type or disulfide-containing arrestin-3 (10 μg) was added to the mixture with and without 100 μM IP_6. The samples were washed with buffer (20 mM MOPS, pH 7.4, 150 mM NaCl, 25 mM imidazole) and eluted with 100 μl of the same buffer containing 250 mM imidazole. The eluate was methanol precipitated, and the JNK3 bound arrestin-3 (residues 1–393) was visualized by both Coomassie blue staining and Western blot, quantified using the QuantityOne software, and the data were analyzed using Prism. For the disulfide- linked bands, measurements were made in quadruplicate and one-way ANOVA was used to compare JNK3 binding to disulfide-containing arrestin-3.

CHAPTER 5

PEPTIDE MINI-SCAFFOLD FACILITATES JNK3 ACTIVATION IN CELLS

This article was published in Scientific Reports (4). Xuanzhi Zhan was the first author, and Henriette Stoy, Tamer Kaoud, **Nicole A. Perry,** Qiuyan Chen, Alejandro Perez, Sylvia Els-Heindl, Jack V. Slagis, T.M. Iverson, Annette G. Beck-Sickinger, Eugenia V. Gurevich, Kevin N. Dalby, and Vsevolod V. Gurevich contributed to this work. Specific contribution: MBP pull-down experiments.

5.1 Introduction

The spatial and temporal organization of proteins within a cell is critical for coordinating essential activities (148). Appropriate cellular response to external or internal stimuli often requires precise orchestration by scaffold proteins, which determine the specificity and precise time course of signaling. In particular, the specificity of signal transduction through mitogen activated protein kinase (MAPK) cascades is highly dependent on scaffold proteins (149-151). MAPK signaling is involved in the regulation of key cellular behaviors, from proliferation to differentiation and apoptotic death (151). The overall architecture of three-kinase MAPK cascades is conserved from yeast to mammals (152). Most cells have multiple MAPKs, MAPK kinases (MAPKKs), and MAPKK kinases (MAPKKKs), so signaling outcome is often determined by scaffolds organizing particular MAPKKK-MAPKK-MAPK complexes (62,149-151).

The c-Jun NH_2-terminal protein kinases (JNKs) belong to the MAPK family. JNKs regulate normal physiological processes of cell proliferation, apoptosis, differentiation, and

migration (153). JNKs were also implicated in many diseases, from cancer to neurological and immunological disorders (154-156). Full activation of all JNKs requires double phosphorylation of the T-X-Y motif in the activation loop by two upstream kinases, MKK4 (tyrosine) and MKK7 (threonine) (157). Similar to other MAPKs, JNK activation is dependent on scaffolding proteins, such as JIPs (158). Arrestins, which specifically bind active phosphorylated G protein-coupled receptors (GPCRs), were first discovered as negative regulators of GPCR signaling via G proteins (94,159). Among the four arrestin subtypes expressed in vertebrates (78), only arrestin-3 promotes the activation of JNK3 (160), as well as ubiquitous JNK1/2 (161) in cells, acting as a scaffold that brings together MAPKKK ASK1 (160,162), MAPKKs MKK4 (160,162,163) and MKK7 (161,164), and several isoforms of JNK1/2/3 (160-162,165,166). Recently we identified the first 25 residues of arrestin-3 as the key JNK3 binding site (167). Here we demonstrate that this short arrestin-3-derived peptide also binds ASK1 and MKK4/7 and facilitates JNK3 activation in intact cells. This is the smallest JNK cascade scaffold discovered so far. Its size paves the way to designing small molecule mimics that can be used as tools for targeted manipulation of anti-proliferative and often pro-apoptotic JNK signaling in cells.

5.2 Results and Discussion

We recently found that while three elements in both arrestin-3 domains are involved in JNK3 binding, the peptide representing the first 25 residues of arrestin-3 (T1A) is the key interaction site (167). This opens up three possibilities. First, if T1A only binds JNK3, but not the other kinases in the cascade, it could recruit JNK3 away from functional scaffolds, thereby suppressing JNK3 activation. Second, if T1A binds several kinases in the JNK3 activation module, but does not promote JNK3 phosphorylation, it might act as a dominant-negative silent scaffold,

similar to arrestin-3-KNC mutant we recently described (66). Finally, if T1A binds the same kinases as arrestin-3 and facilitates the signaling in the JNK3 cascade, it would be the smallest active MAPK scaffold known, which opens new avenues for the manipulation of MAPK signaling in cells for research and therapeutic purposes.

To determine the functional capabilities of T1A peptide we took advantage of the availability of purified MKK4 and MKK7, both of which activate JNK3 (157) and were shown to bind full-length arrestin-3 (164). We expressed T1A in *E. coli* as an MBP-fusion and purified it on an amylose column (167). The ability of purified GST-MKK4 or GST-MKK7 (**Fig. 5.1**), with GST as negative control, to bind MBP-T1A immobilized on an amylose column was tested in an *in vitro* pull-down assay, where MBP and MBP-arrestin-3 served as negative and positive controls, respectively (**Fig. 5.1**). T1A effectively retained both kinases, but not control GST (**Fig. 5.1**). Interestingly, similar to full-length arrestin-3, T1A peptide demonstrated stronger interaction with MKK4 than with MKK7 (Fig. 1B, lower panel). Thus, in addition to JNK3 (167), T1A peptide binds both MKKs known to phosphorylate it. Since the pull-down was performed with purified proteins, the data prove that the interactions of T1A with MKK4 and MKK7 are direct and do not involve any intermediaries or helpers. Next, we tested whether T1A binds the uppermost kinase in the cascade, ASK1. Because ASK1 is not available in purified form, we co-expressed HA-tagged ASK1 and YFP-tagged T1A (using YFP as a control) in COS7 cells, lysed the cells, and immunoprecipitated YFP constructs with anti-GFP antibody (**Fig. 5.1**). We found that HA-ASK1 was effectively co-immunoprecipitated with YFP-T1A, but not with control YFP (Fig. 1C). Thus, in addition to JNK3 (167), T1A peptide binds all upstream kinases of its activation cascade, ASK1, MKK4, and MKK7 (**Fig. 5.1**).

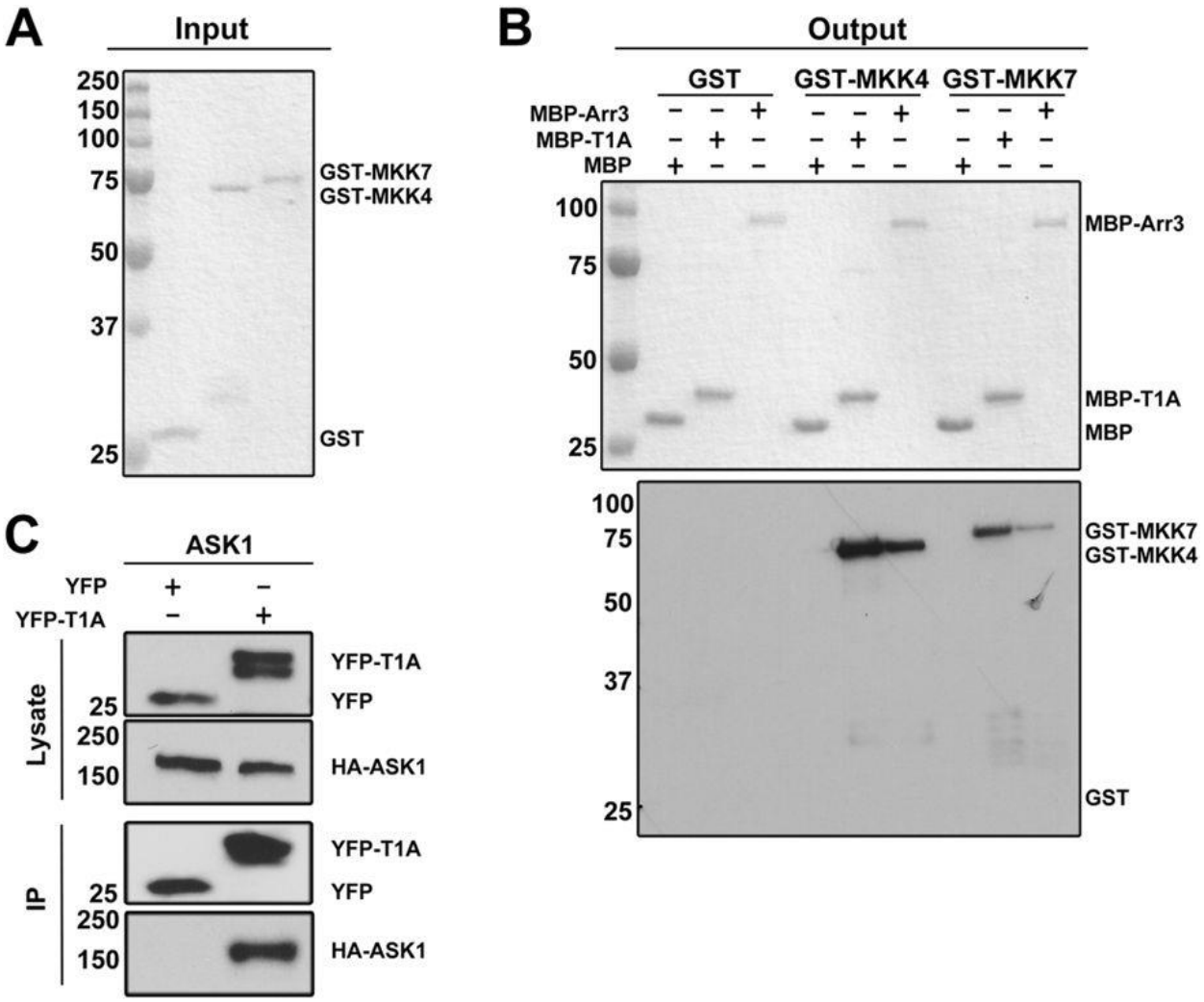

Fig. 5.1. MAPK and arrestin interaction. (A) Purified GST (control), GST-MKK4, and GST-MKK7 (Coomassie staining) **(B)** Top: Coomassie staining of MBP (control), MBP-T1A, and MBP-arrestin-3 bait eluted from amylose beads. Lower blot: GST-MKK4 and GST-MKK7 retained by MBP-T1A and MBP-arrestin-3. Pull-down was performed as described in methods. **(C)** HA-ASK1 was co-immunoprecipitated with YFP-T1A, but not the YFP control, from cells coexpressing these proteins (top blots: lysate; bottom blots: proteins immunoprecipitated with anti-GFP antibody).

Next, we tested whether T1A acts as a scaffold facilitating signaling. To this end, we used experiments with purified proteins, because they provide the most definitive data supporting a direct interaction. As purified ASK1 is not available, we reconstituted MKK4-JNK3 and MKK7-JNK3 modules in the absence and presence of varying concentrations of synthetic purified T1A peptide and measured JNK3 phosphorylation (**Fig. 5.2**). In both cases we obtained bell-shaped curves reflecting JNK3 phosphorylation level as a function of T1A concentration (**Fig. 5.2**). This dependence, where signaling is increased at lower scaffold concentrations and decreased at higher, was also found for scaffolding of these modules by full-length arrestin-3 (164). It is believed to be a characteristic of simple scaffolds, which act by bringing the enzyme and substrate together, as lower scaffold concentrations make the formation of complete scaffold-enzyme-substrate ternary complexes likely, whereas higher concentrations increase the probability of formation of incomplete enzyme-scaffold and substrate-scaffold binary complexes, suppressing the signaling (168,169). The optimal concentration of a scaffolding protein for signaling depends on its affinity for the proteins it scaffolds (164,168,169).

Our previous work suggested that the efficiency of JNK3 phosphorylation in the complex that includes MKK4 and arrestin-3 is higher than the efficiency of JNK3 phosphorylation by MKK4 in the absence of arrestin-3 (164). Since these experiments were performed with pure components, the data show that simultaneous direct binding to T1A of MKK4/7 (**Fig. 5.1**) and their substrate JNK3 (167) places MKKs into a favorable position to phosphorylate JNK3 (**Fig. 5.2**). Previously we found that the optimal concentrations of arrestin-3 for scaffolding MKK4-JNK3 and MKK7-JNK3 modules are ~0.6 μM and ~ 6 μM (164), reflecting lower affinity of arrestin-3 for MKK7 than for MKK4 (164). Interestingly, the optimal concentration of T1A for promoting JNK3 phosphorylation by MKK4 is lower than for MKK7-JNK3 module (**Fig. 5.2**), in

line with more avid binding of this peptide to MKK4 (**Fig. 5.1**). Intriguingly, in both cases optimal T1A concentrations were ~10-times lower than those of full-length arrestin-3. These results suggest that T1A has higher affinity for MKKs and/or JNK3, in line with its ability to retain more MKKs than arrestin-3 (**Fig. 5.1**). This phenomenon might be explained by greater accessibility of T1A peptide when it is free and not in the context of full-length arrestin-3, where it is partially shielded by other elements of the N-domain (92).

To test whether T1A can promote JNK3 phosphorylation by MKKs in cells, we co-expressed MKK4 or MKK7 with YFP-T1A in COS7 cells, using YFP and full-length arrestin-3 as negative and positive controls, respectively (**Fig. 5.2**). We found that YFP-T1A, but not YFP, increases JNK3 phosphorylation by both MKKs, similar to arrestin-3. Thus, T1A is necessary and sufficient to promote the signaling in MKK4/7-JNK3 modules both *in vitro* and in intact cells.

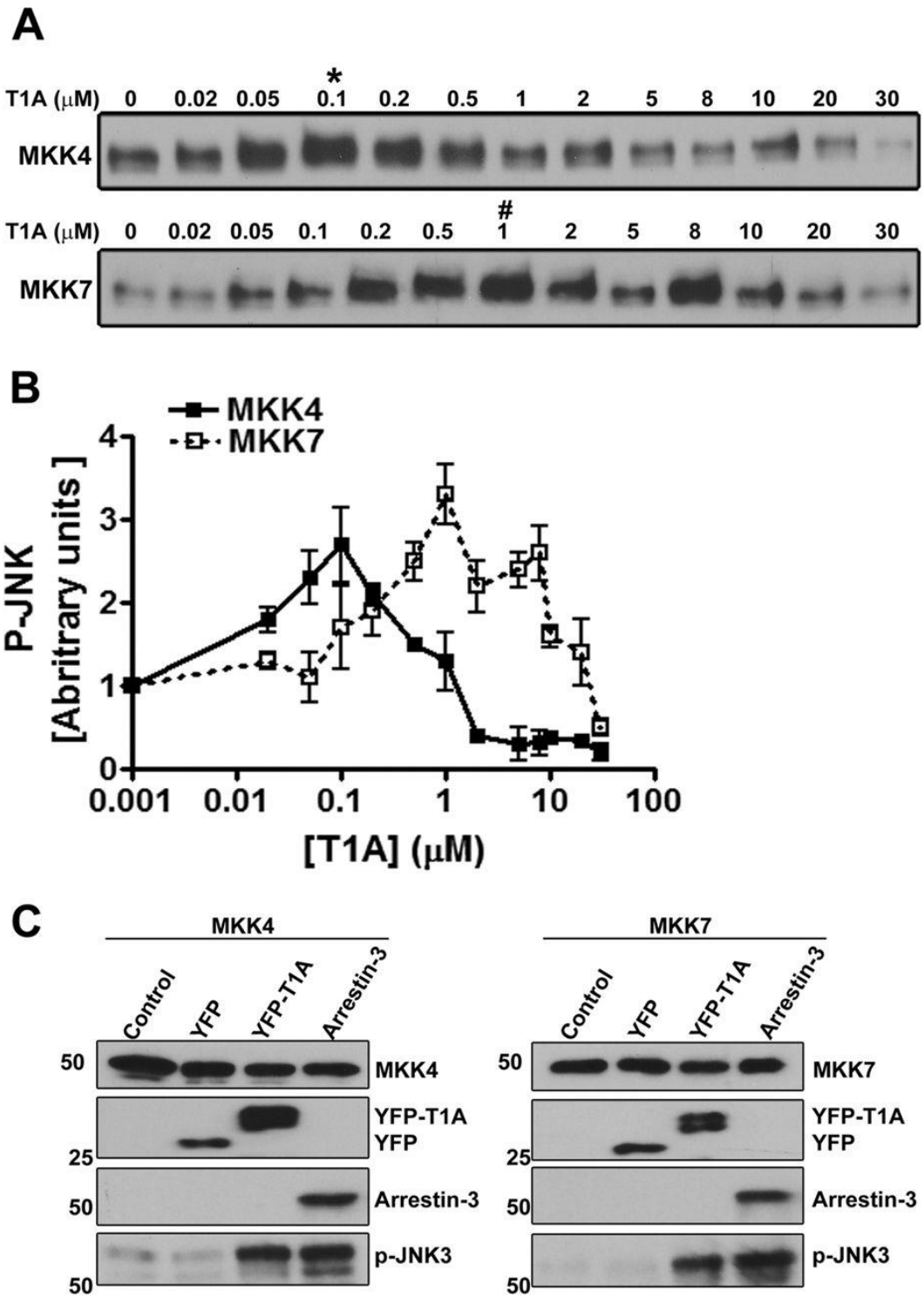

Fig. 5.2. The T1A scaffold. (A) Representative autoradiograms showing JNK3α2 phosphorylated by purified MKK4 (upper panel) and MKK7 (lower panel) at the indicated concentration of synthetic purified T1A peptide (10-s incubation). **(B)** Quantification of JNK3α2 phosphorylation by MKK4 and MKK7. **(C)** JNK3α2 phosphorylation by MKK4 and MKK7 in COS7 cells co-expressing JNK3α2 with MKK4 or MKK7 (control) and YFP, YFP-T1A, or arrestin-3.

T1A constitutes a small part of the arrestin-3 N-domain (92). All arrestins consist of two domains (91-93,170), which fold independently, can be expressed separately, and retain certain functions (162,171,172). Therefore, we tested whether separated domains of arrestin-3, as well as the other ubiquitously expressed non-visual subtype, arrestin-2, which also binds kinases of the JNK3 activation cascade (162), can promote JNK3 phosphorylation in cells. To this end, we expressed in COS7 cells both arrestins and their individual domains with the same HA-tag (to compare their expression on the same blot) along with ASK1 and JNK3 (**Fig. 5.3**). We confirmed that arrestin-3 expression significantly increases JNK3 phosphorylation in cells, whereas arrestin-2 does not (88,160,162), and found no effect of the separated domains of either arrestin (**Fig. 5.3**).

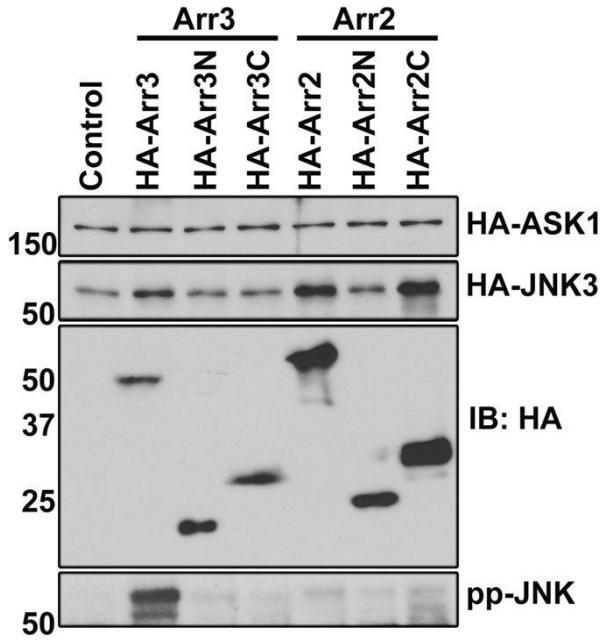

Fig. 5.3. Arrestin domain activation of JNK3. Western blot of lysates of COS7 cells co-expressing HA-ASK1 and HA- JNK3α2 (control), or with HA-tagged full-length arrestin-3 (Arr3), arrestin-2 (Arr2), or separated N- and C-domains of the two non-visual arrestins (Arr3N, Arr2N, Arr3C, Arr2C). Phospho-JNK blot shows that among these constructs only full-length arrestin-3 facilitates JNK3α2 phosphorylation in cells.

T1A effectively enhanced JNK3 phosphorylation by MKK4 and MKK7 (**Figs. 5.1, 5.2**), whereas full-length arrestin-3 facilitates JNK3 phosphorylation upon co-expression with ASK1 (88,160,162,165), which phosphorylates and activates MKKs. If the arrestin-3 N-domain fails to promote the activation of JNK3 because it can only scaffold MKK4/7-JNK3 modules, then the T1A peptide, which constitutes only a part of the arrestin-3 N-domain, would not be expected to promote JNK3 phosphorylation in the presence of ASK1 in cells. To test this, we co-expressed YFP fusions of T1A, and two other JNK3-binding peptides, T3 and T6 (**Fig. 5.4**) (167), with JNK3 and ASK1 in COS7 cells and monitored JNK3 phosphorylation, using YFP and arrestin-3 as negative and positive controls, respectively (**Fig. 5.4**). As expected, arrestin-3 increased the level of JNK3 phosphorylation (**Fig. 5.4**). T1A, but not other peptides, was also active, and the effect of T1A was greater than that of full-length arrestin-3 (**Fig. 5.4**). To test whether T1A still functions as a simple scaffold in intact cells in the presence of over-expressed ASK1, as in case of MKK4/7-JNK3 signaling modules (**Fig. 5.2**), we co-expressed ASK1 and JNK3 with YFP (control) and varying amounts of YFP-T1A (**Fig. 5.4**). The dose-response curve for T1A in these experiments was also biphasic, with a clear optimum, indicating that T1A is a simple scaffold of the three-kinase cascade, similar to full-length arrestin-3 (163).

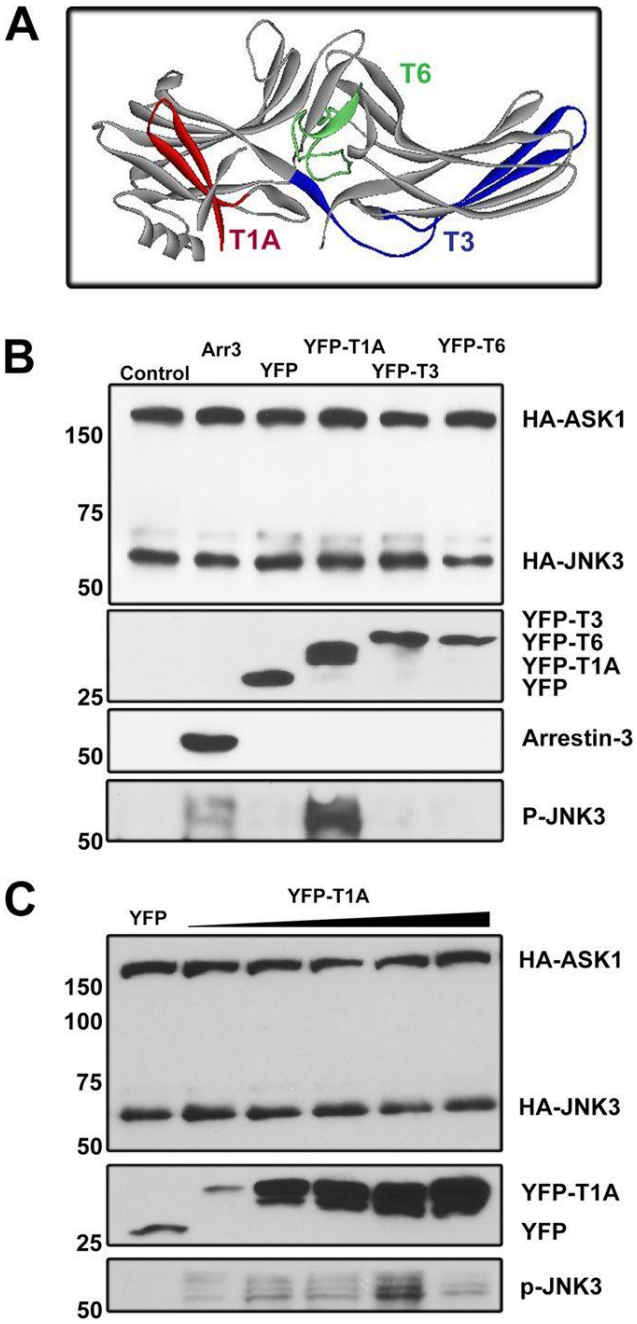

Fig. 5.4. The T1A peptide increases JNK3 phosphorylation in cells. The structure of arrestin-3 (PDB: 3P2D) with the three peptides implicated in JNK3 binding shown in red (T1A), blue (T3), and green (T6). **(B)** COS7 cells co-expressed HA-ASK1 and HA-JNK3α2 without (control), or with full-length arrestin-3 (Arr3), YFP, or indicated YFP-tagged JNK3-binding peptides. The upper three blots show expression levels of indicated proteins; the lower blots show that T1A facilitates JNK3α2 phosphorylation more efficiently than full-length arrestin-3. **(C)** COS7 cells co-expressed HA-ASK1 and HA- JNK3α2 with YFP (control) or different concentrations of YFP-T1A The upper two blots show expression levels of indicated proteins; the lower blot shows biphasic dependence of JNK3α2 phosphorylation of T1A level.

To test the specificity of T1A action, we compared its ability to bind purified MKK4, MKK7, and JNK3 with that of B1A, a homologous N-terminal peptide from closely related arrestin-2, which differs from T1A only in four positions (**Fig. 5.5**). We found that while both peptides comparably bind MKK4, B1A demonstrates less robust interaction with JNK3 and its other upstream activator, MKK7 (**Fig. 5.5**). To test whether this difference in binding translates into differential activity in cells, we compared the ability of YFP-T1A and YFP-B1A to facilitate JNK3 activation in cells over-expressing ASK1, using YFP-arrestin-3 and YFP as positive and negative controls, respectively. We found that in contrast to T1A, arrestin-2-derived B1A does not function as a scaffold of ASK1-MKK4/7-JNK3 cascade in cells (**Fig. 5.5**), indicating that specific sequence, rather than simple accessibility of this part of arrestins, determines its functional capabilities.

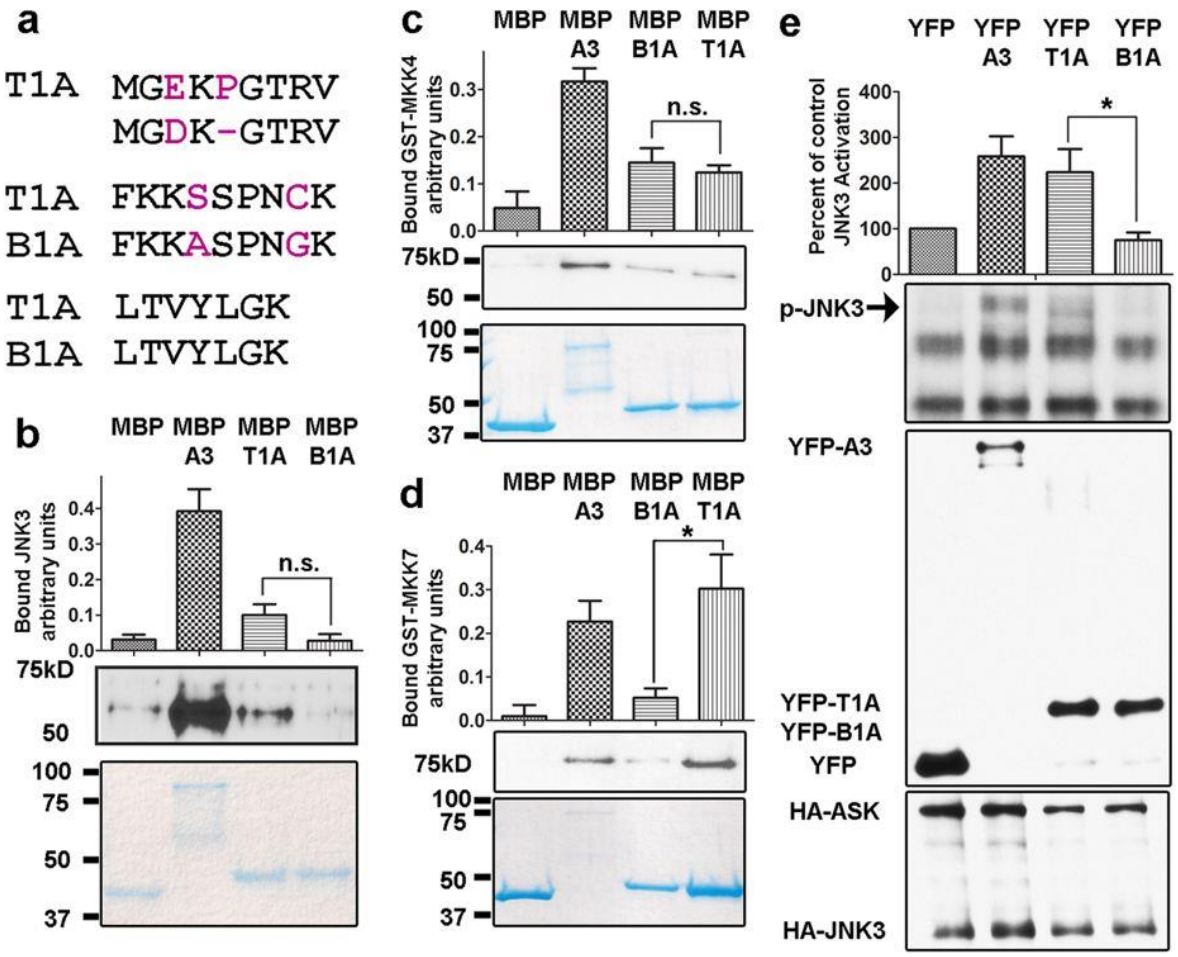

Fig. 5.5. ***In vitro*** **assessment of the T1A peptide. (A)** Sequence comparison of arrestin-3-derived T1A and B1A, derived from arrestin-2, which does not facilitate JNK3 activation. Residues that differ between T1A and B1A are shown in magenta. **(B-D)** Pull-down of purified JNK3, MKK4, and MKK7 by MBP (negative control), MBP-arrestin-3 (positive control), MBP-T1A, and MBP-B1A, was performed as described in Methods. Lower panels, Coomassie gels of loaded MBP-fusions; middle panels, Western blots of retained JNK3, MKK4, and MKK7; upper panels, quantification of Western blots from 3-4 independent experiments. Note that B1A binds MKK4 like T1A, but does not appreciably interact with JNK3 or MKK7. **(E)** COS7 cells co-expressed HA-ASK1 and HA-JNK3 with YFP (negative control), YFP-arrestin-3 (Arr3, positive control), YFP-T1A, or YFP-B1A. Lower two blots show expression levels of indicated proteins; upper blot and bar graph (quantification of JNK3 phosphorylation in four independent experiments) show that T1A facilitates JNK3 phosphorylation, whereas B1A does not. *p<0.05; n.s., not significant.

Thus, the first 25 residues contained in the T1A peptide are primarily responsible for the ability of arrestin-3 to scaffold the ASK1-MKK4/7-JNK3 signaling module. The lack of the activity of the arrestin-3 N-domain (**Fig. 5.3**), which contains the T1A peptide, along with facilitation of JNK3 phosphorylation in exactly the same experimental paradigm by T1A (**Fig. 5.4**), clearly indicates that when separated, this peptide is a lot more accessible than in the context of arrestin-3 or its N-domain. It is tempting to speculate that receptor binding of arrestin-3 stimulates its ability to promote JNK3 activation (160) by increasing the accessibility of the T1A element to relevant kinases. Significant flexibility of receptor-bound arrestins revealed by biophysical methods (111,173) supports this idea. While the crystal structure of arrestin-3 in complex with any GPCR is not available, the only existing structure of the arrestin-receptor complex, that of visual arrestin-1 bound to rhodopsin (174), is consistent with this hypothesis. Arrestin-3 elements that promote signaling leading to the activation of other MAPKs, such as ERK1/2 (175) and p38 (176), also need to be identified. The activation of these two kinases is strictly dependent on arrestin binding to the receptor (175,176), suggesting that arrestin elements that change conformation and/or become more exposed upon GPCR interaction are likely the prime suspects.

Our data identify a relatively short arrestin-3-derived peptide as an effective scaffold of the ASK1-MKK4/7-JNK3 signaling cascade, making it the smallest MAPK scaffold ever reported. However, T1A can be large enough to bind all the kinases involved simultaneously. Each residue has a structure –NH-CH(R)-CO-, with each bond >1.4A. Thus, taking into account angles, a single reside has a length of ~3A. Therefore, a 25-residue peptide in fully extended conformation can achieve a length of up to ~75A, which is similar to the maximum “wingspan” (the distance between the far tips of the two arrestin domains) of all arrestins (91-93,170). Nonetheless, limited size of

T1A opens the prospect of designing peptides and/or non-peptide small molecule mimics that can be used as tools to manipulate MAPK signaling for research and therapy. Many human disorders are caused by excessive cell proliferation (e.g., cancer) or death (e.g., Alzheimer's, Parkinson's, and other neurodegenerative diseases). Targeted activation of JNK family kinases usually has anti-proliferative effect, whereas the activation of ERK1/2 promotes cell survival. Scaffolds facilitating signaling in these pathways might be easier to dose than direct pharmacological activators, making them safer intervention tools. The identification of the shortest active form of the T1A-derived peptide must be the next step in this direction.

5.3 Materials and Methods

Materials. All restriction and DNA modifying enzymes (T4 DNA ligase, Vent DNA polymerase, and calf intestine alkaline phosphatase) were from New England Biolabs (Ipswich, MA). Other chemicals were from sources recently described (161,167).

Terminology. We use the systematic names of arrestin proteins: arrestin-1 (historic names S-antigen, 48 kDa protein, visual or rod arrestin), arrestin-2 (®-arrestin or ®-arrestin1), arrestin-3 (®-arrestin2 or hTHY-ARRX), and arrestin-4 (cone or X-arrestin; for unclear reasons its gene is called "*arrestin 3*" in the HUGO database).

*MBP-fusion protein constructs in pMal and MBP pull-down***.** To make MBP-fusions containing arrestin-2/3 elements, the cDNAs encoding arrestin fragments were subcloned into pMal-p2T (generous gift from Dr. Keiji Tanaka, Tokyo Institute of Medical Science) between Eco RI and Xho I sites in frame with MBP, as described (167). MBP-Arr3 (full-length arrestin-3) was created by subcloning the corresponding cDNA into pMal-p2T between Eco RI and Not I sites (167). All MBP-arrestin-3 fusion proteins contained the same TLVPRGSPGF linker between MBP

and arrestin-3 or its fragments. The MBP protein used as negative control was purified using empty pMal-p2T vector containing the same linker with 10 additional residues: PGRLERPHRD. MBP fusions were purified, as described (167). MBP pull-down was performed, as described (167). Briefly, Indicated MBP fusions (10-30 μg in 50 μL 20 mM Tris/150 mM NaCl) were immobilized on amylose resin (25 μL, 50% slurry, New England Biolabs) for 1 h at 4°C with slight rotation. Purified, as described (177), MKK4/7 (10 μg in 50 μL 20 mM Tris/150 mM NaCl) were added to the immobilized MBP fusions and rotated gently for 2 h at 4°C. Samples were transferred to centrifuge filters (Durapore®-PVDF-0.65μm), washed three times with 50 mM HEPES-Na, pH 7.3, 150 mM NaCl. The proteins were eluted by 100 μl of elution buffer (wash buffer containing 50 mM maltose) by gentle rotation for 5 min at 4°C. Eluates were analyzed by SDS-PAGE and Western blotting.

Kinase purification and in vitro phosphorylation assay. JNK3a2 (164,167), and MKK4 and MKK7 (161,164) were expressed in *E. coli* and purified as previously described (177). The effect of arrestin-3 and MBP-T1A on the phosphorylation of JNK3α2 by MKK7 or MKK4 was analyzed by an *in vitro* kinase assay, as described (163,164). Briefly, the assays were conducted in 10 μL containing the following final concentrations: 50 nM active MKK7 or MKK4, 1μM JNK3α2, and indicated concentrations of arrestin-3 or T1A. The mixtures were incubated individually at 30°C for 10 sec. The reactions were stopped by the addition of 15 μL of Laemmli SDS sample buffer (Sigma) and 2 μl of total reaction sample was subjected to SDS-PAGE (8%) and transferred polyvinylidene difluoride (PVDF) membranes (Millipore, Bedford, MA). Phosphorylated JNK3α2 was visualized by rabbit anti-phospho JNK antibody (Cell Signaling) and the level of JNK phosphorylation was quantified.

Peptide synthesis. The T1A peptide (MGEKPGTRVFKKSSPNCKLTVYLGK),

representing the first 25 residues of arrestin-3, was synthesized using automated synthesis robot (SyroI, MultiSyntech, Witten, Germany) on NovaSyn® TGR R resin (13.5 µmol, Novabiochem, Darmstadt, Germany) with a fluorenylmethyloxycarbonyl chloride (FMOC)/tert-butyl strategy, as described (178). FMOC-amino acids were from Iris Biotech and Novabiochem (Marktredwitz, Germany). Amino acid side chain protecting groups were used as following: trityl (Trt) for Asn and Cys; tBu for Glu, Thr, Ser and Tyr; tert-butyloxycarbonyl (Boc) for Lys; and pentamethyl-2,3-dihydrobenzofuran-5-sufonyl (Pbf) for Arg. Automated FMOC deprotection was carried out with 40% (v/v) piperidine (Sigma-Aldrich, Taufkirchen, Germany) in N,N-dimethylformamide (DMF; Biosolve, Valkenswaard, The Netherlands) for 3 min and 20% (v/v) piperidine in DMF for 10 min. The coupling of the amino acids was carried out twice. FMOC-amino acids were pre-incubated with OxymaPure (Iris Biotech) for 2 min. Following the addition of N,N'-diisopropylcarbodiimide (DIC; Iris Biotech), reaction was incubated for 40 min. After successful synthesis, peptides were cleaved from the resin with 90% trifluoroacetic acid (TFA) and 10% 1,2-ethanedithiol/thioanisole (v/v 3:7). Methionines were reduced with 1,2-ethanedithiol and trimethylsilyl bromide in TFA. Subsequently, peptides were purified on a reversed-phase C18 column (Phenomenex Jupiter 10u Proteo 90 Å: 250 × 21.2 mm; 7.8 µm; 90 Å) and analyzed by MALDI-TOF mass spectrometry (UltraflexII, Bruker, Bremen, Germany) and analytical reversed-phase HPLC on columns Phenomenex Kinetex 5u XB-C18 100 Å (Phenomenex: 250 × 4.6 mm; 5 µm; 100 Å) and Phenomenex Jupiter 4u Proteo 90 Å (Phenomenex: 250 × 4.6 mm; 4 µm; 90 Å). Eluent A was 0.1% TFA in H_2O and eluent B 0.08% TFA in ACN. On both columns, a gradient of 10% eluent B in A to 60% eluent B in A in 40 min was used. Following this procedure, the peptide was ≥ 95% pure (theoretical M_r = 2766.5 Da, experimental ($[M+H]^+$) = 2767.6).

Plasmids, Cell Culture, and Transient Transfection. HA-tagged arrestins and their

separated domains were constructed, as described (171). Full-length arrestin-3 and its fragments with N-terminal YFP tag were constructed by subcloning the cDNA encoding YFP-arrestin-3 or YFP-tagged arrestin-3 fragments cDNAs into pcDNA3.1 between Eco RI and Hind III restriction sites.

COS-7 African green monkey cells were maintained in DMEM supplemented with 10% heat-inactivated FBS (Invitrogen), penicillin, and streptomycin at 37 °C in a humidified incubator with 5% CO_2. The cells were plated at 80–90% confluence and transfected using Lipofectamine 2000 (Invitrogen) according to the manufacturer's instructions. Cells were used 48 h post-transfection and serum-starved overnight before experiments.

Western Blotting and measurement of JNK phosphorylation in intact cells. COS-7 cells were incubated with phosphatase inhibitors (50 mM NaF and 10 mM Na_3VO_4) in serum-free medium for 15 min at 37 °C; washed with cold PBS; and lysed with SDS lysis buffer containing 1% SDS, 10mM Tris (pH7.4), 10 mM NaF, 100 μM Na_3VO_4, 2 mM EDTA, 2 mM benzamidine and 1 mM PMSF. JNKs activity was assayed by Western blotting using an antibody specific for phosphorylated JNK to detect phophorylated (active) JNKs (161,164,167). Whole cell lysates were boiled for 5 min and centrifuged at 10,000 × *g* for 10 min, and the supernatants were used for Western blotting. Protein was measured using the Bio-Rad Coomassie Blue assay. The proteins were resolved on 8% SDS-PAGE and transferred to PVDF membrane (Millipore, Bedford, MA). Blots were incubated with the primary antibodies (Cell Signaling Technology, Inc) anti-phospho-JNK, anti-JNK, anti-HA (6E2) (1:1000 to 1:5000), followed by appropriate HRP-conjugated secondary antibodies. Protein bands were detected by enhanced chemiluminescence (ECL, Pierce), followed by exposure to x-ray film. To quantify phopho-JNKs, we used serial dilutions of anisomycin (1μg/ml)-stimulated HEK-A cell lysates to ensure that all samples were in linear range.

CHAPTER 6

ARRESTIN-3 SCAFFOLDING OF THE JNK3 CASCADE SUGGESTS A MECHANISM FOR SIGNAL AMPLIFICATION

This article was published in the *Proceedings of the National Academy of Sciences (2).* **Nicole A. Perry** was first-author, and Tamer S. Kaoud, Oscar O. Ortega, Ali I. Kaya, David J. Marcus, John M. Pleinis, Sandra Berndt, Qiuyan Chen, Xuanzhi Zhan, Kevin N. Dalby, Carlos L. Lopez, T.M. Iverson, and Vsevolod V. Gurevich contributed to this work.

6.1 Introduction

Scaffold proteins are critical in the regulation of numerous cellular signaling pathways. The action of protein scaffolds is often attributed to their ability to organize signaling cascades by binding and orienting individual components (179). This tethering model, however, can create a conceptual problem regarding signal amplification: a stable complex would prevent rapid biological response (180).

Among the better studied signaling pathways regulated by scaffolds are mitogen-activated protein kinase (MAPK) cascades (1,10,181,182) (**Fig. 6.1)**. MAPK cascades involve three sequentially acting kinases (in general terms, a MAP3K, a MAP2K, and a MAPK). Each kinase becomes competent to phosphorylate downstream substrates when it is both (i) phosphorylated within the activation loop and (ii) liganded with ATP (183). MAPK activity is linked to phosphorylation, so that an "inactive" kinase is unphosphorylated and an "active" kinase has been phosphorylated by upstream kinase(s). The final, activated kinase phosphorylates downstream

substrates and yields a biological response. Protein phosphatases terminate signaling by removing the attached phosphates (184). The mechanistic details of MAPK signaling pathways are still contested (181), although spatial and temporal regulators of MAPK proteins play direct roles in signal specificity (182). Mathematical modeling has provided insights into how an initial signal could be amplified through a nonspecific set of MAPK interactions and shown that amplitude and duration of the signal can determine biological outcomes (185,186).

To elucidate how scaffold proteins modulate MAPK signaling, we focused on arrestin-3 scaffolding of the ASK1-MKK4/7-JNK3 cascade, where biological effects of inappropriate JNK3 activity include neurodegeneration via cellular apoptosis (182,187). Prior studies showed that arrestin-3 scaffolds the JNK3 cascade (10,64,188,189) in both a GPCR-dependent (54,190) and -independent (64,96,121,191) fashion. The mechanism of arrestin-mediated MAPK activation, however, remains poorly understood (192). Here we explore the mechanism of receptor-independent, arrestin-3-dependent signal amplification in the JNK3 pathway by combining experimental and computational approaches. To make measurements more experimentally tractable, we used the arrestin-$3^{(1\text{-}393)}$ protein, which exhibits a pre-activated state in solution, meaning its equilibrium is likely shifted toward the active conformation. This established tool eliminated the need for arrestin activation by GPCRs and non-receptor activators, and we validated the biological relevance using full-length arrestin-3 activated by the non-receptor activator IP_6. Collectively, our data suggest a "conveyor belt mechanism" that is likely generalizable to other scaffolds.

6.2 Results

Purified arrestin-3 and an arrestin-derived T1A peptide directly interact with MKK4,

MKK7, and JNK3 in vitro. To complement previous reports that arrestin-3 interacts with kinases of the JNK3 cascade in cells, we performed an *in vitro* pull-down assay. Since this assay primarily detects high affinity interactions, we focused on the unphosphorylated MAP2Ks and JNK3, which have been suggested as high-affinity arrestin binding partners (64,75,98,193). For these assays we fused MBP to either arrestin-3 or the first 25 amino acids of arrestin-3 (a peptide termed T1A that facilitates JNK3 activation in cells (75)). We tested binding in the presence or absence of physiological concentrations of ATP to assess the role of the kinase domain in the arrestin-3 interaction. Unphosphorylated MKK4 exhibited robust binding to both MBP-arrestin-3 and MBP-T1A in the presence of ATP (**Fig. 6.1B**). The quantities of MKK4 that were pulled down in this assay by MBP-arrestin-3 and MBP-T1A did not differ significantly, suggesting that ATP-liganded MKK4 binds largely to the N-terminus of arrestin-3. Unphosphorylated MKK7 bound more robustly to MBP-arrestin-3 in the presence of ATP (**Fig. 6.1C**). Its binding to MBP-T1A, although weaker than the full-length protein, also showed ATP dependence. These data suggest that MKK4 and MKK7 share binding sites on the N-terminus of arrestin-3 and that ATP-induced conformational changes in the kinase domain facilitate MAP2K binding to arrestin-3.

In the case of unphosphorylated JNK3 (**Fig. 6.1D**) we observed robust binding to full-length arrestin-3, but weak binding to MBP-T1A. This contrasts with the MAP2Ks, where the T1A peptide interacts strongly in each case. The finding that the T1A peptide cannot recapitulate the interaction between unphosphorylated JNK3 and full-length arrestin-3 is consistent with previous report that JNK3 has multiple sites of interaction on arrestin-3, including contact points outside its N-terminus (104). As with the MAP2Ks, unphosphorylated JNK3 binding to arrestin-3 was enhanced by ATP. The binding of doubly phosphorylated JNK3 to either MBP-arrestin-3 or MBP-T1A was not detectable in this assay, suggesting that kinase activation weakens its interaction with

arrestin-3.

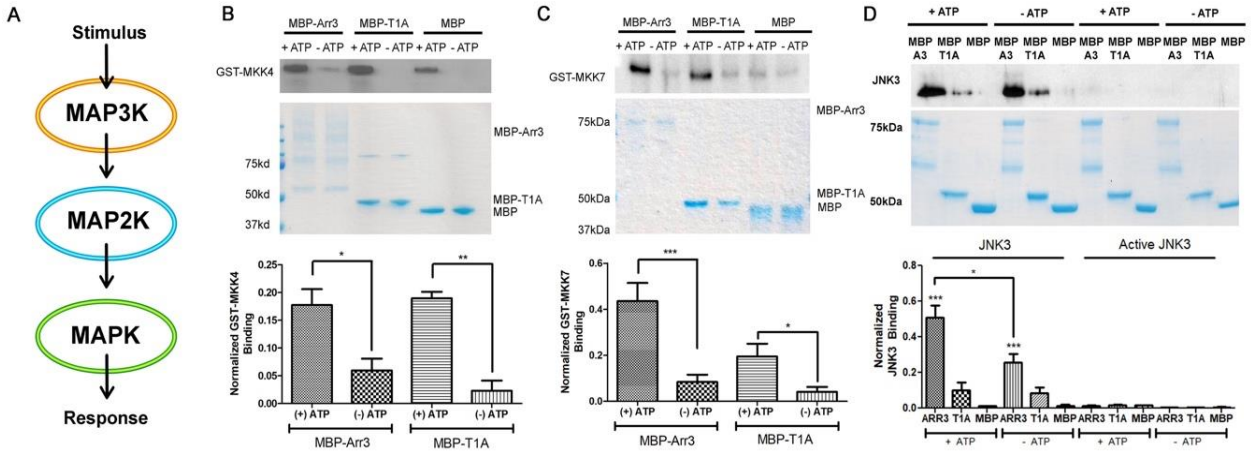

Fig. 6.1. ATP effect on GST-MKK4, GST-MKK7, and His-JNK3 binding to arrestin-3 and T1A peptide. (A) Mitogen-activated protein kinase (MAPK) cascades are three-tiered cascades consisting of a MAP3K, MAP2K, and MAPK. The initial signal or stimulus is propagated through sequential activation (via phosphorylation by an upstream kinase) of each kinase in the cascade. Arrestin-3 acts as a molecular scaffold for these cascades, allowing for signal amplification through production of multiple active MAPKs. **(B-D)** GST-MKK4, GST-MKK7, and His-JNK3 binding to MBP-fusions of arrestin-3 and T1A peptide was determined in the presence and absence of ATP using an in vitro pull-down assay. The upper panel shows a representative Western blot of retained MKK4, MKK7, or inactive and active (doubly-phosphorylated) JNK3, while the lower panel shows a representative Coomassie staining to ensure equal loading of the MBP fusions on the amylose column. Non-specific binding to MBP was subtracted prior to quantitative analysis. Densitometric quantification was performed for each assay using Quantity One software. One-way ANOVA followed by Dunnett's post-hoc test was used to compare the binding in the presence and absence of ATP of each MBP-fusion construct (n=3; *, $p<0.05$; **, $p<0.001$) The student's t-test was used to compare the MBP-arrestin conditions.

The affinities of MKK4/7 and JNK3 for arrestin-3 depend on their activation state. With direct binding of the signaling components established, we next explored how activation altered kinase affinity for arrestin-3. We measured the affinities of MKK4/7 (MAP2Ks) and JNK3 (MAPK) for truncated arrestin-$3^{(1\text{-}393)}$. This arrestin-3 construct likely samples the active conformation more readily, which allowed affinity measurements in the absence of activators. The affinity of full-length ASK1 (MAP3K) was not measured as this kinase does not express well enough in *E. coli*. We measured the affinity of arrestin-3 for all other kinases in different activation states using microscale thermophoresis (MST) (**Fig. 6.2A-H**) (194-196) in the presence of ATP and $MgCl_2$.

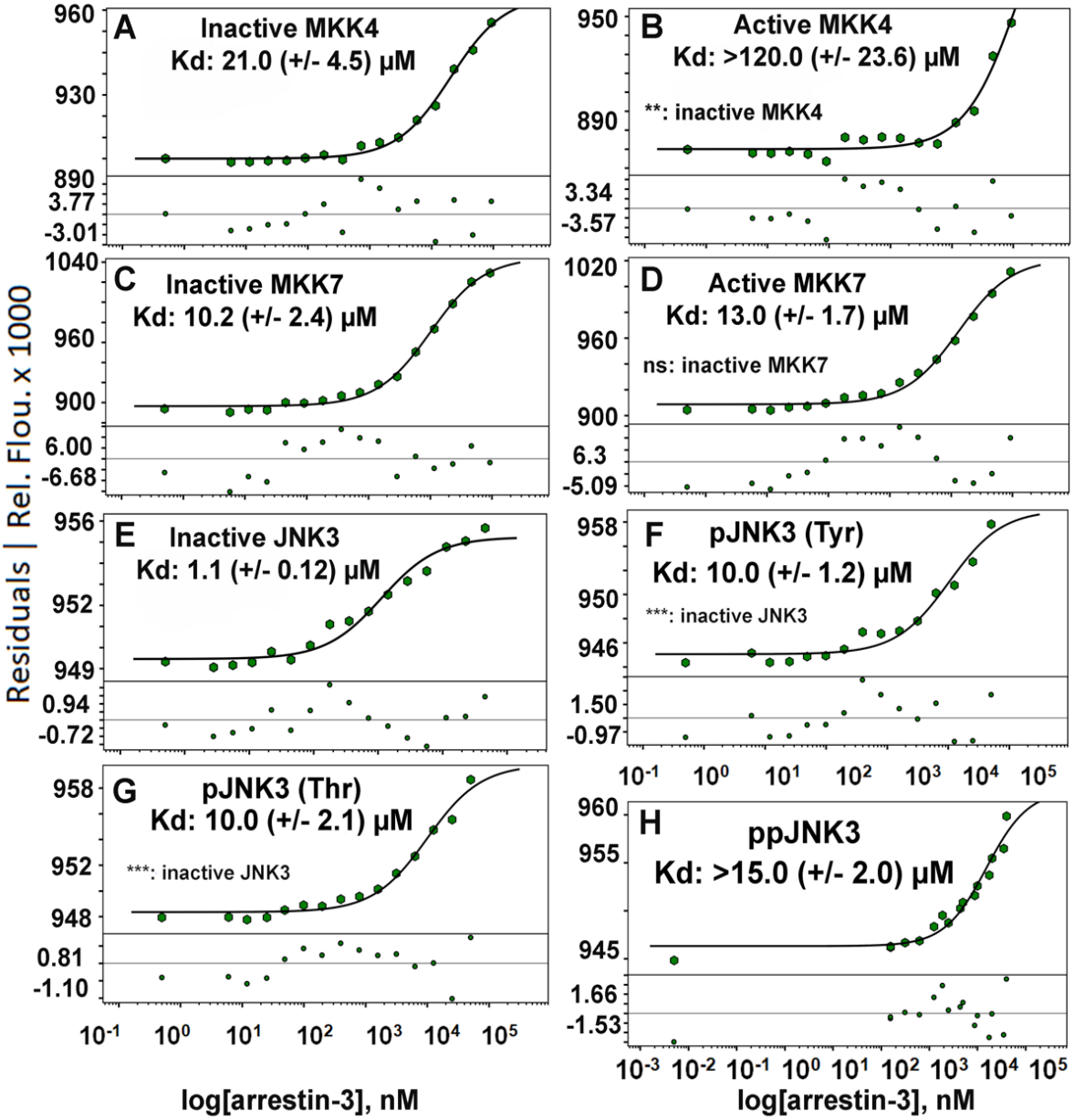

Fig. 6.2. The affinity of arrestin-3 for unphosphorylated and phosphorylated MKK4, MKK7, and JNK3. Average K_d values are shown for each curve (n=3-6). Binding curves for arrestin-3 with unphosphorylated MKK4 **(A)**, phosphorylated MKK4 **(B)**, unphosphorylated MKK7 **(C)**, phosphorylated MKK7 **(D)**, unphosphorylated JNK3 **(E)**, JNK3 phosphorylated at Tyr-223 **(F)**, JNK3 phosphorylated at Thr-221 **(G),** and doubly phosphorylated JNK3 **(H)** in the presence of 1 mM ATP and 2 mM $MgCl_2$ are shown. For the MAP2Ks, MKK4 and MKK7, the preset Thermophoresis and T-jump was used to calculate the isotherm, whereas for the MAPK interactions the preset T-jump was used. Points where the fluorescence differed by more than 10% from the average were not included in the curve fit (**Fig. S1**). Student's two-tailed t-test was used to assess significance of the differences between inactive (unphosphorylated) and active (phosphorylated) MAP2Ks and One-way ANOVA followed by Dunnett's post-hoc test was used to compare inactive JNK3 to singly- or doubly-phosphorylated JNK3 (*, $p<0.05$; **, $p<0.01$, ***, $p<0.001$, n.s., not significant).

Activation of the MAP2Ks MKK4/7 occurs when an upstream MAP3K phosphorylates the conserved phosphorylation motif (SXXS or SXXT) in their activation loops (197). The unphosphorylated form of MKK4 exhibited higher affinity for arrestin-3 than the phosphorylated form, with K_d values of 21 (±4.5) μM for the inactive kinase and >120 (±23.6) μM for active MKK4 (**Fig. 6.2A-B**). Importantly, the active kinase measurement only suggested the lower limit of the K_d value due to ligand-induced fluorescent effect at higher concentrations. However, the maximum concentrations used in the MST assay exceeded typical arrestin-3 intracellular concentrations (198,199), and therefore yield a reasonable estimate of relative protein affinities. For MKK7, the unphosphorylated and phosphorylated form did not show statistically significant differences, with K_d values of 10.2 (±2.4) μM for the inactive and 13 (±1.7) μM for active MKK7 (**Fig. 6.2C-D**).

The two MAP2Ks of the cascade, MKK4 and MKK7, work to fully activate the final effector, JNK3, by phosphorylating Tyr-223 and Thr-221, respectively (98,200). Thus, JNK3 has four potential states: an unphosphorylated (inactive) state, two singly phosphorylated (partially active) states, and one doubly phosphorylated (fully active) state. Affinity measurements between JNK3 and arrestin-3 exhibited the same trend as MKK4, with unphosphorylated JNK3 having a higher affinity than singly or doubly phosphorylated JNK3. Notably, the K_d values of the distinct activation states significantly differed: unphosphorylated JNK3 bound arrestin-3 with high affinity (K_d of 1.1 (±0.12) μM) (**Fig. 6.2E**); singly phosphorylated JNK3 exhibited moderate affinities for arrestin-3, with K_d values of 10 (±1.2) μM for JNK3 pThr-221 (**Fig. 6.2F**) and 10 (±2.1) μM for JNK3 pTyr-223 (**Fig. 6.2G**); whereas doubly phosphorylated JNK3 exhibited lower affinity with a K_d of >15 μM (**Fig. 6.2H**). Interestingly, this effect was less pronounced in the absence of ATP (**Fig. 6.3**).

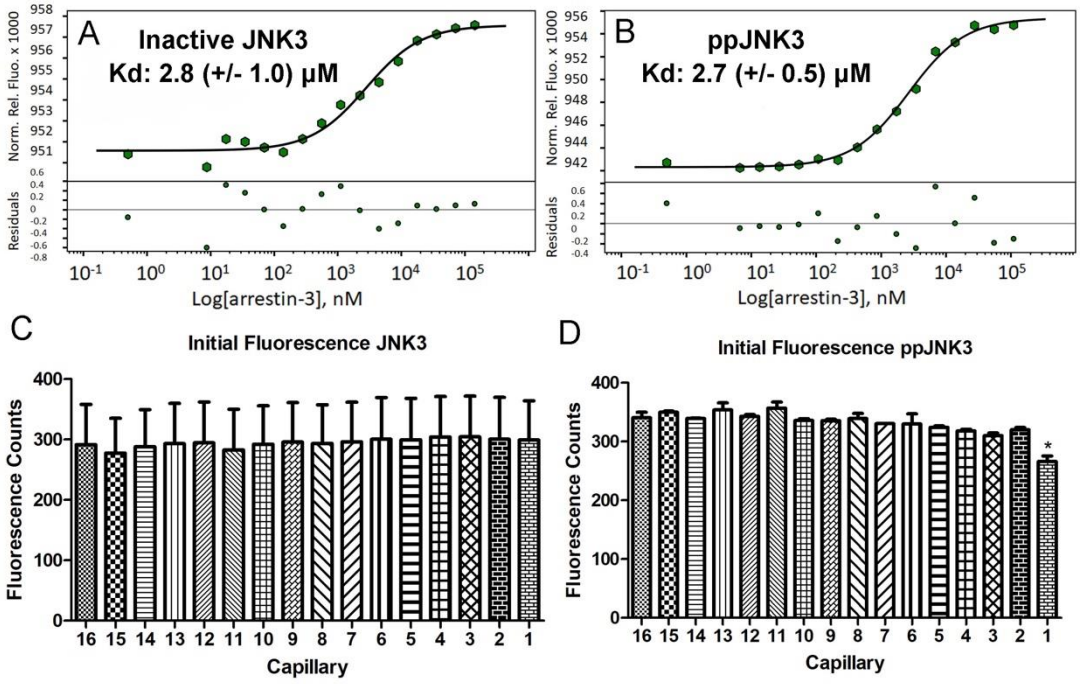

Fig. 6.3. The affinity of arrestin-3 for unphosphorylated and phosphorylated JNK3 measured by MST in the absence of ATP. The K_d values are shown for each curve. **A.** Binding curve for inactive JNK3 and arrestin-3 in the absence of ATP. MST was performed at a constant concentration of Tris-NTA-labeled His-JNK3 (100 nM), and the indicated concentrations of unlabeled arrestin-$3^{(1\text{-}393)}$ (0-72 µM; n=3). **B.** Binding curve for active JNK3 and arrestin-3 in the absence of ATP. MST was performed at a constant concentration of Tris-NTA-labeled His-phosphoJNK3 (100 nM) with a titration with unlabeled arrestin-3 (0-110 µM; n=3). **C,D.** Initial fluorescence was measured using a capillary scan prior to MST analysis. Average values of three experiments are shown for inactive JNK3 **(C),** and doubly phosphorylated JNK3 **(D).** Statistical analysis was performed using NT Analysis Software (NanoTemper technologies GmbH) (*, outside of ±10% interval; these points were excluded from curve analysis). Student's two-tailed t-test was used to assess significance between inactive (unphosphorylated) and active (phosphorylated) JNK3 (** $p<0.01$).

Collectively, the MST affinity measurements indicate that in the presence of ATP, kinase phosphorylation decreases the affinity for arrestin-3. This implies that JNK3 phosphorylation induces its dissociation from arrestin-3, which would vacate the binding site and allow another inactive JNK3 to bind and become phosphorylated.

Kinase phosphorylation alters the binding site on arrestin-3. MAP kinases achieve maximum activity when fully phosphorylated on their activation loop (201). While the structures of both unphosphorylated and phosphorylated members of the JNK3 cascade are not available,

crystal structures of inactive and active ERK2 (40% identical to JNK3) have been determined (201,202). Upon full phosphorylation, ERK2 remodels its active site and slightly rotates the N- and C-terminal lobes of the kinase domain (202). These conformational changes induce allosteric shifts in the surface loops that affect the ERK2 interactions with other macromolecules.

We used peptide array analysis to test whether phosphorylation-dependent conformational changes affected the binding position of each kinase on arrestin-3. This technique takes advantage of the fact that arrestins interact with binding partners via peptide-like surface fragments (46,47,64,203). Based on our recent finding that the first 25 amino acids of arrestin-3 (T1A) are sufficient to scaffold the JNK3 cascade, we used peptides corresponding to this region to assess whether the binding site on arrestin-3 shifted upon kinase activation (75) (**Fig. 6.4**). We used the non-hydrolyzable ATP analog AMP-PNP to minimize assay-to-assay variability resulting from ATP hydrolysis during overnight incubation.

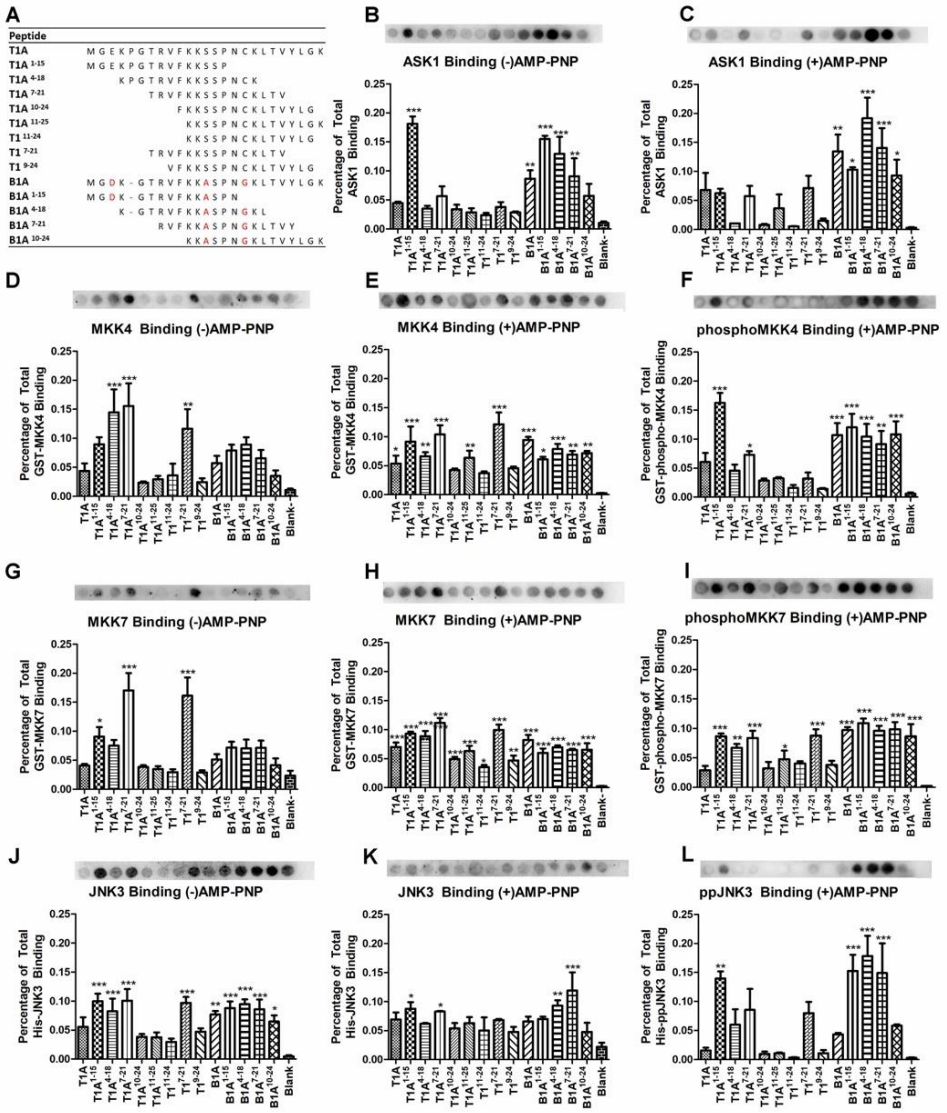

Fig. 6.4. The binding of ASK1, MKK4/7, and JNK3 to arrestin-3 peptides in their unphosphorylated and phosphorylated states. Peptides of the first 25 amino acids of arrestin-3 (T1A) were synthesized as 14-25 amino acid fragments attached to a solid support using ResPep SL (Intavis Bioanalytical Instruments). The amino acid sequences of each peptide and their corresponding names are shown. As a biologically relevant negative control, we added a short scan of the B1A peptide, an N-terminal (homologous to T1A) fragment of arrestin-2, which binds the kinases without facilitating JNK3 activation (204). We also used a blank spot and a 15-mer glycine peptide as negative controls, both of which yielded the same non-specific binding. Sequence differences between the T1A peptide and B1A and B1A-derived peptides are highlighted in red. **B.** The binding of ASK1 in the presence of AMP-PNP, **C.** ASK1 in the absence of AMP-PNP, **D.** GST-MKK4 in the absence of AMP-PNP, **E.** GST-MKK4 in the presence of AMP-PNP, **F.** GST-phosphoMKK4, **G.** GST-MKK7 in the absence of AMP-PNP, **H.** GST-MKK7 in the presence of AMP-PNP, **I.** GST-phosphoMKK7, **J.** JNK3 in the absence of AMP-PNP, **K.** JNK3 in the presence of AMP-PNP, and **L.** phosphoJNK3 (2 mM AMP-PNP and 3 mM $MgCl_2$ when indicated) (n=3-5). Representative peptide array results are shown above graphs displaying experimental averages. Statistical analysis was performed using one-way ANOVA followed by Dunnett's post-hoc test. The statistical significance of the difference of the signal from the blank spot (negative control) is shown (*, $p<0.05$; **, $p<0.01$; ***, $p<0.001$).

Incubation of inactive ASK1 with T1A-derived peptides implicated the first fifteen residues of arrestin-3 in ASK1 binding (**Fig. 6.4B, C**). These residues also participated in binding of the downstream MAP2Ks MKK4/7 (**Fig. 6.4D-I**). Interestingly, unphosphorylated MKK4 and MKK7 demonstrated similar binding patterns, suggesting that they bind overlapping sites that include the T1A region of arrestin-3; however, phosphorylated MAP2Ks exhibited dissimilar binding. One interpretation of this finding is that the binding sites for these active kinases are optimized to stabilize an ideal orientation for acting on JNK3 (193). Both MAP2Ks exhibited an activation-dependent change in the pattern of peptide binding for T1A-derived peptides (**Fig. 6.4E-F, H-I**).

We next assessed binding of final effector JNK3. Unphosphorylated JNK3 exhibited more modest binding to all T1A-derived peptides than did the upstream kinases (**Fig. 6.4K**); however, doubly-phosphorylated JNK3 only bound measurably to the $T1A^{1-15}$ peptide (**Fig. 6.4L**). As the affinity of inactive JNK3 for arrestin-3 in the MST experiments is fairly high, the modest signal observed suggests that JNK3 has additional binding contacts on full-length arrestin-3, in agreement with an earlier report (104) and our pull-down assays (**SI Appendix, Fig. 6.1D**). Importantly, JNK3 activation leads to decreased contact with the T1A region of arrestin-3, which is consistent with both the pull-down assays (**Fig. 6.1**) and the lower affinity observed in the MST measurements (**Fig. 6.2E-H**).

Notably, peptide array analysis revealed that unphosphorylated MKK4 and MKK7 bind to overlapping sites within the T1A peptide and that the active forms of MKK4, MKK7, and JNK3 also share binding regions. It is possible that there are additional contact points for each kinase on arrestin-3 that strengthen the interaction. An alternative interpretation is that only kinases that do not share overlapping sites can bind arrestin-3 simultaneously. In this scenario, the data suggest

that MKK4 and MKK7 cannot bind to arrestin-3 at the same time, whereas inactive JNK3 can form a complex with arrestin-3 and an upstream kinase.

For comparison, we analyzed the binding of the kinases to the B1A peptide, a homologous peptide to T1A that contains the first 25 amino acids of arrestin-2. We observed that binding to B1A was not significantly affected by the presence of AMP-PNP or phosphorylation, suggesting that kinase contact points on B1A retain similar binding affinities over the course of activation. Because signal amplification requires release of the activated kinase, this difference between T1A and B1A binding may underlie the observed inability of arrestin-2 to facilitate the activation of JNK3 in cells (75).

Computational modeling of MAP2K action on JNK3. To identify a biochemical reaction mechanism to explain JNK3 activation, we built the JNK3-activation Reaction Model (JARMv1.0) (**Fig. 6.5A, 6.6A**). JARMv1.0 was encoded using PySB (205) to enable hypothesis testing as we explored plausible mechanisms. We used an *in vitro* kinase activation assay to give the model a dynamic point of reference for calibration. This assay characterized the JNK3 phosphorylation time course, in the presence or absence of arrestin-3, by MKK7 and MKK4 (**Fig. 6.5B-C, 6.6B**). The data showed 2.2-fold more phosphorylation of Thr-221 than Tyr-223 at 60 s incubation when arrestin-3 is present. It also showed that ppJNK3 generation in the presence of arrestin-3 displayed a fold change between 1.2 and 1.8 higher than in the absence of arrestin-3.

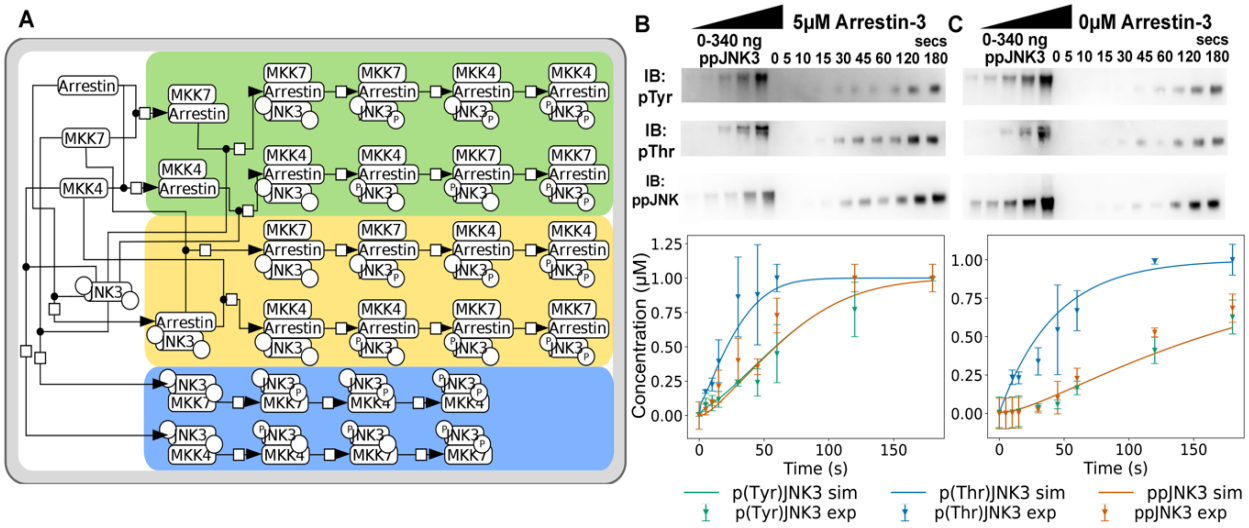

Fig. 6.5. Phosphorylation of inactive JNK3 by upstream kinases MKK4/7. (A) Network of the interactions between MKK4, MKK7, and JNK3 with arrestin-3. Nodes represent the different complexes formed by the interacting species, and the circles in the JNK3 node show the phosphorylation state of the tyrosine (left) and threonine (right) sites. The different orders in which JNK3 can be phosphorylated are highlighted by color: arrestin-3:MKK4/7 formation before JNK3 binding (green); arrestin-3:JNK3 complex formation before MKK4/7 binding (yellow); MKK4/7 binding JNK3 in the absence of arrestin-3 (blue). The convention of Kitano et al. is followed (206). **(B,C)** Representative Western blots showing phosphorylation of inactive JNK3 by MKK4 (upper panel, pTyr), MKK7 (middle panel, pThr), or both kinases (lower panel, ppJNK3) at indicated time points upon co-incubation of the three kinases in the presence of 5 μM arrestin-3$^{(1\text{-}393)}$ **(B)** or in its absence **(C)**. Standards of ppJNK3 (20-340 ng) were used to calculate the ng of singly-phosphorylated or doubly-phosphorylated JNK3 generated over time (n=3). JNK3 phosphorylation at Tyr-185, Thr-187, and both residues are shown for arrestin and no arrestin conditions. Solid lines represent the model simulated trajectories, whereas the symbols show the experimental data used for model calibration.

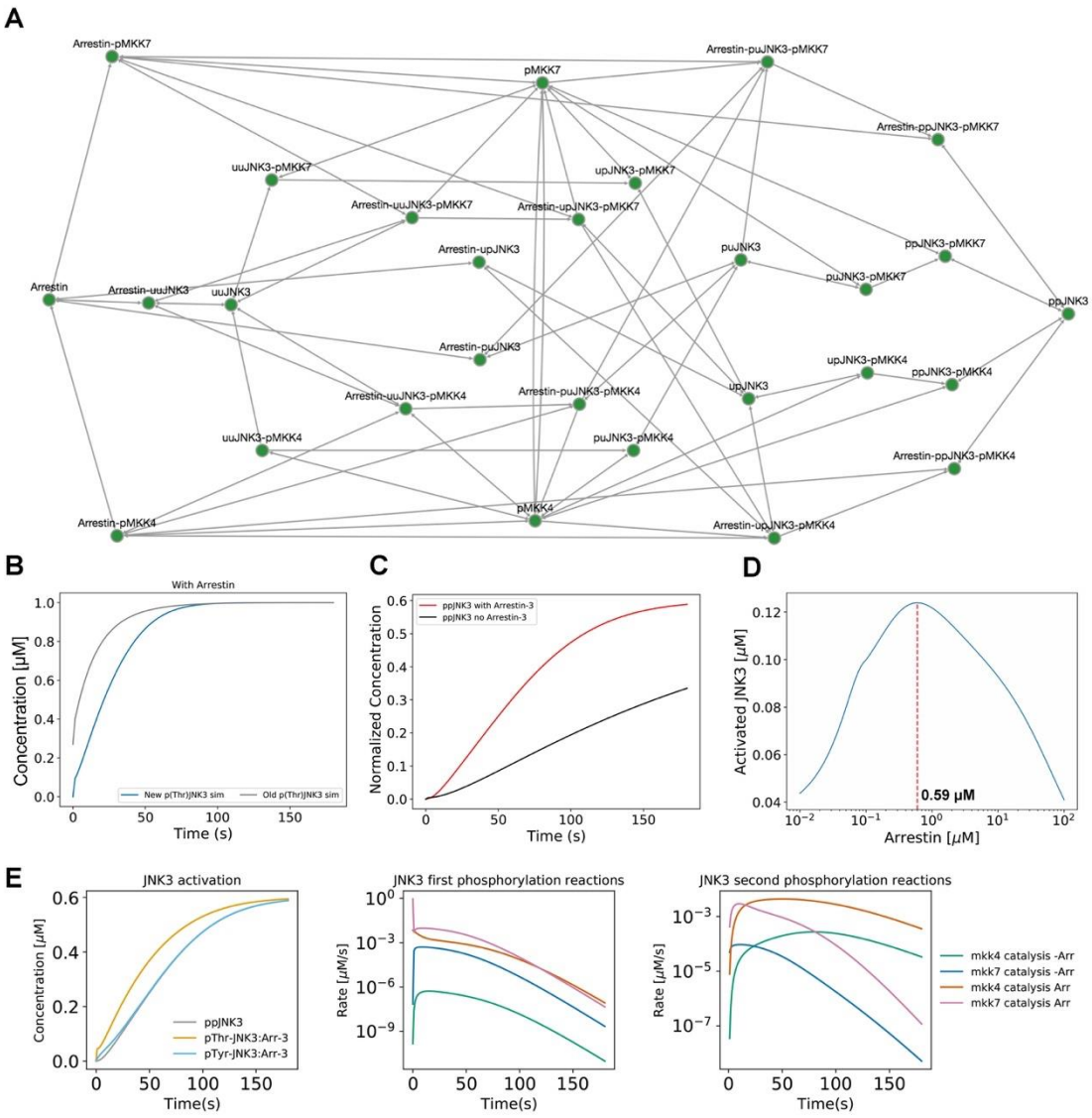

Fig. 6.6. JNK3 activation reaction model. (**A**) The protein-protein interaction networkbetween arrestin-3, MKK4/7 and JNK3. (**B**) Simulated trajectories of Thr-221 phosphorylation in the presence of arrestin-3. As a blind test for JARMv1.0 robustness, the computational model was used to predict phosphorylation of pThr-221 in the presence of data collected using an antibody with limited dynamic range. In this scenario, the experimental results are expected to be inaccurate. The gray line is the proposed trajectory when these inaccurate values for the kinetics of p-Thr221 phosphorylation are used for model calibration and execution. In contrast, the blue line shows the computational model adjusted for the values shown in **Fig. 2B**. This demonstrates that the computational model (gray) accurately predicts the trajectory of the newly collected data (blue) without parameter bias. This validates the model and demonstrates the predicting capabilities of JARMv1.0 for this system in the absence of experimentally determined parameters. **(C)** Simulated model trajectories of doubly phosphorylated JNK3. The red and black lines show the production of ppJNK3 when arrestin-3 is present and absent, respectively. (**D**) Simulated effect of varying arrestin-3 concentration in the system. **(E)** Right panel: corresponds to the time-dependent concentration changes of active (doubly phosphorylated) JNK3, pTyr-JNK3 bound to arrestin-3 and pThr-JNK3 bound to arrestin-3. Center panel: represents the catalysis reaction rate values of singly phosphorylated JNK3. Left panel: shows the catalysis reaction rate values of active (doubly phosphorylated) JNK3.

To populate JARMv1.0 parameters, we used our experimentally determined binding constants (**Fig. 6.2A-H, Fig. 6.7**) and values reported in the literature (99). Remaining parameters were estimated using PyDREAM, a Bayesian parameter inference formalism (207). This yielded parameter probability distributions, constrained by our experimental data, rather than single best-fit values (**Fig. 6.8**). Inspecting these distributions, we observed a few that spanned a narrow parameter range whereas others spanned a broader parameter range. From a statistical perspective, JNK3 activation is less sensitive to parameters with broad distributions, and more sensitive to those with a narrow distribution. The calibration results suggest that the system is most sensitive to the catalytic phosphorylation constants of MKK4 and MKK7 (**Fig. 6.8**). This gave us confidence that experimental measurements provided suitable constraints to explore the dynamics of JNK3 phosphorylation even without direct measurements of other parameters.

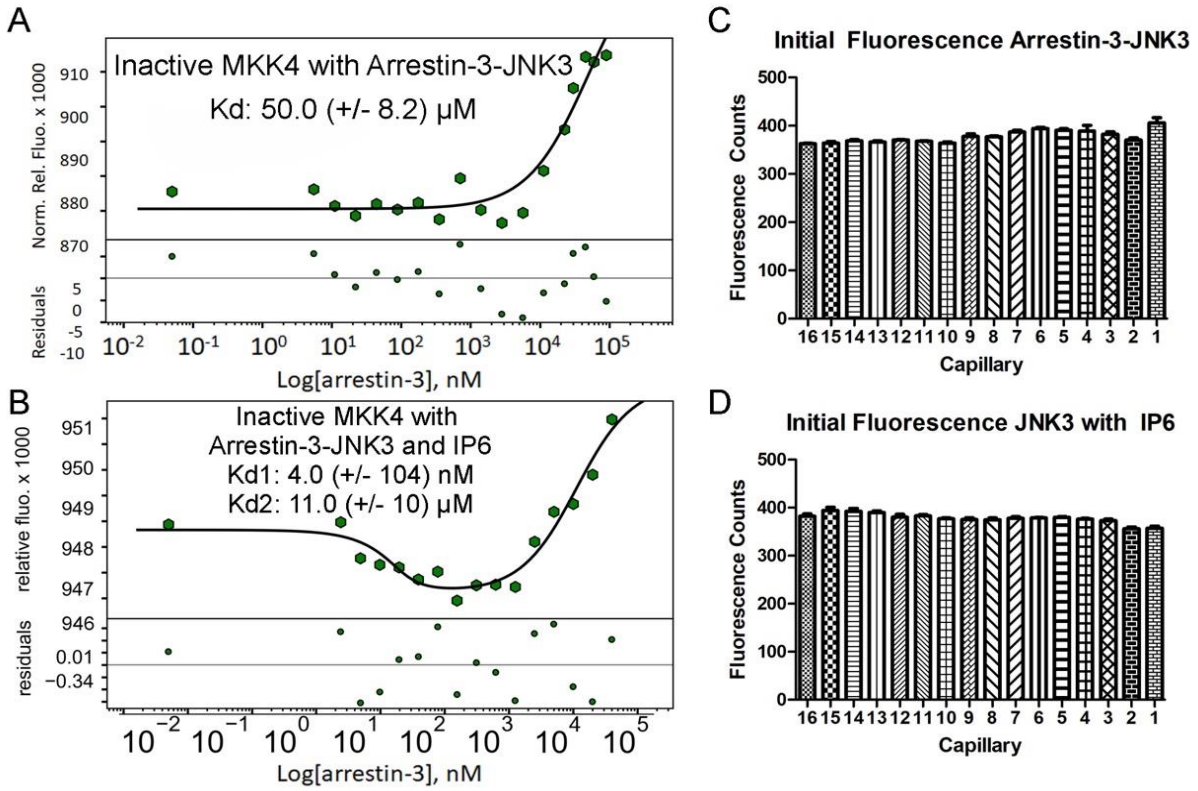

Fig. 6.7. Microscale thermophoresis with an arrestin-3-JNK3 complex or full-length arrestin-3 in the presence of IP_6. The average K_d value is shown. **(A)** The binding curve for arrestin-3-JNK3-His with GST-MKK4 was determined in the presence of 1 mM AMP-PNP and 2 mM $MgCl_2$. MST was performed at a constant concentration of Tris-NTA-labeled arrestin-3-JNK3-His (100 nM), and the indicated concentrations of unlabeled GST-MKK4 (0-90 µM; n=3). Binding curves were calculated using nonlinear regression (curve fit). **(B)** The binding curve for full-length arrestin-3 with inactive JNK3 in the presence of 1 mM AMP-PNP, 2 mM $MgCl_2$, and 100 µM IP_6. MST was performed at a constant concentration of Tris-NTA-labeled His-JNK3 (100 nM) and titrations of full-length arrestin-3 (0-40 µM; n=3). **(C,D)** Initial fluorescence was measured using a capillary scan prior to MST analysis. Average values of three experiments are shown. Statistical analysis was performed using NT Analysis Software (NanoTemper technologies GmbH) (*, outside of ±10% interval; these points were excluded from curve analysis).

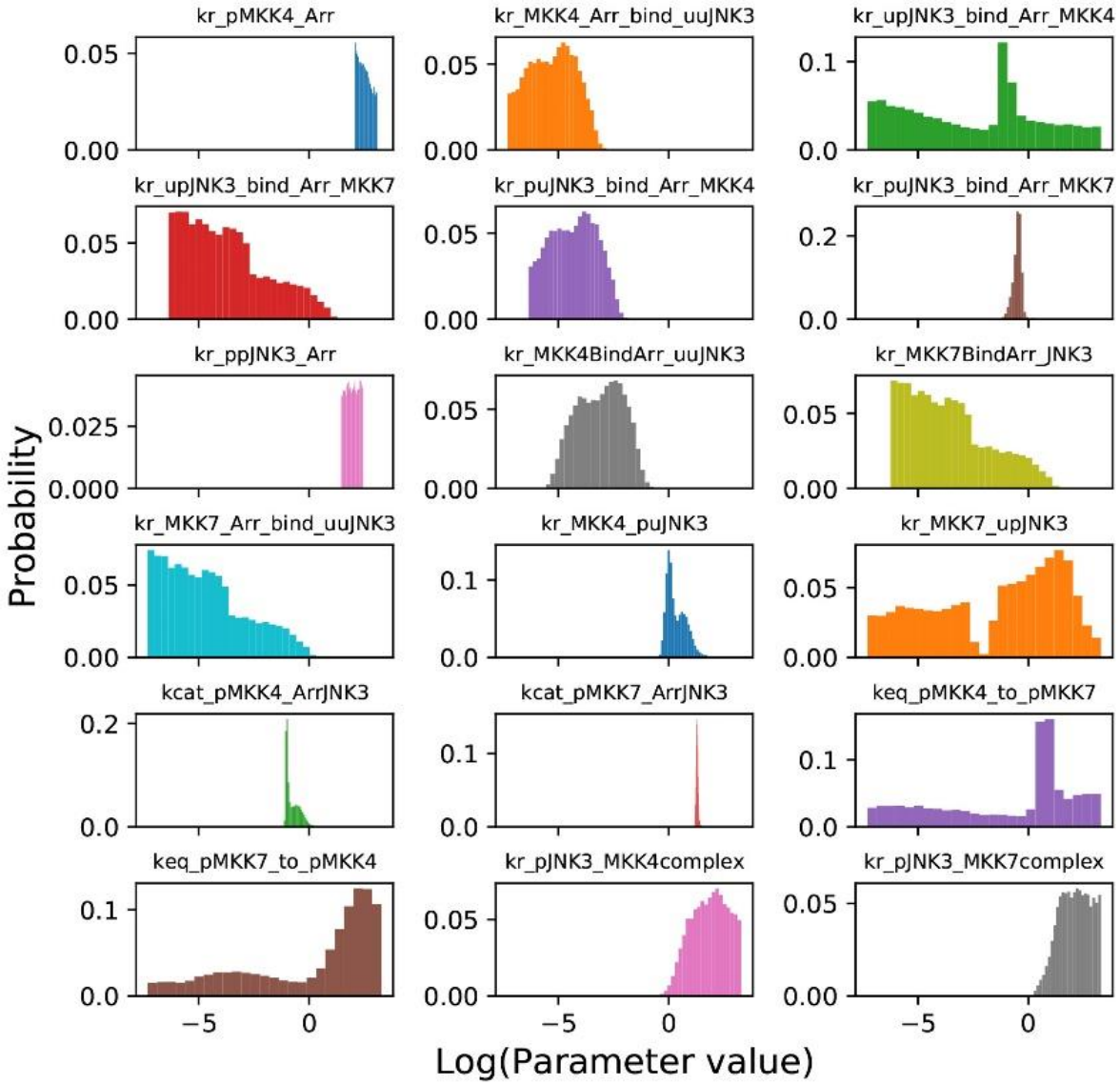

Fig. 6.8. Posterior probability distributions for calibrated JARM kinetic parameters. The x-axis corresponds to the base-10 logarithm range for possible values of kinetic parameters in JARM. The y-axis represents the probability of each of the possible parameter values. The resulting distributions provide an idea of the range and likelihood of each parameter value given the experimental data. As shown, some parameters exhibit a broad range of parameters (~3 orders of magnitude) but the key catalytic parameters for arrestin are well constrained. Parameter values were obtained as described in *SI Methods.* Parameter names with the prefix 'kr', 'kcat' and 'keq' correspond to the reverse, catalysis (sec^{-1} units) and forward ($(uM*sec)^{-1}$ units) rate constants, respectively.

Calibrated JARMv1.0 showed that the time-dependent concentrations of singly phosphorylated JNK3 in complex (pTyr-JNK3:Arrestin-3, pThr-JNK3:Arrestin-3) or doubly phosphorylated JNK3 (ppJNK3), exhibit nonlinear dynamics that emerge from multiple simultaneous reactions (**Fig 6.5B,C, top, Fig. 6.6E**). Our Bayesian calibration estimated that the catalytic constant of JNK3 phosphorylation by MKK7 is 2 orders of magnitude faster than the one of JNK3 phosphorylation by MKK4 (**Fig. 6.8**). This leads to rapid consumption of unphosphorylated JNK3 and pTyr-JNK3, whereas pThr-JNK3 accumulates in the system over time. In addition, the reaction rate of MKK4 second phosphorylation on the arrestin-3 scaffold is up to one order of magnitude faster than all other second phosphorylation events with or without arrestin-3 (**Fig 6.5B,C, bottom**). Taken together, these data suggest that MKK4 phosphorylation is the rate-limiting step in the JNK3 activation pathway, but multiple interactions take place to accomplish this outcome. This is consistent with active MKK4 having a lower affinity for arrestin-3 (**Fig. 6.2A-B**).

JARMv1.0 also showed that the reactions involving arrestin-3 increase the yield of doubly phosphorylated JNK3 3-fold at early time points (24 secs) (**Fig. 6.6C**) relative to the reaction system without arrestin-3. Previous studies have shown that less than 50% dual phosphorylation over total JNK expression can lead to a robust physiological response (208-210). JARMv1.0 execution places the optimal concentration of arrestin-3 for maximal JNK3 phosphorylation around ~0.59 μM (**Fig. 6.6D**).

Release of active JNK3 from arrestin-3 is necessary for signal amplification. Signal amplification requires activation of multiple downstream signaling molecules following a single upstream stimulus. To test the biological role of the release of activated JNK3 from arrestin-3, we engineered an arrestin-3-JNK3 fusion and expressed it in HEK293 arrestin-2/3 knockout cells

(211) (**Fig. 6.9**). After 48 h, we assessed the level of JNK3 activation in cells expressing free arrestin-3 or the arrestin-3-JNK3 fusion. We found significantly less JNK3 phosphorylation in cells expressing arrestin-3-JNK3 fusion than in cells expressing free arrestin-3 (**Fig. 6.9B**). Importantly, the JNK3 within the arrestin-3-JNK3 fusion was effectively phosphorylated (~95 kDa band on ppJNK3 blot, **Fig. 6.9A**), demonstrating that the fused proteins are functional. These data provide the first evidence that the release of activated JNK3 increases JNK3 phosphorylation. This supports computational and experimental prediction that once phosphorylated, active JNK3 must dissociate from arrestin-3 to allow an inactive JNK3 molecule to bind, ensuring signal amplification.

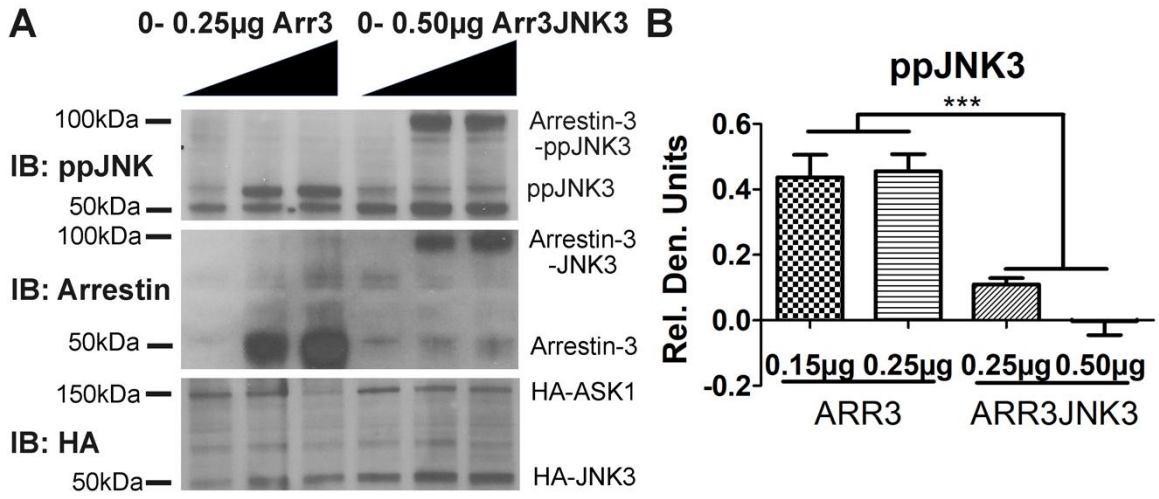

Fig. 6.9. JNK3 phosphorylation in cells expressing arrestin-3 or arrestin-3-JNK3 fusion. HEK293 arrestin-2/3 knockout cells were transfected with HA-ASK1 (0.1µg), HA-JNK3 (0.65µg), and either arrestin-3 (0-0.25µg) or arrestin-3-JNK3 (0-0.5µg) DNA for 48 h. **A.** The cells were lysed and analyzed by Western using antibodies against ppJNK (Cell Signaling, #9255S), arrestin (rabbit polyclonal F431 antibody, (211)), and HA (Cell Signaling, #3724). QuantityOne software was used to analyze the ppJNK3 bands by densitometry. **B.** The quantification of ppJNK3. The background was subtracted for each respective grouping (arrestin-3 and arrestin-3-JNK3) and the intensity of individual bands was divided by the sum total of band intensities (to eliminate the effect of exposure). Statistical analysis was performed using OneWay ANOVA followed by Dunnett's post-hoc test with correction for multiple comparisons (*, $p<0.05$; **, $p<0.01$; ***, $p<0.001$) (n=5).

6.3 Discussion

Since the discovery of the first signaling scaffold (180), scaffold proteins have been the focus of numerous studies as they provide a simple mechanism for information flow in complex intracellular pathways. Prior studies have focused on how scaffold proteins exert their effects through simple tethering and localization of pathway components. There are, however, potential drawbacks to the simple tethering model. Most notable is the sequestration of signaling components leading to a reduction in signal (212). Despite the plethora of literature dedicated to protein scaffolding, the field lacks evidence on how protein scaffolds amplify signals.

It has been long established in the field that arrestin-mediated signaling occurs through both GPCR-dependent (54,190) and GPCR-independent (64,96,121,191) pathways. For example, studies supported the concept that GPCR-bound arrestin-3 increased JNK3 activation, but also demonstrated that the receptor was not obligatory for this function (97,213). Essentially, in cells overexpressing upstream MAP3K ASK1, arrestin-3 facilitated JNK3 phosphorylation in the absence of receptor activation. Subsequently, an arrestin-3 mutant defective in GPCR binding was found to effectively activate JNK3 (64,96). *In vitro* pre-activated arrestin-$3^{(1\text{-}393)}$ facilitates JNK3 phosphorylation by MKK4 and MKK7 in the absence of GPCRs (214). Finally, a short 25-residue arrestin-3-derived peptide lacking most of receptor-binding elements effectively activated JNK3 *in vitro* and in cells (75). Thus, arrestin-3 can exist in an active (at least in terms of JNK3 activation) conformation without GPCR binding, likely due to its high flexibility revealed by structural work (215) and molecular dynamics modeling (216).

This receptor-independent activation of the JNK3 cascade commences with binding of MAP3K ASK1 to the arrestin scaffold. While ASK1 binds all four isoforms of vertebrate arrestins (64), only arrestin-3 causes an increase in JNK3 phosphorylation (64,192,193). Association of

phosphorylated ASK1 with arrestin-3 is needed for downstream MAP2K activation. Dual phosphorylation of JNK3 by MKK4/7 is required for full activation of JNK3. Early evidence suggested that only MKK4 associates with the arrestin-3 (58), but later studies showed that both MKK4 and MKK7 bind arrestin-3 (214), albeit with different affinities, which is consistent with reported competition of these kinases for arrestin-3 (193). Therefore, we propose that arrestin-3 promotes the phosphorylation and activation of MKK4/7 by complexing with ASK1 (**Fig. 6.10A**). Since our peptide array data show significant overlap of the binding site of inactive MKKs, it is likely that the MKKs exchange on the arrestin-3/ASK1 complex (**Fig. 6.10B-C**).

MKK4/7 phosphorylation of JNK3 on Tyr-223 and Thr-221, respectively, results in its full activation. As previously surmised, MKK4/7 are not expected to bind arrestin-3 simultaneously. Evidence suggests that kinase scaffolding by arrestin-3 could enhance recruitment of additional cascade components via interaction with the arrestin-bound kinases (58); for example, it is well-established that MAPKs form complexes with cognate MAP2Ks and MAP3Ks through docking interactions (217). This type of recruitment would explain how an activated kinase with low affinity for arrestin-3 (i.e. phosphoMKK4) stays associated with the complex and activates its substrate. MST measurements of arrestin-3-JNK3 fusion protein binding to inactive MKK4 (**Fig. 6.7A,C**) yielded a decrease in affinity when compared to arrestin-3 alone (**Fig. 6.2A**). Thus, both the MAP2K and MAPK can bind simultaneously to arrestin-3.

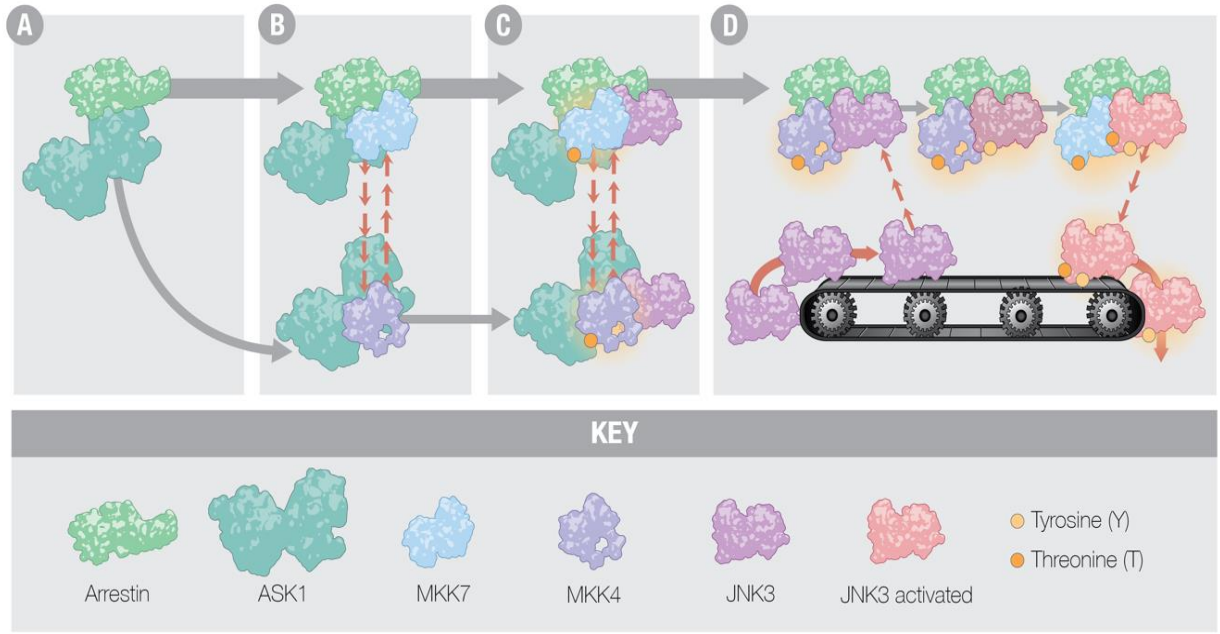

Fig. 6.10. The model of arrestin-3-mediated JNK3 activation. While this model depicts a precise ordering of ASK1 followed by MKK4/7 and finally JNK3, this has yet to be experimentally validated. **A.** The upstream MAP3K, apoptosis signal-regulating kinase 1 (ASK1), binds to arrestin-3 in preparation for activation of MKK4/7. **B.** MKK4 and MKK7 exchange on arrestin-3 and become activated by ASK1. Both the inactive and active forms of MKK7 have higher affinity for arrestin-3, making it likely that MKK7 is bound more frequently than MKK4, which is supported by our computational modeling (see **Fig. 6.5**). **C.** Inactive JNK3 (purple) binds arrestin-3 so that it may become activated by MKK4 and MKK7. **D.** Single phosphorylation of JNK3 on either its threonine or tyrosine residues (partially-active JNK3 shown in purple/red) reduces its affinity for arrestin-3; full phosphorylation results in a greater decrease in affinity, allowing JNK3 to dissociate from arrestin-3 to vacate the site where another inactive JNK3 molecule can bind (active JNK3 shown in red).

Global arrestin concentration changes throughout development: in early neural development it is 7-32 nM, while in late development it is closer to 200 nM (218). For our reported K_d values to be physiologically relevant, local cellular concentrations of arrestin would have to be higher. This is well-documented for arrestin in the literature. For example, arrestins are recruited to GPCRs in the plasma membrane (6,219,220) and to microtubules (121), and it is likely that non-receptor activators also influence local concentration; indeed, IP6 results in arrestin oligomerization (3,221). Therefore, the reported K_d values are consistent with this mechanism being a physiologically relevant.

To make investigation of this phenomenon experimentally tractable, we employed modified protein tools, including fusion proteins for pull-down assays and His-tagged kinases for the MST measurements. We also used a pre-activated arrestin-$3^{(1\text{-}393)}$, an established tool in the arrestin field for studying processes affected by activated arrestin (3,67,132,222-224) that eliminates the need for arrestin activation by GPCRs or non-receptor activators. These modifications did not affect the key conceptual conclusions, as evidenced by the experiments with full-length arrestin-3 in the presence of IP_6 (**Fig. 6.7B, D**). If anything, we might have underestimated the affinity of arrestin-3 for members of the JNK3 cascade, as in-cell experiments (**Fig. 6.9**) suggest that the presence of arrestin-3 has a much greater effect on JNK3 activity in the cell than the *in vitro* data and modeling indicate.

Based on our data, we propose a "conveyor belt" mechanism of JNK3 activation, where an active JNK3 molecule is exchanged for an inactive JNK3 on an arrestin-3/MKK complex leading to signal amplification (**Fig. 6.10D**). This exchange is important biologically; formation of a tight complex would prevent the release of the downstream activated kinase and inhibit physiological response (180). It remains to be elucidated whether this is a unique characteristic of arrestin-3-mediated scaffolding, or whether other scaffolds of JNK activation cascades employ the same mechanism. Our data provide new insight into the mechanism of arrestin-3 scaffolding of the ASK1-MKK4/7-JNK3 cascade; most notably, a >15-fold weaker affinity of doubly phosphorylated JNK3 for arrestin-3 than inactive JNK3, and our model analysis shows a 2 order of magnitude faster phosphorylation of JNK3 by MKK7 compared to MKK4. Careful comparison of active and inactive JNK3 binding to other purified scaffold proteins is necessary to determine whether this conveyor belt model is applicable to other scaffolds.

6.4 Materials and Methods

Protein Purification. Full length arrestin-3 and its truncated form (residues 1-393), ASK1, GST-MKK4-His_6, GST-MKK7-His_6, JNK3-His_6, and MBP-fusion proteins were purified, as described previously (3,225-228). In brief, MKK4 and MKK7 were cloned into a pGEX-4T1 vector with an N-terminal cleavable GST-tag and a C-terminal cleavable His-tag. To generate activated MKK4 and MKK7, 4 μM GST-MKK4 or GST-MKK7 and 2 μM GST-MEKK1c (catalytic domain) were incubated at 30°C for 1 h in the presence of 4 mM ATP in 10 mL activation buffer (25 mM HEPES pH 7.5, 20 mM $MgCl_2$, 0.1 mM EDTA, 0.1 mM EGTA, 2 mM dithiothreitol). Proteins were re-purified via size exclusion chromatography on a Superdex S200 Increase 10/300 GL column equilibrated with 25 mM HEPES-Na, pH 7.5, 100 mM KCl, 0.1 mM EDTA, 0.1 mM EGTA and 2 mM TCEP to separate activated GST-MKK4/7 from constitutively active GST-MEKK1c. JNK3-His was cloned into the pTrc-His2 vector with a C-terminal His-tag. Active JNK3 was prepared in the presence of active MAP2Ks, 4mM ATP, 20 mM $MgCl_2$, 0.1 mM EDTA, 0.1 mM EGTA, and 2 mM dithiothreitol.

Microscale Thermophoresis. MST was performed using the Monolith NT.115 instrument (NanoTemper Technologies GmbH). Binding was measured between arrestin-3 (in 20 mM MOPS pH 7.5, 150 mM NaCl, and 2 mM TCEP) and a His-tagged kinase. The His-tagged proteins were labeled using the MO-L008 Monolith™ His-Tag Labeling Kit RED-tris-NTA following the manufacturer's protocol (100 nM final concentration of kinase in PBS-T buffer). This labeling dye has recently been described as the optimal conjugate for oligohistidine-tags (229). An experiment with a control His peptide was performed to demonstrate that the His-tag did not interfere with binding. A 16-step dilution series was prepared by adding 10 μL buffer (20 mM MOPS pH 7.5, 150 mM NaCl, 2 mM TCEP, 0.05% Tween-20) to 15 tubes. 20 μL of 43-110 μM arrestin-$3^{(1-393)}$

was placed in the first tube, and 10 µL was transferred to the second tube and mixed well by pipetting (1:1 dilution series). The final tube did not contain any arrestin-3 and was used as a blank. 10 µL of the binding partner (inactive or phosphorylated His-kinase in the presence of 1 mM ATP and 2 mM $MgCl_2$) was added to each tube of the dilution series (final concentration 50 nM). The samples were incubated on ice for 15 minutes before being transferred to Standard Monolith NT™ Capillaries. The capillaries were scanned using the MST instrument (40% LED, 40% MST power). The preliminary capillary scan did not show a significant difference in the amount of fluorescently labeled His-kinase during experimentation except for several high concentrations of arrestin-3. An SDS-denaturation test was performed, and it was determined that at high concentrations of arrestin-3, several samples exhibited ligand dependent fluorescent changes. These data was excluded from further analysis. All data were analyzed using PALMIST (145,194). Measured fluorescence was normalized and averaged, and the binding constants were determined using a global fit calculation and a 1:1 fitting model (except for the IP_6 model where a 1:2 macro fit was chosen). The preset Thermophoresis + T-jump was used to calculate binding isotherms for the MAP2Ks, while the preset T-jump was used for the JNK3 interactions. Inactive and active kinase forms were compared using either a Student's two-tailed t-test (MAP2Ks: MKK4 and MKK7) or One-way ANOVA followed by Dunnet's post-hoc test (JNK3) using the inactive kinase form as the control. Of note, for **Fig. 6.2B** and **Fig. 6.2H** we were only able to obtain the lower boundary K_d values. To perform the Student's t-test we assumed that the values obtained from the lower boundary followed a normal distribution, which allowed us to determine significant difference.

MBP Pull-down. N-terminal MBP-fusion proteins including full-length bovine arrestin-3 and sequences corresponding to the indicated arrestin elements were designed and purified, as previously described (75,104). In brief, arrestin-3 or arrestin-3 fragments were subcloned into a

pMal-p2T vector with a 10 amino acid linker, TLVPRGSPGF, between MBP and arrestin-3 or its fragments. Purified MBP was used as a negative control in all pull-down experiments and non-specific binding was subtracted from the total observed binding for each construct. MBP-fusion proteins (10-30 μg in 50 μL of 20 mM Tris/150 mM NaCl) were immobilized on amylose resin (25 μL, 50% slurry, New England Biolabs) for 1 h at 4 °C with slight rotation. Prey protein (GST-MKK4, GST-MKK7, or His-JNK3, 10 μg in 50 μL of 20 mM Tris/150 mM NaCl) was added to the immobilized MBP constructs and incubated with gentle rotation for 2 h at 4 °C in the presence or absence of 2 mM ATP and 4 mM $MgCl_2$. Samples were transferred to centrifuge filters (Durapore®-PVDF-0.65 μm), washed three times with 50 mM HEPES-Na, pH 7.3, 150 mM NaCl. Elution buffer (100 μL 50 mM maltose in wash buffer) was added, the samples were rotated gently for 5 min at 4 °C before centrifugation. Protein in eluates was precipitated by the addition of 1 mL of methanol, and centrifugation at maximum speed for 10 min. The pellets were air dried, dissolved in SDS sample buffer (30 μL Laemmli, 2x) and analyzed by SDS-PAGE and Western blotting, as described (104). Statistical analysis was performed using One-way ANOVA followed by Dunnett's post-hoc test.

Peptide Array Synthesis. The ResPep SL peptide synthesizer was used with conventional SPOT synthesis protocols using peptides ranging from 14 to 25 residues in length, as previously described (230). Both a blank spot and a 15-mer glycine peptide were used as negative controls, and non-specific binding to these controls was not statistically different. Peptides were assembled by the ResPep SL on solid support via a peptide amide linker using Fmoc-chemistry. The sequences of the peptides were derived from the first 25 amino acids of bovine arrestin-3, which function as an effective scaffold of ASK1-MKK4/7-JNK3 cascade in cells (75). After synthesis, the amino-protecting group was removed using piperidine (20% (v/v) solution in

dimethylformamide) followed by extensive washing. The membranes were then submerged in a solution of 95% trifluoroacetic acid (TFA) and 3% triisopropylsilane for 1 h with agitation. Following removal of the TFA solution, the membranes were washed in dichloromethane four times 10 min each, followed by four 10 min washes in dimethylformamide and two 2 min washes in ethanol. The membranes were then dried in the hood and stored at 4°C.

Peptide Membrane Blots. Dried membranes were soaked in 100% ethanol for 5 min and then rehydrated by washing twice in water for 5 min. The membranes were then incubated in blocking solution (5% non-fat dry milk in Tris-buffered saline (TBS) with 0.1% Tween 20) for 1 h. The membranes were washed five times for 5 min before overnight incubation at 4°C with the prey protein (0.3-0.5 µM, depending on the protein construct) in binding buffer, (20 mM HEPES pH 7.3, 50 mM KCl, 0.1 mM EDTA, 0.1 mM EGTA, 10% glycerol, 2 mM ATP, 4 mM $MgCl_2$). The following morning, the membranes were rinsed five times for 5 min in TBS with 0.1% Tween 20. Membranes were incubated with the appropriate primary antibody for 1 h at room temperature, washed five times for 5 min in TBS with 0.1% Tween 20 (SAPK/JNK Rabbit Cell Signaling, 1:1,000 dilution, #9252P; GST Rabbit Cell Signaling, 1:1,000 dilution, #2622; ASK1 Rabbit Cell Signaling, 1:1,000 dilution, #3762). The corresponding HRP-conjugated secondary antibody (1:10,000 dilution) was prepared in TBS with 0.1% Tween 20, incubated with the membrane for 1 h, followed by two 5 min washes in TBS at room temperature. The spots were visualized using the SuperSignal West Pico Stable Peroxide Solution kit from ThermoScientific. Images were obtained using the Bio-Rad Gel Doc Imager and analyzed by densitometry using ImageJ protein array analyzer. For ResPep analysis, the signal in individual dots was measured as a percentage of total binding density detected on the membrane. This allowed for comparison across all peptide experiments. Statistical analysis was performed using one-way ANOVA followed by Dunnett's

post-hoc test using GraphPad Prism5.

Computational Modeling. The JNK3 activation reaction model (JARMv1.0) was implemented in Python using the PySB framework (205) that allows users to build mathematical models of biochemical systems as Python programs. In all, JARMv1.0 included 28 biochemical species, 60 chemical reactions, and 44 free parameters. When this program is executed, a set of rules is translated to 28 ordinary differential equations (ODEs) using the mass action kinetics formalism. Since the ODEs generated by JARM require rate constants instead of K_D values, all experimental K_D were converted into rate parameters using the equation $K_D=k_r/k_f$. For the model calibration, k_f rates were set within the "average enzyme" distribution of specificity constants (231-233), whereas the k_r were allowed to change. Out of linear range values at initial time points and higher than theoretical maximum values in the time-course data (Fig. 2A) were set to zero and the theoretical maximum, respectively. We then applied scaling normalization to both the time-course data and the simulated trajectories. Model calibration was then performed using the PyDREAM package (207), which is a python implementation of the (Multiple-Try) Differential Evolution Adaptive Metropolis ($DREAM_{(ZS)}$) algorithm (234). To reduce the number of model parameters to calibrate, we used the experimentally measured dissociation constants for the interactions between MKK4/7, JNK3, and arrestin-3, and literature values for the interactions between MKK4/7 and JNK3 alone (235). We assumed that the catalytic constants for JNK3 phosphorylation were the same within a scaffold complex and in solution (supported by **Fig. 6.7**). The model was pre-equilibrated to allow complexes to form before the reaction is initiated. Parameter prior probabilities were specified as uniform distributions with the lower and upper boundary set with the lowest and highest values from the protein–protein kinetic interaction data and structures (PPKIDS) dataset (236), indicating a lack of knowledge about the likely parameter

values. Literature-based values and experimental measures were fixed. The fit of simulated trajectories to experimental data was measured using the sum of the squared differences:

$$\chi^2 = \sum_t \sum_i \frac{1}{2\sigma^2_{data}} [x^i_{model}(t;\Theta) - x^i_{data}(t)]^2$$

Where *t* is the time span of the simulation and experiments, $\Theta = (\theta_1, \ldots, \theta_n)$ are the parameters of the model, x^i_{model} are the simulations of the model under condition *i and* $x^i_{data}\ (t)$ is the experimental data under condition *i*. This function corresponds to the negative log of the likelihood in the Bayesian framework assuming the measurement errors at time *t* have a normal distribution. By minimizing this function, we find probable parameter sets that fit the experimental data within the constraints that the network interactions and the network kinetics imposes. To further constraint the model, we added the requirement that thermodynamic cycles present in the interaction network (**Fig. 6.6A**) must obey detailed balance/free energy conservation in the likelihood function.

The DREAM$_{(ZS)}$ algorithm was ran using PyDREAM with five chains that started in parameter locations provided by previous calibrations using the Particle Swarm Optimization algorithm (237). Each chain sampled 500,000 parameter sets and the first 250,000 samples were discarded as burn-in. All chains were tested for convergence using the Gelman-Rubin criterion. To measure the goodness of fit of the calibrated model to the experimental data we use the χ^2 statistic. A good fit would correspond to a χ^2value that is approximately equal to the number of experimentally obtained data points. Using the 5000 most likely parameters obtained from the calibration we obtained a χ^2value of 32.32 (±0.09). Given that we measured 36 experimental points for pTyr-JNK3 and pThr-JNK3 reactions, we conclude that the model shows a reasonable fit to the experimental data.

All code used to build the model, fit the model parameters and perform analysis is freely distributed as open-source software and available in the Lopez lab GitHub repository

(github.com/LoLab-VU/JARM).

In vitro kinase activation assay. The ability of purified active MKK4 and MKK7 to phosphorylate inactive JNK3 in the presence of arrestin-3 was tested using an in vitro activation assay. A stock tube of kinase mix (10 mM HEPES pH 7.3, 5 mM $MgCl_2$, 100 mM NaCl, 2 mM TCEP) was prepared with pMKK4 (0.05 µM), pMKK7 (0.05 µM), arrestin-$3^{(1\text{-}393)}$ (5 µM), and inactive JNK3 (0.5 µM). Each reaction was performed in a volume of 20 µL in a 30°C water bath for the indicated time (0-180 secs). Reactions were initiated by adding 2 µL 10 mM ATP (1 mM final concentration) and quenched with 20 µL SDS buffer. Western analysis using pTyr (Cell Signaling, 1:2000 dilution, #8954S) or pThr (Cell Signaling, 1:5000 dilution, #9391S) antibodies was used to assess JNK3 phosphorylation. Known concentrations of ppJNK3 (20 – 340 ng) were used as standards in all experiments. Bands were quantified using Quantity One software (Bio-Rad) and phospho-JNK3 (ng) was plotted as a function of time (sec).

Recombinant pcDNA3-arrestin-3-JNK3 construction. To make the arrestin-3-JNK3 fusion the cDNAs encoding full-length arrestin-3 and full-length JNK3 were subcloned into a pcDNA3 vector between EcoRI and NotI sites. All restriction enzymes were from New England Biolabs (Ipswich, MA). The final construct consisted of full-length arrestin-3 followed immediately by full-length JNK3 without an additional linker between the coding sequences.

JNK3 phosphorylation assay in HEK293 arrestin-2/3 knockout cells. HEK293 arrestin-2/3 knockout cells (a generous gift from Dr. Asuka Inoue, Graduate School of Pharmaceutical Sciences, Tohoku University) were maintained in DMEM solution containing 10% FBS (Invitrogen), penicillin, and streptomycin at 37°C and 5% CO_2. Cells were transfected at 90-100% confluency in 6-well plates with pcDNA3-HA-ASK1 (0.1ug), pcDNA3-HA-JNK3α2 (0.65µg), and pcDNA3-arrestin constructs (0-0.5µg) at a 1:2.5 ratio of DNA:Lipofectamine 2000

(Invitrogen). At 48 hr post-transfection, the cells were lysed with 400 μL RIPA buffer and spun at 15,000xg to pellet debris. The supernatant was mixed 1:1 with 2x SDS sample buffer (Sigma), the proteins were subjected to 10% SDS-PAGE, and transferred to PVDF membrane (Millipore, Bedford, MA). Membranes were blocked by 1% non-fat dry milk in TBS/Tween-20, incubated with respective primary antibodies (Cell Signaling Technology, Inc.): anti-HA (#3724), anti-phospho-JNK (#9255S), and anti-arrestin (rabbit polyclonal F431 antibody (211)), followed by the appropriate HRP-conjugated secondary antibodies (Jackson ImmunoResearch Laboratories, Inc., West Grove, PA). Bands were detected by X-ray film using enhanced chemiluminescence (ECL, Pierce) and quantification was done using the software Quantity One (BioRad, Hercule, CA).

CHAPTER 7

ERK2 INTERACTION WITH NONVISUAL ARRESTINS SUGGESTS A MECHANISM FOR PREFERENTIAL ACTIVATION

This article is in preparation for Nature Structure and Molecular Biology. **Nicole A. Perry** will be the first author and Ali I. Kaya, Pankaj Sharma, Sergey Vishnivetskiy, Ji Young Park, Ka Young Chung, Andrea Piserchio, Ranajeet Ghose, Tamer N. Kaoud, Kevin N. Dalby, Changxiu Qu, Fan Yang, Ruirui Li, Jinpeng Sun, Ya Zhuo, Candice S. Klug, T.M. Iverson, and Vsevolod V. Gurevich contributed to this work.

7.1 Introduction

Arrestins are multifunctional proteins originally discovered for their role in the desensitization and internalization of G protein-coupled receptors (GPCRs) (27,45,238). This classical paradigm has been expanded to include arrestin-mediated signaling, which can occur in a receptor-dependent or -independent fashion. The non-visual arrestins have been shown to interact with >100 effectors (9), notably including clathrin and AP-2 (6,239), Src family tyrosine kinases (51,57), and members of mitogen-activated protein kinase (MAPK) cascades (10,77,193,240,241). Perhaps one of the most intensely characterized effector interactions is that of the non-visual arrestins with ERK2 (242).

The non-visual arrestins were first shown to facilitate signaling of extracellular signal-regulated kinase 1/2 (ERK1/2) following activation of the angiotensin II type 1a receptor (AT1aR) (242). Not only did ERK2 colocalize with AT1aR-arrestin complexes, but ERK2 phosphorylation

was also enhanced by co-expression of upstream kinase cRaf-1, which suggested that arrestin could function as a protein scaffold for the cRaf-1/MEK/ERK2 cascade. Initial models of arrestin-mediated cellular signaling were restricted to this receptor-dependent activation of arrestin (51,58,242); in fact, ERK1/2 interaction with arrestin was demonstrated to be greatly facilitated by GPCR stimulation (64,242).

Several studies have demonstrated that both non-visual arrestins (arrestin-2 and arrestin-3, a.k.a. β-arrestin1 and 2) promote the activation of ERK1/2 (64,67,241-245). These two isoforms of arrestin are ubiquitously expressed and share a high degree of sequence and structural similarity (246). Considerable effort has been made to elucidate the difference between the two isoforms including studies of isoform-selective knockout mice (247). Although several functional specializations have been established (6,248), ERK1/2 signaling seems to involve both isoforms of arrestin (249,250).

Here we examine the differences in binding interfaces between the non-visual arrestins and ERK2. We demonstrate that both arrestin-2 and arrestin-3 can bind ERK2, but that the binding modes are likely dissimilar. This is supported by a combination of biophysical and structural techniques, most notably HDX-MS experiments between arrestin-$2^{1\text{-}387}$ and ERK2, and SAXS analysis of a tethered arrestin-3-ERK2 construct. Collectively, these data identify molecular details of the arrestin/ERK2 interface and suggest potentially diverse roles of the two arrestin isoforms in ERK2 activation.

7.2 Results

Arrestin-2/3$^{1\text{-}393}$ exhibit increased affinity for ERK2 compared to full-length proteins. Co-immunoprecipitation studies identified ERK2 as an interacting partner of the non-visual arrestins

over 15 years ago (59); however, a direct interaction between the two proteins wasn't confirmed until much later using the model receptor light-activated, phosphorylated rhodopsin (67). This study found that receptor-associated arrestins (arrestin-1/2/3) readily bind ERK2, but only the non-visual arrestins interact with ERK2 in a receptor-independent fashion. To confirm this interaction, we analyzed the affinities of free purified non-visual arrestins for ERK2 using microscale thermophoresis (MST). MST is a biophysical technique that detects changes in fluorescence that result from the movement of molecules in a temperature gradient (196,251).

We first tested the affinities of full-length, bovine arrestin-2/3 for ERK2. Previous work has indicated that ERK2 prefers receptor-bound arrestins (67); therefore, we expected a low affinity interaction since our full-length proteins are likely in the basal conformation. Indeed, full-length arrestin-2 bound ERK2 with K_d >45 (±11) μM and full-length arrestin-3 with K_d >47 (±4.7) μM (**Fig. 7.1A,B**). In contrast, when we measured the affinities of arrestin-2/3$^{1\text{-}393}$, constructs with C-terminal deletions that make them more likely to assume active (receptor-bound-like) conformation, we observed significantly stronger interactions (**Fig. 7.1C,D**). The 1-393 truncation is an established tool in the arrestin field for studying effects of an activated arrestin conformation (3,67,132,222-224) and alleviates the need for activation by GPCRs or non-receptor activators. Arrestin-2$^{1\text{-}393}$ exhibited two binding affinities, a high affinity interaction of 8.4 (±1.7) nM and a lower affinity interaction of 8.4 (±2.3) μM, while arrestin-3$^{1\text{-}393}$ displayed only one affinity for the interaction with a K_d 2.1 (±0.6) μM. Collectively these results suggest that active arrestin is the preferred conformation for the ERK2 interaction.

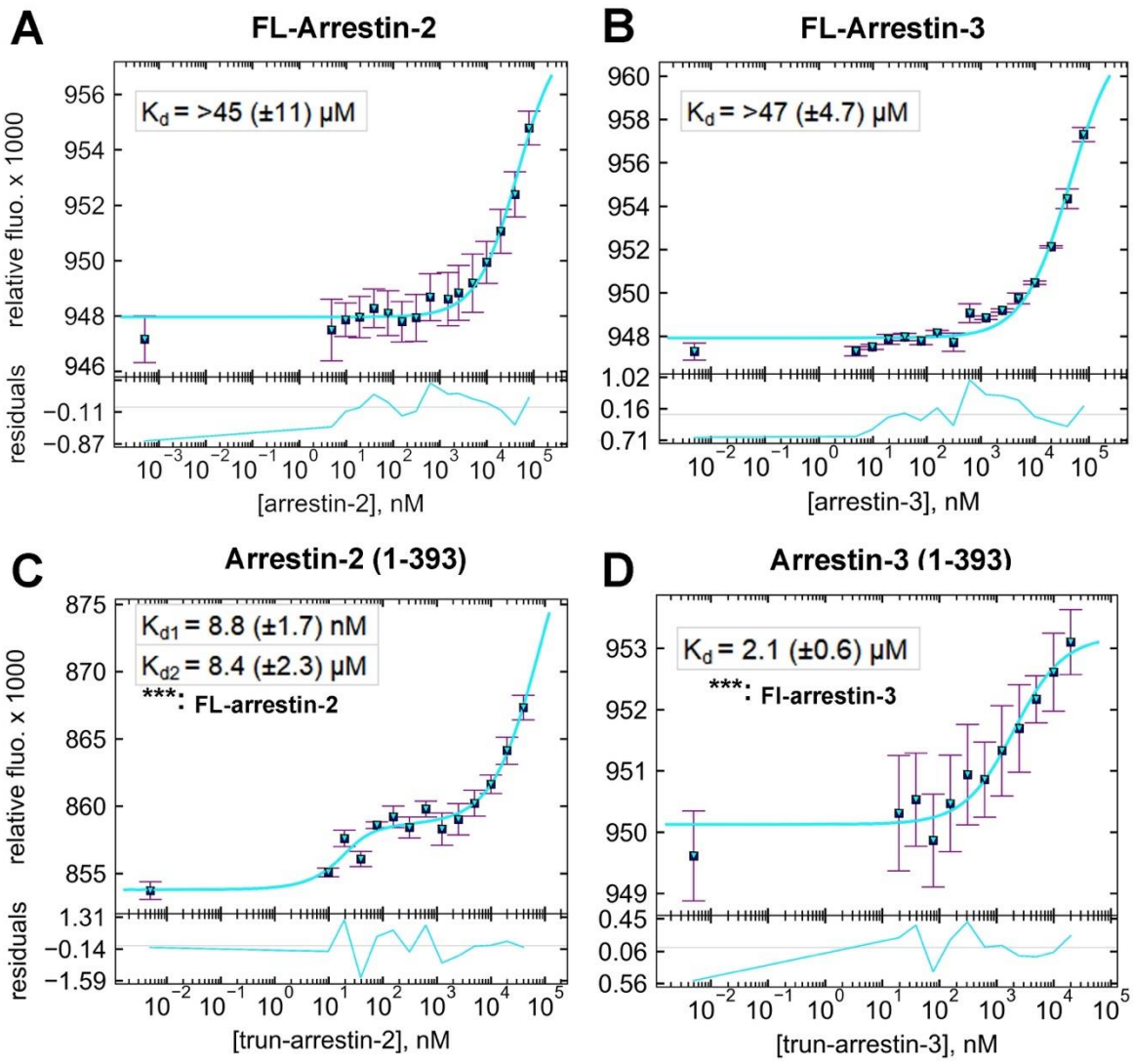

Fig. 7.1. Microscale thermophoresis of ERK2 with nonvisual arrestin constructs. Average K_d values are shown for each curve (n=3). Binding curves for unphosphorylated ERK2 with full-length arrestin-2 **(A)**, full-length arrestin-3 **(B)**, truncated arrestin-$2^{(1\text{-}393)}$ **(C)**, and truncated arrestin-$3^{(1\text{-}393)}$ **(D)** in the presence of 1 mM ATP and 2 mM $MgCl_2$ are shown. The preset T-jump was used to calculate the isotherm. One-way ANOVA followed by Tukey's post-hoc test was used to assess significant differences between full-length constructs and their truncated counterparts (***, $p<0.001$).

Interaction kinetics for full-length arrestin-2/3 binding ERK2. After we determined the relative affinities of the nonvisual arrestins for ERK2, we decided to assess whether there are kinetic differences in ERK2 binding between arrestin-2 and arrestin-3. To this end, we used surface plasmon resonance (SPR), an *in vitro* optical method that detects the kinetics of an interaction through changes in refractive index (252). This technique requires that one biomolecule is

immobilized on a flow cell (the ligand) while the binding partner is injected over the immobilized surface (the analyte). For our measurements, we immobilized full-length, human arrestin-2/3 on the sensor chip and flowed ERK2 over the surface of the cell (**Fig. 7.2, Fig. 7.3**). We first tested binding to full-length arrestin-2 and were surprised to find a high affinity interaction with a K_d 7.4 (±0.18) nM (**Fig. 7.2A**). This was in stark contrast to our previous measurements by MST (Fig. 1). A similar high affinity interaction was detected for full-length arrestin-3 with a K_d 83.1 (±0.97) nM (**Fig. 7.2B**). While the association measurements for both nonvisual arrestins were similar (k_a 257,000 ±2,870 Ms^{-1} for arrestin-2 and k_a 207,000 ±21,700 Ms^{-1} for arrestin-3), the dissociation constants were significantly different (k_d 0.0019 ±0.0003 s^{-1} for arrestin-2 and k_d 0.017 ±0.002 s^{-1} for arrestin-3). Thus, full-length arrestin-2 dissociates from ERK2 much faster than full-length arrestin-3.

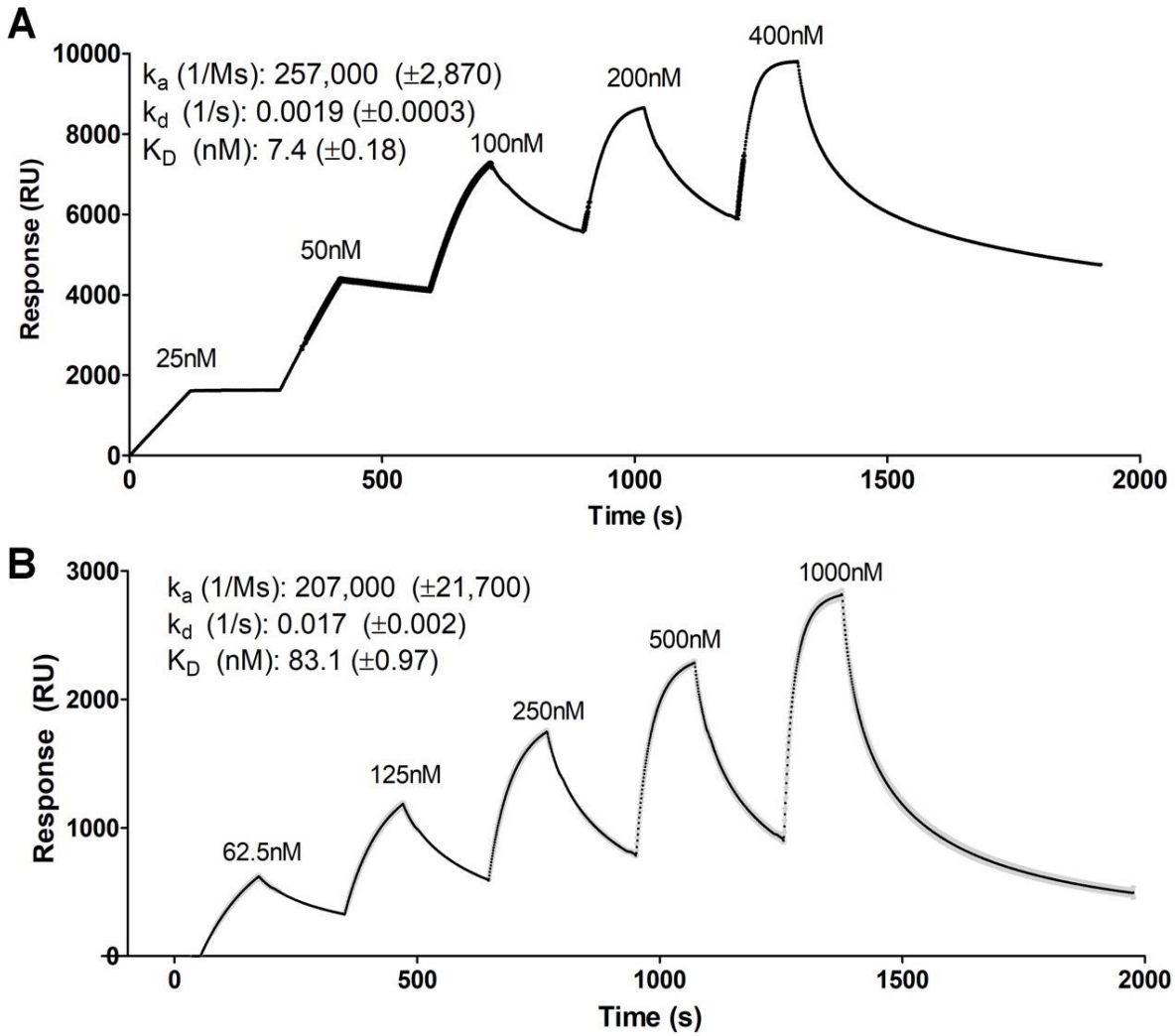

Fig. 7.2. Surface Plasmon Resonance (SPR) of His-full-length-arrestins (ligand) with His-ERK2 (analyte). SPR was performed on the Biacore X100 instrument using the nitrilotriacetic acid (NTA) sensor chip and amine-coupling kit (GE Healthcare Life Sciences). **(A)** Human His-arrestin-2 was first immobilized on the NTA chip. His-ERK2 was then flowed over two flow cells (one reference and one with arrestin-2 coupled) and binding was detected at various concentrations (0-400 nM ERK2, 1:1 serial dilution). **(B)** Human His-arrestin-3 was first immobilized on the NTA chip. His-ERK2 was then flowed over two flow cells (one reference and one with arrestin-3 coupled) and binding was detected at various concentrations (0-1000 nM ERK2, 1:1 serial dilution). Association and dissociation kinetics were calculated using the Biacore-provided evaluation software. Shown is the average response (black) with standard error (gray) (n=3).

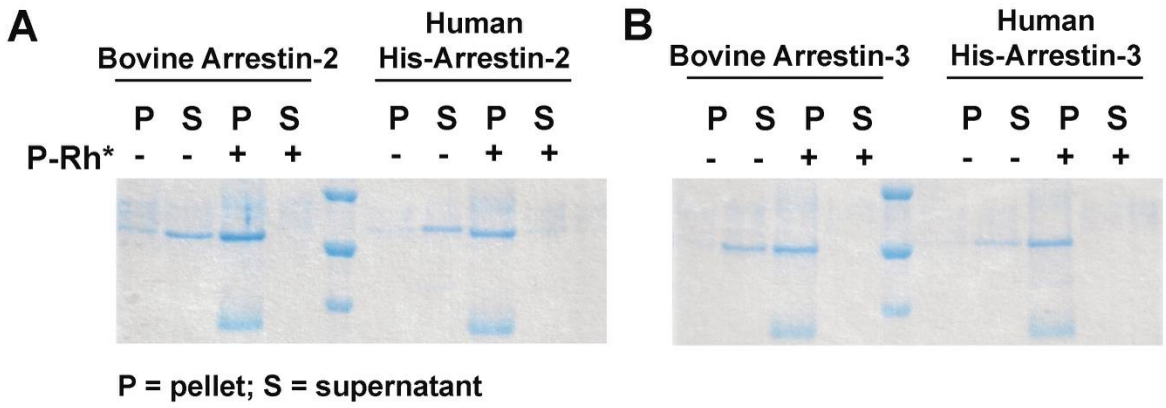

Fig. 7.3. Testing functionality of His-arrestin-2/3 using rhodopsin pull-down assays. (A) Arrestin-2 and **(B)** arrestin-3 binding to light-activated phosphorylated rhodopsin in native membranes. Rhodopsin is concentrated in the membrane pellet and, therefore, functional arrestin is expected to co-pellet with the receptor.

Measuring the binding affinity of two proteins requires that the reaction is at equilibrium by the time the measurement is taken. While an MST experiment is aptly defined as an equilibrium experiment – a function of one protein concentration – the SPR measurements are kinetic, or determined by the rates of the forward and reverse reactions (253). For an equilibrium experiment to yield optimal results, one must use the lowest concentration of all protein components that can be measured accurately. Our MST assay used change in fluorescence intensity as a readout, with a low concentration of fluorescently-labeled ERK2 and a wide range of concentrations for our arrestin constructs (**Fig. 7.1**). Since our MST assays required a rather high concentration of arrestin to saturate the reaction (~20 μM), it is possible that our reported K_d values are higher than the actual binding affinity. For this reason, we conducted additional SPR experiments, which allowed us to observe changes in affinity over varied concentration and time.

Peptides of arrestin-2/3 retain the ability to bind ERK2. To delineate where ERK2 interacts on arrestin-2/3, we used an *in vitro* pull-down assay to detect the binding of peptides from the non-receptor-binding surface of arrestin-2/3 and ERK2 (**Fig. 7.4**). This method has been well-established in our laboratory for the detection of direct interactions between two proteins (254) and is suitable for the initial screening of protein-protein interactions. For this study, we

immobilized MBP-fusions of arrestin-2/3-derived peptides onto amylose resin and incubated with ERK2 as our "prey." For the arrestin-2-derived peptides, we detected statistically significant binding of ERK2 only to full-length arrestin-2 (**Fig. 7.4A**), while in case of arrestin-3-derived peptides we detected binding to both MBP-T1 (residues 1-52) and MBP-T7 (residues 345-409) (**Fig. 7.4B, Fig. 7.5**).

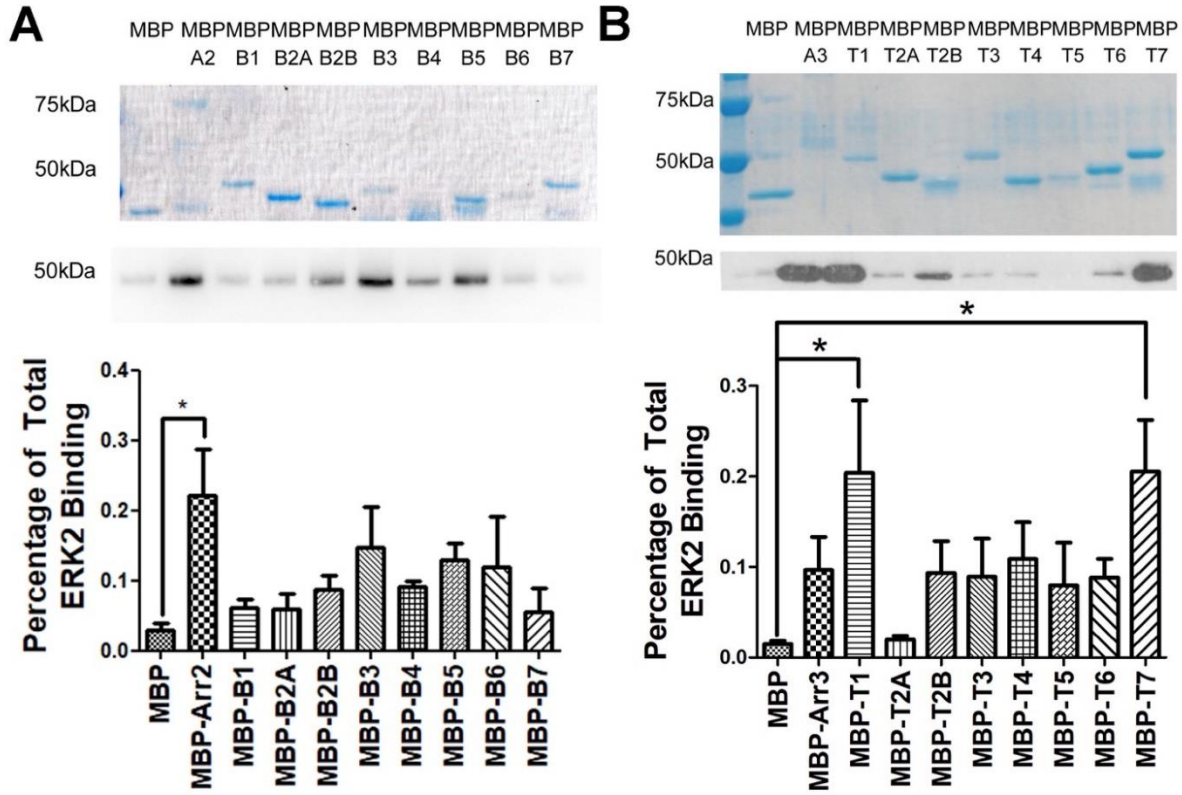

Fig. 7.4. Pull-down assay using MBP-fusions of arrestin-2/3 to bind ERK2. (A) Representative Coomassie Blue Staining (upper) and Western analysis (lower) for a pull-down assay using MBP-arrestin-2 (5 µg) as prey and human ERK2 (5 µg) as bait. **(B)** Representative Coomassie Blue Staining (upper) and Western analysis (lower) for a pull-down assay using MBP-arrestin-3 (5 µg) as prey and human ERK2 (5 µg) as bait. ERK2 binding was quantified using Quantity One 1-D Analysis software (Bio-Rad) to analyze densitometry. Binding was reported as a percentage of total bound ERK2 and statistical analysis was performed using One-way ANOVA followed by Tukey's Multiple Comparison Test (*, $p<0.05$). Peptide residues are listed in **Fig. 7.5**.

A

PEPTIDES		AMINO ACIDS	SEQUENCE
B1	M1-R51	52	MGDKGTRVFKKASPNGKLTVYLGKRDFVDHIDLVEPVDGVVLVDPEYLKER
B2A	S86-L108	23	SFPPAPEDKKPLTRLQERLIKKL
B2B	G109-L123	15	GEHAYPFTFEIPPNL
B3	V171-I207	37	VQYAPERPGPOPTAETTRQFLMSDKPLHLEASLDKEI
B4	Y208-N225	18	YYHGEPISVNVHVTNNTN
B5	S265-R285	21	SSTFCKVYTLTPFLANNREKR
B6	G286-I317	32	GLALDGKLKHEDTNLASSTLLREGANREILGI
B7	M352-G398	47	MHPKPKEEPPHREVPEHETPVDTNLIELDTNDDDIVFEDFARQRLKG

B

PEPTIDES		AMINO ACIDS	SEQUENCE
T1	M1-R52	52	MGEKPGTRVFKKSSPNCKLTVYLGKRDFVDHLDKVDPVDGVVLVDPDYLKDR
T2A	A87-L109	23	AFPPTPNPPRPPTRLQERLLRKL
T2B	G110-L124	15	GQHAHPFFFTIPQNL
T3	V172-L208	37	VQFAPEKPGPSAETTRHFLMSDRSLHLEASLDKEL
T4	Y209-T226	18	YYHGEPLNVNVHVTNNST
T5	S266-R286	21	SSTFCKVYTITPLLSNNREKR
T6	G287-1318	32	GLALDGKLKHEDTNLASSTIVKEGANKEVLGI
T7	M345-C409	47	MHPKPHDHIALPRPQSAVPETDAPVDTNLIEFETNYATDDDIVFEDFARLRLKGLKDEDYDDQFC

Fig. 7.5. Peptide sequences for the non-receptor surface of the nonvisual arrestins. (A) Arrestin-2-derived peptide fragments. **(B)** Arrestin-3-derived peptide fragments.

Peptide arrays reveal which elements of arrestin-2/3 bind ERK2. To further probe the interaction interface between the non-visual arrestins and ERK2 we used peptide arrays, a method that allows parallel synthesis and screening of hundreds of peptides (255). We initially screened peptides that covered the non-receptor-binding surface of arrestin-2/3 for ERK2 interaction. As could be expected based our pull-down studies (**Fig. 7.6**), different elements of the two non-visual arrestins interacted most strongly with ERK2. Arrestin-2-derived ERK2-binding peptides concentrated in the B4/B5 region of the protein (corresponding to residues Y208-R285) whereas ERK2-binding peptides of arrestin-3 were found in the T1 (M1-R52), T2A (A87-L109), T6 (G287-I318), and T7 (M345-C409) regions. The peptides that displayed the highest binding were also dissimilar. The arrestin-2 B5 peptide, CKVYTLTPFLANNRE, displayed the greatest binding, in contrast to arrestin-3, where T1 peptide, MGEKPGTRVFKKSSPN, showed the highest binding. This suggests that there could be binding and mechanistic differences in the interaction of the two non-visual arrestins with ERK2.

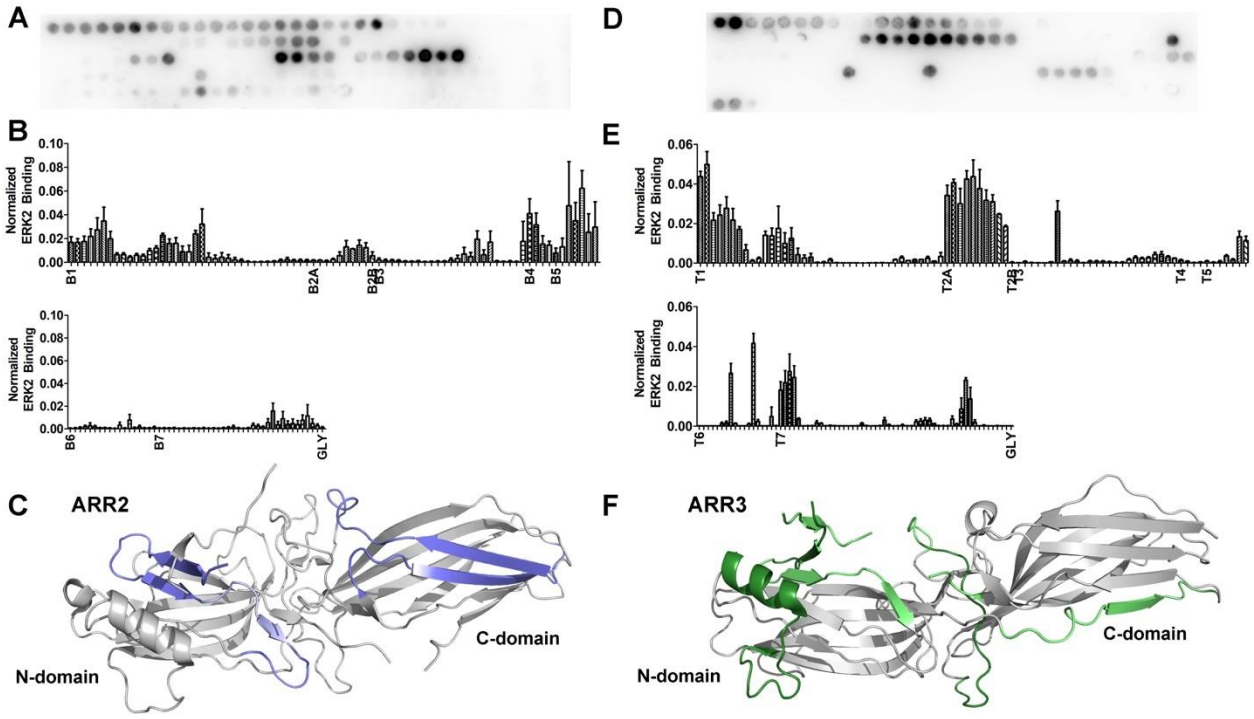

Fig. 7.6. The binding of ERK2 to arrestin-2- and arrestin-3-derived peptides. (A) Peptides of the non-receptor surface of arrestin-2 were synthesized as 15-mer amino acid fragments using ResPep SL (Intavis Bioanalytical Instruments) (1 amino acid shifts). A representative peptide array of His-ERK2 binding to arrestin-2 peptides is shown. **(B)** Quantification of ERK2 binding to the arrestin-2-derived peptide array was performed using the peptide array analyzer on ImageJ (256) (n=3). **(C)** ERK2 binding displayed on the arrestin-2 (PDB 2WTR). Conditional formatting in Excel was used to detect peptides that exhibited moderate to strong binding to ERK2 (defined as >10% of the intensities). For arrestin-2, moderate binding is highlighted in light blue while strong binding is highlighted in slate. **(D)** Peptides of the non-receptor surface of arrestin-3 were synthesized as 15-mer amino acid fragments using ResPep SL (Intavis Bioanalytical Instruments) (1 amino acid shifts). A representative peptide array of His-ERK2 binding to arrestin-3 peptides is shown **(E)** Quantification of ERK2 binding to the arrestin-3-derived peptide array was performed using the peptide array analyzer on ImageJ (256) (n=3). **(F)** Arrestin-3 (PDB 3P2D (215)) crystal structures. Conditional formatting in Excel was used to detect peptides that exhibited moderate to strong binding to ERK2 (defined as >10% of the intensities). For arrestin-3, moderate binding is highlighted in lime while strong binding is highlighted in forest. The peptide with the highest binding for arrestin-2 was in peptide B5, CKVYTLTPFLANNRE, while the peptide with the highest binding for arrestin-3 was the most N-terminal, MGEKPGTRVFKKSSPN. Peptide residues are listed in **Fig. 7.5**.

Localization of arrestin-binding elements in ERK2[3]. Next we assessed the binding of arrestin-2/3$^{1\text{-}393}$ to ERK2-derived peptides (**Fig. 7.7**). Again, we detected a significant difference between the arrestin-2$^{1\text{-}393}$ and arrestin-3$^{1\text{-}393}$. While arrestin-2$^{1\text{-}393}$ displayed fewer high intensity interactions with the ERK2 peptides (**Fig. 7.7A-C**), arrestin-3$^{1\text{-}393}$ interacted quite strongly with several regions (**Fig. 7.7D-E**). This could reflect the overall difference in conformational flexibility of arrestin-2 and -3, as arrestin-3 was shown to be more flexible than arrestin-2 (257).

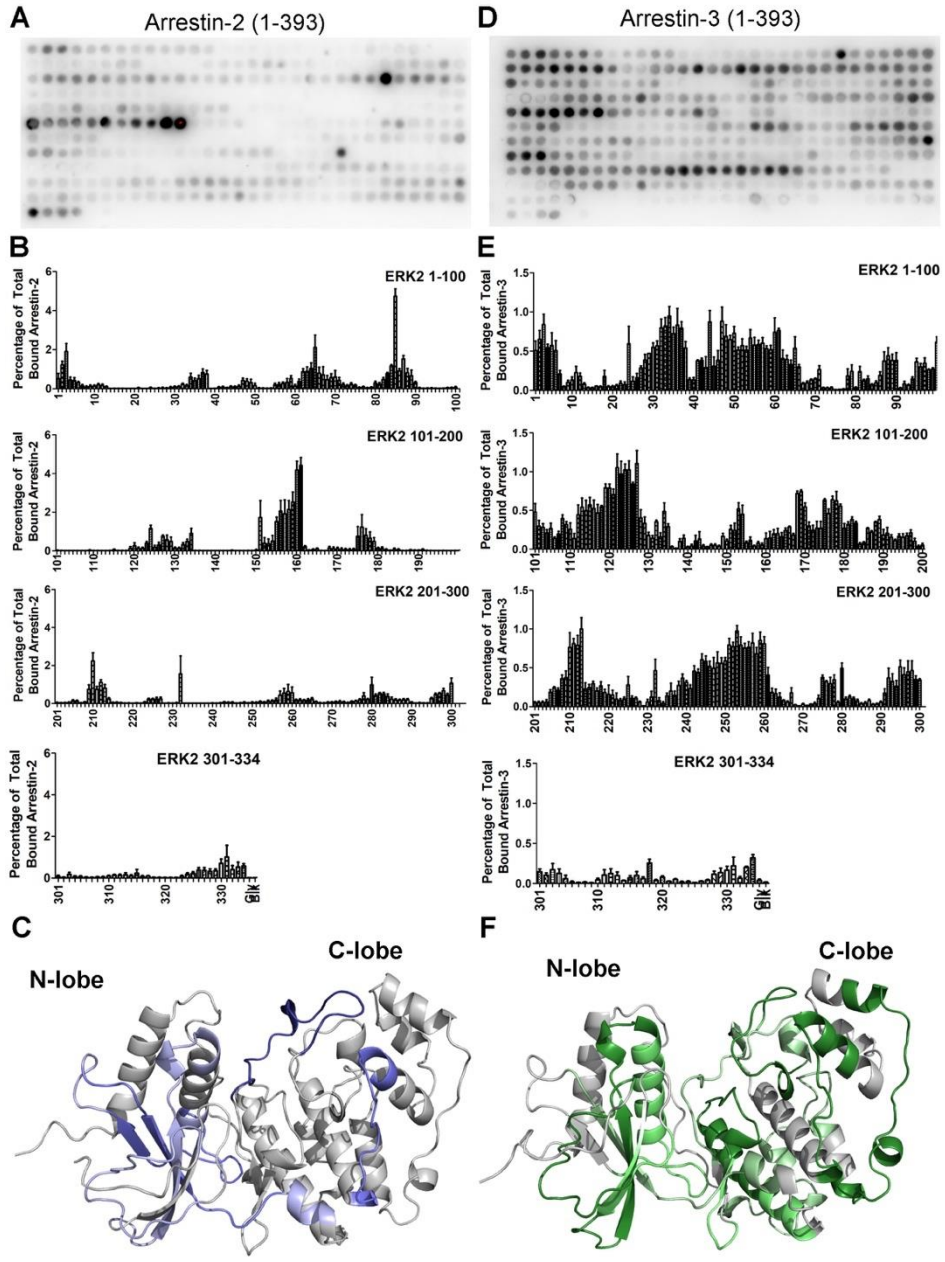

Fig. 7.7. The binding of arrestin-2 or arrestin-3 to ERK2-derived peptides. (A) Peptides of ERK2 were synthesized as 15-mer amino acid fragments using ResPep SL (Intavis Bioanalytical Instruments) (1 amino acid shifts). A representative peptide array of arrestin-$2^{1\text{-}393}$ binding to ERK2 peptides is shown. **(B)** Quantification of ERK2 binding to the ERK2-derived peptide array was performed using the peptide array analyzer on ImageJ (256) (n=4). **(C)** Arrestin-$2^{1\text{-}393}$ binding displayed on ERK2 (PDB 1ERK (201)). **(D)** Peptides of ERK2 were synthesized as 15-mer amino acid fragments using ResPep SL (Intavis Bioanalytical Instruments) (1 amino acid shifts). A representative peptide array of arrestin-$3^{1\text{-}393}$ binding to ERK2 peptides is shown. **(E)** Quantification of ERK2 binding to the ERK2-derived peptide array was performed using the peptide array analyzer on ImageJ (256) (n=3). **(G)** Arrestin-$3^{1\text{-}393}$ binding displayed on ERK2 (PDB 1ERK(201)). Conditional formatting in Excel was used to detect peptides that exhibited moderate to strong binding to ERK2. For arrestin-$2^{1\text{-}393}$, weak binding is highlighted in light blue, moderate binding in slate, and strong binding in deep blue. For arrestin-$3^{1\text{-}393}$, weak binding is highlighted in pale green, moderate binding in lime, and strong binding in forest.

Elucidation od arrestin-binding ERK2 elements and ERK2-binding arrestin elements by HDX-MS. To identify ERK2 eements involved in arrest binding in solution we also used hydrogen/deuterium exchange (HDX) mass spectrometry (MS). This technique is most frequently used to study protein dynamics, protein-ligand interactions, membrane proteins, and intrinsically disordered proteins (258). In brief, proteins are incubated in a deuterated solvent (D_2O) that exchanges with the amide backbone to reveal which regions of the protein are solvent exposed. We performed HDX-MS using several arrestin constructs (full-length arrestin-2/3, arrestin-2^{1-387}, arrestin-2^{1-361}, arrestin-3^{1-385}, arrestin-3^{1-362}); however, we only detected profile changes in case of arrestin-2^{1-387}.

HD exchange in eight peptides of ERK2 was affected by co-incubation with C-terminally truncated arrestin-2^{1-387} (**Fig. 7.8**). While three of these peptides localized to the N-lobe of ERK2 (**Fig. 7.8A-C**), the remaining five were in the the C-lobe (**Fig. 7.8D-H**). This suggests that ERK2 has several binding sites for arrestin-2^{1-387}. The changes in arrestin-2^{1-387} were found almost exclusively in the C-domain, with an additional interaction surface located in the flexible C-tail (**Fig. 7.9**), which was also implicated by the peptide array data (**Fig. 7.6C,G**).

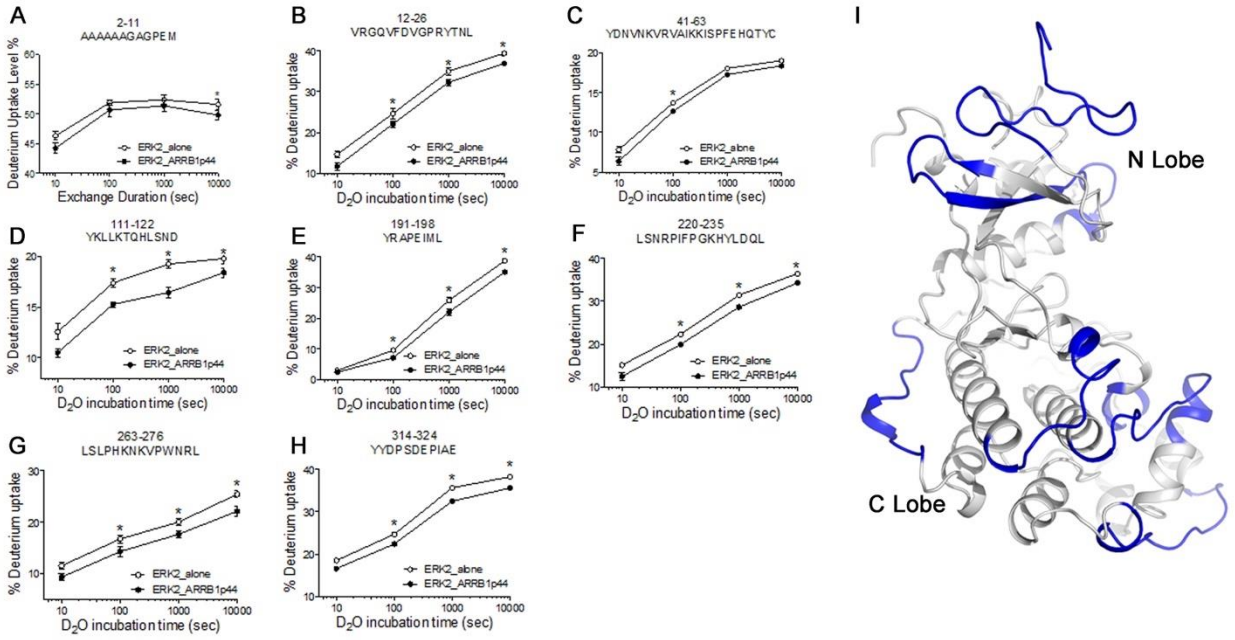

Fig. 7.8. ERK2 HDX-MS profile change upon co-incubation with C-terminal truncated arrestin-2$^{1\text{-}387}$. Co-incubation of ERK2 with truncated arrestin-2$^{1\text{-}387}$ resulted in the above HDX-MS profile: **(A)** residues A2-M11, **(B)** residues V12-L26, **(C)** residues Y41-C63, **(D)** residues Y111-D122, **(E)** residues Y191-L198, **(F)** residues L220-L235, **(G)** residues L263-L276, and **(H)** residues Y314-E24. **(I)** HDX-MS profile changes displayed on ERK2 (PDB 2ERK (259)).

No change in HDX-MS profiles was observed for full-length arrestin-2 or truncated arrestin-2$^{1\text{-}361}$. In addition, no changes were observed for full-length arrestin-3, truncated arrestin-3$^{1\text{-}385}$, or truncated arrestin-3$^{1\text{-}362}$.

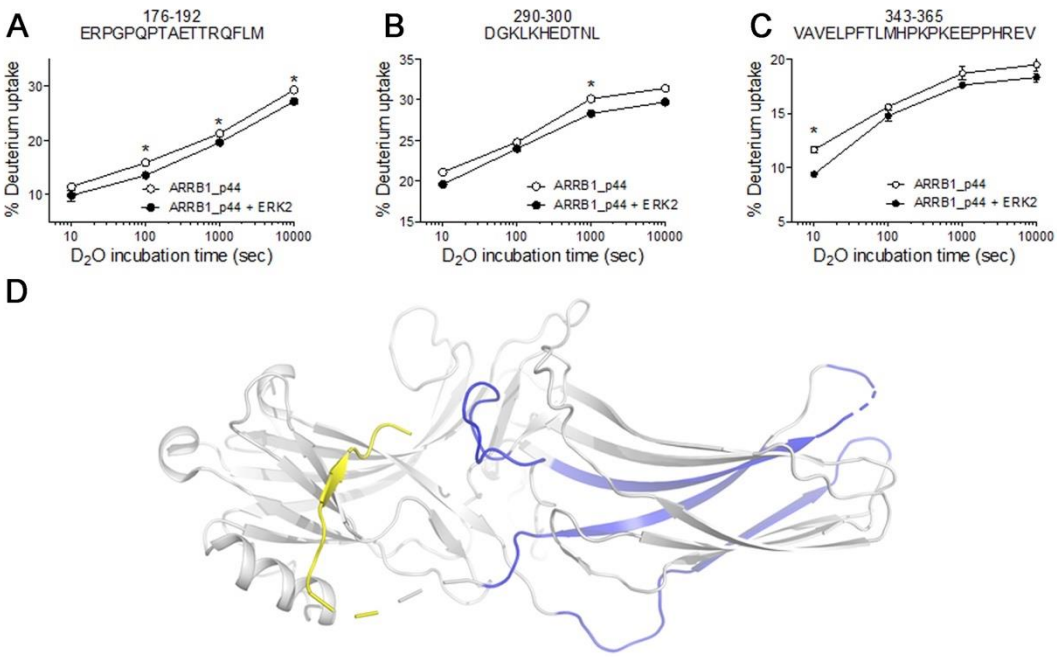

Fig. 7.9. Truncated arrestin-2$^{1\text{-}387}$ HDX-MS profile change upon co-incubation with ERK2. Co-incubation of ERK2 with truncated arrestin-2$^{1\text{-}387}$ resulted in the above HDX-MS profile: **(A)** residues E176-M192, **(B)** residues D290-L300, and **(C)** residues V343-V365. **(I)** HDX-MS profile changes displayed on arrestin-2 (PDB 1G4R (223)).

No change in HDX-MS profiles was observed for full-length arrestin-2 or truncated arrestin-2$^{1\text{-}361}$. In addition, no changes were observed for full-length arrestin-3, truncated arrestin-3$^{1\text{-}385}$, or truncated arrestin-3$^{1\text{-}362}$.

^{19}F-NMR and fluorescence quenching experiments reveal the relative orientation of ERK2 on arrestin-2$^{1\text{-}387}$. To test arrestin-2-ERK2 interaction we also performed fluorine-19 nuclear magnetic resonance spectroscopy (^{19}F-NMR) (**Fig. 7.10**) and fluorescence quenching experiments (**Fig. 7.11**). For ^{19}F-NMR experiments, 3,5-difluorotyrosine (F2Y) was incorporated at position 226 in ERK2 and position 349 in arrestin-2$^{1\text{-}365}$. The ^{19}F-NMR spectra showed that both F2Y positions exhibited downfield shifts with arrestin-2$^{1\text{-}365}$ and ERK2, respectively. These data also suggest that the C-lobe of ERK2 and the C-domain of arrestin-2 interact.

For the fluorescence quenching experiments, we incorporated tryptophan residues into specific locations in ERK2 and used the quenching of fluorescent label bimane by tryptophan (260) as readout. Cysteine-less arrestin-2$^{1\text{-}365}$ was used as the backbone for generation of two single-cysteine mutants, arrestin-2$^{1\text{-}365}$ 300C and arrestin-2$^{1\text{-}365}$ 357C. These mutants were labeled with bimane, and a reduction in its fluorescence indicated the proximity of a Trp residue. Bimane at 300C in arrestin-2$^{1\text{-}365}$ came close to

tryptophanes 47 and 62 in ERK2 (**Fig. 7.11B**) while the bimane at 357C in arrestin-$2^{1\text{-}365}$ 357C came in the vicinity of tryprophanes 111, 123, 226/231, and 265 (**Fig. 7.11C**). This suggests that the N-lobe of ERK2 is oriented toward the gate-loop of arrestin-2 while the C-lobe of ERK2 interacts with the C-terminal linker.

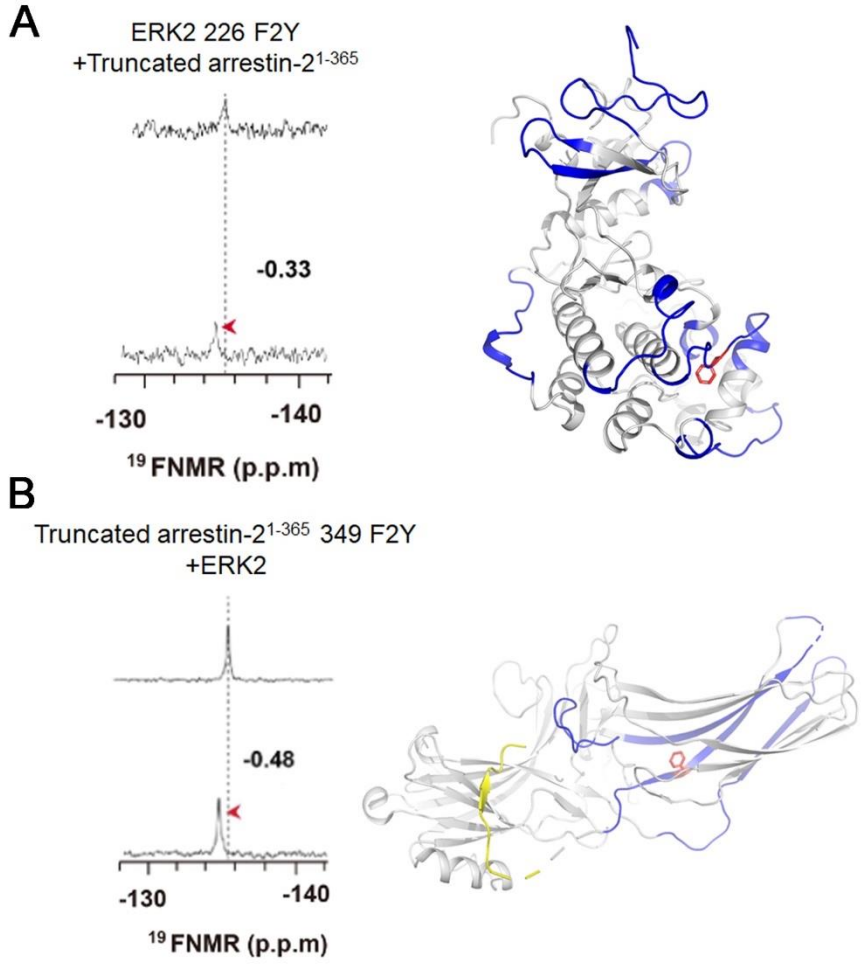

Fig. 7.10. ^{19}F-NMR reveals conformational change in response to the complex formation of the ERK2 and the arrestin-$2^{1\text{-}365}$.

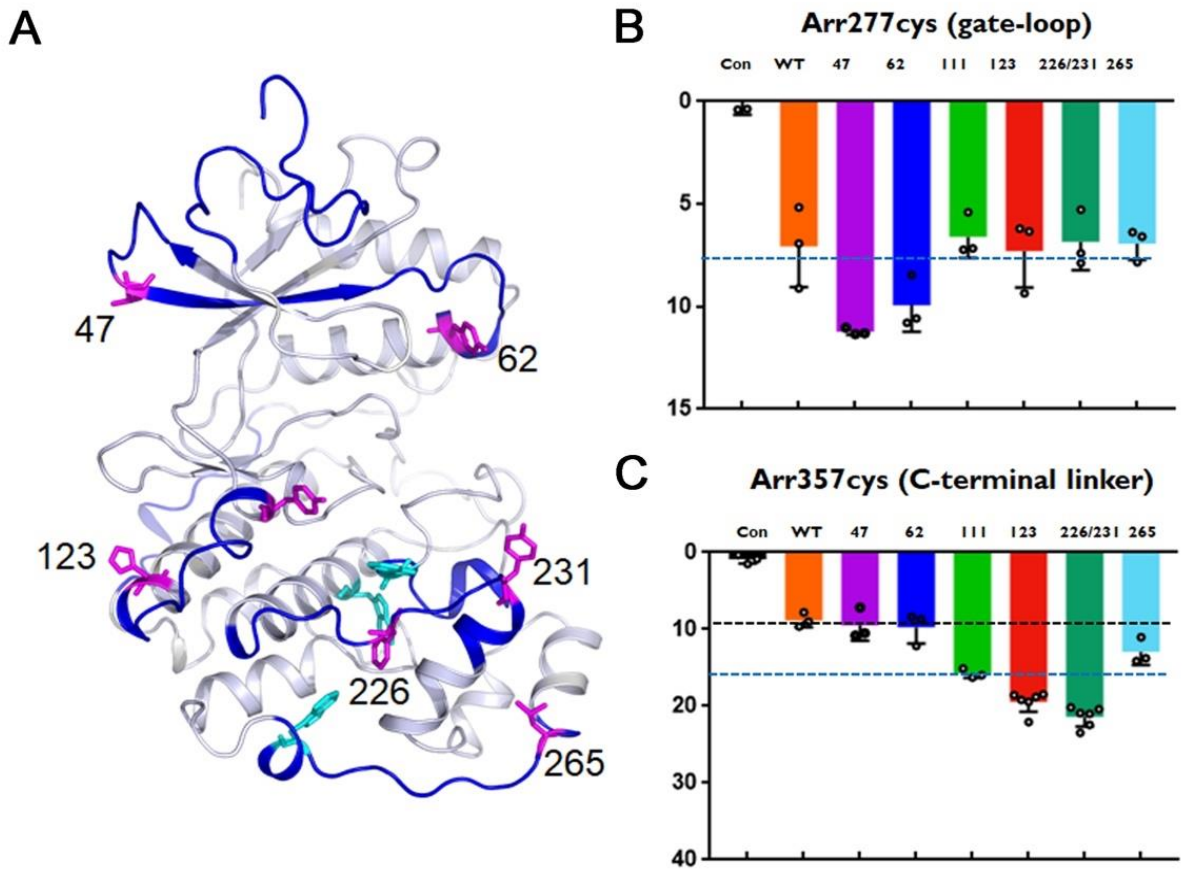

Fig. 7.11. Fluorescence quenching experiment shows interaction surfaces of truncated arrestin-2 with ERK2. (A) Magenta-colored regions are switched to tryptophan, and two residues from cysless arrestin-2 (357 or 300) are labeled with bimane.

CW-EPR positions ERK2 on arrestin-3$^{1\text{-}393}$. To further probe the interaction sites between arrestin-3$^{1\text{-}393}$ and ERK2, we employed site-directed spin labeling (SDSL) and continuous-wave electron paramagnetic resonance spectroscopy (CW EPR) under two different conditions: arrestin-3$^{1\text{-}393}$ alone, and arrestin-3$^{1\text{-}393}$ mixed with ERK2 at a 1:2 molar ratio (**Fig. 7.12**). The EPR spectra for each condition were overlaid and compared to reveal any spectral shape changes. A broadening of the spectral line indicated that the motion of the spin label was restricted and slowed down, which suggested the residue was involved in a protein-protein or tertiary contact. No change in the spectrum indicated that either the labeled arrestin-3 mutant did not bind to ERK2 or that the studied site was not directly involved in the arrestin-3/ERK2 interaction.

Several sites were found to show medium or small spectral changes due to ERK2 binding, mostly on distal loops and flexible regions of the two domains, including sites at 193, 266, 313 and 331 (**Fig. 7.12**). Specifically, spin labels at these sites became more immobilized upon binding to ERK2, indicating they might be involved in a direct structural contact with ERK2 or undergoing conformational changes due to binding. Although small decreases in spin label mobility were found at several sites of arrestin-3, the changes were not dramatic enough to definitively map ERK2 binding on arrestin-3. Therefore, our arrestin3/ERK2 spectra suggest that the spin labeled free arrestin-3 mutants did not bind to ERK2 very tightly at the concentrations used in the experiment (50 μM arrestin-3: 100 μM ERK2).

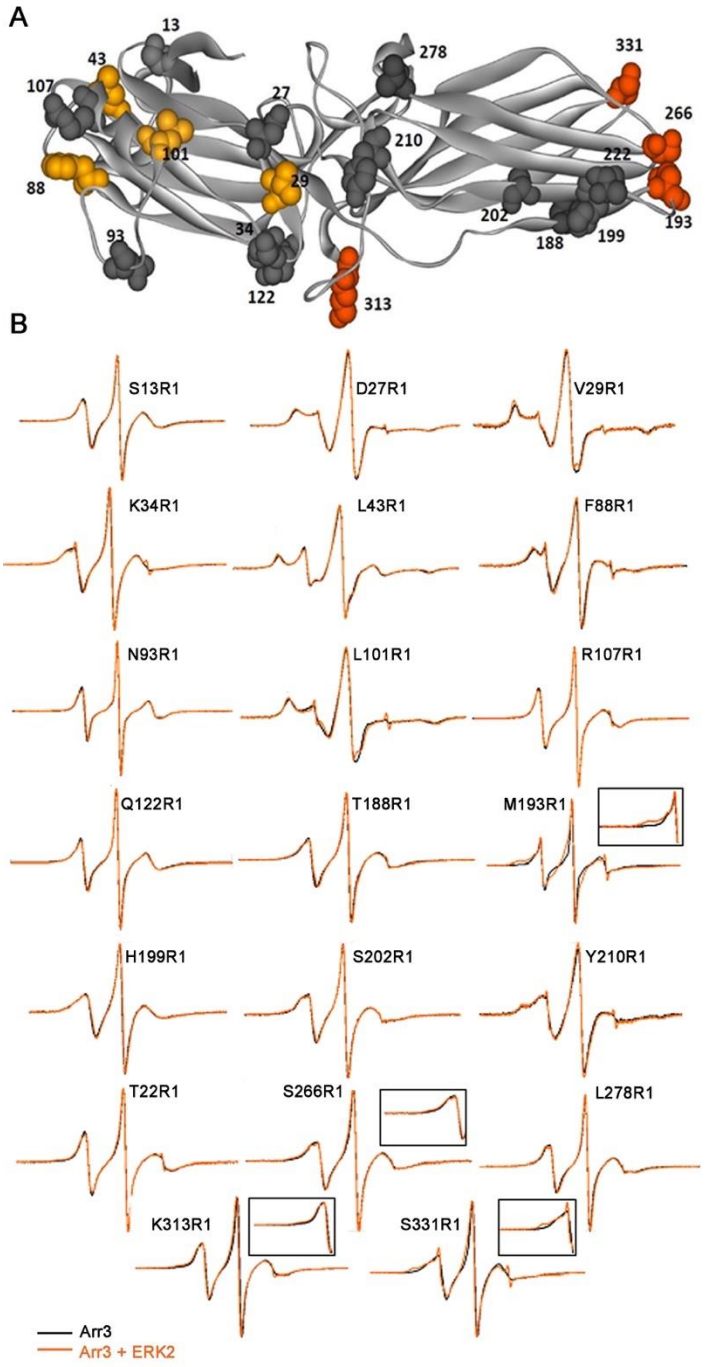

Fig. 7.12. ERK2 binding sites on arrestin-3 using CW EPR. (A) Map of spectral changes upon mixing with ERK2 on the crystal structure of arrestin-3 (PDB 3P2D). Dark orange residues were found to have small to medium spectral line shape changes, while residues colored by light orange and gray are found to have slight or no changes in their EPR spectra, respectively. **(B)** Overlays of center line height-normalized X-band EPR spectra of 20 sites on arrestin- 3 (50 μM) in the absence and presence of unphosphorylated cysless ERK2 (100 μM). Black lines represent arrestin-3 protein alone in the buffer (50 mM MOPS, 100 mM NaCl, pH7.0), and orange lines represent the mixture of arrestin-3 and ERK2. R1 indicates the spin label side chain. Arrows indicate spectral changes due to ERK2 binding and the magnified regions of the spectra highlight medium changes on sites V29R1, L101R1, M193R1 and S331R1 of arrestin-3 upon ERK2 binding.

Small-angle X-ray scattering demonstrates ERK2 orientation on arrestin-3$^{1\text{-}393}$ in solution. Small-angle X-ray scattering (SAXS) is a powerful structural technique to study the shape of biological macromolecules in solution (261). To this effect, we used a construct of arrestin-3 tethered to ERK2 (arrestin-3-ERK2) via a flexible linker (**Fig. 7.13**). We were successful in obtaining an envelope of the fusion construct (**Fig. 7.13A**) with an estimated molecular weight of 115 kDa, D_{max} of 138 Å, and an R_g of 37.7 Å (**Fig. 7.13B,C**). Using the combined data from our peptide array and CW-EPR experiments, we modeled arrestin-3 (PDB 3P2D (215)) and ERK2 (PDB 1ERK(201)) into the envelope. This positioning showed that the C-domain of arrestin-3 resulted in the greatest interface with the N-lobe of ERK2.

Arrestin-3-ERK2-His$_{10}$ undergoes phosphorylation in cells without disrupting native ERK2 activation. To test whether our arrestin-3-ERK2 construct was functional, we transfected HEK293 arrestin-2/3 knockout cells with either monomeric arrestin-3 or arrestin-3-ERK2 and β2-adrenergic receptor and measured ERK2 phosphorylation over a 45 min time course (**Fig. 7.13D,E**). Both transfection of the monomeric arrestin-3 and the arrestin-3-ERK2 construct led to typical ERK2 phosphorylation curves with a peak at 5 min. The ERK2 present in the arrestin-3-ERK2 construct was also able to be phosphorylated, confirming that the construct retains functionality.

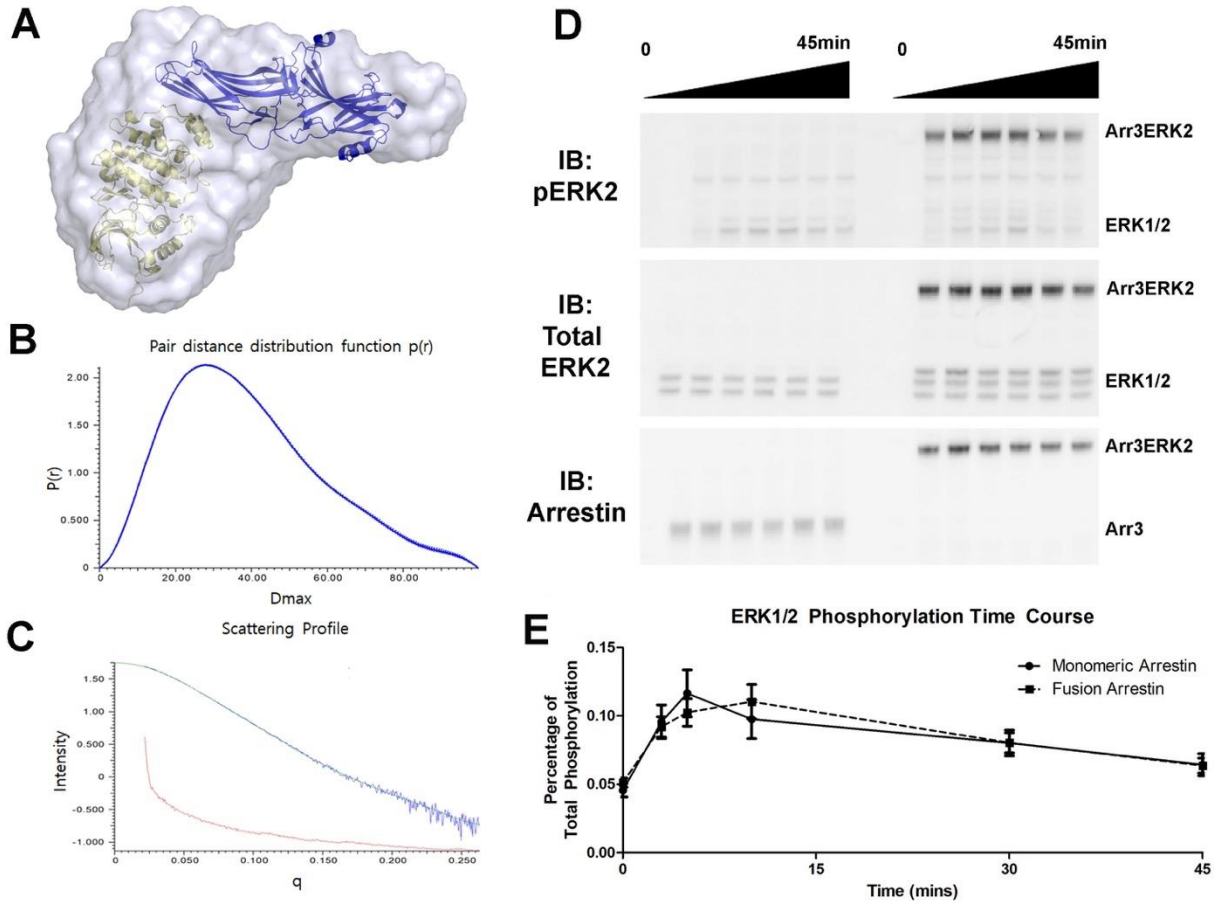

Fig. 7.13. Small-angle X-ray Scattering (SAXS) of an arrestin-3-ERK2 construct. (A) SAXS envelope of an arrestin-3-ERK2 construct. **(B)** Pair distance distribution function and **(C)** scattering profile for the SAXS envelope. **(D)** K/O Arr2/3 HEK293 cells were transfected with β2-adrenergic receptor (0.3μg) and either monomeric arrestin-3 (0.1μg) or an arrestin-3-ERK2 fusion (1.5μg). After 48 hrs, the cells were incubated with 10μM isoproterenol for a time course of 45 mins before lysis with 400μL SDS buffer. Western analysis was performed with antibodies against phosphorylated ERK1/2 (Cell Signaling Technology, #9101, 1:1,000), total ERK1/2 (Cell Signaling Technology, #4695, 1:1,000), or arrestin (F431, 1:5,000). **(E)** Quantity One software was used to analysis band intensity of phosphorylated ERK2 and plotted as a percentage of total phosphorylation.

7.3 Discussion

Although arrestins were first discovered for their role in the desensitization of GPCRs, arrestin-dependent signaling has emerged as an important set of pathways (51,98,227,249,262). Of the identified interacting partners (9), the scaffolding of the Raf1-MEK1/ERK1/2 cascade by the non-visual arrestins is perhaps one of the best characterized (64,67,241-245). However, despite extensive work on arrestin-facilitated ERK activation, less is known concerning the regulation of arrestin-dependent ERK signaling. In fact, several recent studies challenged the previously accepted signaling paradigm (263-265). Identifying the mechanisms through which the nonvisual arrestins facilitate ERK signaling will shed light on the complex role of arrestins in signal regulation.

Here, we assessed ERK2 binding by the non-visual arrestins to determine whether there are mechanistic differences between the two isoforms. Using a combination of biophysical and structural techniques, we found that the interfaces used by each arrestin isoform to bind ERK2 are dissimilar, suggesting that the functional role of the two non-visual arrestins in ERK2 activation may be non-redundant. Since ERK1/2 activation affects cell growth, migration, proliferation, and survival, it is likely that this differential regulation impacts cell fate (54).

Studying protein-protein interactions and their associated binding site residues is critical for understanding how the proteins are involved in cellular processes. For example, outlining an interaction surface can provide a clearer picture of cellular mechanisms and help in the design of small molecules or protein mimetics that block the interaction. The binding sites for ERK2 on the non-visual arrestins have not been previously mapped; however, several studies have suggested that ERK2 contacts multiple points on both arrestin domains (64,67,242). Our data are consistent with this finding (**Figs. 7.1-7.7**). It has also been proposed that ERK2 binds preferentially to

GPCR-activated arrestin conformation(s) (242). This is supported by higher ffinity of C-terminally truncated "pre-activated" arrestin-2/3$^{1\text{-}393}$ mutants (**Fig. 7.1**). Also, we only observed ERK2 activation in the presence of activated β2-adrenergic receptor in cells (**Fig. 12**).

Taken collectively, our data strongly indicate that the C-domain of both nonvisual arrestins is the primary site of interaction with ERK2 (**Fig. 7.9-11, 7.12-13**). Since previous studies have shown that arrestin acts as a molecular scaffold for the cRaf-1/MEK/ERK2 cascade (51,58,242), it is tempting to speculate that the upstream kinases interact mainly with the N-domain of arrestin. It is also possible, however, that the kinases assemble on arrestin at different intervals and that the binding sites overlap. More work is needed with the upstream kinases to determine which scenario is more likely.

All vertebrates have two isoforms of nonvisual arrestins, whereas most invertebrates and protochordates have only one homolog (266). This functional redundancy leaves many questions, foremost of which being the benefit of having two homologs. Our data directly comparing the two arrestins demonstrate clear distinctions in the binding interfaces between arrestin and ERK2 (**Figs. 7.4, 7.6, 7.7**) in addition to changes in binding kinetics (**Fig. 7.2**). Furthering our understanding of these fine molecular differences could lead to information regarding functional interactions with ERK2 and determine whether one nonvisual arrestin is better suited to ERK2-mediated signaling over the other.

Overall, we have shown that both nonvisual arrestins bind ERK2 and that there are distinct interaction interfaces in the two isoforms. This may suggest that one isoform is better suited to ERK2 binding and scaffolding of the cRaf-1/MEK/ERK2 cascade. Our detailed analysis of the ERK2/arrestin interface provides the first map of arrestin binding ERK2, which could help in the design of novel therapeutics that target the protein interaction.

7.4 Materials and Methods

Protein Purification. Full length arrestin-2/3, its truncated form (residues 1-393), cysless arrestin-3, NpT7-5 His_6-ERK2, and MBP-fusion proteins were purified, as described previously (104,226,267). The plasmids for human His-arrestin-2/3 were generously provided by Dr. Dmitry B. Veprintsev from the Paul Scherrer Institut in Switzerland. In brief, His-arrestin was purified on a His-trap column (GE Healthcare) using a gradient of 40-500 mM imidazole in running buffer (20 mM Bis-Tris propane pH 7.0, 500 mM NaCl, 10% v/v glycerol, and 8 mM 2-mercapto-ethanol). The eluate was immediately subjected to overnight dialysis (20 mM Bis-Tris propane pH 7.0, 120 mM NaCl, 10% v/v glycerol and 14.3 mM 2-mercapto-ethanol) and then buffer exchanged using size exclusion chromatography on a Superdex S200 Increase 10/300 GL column equilibrated with 20 mM MOPS, pH 7.5, 150 mM NaCl, and 2 mM TCEP. For HDX-MS, the cDNAs of human ERK2 and *Rattus norvegicus* (Rat) arrestin-2/3 were inserted into pET28a vectors and transformed to the *Escherichia coli* (E. coli) BL21(DE3). The C-terminal truncation constructs (arrestin-2^{1-361}, arrestin-2^{1-387}, arrestin-3^{1-362}, and arrestin-3^{1-385}) were generated using a site-directed mutagenesis kit (Stratagen). The transformed cells were grown in LB broth (Miller) medium at 37°C until the OD_{600} reached 0.4–0.6, after which protein expression was induced with 0.5 mM IPTG for 4 hours at 30°C for ERK2 and 0.03 mM IPTG for 24 hours at 16°C for arrestins. The bacterial cells were harvested by centrifuge (3800 rpm, 20 min. 4°C) and stored at -80°C. Protein purification was performed as previously described (268). The arrestin-3-ERK2-His_{10} purification was divided into three steps: HisTrap, Q/SP, and size-exclusion chromatography. The initial HisTrap purification was performed over a gradient of 15-300 mM imidazole in running buffer (25 mM Tris-HCl pH 7.5, 500 mM NaCl, 10% glycerol, 1 mM TCEP, and 100 µM PMSF). The eluted fractions were analyzed using SDS-PAGE and loaded onto a Q/SP column (GE Healthcare) at approximately 50

mM NaCl (dilution was performed on column in 25 mM Tris-HCl pH 7.5, 10% glycerol, and 1 mM TCEP). The construct was eluted over a gradient of 800 mM NaCl. Finally, size exclusion chromatography was used to exchange arrestin-3-ERK2-His_{10} into its storage buffer (20 mM MOPS pH 7.5, 150 mM NaCl, 1 mM TCEP, and 5% glycerol).

Microscale Thermophoresis (MST). MST was performed using the Monolith NT.115 instrument (NanoTemper Technologies GmbH). Binding was measured between bovine arrestin constructs (full-length arrestin-2/3, $arrestin2/3^{1-393}$; 20 mM MOPS pH 7.5, 150 mM NaCl, and 2 mM TCEP) and His_6-ERK2. His_6-ERK2 was labeled using the MO-L008 Monolith™ His-Tag Labeling Kit RED-tris-NTA following the manufacturer's protocol (100 nM final concentration of kinase in PBS-T buffer), which has been described as the optimal conjugate for oligohistidine-tags (229). A 16-step dilution series was prepared by adding 10 µL buffer (20 mM MOPS pH 7.5, 150 mM NaCl, 2 mM TCEP, 0.05% Tween-20) to 15 tubes. 20 µL of 40 µM arrestin was placed in the first tube, and 10 µL was transferred to the second tube and mixed well by pipetting (1:1 dilution series). The final tube did not contain any arrestin and was used as a blank. 10 µL of inactive His_6-ERK2 in the presence of 1 mM ATP and 2 mM $MgCl_2$ was added to each tube of the dilution series (final concentration ~50 nM). The capillaries were scanned at 40% LED and 40% MST power. All data were analyzed using PALMIST (145,194). Measured fluorescence was normalized and averaged, and the binding constants were determined using a global fit calculation and a 1:1 fitting model. The preset Thermophoresis + T-jump was used to calculate binding isotherms.

Surface Plasmon Resonance (SPR). Surface plasmon resonance experiments were performed with a Biacore X100 instrument. Full-length human His-arrestin-2/3 constructs were immobilized on a nitrilotriacetic acid sensor chip (NTA, GE Healthcare), which permits repeated

immobilization, stripping, and regeneration of His-tagged proteins (269). The running buffer (10 mM HEPES pH 7.3, 150 mM NaCl, 50 μM EDTA, 0.005% Tween-20) was prepared fresh and filtered using a 0.2 μM pore size. An amine coupling kit (GE Healthcare) was used in conjunction with the capture method described by Kimple et al. (269) to fuse the His-arrestin-2/3 constructs in a non-random orientation. His-ERK2 flowed over the immobilized-arrestin surface at concentrations ranging from 0-1 μM and response units were recorded. A reference flow cell was used to subtract background interaction and was treated identically to the arrestin-coupled cell. The chip surface was then regenerated by removal of the His-arrestin-2/3 with regeneration buffer (350 mM EDTA in running buffer). Data were calculated using the Biacore-provided evaluation software (GE Healthcare Life Sciences) with a 1:1 fitting model.

Rhodopsin pull-down assays. Rhodopsin pull-down assays were conducted as previously described (270). In brief, arrestin proteins (3.4 μg) were incubated in 25 μL of binding buffer (50 mM Hepes·K pH 7.4, 100 mM potassium acetate, and 2 mM EDTA) with (+) or without (−) 5 μg of phosphorylated light-activated rhodopsin (P-Rh*) in native membranes for 5 min at 37 °C. The samples were cooled on ice, loaded on top of a 30-μL cushion of 0.2 M sucrose in binding buffer, and centrifuged for 10 min at 350,000 × g in a TLA120 rotor in an Optima TLX ultracentrifuge (Beckman-Coulter). The supernatants were carefully removed, and 25 μL of 2× SDS sample buffer (Sigma) was added. The pellets (containing rhodopsin in samples where P-Rh* was present) were dissolved in 30 μL of 2× SDS (Sigma) sample buffer. One-third of each sample was resolved on discontinuous 10% polyacrylamide gel electrophoresis. The gels were stained with Coomassie blue.

MBP Pull-down. N-terminal MBP-fusion proteins including full-length bovine arrestin-2/3 and sequences corresponding to the indicated arrestin elements were designed and purified as

previously described (75,104). All arrestin fragments were subcloned into a pMal-p2T vector with a 10 amino acid linker, TLVPRGSPGF, between MBP and full-length arrestin-2/3 or its fragments. Purified MBP was used as a negative control in all pull-down experiments and non-specific binding was subtracted from the total observed binding for each construct. MBP-fusion proteins (10 μg in 50 μL of 50 mM HEPES-Na, pH 7.3/150 mM NaCl) were immobilized on amylose resin (25 μL, 50% slurry, New England Biolabs) for 1 h at 4 °C with slight rotation. Prey protein (His_6-ERK2, 10 μg in 50 μL of 20 mM Tris/150 mM NaCl) was added to the immobilized MBP constructs and incubated with gentle rotation for 2 h at 4 °C. Samples were transferred to centrifuge filters (Durapore®-PVDF-0.65 μm) and washed three times with 50 mM HEPES-Na, pH 7.3, 150 mM NaCl. Proteins were eluted with 100 μL 50 mM maltose in wash buffer. Proteins were concentrated using methanol precipitation. The pellets were air dried, dissolved in SDS sample buffer (30 μL Laemmli, 2x) and analyzed by SDS-PAGE and Western blotting, as described (104). Statistical analysis was performed using One-way ANOVA followed by Dunnett's post-hoc test.

Peptide Array Synthesis. The ResPep SL peptide synthesizer was used with conventional SPOT synthesis protocols using peptides with 15 residues in length, as previously described (230). Both a blank spot and a 15-mer glycine peptide were used as negative controls, and non-specific binding to these controls was not statistically different. Peptides were assembled by the ResPep SL on solid support via a peptide amide linker using Fmoc-chemistry. The sequences of the peptides were derived from either bovine arrestin-2, bovine arrestin-3, or human ERK2. After synthesis, the amino-protecting group was removed using piperidine (20% (v/v) solution in dimethylformamide) followed by extensive washing. The membranes were then submerged in a solution of 95% trifluoroacetic acid (TFA) and 3% triisopropylsilane for 1 h with agitation. Following removal of the TFA solution, the membranes were washed in dichloromethane four

times 10 min each, followed by four 10 min washes in dimethylformamide, and two 2 min washes in ethanol. The membranes were then dried in the hood and stored at 4°C.

Peptide Membrane Blots. Dried membranes were soaked in 100% ethanol for 5 min and then rehydrated by washing twice in water for 5 min. The membranes were then incubated in blocking solution (5% non-fat dry milk in Tris-buffered saline with 0.1% Tween 20 (TBS-T)) for 1 h. The membranes were washed five times for 5 min before overnight incubation at 4°C with the prey protein (0.5 µM) in binding buffer (20 mM MOPS pH 7.5, 150 mM NaCl, 2 mM TCEP). The following morning, the membranes were rinsed five times for 5 min in TBS-T. Membranes were incubated with the appropriate primary antibody for 1 h at room temperature, then washed five times for 5 min in TBS-T (p44/42 MAPK ERK1/2 #9102S, anti-arrestin rabbit polyclonal F431 antibody (211)). The corresponding HRP-conjugated secondary antibody (1:10,000 dilution) was prepared in TBS-T, incubated with the membrane for 1 h, followed by two 5 min washes in TBS-T at RT. The spots were visualized using the SuperSignal West Pico Stable Peroxide Solution kit from ThermoScientific. Images were obtained using the Bio-Rad Gel Doc Imager and analyzed by densitometry using ImageJ protein array analyzer. For ResPep analysis, the signal in individual dots was measured as a percentage of total binding density detected on the membrane. This allowed for comparison across all peptide experiments. Statistical analysis was performed using one-way ANOVA followed by Dunnett's post-hoc test using GraphPad Prism5.

Hydrogen Exchange Mass Spectrometry (HDX-MS). Purified arrestin-$2^{1\text{-}387}$ and ERK2 proteins were prepared at 80 µM in 20 mM Hepes pH 7.4, 150 mM NaCl. Equal volumes of proteins were mixed and incubated at RT for 2 h resulting in a final concentration of 40 µM. Hydrogen/deuterium exchange was initiated by mixing 3 µL protein with 27 µL D_2O buffer (20 mM HEPES, pD 7.4, 150 mM NaCl and 10% glycerol in D_2O) and incubated for 10, 100, 1,000,

or 10,000 sec at 4°C. The mixtures were quenched by adding 30 µL ice-cold quench buffer (100 mM NaH_2PO_4 pH 2.01 and 20 mM TCEP). For non-deuterated samples (ND), 3 µL of protein complex was mixed with 27 µL of H_2O buffer (20 mM HEPES, pH 7.4, 150 mM NaCl in H_2O) and quenched with 30 µL ice-cold quench buffer. The quenched samples were digested on line by passing through an immobilized pepsin column (2.1 × 30 mm) (Life Technologies, Carlsbad, CA, USA) at a flow rate of 100 µL/min with 0.05% formic acid in H_2O at 12℃. Peptide fragments were subsequently collected on a C18 VanGuard trap column (1.7 µm × 30 mm) (Waters, Milford, MA, USA) for desalting with 0.05% formic acid in H_2O. Peptic peptides were then separated by ultra-pressure liquid chromatography over an ACQUITY UPLC C18 column (1.7 µm, 1.0 mm × 100 mm) (Waters, Milford, MA, USA) at 40 µL/min with an acetonitrile gradient created by two pumps: mobile phase A (0.15% formic acid in H20) and B (0.15% formic acid in acetonitrile). The gradient started with 8% B and increased to 85% B over the next 8.5 min. To minimize the back-exchange of deuterium to hydrogen, the sample, solvents, trap, and UPLC column were all maintained at pH 2.5 and 0.5℃ during analysis. Mass spectral analyses were performed with a Xevo G2 QTof equipped with a standard ESI source (Waters, Milford, MA, USA). The mass spectra were acquired in the range of m/z 100–2000 for 12 min in positive ion mode. Peptides were identified in ND samples with ProteinLynx Global Server (PLGS) 2.4 (Waters, Milford, MA, USA). The following parameters were applied: monoisotopic mass, nonspecific for the enzyme while allowing up to 1 missed cleavage, MS/MS ion searches, automatic fragment mass tolerance, and automatic peptide mass tolerance. Searches were performed with the variable methionine oxidation modification, and the peptides were filtered with a peptide score of 6. To process HDX-MS data, the amount of deuterium in each peptide was determined by measuring the centroid of the isotopic distribution using DynamX 2.0 (Waters, Milford, MA, USA).

Incorporation of F2Y into ERK2 and truncated arrestin2$^{1\text{-}365}$. Plasmids of ERK2/226/F2Y and truncated arrestin 2$^{1\text{-}365}$/349/F2Y were generated using the Quick Change Mutagenesis kit (ThermoFisher Scientific) and co-transformed into BL21 (DE3) with pEVOL-F2YRS (271). Cells were induced with 0.3 mM IPTG, 0.02% L-arabinose, and 0.5 mM F2Y when OD600 reached 1.0-1.2. The cells were harvested after growing an additional 14 h at 25°C. Protein purification for F2Y proteins was performed as described previously (134,272,273).

^{19}F NMR experiments. F2Y incorporated arrestin-2$^{1\text{-}365}$ was concentrated to 50 μM and mixed with or without an equal molar concentration of ERK2 by end-to-end rotation in binding buffer (20mM Tris-HCl pH 8.0, 150mM NaCl, 10% D2O) at RT for 30 min. Data were then collected at 25°C using an Agilent OD2 600 spectrometer fitted with a 5-mm broad band probe. The ^{19}F 90° pulse lengths were 9.9 μs and the spectra were obtained by using 15,000 scans and a recovery delay of 1 sec. Data were processed using 10-Hz Lorentzian line broadening and were referenced to an internal TFA standard (76.5 ppm.). The same procedure was used to assess the interaction of F2Y incorporated ERK2 and arrestin-2$^{1\text{-}365}$.

Fluorescence Quenching with Bimane. Wild-type ERK2 and tryptophan mutants were purified and exchanged into an interaction buffer (10 mM HEPES, 150 mM NaCl, pH 7.4) in addition to cysless arrestin-2$^{1\text{-}365}$ purification and exchange into a labeling buffer *(*10 mM MES, 150 mM NaCl, pH 6.5*).*). Arrestin-2$^{1\text{-}365}$ was concentrated to 50 μM and labeled with bimane to a final concentration of 0.5 mM. Excess dye was removed through another cycle of buffer-exchange into the interaction buffer following 4 h incubation at RT. ERK2 and arrestin-2$^{1\text{-}365}$ were mixed at 2 μM in 100 μl interaction buffer and samples were placed in a MicroFluor 96-well fluorescent plate. Samples were excited at 390 nm and the emitted fluorescence was measured from 420 to 600 nm using a 2 nm step size. Each data point was integrated for 0.2 s. Spectra were analyzed

using GraphPad Prism 7.

Recombinant pcDNA3-arrestin-3-ERK2 construction. To make the arrestin-3-ERK2-His_{10} fusion the cDNAs encoding full-length bovine arrestin-3 and full-length human ERK2 were subcloned into a pcDNA3 vector between BamHI and HindIII sites. All restriction enzymes were from New England Biolabs (Ipswich, MA). The final construct consisted of full-length arrestin-3 followed by a PreScission protease site (GSLEVLFQGPGS), full-length ERK2, a thrombin cleavage site (GSLVPRGSGS), and a His_{10} tag.

Continuous-wave EPR. Cysteine substitutions were introduced into 20 sites on otherwise cysless arrestin-$3^{1\text{-}393}$. This variant was purified and spin-labeled with MTSL, as described previously (142). Spectroscopy data were collected using a Bruker E580 operating at Q-band and equipped with an EN5107D2 resonator. Samples contained 20% deuterated glycerol as a cryoprotectant and 50 μM arrestin-$3^{1\text{-}393}$ with 100 μM ERK2 and were run at 80 K following flash freezing in a dry ice and acetone mixture. Acquired data were phase and background corrected, plotted and analyzed for distance distributions in the same way for each data set using the algorithms included in the LongDistances software program (143) written by C. Altenbach (University of California-Los Angeles, CA).

ERK2 phosphorylation assay in HEK293 arrestin-2/3 knockout cells. HEK293 arrestin-2/3 knockout cells (a generous gift from Dr. Asuka Inoue, Graduate School of Pharmaceutical Sciences, Tohoku University) were maintained in DMEM solution containing 10% FBS (Invitrogen), penicillin, and streptomycin at 37°C and 5% CO_2. Cells were transfected at 90-100% confluency in 6-well plates with pcDNA3-arrestin constructs (0-0.25 μg) or pcDNA3-arrestin-ERK2-His10 constructs (0-1.5 μg) and 0.3 μg of β2-adrenergic receptor at a 1:2.5 ratio of DNA:Lipofectamine 2000 (Invitrogen). At 48 hr post-transfection, the cells were incubated with

10 μM agonist isoproterenol (Sigma) over the indicated time-course (0-45 mins). Cells were then lysed with 400 μL RIPA buffer and spun at 15,000xg to pellet debris. The supernatant was mixed 1:1 with 2x SDS sample buffer (Sigma), the proteins were subjected to 10% SDS-PAGE, and transferred to PVDF membrane (Millipore, Bedford, MA). Membranes were blocked by 1% non-fat dry milk in TBS-T and incubated with respective primary antibodies (Cell Signaling Technology, Inc.): anti-totalERK2 (#9102S), anti-phospho-ERK2 (#9101S), and anti-arrestin (rabbit polyclonal F431 antibody (211)). After washing, membranes were incubated with the appropriate HRP-conjugated secondary antibodies (Jackson ImmunoResearch Laboratories, Inc., West Grove, PA). Bands were detected using the Bio-Rad Gel Doc Imager with enhanced chemiluminescence (ECL, Pierce) and quantification was done using the software Quantity One (BioRad, Hercule, CA).

Small angle X-ray Scattering (SAXS). SAXS data were collected at the Advanced Photon Source (beamline BioCAT-18) in Lemont, Illinois, as described (274). Arrestin-3-ERK2-10XHis was purified as described above and subjected to in-line Size Exclusion Chromatography (SEC) coupled to SAXS (SEC-SAXS) on a Superdex S200 Increase 10/300 GL column equilibrated with 20 mM MOPS, pH 7.5, 150 mM NaCl, 2 mM TCEP, and 5% glycerol. The standard experimental set-up was used: Pilatus 1M detector from Dectris (Switzerland), a distance of 3.5 m from sample to detector, and a temperature-controlled quartz capillary (1.5 mm 1D, 1.52 mm OD) flow cell.

CHAPTER 8

ARRESTIN-3 INTERACTION WITH MATERNAL EMBYONIC LEUCINE ZIPPER KINASE

This article is in preparation for submission to the Journal of Molecular Biology. **Nicole A. Perry** will be first author and Kevin P. Fialkowski, Ali I. Kaya, Juliana M. Taliaferro, Vsevolod V. Gurevich, Kevin N. Dalby, and T.M. Iverson contributed to this work.

8.1 Introduction

Maternal embryonic leucine-zipper kinase (MELK) is a novel serine/threonine kinase of the AMPK/Snf1 family (275). Unlike other family members, MELK does not require an upstream kinase activator and can self-activate via auto-phosphorylation *in vitro* (276). MELK is highly conserved across species and is thought to play a role in cell cycle regulation, proliferation, and mitosis (275).

While the functions and regulatory mechanisms of MELK are just starting to be elucidated, MELK has been linked to several cell fate-related processes. One group demonstrated that in mice MELK induces phosphorylation and activation of apoptosis signal-regulating kinase 1 (ASK1), a kinase that activates cell death pathways (277). In contrast, several studies showed that overexpression of MELK results in aggressive cell proliferation and that the kinase may function as a driver oncogene (278,279). These contradictory conclusions suggest that the role of MELK in pro- and anti-apoptotic pathways may be context-dependent.

Many signaling proteins have been identified as regulators of MELK activity. Several

prominent examples include c-Jun N-terminal kinases (JNKs)(280), transcription factor FOXM1 (281,282), and zinc-finger-like protein 9 (Zpr9) (283). While these interacting partners and overexpression of MELK in various cancers demonstrate the physiological importance of MELK, the molecular mechanisms underlying these interactions remain unclear. More studies are needed to determine the exact role of MELK in disease progression.

Here, we describe a novel interacting partner for MELK, arrestin-3. While the arrestin proteins are best known for their role in the desensitization and internalization of G-protein coupled receptors (GPCRs), they also act as protein scaffolds for various effectors, including several mitogen-activated protein kinase (MAPK) cascades (2,4,58,64,77,193,240). This arrestin-mediated signaling can be both a GPCR-dependent and GPCR-independent process. We used a combination of biophysical techniques and in-cell assays to show that the interaction between the MELK kinase domain and arrestin-$3^{1\text{-}393}$ is biologically relevant. It is tempting to speculate that arrestin-3 binding to MELK results in specific subcellular localization to direct cell fate signaling pathways. Thus, the arrestin-3 interaction with MELK may be a promising therapeutic target.

8.2 Results

Pull-down assay of MELK$^{1\text{-}326,T167E}$ with arrestin-3$^{1\text{-}393}$. Two separate *in vitro* pull-down assays were conducted to assess binding of the MELK kinase domain (residues 1-326) to truncated arrestin-3 (residues 1-393, denoted below as arrestin-$3^{1\text{-}393}$). This truncated version of arrestin-3 is an established model for both GPCR-dependent and GPCR-independent arrestin activation (2,3,58,96-98,104) as it shifts the equilibrium from a "basal" conformation to an "active" conformation. For MELK, we used the T167E mutant (denoted MELK$^{1\text{-}326,T167E}$), a well-characterized mimic of the constitutively phosphorylated state (284), to favor an activated kinase

state. The full-length mammalian kinase consists of 651 residues and includes the kinase domain (KD), a ubiquitin-associated (UBA) domain, a TP dipeptide-rich domain, and a kinase-associated 1 (KA1) domain (284). We were interested in the interaction between active forms of each of these proteins because we hypothesized that this would be the favored conformation state for each protein.

We evaluated whether there was a species difference in the interaction between $MELK^{1-326,T167E}$ and $arrestin\text{-}3^{1-393}$ by comparing mouse and human constructs (**Fig. 8.1A**). Within the kinase domain of MELK, these homologs share 94% sequence identity. The MELK kinase domain of both species exhibited strong binding to $arrestin\text{-}3^{1-393}$ that was not statistically different (Fig. 1A).

We next tested human $MELK^{1-326,T167E}$ binding to $arrestin\text{-}3^{1-393}$ in the presence of physiological concentrations of ATP and $MgCl_2$. The ATP-binding pocket is located between the N- and C-lobes of the MELK kinase domain, and ATP likely affects the conformation of this domain (284). In the presence of ATP and $MgCl_2$ the $MELK^{1-326,T167E}$ interaction with $arrestin\text{-}3^{1-393}$ was enhanced (**Fig. 8.1B**). This suggests that the conformation of the kinase domain plays a role in the interaction of $MELK^{1-326,T167E}$ with $arrestin\text{-}3^{1-393}$.

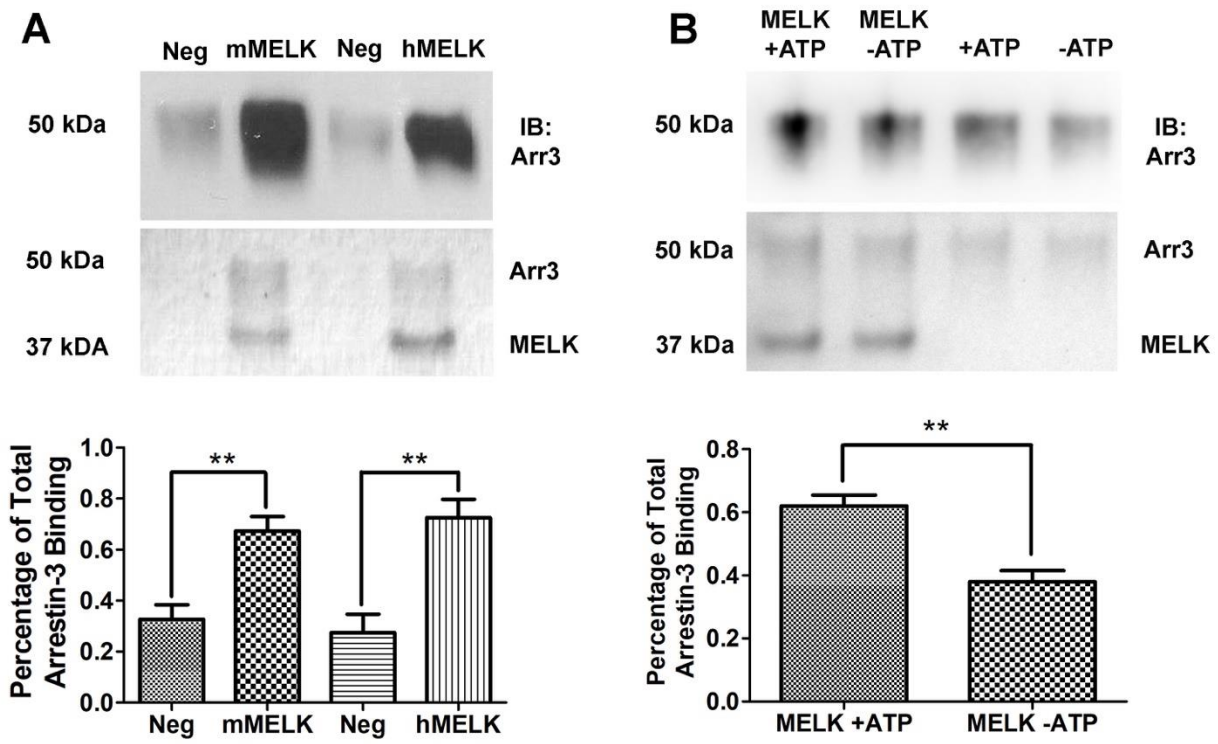

Fig. 8.1. Pull-down analysis of MELK$^{1\text{-}326,T167E}$ with truncated arrestin-3$^{1\text{-}393}$. (A) Analysis of mouse MELK$^{1\text{-}326,T167E}$ (10 µg) and human MELK$^{1\text{-}326,T167E}$ (10 µg) binding to bovine arrestin-3$^{1\text{-}393}$ (10 µg). Top: Representative Western blot of the eluates using an anti-arrestin-3 antibody (1:10,000, F431). Middle: Representative Coomassie staining of the eluates. Bottom: Quantification of arrestin-3 binding using densitometry. Intensity was compared to the negative control (beads alone) and binding is shown as a percentage of total arrestin-3 applied (n=3). **(B)** Analysis of human MELK$^{1\text{-}326,T167E}$ (10 µg) binding to bovine arrestin-3$^{1\text{-}393}$ (10 µg) in the absence or presence of 2 mM ATP and 4 mM $MgCl_2$. Top: Representative Western blot of the eluates using an anti-arrestin-3 antibody (1:10,000, F431). Middle: Representative Coomassie staining of the eluates. Bottom: Quantification of arrestin-3 binding using densitometry. Intensity was compared to the negative control (beads alone) and binding is displayed as a percentage of total arrestin-3 applied (n=4). Statistical analysis was performed using Student's two-tailed paired T-test (**, $p<0.01$).

Affinity of MELK$^{1\text{-}326,T167E}$ for arrestin-3$^{1\text{-}393}$. MicroScale Thermophoresis (MST) quantifies biomolecular interactions using the directed movement of molecules along a temperature gradient (196). To measure the affinity of human MELK$^{1\text{-}326}$ for arrestin-3$^{1\text{-}393}$, we used increasing concentrations of arrestin-3$^{1\text{-}393}$ (0-40 µM) in the presence of fluorescently-tagged MELK$^{1\text{-}326,T167E}$ (50 nM) and physiological concentrations of ATP and $MgCl_2$. In this assay, MELK$^{1\text{-}326,T167E}$ exhibited high affinity for arrestin-3$^{1\text{-}393}$ with a K_d value of 130 ± 35 nM (**Fig. 8.2**). It should be noted that this interaction occurs in the absence of several MELK domains, most notably the TP dipeptide-rich domain and the KA1 domain. These domains may be involved in

autoinhibition of the kinase and could impact the affinity for arrestin-3 (285).

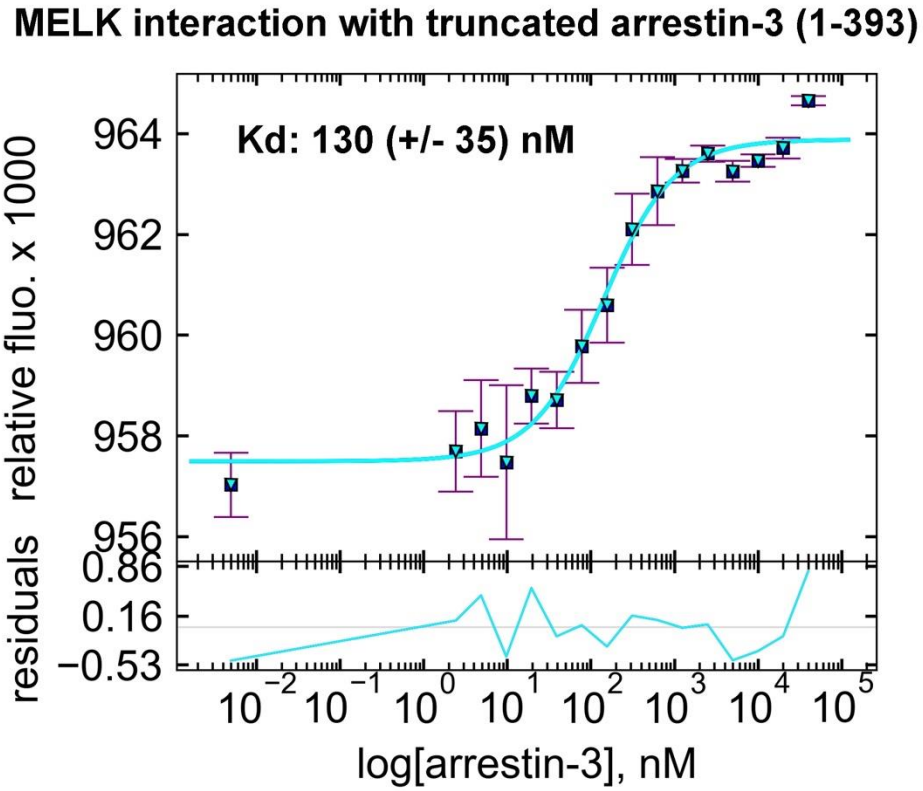

Fig. 8.2. The affinity of MELK$^{1\text{-}326,T167E}$ for arrestin-3$^{1\text{-}393}$ in the presence of ATP. A binding curve for bovine arrestin-3$^{1\text{-}393}$ with human MELK$^{1\text{-}326,T167E}$ in the presence of 1 mM ATP and 2 mM $MgCl_2$ is shown with the average K_d value (n=3). Microscale thermophoresis was performed at a constant concentration of Tris-NTA-labeled His-MELK$^{1\text{-}326,T167E}$ (50 nM) with a serial dilution of arrestin-3$^{1\text{-}393}$ (0-40 µM). The binding isotherm was calculated using preset T-jump in the software PALMIST (145,146) and the graph was created in the program GUSSI.

Mapping the arrestin-3 binding site for MELK$^{1\text{-}326,T167E}$. Defining interface surfaces between proteins is crucial to understanding many biological processes and signaling pathways. Protein-protein interactions are studied using a wide variety of techniques and can be probed using full-length proteins, separated protein domains, or peptides. Two distinct advantages of using peptides to study protein-protein interactions are the ease of synthesis and the ability to identify specific interaction sites (286). Peptide arrays provide investigators with the ability to narrow down a complex interaction surface to a specific binding site(s) (287).

To identify which regions of arrestin-3 are important for the interaction with the MELK$^{1-326,T167E}$, we performed a 15-mer peptide scan of full-length arrestin-3 using 1 amino acid shifts (**Fig. 8.3A**). Conditional formatting was used to separate peptides based on their binding strength and to map interaction regions on the basal arrestin-3$^{1-393}$ crystal structure (PDB 3P2D) (92) (**Fig. 8.3B**). Notably, all interacting peptides localized to the non-receptor binding surface of arrestin-3$^{1-393}$. Closer examination of the binding quantification revealed several regions of high interaction: first, residues A87-P125 that include the □-helix involved in the three-element interaction (92); second, residues E207-N224 and F269-N300 that encompass several β-strands of the C-domain; and finally, the region corresponding to the C-tail of arrestin-3 (**Fig. 8.3C**). Peptides including residues S164-Q173 were excluded despite displaying strong binding because of surface inaccessibility in the crystal structure (92). This region contains several hydrophobic residues and appears to be a false positive. It should be noted that the distal C-terminus of vertebrate arrestins has never been observed in crystal structures (35,92,93,116,288,289), suggesting that it is highly flexible. Peptides corresponding to this region exhibited high binding to MELK$^{1-326,T167E}$. As the arrestin C-tail is released upon receptor binding (30,33,290,291), it is possible that the arrestin-MELK interaction is enhanced by arrestin-3 activation. This is

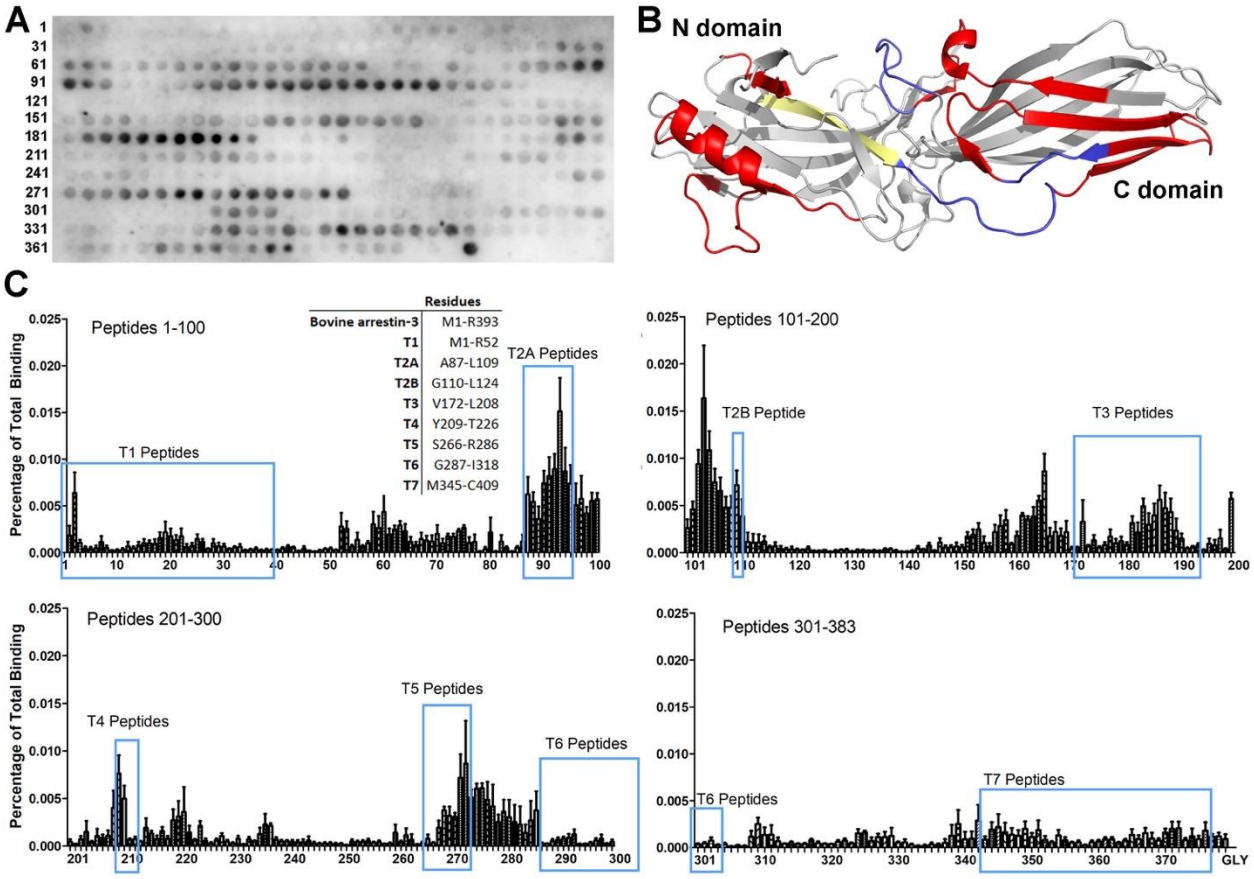

Fig. 8.3. MELK$^{1-326}$ interaction sites on arrestin-3. (A) Peptide scan (15-mer) of bovine arrestin-3-derived peptides (residues 1-393, 1 amino acid shifts). **(B)** Map of interaction sites for MELK$^{1-326}$ on arrestin-3 (PDB 3P2D (92)). Peptides calculated to be in the top 10% for binding to MELK$^{1-326,T167E}$ are highlighted in red, while those with moderate binding are displayed in sky blue. The peptide S164-Q173 (shown in yellow) demonstrated binding within the top 10% but is likely a false positive due to its surface inaccessibility in both basal (92) and active (3) arrestin-3 structure. **(C)** Quantified binding of MELK$^{1-326,T167E}$ to arrestin-3-derived peptides. Binding was measured as a percentage of total intensity on the membrane. A 15-mer glycine peptide was used to detect non-specific interaction with the membrane. Inset: Peptide segments corresponding to the non-receptor surface of arrestin-3. The corresponding regions are highlighted in blue on the quantification.

supported by the high level of binding observed between MELK$^{1\text{-}326,T167E}$ and our pre-activated arrestin-3 construct.

Mapping the MELK site for arrestin-3$^{1\text{-}393}$ binding. To date, crystallization of MELK has been restricted to the catalytic domain (292-295). To characterize which sites on MELK are important for its interaction with arrestin-3$^{1\text{-}393}$, we engineered a peptide array corresponding to full-length MELK using 3 amino acid shifts (**Fig. 8.4A**). Although shifting by 3 amino acids restricts the ability to parse out false positives, we wanted to determine whether MELK domains other than the kinase domain are involved in its interaction with arrestin-3$^{1\text{-}393}$.

Quantification of the arrestin-3$^{1\text{-}393}$ binding revealed several MELK regions responsible for the interaction (**Fig. 8.4B**). The region of highest binding that can be observed in the crystal structure involved residues I82-P135, which correspond to the C-lobe of the kinase domain (highlighted in red in **Fig. 8.4C**). Moderate binding was also detected for residues V271-D285 at the beginning of the UBA domain. No interaction with arrestin-3$^{1\text{-}393}$ was detected in the activation segment (residues D150-E178) of MELK. Of note, significant binding was also detected for residues N562-L582 in the KA1 domain. This domain is thought to be involved in autoinhibition of the kinase and is important for its membrane association (296,297).

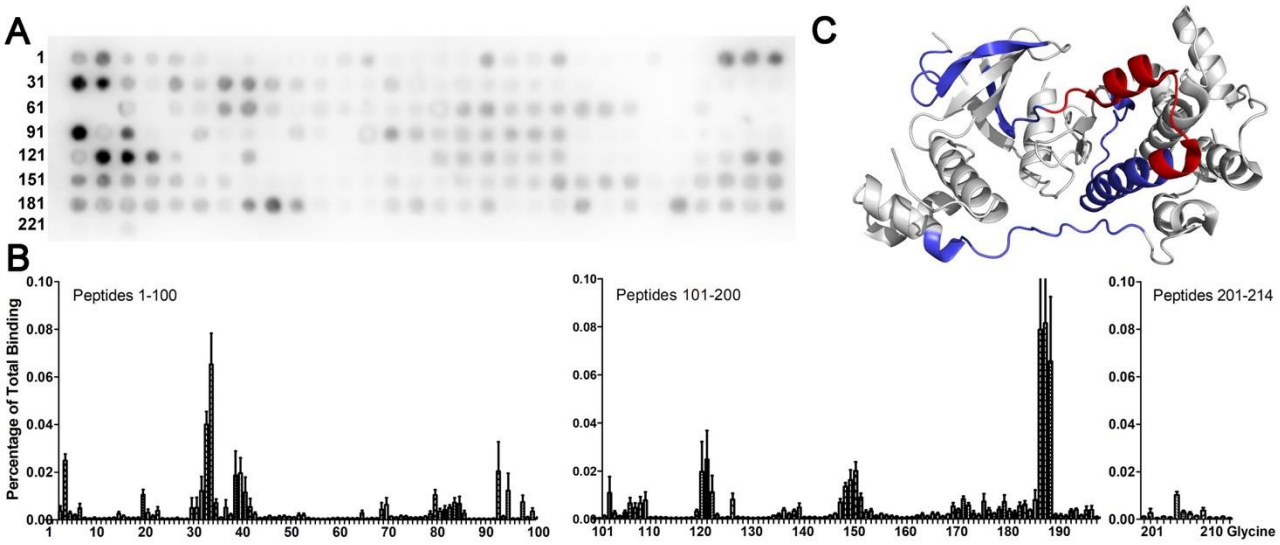

Fig. 8.4. Arrestin-3$^{1\text{-}393}$ interaction sites on MELK$^{1\text{-}651}$. (A) Peptide scan using 15-mers derived from human MELK (residues 1-651, 3 amino acid shifts). **(B)** Quantified binding of arrestin-3$^{1\text{-}393}$ to MELK-derived peptides. Arrestin-3$^{1\text{-}393}$ binding was measured as a percentage of sum total of the intensity of all spots. **(C)** Map of interaction sites for arrestin-3$^{1\text{-}393}$ on MELK (PDB 4BL1 (292)). Peptides that exhibited high binding to arrestin-3$^{1\text{-}393}$ are highlighted in red, while those with moderate binding are displayed in blue. Only 347 residues are visible in the crystal structure (up to peptide 107 in the array). Peptides 188-190, with the sequence NVTTTRLVNPDQLLNEIMSIL from the C-terminal KA1 domain, demonstrated the highest binding.

Arrestin-3$^{1\text{-}393}$ and MELK$^{1\text{-}326,T167E}$ coimmunoprecipitate in cells. We next used coimmunoprecipitation to test the ability of the MELK kinase domain and arrestin-3$^{1\text{-}393}$ to interact in the physiologically relevant environment of living cells (**Fig. 8.5**). While coimmunoprecipitation is a suitable method for detecting biologically relevant interactions, it does not detect low-affinity and/or transient interactions. We observed a modest binding of arrestin-3$^{1\text{-}393}$ and MELK$^{1\text{-}326,T167E}$ at a 1:1 transfection ratio. Thus, the arrestin-3-MELK interaction observed *in vitro* occurs in cells and is likely biologically relevant.

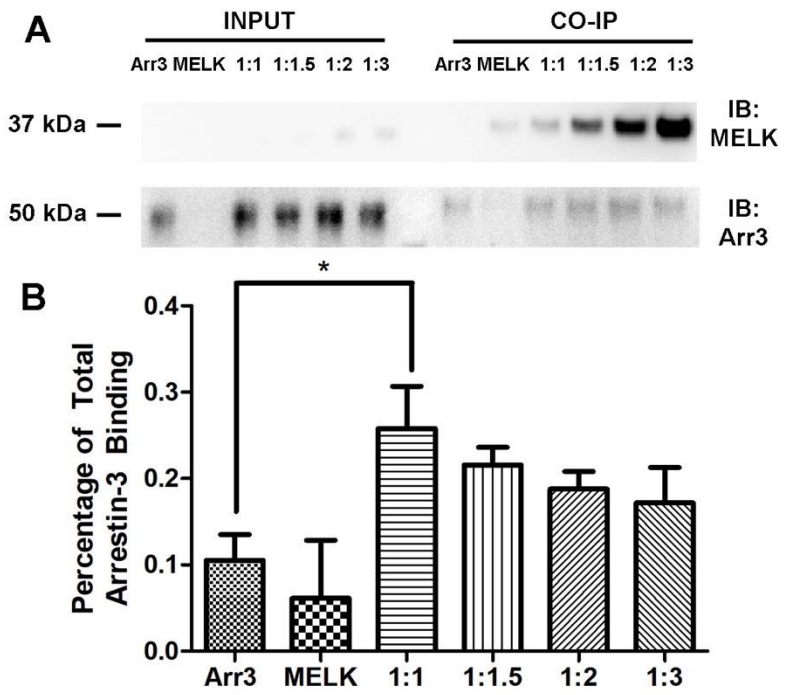

Fig. 8.5. Co-immunoprecipitation of MELK$^{1-340}$ with arrestin-3$^{1-393}$ co-expressed in cells. (A) Western analysis of coimmunoprecipitation. HEK293 arrestin-2/3 knockout cells were transfected with HA-arrestin-3$^{1-393}$ (1 µg), FLAG-MELK$^{1-340}$ (1 µg), or plasmids encoding arrestin and MELK at indicated ratios for 48 h prior to immunoprecipitation with FLAG primary antibody. Western analysis was performed using an arrestin-3 (1:10,000; F431) and FLAG (1:1,000; F3165 Sigma) antibody. **(B)** Arrestin-3$^{1-393}$ co-immunoprecipitation with MELK$^{1-340}$ was quantified using densitometric analysis of arrestin-3 blots. Statistical analysis was performed using One-way ANOVA followed by Tukey's post hoc test with correction for multiple comparisons (*, $p<0.05$).

Cellular proliferation is decreased by co-expression of arrestin-3$^{1-393}$ with the MELK$^{1-340}$.

Over-expression of MELK has been demonstrated in several cancer types and is often linked to poor disease prognosis (278). To measure the effect of arrestin-3$^{1-393}$, a MELK fragment containing the kinase and UBA domain (MELK$^{1-340}$; residues 1-340), and arrestin-3$^{1-393}$/MELK$^{1-340}$ co-expression on cellular proliferation, we directly measured DNA synthesis using 5-ethynyl-2'-deoxyuridine (EdU) incorporation as a readout. EdU is a nucleoside analog of thymidine that is readily incorporated into replicating DNA and can be detected using fluorescent azides (298). HEK293 arrestin-2/3 knockout cells were incubated in media with or without EdU following transfection. Cells were then fixed and incubated with Alexa Flour 488 picolyl azide, whereupon flow cytometry was used to determine the percentage of S-phase cells in the population (**Fig. 8.6**).

Untransfected cells and cells transfected with a 1:1 µg mixture of arrestin-3^{1-393}/$MELK^{1-340}$ without EdU treatment were used as negative controls for gating purposes (gray trace in **Fig. 8.6A**, gating schematic shown in **Fig. 8.6B**). Three replicates yielded the following percentages of S-phase cells: 22.6 ± 9.1% for arrestin-3^{1-393} transfection, 39.7 ± 6.8% for $MELK^{1-340}$ transfection, and 16.8 ± 7.5% for 1:1 mixture of the proteins. Thus, the increase in S-phase cells observed with $MELK^{1-340}$ expression is significantly reduced in the presence of arrestin-3^{1-393}.

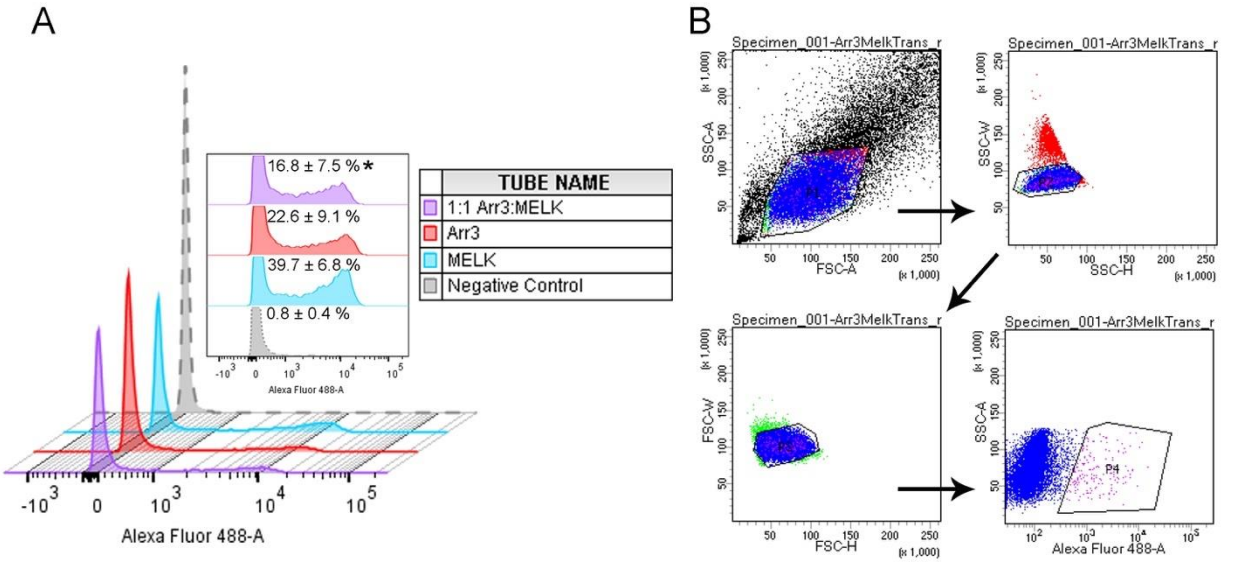

Fig. 8.6. Cellular proliferation upon co-expression of $MELK^{1-340}$ and arrestin-3^{1-393} as detected by flow cytometry. HEK293 knockout cells for arrestin-2/3 were transfected with HA-arrestin-3^{1-393} (1 µg) (red), FLAG-$MELK^{1-340}$ (1 µg) (blue), or a fixed ratio of the two proteins (1 µg:1 µg) (purple), and cellular proliferation was measured using the Click-iT™ EdU Alexa Fluor 488 Imaging Kit (ThermoFisher Scientific) in combination with flow cytometry. **(A)** A representative histogram shows data from cells labeled with Alexa Fluor 488 picolyl azide analyzed on a 3-laser LSRII (BD Biosciences). The inset shows the relative heights of the second distribution (Alexa Fluor 488 positive cells) with the percentages of cells in S-phase for combined experiments (n=3). Analysis was completed on FlowJo 10.1.5 (FlowJo LLC). The first distribution represents cells that are not proliferating, while the second distribution represents cells in S-phase. **(B)** The gating strategy used for histogram generation. Cells were initially sorted by scatter (SSC-A by FSC-A) (P1) to determine the population of living cells, then by single cells (SSC-W by SSC-H) (P2), then singlets (FSC-W by FSC-H) (P3), and finally by cells positive for Alexa Flour 488 (SSC-A by Alexa Fluor 488) (P4).

8.3 Discussion

MELK is activated by a variety of extracellular stimuli including H_2O_2 and tumor necrosis factor-α (299). Additionally, MELK activity can be regulated by protein-protein interactions. For example, mitosis-promoting factor (MPF) and mitogen-activated protein kinases (MAPKs) can directly phosphorylate MELK *in vitro* and enhance its kinase activity (300). Finally, MELK is the only member of the AMP-activated protein kinase (AMPK) subfamily that undergoes autophosphorylation and autoinhibition (285).

While the role of MELK in cell survival continues to be an area of active research, several downstream targets have been implicated. MELK increases transcription of oncogenes through interactions with transcription factors (FOXM1 (281,301), EIF4B (302), ZPR9 (285), and NIPP1 (285)), aids in DNA damage repair via regulation of p53 and ATM (280,301), and acts as a cell cycle regulator (303). MELK also activates proteins that induce cell death, such as ASK1 (277) and Smads (304). Here, we demonstrate that MELK can interact with arrestin-3 and that the interaction changes the effect of MELK on cell survival.

The arrestins are best known for their role in the desensitization and internalization of G protein-coupled receptors (GPCRs) (28). Arrestins also act as critical regulators of signal transduction by binding a wide array of protein partners (9). The best characterized interacting partners include the internalization machinery components clathrin and AP-2 (11,45), Src family tyrosine kinases (51,305), mitogen-activate protein kinase and their upstream activator kinases (58,96,98,181,193), and E3 ubiquitin ligases (203,306). Notably, a key regulatory role of the arrestin proteins is their ability to act as scaffolds/adaptors for kinases and phosphatases (9). The arrestins likely orient kinases and their substrates and bring them into close proximity to facilitate signaling (2,67,98).

Here we showed that MELK$^{1-326}$, which contains the kinase and UBA domains, interacts with arrestin-3$^{1-393}$ (**Figs. 8.1** and 8.**2**). The MELK$^{1-326}$ construct also contains a T167E mutation that mimics an activated kinase conformation (307). This suggests that our *in vitro* binding studies reflect a high affinity interaction of an active kinase with a preactivated conformation of arrestin-3$^{1-393}$. More studies will need to be done to determine whether this is the preferred interaction or whether the inactive kinase is favored, as we recently established for JNK3 and its activators MKK4 and MKK7 (2).

To further isolate the interaction surface between the two proteins, we performed several peptide array studies that covered the full-length of bovine arrestin-3 and human MELK (**Figs. 8.3,8.4**). The arrestin-3-derived peptide experiments largely mapped the MELK "footprint" onto several β-strands of the C-domain and the N-domain α-helix involved in the three-element interaction. This suggests that MELK$^{1-326,T167E}$ can bind elements in both domains and may require multiple sites for the observed high affinity interaction (**Fig. 8.2**). This is similar to our previous finding that each kinase in the ASK1-MKK4/7-JNK3 and cRaf-MEK1-ERK1/2 cascades (64), as well as E3 ubiquitin ligase parkin (203) engage both arrestin domains. When we assessed arrestin-3$^{1-393}$ interaction with MELK-derived peptides, we found the greatest binding in the KA1 domain and a section of the C-lobe. While it is difficult to discern possible binding mechanisms without structural information, it is tempting to speculate that arrestin-3$^{1-393}$ binding the KA1 domain prevents MELK autoinhibition and promotes kinase activity. Further experimentation is necessary to test this hypothesis.

To validate our *in vitro* findings in a more biological context we assessed the MELK$^{1-340}$/arrestin-3$^{1-393}$ interaction in living cells (**Fig. 5**). The MELK$^{1-340}$ construct does not contain the T167E mutation and could therefore reflect either an inactive or active conformation, depending

on its phosphorylation state. We observed a modest binding of MELK$^{1-340}$ and arrestin-3$^{1-393}$ that suggests that these proteins can interact in the cell.

Most intriguing, perhaps, were our cell proliferation results that reflected how arrestin-3$^{1-393}$ may modulate MELK$^{1-340}$ activity (**Fig. 8.6**). When transfected alone, MELK$^{1-340}$ was found to generate 39.7 ± 6.8% of S-phase cells. This was considerably higher than the arrestin-3$^{1-393}$ transfected cells. Upon co-transfection, the percentage of S-phase cells dropped back to arrestin-3$^{1-393}$ levels. While more work will be needed to further characterize this mechanism, it appears that MELK$^{1-340}$ interaction with arrestin-3$^{1-393}$ does not favor cell proliferation. Whether this is due to arrestin-3$^{1-393}$ binding inhibiting MELK$^{1-340}$ interactions with downstream effectors remains to be elucidated.

In conclusion, we discovered a novel interacting partner of MELK: arrestin-3$^{1-393}$. This interaction could provide an interesting avenue for modulating MELK activity that is not exploited by currently available pharmaceuticals.

8.4 Materials and Methods

Purified proteins. Arrestin-3$^{1-393}$ was purified as previously described (226,227). For MELK expression, a BL21 DE3 pLysS glycerol stock of MELK T167E (residues 1-326) in pET21b was used to inoculate 120 mL starter culture overnight at 30°C, 205 rpm. Each 1 L was inoculated using 10 mL overnight culture. Expression was induced with 500 µM IPTG after cells reached an OD 0.6, and the temperature was reduced to 17 °C for ~18 h. The cells were pelleted by centrifugation at 6,000xg, 10 min. The pellets were subjected to one cycle of freeze-thaw before adding the lysis buffer (20 mM Tris-HCl pH 7.5, 300 mM NaCl, 50 mM imidazole, 25 µL DNAse, 500 µL Pepstatin A, 100 µL leupeptin, 2 mM TCEP). The crude lysate was sonicated for

4 min (5 sec on, 10 sec off, 75% amplitude) before pelleting debris at 18,000xg for 30 min.

The clarified lysate was loaded onto a HisTrap column (GE) at 2.5 mL/min in wash buffer (20 mM Tris-HCl pH 7.5, 300 mM NaCl, 50 mM imidazole). Bound protein was eluted with a 0-200 mM imidazole gradient in elution buffer (20 mM Tris-HCl pH 7.5, 300 mM NaCl). The fractions were analyzed by SDS-PAGE. Pooled fractions containing $MELK^{1-326}$ were concentrated and further purified using size exclusion chromatography on a Superdex S200 Increase 10/300 GL column equilibrated with 25 mM HEPES pH 7.3, 300 mM NaCl and 2 mM TCEP.

In vitro pull-down assay. Ni-NTA agarose resin (Qiagen) was rinsed three times with wash buffer (20 mM Tris-HCl pH 7.5, 150 mM NaCl, 10 mM imidazole pH 7.5, 0.1 mM BSA) and 25 µL of the 50% slurry was aliquoted into each tube. His- $MELK^{1-326,T167E}$ (10 µg in 25 µL wash buffer) was immobilized on agarose resin for 1 h at 4°C with gentle rotation. Arrestin-3^{1-393} (10 µg in 50 µL wash buffer) was added to the suspension with slight rotation for 2 h at 4°C in the presence or absence of 2 mM ATP and 4 mM $MgCl_2$. Samples were transferred to centrifuge filters (Durapore® PVDF-0.65 µm) and washed quickly with 900 µL 50 mM HEPES pH 7.3 and 150 mM NaCl. Proteins were eluted with 100 µL 50 mM HEPES pH 7.3, 150 mM NaCl, and 100 mM imidazole. The eluates were immediately precipitated in 90% methanol, air dried, and dissolved in SDS sample buffer (40 µL Laemmli 2x). The samples were analyzed using SDS-PAGE and Western blotting, as described (104).

Microscale thermophoresis. MST experiments were performed using the Monolith NT.115 instrument (NanoTemper Technologies GmbH). The Monolith™ His-Tag Labeling Kit RED-tris-NTA was used to label human His-$MELK^{1-326,T167E}$ following the manufacturer's protocol (100 nM final concentration of His-$MELK^{1-326,T167E}$ in PBS-T buffer). Purified arrestin-3^{1-393} was diluted to a starting concentration of 80 µM in MST buffer (20 mM MOPS pH 7.5, 150 mM NaCl,

2 mM TCEP, 0.05% Tween-20). A 16-step dilution series was prepared by aliquoting 10 µL of MST buffer to 15 tubes. A 20 µL aliqout of the prepared arrestin-$3^{1\text{-}393}$ sample was placed in the first tube, and 10 µL was transferred to the second tube and mixed well by pipetting (1:1 dilution series). The final tube did not contain any arrestin-$3^{1\text{-}393}$ and served as a blank. To all tubes, 10 µL of labeled His-$MELK^{1\text{-}326,T167E}$ in the presence of 1 mM ATP and 2 mM $MgCl_2$ was added. After 15-30 min incubation on ice, the samples were transferred to Standard Monolith NT™ Capillaries. Each capillary was scanned using the MST instrument (40% LED, 40% MST power) and data were analyzed using PALMIST (145,146). Measured fluorescence was normalized and averaged, and the data were fit using a 1:1 binding model. The preset T-jump was used to calculate binding isotherms. All data were displayed using GUSSI.

Peptide Array Synthesis. The ResPep SL peptide synthesizer was used with standardized SPOT synthesis protocols using 15-residue peptides, as previously described (230). A 15-mer glycine peptide was used as a negative control in all experiments. Peptide assembly was conducted on solid support by the ResPep SL via a peptide amide linker using Fmoc-chemistry. The sequences were derived from either the full-length bovine arrestin-3 or full-length human MELK. After peptide synthesis, the amino protecting group was removed using piperidine (20% (v/v) solution in dimethylformamide) and extensive washing. The membranes were immersed for 1 h in a solution of 95% trifluoroacetic acid (TFA) and 3% triisopropylsilane with slight agitation. After the TFA solution was removed, the membranes were washed in dichloromethane four times 10 min each, after which they were washed in dimethylformamide four times 10 min each, and finally washed in ethanol two times 2 min each. The membranes were dried under the hood and stored at 4°C.

Peptide Membrane Blots. Dried membranes were activated by soaking in 100% ethanol for

5 min at room temperature and rehydrated by rinsing two times 5 min in water. The membranes were then blocked in a 20 mL solution of 5% non-fat dry milk in Tris-buffered saline with 0.1% Tween-20 (TBS-T) for 1 h. Then the membranes were washed three times 5 min each in TBS-T before overnight incubation with prey protein (0.2 µM $MELK^{1-326,T167E}$ or 0.3 µM $arrestin\text{-}3^{1-393}$) in binding buffer (MELK: 20 mM Tris-HCl, pH 7.5, 300 mM NaCl, 5 mM DTT; arrestin-3: 20 mM MOPS pH 7.5, 150 mM NaCl, 2 mM TCEP). The following day the membranes were washed three times for 5 min each in TBS-T at room temperature and then incubated with primary antibody (1:1,000 Aviva anti-MELK or 1:5,000 anti-arrestin rabbit polyclonal antibody F431 (226)) for 1 h at room temperature. The membranes were then washed three times 5 min each in TBS-T, incubated for 1 h with the corresponding HRP-conjugated secondary antibody (1:4,000 dilution; Abcam) in TBS-T, and washed three times 5 min each in TBS-T. The membranes were developed using a peroxide solution (SuperSignal West Pico) and visualized using a Bio-Rad Gel Doc Imager. Individual dots were analyzed by densitometry using a protein array analyzer (ImageJ). Individual dot density was expressed as a percentage of total binding across the entire membrane. Peptides were mapped onto either the arrestin-3 structure (PDB 3P2D (92)) or MELK structure (PDB 4BL1; to be published (292)) using conditional formatting in Excel (color scales) to identify the highest and lowest intensity values in relation to one another.

Co-immunoprecipitation of $MELK^{1-340}$ with $arrestin\text{-}3^{1-393}$ in cells. HEK293 arrestin-2/3 knockout cells (308,309) were transfected with HA-arrestin-3 (1 µg), FLAG-MELK-340-WT (1 µg), or a fixed ratio of the two proteins for 48 h. Cells were washed in phosphate-buffered saline (PBS) before incubation with RIPA buffer (Sigma) for 1 h. Lysed cells were centrifuged for 10 min at maximum speed (10,000xg) and the supernatant was mixed with suspended with 50 µL Protein G Sepharose (supplied as aqueous ethanol suspension; Sigma; washed with PBS) for 1 h

to preclear the samples. Samples were then centrifuged at low speed (3200xg) to remove the beads and incubated overnight with primary antibody (Anti-FLAG; 1:1,000; F3165 Sigma). The next morning, the samples were incubated with Protein G Sepharose for 2 h to capture the FLAG-MELK$^{1\text{-}340}$. The beads were then washed with lysis buffer (20 mM Tris-HCl pH 7.5, 150 mM NaCl, 1% NP-40, 0.5% sodium deoxycholate). Finally, the samples were eluted with 100 µL SDS buffer. Both cell lysates and co-immunoprecipitated samples were subjected to Western blotting using antibodies against arrestin (1:10,000; polyclonal rabbit F431 (226)) and MELK (1:1,000; F3165 Sigma).

Cellular Proliferation Assay. HEK293 arrestin-2/3 knockout cells were either left untransfected or transfected with HA-arrestin-3 (1 µg), FLAG-MELK$^{1\text{-}340}$ (1 µg), or a fixed ratio of the two plasmids for 46 h prior to treatment with 10 mM EdU (5-ethynyl-2'-deoxyuridine) for 2 h. Cells were then detached from support using 0.025% trypsin and the reaction was quenched with DMEM medium (10% FBS, 1% Pen/Strep). Cells were immediately washed with 3 mL of 1% bovine serum albumin (BSA) in PBS and centrifuged at 700xg. The pellet was then fixed for 15 min at room temperature with 4% paraformaldehyde in PBS and the wash step was repeated. A 100 µL saponin-based permeabilization and wash reagent was used to prepare the cells for the Click-iT™ reaction (ThermoFisher Scientific).

A Click-iT™ reaction mixture was prepared using PBS, copper protectant, reaction buffer additive, and picolyl azide fluorescent dye following manufacturer's instructions (ThermoFisher Scientific). Cells were incubated with 500 µL of the mixture for 30 min prior to a final wash with saponin-based permeabilization and wash reagent. Cells were resuspended in 500 µL buffer and analyzed using flow cytometry. Flow analysis was performed using a 3-laser LSRII (BD Biosciences). Analysis of flow cytometry data was performed using FlowJo 10.1.5 (FlowJo LLC).

SECTION B: ARRESTIN INTERACTION WITH G PROTEIN-COUPLED RECEPTORS

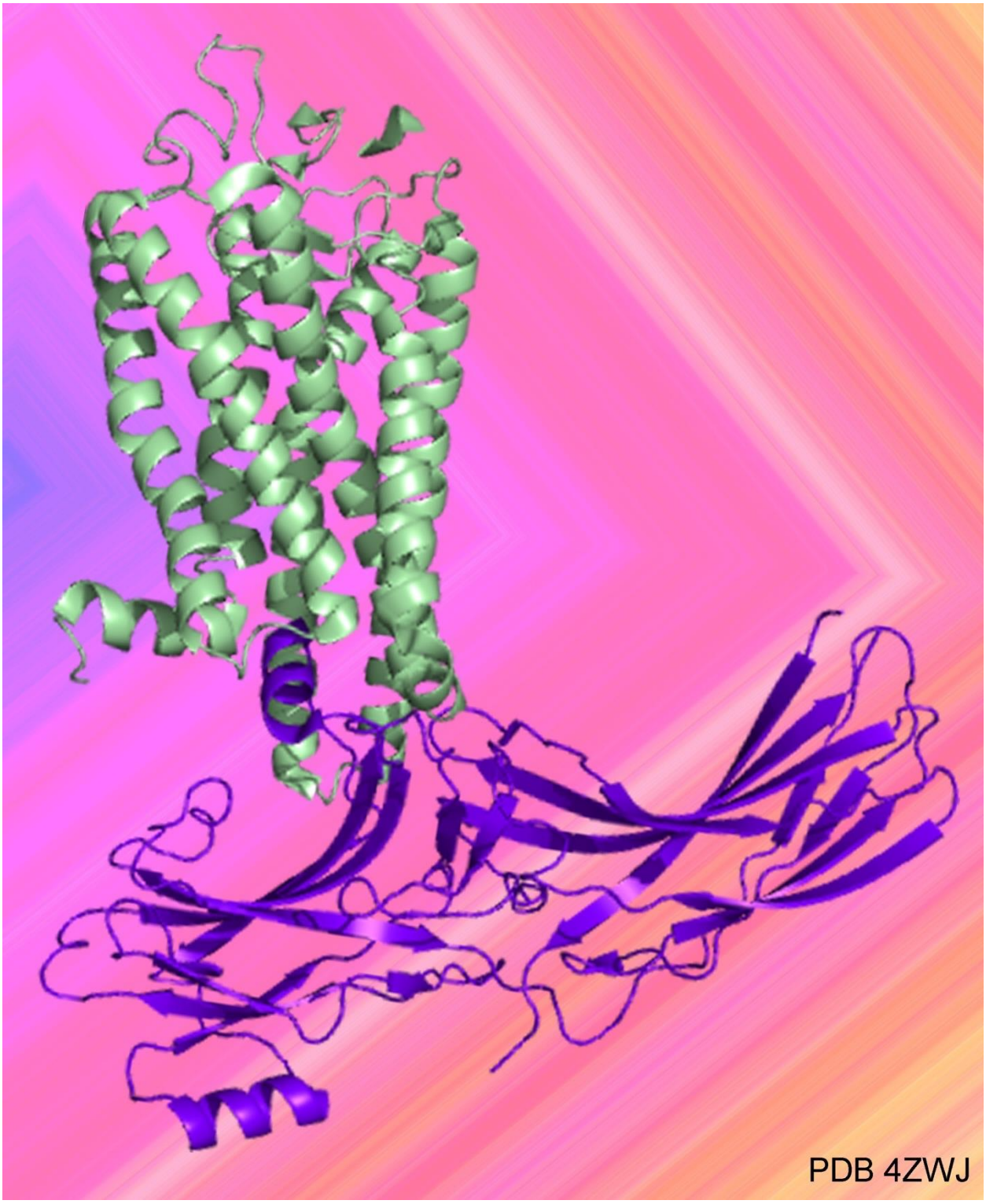

CHAPTER 9

DIFFERENTIAL MANIPULATION OF ARRESTIN-3 BINDING TO BASAL AND AGONIST-ACTIVATED G PROTEIN-COUPLED RECEPTORS

This article was published in Cellular Signaling (310). Susanne Prokop was first author, and **Nicole A. Perry,** Sergey A. Vishnivetskiy, Andras D. Toth, Asuka Inoue, Graeme Milligan, T.M. Iverson, Laszlo Hunyady, and Vsevolod V. Gurevich contributed to this work. Relation to dissertation work: While most of the work outlined in this thesis converys arrestin-mediated signaling through MAP kinase cascades, this chapter details arrestin interaction at the receptor level.

9.1 Introduction

Dysfunction of G protein-coupled receptor (GPCR) signaling plays an important role in the pathogenesis of numerous human diseases (311,312). For example, gain-of-function mutations that result in excessive activity or elevated ligand production that over-stimulates normal receptors can each cause endocrinological disorders and malignant tumors (311,313,314). Because receptor activity is crucial for normal cell function, it is tightly controlled by several regulatory mechanisms. Active receptors are phosphorylated by specific GPCR kinases, whereupon arrestin proteins bind active phosphoreceptors (159). Conceivably, the introduction of strong negative regulators into pathological cells, such as enhanced arrestins that bind unphosphorylated GPCRs, can suppress excessive signaling and potentially correct these problems.

Wild type (WT) arrestins bind active phosphorylated GPCRs (315,316), thereby terminating G protein signaling (317), and facilitating receptor internalization (318). Thus,

enhanced arrestins that do not require receptor phosphorylation can potentially be used in compensational therapy aiming at suppression of excessive G protein-mediated signaling (319,320). Vertebrates have more than 800 GPCRs (321,322) and only four different arrestins (78). Arrestin-1 and -4 are expressed in the visual system (323), whereas arrestin-2 and -3 (also known as β-arrestin1 and 2) are ubiquitously expressed, and each regulates hundreds of receptors. Previous work established that arrestins can be "pre-activated" by mutations destabilizing their basal conformation, thereby increasing their binding to GPCRs (324-326). Enhanced arrestin-1 was shown to partially compensate for defects of rhodopsin phosphorylation in vivo (320). Similarly, enhanced non-visual arrestins could reduce the signaling of hyperactive GPCRs. But as arrestin-2 and -3 are fairly promiscuous (327), enhanced non-visual arrestins would likely have unwanted side effects as they would simultaneously affect the function of all receptors expressed in the same cell. Thus, to make enhanced non-visual arrestins useful as therapeutic agents, their receptor specificity must be dramatically increased.

The feasibility of engineering arrestin-2 and -3 with enhanced receptor selectivity is suggested by strict selectivity of visual arrestin-1, exclusively expressed in photoreceptor cells, for photopigments. Arrestin-1 binds to phosphorylated light-activated (P-Rh*) rhodopsin much better than other receptors (328,329). Earlier studies identified elements (329) and individual residues on the receptor-binding surface (330) responsible for receptor preference of arrestins. The exchange of ten non-identical residues on the receptor-binding surface can change arrestin-1 preference to that of arrestin-2, and vice versa (330). Point mutations at these positions were shown to increase the preference of arrestin-3 for some cognate receptors over others up to 4-fold, whereas double mutations yielded 50-fold differential in the binding to M_2 muscarinic over β_2-adrenergic receptor (331). Comparison of crystal structures (109,332) and primary sequences of arrestin-1 and -2

additionally identifies a key valine residue in arrestin-1 that stabilizes its N-domain, and likely contributes to its high selectivity for rhodopsin, as demonstrated by a dramatic increase in the binding to non-cognate M_2 muscarinic receptor of arrestin-1 with a single Val83Ser mutation (332). However, mutations of the ten "receptor-discriminator" residues identified in the arrestin-1/arrestin-2 chimeras did not affect arrestin-3 binding to some of the GPCRs tested, including the D_1 dopamine (331) or Y_1 neuropeptide (117) receptors, while many of the same mutations dramatically change arrestin-3 binding to D_2 dopamine and Y_2 neuropeptide receptors. Here we took advantage of the recent crystal structure of arrestin-1 in complex with rhodopsin (25), which identified additional elements, including the middle-loop and C-loop, both of which engage the receptor and therefore might play a role in arrestin selectivity. We used four model GPCRs (M_2 muscarinic, b_2-adrenergic, D_1 dopaminergic, and D_2 dopaminergic) and show that mutations in these regions of arrestin-3 differentially affect its basal and agonist-induced binding.

9.2 Results

Highly conserved lysine in the middle-loop differentially affects basal receptor binding. All four vertebrate arrestins exhibit remarkable conservation of their structures, consisting of two "cup-like" domains (102,109,110,116,129,332) (Fig. 9.1A). Within this context, the receptor-binding surface of arrestins comprises the concave sides of the N- and the C-domains, as well as the central loops (30,31,108,330,333,334). The "middle-loop" (335), also called "139-loop" in arrestin-1 (40,336), is a flexible region, connecting β-strands VIII and IX in the N-domain, forming part of the central crest on the receptor interaction surface (Fig. 9.1A, *blue*). It has been reported that the middle-loop plays an important role in the high selectivity of visual arrestin-1 for P-Rh* (40,337), but its functional role in non-visual arrestins has not been reported in the literature.

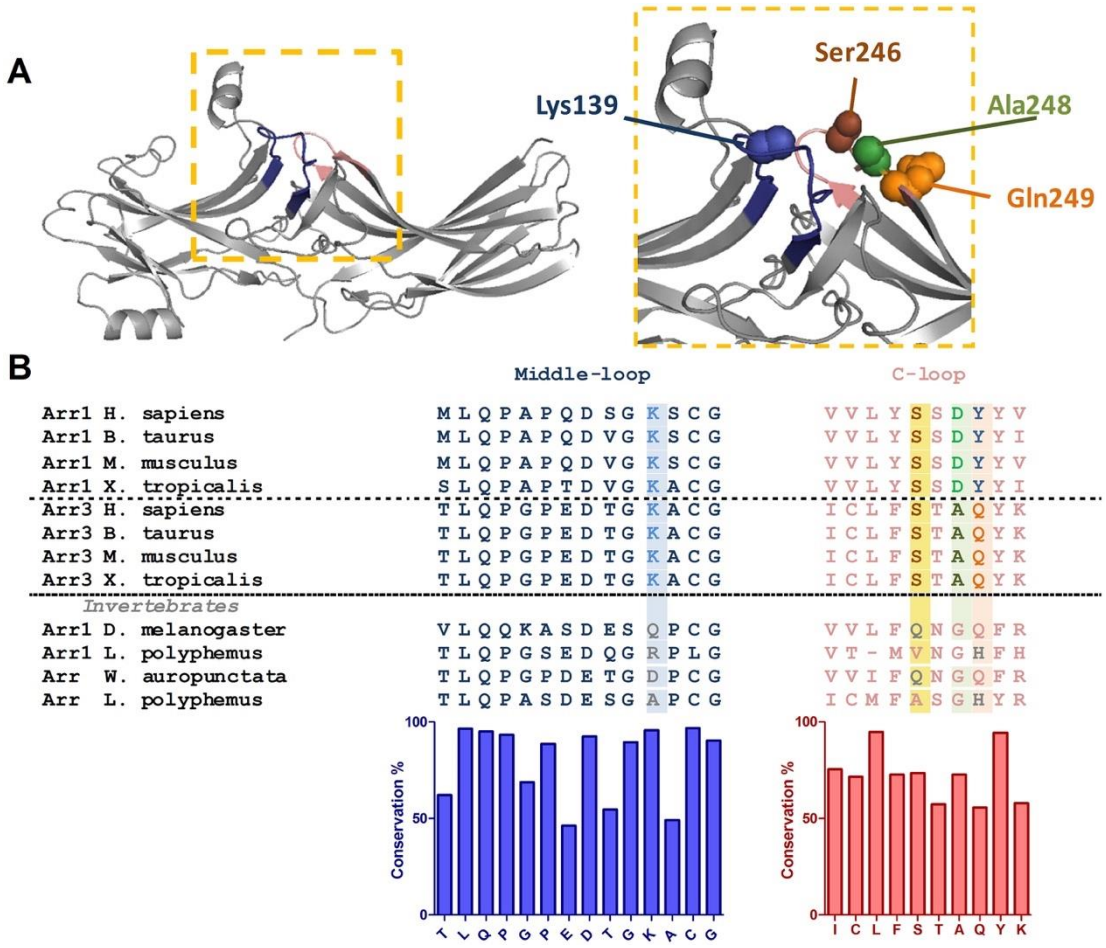

Fig. 9.1. Structure and sequence of the middle and C-loops of arrestins. A. Crystal structure of rhodopsin-bound arrestin-1 (Protein Data Bank entry 4ZWJ (25)). The middle and C-loops are shown in blue and pink, respectively. Residues mutated in this study are shown as CPK models. **B.** Multiple sequence alignment of arrestin-1 (Arr1), arrestin-3 (Arr3) and arrestin homologs (Arr) from invertebrate species. Residues mutated in this study are highlighted. Bar graph under the alignment shows the extent of residue conservation at each position.

Multiple sequence alignment of the middle-loop region shows that lysine139 (in bovine arrestin-3) is highly conserved among all four arrestin subtypes in vertebrates (Fig. 9.1B). However, various residues (Ile, Ala, Asp, Gln, Arg) are found in invertebrate arrestins in position homologous to Lys139 in arrestin-3 (Fig. 9.1B; see also (78)). Available structures suggest that a putative salt bridge involving this conserved lysine anchors the middle-loop to the receptor-binding "finger loop" in the basal state of vertebrate arrestins (109,337). To test the role of lysine139 in arrestin-3, we substituted it with residues found in the equivalent position in non-

vertebrate species. The wide variety of homologues provides interesting substitutions: uncharged (Gln, Ile, Ala), acidic (Asp), and other positively charged (Arg) residues have all appeared at the corresponding position during evolution, among which Ile and Ala represent the least conservative substitutions according to substitution matrices (338).

To measure arrestin interactions with GPCRs co-expressed in the same cell, we used bioluminescence resonance energy transfer (BRET) between receptors C-terminally tagged with Renilla luciferase and arrestins N-terminally tagged with Venus, as described (114,117,319,331). The middle-loop mutations were introduced in arrestin-3 carrying an Ala87Val mutation, which is expected to increase its receptor selectivity (331). This Val residue is involved in multiple hydrophobic interactions in arrestin-1, and thus responsible for the rigidity of the N-domain, which is proposed to ensure selective rhodopsin binding. The Ala87Val base mutant was used because it was expected to predispose arrestin-3 to higher receptor selectivity, by making its N-domain less flexible. As a negative control, we used the arrestin-3-KNC mutant, in which 12 key receptor-binding residues are replaced with alanines. Arrestin-3-KNC does not demonstrate basal or agonist-induced binding to any GPCR tested so far (114,117,331). It is the most appropriate control for bystander BRET, as it has the same molecular weight and therefore is expected to diffuse at the same rate as other arrestin-3 variants.

We tested several Class A GPCRs: b_2-adrenergic (β_2AR), D_1 (D_1R) and D_2 (D_2R) dopamine, and M_2 muscarinic (M_2R) receptors. In the case of visual arrestin-1, certain mutations in the middle-loop "loosened up" the basal state of the molecule and facilitated arrestin-1 binding to P-Rh* and non-preferred forms of rhodopsin, light-activated unphosphorylated (Rh*) and inactive phosphorylated (P-Rh) (337,339). Therefore, we first investigated possible "pre-docking" of the arrestin-3 middle-loop mutants to the receptors without agonist stimulation (Fig. 9.2A). In

the case of β_2AR, Lys139 substitutions did not significantly affect basal arrestin binding, whereas we observed receptor-specific changes with the other three GPCRs. The most dramatic were the effects of Lys139Ile substitution, which increased pre-docking to M_2R more than 3-fold, while decreasing basal interactions with D_1R and D_2R (Fig. 9.2A). Interestingly, while none of the other Lys139 substitutions affected basal binding of arrestin-3 to M_2R, D_2R, or b_2AR, most of them reduced basal binding to D_1R to varying degrees (Fig. 9.2A).

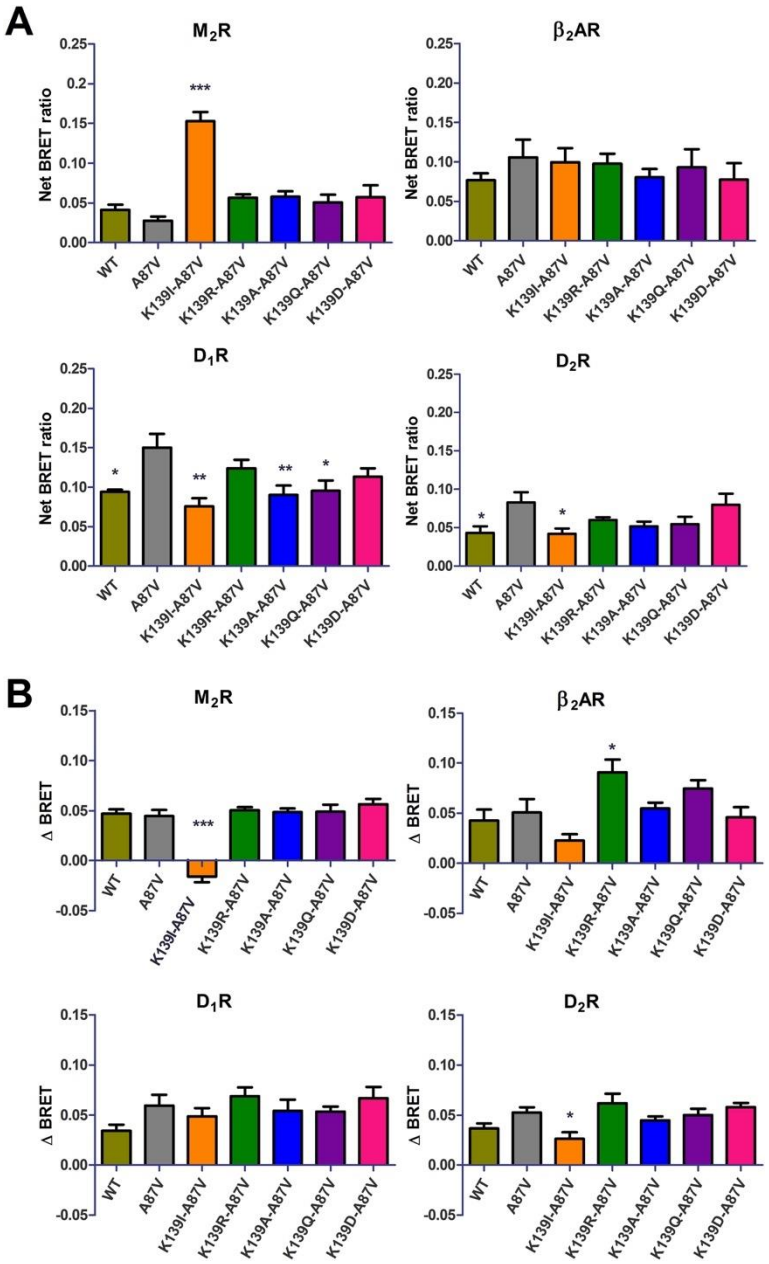

Fig. 9.2. Basal and agonist-induced binding of Lys139 mutants to GPCRs. A. Basal (agonist-independent) association of the indicated luciferase-tagged receptor and wild type or mutant Venus-Arrestin-3 in COS-7 cells at 10 minutes of vehicle treatment. Nonspecific (bystander) BRET was measured using non-receptor-binding arrestin-3 mutant (Arrestin3-KNC(114,331)). Net BRET ratio was calculated by subtracting non-specific BRET from the raw BRET data in each experiment. **B.** The agonist-induced arrestin-3 recruitment to indicated receptors. The BRET change (ΔBRET) was determined by the difference between the BRET ratio between ligand and vehicle treated cells (nonspecific BRET was subtracted from both). Means ± S.E. of at least three independent experiments are shown. Each experiment was performed in quadruplicate. Statistical significance was determined by one-way ANOVA, followed by Dunnett's post-hoc test: *, $p < 0.05$; **, $p < 0.01$; ***, $p < 0.001$, as compared with A87V base mutant binding to each receptor.

The effects of Lys139 substitutions on agonist-induced binding to the tested receptors were remarkably different. The Lys139Ile mutation, which greatly increased the binding to inactive M_2, essentially eliminated agonist-induced increase in binding to this receptor (Fig. 9.2B). Apparently, the interaction between basal M_2R and arrestin3-Lys139Ile mutant reached the maximum possible extent, so that the presence of M_2 agonist could not further increase binding. None of the other Lys139 substitutions appreciably affected agonist-induced increase of M_2 interaction. The conservative Lys139Arg substitution enhanced agonist-induced binding to the b_2-adrenergic receptor, whereas other mutations did not significantly affect it. The interactions with activated D_1R were not perturbed by Lys139 substitutions, whereas the effect of D_2R agonist quinpirole was reduced by the Lys139Ile mutation (Fig. 9.2B).

The effects of the perturbation of arrestin-3 C-loop. A recent crystal structure of the visual arrestin-1-rhodopsin complex revealed a direct interaction between the C-loop of arrestin-1 (Fig. 1A, pink) and the receptor (25,142). The C-loop connects two b-strands in the C domain of all arrestins and is found in close proximity to the middle-loop in the basal conformation (102,109,110,332). To test the role of this loop in receptor binding, we generated single mutations in the C-loop at three selected positions: Ser246, A248 and Q249. These residues were replaced with residues in homologous positions of invertebrate arrestins (78) in the context of the Ala87Val arrestin-3.

Gln249 is the least conservative position of the C-loop (Fig. 9.1B). While Gln dominates in non-visual arrestins, Tyr and Phe are found at the corresponding place in visual arrestin-1. The Gln249His substitution somewhat increased the basal binding to β_2AR and D_1R, but the increase of BRET signal upon isoproterenol or dopamine stimulation were not different from WT arrestin-3.

The replacement of Ala248 with a larger hydrophobic residue Val, yielded enhanced receptor binding upon activation in case of two class A receptors out of four tested (Fig. 9.3): β_2AR and D_2R both bound Ala248Val mutant better than WT arrestin-3 or base mutant Ala87Val. However, the basal arrestin-3 binding to these receptors was not affected by Ala248 mutation. The Ala248Val substitution reduced arrestin-3 interaction with inactive D_1R.

Interestingly, neither glutamate nor glutamine substitution of Ser246 in the same loop where Ala248 and Gln249 are localized affected the binding to the four receptors tested (Fig. 9.3).

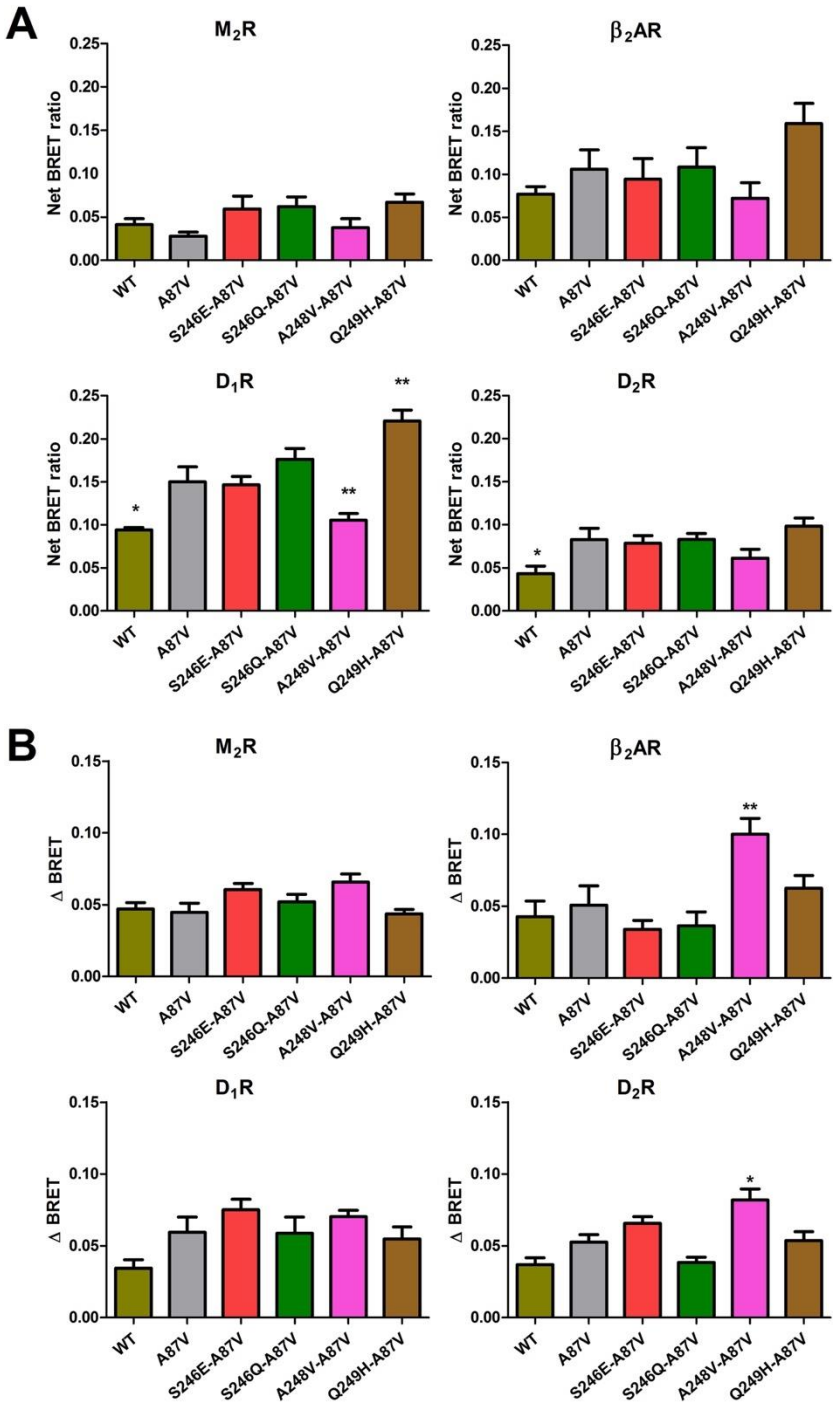

Fig. 9.3. The effect of C-loop mutations on basal and agonist-induced receptor binding. A. Basal BRET (net BRET ratio) and **B.** agonist-induced BRET change (delta BRET) between indicated luciferase-tagged receptors and Venus-tagged arrestin-3 C-loop mutants was calculated, as described in the legend to Fig. 2. The cells were stimulated for 10 minutes with the appropriate agonist. BRET ratio obtained with negative control (arrestin-3 KNC (66,117)) was subtracted. Means ± S.E. of at least three independent experiments are shown. Each experiment was performed in quadruplicate. Statistical significance was determined by one-way ANOVA: *, $p < 0.05$; **, $p < 0.01$; ***, $p < 0.001$, as compared with A87V base mutant binding to each receptor.

Middle and C-loop of arrestin-3 participate in rhodopsin binding. The crystal structure of the rhodopsin-arrestin-1 complex identifies global conformational changes in receptor-bound arrestin-1 as compared to basal arrestin-1, including an increase in the distance between the middle-loop and C-loop. This particular conformational rearrangement forms cleft that allows binding of the second intracellular loop of rhodopsin (25). Arrestin-3 is not a cognate interaction partner of rhodopsin, but can bind to P-Rh*, although it yields lower binding than arrestin-1 (325,328). To test whether the same interaction interface drives non-visual arrestin binding to rhodopsin, we incorporated radiolabeled leucine into untagged arrestin-3 mutants (340,341) and performed *in vitro* binding to rhodopsin (325,341). We found that the Lys139Ile mutation of arrestin-3 significantly reduced P-Rh* binding, whereas arrestin-3 harboring other substitutions exhibited binding that was not statistically different from WT (Fig. 9.4). Intriguingly, a recent report indicates that when the analogous residue in mouse arrestin-1 (Lys 142) is substituted, the conservative Lys142Arg and, to a lesser extent, Lys142His mutation enhanced binding to both P-Rh*, and Rh*, whereas alanine and glutamine substitutions did not affect the binding (337). Our test of arrestin-3 mutants yielded similar results (Fig. 9.4). Among C-loop mutations, Ala248Val enhanced arrestin-3 binding, whereas the others did not (Fig. 9.4).

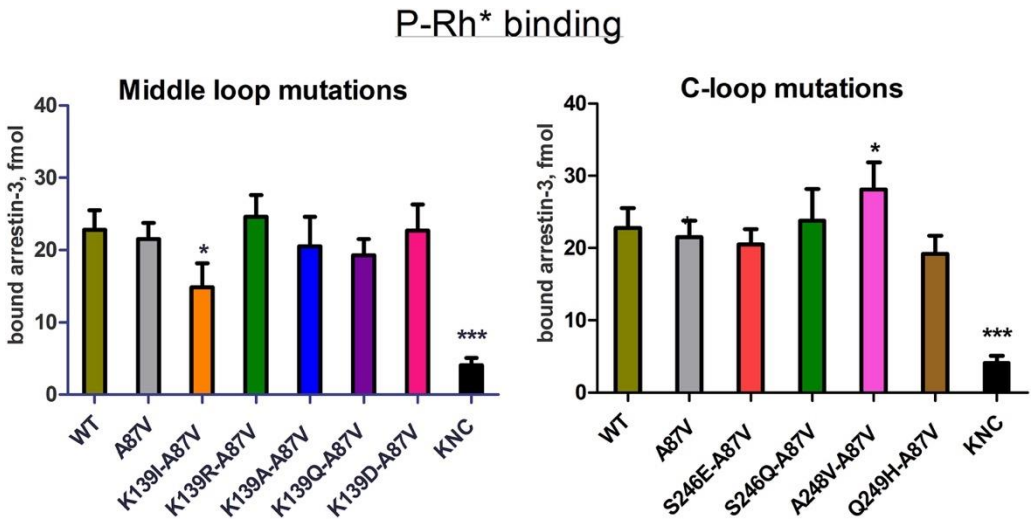

Fig. 9.4. Direct binding of arrestin-3 mutants to light-activated phosphorylated rhodopsin. WT and mutant forms of arrestin-3 produced in cell-free translation in the presence of radiolabeled leucine (2 nM) were incubated with 0.3 μg of light-activated phosphorylated rhodopsin (P-Rh*) for 5 min at 37 °C. Free and rhodopsin-bound arrestin was separated by gel filtration on 2-ml Sepharose 2B-CL columns. The amount of bound arrestin eluting with rhodopsin-containing membranes was quantified by scintillation counting. Non-specific binding (in the absence of rhodopsin) was subtracted. Means ± S.D. of three independent experiments performed in duplicate are shown. The data were analyzed by one-way ANOVA with arrestin type as the main factor, followed by Dunnett's post-hoc test.

Agonist-independent receptor recruitment of arrestin-3-Lys139Ile mutant. Muscarinic acetylcholine receptors display measurable constitutive activity in heterologous expression systems (342). This raises the possibility that the high basal binding of arrestin-3-Lys139Ile is due to its interaction with a spontaneously active pool of M_2 receptors. Therefore, we tested whether the mutant binds the truly inactive receptors, by incubating cells with atropine, a known inverse agonist of the M_2 receptor (342). We found that atropine pretreatment did not decrease the binding of arrestin-3-Lys139Ile, and the agonist-independent binding of the WT arrestin-3 or the A87V base-mutant were not altered, either (Fig. 9.5). As expected, atropine pretreatment prevented all carbachol-induced BRET changes. These data support the conclusion that the Lys139Ile mutant binds the inactive conformation of M_2R.

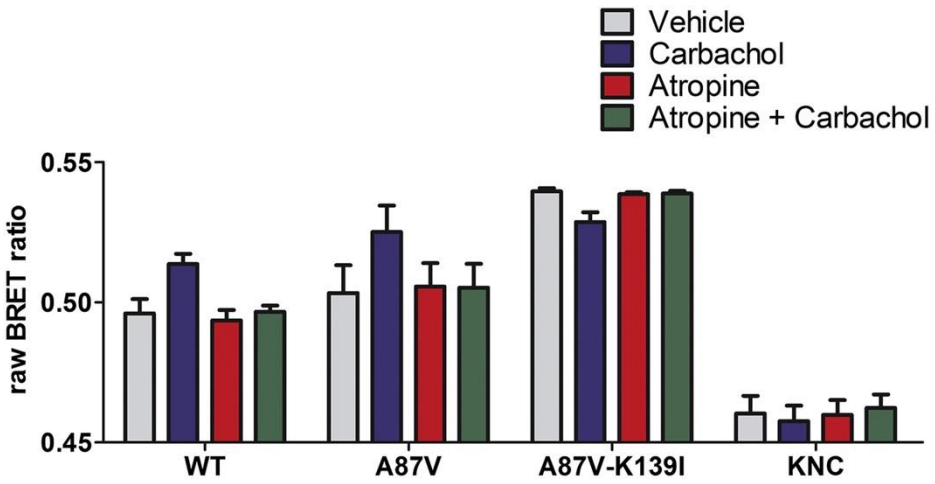

Fig. 9.5. Lys139Ile mutant binds inactive M_2R. COS-7 cells co-expressing M_2R-RLuc8 and indicated form of Venus-arrestin-3. Cells were pretreated for 5 minutes with vehicle or 10 μM inverse agonist atropine (342), and stimulated with carbamylcholine as in Fig. 2. Raw BRET ratios are shown. Basal arrestin-3 binding was not altered by atropine treatment. *,$p<0.05$ (vs. vehicle control), analyzed with one-way repeated measures ANOVA, followed by Dunnett post-hoc test. Atropine prevented the effects of carbachol. #,$p<0.05$ (significant interaction between the two treatments), analyzed with two-way repeated measures ANOVA, followed by Bonferroni post-hoc test.

As high agonist-independent binding of arrestin-3-Lys139Ile mutant (Fig. 9.2) is unusual, we tested it using co-immunoprecipitation as an independent method (Fig. 9.6). To this end, we transfected HEK293 cells made deficient for both non-visual arrestins using CRIPR/Cas9 (308) to exclude endogenous arrestin competition, with the same HA-M_2R-RLuc8 and Venus-arrestin-3-Lys139Ile constructs used for BRET (Fig. 9.2), immunoprecipitated the receptor with anti-HA antibody, and blotted for Venus. In these experiments we used WT arrestin-3 as a positive control and arrestin-3-KNC that does not bind receptors (114,117,331), as a negative control (Fig. 9.5). We found that arrestin-3-Lys139Ile binds M_2 muscarinic receptors in the absence of agonists, and the addition of saturating agonist 10 μM carbamylcholine does not further increase its binding (Fig. 9.5). In full agreement with BRET data (Fig. 9.2), if anything, the addition of the agonist slightly suppresses the interaction of this mutant with M_2R, although in neither case this trend rose to statistical significance (Fig. 9.5).

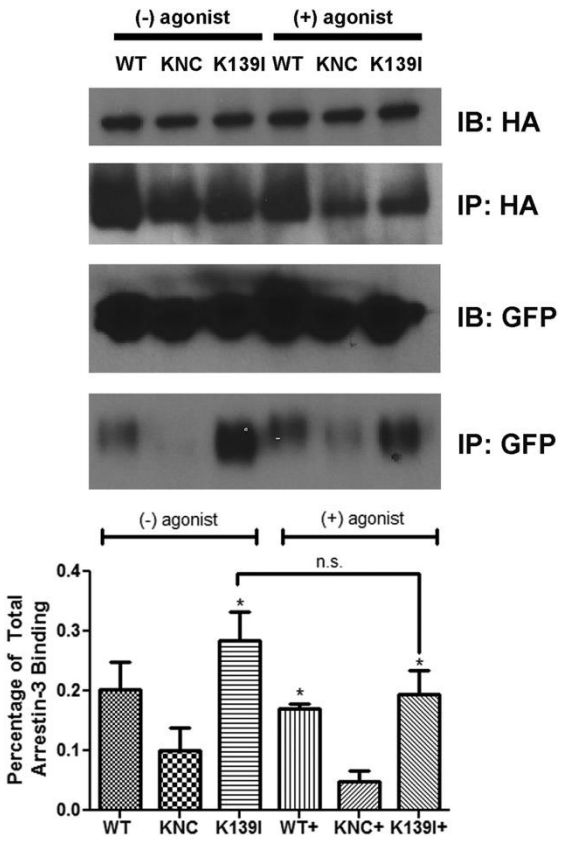

Fig. 9.6. Co-immunoprecipitation of Venus-arrestin constructs with M_2R. HEK arrestin-2/3 KO cells (308) were co-transfected with Venus-arrestin constructs and HA-M2R-RLuc8. After 48 h, the cells were incubated in either serum-free media alone, or serum-free media with 10 μM carbamylcholine for 15 min. The cells were lysed in IP buffer (50 mM Tris-HCl pH 7.5, 2 mM EDTA, 250 mM NaCl, 10% glycerol, 0.5% NP-40, 20 mM NaF, and 1mM $NaVO_3$) and the supernatant was cleared by centrifugation at max speed for 15 min, then pre-cleared with protein G agarose. The supernatant was immunoprecipitated using a rat HA antibody against HA-M2R-Rluc8. The input (IB) and immunoprecipitated material (IP) were subjected to Western blotting to detect HA and GFP, as indicated. The GFP blot of the immunoprecipitated samples was analyzed using Versadoc. The results were statistically analyzed using one-way ANOVA followed by Dunnett's post-hoc test. The difference with KNC is shown (*, $p<0.05$, n=3). The effect of agonist treatment on Venus-arrestin-3 (K139I) was not statistically significant (n.s.).

9.3 Discussion

Arrestins preferentially bind active phosphorylated GPCRs, precluding their coupling to G proteins, facilitating receptor internalization, and/or facilitating G protein-independent signaling (94,343,344). Vertebrates express only four arrestin subtypes (78), as compared to hundreds of different GPCRs (321,322). Arrestin-1 and arrestin-4 are specialized visual proteins, and are expressed at fairly high levels in photoreceptor cells, where they bind photopigments (49,323,345).

The two non-visual subtypes, arrestin-2 and -3, are ubiquitously expressed and bind hundreds of different GPCRs (78,94,327,346-349). Non-visual arrestins also interact with numerous non-receptor signaling proteins (79), orchestrating a second, G protein-independent wave of GPCR signaling (78,350,351).

Arrestin-3 is the most promiscuous of the two non-visual subtypes: it interacts with a wide variety of GPCRs (102,327,349). Previously, by manipulating the residues on the receptor-binding surface that determine receptor specificity of arrestins (329,330), we constructed arrestin-3 mutants with up to 50-fold preference for some GPCR subtypes over others (331). In the first set of point mutants the effects of substitutions on agonist-independent "pre-docking" and agonist-induced increase in arrestin binding to β_2AR, M_2R, D_1R and D_2R appeared to correlate (331). More extensive mutagenesis of the same regions yielded variants of arrestin-3 that showed virtually no "pre-docking", but normally responded to agonist challenge of neuropeptide Y receptors Y_1 and Y_2 (117). None of the mutations tested affected arrestin-3 interactions with D_1R and Y_1 receptor significantly (117,331), suggesting that additional residues might be involved. The crystal structure of the arrestin-1-rhodopsin complex (25) revealed direct contacts between rhodopsin and two loops in the central "crest" of the arrestin-1 molecule (Fig. 9.1A), the middle loop (335) and the C-loop (25).

Pre-activating mutations destabilize the basal conformation of arrestin, suggesting that fully active arrestin conformation can only be stable in its receptor-bound state. The first crystal structure of pre-activated arrestin-1 in complex with a constitutively active rhodopsin mutant has recently been solved (25,142), revealing new aspects of the arrestin-receptor interaction. The structure showed that several distinct contact surfaces mediate arrestin-1 binding to rhodopsin (25). One of the critical interaction sites in the center of arrestin molecule is created by the middle and

the C-loop, coming from the N- and C-domain, respectively. Receptor binding is accompanied by global conformational changes in arrestin, including ~20° rotation between the N- and C-domain (25,37,101).

The middle loop is highly flexible both in free arrestin-1 (109,129) and in the rhodopsin complex (25). Intramolecular distance measurements in arrestin-1 revealed large movement of the middle loop (339). Deletions in this element (called "139-loop" in arrestin-1) enhanced arrestin-1 binding to phosphorylated, light activated rhodopsin (P-Rh*) and non-preferred forms, light-activated unphosphorylated, inactive phosphorylated rhodopsin, and phospho-opsin (337,339). Perturbations in this region also dramatically reduced thermal stability of the protein (337). These results suggest that the presence of this loop contributes to the high selectivity of arrestin-1 for P-Rh* and stabilizes the basal conformation. Structural data also suggest the existence in the basal state of a salt bridge between Lys142 in the middle-loop and Asp72 in the finger loop (residue numbers correspond to bovine arrestin-1), which might contribute to the stability of the basal conformation.

Here we tested nine mutations in the middle and C-loops of arrestin-3 (Figs. 9.2-9.4). The results are consistent with the hypothesis that these elements directly participate in the binding to non-phosphorylated parts of GPCRs, in agreement with the structure of the arrestin-1-rhodopsin complex, where these elements directly contact the receptor (25). Various middle loop and C-loop mutations increase (Lys139Arg, Ala248Val) or decrease (Lys139Ile) GPCR binding in receptor-specific manner (Figs. 9.2-9.4). Based on the current model of arrestin activation (315,352), arrestin binding to the receptor can be increased via two distinct mechanisms: destabilization of the basal conformation (320,337,339,353-355) or changing the residues that contact the receptor (31,356). The mutations of the first type tend to increase the binding to all GPCRs indiscriminately

(325,326). Since the effects of the mutations tested here are receptor subtype-specific (Figs. 9.2-9.4), it is likely that targeted residues are in the arrestin-receptor interface, similar to previously characterized mutants (117,331).

However, there is a difference. All earlier constructed mutants with enhanced receptor specificity demonstrated lower than WT arrestin-3 binding to some receptors. The specificity was achieved by large reduction of binding to some GPCRs with minimal to no reduction of the interactions with others (117,331). Several mutants tested here demonstrate an increase in binding to certain GPCRs: Lys139Ile dramatically enhances the binding to inactive M_2R, to the level where agonist stimulation of this receptor does not produce any effect (Fig. 9.2). Interestingly, the same mutation reduces arrestin-3 binding to D_1 and D_2 dopaminergic receptors (Figs. 9.2,9.4). While none of the previously tested mutations appreciably affected arrestin-3 binding to D_1R, one mutation in this series, Gln249His, enhanced it, whereas two others, Lys139Ile and Ala248Val, decreased it (Figs. 9.2,9.3). In fact, Ala248Val selectively reduced the binding to D_1R, while increasing the binding to rhodopsin, D_2R, and b_2AR (Figs. 3,4). Thus, manipulation of these residues, which are likely engaged by the receptor directly, yielded arrestin-3 variants where receptor preference was achieved by selective increase in the binding to some GPCRs, rather than solely by receptor-specific reduction of the binding (Figs. 2,3,7). For the sake of clarity, we presented receptor preference of the biased arrestin mutants as radar charts, which show that some point mutations yield 2-5-fold selectivity toward certain receptors over others (Fig. 9.7). Importantly, the magnitude and direction of bias is strongly dependent on the activation state of the receptors (Fig. 9.7).

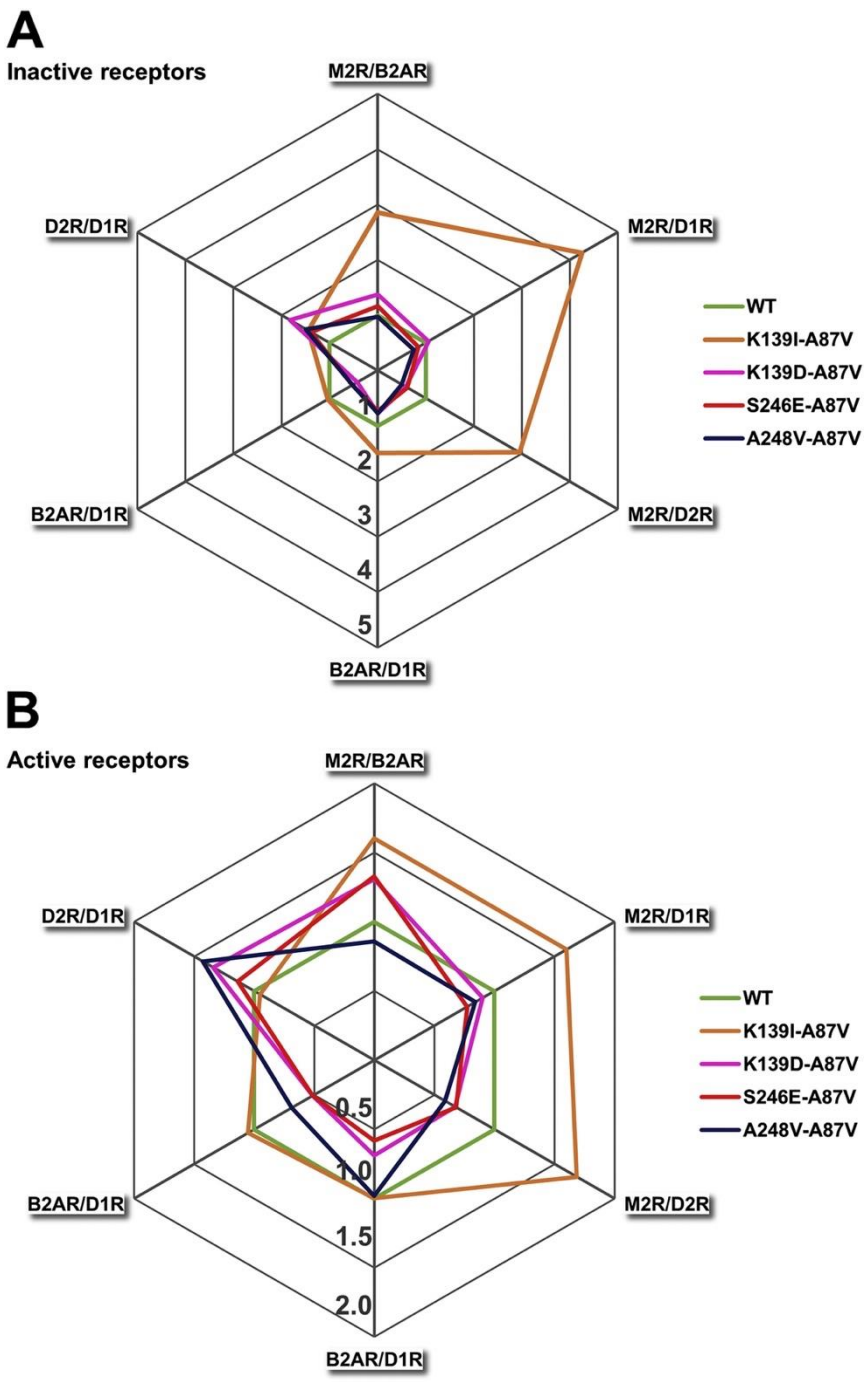

Fig. 9.7. Receptor selectivity of arrestin-3 mutants. Each receptor pair is provided as radially arranged axis that starts from the centre. The relative binding of each arrestin-3 mutant was plotted along all axes, and the connected values create a polygon. The binding ratio of WT arrestin-3 was set at 1 for each receptor pair. If the relative binding is greater than 1, the indicated arrestin has a preference for the first member of the receptor pair (receptor1/receptor2). Panel A shows the basal arrestin interactions. The green regular hexagon indicates WT arrestin. Only those mutants are highlighted that have at least a 1.5-fold bias against one receptor. Panel B shows the selectivity of the arrestin3 mutants after ligand treatment.

Cellular signaling is regulated by a complex network of protein-protein interactions (148,357,358). The majority of the therapeutically used agents are small molecules, which have limited ability to interact with flat or disordered protein elements mediating these interactions (359,360). Manipulation of these interactions by changing expression levels of proteins involved affects every function of proteins in question, not the one function that needs to be targeted (13). Custom-designed signaling proteins can overcome this limitation, and selectively enhance or disrupt individual protein-protein interactions (7,83,331,361). Arrestins play a role in many critical cellular functions, including cell death and survival (78,350,362-364). All of their effects are mediated through direct binding to other proteins, which gives arrestins exceptional potential in protein-based therapy (331). The putative usefulness of an enhanced arrestin molecule in compensational gene therapy has already been proven with an enhanced form of arrestin-1, which prolonged photoreceptor survival and improved rod function in rhodopsin kinase-deficient mice (320). Non-visual arrestins can be pre-activated by homologous mutations (325,326,365,366). Enhanced versions of non-visual arrestins can quench hyperactive GPCRs in all cell types where excessive receptor signaling underlies disease state (311,312). However, broad receptor specificity of non-visual arrestins does not allow specific targeting of the receptor of interest. Our data demonstrate that there are many ways of narrowing receptor specificity of even the most promiscuous non-visual subtype, arrestin-3, paving the way to the construction of arrestin mutants with therapeutic potential.

9.4 Conclusions

Here we show that the middle-loop (called 139-loop in arrestin-1) and the C-loop are important parts of the receptor-binding surface of arrestin-3, and that the manipulation of these

elements yields subtype-selective changes of non-visual arrestin interactions with different GPCRs. One of the introduced mutations, Lys139Ile, has resulted in high-affinity basal (agonist-independent) binding of arrestin-3 to M_2 muscarinic receptor, while reducing the agonist-induced interaction with D_2 dopamine receptor. Subtype-specific increase in receptor binding described here can enhance the specificity of non-visual arrestins in a different way than in previous studies, where a decrease of arrestin-3 binding to certain receptor subtypes enhanced the receptor specificity of arrestin-3.

9.5 Materials and Methods

Materials. Restriction endonucleases and other DNA modifying enzymes were from New England Biolabs (Ipswich, MA). Cell culture reagents and media were from Mediatech-Corning (Manassas, VA), Life-technologies (Carlsbad, CA), or PAA Laboratories GmbH (Pasching, Austria). Luciferase substrate coelenterazine *h* was from NanoLight Technology (Pinetop, AZ). DNA purification kits were from Zymo Research (Irvine, CA). All other reagents were from Amresco (Solon, OH) or Sigma-Aldrich (St Louis, MO).

Mutagenesis and plasmid construction. Plasmids encoding short splice variant of bovine arrestin-3 (367) with unique restriction sites introduced by silent mutations were used to introduce mutations on the background of Ala87Val base mutant (which is expected to be predisposed to higher receptor selectivity), as described (117,331). To generate all mutants, oligonucleotides harboring the desired substitutions were used as forward primers and an oligonucleotide downstream from the far restriction site was used as a reverse primer for PCR. Resulting fragments of various lengths and an appropriate primer upstream of the near restriction site were then used as reverse and forward primers, respectively, for the second round of PCR. Restriction sites Bam*H*I

and Bsi*W*I were used to introduce indicated Lys139 substitutions and Bsi*W*I and XbaI to introduce mutations in the C-domain. The resulting fragments were purified, digested with the respective enzymes, and subcloned into the suitably digested pGEM-2 plasmid (Promega; Madison, WI) encoding WT bovine arrestin-3 with engineered restriction sites (331).

Direct in vitro Binding Assay. In vitro transcription, translation, preparation of light-activated phosphorylated rhodopsin (P-Rh*), and in vitro direct binding assay were performed, as previously described (330,340).

Bioluminescence Resonance Energy Transfer (BRET) Assay. COS-7 cells were transfected using Lipofectamine 2000 (2µl Lipofectamine/1µg DNA) in 6 well plates. We have previously determined the amounts of plasmid DNA to produce sufficient excess of arrestin-3 over receptor and therefore saturate the BRET signal (114,331). 48 hours after transfection, the appropriate ligands (agonist carbachol (carbamoylcholine) and inverse agonist atropine for M_2R, agonists isoproterenol for β_2AR, dopamine for D_1R, and quinpirole for D_2R) were used at 10 µM. After stimulation, 5 µM luciferase substrate coelenterazine *h* was added, and BRET was measured between RLuc8-tagged receptors, and Venus-tagged arrestins, as previously described (114,117,331). BRET measurements for Figure 9.5 were performed with Varioskan Flash Multimode Reader (Thermo Scientific, Waltham, MA).

Co-immunoprecipitation. HEK293 arrestin-2/3 KO cells (308) were co-transfected with HA-M_2R-RLuc8 (0.5 µg) and a Venus-Arrestin construct (0.25-1 µg) using Trans-Hi™ DNA transfection reagent (1 µg DNA: 3 µL reagent) in 6-well plates. At 48 hours post-transfection, the cells were incubated in either serum-free DMEM or serum-free DMEM with 10 µM carbachol (carbamoylcholine) for 15 min. After stimulation, the cells were lysed in IP buffer (50 mM Tris-HCl pH 7.5, 2 mM EDTA, 250 mM NaCl, 10% glycerol, 0.5% NP-40, 20 mM NaF, and 1mM

$NaVO_3$) and incubated at 4°C for 1 h. The lysates were then centrifuged (max speed, 15 min) and the supernatants were pre-cleared by incubation for 1 h with 25 µL protein G agarose beads. The beads were pelleted by centrifugation, a 30 µL aliquot was removed for input analysis, and the remaining lysates were incubated overnight at 4°C with 1 µg of anti-HA antibody (Sigma-Aldrich, 3F10). The next morning 50 µL protein G agarose beads were added and incubated for an additional 2 h. The beads were then washed three times with 1 mL of ice-cold IP buffer before elution with 35 µL of SDS sample buffer (Sigma-Aldrich, Laemmli 2X) at room temperature. Samples were analyzed by Western blot. Co-immunoprecipitated arrestins were quantified on blots using the QuantityOne Software (BioRad). The results from three independent experiments were statistically analyzed using one-way ANOVA followed by Dunnett's post-hoc test ($p<0.05$ was considered significant).

Data Analysis and Statistics. GraphPad Prism 5.0 was used to plot the results of BRET experiments (Figs. 9.2-9.3), direct binding assay (Fig. 9.4), and to statistically analyze them, as described (331). Protein sequences for multiple sequence alignments were taken from OMA database (368). To characterize the level of residue conservation, entropy was calculated for each amino acid position.

SECTION C: THERAPEUTIC POTENTIAL OF THE ARRESTIN PROTEINS

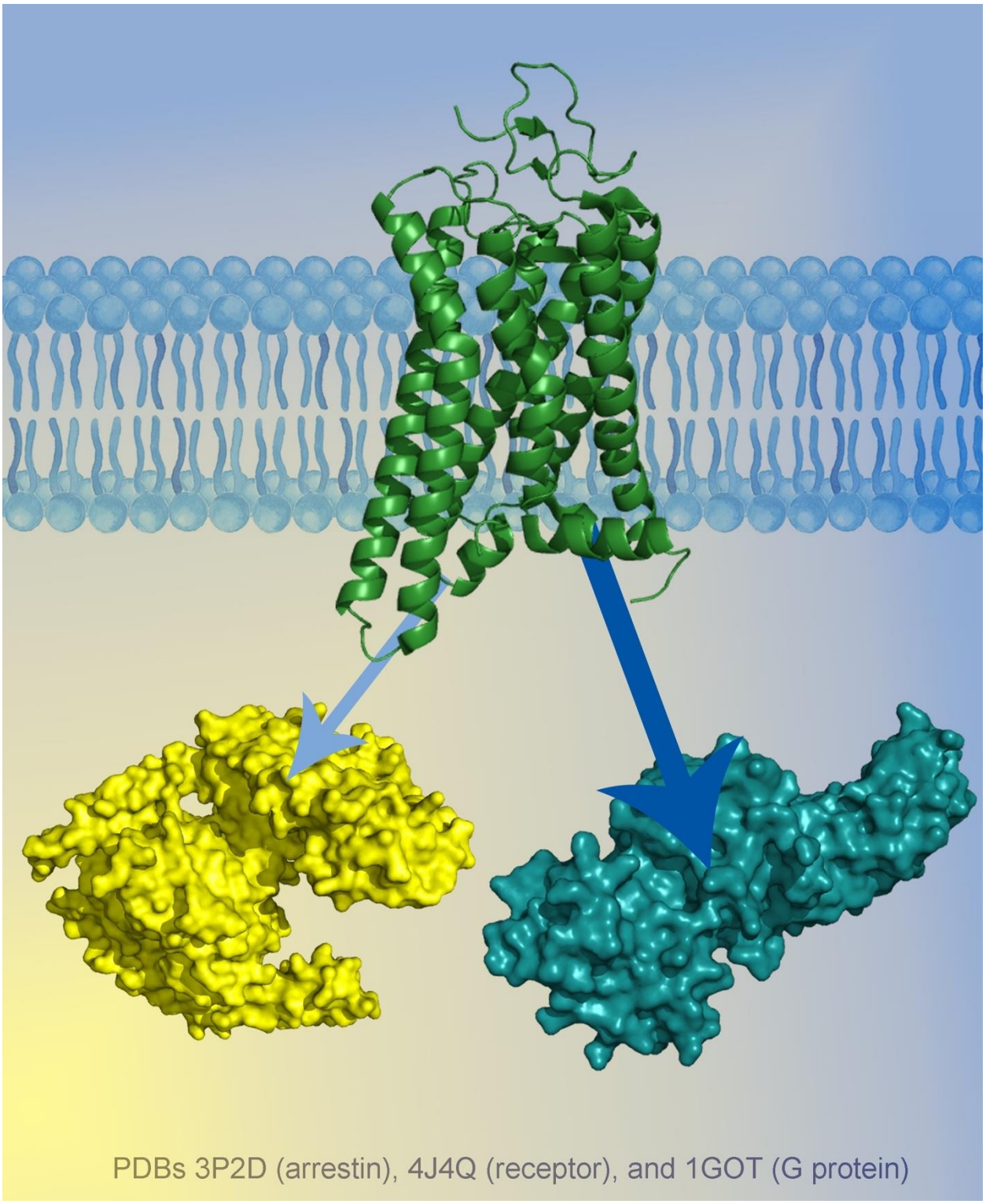

CHAPTER 10

β-ARRESTIN-2 IS AN ESSENTIAL REGULATOR OF PANCREATIC β-CELL FUNCTION UNDER PHYSIOLOGICAL AND PATHOPHYSIOLOGICAL CONDITIONS

This article was published in Nature Communications (369). Lu Zhu was first author, and Joana Almaca, Prasanna K. Dadi, Hao Hong, Wataru Sakamoto, Mario Rossi, Regina J. Lee, Nicholas C. Vierra, Huiyan Lu, Yinghong Cui, Sara M. McMillin, **Nicole A. Perry,** Vsevolod V. Gurevich, Amy Lee, Bryan Kuo, Richard D. Leapman, Franz M. Matschinsky, Nicolai M. Doliba, Nikhil M. Urs, Marc G. Caron, David A. Jacobson, Alejandro Caicedo, and Jurgen Wess contributed to this work. Specific contribution: Guidance/assistance with MBP pull-down experiments. Relation to dissertation work: This chapter invesitages arrestin-3 function in an *in vivo* system and demonstrates how arrestin-3 regulates pancreatic function.

10.1 Introduction

The two members of the β-arrestin family, β-arrestin-1 and -2 (barr1 and barr2; also known as arrestin-2 and arrestin-3, respectively) are widely expressed throughout the body (370). Both β-arrestins regulate a wide array of important physiological functions (189,371,372). It is well known that the β-arrestins bind to ligand-activated G protein-coupled receptors (GPCRs) and that this process interferes with receptor/G protein coupling and promotes GPCR internalization via clathrin-coated pits (238,373).

However, during the past decade, it has become increasingly clear that β-arrestins also

represent signal transducers in their own right, primarily by acting as adaptor proteins for various signaling proteins and their effector pathways (189,241,374-376). It is likely that these non-canonical β-arrestin functions can be exploited for the development of novel classes of clinically useful drugs, including β-arrestin-biased agonists (375,376).

Studies with whole body barr1 and barr2 knockout (KO) mice have shown that β-arrestins play important roles in several key metabolic functions including the maintenance of euglycemia and peripheral insulin sensitivity (372,377,378). However, the metabolic phenotypes displayed by these mutant animals are often difficult to interpret, primarily for two reasons. First, β-arrestins are expressed in most tissues and cell types, making it difficult to determine which cellular pathways in which particular tissues contribute to the observed metabolic deficits. Moreover, since the two β-arrestins regulate many important developmental functions (379,380), it is also possible that the metabolic phenotypes displayed by adult whole body barr1 and barr2 KO mice are modulated by compensatory developmental changes.

To circumvent these difficulties, we inactivated the *barr1* or *barr2* genes in a conditional fashion in specific, metabolically relevant cell types of adult mice. In the present study, we analyzed a mouse strain in which we conditionally inactivated the *barr2* gene in β-cells of adult mice (β-barr2-KO mice). At present, very little is known about the potential role of barr2 in regulating β-cell function. Two recent studies reported contradictory results regarding the role of barr2 in modulating insulin secretion, probably due to problems associated with the use of whole body barr2 KO mice (see above (381,382)). We hypothesized that detailed metabolic studies with β-barr2-KO mice should lead to unambiguous and novel insights into the role of β-cell barr2 in regulating β-cell function and whole-body glucose homeostasis.

We found that β-barr2-KO mice show several striking metabolic deficits, including greatly

impaired glucose-stimulated insulin secretion (GSIS) and Ca^{2+} entry into β-cells, and a pronounced reduction of glucose tolerance when β-barr2-KO mice consume a high-fat diet. We provide strong evidence that barr2 is required for the proper activation of CAMKII and that disruption of this pathway can fully account for the metabolic deficits observed with the β-barr2-KO mice. Moreover, knockdown of *barr2* expression virtually abolishes GSIS in human β-cells. Our findings may lead to the development of novel drugs aimed at modulating barr2 function in β-cells for therapeutic purposes.

10.2 Results

Conditional inactivation of barr2 in β-cells of adult mice. The two β-arrestins regulate many important developmental processes (379,380). To avoid potential developmental changes due to barr2 deficiency, we used a conditional gene deletion strategy to selectively inactivate the *barr2* gene in β-cells of adult mice. Previous studies have shown that tamoxifen (TMX) induces Cre activity in *Pdx1-Cre-ER^{TM}* transgenic mice selectively in pancreatic β-cells (383,384). We therefore crossed *Pdx1-Cre-ER^{TM}* mice (genetic background: C57BL/6) with homozygous floxed *barr2* mice in which exon 2 was flanked by loxP sites (*fl/fl barr2* mice; genetic background: C57BL/6J (385)). Subsequent matings led to the generation of *fl/fl barr2-Pdx1-Cre-ER^{TM}* mice and *fl/fl barr2* control littermates. Previous studies demonstrated that TMX-treated *Pdx1-Cre-ER^{TM}* mice do not show any changes in β-cell function, as compared to wild-type (wt) littermates (314). For this reason, *fl/fl barr2* littermates served as control animals throughout this study. All animals used were maintained on a C57BL/6 background.

We injected *fl/fl barr2-Pdx1-Cre-ER^{TM}* mice and their control littermates (8-week-old males) for 6 consecutive days with TMX (1 mg i.p. per mouse per day) to induce Cre activity and

barr2 inactivation selectively in pancreatic β-cells (383,384). Two weeks after the last TMX injection, we used qRT-PCR to determine *barr2* expression levels in different mouse tissues. As expected, *barr2* transcript levels were greatly reduced in pancreatic islets from TMX-treated *fl/fl barr2-Pdx1-Cre-ER^{TM}* mice, as compared to TMX-treated control littermates (*fl/fl barr2* mice). The expression of islet barr2 protein was also dramatically reduced in the TMX-treated *fl/fl barr2-Pdx1-Cre-ER^{TM}* mice. Most likely, the residual expression of *barr2* in the *fl/fl barr2-Pdx1-Cre-ER^{TM}* islets is due to *barr2* expression by islet cells that are non-β-cells (i.e. α-cells). We also found that TMX-induced reduction of *barr2* expression was selective for islets/β-cells. Importantly, deletion of the *barr2* gene in mouse islets/β-cells did not lead to significant compensatory changes in *barr1* transcript or protein levels in islets or other tissues. For the sake of simplicity, we refer to the TMX-treated *fl/fl barr2-Pdx1-Cre-ER^{TM}* mice as 'β-barr2-KO mice' below.

Stimulated insulin release is impaired in β-barr2-KO islets. Immunohistochemical studies demonstrated that the lack of barr2 in β-cells had no detectable effect on overall islet/β-cell architecture. Similarly, β-cell barr2 deficiency had no significant effect on total pancreatic insulin and islet insulin content (ng insulin per islet: β-barr2-KO, 142±9; control, 133±10; 26 independent islet preparations from 6 mice per group (8-week-old males)).

To assess the effects of barr2 deficiency on β-cell function, we performed islet perfusion experiments. We made the striking observation that glucose (16 mM)-induced insulin release was greatly reduced in the β-barr2-KO islets, as compared to control islets (Fig. 10.1a, b). Calcium imaging experiments demonstrated that glucose-induced increases in intracellular calcium levels ($[Ca^{2+}]_i$) were also severely blunted in the mutant islets (Fig. 10.1c, d).

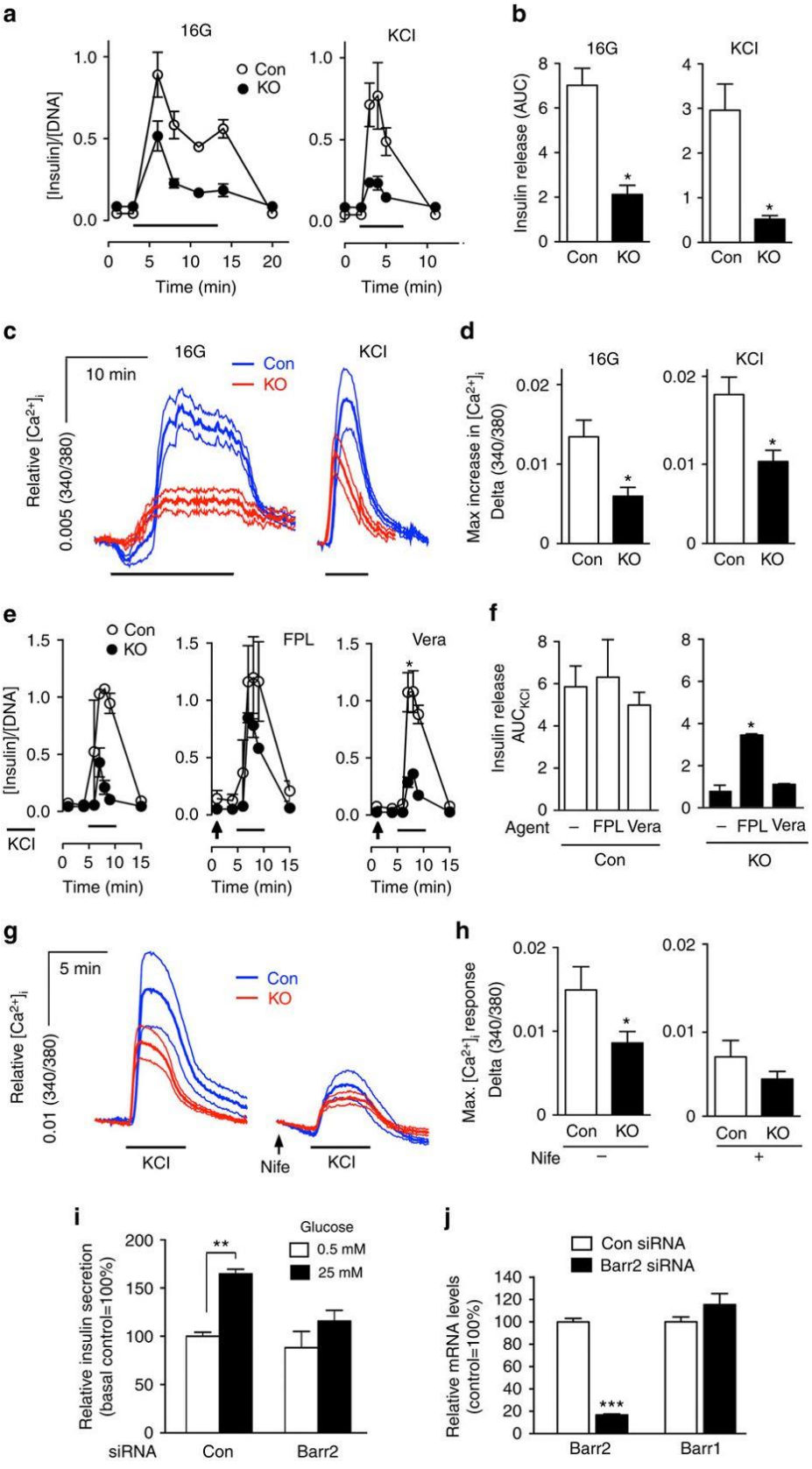
a
16G
KCl
Con
KO
[Insulin]/[DNA]
Time (min)
b
16G
KCl
Insulin release (AUC)
Con
KO
c
16G
KCl
10 min
Con
KO
Relative [Ca2+]i
0.005 (340/380)
d
16G
KCl
Max increase in [Ca2+]i
Delta (340/380)
e
Con
KO
FPL
Vera
[Insulin]/[DNA]
KCl
Time (min)
f
Insulin release
AUCKCl
Agent
–
FPL
Vera
Con
KO
g
5 min
Con
KO
Relative [Ca2+]i
0.01 (340/380)
KCl
Nife
h
Max. [Ca2+]i response
Delta (340/380)
Nife
i
Glucose
0.5 mM
25 mM
Relative insulin secretion
(basal control=100%)
siRNA
Con
Barr2
j
Con siRNA
Barr2 siRNA
Relative mRNA levels
(control=100%)
Barr2
Barr1

Fig. 10.1. β-barr2-KO islets show reduced insulin and $[Ca^{2+}]_i$ responses and impaired function of L-type Ca^{2+} channels (LTCCs). (**a**) Insulin secretion studied with perifused pancreatic islets. Insulin secretion was studied using islets from control and β-barr2-KO mice stimulated with 16 mM glucose (16G) for 15 min or with KCl (25 mM) for 5 min, respectively. Thick horizontal bars indicate the 16G/KCl stimulation periods. All data are given as means ± s.e.m. Insulin secretion was normalized to DNA content (n=3 perifusions per genotype; islets were isolated from 6 male mice per genotype). (**b**) Quantification of the data shown in (a); *p< 0.05 (Student's t-test). Data are given as means ± s.e.m. (**c**) Increases in $[Ca^{2+}]_i$ studied with isolated pancreatic islets. Increases in $[Ca^{2+}]_i$ were recorded using control and β-barr2-KO islets following glucose (16G) or KCl (25 mM) stimulation, respectively. Thick horizontal bars indicate the 16G/KCl stimulation periods. Traces represent average responses (thick lines in the middle) and associated s.e.m. (thin lines above and below the thick lines) from 8-12 islets. Islets were isolated from 6 male mice per genotype. (**d**) Quantification of the data in (c) showing maximum $[Ca^{2+}]_i$ amplitudes after glucose or KCl stimulation. *p< 0.05 (Student's t-test). (**e**) KCl-induced insulin secretion studied with perifused pancreatic islets under different experimental conditions. Insulin secretion from islets of control and β-barr2-KO mice was stimulated with KCl (25 mM; thick horizontal bars), either in the absence of other drugs (left panel), or in the presence of the selective LTCC activator FPL64176 (FPL, 10 µM; center panel), and the selective Na^+ channel opener veratridine (Vera, 10 µM; right panel). Arrows indicate when drugs were added to the medium. All data represent means ± s.e.m. (n=3 perifusions per condition; islets were isolated from 6 male mice per genotype). Asterisks denote significant differences at time points 7, 8, and 9 min. *p<0.05 (two-way repeated measures ANOVA followed by Bonferroni post-tests). (**f**) Quantification of the data shown in (e); *p<0.05. (**g**) KCl-induced increases in $[Ca^{2+}]_i$ studied with isolated pancreatic islets under different experimental conditions. Traces of $[Ca^{2+}]_i$ responses to KCl (25 mM) in the absence (left panel) or presence (right panel) of the selective LTCC blocker nifedipine (Nife, 10 µM; arrow). Traces represent average responses (thick lines in the middle) and associated s.e.m. (thin lines above and below the thick lines). Islets were isolated from 6 male mice per genotype (n=6-8 islets per genotype). (**h**) Quantification of the data in (c) showing maximum $[Ca^{2+}]_i$ amplitudes following KCl stimulation in the absence (left panel) or presence of nifedipine (Nife; right panel). Data represent means ± s.e.m. (*p< 0.05, Student's t-test). AUC, area under the curve. **(i)** *Barr2* knockdown greatly reduces GSIS in human β-cells. Human EndoC-βH1 cells were stimulated with glucose (25 mM) after treatment of cells with scrambled control siRNA (Con) or *barr2* siRNA (means ± s.e.m., n=3; **p<0.01, as compared to the indicated control group, two-way ANOVA followed by Tukey's post-test). **(j)** Effective knockdown of *barr2* expression in human EndoC-βH1 cells following treatment with *barr2* siRNA (con = scrambled control siRNA). *barr2* and *barr1* mRNA levels were determined via real-time qRT-PCR and were normalized relative to the expression of *GAPDH*. Data are expressed as means ± s.e.m.(n=3; ***p<0.001, Student's t-test).

Exposure of β-cells to high concentrations of glucose leads to enhanced glucose metabolism, closure of ATP-sensitive K^+ channels (K_{ATP} channels), β-cell membrane depolarization, influx of Ca^{2+} through voltage-gated calcium channels, and an increase in $[Ca^{2+}]_i$ which in turn triggers the exocytosis of insulin-containing granules. To test the hypothesis that the functional impairments displayed by β-barr2-KO islets were caused by signaling deficits downstream of glucose-induced closure of K_{ATP} channels, we directly depolarized β-cell membranes by treating perifused islets with KCl (25 mM). Strikingly, KCl-induced insulin secretion and increases in $[Ca^{2+}]_i$ were reduced to a similar degree in β-barr2-KO islets, as compared to glucose-treated β-barr2-KO islets (Fig. 10.1a-d). This observation strongly suggests that barr2 facilitates insulin release through a pathway that is located downstream of glucose-induced inactivation of K_{ATP} channels.

Barr2 promotes β-cell L-type Ca^{2+} channel function. Since the lack of β-cell barr2 led to greatly diminished glucose- and KCl-induced increases in $[Ca^{2+}]_i$, we hypothesized that Ca^{2+} influx was impaired in β-cell barr2-KO islets. GSIS is driven mainly by Ca^{2+} influx via L-type Ca^{2+} channels (LTCCs; (386)). To examine the potential role of LTCCs in the functional deficits displayed by barr2-KO islets, we treated islets with FPL64176, a selective activator of LTCCs. In this set of experiments, insulin secretion was triggered by direct membrane depolarization with KCl (25 mM). FPL64176 had no significant effect on KCl-stimulated insulin secretion in control islets (Fig. 10.1e, f). In contrast, FPL64176 greatly amplified the weak insulin response observed with KCl-stimulated β-barr2-KO islets (Fig. 10.1e, f). For control purposes, we carried out similar experiments with veratridine, a selective activator of Na^+ channels. In contrast to FPL64176, veratridine had no significant effect on KCl-induced insulin release in control or β-barr2-KO islets (Fig. 10.1e, f).

As already shown in Fig. 10.1d, KCl-induced elevations in $[Ca^{2+}]_i$ were greatly reduced in barr2-deficient β-cells (Fig. 10.1g, h). Strikingly, in the presence of nifedipine (10 μM), a selective blocker of LTCCs, KCl-induced $[Ca^{2+}]_i$ responses were not significantly different in β-barr2-KO and control islets (Fig. 10.1g, h).

Taken together, the outcome of these pharmacological studies strongly suggests that the lack of barr2 interferes with the proper function of LTCCs in β-cells.

In mouse β-cells, the predominant LTCCs are $Ca_V1.2$ and $Ca_V1.3$ (387). qRT-PCR studies with RNA prepared from β-barr2-KO and control islets demonstrated that the expression levels of *$Ca_V1.2$* and *$Ca_V1.3$* (α subunits) remained unaffected by the lack of barr2. This observation indicates that the impaired activity of LTCCs observed with β-barr2-KO islets is not due to altered LTCC expression levels. The expression levels of other key β-cell genes remained unaffected by the lack of barr2 in β-cells.

Barr2 knockdown greatly reduces GSIS in human β-cells. To confirm that barr2 is also a critical regulator of insulin release in human β-cells, we carried out insulin secretion studies with EndoC-βH1 cells, an immortalized human pancreatic β-cell line (388). Treatment of EndoC-βH1 cells with *barr2* siRNA resulted in a ~80% reduction in *barr2* expression while *barr1* transcript levels remained unaffected (Fig. 10.1j). Following treatment with 25 mM glucose, control EndoC-βH1 cells treated with scrambled control siRNA showed a significant increase in GSIS (Fig. 10.1i). In contrast, GSIS was virtually abolished in cells treated with *barr2* siRNA (Fig. 10.1i), indicating that barr2 is also essential for insulin release in human β-cells.

EM analysis of β-cell dense core vesicles. Since glucose/KCl-stimulated insulin secretion was impaired in β-barr2-KO islets, we next examined whether the lack of barr2 affected the total number of β-cell dense core vesicles (DCVs) and the density of plasma membrane-docked DCVs.

To obtain these parameters, we employed serial block-face scanning electron microscopy (SBF-SEM) using pancreatic islets prepared from control and β-barr2-KO mice (see Methods for details). This analysis demonstrated that the total number of β-cell DCVs remained unaffected by the absence of barr2. Similarly, control and barr2-deficient β-cells did not differ significantly from each other in the number of DCVs docked to the β-cell plasma membrane. These data clearly indicate that barr2 deficiency does not affect the total number and distribution of β-cell DCVs.

Lack of β-cell barr2 causes electrophysiological deficits. To directly study the role of barr2 in regulating the activity of β-cell voltage-dependent Ca^{2+} channels (VDCCs)/LTCCs, we carried out electrophysiological recordings studying β-cells from control and β-barr2-KO mice. Initially, we measured VDCC currents in response to 10 mV voltage steps from -70 to +70 mV. The β-cells were first held at -80 mV in low glucose (3 mM) for 3 min to limit Ca^{2+} influx and prevent Ca^{2+}-induced changes in VDCC activity before the first recording. Interestingly, barr2-deficient β-cells showed significantly reduced VDCC currents in response to voltage steps between 0 and 20 mV when compared with control β-cells (Fig. 10.2a, b). Despite the decrease in VDCC currents, the lack of barr2 did not affect the kinetics of VDCC activation or inactivation (Fig. 10.2c, d). These data strongly support the concept that barr2 is required for efficient glucose-stimulated Ca^{2+} entry into β-cells by increasing the activity of VDCCs.

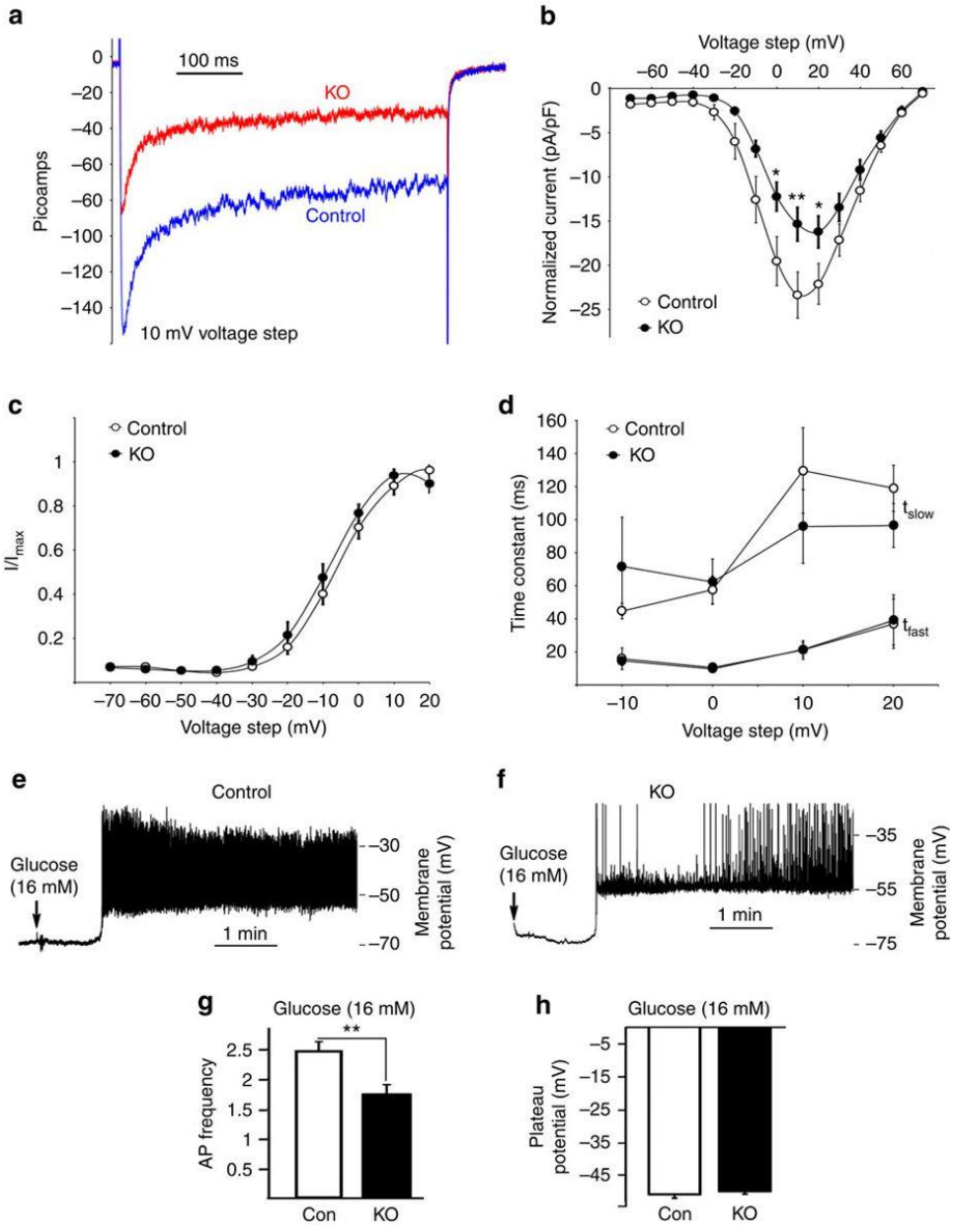

Fig. 10.2. Lack of barr2 in β-cells causes a strong reduction in VDCC amplitude and action potential firing frequency. (**a**) Voltage-dependent Ca^{2+} channel (VDCC) currents recorded from β-cells of control and β-barr2-KO mice in response to voltage steps of 10 mV from -70 mV to 70 mV. (**b**) Normalized average β-cell VDCC currents at the indicated voltage steps (control, n=15 islets; β-barr2-KO, n=13 islets). (**c**) Activation of β-cell VDCCs in response to the indicated voltage steps. (**f**) Time constants of VDCC inactivation in response to the indicated voltage steps (fast (τ_{fast}) and slow (τ_{slow})). (**e, f**) Electrical activity of representative β-cells from a control (e) and a β-barr2-KO mouse (f) in response to 16 mM glucose. (**g**) β-Cell action potential (AP) firing frequency recorded 2.5 min after glucose (16 mM) treatment (control, n=13 islets; β-barr2-KO, n=19 islets). (**h**) Plateau potential from where β-cell APs occurred 2.5 min after glucose (16 mM) treatment (control, n=13 islets; β-barr2-KO, n=19 islets). The data shown in (B)-(D) and (G)-(H) comprise experiments derived from 5 independent islet isolations using different sets of control and β-barr2-KO mice (adult males). Data represent means ± s.e.m. (*p< 0.05; **p<0.01; Student's t test).

After glucose-dependent depolarization of the β-cell membrane, activation of VDCCs results in the upstroke of action potential (AP), which is the primary electrical signal of the β-cell (389). To assess how changes in VDCC activity affect β-cell AP firing, we monitored the membrane potential of mouse β-cells in response to 16 mM glucose. The glucose-stimulated plateau potential from where APs occurred was similar for control and barr2-KO β-cells (-51.2 ± 1.1 mV and -50.2 ± 0.88 mV, respectively; Fig. 10.2h). In striking contrast, AP firing frequency measured 2.5 min after 16 mM glucose was greatly reduced in barr2-KO β-cells (1.73 ± 0.17 Hz), as compared with control β-cells (2.47 ± 0.14 Hz) (Fig. 10.2e-g). These data clearly indicated that barr2 increases β-cell AP firing frequency by augmenting VDCC activity.

Lack of barr2 has no effect on β-cell K^+ channels. We next studied potential effects of barr2 deficiency on the activities of the two major β-cell K^+ channels, the delayed rectifier voltage-gated K^+ channel (K_V) and the ATP-sensitive K^+ channel (K_{ATP}). K_v currents were recorded from control and barr2-deficient β-cells in response to 10 mV voltage steps from -70 to 70 mV (Fig. 10.3a, b). The resulting K_v currents were not significantly different between control and barr2-deficient β-cells. Moreover, K_v currents were inhibited by tetraethylammonium (TEA, 10 mM) to the same extent in the presence or absence of barr2 (Fig. 10.3c). We also recorded K_{ATP} currents from control and barr2 KO β-cells by removing intracellular ATP and recording the resulting K^+ currents in response to a voltage ramp from -120 to -40 mV (Fig. 10.3d). This analysis showed that barr2 deficiency had no significant effect on the activity of K_{ATP} currents (Fig. 10.3d). Moreover, the lack of barr2 did not affect the ability of tolbutamide (200 μM) to inhibit K_{ATP} currents (Fig. 10.3d). Thus, the lack of barr2 in β-cells has no detectable effect on β-cell K_v or K_{ATP} channels.

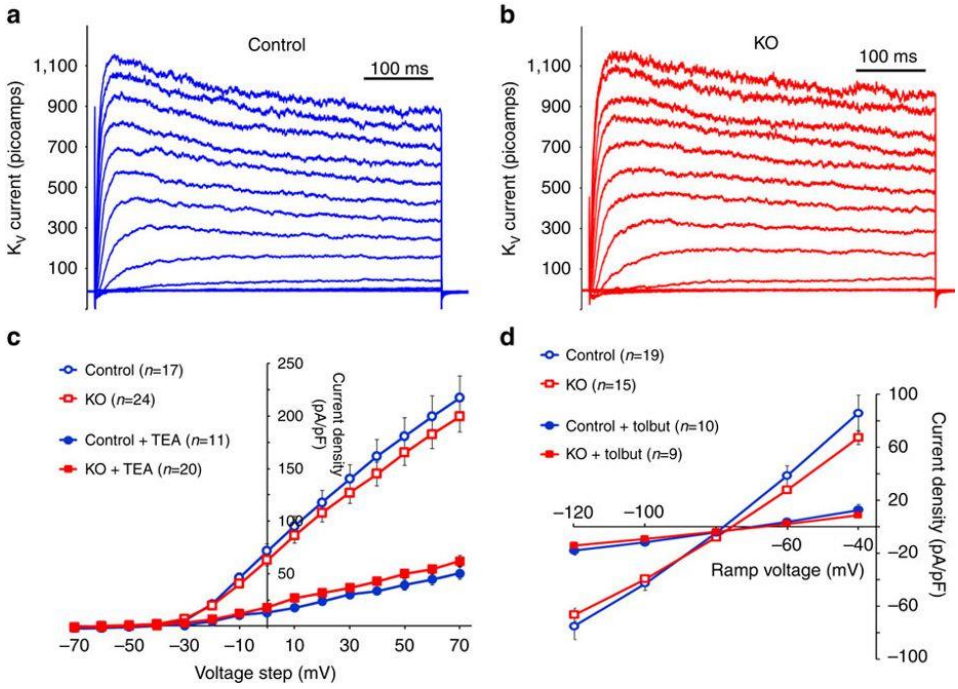

Fig. 10.3. Barr2 deficiency does not affect β-cell K_v and K_{ATP} channel currents. (**a**) Representative K_v current traces from a control β-cell during 10 mV voltage steps from -70 to 70 mV. (**b**) Representative K_v current traces from a barr2-deficient (KO) β-cell during 10 mV voltage steps from -70 to 70 mV. (**c**) Summary of β-cell K_v currents recorded from control and KO β-cells at the indicated voltages and following inhibition with tetraethylammonium (TEA; 10 mM). Data are given as means ± s.e.m. (**d**) K_{ATP} current recordings (induced by removal of intracellular ATP) from control and barr2-deficient (KO) β-cells at the indicated voltages and following inhibition with tolbutamide (Tolbut; 200 μM). Data are presented as means ± s.e.m.

GPCRs promote GSIS in the absence of β-cell barr2. The activity of pancreatic β-cells is modulated by several GPCRs including the M_3 muscarinic receptor (390) and the GLP-1 receptor (391). Since β-arrestins are well-known regulators of GPCR function, we studied whether M_3 and GLP-1 receptor-mediated augmentation of GSIS was altered in β-barr2-KO islets. In the presence of a stimulatory concentration of glucose (16 mM), the muscarinic agonist, oxotremorine-M (Oxo-M; 10 μM), and GLP-1 (100 nM) amplified insulin secretion in a similar fashion in β-barr2-KO and control islets (data not shown), suggesting that barr2 deficiency does not interfere with the ability of these two GPCRs to augment GSIS.

Consistent with the insulin data, Ca^{2+} responses to Oxo-M and exendin-4, a GLP-1 analog

with increased hydrolytic stability, were significantly increased in the presence of a stimulatory concentration of glucose (16 mM) (data not shown). Moreover, β-cell barr2 deficiency did not interfere with the ability of the two agonists to promote increases in $[Ca^{2+}]_i$ (data not shown). In fact, Oxo-M treatment of β-barr2-KO islets led to a significantly greater elevation of $[Ca^{2+}]_{i,}$ as compared to Oxo-M-treated control islets. The molecular mechanisms underlying this effect, which may involve impaired desensitization of the M_3 muscarinic receptor, remain to be explored in future studies.

We also stimulated β-barr2-KO and control islets with Oxo-M (10 μM) in the absence of extracellular Ca^{2+}. Under these conditions, muscarinic agonists, such as Oxo-M, stimulate increases in β-cell $[Ca^{2+}]_i$ via G_q-dependent activation of IP_3 receptors, triggering Ca^{2+} release from ER Ca^{2+} pools (392). We found that the Oxo-M-induced increases in $[Ca^{2+}]_i$ were similar in β-barr2-KO and control islets (data not shwon), suggesting that β-cell barr2 deficiency does not affect Ca^{2+} release from ER stores.

β-Barr2-KO mice show striking metabolic deficits in vivo. To investigate whether the functional impairments observed with β-barr2-KO islets in vitro were associated with metabolic deficits in vivo, we subjected β-barr2-KO and control mice to a series of in vivo metabolic studies. Interestingly, β-barr2-KO mice consuming regular chow showed only mild metabolic phenotypes (Fig. 10.4a-c). The mutant mice displayed a trend toward reduced GSIS (Fig. 10.4a). However, β-barr2-KO mice and control littermates showed a similar degree of glucose tolerance (i.p. glucose tolerance test; Fig. 10.4b) and insulin sensitivity (0.75 U insulin kg^{-1} i.p.; Fig. 10.4c). Moreover, basal plasma insulin levels were not affected by β-barr2-deficiency (data not shown).

In contrast, when β-barr2-KO mice were maintained on a calorie-rich, high-fat diet (HFD), they showed pronounced metabolic impairments. Strikingly, GSIS was essentially abolished in

HFD β-barr2-KO mice (Fig. 10.4d). Consistent with this finding, HFD β-barr2-KO mice displayed greatly impaired glucose tolerance and a significant increase in fasting blood glucose levels (Fig. 10.4e). In both groups of mice, the HFD induced a similar degree of reduced insulin sensitivity (Fig. 10.4f). β-Cell barr2 deficiency had no significant effect on basal plasma insulin levels (data not shown).

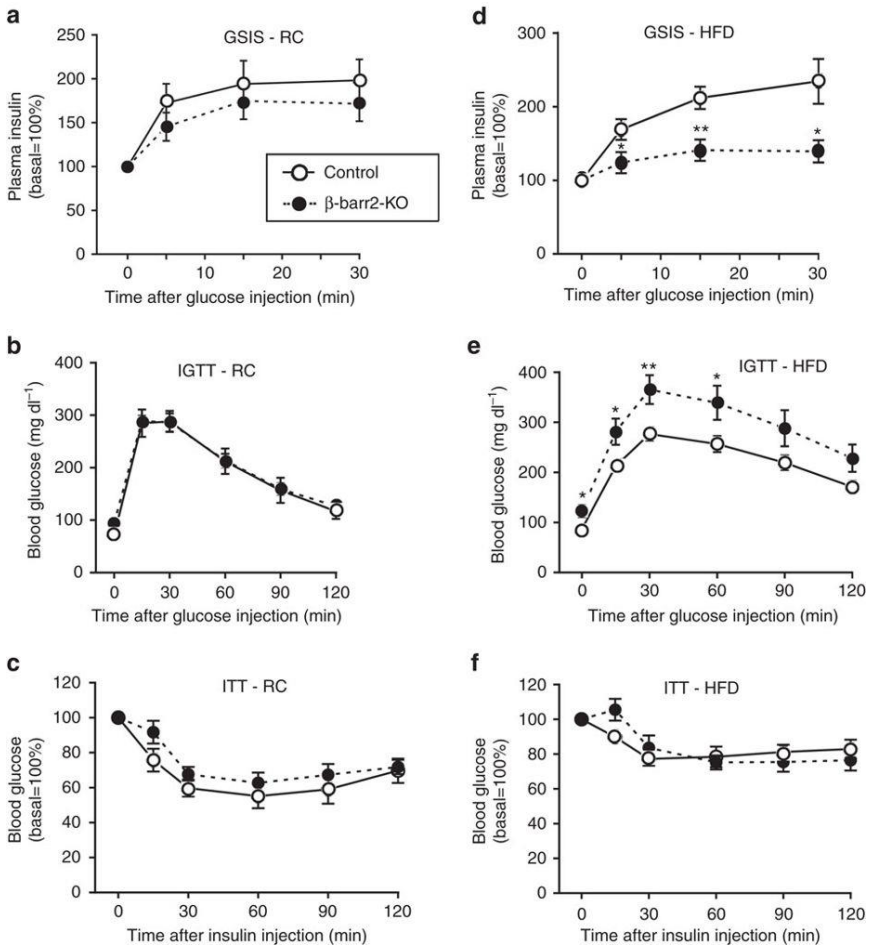

Fig. 10.4. In vivo metabolic studies with mice lacking barr2 in pancreatic β-cells. (**a-c**) In vivo metabolic tests carried out with β-barr2-KO mice and control littermates maintained on regular chow (RC). (**a**) Glucose-induced insulin secretion (GSIS; 2 g glucose/kg i.p.). (**b**) I.p. glucose tolerance test (IGTT; 2 g glucose/kg i.p.). (**d**) Insulin tolerance test (ITT; 0.75 U insulin/kg i.p.). (**d-f**) β-barr2-KO mice and control littermates were maintained on a high-fat diet (HFD) and subjected to the same tests as in (A-C). In (d) and (e), the glucose dose was reduced to 1 g/kg (i.p.). In (F), the insulin dose was 1 U/kg (i.p.). Mice were maintained on the HFD for at least 8 weeks. All studies were carried out with male mice (mouse age: RC, 10-16 weeks; HFD, 16-22 weeks). Data are given as means ± s.e.m. (8-12 mice per group). *$p<0.05$, **, $p<0.01$, as compared to the corresponding control value (Student's t-test).

Islet morphometric studies showed that β-cell mass was unaltered in HFD β-barr2-KO mice, as compared with HFD control littermates (data not shown). Also, consumption of the HFD caused similar weight gain in control and barr2-KO mice (data not shown). Collectively, these data strongly support the notion that the pronounced metabolic deficits observed with HFD β-barr2-KO mice are due to impaired insulin secretion, consistent with the in vitro insulin release studies.

Barr2 is essential for β-cell function by regulating CAMKII. Our next goal was to identify the cellular pathway through which barr2 exerts its beneficial effects on β-cell function including insulin release. We recently found that conditional inhibition of CAMKII in β-cells leads to severe deficits in β-cell function, associated with impaired glucose homeostasis in vivo (393,394). Interestingly, the metabolic in vitro and in vivo phenotypes that we observed with this mouse model are strikingly similar to those displayed by the β-barr2-KO mutant mice. We therefore hypothesized that barr2 might be required for the proper activity of CAMKII in β-cells.

To test this hypothesis, we incubated β-barr2-KO and control islets with AIP2 (autocamtide-2 related inhibitory peptide II), a cell-permeable, selective peptide inhibitor of CAMKII (394,395). We found that AIP2 (5 μM) treatment of control islets greatly reduced glucose- and KCl-dependent increases in insulin secretion and [Ca^{2+}_i] (Fig. 10.5a, b). Notably, these impairments were similar in magnitude to those observed with β-barr2-KO islets that had not been exposed to AIP2 (Fig. 10.5a, b). In contrast to the control islets, β-barr2-KO islets showed little or no sensitivity to AIP2 treatment (Fig. 10.5a, b).

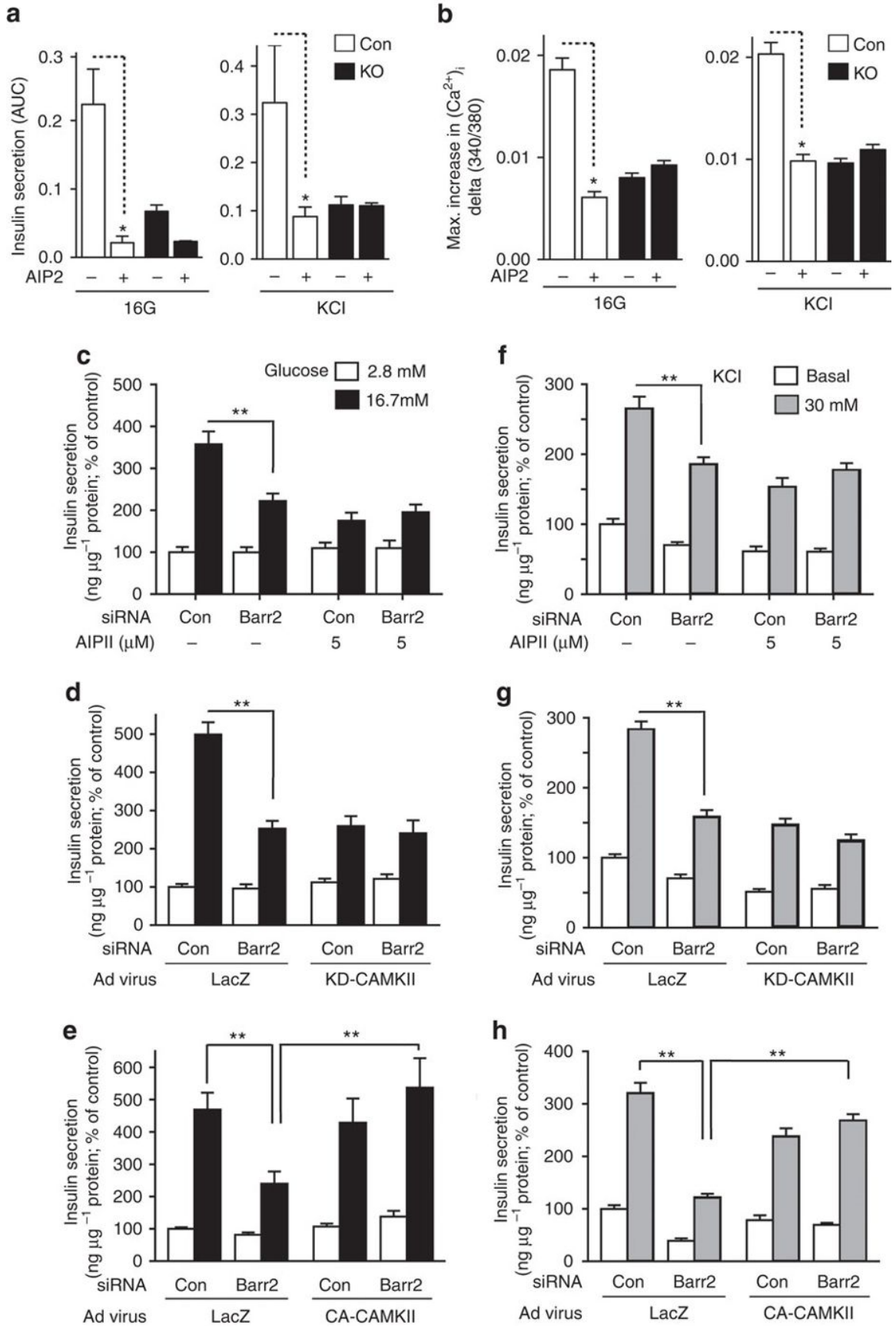
a
Insulin secretion (AUC)
0.3
0.2
0.1
0.0
AIP2
– + – +
16G
0.4
0.3
0.2
0.1
0.0
– + – +
KCl
Con
KO
b
Max. increase in $(Ca^{2+})_i$ delta (340/380)
0.02
0.01
0.00
AIP2
– + – +
16G
0.02
0.01
0.00
– + – +
KCl
Con
KO
c
Glucose
2.8 mM
16.7mM
Insulin secretion (ng µg^{-1} protein; % of control)
500
400
300
200
100
0
**
siRNA Con Barr2 Con Barr2
AIPII (µM) – – 5 5
f
KCl
Basal
30 mM
Insulin secretion (ng µg^{-1} protein; % of control)
300
200
100
0
**
siRNA Con Barr2 Con Barr2
AIPII (µM) – – 5 5
d
Insulin secretion (ng µg^{-1} protein; % of control)
500
400
300
200
100
0
**
siRNA Con Barr2 Con Barr2
Ad virus LacZ KD-CAMKII
g
Insulin secretion (ng µg^{-1} protein; % of control)
300
200
100
0
**
siRNA Con Barr2 Con Barr2
Ad virus LacZ KD-CAMKII
e
Insulin secretion (ng µg^{-1} protein; % of control)
600
500
400
300
200
100
0
** **
siRNA Con Barr2 Con Barr2
Ad virus LacZ CA-CAMKII
h
Insulin secretion (ng µg^{-1} protein; % of control)
400
300
200
100
0
** **
siRNA Con Barr2 Con Barr2
Ad virus LacZ CA-CAMKII

Fig. 10.5. Role of CAMKII in mediating the stimulatory effects of barr2 in islets/β-cells. (**a**) Stimulation of insulin release by glucose (16G, left panel) and KCl (25 mM, right panel) from control and β-barr2-KO islets, in the absence or presence of a selective CAMKII inhibitor (AIP2, 5 μM). Islets were incubated for 30 min with AIP2 prior to glucose or KCl stimulation. AIP2 significantly inhibited insulin secretion in control islets but had no significant effect on insulin release from β-barr2-KO islets (*p< 0.05, one-way ANOVA followed by Tukey's post-test; n=3 perifusions per condition; islets were isolated from 6 male mice per genotype; means ± s.e.m.). AUC, area under the curve. (**b**) Maximum amplitudes of $[Ca^{2+}]_i$ responses (delta 340/380 nm) to 16G (left panel) and KCl (25 mM, right panel) in control and β-barr2-KO islets in the presence or absence of AIP2 (5 μM). Maximum $[Ca^{2+}]_i$ responses were defined as the difference between maximum and basal 340/380 nM values. AIP2 significantly inhibited 16G- and KCl-induced increases in $[Ca^{2+}]_i$ in control islets but had no significant effect on $[Ca^{2+}]_i$ responses in β-barr2-KO islets (*p< 0.05, one-way ANOVA followed by Tukey's post-test; n=6 islets per condition; islets were isolated from 6 male mice per genotype; means ± s.e.m.). (**c-e**) Glucose (16.7 mM)-stimulated insulin secretion by glucose (GSIS) in MIN6 cells (stimulation period: 1 hr). Prior to insulin secretion studies, cells were treated with either scrambled control siRNA (Con) or *barr2* siRNA. (**c**) GSIS in the presence of a selective CAMKII inhibitor (AIP2, 5 μM). AIP2 significantly inhibited insulin secretion in control cells but had no effect on insulin release in *barr2* knockdown cells. (**d**) GSIS studied with cells infected with adenoviruses coding for KD-CAMKII (a dominant negative mutant of CAMKII) or LacZ (control). (**e**) GSIS studied with cells infected with adenoviruses coding for CA-CAMKII (a constitutively active version of CAMKII) or LacZ (control). (**f-h**) KCl-induced stimulation of insulin secretion in MIN6 cells (stimulation period: 1 hr). Prior to insulin release studies, cells were treated with either scrambled control siRNA (Con) or *barr2* siRNA. Cells were exposed to AIP2 or different adenoviruses, as indicated in (A-C). Data are given as means ± s.e.m. from three independent experiments carried out in hexuplicate. *p<0.05, **p<0.01, as compared to the indicated control group (two-way ANOVA followed by Tukey's post-test).

We obtained very similar results when we studied the effect of AIP2 on GSIS and KCl-induced insulin secretion in cultured mouse β-cells (MIN6 cells) treated with either scrambled control siRNA or *barr2* siRNA (Fig. 10.5c, f). qRT-PCR experiments showed that *barr2* siRNA-mediated knockdown of *barr2* expression in MIN6 cells did not lead to compensatory changes in *barr1* expression levels (data not shown). Besides using a peptide inhibitor (AIP2), we also disrupted CAMKII function by infecting MIN6 cells with an adenovirus coding for a dominant negative version of CAMKII (KD-CAMKII (396)). A pharmacologically inert adenovirus coding for lacZ was used for control purposes. This alternative strategy to inhibit CAMKII function resulted in a pattern of insulin responses that was very similar to that seen with AIP2-treated MIN6 cells or pancreatic islets (Fig. 10.5d, g).

The CAMKII inhibition data strongly suggested that barr2 is a component of a β-cell signaling pathway that is required for CAMKII activation. To examine whether barr2 acts upstream or downstream of CAMKII, we infected MIN6 cells treated with either scrambled control siRNA or *barr2* siRNA with an adenovirus coding for a constitutively active version of CAMKII (CA-CAMKII (396)). Expression of CA-CAMKII in MIN6 cells treated with control siRNA had no significant effect on glucose (16.7 mM)- or KCl (30 mM)-induced insulin secretion (Fig. 10.5e, h). Remarkably, expression of CA-CAMKII in cells treated with *barr2* siRNA completely rescued the pronounced deficits in glucose- and KCl-induced insulin secretion caused by *barr2* knockdown (Fig. 10.5e, h). In contrast to AIP2, a membrane-permeable control peptide (Drosophila antennapedia homeodomain leader peptide) had no significant effect on glucose- and KCl-stimulated insulin secretion in MIN6 cells (note that this sequence is part of the AIP2 peptide) (data not shown).

We next examined whether the deficits in GSIS observed with β-barr2 KO islets could also

be rescued by a constitutively active version of CAMKII. Specifically, we infected β-barr2 KO and control islets with adenoviruses coding for CA-CAMKII or GFP (control) (Fig. 10.6). After a 30 min pre-incubation, the islets were incubated in low or high glucose buffer (2.8 mM or 28 mM glucose, respectively) for 1 hr. We found that treatment of β-barr2 KO islets with the CA-CAMKII virus efficiently rescued the impairment in GSIS caused by barr2 deficiency (Fig. 10.6).

Taken together, these findings strongly suggest that barr2 acts upstream of CAMKII in pancreatic β-cells.

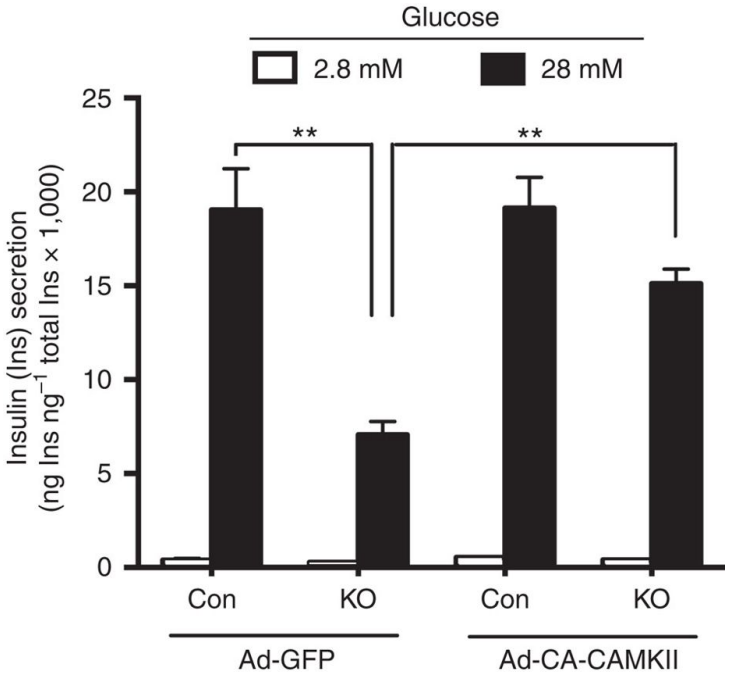

Fig. 10.6. Deficits in GSIS in β-barr2 KO islets are rescued by a constitutively active CAMKII mutant (CA-CAMKII). Islets prepared from β-barr2 KO mice or control littermates were infected with adenoviruses coding for CA-CAMKII or GFP (control). After pre-incubation of islets with insulin secretion buffer for 30 min, islets were incubated in low or high glucose buffer (2.8 mM or 28 mM glucose, respectively) for 1 hr. Data are given as means ± s.e.m. (n=4-8). **$p<0.01$, as compared to the indicated control group (two-way ANOVA followed by Tukey's post-test).

Barr2 deficiency prevents synapsin I phosphorylation. CAMKII is known to stimulate insulin secretion via phosphorylation of various signaling proteins involved in insulin exocytosis, including synapsin I (393,397,398). CAMKII activation is also associated with its auto-phosphorylation at Thr-286 (399). Consistent with these findings, Western blotting studies demonstrated that KCl (30 mM) treatment of MIN6 cells increased both CAMKII auto-phosphorylation and synapsin I phosphorylation (Fig. 10.7a-c). Strikingly, these phosphorylation events were completely abolished in barr2-deficient cells (Fig. 10.7a-c). We obtained similar results when we carried out CAMKII and synapsin I phosphorylation studies with control and β-barr2-KO islets (Fig. 10.7d-f). Importantly, total CAMKII levels were similar in control and β-barr2 KO islets (Fig. 10.7g).

*Stimulated CAMKII activity is reduced in β-barr2 KO islets***.** We also performed CAMKII activity assays with control and β-barr2 KO islets. These experiments were carried out at two different concentrations of glucose (2.8 and 28 mM, respectively), either in the presence or absence of Ca^{2+}/calmodulin. The lack of barr2 had no significant effect on total CAMKII activity measured in the presence of Ca^{2+}/calmodulin (data not shown), consistent with the observation that β-cell barr2 deficiency did not affect total CAMKII expression levels (Fig 10.7g). However, in the presence of a stimulatory concentration of glucose (28 mM), β-barr2 KO islets displayed a significant reduction in autonomous (Ca^{2+}/calmodulin-independent) CAMKII activity (data not shown), in good agreement with the results of the CAMKII autophosphorylation studies (Fig. 10.7e).

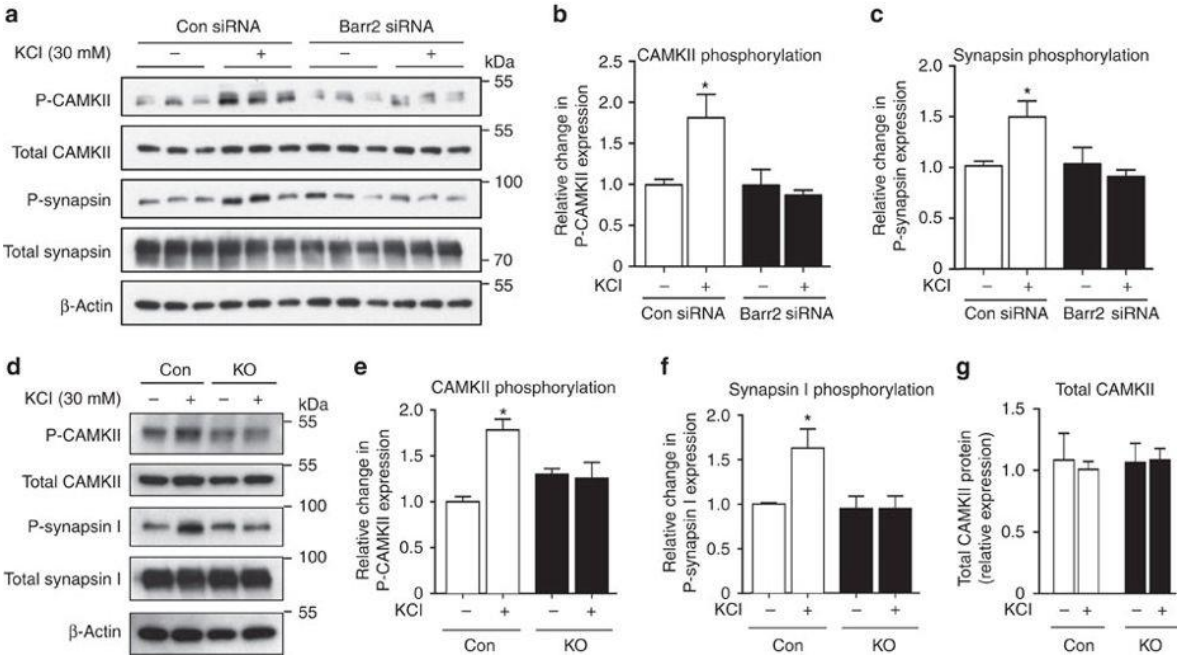

Fig. 10.7. CAMKII and synapsin I phosphorylation and barr2/CAMKII co-immunoprecipitation/co-localization studies. (**a-f**) Western blotting studies. (**a-c**) KCl (30 mM) stimulation of MIN6 cells treated with scrambled control siRNA (Con) promotes the phosphorylation of CAMKII (a, b) and synapsin I (a, c). These responses are abolished after treatment of MIN6 cells with *barr2* siRNA. (**b, c**) Quantification of CAMKII and synapsin I phosphorylation data derived from immunoblotting experiments normalized by total CAMKII or total synapsin I expression, respectively. (**d-f**) Data represent means ± S.E.M. of three independent experiments carried out in triplicate. *p<0.05, **p<0.01, as compared to the non-stimulated control group (one-way ANOVA followed by Tukey's post-test). (**d-f**) Western blotting experiments similar to those shown in (a-c) were carried out with pancreatic islets prepared from barr2-KO mice (KO) and control littermates (12-week old males). (**g**) Total CAMKII expression levels in control and β-barr2 KO islets determined in immunoblotting studies using a pan-CAMKII antibody. Protein levels are expressed relative to the expression of β-actin. Data represent means ± s.e.m. of three or four independent experiments (b, c, e-g). *p<0.05, as compared to the non-treated control group (one-way ANOVA followed by Tukey's post-test).

Detection of barr2/CAMKII complexes in mouse islets. We next used a co-immunoprecipitation strategy to explore the possibility that barr2 can form a complex with CAMKII in native mouse β-cells (pancreatic islets). Specifically, we subjected lysates prepared from wt mouse pancreatic islets to immunoprecipitation with either an anti-CaMKII antibody or goat IgG (negative control). Immunoprecipitated proteins were then probed via Western blotting with an anti-barr2 antibody. Using this approach, we detected barr2 protein as a ~50 kDa species in the immunoprecipitates (Fig. 10.8a). As expected, control IgG immunoprecipitates did not yield any detectable immunoreactive bands (barr2 or CaMKIIδ indicative of the selectivity of the CaMKIIδ antibody used (Fig. 10.8a). These findings strongly support the existence of barr2/CAMKII complexes in native mouse islets (β-cells).

In mouse pancreatic β-cells, the $Ca_V1.2$ channel is one of the predominant LTCCs (387). To examine whether barr2 has access to $Ca_V1.2$ in native β-cells, we subjected lysates prepared from wt mouse pancreatic islets to the same immunoprecipitation strategy described above. By using anti-$Ca_V1.2$ (α_1 subunit) and anti-barr2 antibodies, we were unable to demonstrate the existence of barr2/$Ca_V1.2$ complexes (Fig. 10.8a). This observation indicates that barr2 does not have access to LTCCs.

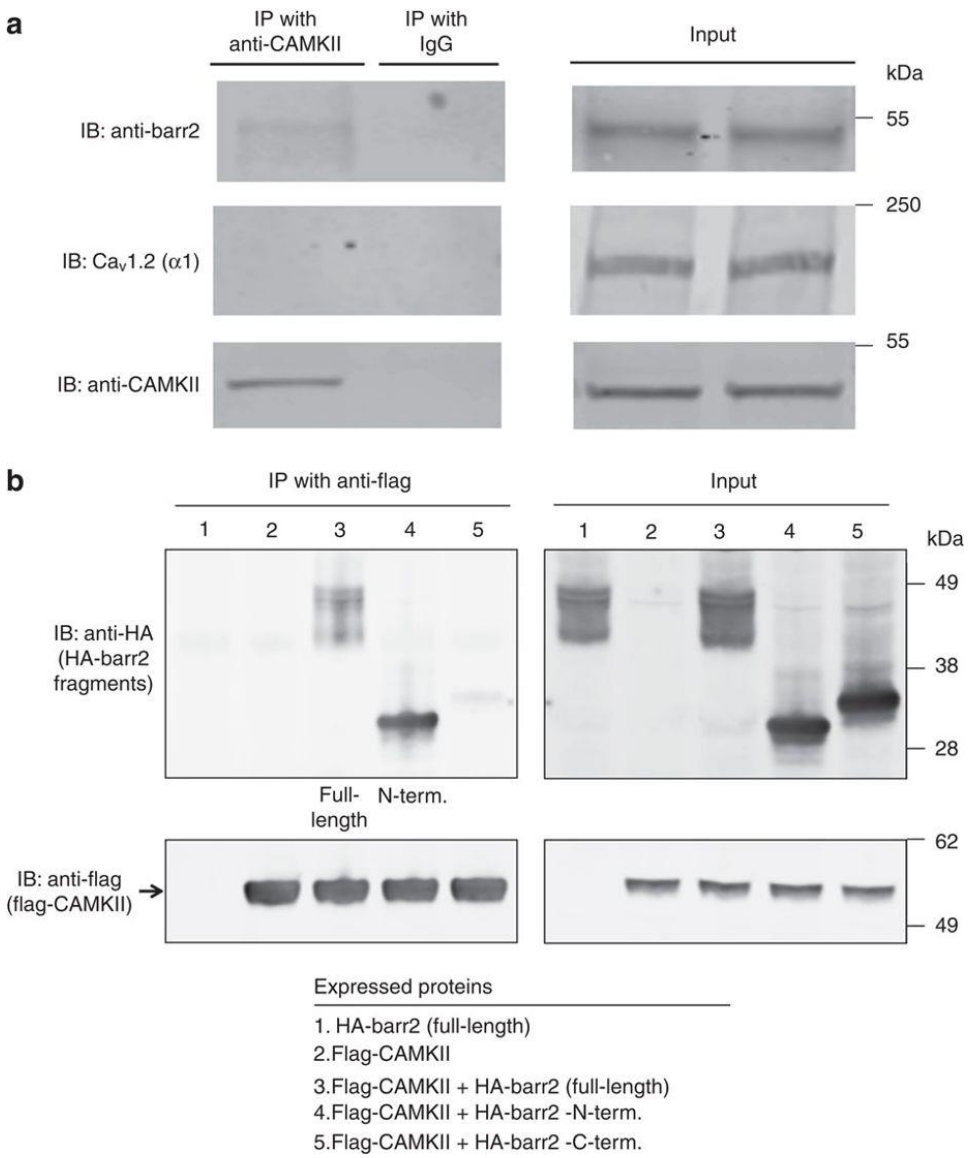

Fig. 10.8. Co-immunoprecipitation of barr2/CAMKII complexes. (a) Studies with wt mouse pancreatic islets. Lysates prepared from wt mouse pancreatic islets were subjected to immunoprecipitation with either an anti-CaMKII δ antibody or goat IgG (negative control). Immunoprecipitated proteins were then probed with anti-barr2, anti-CaMKII (pan), and anti-$Ca_V1.2$ (α_1 subunit) antibodies. Note that barr-2, but not $Ca_V1.2$, could be co-immunoprecipitated with CAMKII. **(b)** Co-immunoprecipitation studies with transfected HEK293T cells. HEK293T cells were transfected with the indicated plasmids. All barr2 constructs carried an N-terminal HA epitope tag (HA-barr2-N-term: barr2 residues 1-181; HA-barr2-C-term: barr2 residues 180-408). In addition, cells were infected with an adenovirus coding for flag-CaMKIIδ (lanes 2-5) or an empty control virus (lane 1). Flag-CaMKIIδ was immunoprecipitated from cell lysates with an anti-flag antibody, followed by immunoblotting studies to detect co-immunoprecipitated barr2/barr2 fragments. This analysis indicated that the barr2-N-domain (similar to full-length barr2), but not the barr2-C-domain, was clearly detectable in the immunoprecipitates. The blots shown are representative of two or three independent experiments.

*Role of the N-terminal barr2 domain in CAMKII complexes***.** β-Arrestins consist of two major regions, the N- and C-terminal domains (barr2-N-domain: residues 1-181; barr2-C-domain: 180-408). To explore which of these two domains is involved in the formation of protein complexes containing barr2 and CAMKII, we carried out additional co-immunoprecipitation studies using co-transfected HEK293T cells. Cells were transfected with plasmid DNAs coding for full-length barr2, the barr2-N-domain, or the barr2 C-domain (all constructs carried an N-terminal HA tag). Subsequently, cells were infected with an adenovirus coding for flag-CAMKII or a control virus. Following cell lysis, flag-CAMKII was immunoprecipitated with an anti-flag antibody. Western blotting studies showed that the barr2-N-domain, but not the barr2-C-domain, was clearly detectable in the immunoprecipitates (Fig. 10.8b). This finding suggests that the N-domain of barr2 is critically involved in the formation of protein complexes containing barr2 and CAMKII.

Purified barr2 does not interact with purified CAMKII. To examine whether barr2 was able to bind to CAMKII directly, we studied the ability of purified barr2 fused to the C-terminus of maltose-binding protein (MBP-barr2 (104)) to interact with purified CAMKII (CAMKIIδ). Pull-down assays failed to demonstrate a direct interaction between MBP-barr2 and CAMKII (data not shown). In contrast, as reported previously (104), purified MBP-barr2 was able to bind to purified JNK3 (JNK3α2, positive control).

In vivo studies with mice overexpressing barr2 in β-cells. Since the lack of barr2 in β-cells led to impaired glucose homeostasis (Fig. 10.4), we hypothesized that enhanced signaling via barr2 in β-cells might promote GSIS and improve glucose tolerance. To test this hypothesis, we generated transgenic mice which selectively overexpressed an HA-tagged version of barr2 in pancreatic β-cells (for details, see Methods). In the following, we refer to these mice as *RIPII-*

barr2 Tg mice.

We subjected *RIPII-barr2* Tg mice and their wt littermates to the same in vivo metabolic tests as β-barr2-KO mice. In general, the phenotypes displayed by the *RIPII-barr2* Tg mice were opposite to those observed with the β-barr2-KO mice (Fig. 10.9).

When mice were maintained on regular chow (RC), GSIS was greatly enhanced in *RIPII-barr2* Tg mice, as compared to their wt littermates (Fig. 10.9a). The transgenic mice also showed a trend toward improved glucose tolerance (Fig. 10.9b). In an insulin tolerance test (ITT), *RIPII-barr2* Tg mice and wt littermates showed a similar degree of insulin sensitivity (Fig. 10.9c). Moreover, as compared to wt littermates, fed blood glucose levels were significantly lower in the transgenic mice consuming regular chow.

When maintained on a calorie-rich HFD, *RIPII-barr2* Tg mice and wt littermates showed a similar degree of weight gain (data not shown). Moreover, insulin sensitivity remained unaffected by the presence of the *RIPII-barr2* transgene (ITT; Fig. 10.9f). Strikingly, however, the transgenic mice displayed both a pronounced increase in GSIS (Fig. 10.9d) and greatly improved glucose tolerance (Fig. 10.9e). Fed and fasting blood glucose levels were significantly lower in the HFD transgenic mice, as compared to the corresponding wt littermates (data not shown). Thus overexpression of barr2 in β-cells greatly ameliorated the key metabolic deficits associated with the consumption of a HFD.

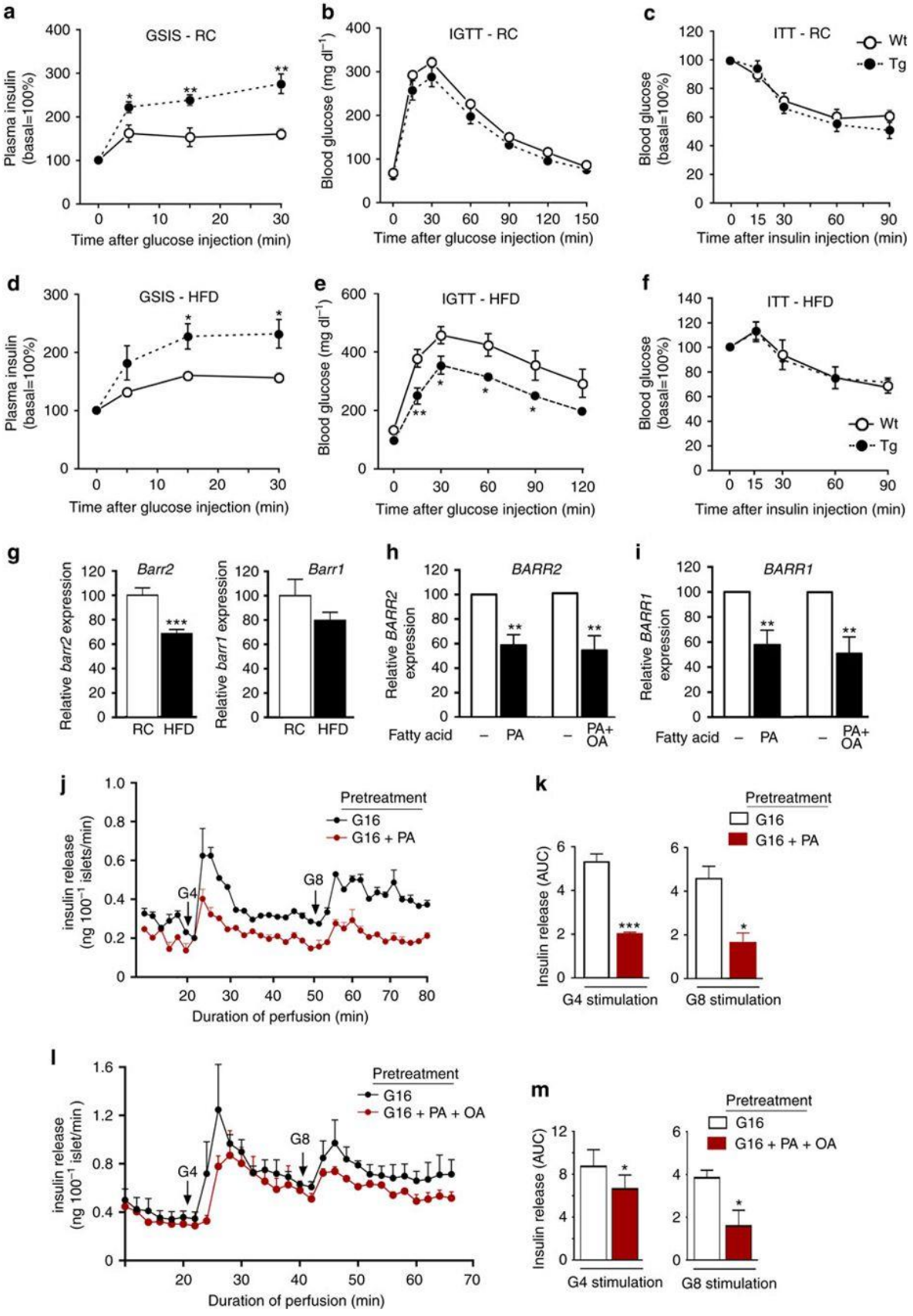
a
GSIS - RC
Plasma insulin (basal=100%)
Time after glucose injection (min)
b
IGTT - RC
Blood glucose (mg dl−1)
Time after glucose injection (min)
c
ITT - RC
Wt
Tg
Blood glucose (basal=100%)
Time after insulin injection (min)
d
GSIS - HFD
Plasma insulin (basal=100%)
Time after glucose injection (min)
e
IGTT - HFD
Blood glucose (mg dl−1)
Time after glucose injection (min)
f
ITT - HFD
Wt
Tg
Blood glucose (basal=100%)
Time after insulin injection (min)
g
Barr2
Relative barr2 expression
RC HFD
Barr1
Relative barr1 expression
RC HFD
h
BARR2
Relative BARR2 expression
Fatty acid – PA – PA+ OA
i
BARR1
Relative BARR1 expression
Fatty acid – PA – PA+ OA
j
Pretreatment
G16
G16 + PA
insulin release (ng 100−1 islets/min)
G4
G8
Duration of perfusion (min)
k
Pretreatment
G16
G16 + PA
Insulin release (AUC)
G4 stimulation
G8 stimulation
l
Pretreatment
G16
G16 + PA + OA
insulin release (ng 100−1 islet/min)
G4
G8
Duration of perfusion (min)
m
Pretreatment
G16
G16 + PA + OA
Insulin release (AUC)
G4 stimulation
G8 stimulation

Fig. 10.9. In vivo studies with transgenic mice overexpressing Barr2 in pancreatic β-cells. (**a-c**) In vivo metabolic tests carried out with *RIPII-barr2* Tg mice (Tg) and wild-type (wt) littermates maintained on regular chow (RC). (**a**) Glucose-induced insulin secretion (GSIS; 2 g glucose/kg i.p.). (**b**) I.p. glucose tolerance test (IGTT; 2 g glucose/kg i.p.). (**c**) Insulin tolerance test (ITT; 0.75 U insulin/kg i.p.). (**d-f**) *RIPII-barr2* Tg mice (Tg) and wt littermates were maintained on a high-fat diet (HFD) and subjected to the same tests as in (A-C). In (D) and (E), the glucose dose was reduced to 1 g/kg (i.p.). In (F), the insulin dose was 1 U/kg (i.p.). Mice were maintained on the HFD for at least 8 weeks. All studies were carried out with male mice (mouse age: RC, 8-12 weeks; HFD, 16-20 weeks). Data are given as means ± s.e.m. (6-9 mice per group); *p<0.05, **, p<0.01, as compared to the corresponding wt value (Student's t-test). (**g**) *Barr2* expression is reduced in islets of mice maintained on a HFD. Total RNA was prepared from pancreatic islets of wt mice (16-week old male C57BL/6NTac mice; 8 mice per group). Mice were maintained on either regular chow (RC) or on a HFD (for 8 weeks). Gene expression levels were determined via real-time qRT-PCR. Transcript levels were normalized relative to the expression of *β-actin* (for primer sequences, see Methods). Data represent means ± s.e.m. (***p<0.001; Student's t-test). (**h, i**) Reduced β-arrestin expression in human islets cultured in glucose-rich medium (16 mM) in the presence of 0.5 mM palmitic acid (PA) or a 2:1 mixture of PA and oleic acid (PA + OA; total fatty acid concentration: 0.5 mM) for three days. Relative *BARR2* (h) and *BARR1* (i) expression levels were determined by qRT-PCR (internal control gene: *β-ACTIN)*. *BARR2* and *BARR1* expression levels determined with islets that had not been exposed to PA or PA + OA were set equal to 100 in each individual experiment. Data are given as means ± s.e.m. (n=3 per group; islets were prepared from six different donors). **p<0.01, Student's t-test. (**j, l**) Impaired insulin secretion in human islets cultured in glucose-rich medium (16 mM) in the presence of 0.5 mM PA or a 2:1 mixture of PA and OA (total fatty acid concentration: 0.5 mM) for three days. Insulin release in response to 4 and 8 mM glucose (G4 and G8, respectively) was monitored using an islet perifusion system. Note that isolated human islets are far more sensitive to glucose than mouse or rat islets explaining why both G4 and G8 strongly promote insulin release in control islets. (400)

Decreased barr2 expression in islets from HFD mice. To examine whether the consumption of a HFD affects *barr2* expression in pancreatic islets, we carried out qRT-PCR studies using RNA prepared from islets of wt mice (16-week old male C57BL/6NTac mice) maintained on RC or a HFD. We found that HFD mice showed a significant reduction (by ~30%) of islet *barr2* expression (Fig. 10.9g). We also noted a trend toward reduced *barr1* expression levels in HFD mice (Fig. 10.9g).

*Glucolipotoxicity affects BARR2/1 levels in human islets***.** Elevated blood glucose and fatty acid levels are known to have deleterious effects on β-cell function including GSIS[40]. This phenomenon, referred to as "glucolipotoxicity", is predicted to play an important role in the pathogenesis of type 2 diabetes (T2D) (401). To mimic this process in human pancreatic islets in vitro, we exposed human islets for three days to high concentrations of glucose (16.7 mM) and palmitic acid (0.5 mM). Islet perifusion studies showed that GSIS was significantly reduced in human islets cultured in the presence of palmitic acid, as compared to islets cultured in its absence (Fig. 10.9j, k).

To explore whether glucolipotoxic conditions affected the expression levels of β-arrestins in human islets, we carried out qRT-PCR experiments using total RNA prepared from human islets that had been cultured for three days in glucose (16.7 mM)-rich medium either in the presence or absence of palmitic acid (0.5 mM). This analysis showed that both *BARR2* and *BARR1* expression were significantly reduced (by ~30-40%) under glucolipotoxic conditions (Fig. 10.9h, i). We obtained very similar results when we exposed human islets to a 2:1 mixture of palmitic and oleic acid (total fatty acid concentration: 0.5 mM) (Fig. 10.9h, i, l, m).

10.3 Discussion

Barr2, similar to barr1, can act as a scaffold to coordinate the activity of many important signaling proteins (19,189,374). Here we report the novel finding that barr2 expressed by pancreatic β-cells is required for proper β-cell function, both in mouse and human β-cells. We provide strong evidence that the presence of β-cell barr2 is critical for the proper function of CAMKII, a multi-functional Ser/Thr protein kinase. This novel, non-canonical activity of barr2 does not seem to require barr2 interactions with β-cell GPCRs.

Several lines of evidence suggest that the in vitro and in vivo phenotypes displayed by the β-barr2-KO mice are caused by impaired CAMKII function. First, the biochemical, electrophysiological, and metabolic deficits displayed by the β-barr2-KO mice closely mimic those described for a mutant mouse strain expressing a dominant negative version of CAMKII selectively in β-cells (393). These deficits also include impaired Ca^{2+} influx through LTCCs/VDCCs (Figs. 10.1, 10.2), suggesting that the deficits in Ca^{2+} influx caused by β-cell barr2 deficiency are most likely a consequence of impaired CAMKII activity. Consistent with this observation, co-immunoprecipitation studies using lysates from wt mouse islets demonstrated that barr2 forms a complex with CAMKII, but not with LTCCs (Fig. 10.8a). In addition, we found that expression of a constitutively active version of CAMKII in cultured β-cells (Fig. 10.5e, h) or wt mouse islets (Fig. 10.6) rescued the deficits in insulin secretion caused by barr2 deficiency. CAMKII also promotes insulin secretion via phosphorylation of various signaling proteins involved in insulin exocytosis, including synapsin I (393,397,398). CAMKII activation is dependent on its auto-phosphorylation at Thr-286 (399). Strikingly, we found that both synapsin I phosphorylation and CAMKII auto-phosphorylation were abolished in barr2-deficient β-cells (Fig. 10.7a-f).

In this context, it should be mentioned that Xiao et al. (79) demonstrated the formation of β-arrestin/CAMKII complexes following angiotensin II type 1a receptor activation in cultured cells. Moreover, Mangmool et al. (402) reported that β-arrestin-CAMKII-Epac1 complexes are functionally important in the mouse heart.

Taken together, these observations strongly support the concept that barr2 is required for the proper function of CAMKII in pancreatic β-cells and that impaired CAMKII activity can fully account for the deficits displayed by the β-barr2-KO mutant mice. Our findings, in combination with previous studies (79), are consistent with a model in which β-cell barr2, as part of a complex that includes CAMKII and probably other proteins, functions as a critical positive regulator of CAMKII function.

Hudmon et al. (403) demonstrated that the pore-forming α subunit of LTCCs ($Ca_v\alpha1.2$) is a CAMKII substrate and that tethering of CAMKII to LTCCs facilitates Ca^{2+} influx. It is therefore possible that a similar mechanism is operative in pancreatic β-cells. However, this notion remains to be tested experimentally.

Interestingly, while islets prepared from β-barr2-KO mice showed pronounced deficits in calcium homeostasis and glucose- or KCl-stimulated insulin secretion (Fig. 10.1), GSIS was only slightly reduced and glucose tolerance remained largely normal in β-barr2-KO mice consuming standard chow (Fig. 10.4a, b). One possible explanation for the discrepancy between the in vitro and in vivo findings is that other factors, such as islet innervation, hormonal stimulation of β-cells, or the involvement of non-β-cell pathways allow β-barr2-KO mice to maintain normal glucose homeostasis when maintained on regular chow. The identity of these pathways remains to be elucidated.

In contrast, when mice were fed a calorie-rich HFD, in vivo studies showed that GSIS was

virtually abolished in β-barr2-KO mice (Fig. 10.4d). Consistent with this finding, HFD β-barr2-KO mice showed a striking exacerbation of glucose intolerance (Fig. 10.4e) and greatly increased fed and fasting blood glucose levels. One possible explanation for the observation that β-cell barr2 deficiency causes pronounced metabolic deficits only in HFD mice is that barr2-independent signaling pathways are able to maintain normal β-cell function in healthy islets in vivo (regular chow mice). When β-cell function is compromised by the glucolipotoxic effects of a long-term HFD, these barr2-independent signaling pathways are probably no longer able to compensate for the deficits in β-cell function caused by the lack of barr2. Interestingly, mice lacking the exchange protein activated by cAMP islet/brain isoform 2A (EPAC2A KO mice) showed diet-dependent in vivo metabolic changes similar to those displayed by the β-barr2-KO mice (404).

Two recent reports described the function of pancreatic islets prepared from whole body barr2-KO mice that lacked barr2 throughout development (381,382). In contrast to our findings, Ravier et al. (381) reported that glucose-stimulated increases in insulin release and $[Ca^{2+}]_i$ were unchanged in islets prepared from whole body barr2-KO mice. Zhang et al. (382) demonstrated that GSIS was reduced in islets from whole body barr2-KO mice in a static islet incubation assay, similar to our findings with perifused β-barr2-KO islets. This deficit in GSIS was associated with a reduction in pre-docked insulin vesicles. However, we found that the total number and the density of pre-docked insulin granules were similar in β-barr2-KO and control islets. The most likely explanation for these discrepant observations is that the inactivation of *barr2* in essentially all body cells affects β-cell function in an indirect fashion and that the absence of barr2 during development is likely to trigger unpredictable changes in β-cell function and glucose homeostasis.

The two β-arrestins, barr1 and barr2, share a high degree of sequence identity (78% at the amino acid level) and act in a similar fashion in many but not all experimental systems (19).

Sonoda et al. (405) demonstrated that barr1 knockdown in cultured β-cells (INS-1 cells) led to a marked decrease in GLP1 receptor-mediated insulin secretion, implicating barr1 in the regulation of insulin secretion. Clearly, studies with conditional, β-cell-specific β-barr1-KO mice are needed to explore the potential role of barr1 in regulating β-cell function and whole body glucose homeostasis under in vivo conditions.

In patients with T2D and obese individuals, plasma free fatty acid levels are usually elevated, contributing to impaired β-cell function including reduced GSIS (406). Interestingly, we showed that exposure of isolated human pancreatic islets to glucolipotoxic conditions that impair β-cell function led to significant reductions in *BARR2* and *BARR1* expression levels (Fig. 10.9h, i). This finding, together with our observation that *barr2* knockdown impairs GSIS in both mouse and human β-cells (Fig. 10.1), suggests that strategies that promote barr2 expression and/or function in β-cells may prove beneficial for restoring impaired β-cell function. Consistent with this notion, pancreatic islets prepared from HFD mice showed reduced *barr2* levels (Fig. 10.9g) and barr2 overexpression in β-cells greatly ameliorated obesity-associated metabolic deficits (Fig. 10.9d, e).

In conclusion, we report the novel finding that barr2 is required for the proper function of pancreatic β-cells in vitro and in vivo. Several lines of evidence indicate that barr2-dependent activation of CAMKII represents the key mechanism through which barr2 exerts its beneficial effects on insulin release and Ca^{2+} entry into β-cells. These findings suggest the intriguing possibility that modulating barr2 function in β-cells may represent a potential new therapeutic approach for the treatment of T2D.

10.4 Materials and Methods

Generation of mice lacking barr2 in pancreatic β-cells. The generation of homozygous floxed *barr2* mice (*fl/fl barr2* mice) in which exon 2 is flanked by loxP sites is described in a separate publication (385). These floxed mice were obtained on a pure C57BL/6J background. *Pdx1-Cre-ER^{TM}* mice with a mixed genetic background were kindly provided by Dr. Doug Melton (Harvard University). We backcrossed the *Pdx1-Cre-ER^{TM}* mice for 10 generations onto a C57BL/6 background. Subsequently, we intermated the backcrossed *Pdx1-Cre-ER^{TM}* mice with the *fl/fl barr2* mice to generate *fl/fl barr2-Pdx1-Cre-ER^{TM}* mice and *fl/fl barr2* control littermates. When these mice were 8 weeks old, we injected them for 6 consecutive days with TMX (Sigma) suspended in corn oil (Sigma) (1 mg i.p. per mouse per day). All animals used were maintained on a C57BL/6 background.

All experiments were conducted according to US National Institutes of Health Guidelines for Animal Research and were approved by the NIDDK Institutional Animal Care and Use Committee.

Generation of mice overexpressing barr2 in β-cells. An HA-tagged version of rat *barr2* (Addgene) was used to generate a transgene construct in which the expression of *barr2* was under the transcriptional control of the *RIPII* promoter (390,407). The resulting 4.1 kb transgene was isolated, purified, and microinjected into the pronuclei of ova prepared from C57BL/6 mice (Taconic) (390). *RIPII-barr2* transgenic mice were identified via PCR analysis of tail DNA (see next paragraph). All mice were maintained on a pure C57BL/6NTac background.

PCR genotyping of mutant mice. Floxed *barr2* mice*:* The following PCR primer pair flanking exon 2 was used to distinguish between the wt *barr2* allele and the floxed *barr2* allele: forward primer, 5'-GAGTCACTGTATGGGTCCCTG-3'; reverse primer, 5'-

TTGCTGTTCGATGCTACATAACTC-3'. The use of these primers results in PCR products of the following sizes: wt allele, 349 bp; floxed allele, 507 bp. To detect the *Pdx1-Cre-ER*^{TM} transgene, we used the following PCR primers (size of PCR product, 400 bp): forward primer, 5'-CCTGGAAAATGCTTCTGTCCG-3'; reverse primer, 5'-CAGGGTGTTATAAGCAATCCC-3'.

RIPII-barr2 transgenic mice: To detect the *RIPII-barr2* transgene, we used the following PCR primers (size of PCR product, 618 bp): forward primer, 5'- AGTTCTGCTACCCATACGAC -3'; reverse primer, 5'- CTCCTTAGTCTCCTCCTCTTAT -3'. The following PCR cycling conditions were used: 95 °C for 5 min followed by 35 cycles at 95 °C for 30 s, 55 °C for 30 s, and 72 °C for 1 min.

Mouse maintenance and diet. Mice were fed ad libitum and kept on a 12-hr light, 12-hr dark cycle. Unless stated otherwise, all experiments were carried out with male littermates that were 10-20 weeks old and maintained on a standard mouse chow (4% (w/w) fat content; Zeigler). In a subset of experiments, 8-10-week-old male mice were switched to a high-fat diet (35.5 % (w/w) fat content; # F3282, Bioserv) for at least 8 weeks.

Morphometric analysis of pancreatic islets. Pancreata were fixed overnight in 4% paraformaldehyde/phosphate-buffered saline, and embedded in paraffin. For each pancreas, three consecutive 5 µm-thick sections from six distinct levels, 150 µm apart, were mounted on slides and subjected to standard hematoxylin/eosin staining. To determine β-cell mass, we used three mice per genotype (5-month-old males). Six whole pancreatic sections per animal (150 µm apart) were blocked with normal goat serum for 1 hr,and incubated overnight at 4 ^{o}C with a guinea-pig anti-insulin antibody (Thermo Scientific, PA1-26938, dilution 1:100) and a rabbit anti-glucagon antibody (Thermo Scientific, RB-1422-A1, dilution 1:100). The two primary antibodies were detected with Alexa Fluor 555 goat anti-guinea pig (red color, Invitrogen, A21435, dilution 1:500)

or Alexa Fluor 488 goat anti-rabbit (green color, Invitrogen, A11034, dilution 1:500), respectively. All sections were counterstained with DAPI (Vectashield mounting medium with DAPI, Vector Laboratories) to visualize nuclei (blue color). For β-cell mass analysis, slides were imaged on a Keyence digital microscope (BZ-9000) with a lens CFI Plan Apo 4x attached. Image acquisition and measurement of total pancreatic and β-cell specific area for each section were performed using BZ-II Viewer and BZ-II Analyzer software (version 2.1; Keyence). To determine β-cell mass, we calculated the ratio of islet cross-sectional area to total pancreatic area multiplied by pancreatic weight.

Drugs used for insulin release studies. Drugs employed for insulin release studies were purchased from Tocris Bioscience (nifedipine, FPL64176, oxotremorine-M, exendin-4, veratridine), Sigma (GLP-1), or Millipore (AIP2). The Drosophila homeoprotein Antennapaedia leader peptide (RQIKIWFQNRRMKWKK) was obtained from GenScript.

Mouse Islet perifusion studies. Islets were isolated from pancreata of control and mutant mice after collagen digestion (408). Dynamic measurements of insulin secretion were performed by using a high-capacity, automated islet perifusion system (Biorep Perifusion V2.0.0) (408-410). A low pulsatility peristaltic pump pushed HEPES-buffered solution (composition in mM: 125 NaCl, 5.9 KCl, 2.56 $CaCl_2$, 1 $MgCl_2$, 25 HEPES, and 0.1% BSA; pH 7.4) at a perifusion rate of 100 µl/min through a column containing 100 pancreatic islets immobilized in Bio-Gel P-4 Gel (BioRad). In all perifusion experiments, basal glucose concentrations were adjusted to 3 mM. Stimuli (16 mM glucose for 15 min or 25 mM KCl for 5 min, respectively) were applied with the perifusion buffer. The perifusate was collected in an automatic fraction collector designed for a 96 well plate format. The columns containing the islets and the perifusion solutions were kept at 37 ºC, and the perifusate in the collecting plate was kept at < 4 ºC. Perifusates were collected every

minute. Insulin release in the perifusate was determined with an ultra-sensitive mouse insulin Elisa kit (Mercodia). DNA extracted from islets was quantified using the PicoGreen kit (Invitrogen) and used for normalization of islet size and number. We calculated the area under the curve (AUC) over the 15-min stimulation period with high glucose or the 5-min KCl stimulation period to determine the total amount of insulin secreted during these stimulatory conditions.

Cytoplasmic Ca^{2+} measurements. To determine cytoplasmic Ca^{2+} concentrations ($[Ca^{2+}]_i$), we used a Fura-2-based imaging procedure (408-410). Mouse pancreatic islets were immersed in HEPES-buffered solution. Glucose was added to a final concentration of 3 mM. Islets were incubated in Fura-2 AM (2 μM) for 1 hr and placed in a small-volume imaging chamber (Warner Instruments). Stimuli were applied with the bathing solution. Islets loaded with Fura-2 were alternatively excited at 340 and 380 nm with a monochromator light source (Cairn Research Optoscan Monochromator, Cairn Research Ltd, Faversham, UK). Images were acquired with a Hamamatsu camera (Hamamatsu Corp., Japan) attached to a Zeiss Axiovert 200 microscope (Carl Zeiss, Jena, Germany). Changes in the 340/380 nm fluorescence emission ratio after addition of high glucose (16 mM) or KCl (25 mM) were analyzed over time in individual islets using MetaFluor imaging software. Peak changes in the fluorescence ratio were measured to compare response profiles between islets (delta $[Ca^{2+}]_i$ = (maximum 340/380 value) - (baseline 340/380 value)). In all experiments, the basal concentration of glucose was 3 mM.

Determination of pancreatic insulin content. Total pancreatic insulin content was measured by using an acid-ethanol method.

Immunohistochemistry and imaging studies (mouse islets). Immunohistochemical stains were performed using standard procedures. Fluorescent images were captured and processed under identical parameters with a Zeiss Imager D1 fluorescent microscope. Confocal images were

obtained and processed using an LSM 700 confocal microscope with a 20×/0.45 N-Achroplan objective (Zeiss, Germany). The antibodies used are included in Supplementary Table 2.

Western blotting studies. Western blotting studies were carried out with lysates prepared from MIN6 cells or isolated pancreatic islets by using standard techniques (411). Protein bands were quantitated by using ImageJ software (NIH). The antibodies used are listed in Supplementary Table 2. Original uncropped blots are presented in Supplementary Fig. 16 and 17.

Determination of gene expression levels via qRT-PCR. Gene expression levels were measured via qRT-PCR using total RNA prepared from different mouse tissues, human pancreatic islets or cultured MIN6 cells. The PCR primers used for qRT-PCR experiments are listed in Supplementary Table 3.

Perforated patch electrophysiology. β-Cells on the periphery of islets were sealed in voltage clamp at -80 mV (>2 giga-ohm seal). Patch electrodes were pulled with tip resistance between 3–4 micro-ohms and loaded with intracellular solution containing (in mM) 140 KCl, 1 $MgCl_2[H_2O]_6$, 10 EGTA, 10 HEPES (pH 7.25 adjusted with KOH) and the pore-forming antibiotic amphotericin B (Sigma) (412). After perforation of the plasma membrane by amphotericin B, the cell was transitioned to current clamp mode (412). Islets were treated with 3- or 16-mM glucose dissolved in Krebs-Ringer-buffer (KRB) of the following composition (in mM): 119 NaCl, 2 $CaCl_2$, 4.7 KCl, 10 HEPES, 1.2 $MgSO_4$, and 1.2 KH_2PO_4 (pH 7.35 adjusted with NaOH). The starting glucose concentration was 3 mM and was followed by 16 mM glucose for 10-20 min. The frequency of action potential firing in response to 16 mM glucose was determined.

*Whole cell voltage clamp electrophysiological recordings***.** VDCCs, K_{ATP} and K_V currents were recorded from dispersed, primary mouse β-cells with the whole cell voltage clamp technique (393). Patch electrodes were pulled with tip resistance between 3–4 micro-ohms. For VDCC

recordings, patch electrodes were loaded with intracellular solution containing (in mM): 102 CsCl, 10 tetraethylammonium chloride, 0.1 tolbutamide, 10 EGTA, 1 $MgCl_2$, 3 Na_2ATP, 5 HEPES, pH 7.4, adjusted with CsOH. Whole β-cell seals (>1 giga-ohm) were made in KRB buffer in the presence of 3 mM glucose followed by perifusion with a modified, high Ca^{2+}-containing KRB buffer of the following composition (in mM): 82 NaCl, 20 tetraethylammonium chloride, 0.1 tolbutamide, 30 $CaCl_2$, 5 CsCl, 1 $MgCl_2$, 0.1 EGTA, 10 glucose, 5 HEPES, pH 7.4, adjusted with NaOH. After perfusion of β-cells for 3 min with this buffer, the first voltage step recording protocol was initiated. Subsequently, K_V and K_{ATP} voltage clamp recordings were performed and analyzed using Clampfit software (Molecular Devices) (393).

Preparation of islets for electron microscopic studies. Male mice (age: 2-3 months) were anaesthetized with ketamine (50 mg kg^{-1} i.p.). Collagenase solution (Sigma) was injected into the bile duct to inflate the pancreas. After digestion, islets were manually selected and washed in Krebs-Ringer HEPES buffer and cultured overnight in RPMI-1640 medium (Invitrogen) before further experiments (413,414).

To prepare specimens for serial block-face scanning electron microscopy (SBF-SEM), a heavy metal staining procedure was used to fix and stain islets (415). After staining, the samples were dehydrated and embedded in Epon-Araldite according to standard protocols.

To minimize specimen charging by the electron beam of the SEM, each epon-embedded islet was mounted on an empty resin block and trimmed under a microtome until the stained islet became exposed in the block. The block was subsequently remounted by gluing the exposed face downwards on an aluminum specimen pin (Gatan) using CircuitWorks Conductive Epoxy (CW2400) so that the tissue could maintain electrical contact with the pin. Each specimen block was then trimmed again to expose the opposite side of the islet and coated with 40-100 nm gold

using a Quorum Q150RS sputter coater (EM Sciences).

SBF-SEM. The trimmed, epon-embedded, stained blocks were imaged using a Gatan 3View serial block-face imaging system installed on a Zeiss SIGMA-VP (variable pressure) SEM. The SEM was operated in high-vacuum mode, with an accelerating voltage of 1.5 kV and a standard 30 µm condenser aperture. Block face images were collected with a pixel size of 9.9 nm in the x-y plane with removal of 50 nm slices along the z-axis, and a pixel dwell time of 1.5 µs. The resulting image series were aligned using Digital Micrograph software (Gatan) and uploaded to Amira software (FEI Inc.) for 3D visualization and quantitative analysis of individual beta cells from each genotype.

*Determination of the total number of dense-core vesicles***.** The total number of dense core vesicles (DCVs) per β-cell was estimated by utilizing a combination of 3D volume measurements and 2D vesicle density measurements (416). The cellular, nuclear, and mitochondrial volumes per β-cell were measured using Amira software, after which the nuclear and mitochondrial volumes were subtracted from the cell volume to determine the volume available to DCVs. To determine the average vesicle density in each β-cell, five vesicle-rich squares of size 2 µm x 2 µm were extracted from SBF-SEM planes at roughly even intervals throughout each cell. In each square, the number of DCVs per unit area n_{gran} was determined and the average n_{gran} was used to calculate the number of DCVs per unit volume ρ_{gran}:

$$\rho_{gran} = \frac{n_{gran}}{D_{dense\ core} + d}$$

where $D_{dense\ core}$ is the average diameter of the vesicle's dense core, and d is the slice thickness. The average DCV dense core diameter has been previously measured to be 240±42 nm (417). Measurements of ρ_{gran} were multiplied with available DCV volumes to yield estimates of the total DCV number in each β-cell.

*Measurement of the density of docked DCVs***.** The density of DCVs docked at the plasma membrane in each β-cell was determined by first selecting a single region along the cell membrane with a surface area of at least 30 μm^2. Surface areas of selected regions were computed in Digital Micrograph using the software's measurement tools to determine the width and height of the region. Successive slices throughout the 3D dataset were then examined to manually count the number of DCVs in direct contact with the membrane at any instance in the selected region.

Physiological studies. In vivo metabolic tests were performed using standard procedures. In brief, to measure glucose tolerance (IGTT), mice were fasted overnight for 12 hr. Blood glucose concentrations were determined using blood collected from the tail vein immediately before and 15, 30, 60, 90 and 120 min after i.p. injection of glucose (regular chow, 2 g kg^{-1}; HFD, 1 g kg^{-1}). To obtain a measure of peripheral insulin sensitivity (ITT), mice were fasted for 4 hr, and blood glucose concentrations were measured before and at the indicated time points after i.p. injection of human insulin (regular chow, 0.75 U kg^{-1}; HFD, 1 U kg^{-1}; Novo Nordisk). Blood glucose levels were determined using an automated blood glucose reader (Glucometer Elite Sensor; Bayer). To study glucose-stimulated insulin secretion (GSIS), mice were fasted overnight for 12 hr, and then injected with the same doses of glucose (i.p.) as used for the IGTT. Blood samples were collected from the tail vein at different time points (0, 5, 15 and 30 min) and centrifuged for plasma collection (3,000 g, 5 min, 4 ^{o}C). Plasma insulin concentrations were determined by using an ELISA kit (Crystal Chem Inc.).

Measurement of CAMKII activity in mouse pancreatic islets. CAMKII activity assays were carried out with isolated mouse pancreatic islets (418). In brief, islets (200-300/tube) were pre-incubated in KRBH buffer with 2.8 mM glucose for 15 min at 37 °C, and then transferred to either low glucose (2.8 mM) or high glucose (28 mM) KRBH buffer. After a 2.5 min incubation period,

islets were sonicated on ice with 50 µl of lysis buffer containing 20 mM Tris/HCl, pH 8.0, 2 mM EGTA, 2 mM EDTA, 10 µg/ml aprotinin, 2 mM DTT, 1 mM PMSF, and proteinase and phosphorylase inhibitors (Roche). CAMKII activity was determined with a widely used assay kit (SignaTECT Calcium/Calmodulin-Dependent Protein Kinase Assay System, V8161; Promega). This kit involves the use of biotinylated CAMKII peptide substrate to determine CAMKII-dependent phosphorylation. Phosphorylation reactions were initiated by mixing 5 µl of islet homogenate with 25 µl of a solution containing (final concentrations) 50 mM Tris–HCl (pH 7.5), 10 mM $MgCl_2$, 0.5 mM DTT, 0.1 mM ATP, 0.5 µCi [γ^{32}P]-ATP (3000 Ci/mmol, 10 mCi/ml; PerkinElmer), and biotinylated substrate (concentration: 50 µM). Total CAMKII activity was determined in the presence of 1 mM $CaCl_2$ and 1 µM calmodulin. Ca^{2+}-independent, autonomous CAMKII activity was assessed in the presence of 1 mM EGTA and the absence of $CaCl_2$/calmodulin. After a 2 min incubation period at 30 °C, the reaction was terminated by the addition of guanidine hydrochloride (final concentration: 2.5 M). Following a centrifugation step at 12,000 g for 1 min, 10 µl of supernatant was spotted onto a pre-numbered square of membrane impregnated with streptavidin. Membranes were washed and dried according to the manufacturer's instructions. The amount of ^{32}P bound to the membrane squares was measured via a liquid scintillation counting. CAMKII activities were normalized to the amount of protein contained in each sample.

Insulin release studies with cultured β-cells (MIN6 cells). MIN6 cells were a kind gift from Dr. Abner Notkins (NIDCR, NIH) (original source: Dr. J. Miyazaki, University of Osaka, Japan). For gene silencing studies, ~1 x 10^6 MIN6 cells were electroporated with 100 pmoles of mouse *barr2* siRNA or negative control siRNA (SMARTpool siRNA; Dharmacon), according to the manufacturer's instructions (Dharmacon). In a subset of experiments, cells were infected with the

KD-CAMKIIδ or CA-CAMKIIδ adenoviruses (100 MOI (multiplicity of infection)) ~24 hr after electroporation. About 48 hr after electroporation, insulin secretion studies were carried out with transfected/infected MIN6 cells grown in 6-well plates. In brief, cells were pre-incubated with Krebs-Ringer HEPES (KRBH) buffer for 30 min, and then switched to either low glucose (2.8 mM) or high glucose (16.7 mM) KRBH buffer. KCl-induced insulin secretion was monitored via incubation of MIN6 cells with KRBH buffer containing 30 mM KCl (1 hr at 37 ^{o}C; 2.8 mM glucose). The amount of insulin released into the medium was measured by using an ELISA kit (Crystal Chem Inc.).

Adenoviral transduction of mouse pancreatic islets. Mouse pancreatic islets were isolated and transduced with adenoviruses using a published procedure (419) with minor modifications. In brief, islets were isolated from 10- to 16-week-old male mice by collagenase digestion and Histopaque gradient purification. Islets were then immediately transduced at an MOI of 100 with either Ad-GFP or Ad-CA-CAMKIIδ for overnight at 37 °C. After washing, islets were incubated for another 24 hr in RPMI 1640 medium at 37 °C in the presence of 5% CO_2. For insulin secretion assays, islets were first pre-incubated with KRBH buffer for 30 min and then switched to either low glucose (2.8 mM) or high glucose (28 mM) KRBH buffer, followed by a 1 hr incubation at 37 °C. Insulin measurements were carried out as described in the previous paragraph.

*Insulin secretion studies with human EndoC-βH1 cells***.** EndoC-βH1 cells (388) were a kind gift by Dr. Raphaël Scharfmann (INSERM U1016, Institut Cochin, Université Paris Descartes, France). Briefly, EndoC-βH1 cells were cultured in a humidified incubator at 37 °C, 5% CO_2, with DMEM (Life Technologies) containing 1 mg ml^{-1} glucose, 2% albumin from bovine serum fraction V (Equitech), 50 µM 2-mercaptoethanol (Sigma), 10 mM nicotinamide (VWR), 5.5 µg ml^{-1} transferrin (Sigma), 6.7 ng ml^{-1} sodium selenite (Sigma) and penicillin (100 units ml^{-}

^{1})/streptomycin (100 μg ml^{-1}). The culture supports were pre-coated with medium containing ECM (1%; Sigma) and fibronectin (2 μg ml^{-1}; Sigma). Cells were passaged every 5-7 days and maintained at a density of ~6 x 10^6 cells per 10 cm^2 dish. For gene silencing studies, ~1 x 10^6 cells were electroporated with 100 pmoles of human *barr2* siRNA or scrambled control siRNA (SMARTpool siRNA; Dharmacon), according to the manufacturer's instructions (Dharmacon). Two days after plating of the cells, the medium was replaced with DMEM without glucose, and cells were allowed to continue to grow overnight. Insulin secretion studies were then carried out using the same strategy as described above for murine MIN6 cells. In brief, cells were pre-incubated with Krebs-Ringer HEPES (KRBH) buffer with 0.5 mM glucose for 1 hr, and then switched to same KRBH buffer with different concentrations of glucose (0.5 mM or 25 mM, respectively) containing 500 μM IBMX for 1 hr at 37 °C. Insulin concentrations were measured by using a human insulin ELISA kit (Alpco Inc.).

Human pancreatic islets: source and culture. Human pancreatic islets were received from the accredited Human Islet Resource Center at the University of Pennsylvania. Islets were obtained from six individuals, who were normoglycemic at the time of organ isolation. Human islets were then cultured and transferred to the laboratory (420,421). The work with the human islets was carried out at the University of Pennsylvania. Islets are not identified with regard to donor. Only information on diabetes status, gender, age, race, and cause of death is received. Because of these factors, this research is considered non-human research by the Institutional Review Board of the University of Pennsylvania.

Preparation of fatty acid solutions. A 5 mM stock solution of sodium palmitate (Sigma-Aldrich) was prepared by dissolving the fatty acid salt in 10% BSA (Sigma-Aldrich, fraction V, fatty acid-free) in Krebs buffer by continuous stirring for ~4 hr in a 37 °C water bath. The stock

solution was then diluted by Krebs buffer to obtain the final concentration of 0.5 mM sodium palmitate. To prepare a 2:1 mixture of palmitate and oleate (final fatty acid concentration: 0.5 mM), sodium palmitate was dissolved first, followed by the addition of the proper amount of sodium oleate (Sigma-Aldrich).

Perifusion of human islets for insulin release measurements. Handpicked human islets (180 islets per group) were placed on a nylon filter and perfused at a flow rate of 1.2 ml per min in a plastic perifusion chamber (Millipore) (422). The perifusion apparatus consisted of a computer-controlled low-pressure chromatography system (BIO-RAD Econo system) with programmable rates of flow and glucose concentrations in the perfusate, a 37 °C water bath, and a fraction collector (BIO-RAD; model 2128). The perifusion solution was a Krebs buffer (pH 7.4) containing (in mM): 114 NaCl, 5 KCl, 24 $NaHCO_3$, 1 $MgCl_2$ $6H_2O$, 2.2 Ca^{2+}, 1 Pi, 10 HEPES (pH 7.4), and 1% of BSA (Sigma-Aldrich: fraction V, fatty acid-free) equilibrated with 20% O_2 and 5% CO_2 balanced with N_2. Insulin secretion was initiated by incubating islets consecutively with 4- and 8-mM glucose. We applied these rather low glucose concentrations since human islets are far more sensitive to glucose than mouse or rat islets (10 mM glucose causes a maximum insulin response in human islets (422)).The area under curve (AUC) for glucose (4 or 8 mM)-stimulated insulin release was calculated using GraphPad software (Prism 6.0.) qRT-PCR studies with total human islet RNA were carried out in the same fashion as described above for mouse islet RNA.

Co-immunoprecipitation of endogenous barr2/CAMKII complexes. Wt islets (~1,000) were lysed in co-IP lysis buffer containing 20 mM Tris ·HCl (pH 8.0), 137 mM NaCl, 2 mM EDTA, 1% Nonidet P-40, and a mixture of protease and phosphatase inhibitors (Roche). After centrifugation (16,000 x g at 4 °C for 10 min), the supernatant was divided into two aliquots. Immunoprecipitation studies were performed as described (423). In brief, samples were incubated

overnight at 4 °C with either an anti-CaMKIIδ antibody (goat IgG, Santa Cruz) or the same amount of goat IgG (Santa Cruz). After this step, reaction mixtures were incubated with protein A/G PLUS agarose beads (Santa Cruz) for 4 h at 4 °C. The immunoprecipitated proteins were washed three times with a buffer containing 10 mM Tris ·HCl (pH 7.4), 150 mM NaCl, 1 mM EDTA, 1 mM EGTA, and 1% Triton X-100, followed by SDS-PAGE analysis.

Immunoblots were probed with anti-barr2, anti-CaMKII (pan), and anti-$Ca_V1.2$ (α_1 (α1 subunit) antibodies, using the Quick Western Kit (IRDye 680RD, LI-COR Biosciences). Western blots were scanned and validated with an infrared imaging system (Odyssey CLx; LI-COR Biosciences). The antibodies used are listed in the Supplementary Table 2 above.

Co-immunoprecipitation studies using barr2 fragments. HEK293T cells grown in 60-mm plates were transfected with expression plasmids (3 μg each) coding for HA-tagged full-length barr2, the N-domain of barr2 (residues 1-181), or the C-domain of barr2 (residues 180-408). All constructs carried an N-terminal HA epitope tag (171). Subsequently, transfected cells were infected with an adenovirus (100 MOI) coding for flag-CAMKIIδ or an empty control adenovirus (viruses were a kind gift by Dr. Harold Singer, Albany Medical College, NY, USA). About 24 hr after the addition of virus, cells were lysed, and co-immunoprecipitation studies were carried out as described in the previous paragraph. Flag-CAMKIIδ was immunoprecipitated with an anti-flag antibody (anti-flag M2 antibody, Sigma). The HA-tagged barr2 fragments and full-length barr2 were detected via Western blotting using a rabbit anti-HA monoclonal antibody (Cell Signaling).

MBP pull-down assay. Purified CAMKIIδ (CAMKII) was a kind gift by Dr. Andy Hudmon (Indiana University, Indianapolis, Indiana, USA). We followed a pull-down protocol very similar to that described by Zhan et al. (104). In brief, purified MBP-barr2 (ref. 39) or MBP alone (5 μg each) were incubated with purified JNK3 (JNK3α2; positive control) or CAMKII (μg each) and

amylose resin (25 µl; NEB) in 500 µl binding buffer (20 mM Tris-HCl pH 8, 137 mM NaCl, 1% Nonidet P-40, and 2 mM EDTA) supplemented with EDTA-free protease inhibitor (Roche) for 3 hr at 4 °C under gentle rotation. Final protein concentrations were: MBP-barr2 and MBP, ~0.11 µM; JNK3 and CAMKII, ~0.18 µM. The resin was then washed three times with wash buffer containing 10 mM Tris-HCl pH 7.4, 150 mM NaCl, 1 mM EDTA, 1 mM EGTA, and 1% Triton X-100. Bound proteins were eluted with 100 µl buffer containing 50 mM HEPES pH 7.3, 150 mM NaCl, and 50 mM maltose. Eluates were analyzed by SDS-PAGE and Western blotting.

Statistical analysis. Data are expressed as means ± s.e.m. for the indicated number of observations. The statistical tests used are indicated in the figure legends.

Data availability. The authors declare that all data supporting the findings of this study are available within the paper (and its supplementary information files).

CHAPTER 11

HEPATIC β-ARRESTIN-2 IS ESSENTIAL FOR MAINTAINING EUGLYCEMIA

This article was published in Journal of Clinical Investigation (424). Lu Zhu was first author, and Mario Rossi, Yinghong Cui, Regina J. Lee, Wataru Sakamoto, **Nicole A. Perry**, Nikhil M. Urs, Marc G. Caron, Vsevolod V. Gurevich, Grzegorz Godlewski, George Kunos, Minyong Chen, Wei Chen, and Jurgen Wess contributed to this work. Specific contribution: BRET experiments. Relation to dissertation work: This chapter builds on the previous article and details the specific role of arrestin-3 in hepatic cells.

.

11.1 Introduction

Type 2 diabetes (T2D) has emerged as a major health problem world-wide (425). One of the key pathophysiological features of T2D is an increase in hepatic glucose production (HGP) (426-428). HGP is modulated by the activity of several G protein-coupled receptors (GPCRs) including hepatic glucagon receptors (GCGRs) which play a key role in maintaining euglycemia (428-430). The GCGR, which is abundantly expressed in hepatocytes, is coupled to the stimulatory G protein, G_s, which triggers pronounced increases in HGP through a pathway that involves cAMP-mediated activation of PKA (430,431). Importantly, glucagon levels are inappropriately elevated in patients suffering from T2D, suggesting that enhanced GCGR activity may play a central role in the pathophysiology of T2D (428,432).

To explore novel strategies to inhibit GCGR signaling for therapeutic purposes, it is essential to delineate cellular pathways and signaling molecules that modulate GCGR activity.

However, at present, little is known about which processes regulate GCGR function in vivo.

The activity of almost all GPCRs is modulated by a pair of proteins known as β-arrestin-1 and -2 (alternative names: arrestin-2 and -3, respectively) (370,433,434). β-arrestins promote GPCR desensitization and internalization (435) but can also act as signaling proteins in their own right (376). For example, Olefsky and coworkers (405,436) recently identified β-arrestin-mediated signaling pathways that regulate key metabolic functions.

At present, it remains unknown whether hepatic GCGR activity is regulated by β-arrestins in vivo, and, if yes, whether this regulation is physiologically relevant. To address this issue, we generated mutant mice that lack β-arrestin-2 (barr2) or β-arrestin-1 (barr1) selectively in hepatocytes (hep-barr2-KO and hep-barr1 KO mice, respectively). We demonstrate that hep-barr2-KO display pronounced deficits in whole body glucose homeostasis, due to enhanced signaling via hepatic GCGRs. Our findings indicate that hepatic barr2 is critical for maintaining euglycemia by acting as a potent negative regulator of hepatic GCGR signaling in vivo. These new data raise the possibility that strategies that can stimulate or mimic hepatic barr2 activity may prove beneficial to suppress exaggerated hepatic GCGR signaling for therapeutic purposes (428,437).

11.2 Results and Discussion

Generation of mice lacking β-arrestin-2 (barr2) in hepatocytes. To generate hepatocyte-specific barr2 KO mice, we injected floxed *barr2* mice (385) via the tail vein with an adeno-associated virus (AAV) coding for Cre recombinase (AAV-TBG-Cre) (438). For control purposes, we injected another set of floxed *barr2* mice with the AAV-TBG-EGFP virus (438) which codes for EGFP (control mice). Two weeks after virus administration, we monitored *barr2* and *barr1* expression levels using RNA prepared from primary hepatocytes (Fig. 11.1A, C).

Treatment of floxed *barr2* mice with the AAV-TBG-Cre virus resulted in a pronounced and selective reduction of *barr2* mRNA expression in hepatocytes (Fig. 11.1A). Moreover, barr2 protein expression was no longer detectable in hepatocytes from these mice (Fig. 11.1B). *Barr2* deletion in hepatocytes had no significant effect on hepatic *barr1* expression levels (Fig. 11.1C), indicating that barr2 deficiency in hepatocytes does not lead to compensatory changes in the expression levels of *barr1*. Thus, we refer to floxed *barr2* mice treated with the AAV-TBG-Cre virus as 'hep-barr2-KO mice' throughout this study.

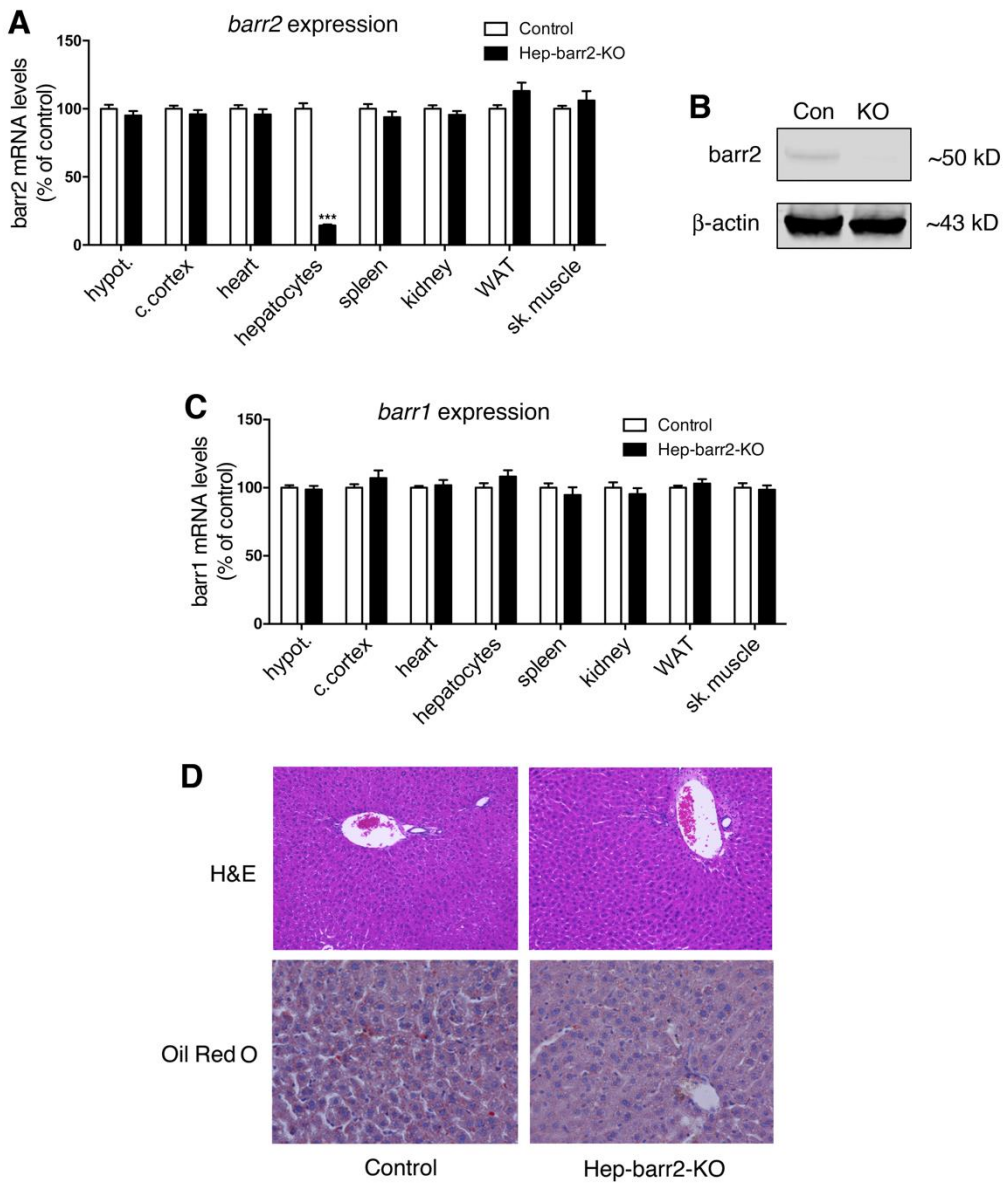

Fig. 11.1. Generation of mutant mice selectively lacking barr2 in hepatocytes (hep-barr2-KO mice) and histochemical studies with liver slices. (**A**) *Barr2* transcript levels are selectively reduced in hepatocytes of hep-barr2-KO mice. (**B**)Representative Western blot indicating the lack of barr2 protein in hepatocytes of hep-barr2-KO mice. The antibody used is selective for barr2 (Cell Signaling; # 3857). (**C**) *Barr1* mRNA levels are not affected by the lack of barr2 in hepatocytes. *Barr2* and *barr1* transcript levels were examined by qRT-PCR using *®-actin* expression as an internal control. Template RNA was prepared from the indicated tissues. Data are given as means ± SEM (3 mice per genotype, 10-week-old males). ***p<0.001, as compared to control (Student's t-test). hypot., hypothalamus; c. cortex, cerebral cortex; WAT, white adipose tissue; sk. muscle, skeletal muscle. (**D**) Lack of barr2 in hepatocytes does not affect mouse liver morphology. Liver sections from fasted hep-barr2-KO mice and their control littermates (10-week-old males) were stained with either H&E (upper panels) or Oil Red O (lower panels). The images shown are representative of results from 10 mice per group.

Hep-barr2-KO mice appeared healthy and had similar whole body and liver weights as their corresponding control mice. Moreover, livers from hep-barr2-KO mice displayed no obvious morphological deficits (Fig. 11.1D).

Hepatic insulin action is not impaired hep-barr2-KO mice. In a previous study, Luan et al. (377) proposed that barr2 is required for proper insulin signaling in hepatocytes, and that the formation of an insulin receptor/barr2 complex is essential for maintaining euglycemia. We therefore reexamined this concept by studying hepatic insulin receptor signaling in the newly generated hep-barr2-KO mice. In contrast to the results obtained with whole body barr2 KO mice (377), we found that hep-barr2-KO mice showed normal insulin sensitivity in an i.p. insulin tolerance test (ITT; Figure 11.2A). Moreover, in contrast to data reported by Luan et al. (377), insulin stimulated the phosphorylation of Akt and GSK3α/β, two signaling proteins that are critically involved in hepatic insulin signaling, to a similar extent in primary hepatocytes prepared from hep-barr2-KO mice and control littermates (Figures 11.2B and 11.2C). Finally, hyperinsulinemic euglycemic clamp studies did not reveal any significant changes in steady-state glucose infusion rates (GIR) between hep-barr2-KO and control mice (Figures 11.2D and 11.2E), in agreement with the ITT data (Figure 11.2A). Plasma insulin levels were similar in hep-barr2-KO and control mice during the final 40 min of the clamp procedure (human insulin in mU/l: 38.7 ± 2.3 and 41.8 ± 4.9, respectively; n=4).

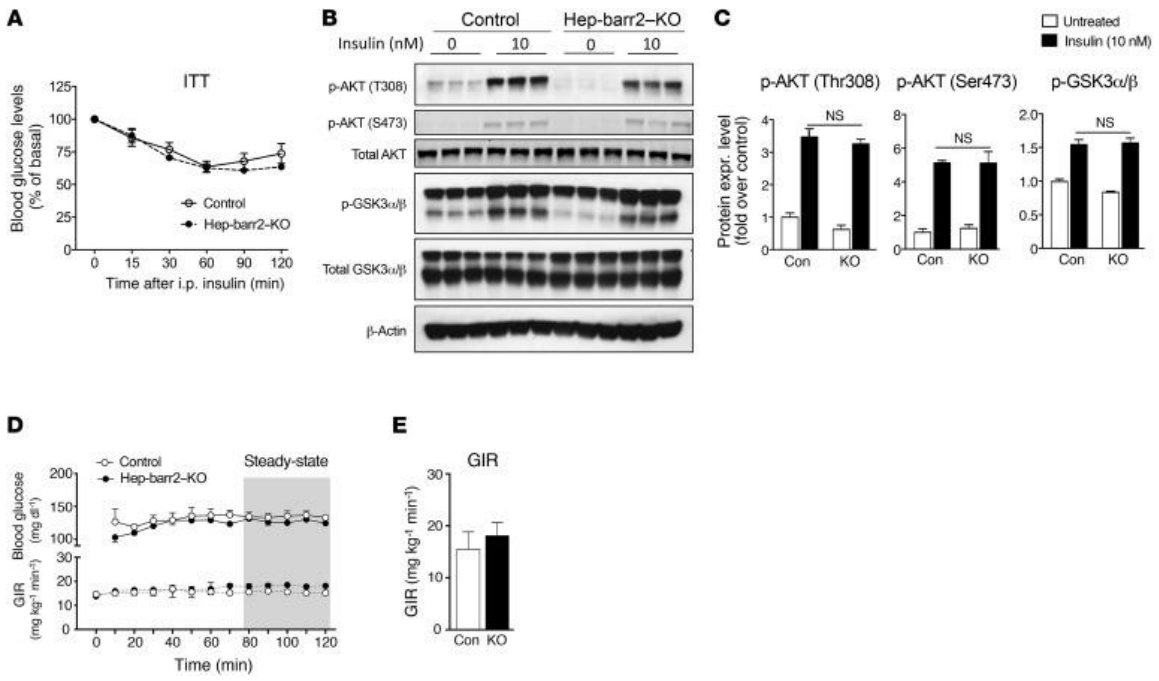

Fig. 11.2. Insulin signaling is not impaired in hep-barr2-KO mice. A) I.p. insulin tolerance test (ITT). Data are given as means ± SEM (n=9 mice per group, 20-week-old males). (**B**) Insulin-induced phosphorylation of Akt and GSK3α/β remains unaffected by the lack of barr2 in hepatocytes. Primary hepatocytes prepared from hep-barr2-KO and control mice were incubated with insulin (10 nM) or saline for 15 min. Cell lysates were used for immunoblotting with the indicated antibodies. Representative blots are shown. (**C**) Quantification via densitometry (NIH ImageJ software) of the immunoblotting data shown in (B). Phospho-protein expression levels were normalized by total Akt or total GSK3 α/β expression, respectively. Data represent means ± SEM (n=5 mice per group, 16-20-week-old males). n.s., no statistically significant difference. (**D, E)** Hyperinsulinemic euglycemic clamp studies. In (D), the time course of blood glucose and glucose infusion rate (GIR) are shown. Data in panel (E) were obtained during the steady-state period of the clamp (gray area in (D)). Values are given as means ± SEM (n=3 or 4 mice per group, 20-week-old males).

These new findings clearly indicate that the lack of barr2 in hepatocytes has no significant effect on insulin sensitivity. One possible reason for the discrepant findings reported by us (this study) vs. Luan et al. (377) is that the previous study examined whole body barr2 KO mice. Since barr2 is expressed in most tissues and cell types (370), hepatic insulin signaling may have been affected indirectly by barr2 deficiency in other tissues. Moreover, since barr2 regulates many important developmental functions (379,380), it is also possible that general barr2 deficiency throughout development triggers compensatory cellular/physiological changes (see, for example, (439)).

Barr2 acts as a potent negative regulator of hepatic glucagon receptor signaling. We next subjected hep-barr2-KO mice and their control littermates to a series of in vivo metabolic tests. Blood glucose levels were significantly increased in both fed and fasted hep-barr2-KO mice. In contrast, plasma insulin and glucagon levels were not significantly different between hep-barr2-KO and control mice.

Interestingly, following an acute dose of i.p. glucose, hep-barr2-KO mice showed significantly impaired glucose tolerance, as compared to their control littermates (Figure 11.3A). I.p. glucose treatment caused comparable changes in plasma insulin, glucagon, and GLP-1 levels in hep-barr2-KO and control mice (Figure 11.4). Since insulin signaling is intact in hep-barr2-KO hepatocytes, we hypothesized that hepatic barr2 deficiency may lead to enhanced hepatic GCGR signaling. To test this hypothesis, we treated hep-barr2-KO mice and their control littermates with a single i.p. dose of an anti-GCGR monoclonal antibody (mAb7.v44; 10 mg/kg). In control experiments, this antibody completely prevented glucagon (16 μg/kg i.p.)-induced increases in blood glucose levels in WT C57BL/6 mice (Figure 11.5). Remarkably, following treatment of hep-barr2-KO mice with the anti-GCGR antibody, the mutant mice did no longer display impaired glucose tolerance (Figures 11.3A and 11.3B). This observation suggests that the impairment in glucose tolerance caused by hepatic barr2 deficiency is probably due to enhanced hepatic GCGR signaling. Consistent with this concept, previous studies have shown that elevated plasma glucagon levels (which are predicted to stimulate GCGR activity) lead to enhanced blood glucose excursions in the postprandial state (440). In addition, the ability of the anti-GCGR antibody to improve glucose tolerance in glucose-injected control mice (compare Figures 11.3A and 11.3B) also clearly indicates that GCGR signaling regulates post-prandial blood glucose levels.

We obtained very similar results when we treated hep-barr2-KO and control mice with the

gluconeogenic substrate, pyruvate (pyruvate tolerance test). In this test, hep-barr2-KO mice showed significantly increased hyperglycemic effects, as compared to their control littermates (Figure 11.3C). This effect was no longer observed after treatment of mice with the anti-GCGR antibody (Figure 11.3D). Importantly, following an acute dose of i.p. glucagon (16 μg/kg), hep-barr2-KO mice showed greatly enhanced blood glucose excursions (glucagon challenge test; Figure 11.3E). Taken together, these observations indicate that barr2 acts as a potent negative regulator of GCGR signaling in hepatocytes.

We also noted that hepatic glycogen and triglyceride levels were significantly reduced in livers from hep-barr2-KO mice (Figures 11.3J and 11.3K). Since glucagon stimulates hepatic glycogen breakdown and fatty acid oxidation and inhibits insulin-dependent lipogenesis (430,441), this observation further supports the notion that GCGR signaling is enhanced in barr2-deficient hepatocytes.

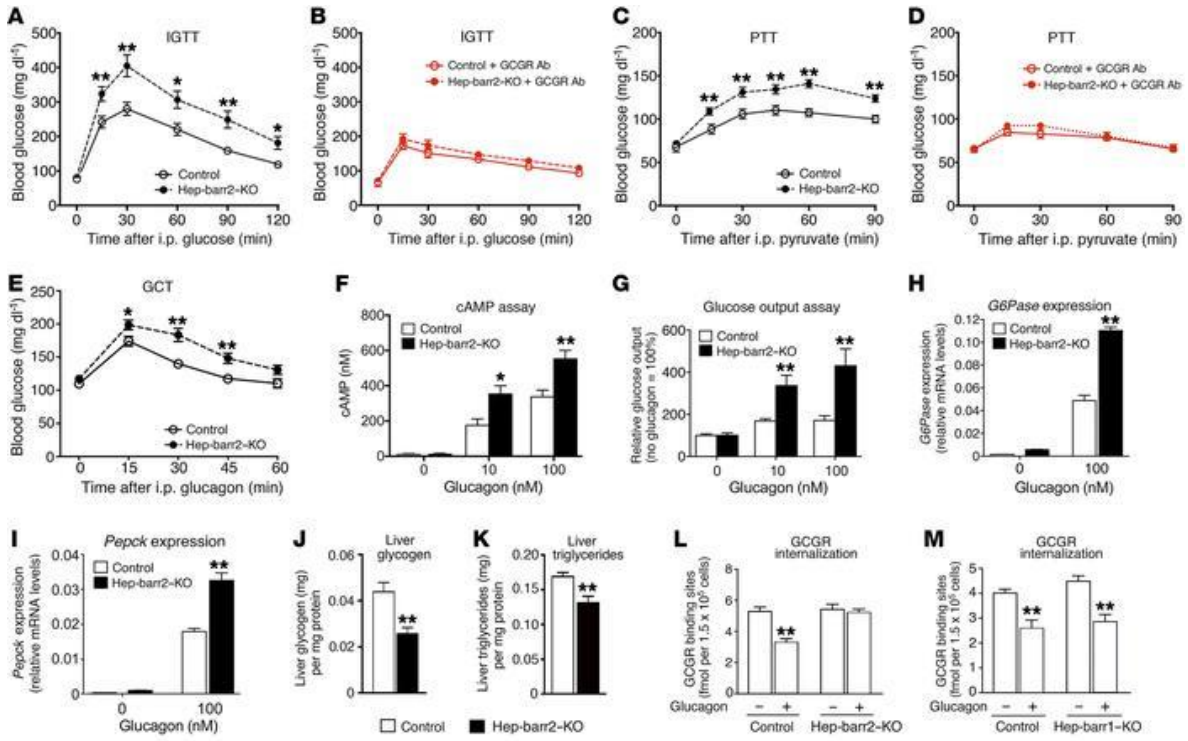

Fig. 11.3. Metabolic phenotyping and GCGR internalization studies. (**A, B**) I.p. glucose tolerance tests (IGTT). (**C, D**) I. p. pyruvate tolerance tests (PTT). In (B) and (D), an anti-GCGR antibody (10 mg/kg i.p) was administered ~24 h prior to glucose or pyruvate injections, respectively. (**E**) I.p. glucagon challenge test (GCT). (**F-I**) In vitro studies with primary mouse hepatocytes. The ability of glucagon to stimulate intracellular cAMP accumulation (F), glucose production (G), and the expression of the *G6pase* (H) and *Pepck* (I) genes was studied using primary hepatocytes prepared from hep-barr2-KO mice and their control littermates. Gene expression data were normalized relative to the expression of *β-actin* (qRT-PCR analysis). Hepatocyte data are given as means ± SEM of at least three independent experiments. (**J, K**) Hepatic glycogen and triglyceride content. All studies were carried out with male mice consuming regular chow (mouse age: 11-20 weeks). Data represent means ± SEM **(**n=8-13 mice per group) (A-K). *p<0.05, **p<0.01, versus control (Student's t-test). (**L, M**) GCGR internalization assays. Primary hepatocytes prepared from hep-barr2-KO (L) or hep-barr1-KO (M) mice and their control littermates were stimulated with glucagon (100 nM) for 30 min at 37 °C. Cell surface GCGRs were labeled with I^{125}-glucagon. Data represent the means ± SEM of three independent experiments, each carried out in triplicate. **p<0.01, versus cells not exposed to glucagon (One way ANOVA followed by Tukey's multiple comparison's test).

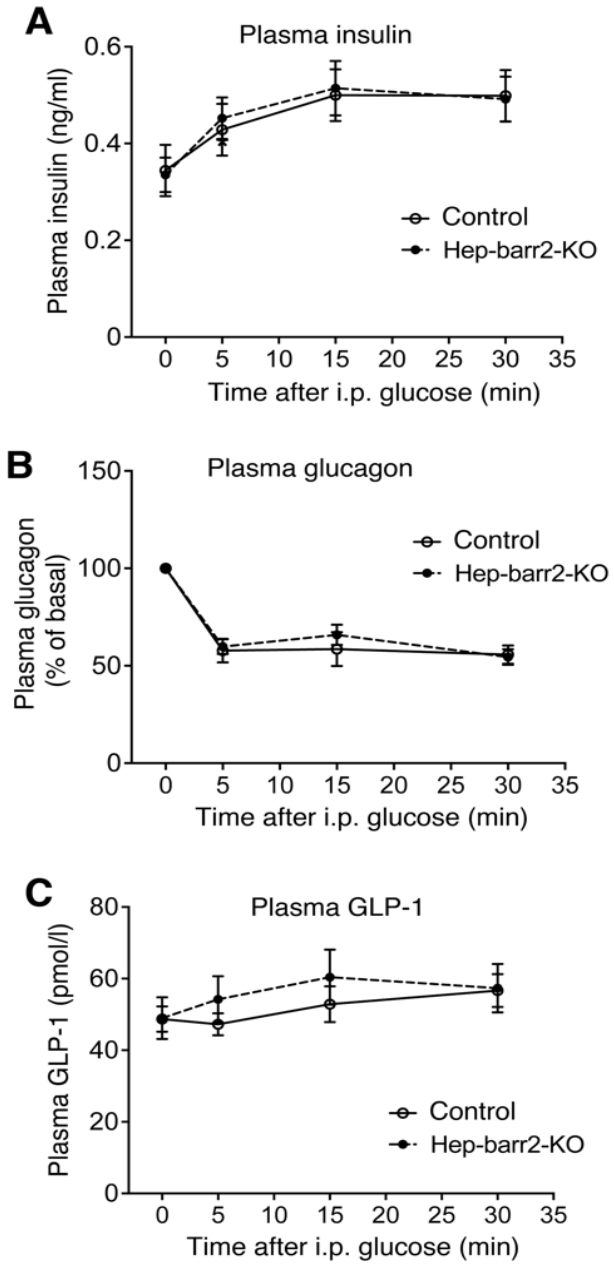

Figure 11.4. Glucose-induced changes in plasma insulin, glucagon, and GLP-1 remain unaffected by hepatic barr2 deficiency. (**A**-**C**) Hep-barr-2 KO mice and control littermates that had been fasted for 12 hr were injected with glucose (2 g/kg i.p.), followed by the measurement of plasma insulin (**A**), glucagon (**B**), and GLP-1 levels (**C**). Basal glucagon levels at time '0' were (in pmol/l): control, 3.89±0.30; hep-barr2-KO, 3.23 ±0.24. Data represent means ± SEM **(**n=7 or 8 mice per group; 12-16-week old males).

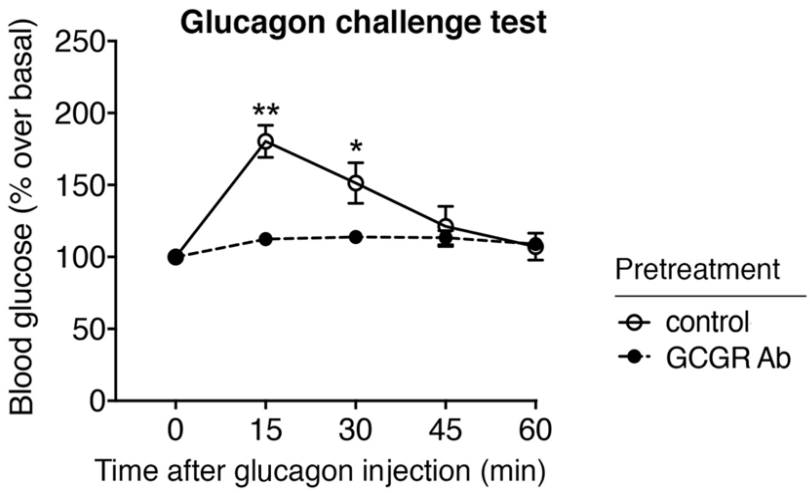

Fig. 11.5. The anti-GCGR antibody blocks glucagon-induced increases in blood glucose levels in WT mice. Male WT mice (14-week-old male C57BL-6NTac mice) were injected with the anti-GCGR antibody (10 mg/kg i.p; see Supplemental Methods for details) or vehicle (control) ~24 h prior to glucagon administration (16 µg/kg i.p.), following a 4 hr fast. For each individual mouse, blood glucose levels at time '0" were set equal to 100%. Data are given as means ± SEM (n=6 per group). *p<0.05,**p<0.01, versus control (Student's t-test).

At the cellular level, glucagon stimulates the production of cAMP via GCGR-mediated activation of G_s (430). To examine whether the lack of hepatic barr2 affected the magnitude of this response, we carried out cAMP assays with primary hepatocytes prepared from hep-barr2-KO mice and their control littermates. Strikingly, glucagon-induced increases in cAMP levels were significantly enhanced in hepatocytes lacking barr2 (Figure 11.3F). We obtained similar results when we knocked down the expression of *barr2* in primary wild-type (WT) mouse hepatocytes by using *barr2* siRNA (Figure 11.6). In this latter case, we monitored the activity of the cAMP/PKA signaling pathway by using a CRE-luciferase reporter.

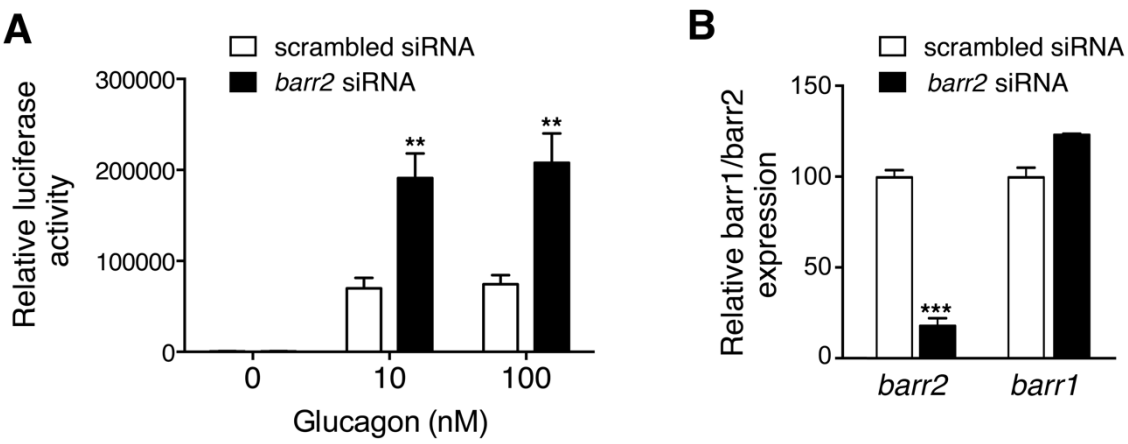

Fig. 11.6. Barr2 knockdown enhances glucagon signaling in primary mouse hepatocytes. WT mouse hepatocytes were transfected with *barr2* siRNA or scrambled control siRNA. Hepatocytes were then infected with adenoviruses coding for the CRE-luc reporter and β -gal (internal control). β-gal activity was used to normalize the results of luciferases assays. (**A**) Following treatment of hepatocytes with *barr2* siRNA, glucagon enhances cAMP/PKA signaling in a CRE-luc reporter assay. (**B**) Efficient reduction of *barr2* expression after treatment of mouse hepatocytes with *barr2* siRNA. *Barr1* transcript levels were not significantly affected by the knockdown of *barr2* expression. *Barr2* and *barr1* mRNA levels were examined by qRT-PCR using β-*actin* expression as an internal control. Data are given as means ± SEM from six independent experiments. **p<0.01,*** p<0.001, as compared to control (Student's t-test).

We also examined whether glucagon-stimulated glucose output differed between primary hepatocytes prepared from hep-barr2-KO and control mice. We found that glucagon-induced glucose output was greatly enhanced (by ~2-3-fold) in barr2-deficient hepatocytes (Figure 11.3G). Consistent with this observation, hepatic barr2 deficiency led to significant increases in glucagon-stimulated *G6pase* and *Pepck* transcript levels (*G6pase* and *Pepck* are the two rate-limiting enzymes of gluconeogenesis) (Figures 11.3H and 11.3I).

I^{125}-glucagon radioligand binding studies with primary hepatocytes showed that the lack of barr2 had no significant effect on GCGR densities (receptor number per cell: control, 2.19±0.12 x 10^4; hep-barr2-KO: 2.25±0.13 x 10^4). In summary, these data strongly support the concept that barr2 represents a potent suppressor of hepatic GCGR signaling in vivo and in vitro.

Mice lacking β-arrestin-1 (barr1) in hepatocytes show normal glucose homeostasis. Like most cell types, mouse hepatocytes express both barr2 and barr1 (377). By employing the same

strategy as described above for the generation of hep-barr2-KO (385), we used floxed *barr1* mice **(**Kim, J., Lefkowitz, R.J., et al., manuscript in preparation) to obtain mutant mice that selectively lacked barr1 in hepatocytes (hep-barr1-KO mice) **(**Figure 11.7A, B). The lack of barr1 had no significant effect on GCGR expression in primary hepatocytes (receptor number per cell: control, 1.66±0.06 x 10^4; hep-barr1-KO: 1.86± 0.08 x 10^4), as determined in I^{125}-glucagon binding studies. Blood glucose, plasma insulin, and plasma glucagon levels remained unaffected by hepatic barr1 deficiency. Moreover, and in striking contrast to the metabolic deficits displayed by the hep-barr2-KO mice, hep-barr1-KO mice did not show any impairments in glucose homeostasis (Figure 11.8). This observation clearly indicates that hepatic GCGR signaling is strongly regulated by barr2 but not by barr1.

GCGR internalization is abolished in hepatocytes lacking barr2. β-Arrestins interact with ligand-activated GPCRs, resulting in receptor-G protein uncoupling and receptor internalization (370,433,442). Both of the processes are critically involved in GPCR desensitization (370). To examine whether barr2 is required for the internalization of endogenous GCGRs, we used I^{125}-glucagon to assess the density of GCGRs present on the surface of primary hepatocytes prepared from hep-barr2-KO or control mice (Figure 11.3L). Prior to glucagon treatment, cell surface GCGR densities were similar in KO and control hepatocytes (Figure 11.3L). Glucagon (100 nM) treatment of control hepatocytes led to the internalization of ~35% of cell surface GCGRs (Figure 11.3L). In striking contrast, glucagon failed to induce GCGR internalization in barr2-deficient hepatocytes (Figure 11.3L). Additional I^{125}-glucagon binding studies showed that glucagon-induced GCGR internalization remained intact in hepatocytes lacking barr1 (Figure 11.3M). These data indicate that hepatic GCGR internalization is mediated by barr2 and that barr1 is not involved in this process. Since receptor internalization contributes to GPCR desensitization (370), it is likely

that the lack of GCGR internalization in barr2-deficient hepatocytes plays a role in enhanced glucagon signaling.

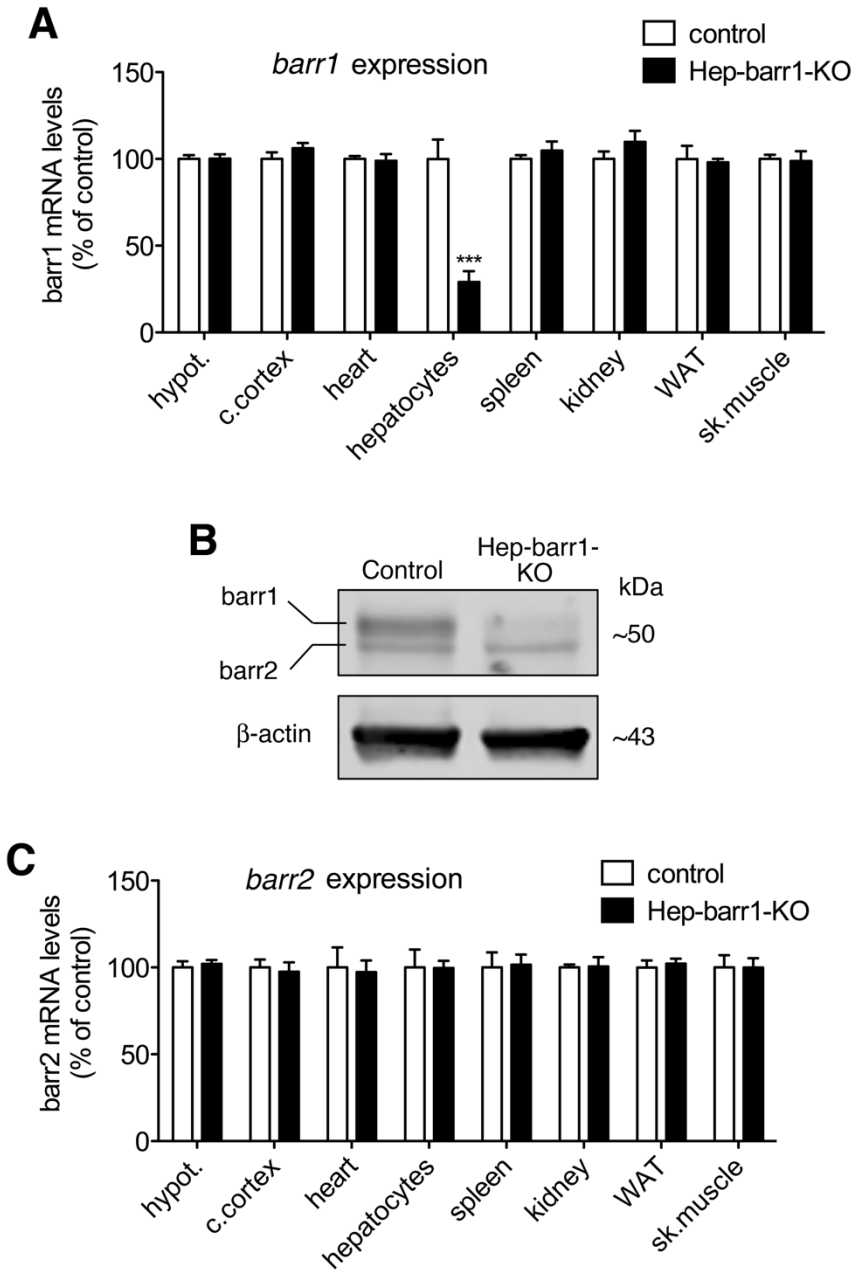

Fig. 11.7. Generation of mutant mice selectively lacking barr1 in hepatocytes (hep-barr1-KO mice). (**A**) *Barr1* transcript levels are selectively decreased in hepatocytes of hep-barr1-KO mice. (**B**) Representative Western blot showing the relative lack of barr1 protein in hepatocytes of hep-barr1-KO mice. ns, non-specific band. (**C**) *Barr2* mRNA levels remain unaffected by hepatocyte barr1 deficiency. Gene expression levels were determined via qRT-PCR using *β-actin* expression as an internal control. Template RNA was prepared from the indicated tissues. Data are given as means ± SEM (3 mice per genotype, 10-week-old males). ***p<0.001, as compared to control (Student's t-test). hypot., hypothalamus; c. cortex, cerebral cortex; WAT, white adipose tissue; sk. muscle, skeletal muscle.

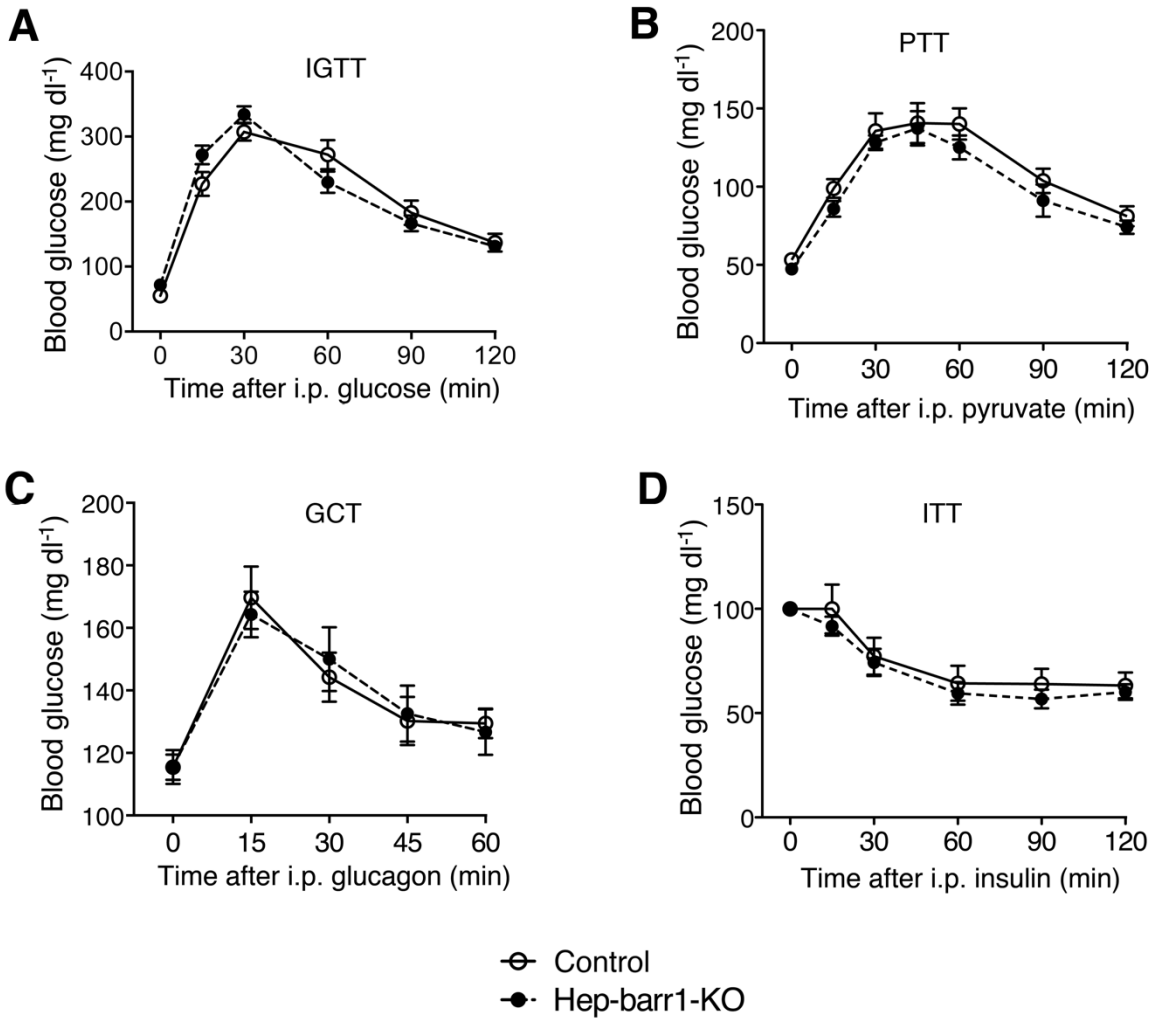

Fig. 11.8. In vivo metabolic studies with hep-barr1-KO mice and their control littermates. (**A**) I.p. glucose tolerance test (IGTT). (**B**) I. p. pyruvate tolerance test (PTT). (**C**) I.p. glucagon challenge test (GCT). (**D**) I. p. insulin tolerance test (ITT). All studies were carried out with male mice maintained on regular chow (mouse age: 12-18 weeks). Data are presented as means ± SEM (n=7-10 mice per group).

To demonstrate that barr2 can directly interact with the GCGR, we carried out BRET studies using COS-7 cells co-expressing a *Renilla* luciferase-tagged version of the GCGR (443) (GCGR-Luc) and a Venus-barr2 fusion protein (V-barr2) (114). Glucagon treatment of co-transfected cells led to concentration-dependent increases in BRET (Figure 11.9A), indicating that the GCGR is able to recruit barr2 in an activity-dependent fashion. Interestingly, BRET studies also showed activated GCGRs were able to interact with barr1 (V-barr1) (Figure 11.9B). Since barr1 recruitment did not interfere with GCGR internalization (Figure 11.3M), it is likely that activated GCGRs induce different conformational changes in barr2 vs. barr1. This phenomenon of conformational flexibility is currently the focus of many laboratories studying β-arrestin function (444).

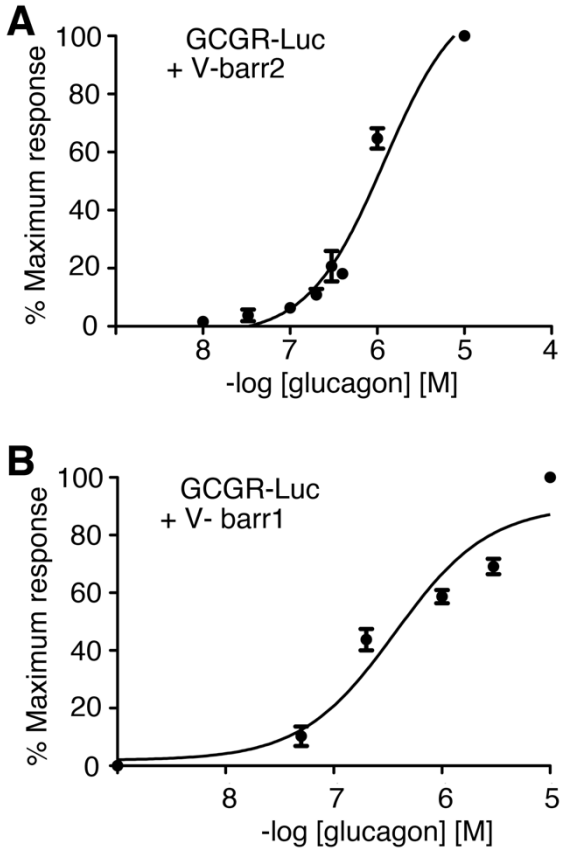

Fig. 11.9. GCGR activation promotes the recruitment of both β-arrestins in BRET assays. The ability of a GCGR-Luc fusion protein to interact with a Venus-tagged version of barr2 (A) or barr1 (B) was studied using BRET in co-transfected COS-7 cells as a readout (see Supplemental Methods for details). Data represent the means ± SEM of three independent experiments.

Lack of β-arrestins has little effect on β-adrenergic receptor signaling in hepatocytes. To test the hypothesis that altered β-adrenergic receptor signaling plays a role in the observed metabolic phenotypes described above, we also treated mouse hepatocytes from control and hep-barr2 (and barr1)-KO mice with isoproterenol (Iso), a β-adrenergic receptor agonist, and then measured increases in intracellular cAMP levels and glucose output (Figures 11.10, 11.11). In comparison to the very pronounced cAMP and glucose responses observed after glucagon (10 nM) treatment, Iso (1 and 10μM)-mediated effects on cAMP accumulation were much smaller and

effects on glucose output were not significantly different from control cells (no drug treatment) (Figures 11.10, 11.11). Following Iso (10 μM) treatment, hep-barr2-KO hepatocytes (Figure 11.10A), but not hep-barr1-KO hepatocytes (Figure 11.11A), showed a small but significant increase in intracellular cAMP levels. Iso was unable to stimulate glucose release in control or mutant hepatocytes (Figures 11.10B, 11.11B). Taken together, these data suggest that altered β-adrenergic receptor signaling does not make a major contribution to the metabolic phenotypes observed with the hep-barr2-KO mice.

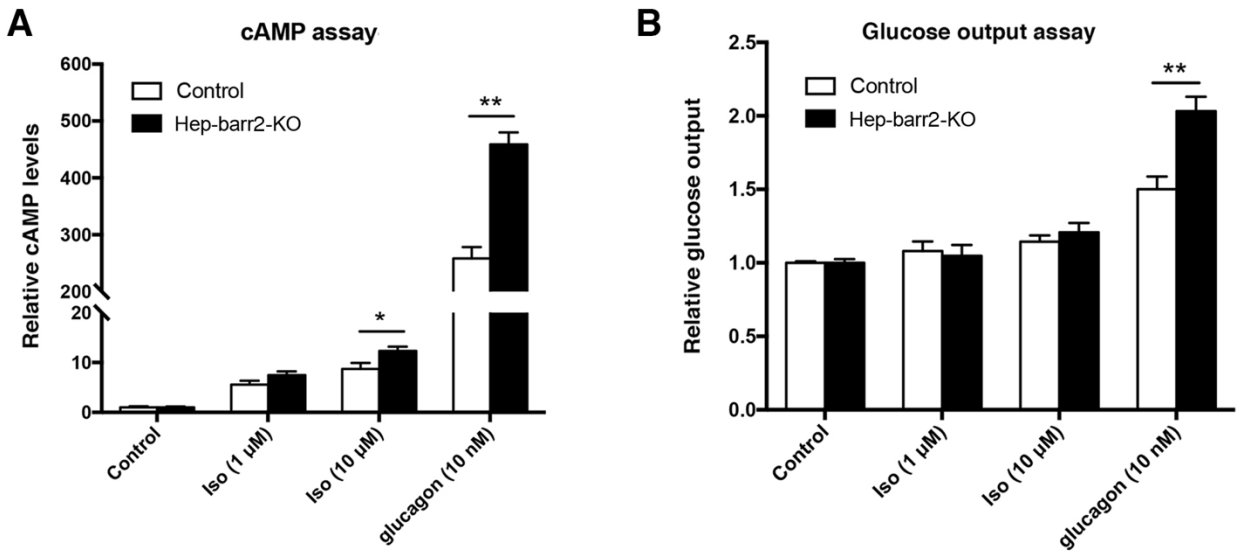

Fig. 11.10. Isoproterenol treatment of primary mouse hepatocytes from control and hep-barr2-KO mice. (A) cAMP assay. The ability of isoproterenol (Iso), a β-adrenergic receptor agonist, and glucagon to stimulate intracellular cAMP accumulation was examined. In each individual experiment, the cAMP response in the absence of drugs was set equal to 1. (B) Glucose output assay. The ability of Iso and glucagon to stimulate glucose release from control and hep-barr2-KO hepatocytes was determined. In each individual experiment, glucose levels in the absence of drugs were set equal to 1. Data are given as means ± SEM of three or four independent experiments. *$p<0.05$,**$p<0.01$, versus control (Student's t-test).

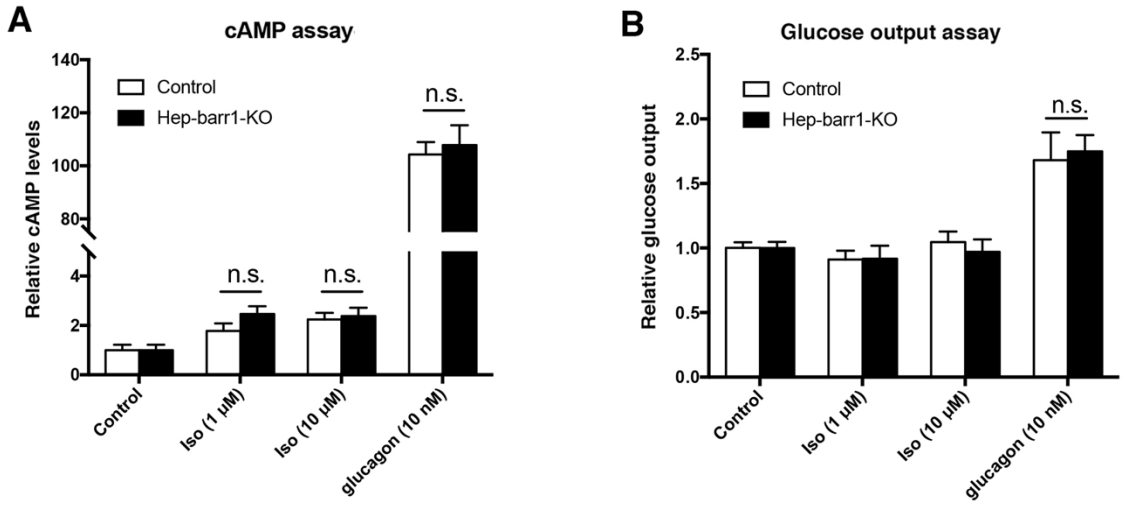

Fig. 11.11 Isoproterenol treatment of primary mouse hepatocytes from control and hep-barr1-KO mice. (A) cAMP assay. The ability of isoproterenol (Iso) and glucagon to stimulate intracellular cAMP production was determined. In each individual experiment, cAMP responses in the absence of drugs were set equal to 1. **(B)** Glucose output assay. The ability of Iso and glucagon to stimulate glucose release from control and hep-barr1-KO hepatocytes was measured. In each individual experiment, glucose levels in the absence of drugs were set equal to 1. Data are given as means ± SEM of three independent experiments. n.s., not significantly different from control (Student's t-test).

PTX treatment does not affect the increase in GCGR-mediated glucose output in hep-barr2-KO hepatocytes. We also examined whether potential signaling of activated GCGRs to G_i (see, for example, ref. (445)) may contribute to the metabolic changes displayed by the hep-barr2-KO mice. Specifically, we monitored glucagon (10 nM)-induced changes in cAMP accumulation and glucose release in hep-barr2-KO hepatocytes, either in the absence of presence of PTX (300 ng/ml). In cAMP assays, glucagon-stimulated cAMP levels were significantly increased in PTX-treated controls cells (Figure 11.12A), suggesting that inactivation of inhibitory, G_i-type G proteins enhances GCGR signaling via G_s. This stimulatory effect of PTX was not observed with glucagon-treated hep-barr2-KO hepatocytes (Figure 11.12A), probably due to the fact that cAMP levels were already maximally activated under these experimental conditions. The presence of PTX had no significant effect on glucagon-induced glucose responses in control and hep-barr2-KO hepatocytes (Figure 11.12B), suggesting that it is unlikely that potential signaling of the GCGR via G_i makes an important contribution to the changes in glucose homeostasis observed with the hep-barr2-KO

mice.

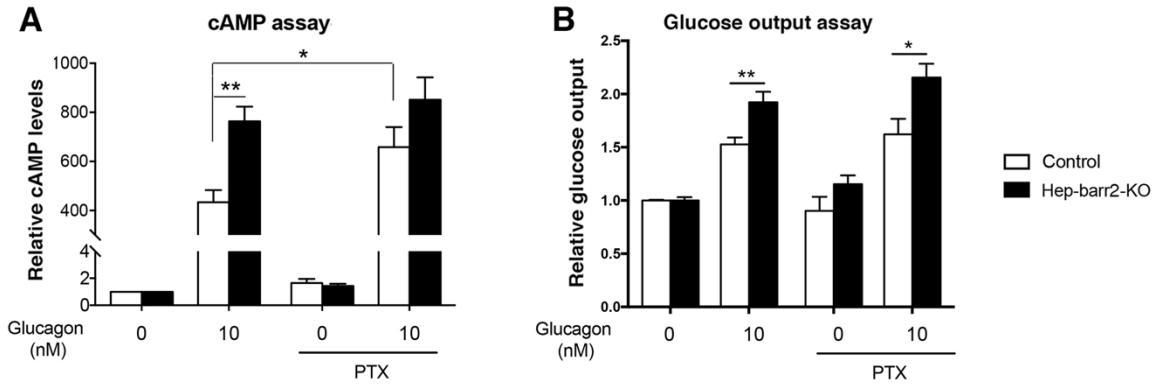

Fig. 11.12. Glucagon treatment of primary mouse hepatocytes from control and hep-barr2-KO mice in the absence or presence of PTX. (A) cAMP assay. The ability of glucagon to stimulate intracellular cAMP accumulation was examined. In each individual experiment, cAMP responses in the absence of drugs were set equal to 1. **(B)** Glucose output assay. The ability of glucagon to promote glucose release from control and hep-barr2-KO hepatocytes was determined. In each individual experiment, glucose levels in the absence of drugs were set equal to 1. Experiments were carried out either in the absence or presence of PTX (300 ng/ml), including a 2 hr pre-incubation. Data are given as means ± SEM of three or four independent experiments. *p<0.05,**p<0.01, versus control (Student's t-test).

Overexpression of barr2 in hepatocytes protects mice against obesity-induced metabolic deficits. Since hep-barr2-KO mice showed impaired glucose tolerance, we hypothesized that overexpression of barr2 in mouse hepatocytes might lead to improved glucose homeostasis. To generate mice that overexpressed barr2 selectively in hepatocytes (hep-barr2-OE mice), we injected WT C57BL/6 mice with an AAV coding for an HA-tagged version of barr2 (51) under the transcriptional control of the hepatocyte-selective thyroxine-binding globulin (TBG) promoter (Figure 11.13A, B). Overexpression of barr2 in hepatocytes had no significant effect on *barr1* expression levels (Figure 11.13A, B).

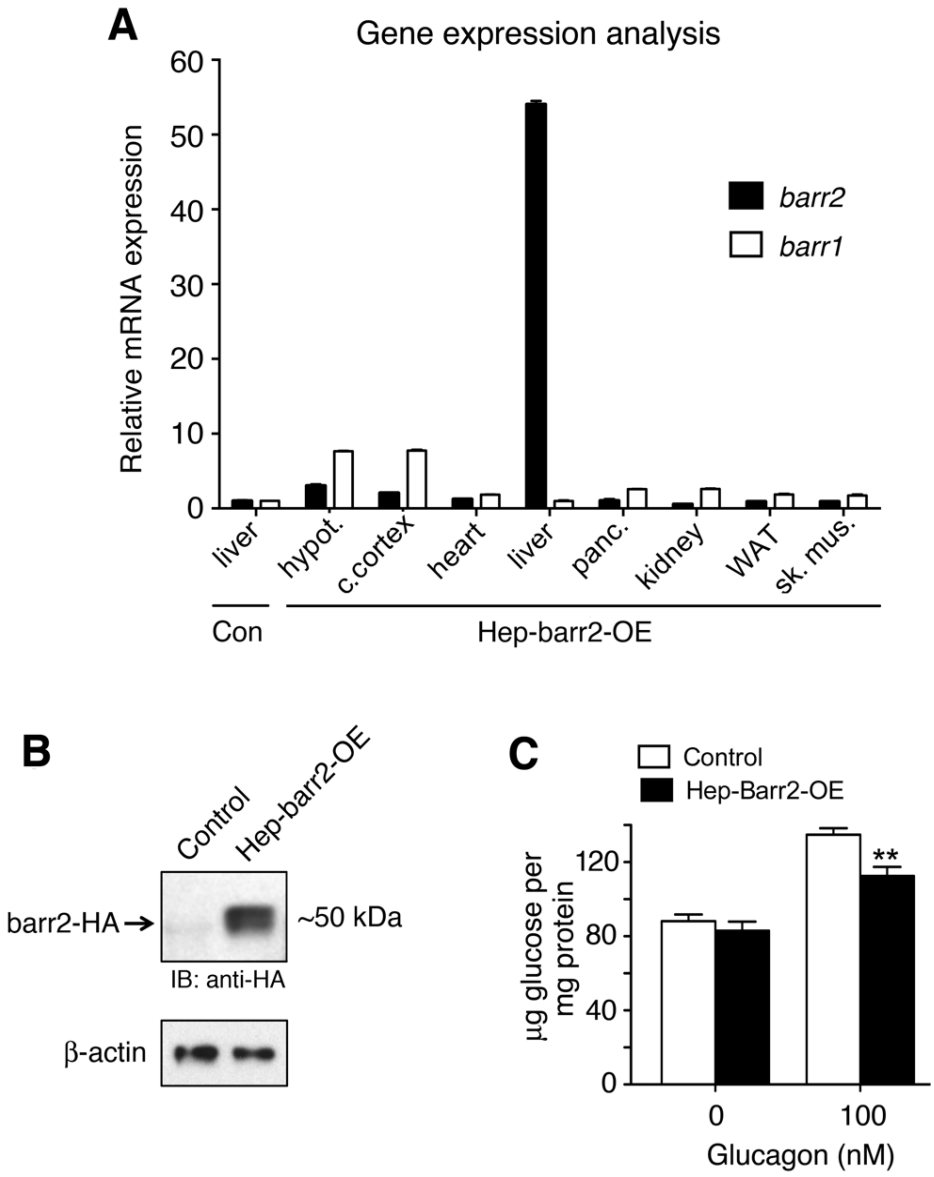

Fig. 11.13. Generation of mutant mice selectively overexpressing barr2 in hepatocytes (hep-barr2-OE mice) and analysis of hepatocyte glucose production. (**A**) *Barr2* transcript levels are selectively increased in the liver of hep-barr2-OE mice. mRNA levels are expressed relative to hepatic *barr2* and *barr1* expression levels in control littermates (=1). *Barr2* and *barr1* transcript levels were examined by qRT-PCR using β-*actin* expression as an internal control. Template RNA was prepared from the indicated tissues. Data are given as means ± SEM (3 mice per genotype, 10-week-old males). hypot., hypothalamus; c. cortex, cerebral cortex, WAT, white adipose tissue; sk. mus., skeletal muscle. (**B**) Representative Western blot demonstrating the expression of barr2-HA in the liver of hep-barr2-OE mice. Please note that the AAV used for generating the hep-barr2-OE mice encoded an HA-tagged version of barr2. (**C**) Glucose production by hepatocytes from hep-barr2-OE mice and control littermates. Glucagon-induced hepatic glucose output is significantly reduced in hepatocytes from hep-barr2-OE mice. Data are given as means ± SEM of three independent experiments, each carried out in duplicate. **$p<0.01$, as compared to control (Student's t-test).

Initially, we subjected hep-barr2-OE mice consuming RC and their control littermates (AAV-TBG-EGFP-injected WT C57BL/6 mice) to a series of in vivo metabolic studies. Hep-barr2-OE mice showed significant decreases in fed blood glucose levels. Plasma insulin and glucagon levels were similar in hep-barr2-OE mice and their control littermates. The hep-barr2-OE mice showed only very minor reductions in blood glucose excursions in glucose and pyruvate tolerance tests (Figure 11.14A, B). Importantly, however, the mutant mice were clearly less sensitive to the hyperglycemic effects of glucagon in a glucagon challenge test (Figure 11.14C). Consistent with this in vivo phenotype, glucagon-stimulated HGP was significantly reduced in primary hepatocytes prepared from hep-barr2-OE mice (Figure 11.13C), further confirming that barr2 represents a potent negative regulator of hepatic GCGR function.

We performed similar metabolic tests with hep-barr2-OE mice and their control littermates maintained on a high-fat diet (HFD) for 6-10 weeks (Figure 11.14E-H). Under these experimental conditions, the control mice showed significantly greater increases in blood glucose levels in all in vivo metabolic assays (as compared to RC control mice), indicative of glucose intolerance, increased gluconeogenesis, and enhanced glucagon sensitivity (Figure 11.14E-G). Strikingly, these metabolic deficits were not observed with hep-barr2-OE mice maintained on the HFD (Figure 11.14E-G). HFD Hep-barr2-OE mice displayed significantly reduced fed and fasting blood glucose levels. Plasma insulin and glucagon levels were not significantly affected by hepatic barr2 overexpression. Moreover, hep-barr2-OE and control mice showed similar glucose responses in an insulin tolerance test (Figure 11.14D, H).

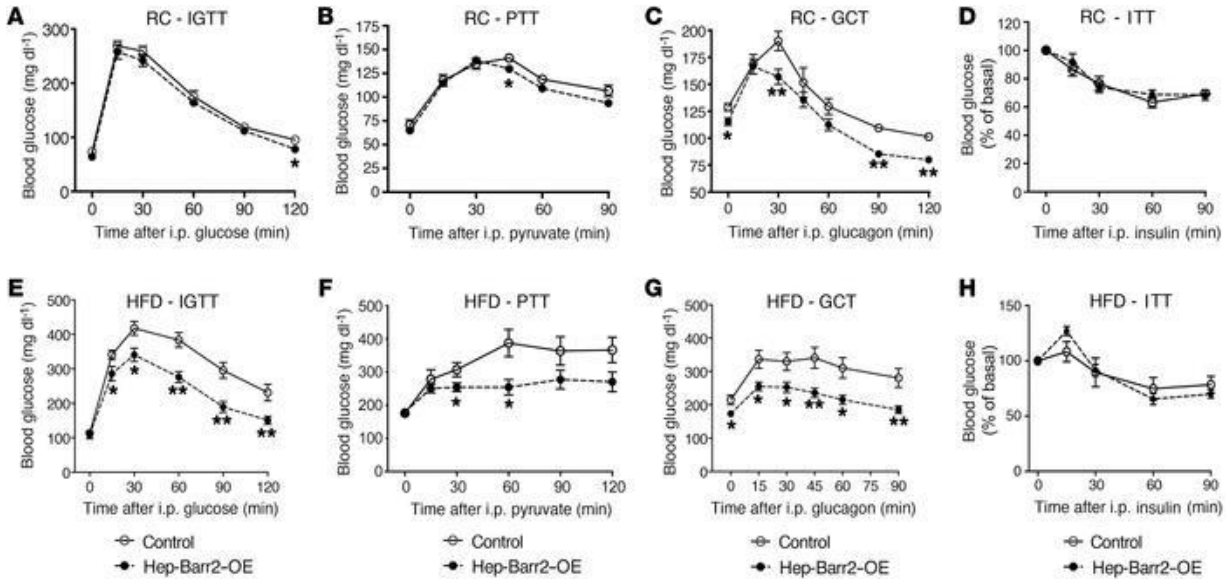

Fig. 11.14. In vivo studies with hep-barr2-OE mice and their control littermates. (**A-H)** In vivo metabolic tests carried out with mice maintained on regular chow (RC) (A-D) or a high-fat diet (HFD) (E-H). Animals were maintained on the HFD for at least 8 weeks. Mice were subjected to i.p. glucose tolerance (IGTT) (**A, E**), pyruvate tolerance (PTT) (**B, F**), glucagon challenge (GCT) (**C, G**), and insulin tolerance (ITT) (**D, H**) tests. Data are given as means ± SEM (8-10 mice per group; 12-16-week old males). *p<0.05,**p<0.01, versus control (Student's t-test).

Interestingly, hepatic *barr2* expression levels were significantly lower in HFD control than in RC control mice. Consistent with this observation, a recent study (377) reported that hepatic barr2 levels are reduced in diabetic individuals. On the basis of these observations, reduced hepatic barr2 activity may contribute to the pathophysiology of T2D.

11.3 Conclusions

In summary, we here demonstrate that hepatic barr2 is critical for maintaining euglycemia. At the cellular level, barr2 acts as a potent negative regulator of hepatic GCGR signaling in vivo and in vitro. Interestingly, hepatic barr1, in contrast to barr2, does not play a role in regulating hepatic GCGR activity and euglycemia, indicating that the two β-arrestins do not have redundant functions in hepatocytes. Our findings suggest that strategies aimed at enhancing the expression or activity of hepatic barr2 or the development of small molecule barr2 mimetics may become

clinically useful for reducing exaggerated hepatic GCGR signaling for the treatment of T2D (428,437).

11.4 Materials and Methods

Mouse maintenance and diet. Mice were fed ad libitum and kept on a 12-h light, 12-h dark cycle. Mice were maintained either on a standard mouse chow (4% (w/w) fat content; Zeigler) or a high-fat diet (35.5 % (w/w) fat content; # F3282, Bioserv). All animal experiments were conducted according to the US National Institutes of Health Guidelines for Animal Research and were approved by the NIDDK Institutional Animal Care and Use Committee.

Generation of mutant mice. To selectively inactivate *barr2* or *barr1* in hepatocytes, we used floxed *barr2* or *barr1* mice in which exon 2 was flanked by loxP sites (*fl/fl barr2* and *fl/fl barr1* mice, respectively). The *fl/fl barr2* mice had a pure C57BL/6 genetic background (385). The *fl/fl barr1* mice were initially obtained on a mixed background (C57BL/6 x 129R1) **(**Kim, J., Lefkowitz, R.J., et al., manuscript in preparation) and then backcrossed for multiple generations (>7) onto a C57BL/6 background (Taconic). The *fl/fl barr2* mice (8-week-old males) were injected, via the tail vein, with an adeno-associated virus (AAV) coding for Cre recombinase (AAV-TBG-CRE; 10^{11} genomic copies per mouse) (438). This virus directs the selective expression of Cre recombinase in hepatocytes (Cre expression is under the transcriptional control of the hepatocyte-selective thyroxine-binding globulin (TBG) promoter). As a result, injection of floxed *barr2* mice with the AAV-TBG-CRE virus led to the selective inactivation of *barr2* in hepatocytes (hep-barr2-KO mice) (Figure 11.1A and B). By using the same strategy, we also generated hep-barr1-KO mice (Figure 11.5). For control purposes, we injected floxed *barr2* or *barr1* mice with another virus, AAV-TBG-EGFP (438), that codes for EGFP which is

physiologically inert. Both viruses were obtained from the Vector Core of the University of Pennsylvania (Philadelphia, PA). We used a similar strategy to generate mice that selectivity overexpressed barr2 in hepatocytes (hep-barr2-OE mice). In this case, wild-type (WT) C57BL/6 mice (8-week-old males; Taconic) were injected with an AAV coding for an HA epitope-tagged version of rat barr2 under the transcriptional control of the TBG promoter (source of plasmid: Addgene; source of virus: Vector Core of the University of Pennsylvania).

Mouse phenotyping studies were initiated two weeks after virus administration.

Isolation of primary mouse hepatocytes and glucose production assay. Primary mouse hepatocytes were isolated from livers of mice that were at least 8 weeks old by using a two-step collagenase perfusion protocol (446). Hepatocytes were cultured in collagen I-coated 6-well plates (5×10^5 cells per well) in DMEM containing 10% FBS (GIBCO-BRL). The medium was changed after 4 h with DMEM supplemented with penicillin (100 U/ml) and streptomycin (100 μg/ml). To stimulate glucose production, the medium was replaced with glucose- and phenol red-free DMEM supplemented with gluconeogenic substrates (20 mM sodium lactate and 2 mM sodium pyruvate, respectively), followed by an overnight incubation step at 37 °C. Subsequently, hepatocytes were incubated in the same medium in the absence or and presence of glucagon (10 and 100 nM) for 4 h at 37 °C. The culture medium was then collected for the measurement of glucose levels using a glucose kit (Sigma).

In a subset of experiments, primary mouse hepatocytes were pre-incubated with or without PTX (300 ng/ml; Tocris) for 2 hr, and the treated with glucagon (10 nM) and isoproterenol (1 and 10 μM).

Physiological studies. All in vivo metabolic tests were performed with male mice (age range: 10-20 weeks) using standard procedures. In brief, prior to i.p. glucose tolerance tests

(IGTT), mice were fasted overnight for 12 h. Blood glucose concentrations were determined using blood collected from the tail vein immediately before and at defined time points after i.p. injection of glucose (regular chow, 2 g/kg; HFD, 1 g/kg). Glucagon challenge tests (GCT) were carried out using mice that had been fasted for 4 h. Blood glucose levels were determined at various time points after i.p. injection of glucagon (hep-barr2-KO mice, 16 μg/kg; hep-barr2-OE mice, 100 μg/kg). For pyruvate tolerance tests (PTT), mice were fasted overnight for ~12 h and then injected i.p. with sodium pyruvate (2 g/kg), followed by the monitoring of blood glucose levels. Insulin tolerance tests (ITT) were carried out with mice that had been fasted for 4 h. Mice were then injected i.p. with human insulin (regular chow, 0.75 U/kg; HFD, 1 U/kg; Novo Nordisk), and changes in blood glucose levels were measured at defined time points. For a subset of studies, mice were injected with an anti-GCGR antibody (10 mg/kg, mAb7.v44; Genentech) (447) 24 h prior to glucose or pyruvate injections. This antibody was a kind gift by Dr. Bernard B. Allan (Genentech Inc., South San Francisco, CA). Blood glucose levels were determined using an automated blood glucose reader (Glucometer Elite Sensor; Bayer). The plasma insulin and glucagon levels shown in the Supplemental Tables were determined by using ELISA (Crystal Chem Inc.) or RIA (Millipore) kits, respectively, following the manufacturers' instructions.

To study glucose-induced changes in plasma insulin, glucagon, and GLP-1 levels (Supplemental Figure 2), mice were fasted overnight for ~12 h and then injected with glucose (2 g/kg i.p.). Blood samples were collected from the tail vein at different time points (0, 5, 15 and 30 min) into EDTA-coated tubes and centrifuged for plasma collection (3,000 g, 5 min, 4 ^{o}C). Glucagon and GLP-1 assays were carried out in the presence of proteinase inhibitor aprotinin and DPP-4 inhibitor (Sigma). Plasma insulin, glucagon, and GLP-1 levels were determined by using commercially available ELISA kits (insulin and GLP-1, Crystal Chem Inc.; glucagon, Mercodia).

The anti-GCGR antibody used in this study (mAb7.v44) is a sequence variant of mAb7 first described by Koth et al. (448). The specificity and biological properties of mAb7.v44 are described in detail by Solloway et al. (449), although mAb7.v44 is not specifically identified by name in this study. In fact, all data shown in the figures labeled 'anti-GCGR', including Fig. S1 (449) were generated by using the mAb7.v44 antibody.

Measurement of hepatic glycogen and triglyceride levels. Liver glycogen was measured with a commercially available glycogen assay kit (Sigma,) according to the manufacturer's protocol. Hepatic triglyceride levels were determined by using a published procedure (450).

CRE-luciferase reporter assay. Initially, primary hepatocytes prepared from WT mice (C57BL/6; Taconic) were treated with either *barr2* siRNA (On Target plus siRNA SMARTpools, GE Dharmacon) or scrambled control siRNA (GE Dharmacon) using Lipofectamine RNAiMAX transfection reagent (Thermo Fisher Scientific). About 12 h later, hepatocytes were infected with adenoviruses coding for CRE-luc (CRE, cAMP response element; luc, luciferase) and β-gal (both viruses were a kind gift by Dr. Rebecca Berdeaux, University of Texas Health Science Center, Houston, TX) (10 M.O.I.). About 24 h after virus treatment, hepatocytes (3×10^5 cells per well) were incubated in 12-well plates for 5 h at 37 °C with 10 or 100 nM of glucagon. After this incubation step, luciferase assays were performed as described previously (451).

cAMP assay. Primary mouse hepatocytes were isolated and resuspended in phenol red-free William's medium at a density of 1×10^6 cells/ml. Media were supplemented with 500 μM IBMX. Subsequently, 5 μl aliquots of the cell suspension were added to white-bottom 384-well plates (~5,000 cells per well) and incubated with increasing concentrations of glucagon (added in a 5 μl volume) for 25 min at 37 °C. After this incubation step, cells were lysed and glucagon-induced changes in intracellular cAMP levels were determined by using a FRET-based cAMP detection

kit, following the manufacturer's protocol (cAMP dynamic 2 kit; Cisbio Bioassays).

In a subset of experiments involving PTX-treated mouse hepatocytes, we used a modified cAMP assay protocol to study cAMP levels in attached cells. Hepatocytes were isolated and cultured in collagen I-coated 6-well plates (5×10^5 cells per well) in culture medium (DMEM with 10% FBS; GIBCO-BRL) supplemented with penicillin (100 U/ml) and streptomycin (100 μg/ml). The medium was replaced with the same medium after 4 h. On the second day, cells were washed once with PBS and phenol red-free William's medium supplemented with 500 μM IBMX was added. Cells were then stimulated with different ligands for 30 min. A subset of cells was pre-incubated with PTX (300 ng/ml) for 2 hr prior to ligand stimulation. After the ligand incubation step, cells were lysed and intracellular cAMP levels were determined by using a FRET-based cAMP detection kit, following the manufacturer's protocol (cAMP dynamic 2 kit; Cisbio Bioassays).

GCGR internalization assay. The internalization of hepatic GCGRs was monitored via radioligand (^{125}I-glucagon) binding as described previously (452). Primary hepatocytes from β-arrestin mutant mice and control littermates were seeded onto collagen-coated 24-well plates (1.5 x 10^5 cells per well). Cells were cultured overnight and then washed twice with warm binding buffer (DMEM containing 0.1% BSA and 20 mM HEPES, pH 7.4) and incubated at 37 ºC for 1 h (starvation step). Hepatocytes were then incubated in the absence or presence of glucagon (100 nM) for 30 min at 37° C. Subsequently, plates were kept on ice and cell surface GCGRs were labeled with 1 nM of ^{125}I-glucagon per well (2200 Ci/mmol; PerkinElmer). Cells were incubated with the radioligand for 2 h at 4° C in a 200 μl volume. Non-specific binding was determined in the presence of 1 μM glucagon. All binding reactions were carried out in triplicate. Unbound ligand was removed by three washes with ice-cold binding buffer. Cells were then lysed in ice-cold 0.8

M NaOH for 1 h. Subsequently, cell lysates were transferred to glass tubes, and radioactivity was measured using a gamma counter (PerkinElmer).

BRET assay. The ability of the GCGR to recruit both β-arrestins was assessed in transfected COS-7 cells using a bioluminescence resonance energy transfer (BRET) assay. A GCGR-*Renilla* luciferase fusion construct (GCGR-Luc) served as the BRET donor (a kind gift by Dr. Eric Xu, Van Andel Research Institute, Grand Rapids, MI). As BRET acceptors, we used plasmids coding for Venus-tagged versions of barr2 (V-barr2) or barr1 (V-barr1), respectively (114). In brief, COS-7 cells were seeded into 100 mm dishes and transfected at 80-90% confluency using Lipofectamine™ 2000 (Invitrogen; 2 μl of Lipofectamine 2000 per 1 μg of DNA). Cells were co-transfected with 0.2 μg of the GCGR-Luc plasmid and 2 μg of V-barr2 (or V-barr1) DNA. BRET measurements were performed as described in detail previously (114). Cells were incubated with increasing concentrations of glucagon (0-10 μM) for 25 min at 28°C, followed by the addition of 5 μM coelenterazine-*h* (luciferase substrate; Nanolight Technology). The resulting BRET data were analyzed using GraphPad Prism 6.04 (GraphPad Software).

Hyperinsulinemic euglycemic clamp study. Clamp studies were performed as described earlier (453). In brief, hep-barr2-KO mice and control littermates (20-week-old males) were catheterized at the left common carotid artery and the right jugular vein. Clamps were performed on unrestrained, conscious mice after 5 h food restriction. The insulin clamp was initiated at t=0 min with a priming bolus (64 mU/kg) of human insulin (Humulin R; Eli Lilly), followed by an infusion (3.6 mU/kg/min) delivered at a pump (CMA Microdialysis) rate of 0.1 μl/min from 0 to 120 min. Euglycemia (~120–150 mg/dl) was maintained during clamps by measuring blood glucose every 10 min and infusing 45% dextrose as necessary. The clamp steady state was achieved within 80-120 min. Glucose infusion rate (GIR) was expressed as mg/kg/min. Plasma

insulin levels (human) during the clamp were determined by using an insulin ELISA kit for human insulin (Crystal Chem).

Western blotting. Mouse tissues or hepatocytes were lysed in RIPA buffer (Sigma) containing proteinase and phosphatase inhibitors (Roche). Protein lysates were subjected to SDS-PAGE after denaturation of proteins at 95 ^{o}C. Immunoblotting studies were performed using standard procedures. Western blots were scanned and validated with an infrared imaging system (Odyssey CLx; LI-COR Biosciences). All antibodies used for Western blotting were from Cell Signaling: βarr2 (Cat# 3857), βarr1 (Cat# 4674), p-Akt-S473 (Cat# 9271), p-Akt-T308 (Cat# 2965), total Akt (Cat# 9272), p-GSK3α/β (Cat# 9331), total GSK3 α/β Cat #5676), anti-HA (Cat# 3724), and β-actin (Cat# 3700).

RNA extraction and qRT-PCR. Total mRNA was extracted from hepatocytes or different mouse tissues using the RNeasy Mini Kit (Qiagen), followed by DNase I treatment (Invitrogen). cDNAs were prepared from total mRNA by using a reverse transcriptase kit (SuperScript® III Reverse Transcriptase, Invitrogen). Gene expression levels were measured via qRT-PCR using QuantiTect primers (Qiagen): QT00495404 (*barr2*), QT00152880 (*barr1*), QT00114625 (*G6Pase*), and QT00153013 (*Pepck*). qRT-PCR studies were carried out as described in detail previously (411). Gene expression data were normalized relative to the expression of *β-actin* (QT01136772).

SECTION D: ADDITIONAL MANUSCRIPTS (UNRELATED TO THE ARRESTIN PROTEINS)

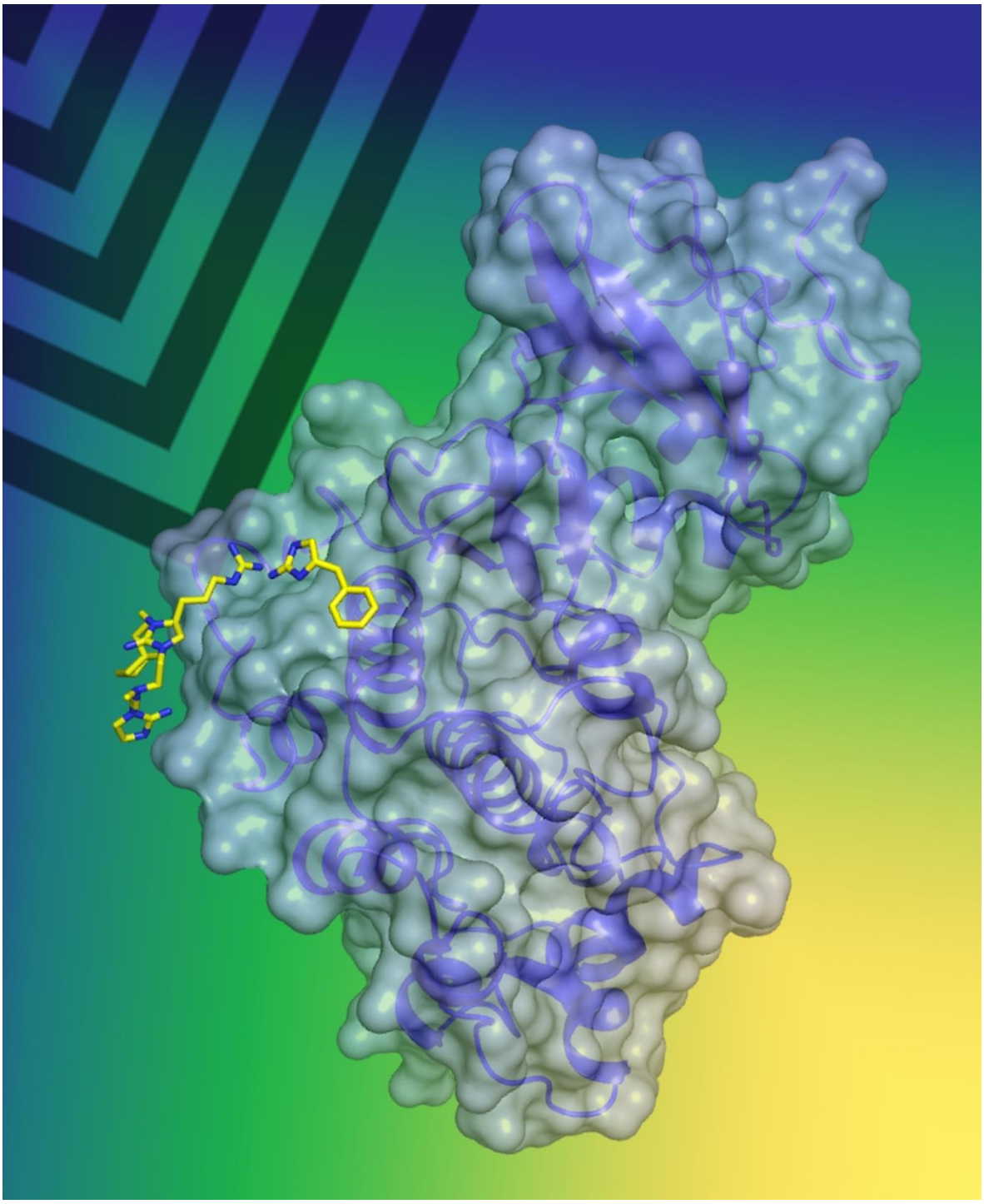

CHAPTER 12

A NOVEL CLASS OF COMMON DOCKING DOMAIN INHIBITORS THAT PREVENT ERK2 ACTIVATION AND SUBSTRATE PHOSPHORYLATION

This article has been submitted to ACS Biological Chemistry. Rachel Sammons was co-first author with **Nicole A. Perry**, and Yangmei Li, Eun Jeong Cho, Andrea Piserchio, Diana Zamora-Olivares, Ranajeet Ghose, Tamer Kaoud, Ginamarie Debevec, Vsevolod V. Gurevich, T.M. Iverson, Marc Giulianottie, Richard A. Houghten, and Kevin N. Dalby contributed to this work. Specific contributions: obtained the crystal structure of ERK2 in complex with 2507-8.

12.1 Introduction

The protein kinome consists of 518 members, representing 1.7% of the human genome (454). Of these kinases, 385 are known Ser/Thr kinases that phosphorylate motifs consisting of only two residues (Ser/Thr-Pro)(454). ERK1/2 alone have over 175 known cellular substrates (455). Additionally, MAPKs like ERK1/2 have highly conserved active sites, so despite their structural and mechanistic similarities, they must each take part in specialized interactions in order to control critical cellular processes. As a result, extensive regulation of these MAPK signaling networks is required to reliably orchestrate specific events. One level of MAPK signaling specificity is achieved through protein docking sites. Docking sites are interfaces of protein-protein interaction that are distinct from catalytic sites. In the case of MAPKs, docking sites can bind substrates in a position that brings specific S/T-P sequences into proximity of the active site in order to facilitate catalysis (456,457). For example, the transcription factor Ets-1 weakly engages

both the FRS and DRS of ERK2 in order to position Thr38 near the ERK2 active site for efficient phosphorylation (458-460). In comparison, the substrate Elk-1 binds the FRS to direct ERK2 to phosphorylate Ser383, but different residues are phosphorylated when Elk-1 binds the DRS (457). The number of protein docking sites, the order in which they are engaged, as well as their positions and arrangement on an enzyme can all influence binding interactions and substrate phosphorylation. Therefore, inhibitors that block these sites can potentially disrupt particular MAPK binding interactions and signaling events, yet leave others unaffected. An additional advantage to targeting these docking sites is that inhibitors do not have to compete with ATP, which is present in cells at millimolar concentrations and binds to MAPKs with high affinity (461,462). Instead, kinase substrates that use these docking sites are typically present in cells at or below their K_m values, so high affinity inhibitors may not be required to block interactions (463,464). Consequently, protein-docking sites on MAPKs offer an alternative approach to classical kinase inhibition that could improve selectivity and block specific signaling events in a tunable manner.

ERK phosphorylates substrates in a signaling cascade that controls cellular processes such as proliferation and survival. Thus, ERK plays a critical role in the development of diseases associated with excessive cell proliferation, like cancer (465,466). ERK is also implicated in cardiac hypertrophy, neurodegenerative diseases, and diabetes (467-470). Consequently, ERK inhibitors are potentially of significant therapeutic value. Here, we focus on identification of ERK inhibitors that target the D-recruitment site (DRS), a protein-protein interaction surface that is distal from the active site of ERK. Classically, linear regions of proteins that bind to the DRS consist of the D-site sequence $\psi_{1\text{-}3}X_{3\text{-}7}\phi X\phi$, where ψ are positively charged residues, ϕ are hydrophobic residues, and X are any residues. The DRS is composed of a hydrophobic groove

located between an ED domain (T157/T158 on ERK2) and an acidic common docking domain (D316 and D319 on ERK2). Though MAPK sequences are highly conserved among the ERK1/2, p38, and JNK subfamilies (471) and all of these subfamily members possess a DRS, it has been shown that kinase-specific DRS inhibitors can be designed (472) and that differences among the D-recruitment sites, particularly in the ED domain, can help confer substrate specificity (473). Though protein-protein interaction sites like the DRS are large and shallow compared to typical druggable features, small-molecule inhibitors have been shown to successfully disrupt expansive protein binding interfaces much larger than the inhibitors themselves (474-477).

The ERK DRS mediates numerous specific interactions, including binding of the upstream activators MEK1/2 (478-480), certain phosphatases like MKP3 (478,481), and the substrates MNK1 (478), caspase-9 (482), p90Rsk-1 (474,483,484), and Ets-1 (459,460). In cancer, several mutations in the ERK DRS confer resistance to upstream Raf/MEK inhibition by preserving ERK activity. For example, the sevenmaker mutant D319N of ERK2 is known to significantly decrease MEK1 binding, while in cells, it is a gain-of-function mutation due to pathway feedback signaling and probable decrease in phosphatase binding (485). DRS mutations are observed in cervical, head, and neck cancers and can be found in the COSMIC database (E322 and D321 alterations in human ERK2 correspond to E320 and D319 in rat ERK2)(486). Distinct DRS mutations have been observed for ERK1 and ERK2 isoforms, suggesting possible non-redundant functions associated with the DRS between the two isoforms (486). Therefore, the DRS is likely of biological importance in cancer, so targeting it with inhibitors could be beneficial. In addition, ERK DRS inhibitors could be valuable tools for understanding signaling events that are mediated by the DRS, both in cancerous and in normal cells.

Several small-molecule ERK DRS inhibitors have been discovered using computer-aided drug design (CADD)(474,487) or *in silico* screening methods (488). This pool of inhibitors was expanded by further *in silico* screening and computational searches for similar compounds, and by synthesis of analogues for SAR studies (475,489,490). CADD and *in silico* screenings have also been used to identify inhibitors of the other known docking site of ERK2, the F-recruitment site (FRS)(491). Biochemical screenings for non-ATP competitive kinase inhibitors are difficult, given that there are multiple mechanisms of kinase inhibition, and high-throughput screenings typically rely on kinase activity assays that focus on the active site. Assays against ERK docking sites must be biased against discovery of ATP-competitive inhibitors. For example, a high-throughput AlphaScreen assay has previously been designed to identify ERK2 FRS inhibitors, utilizing a high ATP concentration to prevent ATP-competitive inhibitors from binding (492). Here, we describe a competition-based screen to identify inhibitors that displace a fluorescent peptide from the DRS of ERK2. The compounds identified from this screening method represent a new structural class of ERK inhibitors. NMR spectroscopy and macromolecular X-ray crystallography data confirmed that these compounds bind to the DRS of ERK2, which opens avenues for the future chemical optimization of ERK DRS inhibitors.

12.2 Results and Discussion

Screening Identified Tripodal Cyclic Guanidino Scaffolds as DRS Inhibitors. To identify reversible inhibitors that bind the DRS of ERK2, we first designed and optimized a screening method suitable for combinatorial ligand libraries. This library format allows high-throughput screening with low resource consumption, i.e. less than 100 samples are needed to screen millions of compounds (493-495). We previously designed a high-throughput screening method to

preferentially detect covalent inhibitors of the ERK2 DRS that react with Cys159 (*in preparation*). In that method, a FITC-tagged peptide (FITC-X-Lig-D) was competitively displaced from the DRS by library compounds, generating a change in fluorescence anisotropy. We modified this protocol to avoid the detection of covalent cysteine-reactive inhibitors by including a reducing agent (2 mM DTT) in each sample. Since the combinatorial libraries contained the solvent DMF, we then tested the effects of DMF concentration on the anisotropy signal for fully bound FITC-X-Lig-D (Figure 12.1). Concentrations of DMF exceeding 0.5 % (v/v) significantly reduced the anisotropy, so this concentration was chosen as a maximum functional limit for the screening. Additionally, we determined the Z-factor for manual 384-well plate preparation by measuring the fluorescence signal for FITC-X-Lig-D samples in a 384-well plate (Supplementary Table S1). The Z-factor was ≥ 0.90 for all fluorescence intensity readings, which indicated that plate preparation was consistent (496).

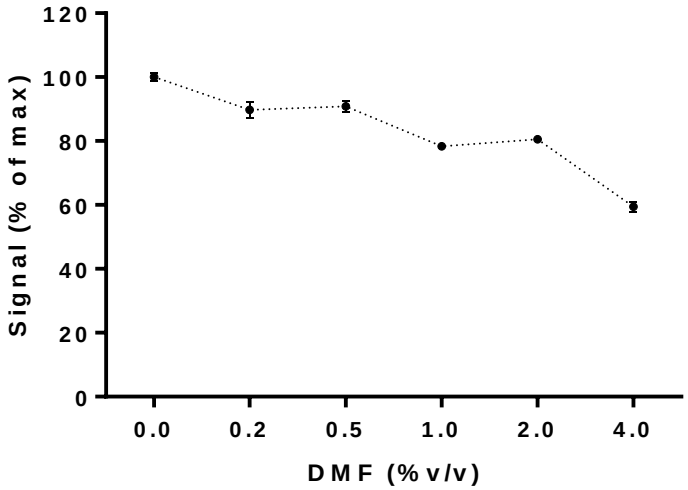

Fig. 12.1. Dependence of maximum anisotropy signal on DMF % (v/v). ERK2 (1 µM) was incubated with 10 nM FITC-X-Lig-D at room temperature in the presence of 0-4 % (v/v) DMF for 1 hr. Anisotropy was measured and normalized to the maximum signal at 0 % (v/v) DMF. All subsequent screening conditions utilized 0.5 % (v/v) DMF.

The screening then proceeded in three phases that allowed for inherent optimization of the structure-activity relationship (Figure 12.2). In Phase I, 78 scaffold ranking samples, each representing a distinct chemical structure with systematically varied functional groups, were screened at 50 and 25 μg/mL in a binding competition assay to identify the active scaffolds that displace the peptide FITC-X-Lig-D from the DRS. The top 5 most active scaffolds that caused the greatest displacement of the fluorescent peptide all contained cyclic guanidino moieties (Table 12.1). 2408 was the most potent hit scaffold, showing at least two-fold more percent signal change in the displacement assay than the rest of the scaffold samples, so it was selected for the second screening phase. Scaffold 2408 consists of a tripodal tris-(2-aminoethyl)amine backbone that connects three cyclic guanidino moieties. It qualitatively has an additional plane of symmetry compared to the other active scaffolds, which could increase its productive binding modes and account for its higher potency. Scaffolds 2407, 2157, 2353, and 2354 contain two cyclic guanidino moieties and all had similar lower potencies against ERK2, further suggesting the importance of the third cyclic guanidino group in 2408. In Phase II of the screening, a mixture-based compound library of scaffold 2408, which contained 9,765,625 compounds formatted into 125 systematically arranged mixture samples, was screened at 50 and 25 μg/mL using the FITC-X-Lig-D displacement assay. All the compounds in the 2408 mixture-based library had 5 functional groups, and the 125 mixture samples were arranged into 5 sub-libraries based on the positions of the functional groups. In each mixture sample, one position was held constant with a single R-group (R) while the remaining positions were systematically varied (X). The hit functional groups for each position on the scaffold

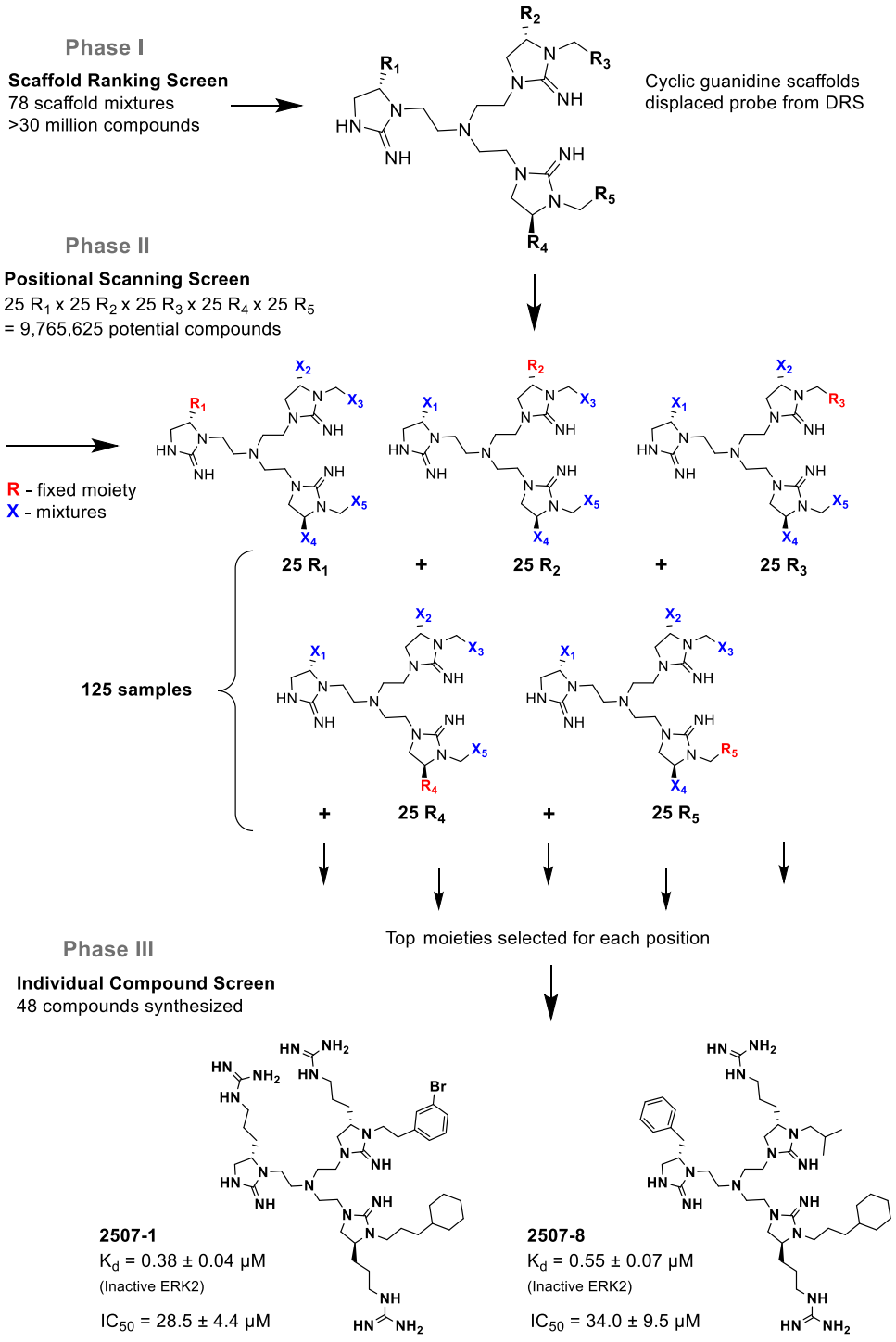

Figure 12.2. Deconvolution of the tripodal cyclic guanidino libraries.

Table 12.1. Top scaffold samples that exhibited highest displacement of fluorescent probe in scaffold screening. Screening results for scaffold ranking library at 25 µg/mL. Scaffold samples were ranked by their average % displacement of the FITC-X-Lig-D probe from the D-recruitment site of ERK2. Data reported as average of 2 replicate samples at mixture dose of 25 µg/mL.

Scaffold Sample #	Structure	Percent (%) signal change
2408	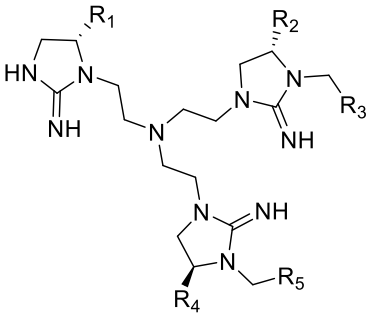	55.7
2407	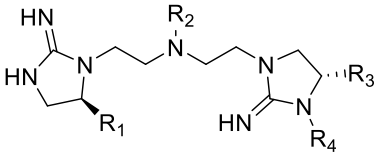	21.2
2353	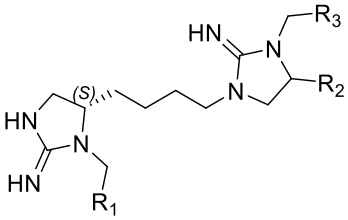	19.5
2157	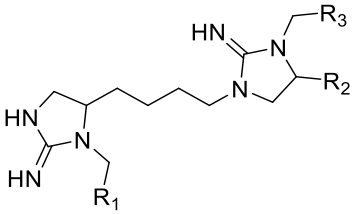	19.4
2354	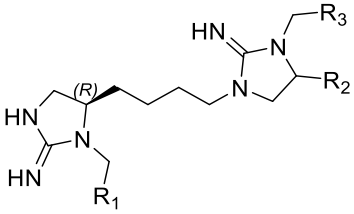	16.3

were selected to generate structures of 48 individual compounds. The individual compounds were then rescreened in Phase III and the resulting top 10 most active compounds were selected as hits and purified for further characterization (Table 12.2).

Hit Compounds Inhibit DRS Interactions in a Dose-Dependent Manner. Next, we measured the dose-dependent change in anisotropy signal for each of the top 10 compounds upon competitive displacement of FITC-X-Lig-D from the DRS of ERK2. Both inactive (unphosphorylated) and active (bis-phosphorylated) forms of ERK2 were tested to evaluate if the conformational changes of ERK2 upon its activation have any effect on DRS binding. The resulting apparent affinities (K_i values) of the compounds for ERK2 ranged from approximately 0.24 – 1.5 μM for each enzyme activation state (Table 12.3). The activation state of ERK2 did not appear to have a dramatic effect on the inhibitor binding affinities; the largest observed difference between inhibitor affinity values for active and inactive forms of ERK2 was 2.4-fold. These results indicated that while there are minor differences between the affinities of each compound for active and inactive ERK2, the compounds all effectively bind to both forms of the enzyme under the assay conditions.

Table 12.2. Top individual compounds resulting from positional scanning of library 2408. Structure-activity relationship and potency of the top 10 individual hit compounds from the 2408 scaffold library. IC_{50} values were measured using a fluorescence assay. ERK2 at 2 nM was incubated with 0-50 µM compounds for 20 minutes prior to reaction with 2 µM sox-Sub-D and 1 mM MgATP. Values shown indicate IC_{50} ± standard error. Compounds are organized according to structural similarities. [A]IC_{50} was too large to be accurately measured

Com-pound 2507-#	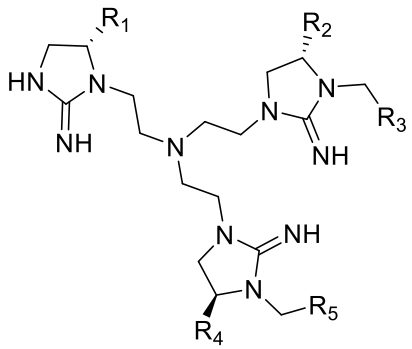					**Dose-response data**
	R1	**R2**	**R3**	**R4**	**R5**	**IC_{50}, µM**
8	benzyl	guanidinopropyl	isopropyl	guanidinopropyl	cyclohexylethyl	34.0 ± 9.5
2			3'-bromobenyl			31.4 ± 4.8
26					4'-methylbenzyl	41.2 ± 4.5
14				4'-fluorobenzyl	cyclohexylethyl	54.8 ± 15.3
1	guanidinopropyl			guanidinopropyl		28.5 ± 4.4
25					4'-methylbenzyl	48.9 ± 7.1
13				4'-fluorobenzyl	cyclohexylethyl	41.8 ± 4.0
37					4'-methylbenzyl	68.7 ± 15.9
16		methylthioethyl			cyclohexylethyl	ND[A]
40					4'-methylbenzyl	60.8 ± 13.4

Table 12.3. Binding affinities of top 10 compounds. Potency of top inhibitors against ERK2. K_i values were determined by anisotropy assay in the same manner as the original screening. Active or inactive ERK2 at 1 μM was incubated with 0-200 μM compounds for 45 minutes at room temperature prior to anisotropy measurements as conducted in the main screening. K_i values were calculated in GraphPad Prism as described in Supplementary Information. Values shown indicate K_i ± standard error of the fit.

ID	Inactive ERK2 K_i, μM	Active ERK2 K_i, μM	Approx. K_i ratio (Active/Inactive)
2507-1	0.383 ± 0.042	0.567 ± 0.122	1.48
2507-2	0.247 ± 0.026	0.584 ± 0.104	2.36
2507-8	0.549 ± 0.066	0.384 ± 0.048	0.70
2507-13	0.351 ± 0.045	0.598 ± 0.085	1.70
2507-14	0.933 ± 0.110	0.660 ± 0.112	0.71
2507-16	1.48 ± 0.11	1.273 ± 0.203	0.86
2507-25	0.611 ± 0.064	0.861 ± 0.138	1.41
2507-26	0.501 ± 0.075	0.404 ± 0.061	0.81
2507-37	0.567 ± 0.066	0.564 ± 0.078	0.99
2507-40	0.938 ± 0.109	0.783 ± 0.092	0.83

The compounds were also tested for their ability to prevent active ERK2 from phosphorylating sox-Sub-D, a fluorescent reporter substrate peptide (Table 12.2). This peptide sequence included the same core sequence of FITC-X-Lig-D without the FITC tag and 6-aminohexanoic acid linker (X). The peptide also contained a phosphorylation consensus sequence such that it can bind to both the DRS and active site of ERK2. The peptide was labeled with the sox moiety, which fluoresces upon chelation with magnesium and peptide phosphorylation. Dose-response curves were obtained for each compound against ERK2 phosphorylation of sox-Sub-D. The resulting IC_{50} values indicated that the relative potency among the 10 compounds was similar to the observed K_i measurements; however, the IC_{50} values for each compound were larger than their respective K_i values by approximately 2 orders of magnitude. This large difference is not expected, though it could be attributed to several factors. First, the substrate/ligand peptides and experimental conditions are distinctly different for the two assays that were employed to determine K_i and IC_{50}. Also, the presence of MgATP which binds the kinase can influence substrate binding

and phosphorylation (497,498). Specifically, bound ATP can induce communication to other binding sites (488,499). Here, the IC_{50} assay required MgATP with large excess of free magnesium (Mg^{2+}) in order to chelate with sox-Sub-D, while the anisotropy dose-response assay did not include MgATP or Mg^{2+}. Combined, these factors could account for the differences in measurements between the two assays.

Characterization of 2507-1 Selectivity. Compound 2507-1 (Figure 12.3A) showed the most potent IC_{50} at 28.5 ± 4.4 μM, so we selected it for further mechanistic evaluation. In [γ-^{32}P] ATP-based dose-response assays, we found that 2507-1 more potently inhibited ERK2 phosphorylation of the substrate Ets-1 compared to the non-fluorescent Sub-D peptide, with an IC_{50} of 5.62 ± 0.96 μM (Figure 12.3B). Meanwhile, the IC_{50} against the Sub-D peptide phosphorylation was measured at 46 ± 14 μM, which is within error of the IC_{50} against sox-Sub-D. Interestingly, 2507-1 was found to be a partial inhibitor of Ets-1 phosphorylation (~77% maximum inhibition), which is consistent with Ets-1 docking at the FRS of ERK2, in addition to the DRS and active site. To validate that 2507-1 does not interact at the FRS, we tested it as an inhibitor of ERK2 phosphorylation of Sub-F, a peptide that only docks at the FRS. The IC_{50} of 2507-1 in this case was not accurately measurable due to exceeding the solubility limits of the compound, so we concluded that 2507-1 does not effectively target the FRS. Knowing that other kinases like p38α and JNK1/2 share similar DRS regions to ERK2, we tested the ability of 2507-1 to inhibit JNK2 phosphorylation of GST-c-Jun *in vitro* (Figure 12.3B). This IC_{50} was measured at 43 ± 6 μM, which indicated that 2507-1 has similar selectivity for JNK2 when compared to ERK2 phosphorylation of Sub-D, but much less selectivity for JNK2 when compared to ERK2 phosphorylation of the more physiologically relevant substrate Ets-1. It is possible that the difference in IC_{50}s observed for 2507-1 inhibition of Ets-1 and Sub-D phosphorylation could be

explained by multiple modes of inhibitor binding that occur with different affinities.

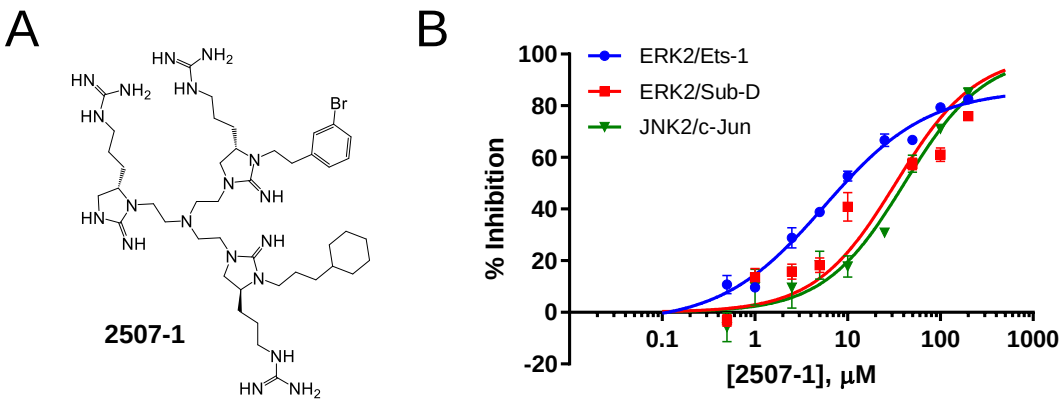

Figure 12.3. Potency and selectivity of 2507-1. (A) Structure of lead compound 2507-1. (B) The ability of 2507-1 to inhibit 2 nM ERK2 phosphorylation of 10 µM Ets-1 and 10 µM Sub-D, as well as 25 nM JNK2 phosphorylation of 2 µM c-Jun, was assessed by ^{32}P assay as described in the Materials and Methods. Enzymes were incubated with 0-200 µM 2507-1 for 30 min prior to reaction initiation by addition of MgATP and substrate. Initial rates ± standard errors are shown fit to standard IC_{50} models.

2507-1 Inhibited ERK2 Activation by Constitutively Active MEK1. Because MEK1 is known to interact at the DRS of ERK2 (478-480), we tested whether 2507-1 would prevent activation of ERK2 by the constitutively active MEK1 mutant, MKK1G7B. We found that 2507-1 blocks ERK2 activation *in vitro* in a dose-dependent manner, with an IC_{50} of 9.9 ± 1.9 µM (Figure 12.4). Thus, this small molecule can potently block ERK2 protein-protein interactions *in vitro*. D-site sequences frequently contain basic residues, such as arginine, that are important for engaging the common docking region of the DRS, which consists of D316 and D319. As mentioned, the sevenmaker mutation D319N causes significant decrease in MEK1 binding to ERK2, and in cells, and acts as a gain-of-function mutation due to signaling pathway feedback and other effects (485). Thus, minor interference in this region can disrupt protein docking. All 10 hit compounds have at least one arginine-like functional group and 2507-1 significantly blocked MKK1G7B activation of ERK2. This indicates that the compounds may function in a similar manner as the D319N mutant by neutralizing the acidic environment of the common docking region.

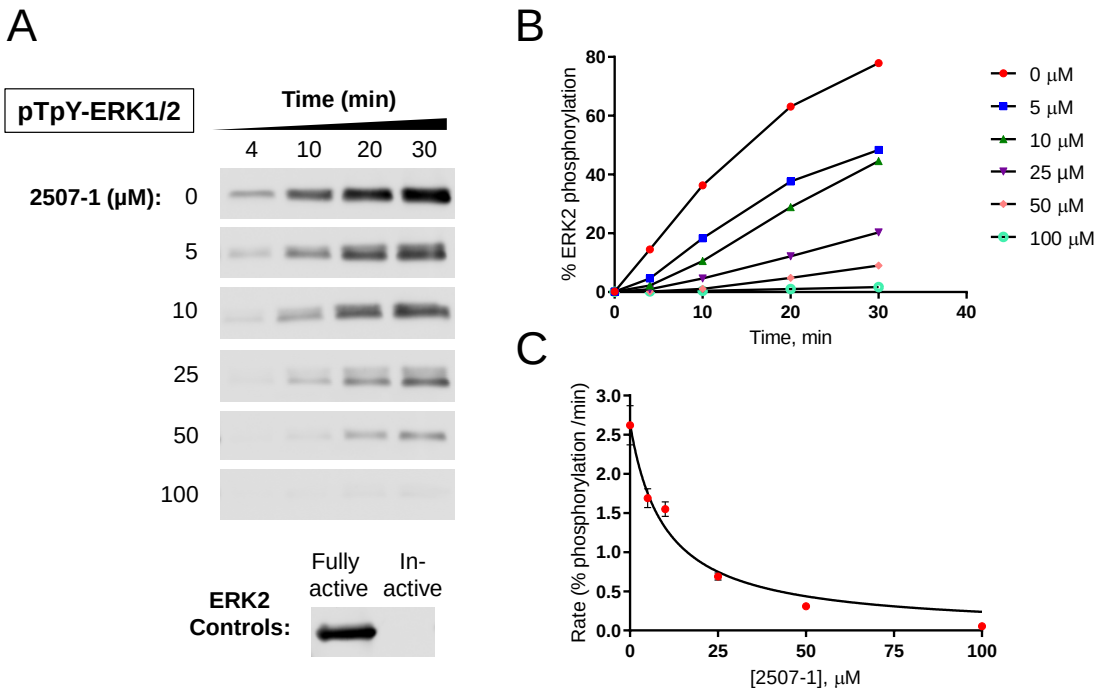

Fig. 12.4. 2507-1 inhibits MKK1G7B phosphorylation of ERK2 *in vitro*. Recombinant ERK2 was incubated with varied concentrations of 2507-1 (0-100 μM) for 10 minutes prior to reaction with MKK1G7B and MgATP as described in Methods. (A) Resulting ERK2 phosphorylation was measured by Western blot. Controls include fully phosphorylated active ERK2 and unphosphorylated inactive ERK2. (B) Densitometry of Western blot, where phospho-ERK signal is normalized to total ERK signal. (C) IC_{50} curve was generated from initial rate measurements of % ERK2 phosphorylation.

Confirmation of DRS Binding by Structural Data. To confirm the binding mode of the hit compounds, we used a combination of NMR and macromolecular X-ray crystallography. For the NMR experiments, inhibitor interactions at particular residues of ERK2 were detected by measuring chemical shift perturbations in response to addition of inhibitor (500). We tested three of the top 10 hit compounds, 2507-1, 2507-8, and 2507-26, by this method in order to observe binding interactions for different R-groups on the 2507 scaffold. As shown in Figure 12.5 for compound 2507-8, most perturbations were localized to the DRS region of ERK2, as was also the case for 2507-1 and 2507-26 (not shown). All three compounds induced chemical shift perturbations above two standard deviations for the following key DRS residues: both common

docking domain residues (D316 and D319), either T157 or T158 of the ED domain, the hydrophobic residues L119, L155, H123, Y126, and a solvent-exposed cysteine residue C159. These results indicated that the compounds likely bind the DRS in the same manner, regardless of their differing R-groups.

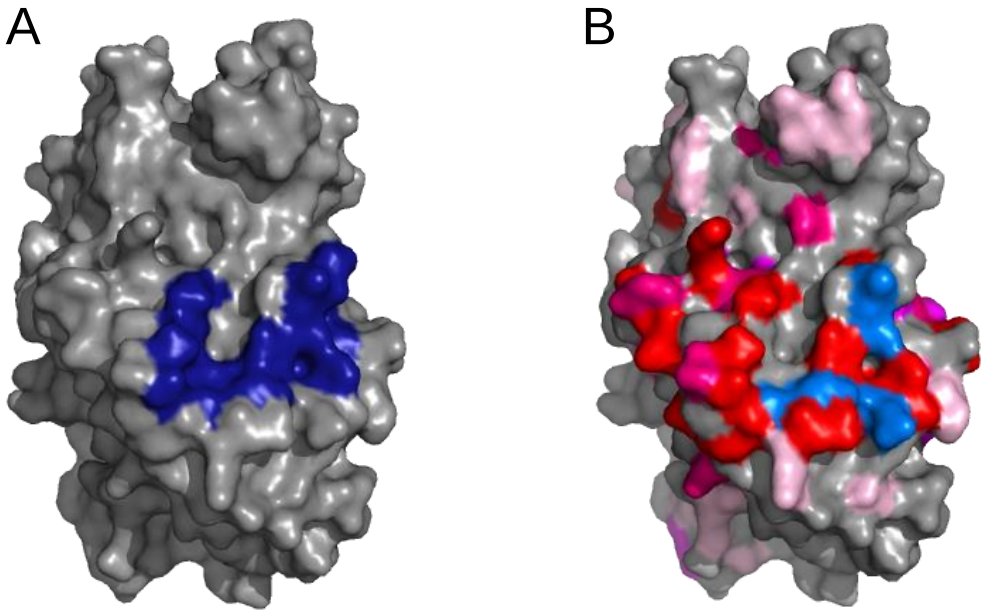

Figure 12.5. Docking of 2507-8 at the DRS via NMR. 2507-8 binding to ERK2 was analyzed by NMR. (A) Structure of ERK2 (PDB ID: 3ERK, grey) showing key DRS residues (dark blue). (B) Solution NMR results showing ERK2 (PDB ID: 3ERK) residues affected by 2507-8 binding. Colors indicate chemical shift perturbations: 1-1.5 S.D.: light pink, 1.5-2 S.D.: magenta, 2-3 S.D.: hot pink, >3 S.D.: red, and perturbations beyond detectable limits: marine. (S.D. = standard deviation).

To ensure that the chemical shift perturbations detected by NMR were not caused by allosteric effects, conformational changes of the protein, or nonspecific binding of the inhibitor, we crystallized compound 2507-8 (Figure 12.6A) in complex with inactive ERK2 and determined the structure with 1.9 Å resolution (Figure 12.6B, Supplementary Table S4). We observed the appearance of new electron density near ERK2 residues 311-318. This electron density was not fully contiguous and was difficult to model with a single molecule of 2507-8 (Figure 12.6C and D). Instead, our best interpretation used two fragments of 2507-8, termed Fragment A and

Fragment B. When considering this model, one possibility is that one or both of the fragments are portions of two intact inhibitor molecules, but only part of each molecule is resolvable. A second possibility is that one or both of the fragments are impurities or degradation products of 2507-8. This may be likely for Fragment B, given that LC-MS analysis of the 2507-8 inhibitor identified Fragment B (*(S)*-4-benzylimidazolidin-2-imine) as an impurity (Supplementary Figure S16). Finally, although it is unlikely given the distance between the two regions, it remains possible that this density is attributed to a single inhibitor molecule, where the structural elements of the inhibitor that link the regions are too flexible for visualization. Nevertheless, both modeled 2507-8 fragments indicate that binding is localized at the DRS and does not occur at the active site of ERK2 (Figure 12.6B).

As predicted, the arginine-like group on Fragment A is located sufficiently close to form ionic interactions with the common docking domain residue D319, in addition to Y129 and Y314 (Figure 12.6E, Figure 12.7). These interactions may stabilize the binding position of this functional group, which is consistent with the observation of clear electron density for Fragment A. Additional hydrophobic interactions engage Fragment A with D316 of the common docking domain, as well as E312, Y315, and P317. In contrast, Fragment B is bound in the hydrophobic groove between the common docking and ED domains. It forms hydrophobic interactions at the key DRS residues H123 and Y126, as well as with D122 and Y314 (Figure 12.6F). Both Fragment A and Fragment B appear to participate in similar binding interactions to those of a peptide derived from the phosphatase HePTP, which has previously been crystallized in complex with ERK2 and is known to bind to the DRS (499). This peptide has been used as a basis for identifying inhibitors of the DRS via computer-aided drug design (487,489). Thus, the HePTP peptide provides further context for the mechanism and binding mode of 2507-8. Interestingly, the phenyl carbon at the

meta-position of Fragment B is approximately 4.5 Å from the C159 side chain, which we have shown to be a suitable target for covalent inhibition of ERK2 (*in preparation, PNAS compound*). Functionalization of the phenyl ring with a cysteine-reactive substituent could generate future covalent ERK inhibitors with greater potency than the reversible inhibitors identified here.

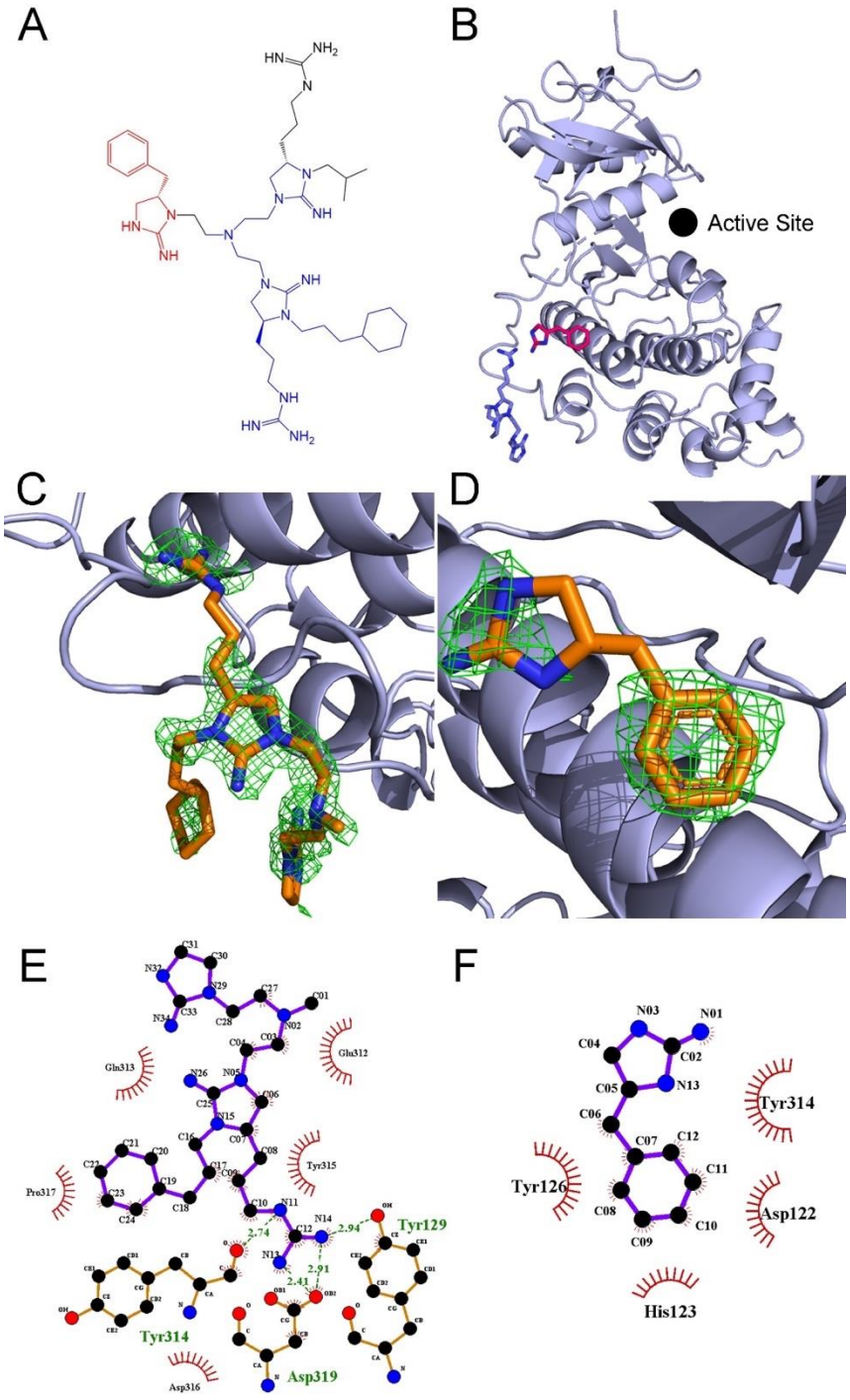

Fig. 12.6. The 1.9Å resolution structure of ERK2 in complex with inhibitor 2507-8. (A) Chemical structure of inhibitor 2507-8 (B) ERK2 (light blue) in complex with inhibitor 2507-8, which was resolved as two fragments termed A and B, that are labeled in blue and red respectively. *The* F_o - F_c composite map contoured at 2.5 σ and calculated in Phenix(140) after the removal of ligands is shown for (C) Fragment A and (D) Fragment B. LigPlot projections of hydrophobic and ionic interactions are shown for (E) Fragment A and (F) Fragment B. Ionic interactions are shown using green dashed lines. Hydrophobic interactions are shown using circular red bursts.

Table 12.4. Crystallographic data collection and refinement statistics.

[a]Numbers in parentheses indicate statistics for the highest shell.
[b]$R_{sym} = \sum|I_i - (I)|/\sum|I_i|$ where I is intensity, I_i is the ith measurement, and (I) is the weighted mean of I.
[c]$R_{work} = \sum\big||Fo| - |Fc|\big|/\sum|Fo|$ where Fo and Fc are the observed and calculated structure factor amplitudes. R_{free} is the same as R_{work} for a set of data omitted from the refinement.
[d]Ramachandran analysis from MOLPROBITY(501).

	ERK2 Inhibitor 2507-8
PDB accession code	6NBS
Data Collection and Processing[a]	
Beamline	21-ID-F
Space groups	$P2_1$
Cell Dimensions: a, b, c (Å)	48.9, 71.2, 60.2
α, β, γ (degrees)	90, 109.4, 90
Resolution (Å)	37.2-1.90 (1.968-1.90)
Total Reflections	137,531
Unique Reflections	30,668
R_{sym}[b] (%)	0.076 (0.565)
<I>/<σ>	35.1 (5.02)
Completeness (%)	99.63
Refinement Statistics	
R_{work}[d] (%)	18.01
R_{free} (%)	22.18
RMS deviations	
Bond (Å)	0.007
Angle (°)	0.822
Ramachandran statistics[e]	
Favored (%)	96.15
Allowed (%)	3.85
Outliers (%)	0.0

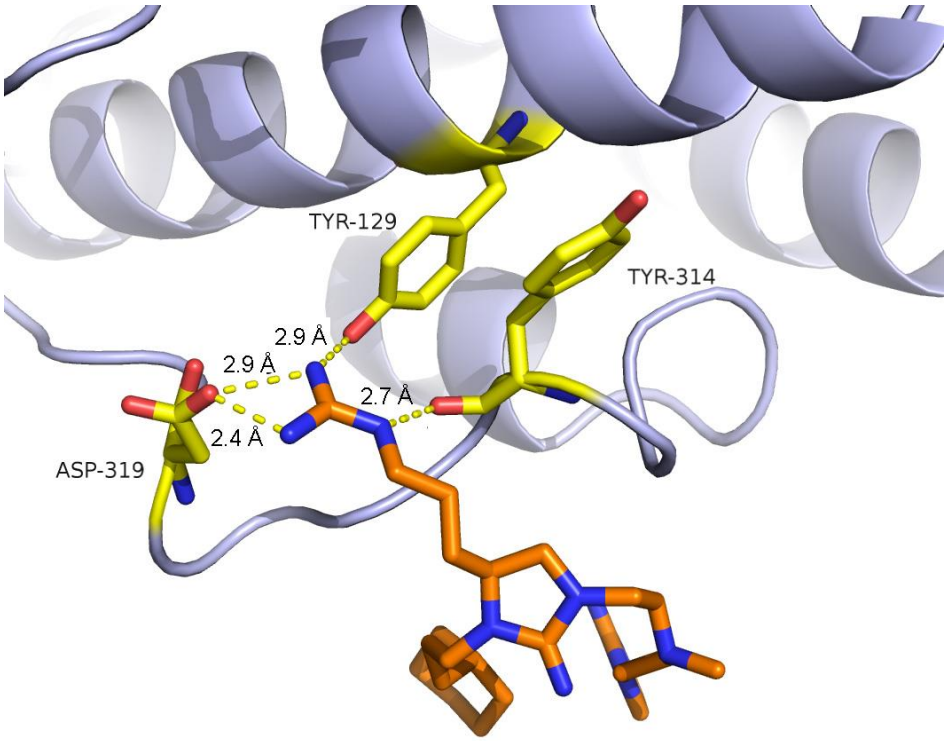

Fig. 12.7. Ionic and hydrogen-bonding interactions between Fragment A and the DRS of ERK2. Three nitrogen atoms in inhibitor 2507-8 interact with residues Tyr129, Tyr314, and Asp319 in ERK2.

12.3 Conclusions

From the binding interactions of 2507-8 and the ability of the hit compounds to inhibit ERK2 activity and activation, it is clear that this class of small molecule is effective at inhibiting ERK2 through the DRS. The structural data showed that small-molecule interactions at the acidic common docking region and the hydrophobic residues adjacent to the ED domain of the DRS are likely the basis of this inhibition. Further structural modifications of these compounds could improve selectivity for ERK or promote covalent inhibition of the solvent-exposed cysteine residue of the DRS. The continued development of these inhibitors has the potential to yield ERK-targeting drugs that do not compete with ATP but instead ensure greater specificity by disrupting critical protein-protein interactions.

12.4 Materials and Methods

Proteins, Peptides, and Buffers. Tag-less ERK2 was expressed, purified, and activated essentially as described (502). Erk2 DNA (NM_053842) was ligated into a pet28a (+) vector that was modified to include a TEV cleavage site for His_6-tag removal. Vector modification and cleavage of the His_6-tag with TEV protease were performed as described (503). ERK2 was activated using the constitutively active MKK1G7B mutant (504). The ERK substrate Ets-1 (residues 1-138) (EtsΔ138) was expressed and purified as previously described (505). GST-c-Jun and active JNK2 were prepared as previously reported (503,506).

The ERK substrate peptides Sub-F and Sub-D were prepared as described (507). Sox-labeled Sub-D (sox-Sub-D) (508,509) and FITC-labeled Lig-D (FITC-X-Lig-D)(510,511) were prepared as previously described. Briefly, sox-labeled sox-Sub-D was synthesized by alkylation of sox-Br (2-bromomethyl-8-tertbutyldiphenylsilyloxy-5- (N, N-dimethyl) sulfonamide quinolone) to Sub-D on resin (508,509). FITC-labeled Lig-D (FITC-X-Lig-D) was prepared by labeling the C-terminus of Lig-D with FITC via a 6-aminohexanoic acid linker on a cysteine residue.

The following buffers were used for all *in vitro* ERK2 assays: Buffer A (25 mM HEPES pH 7.5, 50 mM KCl, 0.1 mM EDTA, 0.1 µM EGTA, 1.3% glycerol, 2 mM DTT, 10 µg/mL BSA, and 0.1% w/v Triton X-100), and Buffer B (25 mM HEPES pH 7.5, 50 mM KCl, 0.1 mM EDTA, 0.1 µM EGTA, 10 mM $MgCl_2$, 2 mM DTT, 10 µg/mL BSA, 0.01% (v/v) Triton X-100, 2% (v/v) DMSO).

Combinatorial Library Screening. All screening samples were prepared in 384-well low-volume black polystyrene plates (Corning) with final volumes of 30 µL per well. Samples were tested in Buffer A with 1 µM ERK2 and 10 nM FITC-X-Lig-D with 0.5% (v/v) DMF. All

anisotropy readings were conducted at room temperature after 1 hour of incubation. Controls included maximal anisotropy signal (full binding of 10 nM FITC-X-Lig-D to 1 μM ERK2 with no inhibitor present), and minimum signal (free 10 nM FITC-X-Lig-D with no ERK2 present). Phase I of the screening tested 78 scaffold-ranking samples at 50 μg/mL and 25 μg/mL, in duplicate. The samples were also tested for intrinsic fluorescence in Buffer A. The top scaffold, 2408 (Table 12.1), was selected for the second phase of the screening: positional scanning of the scaffold R-groups. The 2408 library contained 9,765,625 compounds formatted into 125 systematically arranged mixture samples. The samples were screened at 50 μg/mL and 25 μg/mL in duplicate, with original hit mixtures from Phase I as additional controls. Based on the results of the screening, 48 compounds were selected for individual synthesis (purity ≥ 70%). These compounds, along with two controls (the 2408 scaffold with all R-groups as hydrogens and the original mixture sample 2408-X), were screened at 12.5, and 25 μM. The top 31 compounds from those results were rescreened at 3.125, 6.25, and 12.5 μM. The top 10 compounds were selected for additional purification and further characterization.

Synthesis of 2408 Libraries and Individual Compounds. The synthetic methods for creating the 2408 scaffold and the details for the synthesis and purification of 2507-8 are described in Supplementary Information (Fig. 12.8).

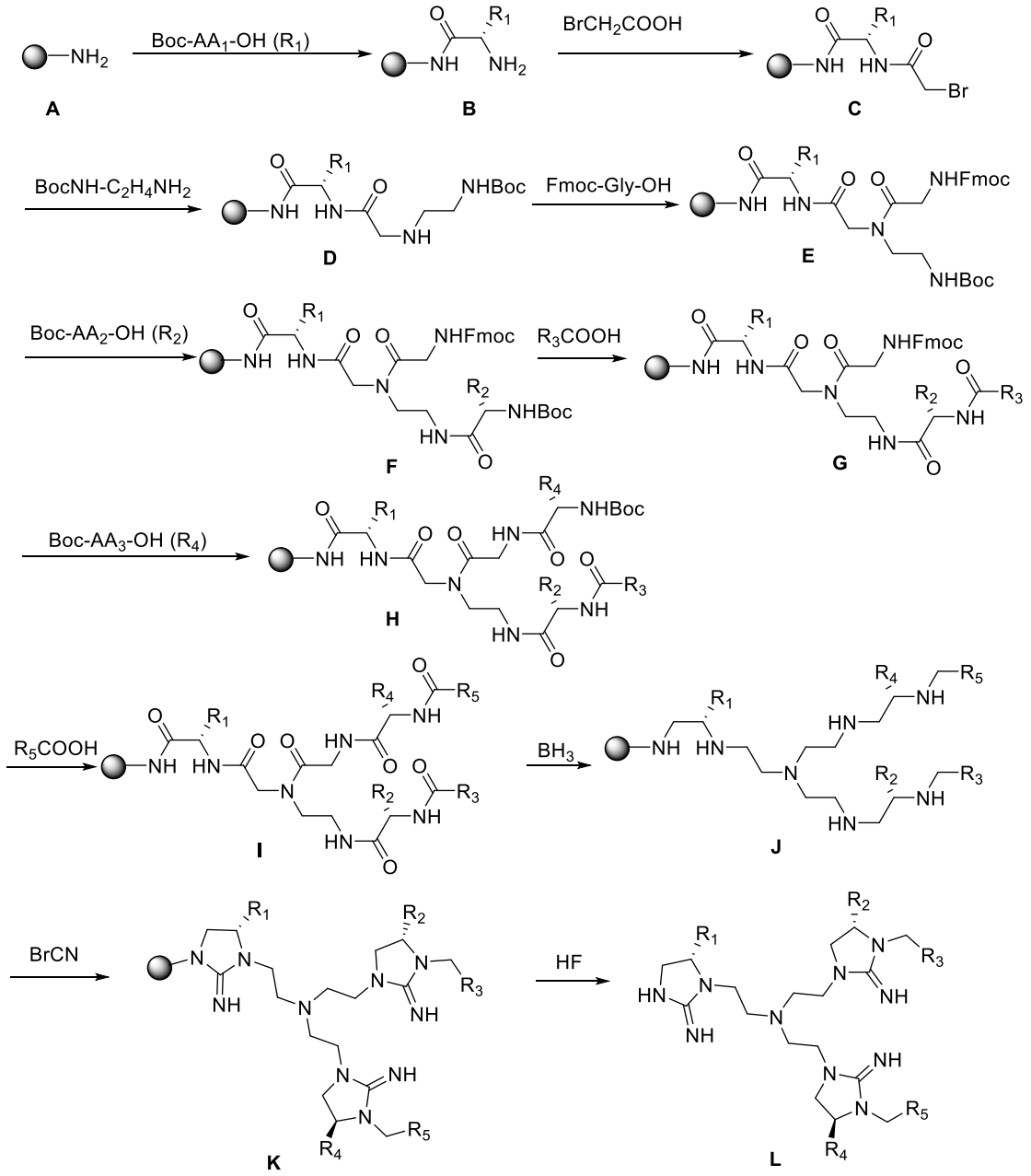

Fig. 12.8. Synthetic approach for tris-(2-(2-iminoimidazolidin-1-yl)ethyl)amines.

D*ose-Response Assays with Fluorescent Reporter*. Compounds at concentrations of 0-100 µM were pre-incubated with 0.5 nM ERK2 at room temperature for 20 minutes. The ability of ERK2 to phosphorylate 2 µM sox-Sub-D in the presence of 1 mM MgATP was then assessed in Buffer B. Reactions were initiated by addition of MgATP and sox-Sub-D and carried out at room temperature in a Synergy H4 plate reader for 10 minutes. Data collection and analysis was conducted as previously described (512).

Anisotropy Dose-Response Assays. 1 µM active or inactive ERK2 was pre-incubated with 10 nM FITC-X-Lig-D and 0, 1, 2.5, 5, 10, 25, 50, 100, and 200 µM of each compound at room temperature for 45 minutes prior to anisotropy measurements as described for the primary screening. The anisotropy dose-response curves were fit to an equilibrium binding model for conditions where the ERK2 concentration is in excess of FITC-X-Lig-D concentration (513). The affinities of active and inactive ERK2 for FITC-X-Lig-D were evaluated for use in the anisotropy binding model.

Quantifying Inhibition of ERK2 Activation In Vitro. The ability of 20 nM MKK1G7B to phosphorylate and activate 1 µM ERK2 was tested in the presence of 0, 50, 100, and 200 µM compound 2507-1 with 10 mM MgATP in Buffer B (with $MgCl_2$ at 0.5 mM). ERK2 was incubated with 2507-1 for 10 minutes at 28ºC prior to initiation with MKK1G7B and MgATP. Reactions were quenched in SDS loading buffer at time points ranging from 0-30 minutes. All quenched samples were loaded into 10% SDS polyacrylamide gels at 52 ng/lane ERK2. Fully active and inactive ERK2 at 52 ng/lane were used as controls. The gels were transferred to Immobilon-FL membranes overnight at 4 ºC. Membranes were then blocked in 4X diluted Odyssey® Blocking Buffer (PBS) (LI-COR) for 1 hr at room temperature. Membranes were incubated in TBST (5% milk) with 1:2,000 antiphospho-p44/42 MAPK (Erk1/2) (Thr202/Tyr204) (E10) mouse mAb (Cell

Signaling Technology), or TBST (5% BSA) with 1:1,000 anti-p44/42 MAPK (Erk1/2) (137F5) rabbit mAb (Cell Signaling Technology) for 1 hour at room temperature and washed with TBST. The membranes were incubated with appropriate secondary antibodies (1:15,000 IRDye® 800CW Goat (polyclonal) anti-rabbit IgG or IRDye® 680RD Goat (polyclonal) anti-mouse IgG (LI-COR)) for 30 min at room temperature. After washing again with TBST and Tris-buffered saline, fluorescence was detected on an Odyssey® Sa imaging system (LI-COR).

^{32}P Assay for Evaluating 2507-1 Selectivity. 2507-1 was tested for its ability to inhibit ERK2 (2 nM) phosphorylation of Ets-1 (10 μM), Sub-D (10 μM), or Sub-F (30 μM), and JNK2 (25 nM) phosphorylation of c-Jun (2 μM). Enzymes were pre-incubated with 0-200 μM 2507-1 at room temperature for 30 min prior to reaction initiation by addition of substrate and [γ-^{32}P] MgATP (1 mM for ERK2 reactions and 500 μM for JNK2 reactions). All reactions were carried out at 28 ºC in Buffer B with reduced $MgCl_2$ (0.5 mM). Sub-F phosphorylation reactions contained final DMSO concentration of 3.2% (v/v) DMSO. Phosphorylated substrate was quantified at 0.5, 1, 1.5, 2, and 4 min time points as previously described (^{32}P protocol)(514) on a Tri-Carb® 2910TR liquid scintillation analyzer (Perkin Elmer).

NMR Spectroscopy. The protocol for producing uniformly labeled ^{2}H,^{13}C,^{15}N kinase has been described elsewhere (500). The NMR data were collected at 25 °C on a 300 μl sample containing 100 μM inactive ERK2, 20 mM potassium phosphate, pH 6.8, 150 mM KCl, 200 μM EDTA and 5.0 mM DTT (10 % $^{2}H_2O$) using a 700 MHz Bruker Avance III spectrometer equipped with a triple resonance cryogenic probe and capable of applying pulsed field gradients along the z-axis. ^{1}H-^{15}N TROSY (515) experiments with 128 transients, a 1.5 s recycling delay and a digital resolution of 8.9 and 18.3 Hz/point in the direct and indirect dimension, respectively, were collected in the absence and presence of a two-fold excess (200 μM) of the ligand (compound

2507-1, 2507-8, or 2507-26). Data were processed using NMRPipe (516) and analyzed using Sparky(517). Chemical shift perturbations based on the previously published partial assignment of ERK2 (500) were calculated as previously described (459).

Expression and Purification of ERK2 for Crystallization. The ERK2 plasmid Npt7-5H6ERK2 was transformed into BL21 *DEM* Gold cells and a single colony was used to inoculate a 100 mL overnight culture in Luria Broth (LB) at 37 ºC. The next morning, 20 mL of culture was added to 1 L of LB supplemented with ampicillin (100 µg/mL) and incubated to an OD of 0.6 at 37ºC and 205 rpm. The cells were induced with IPTG (0.5 mM) and grown for 4-5 hours at 30 ºC before harvesting (6000 rpm, 4 ºC, 10 minutes). Pellets were frozen in liquid nitrogen and kept at -80 ºC until purification.

Cells were resuspended in 30 mL lysis buffer (40 mM Tris-HCl pH 7.0, 1% Triton X-100, 750 mM NaCl, 5 mM imidazole, 0.1 mM PMSF, 2 mM TCEP, 1X protease inhibitor cocktail powder (Sigma)) per 1 L culture. The suspension was sonicated for 3 min (model FB505 (Fisher Scientific), 75% maximum amplitude, in cycles of 5 s on and 10 s off) at 4 ºC. The crude lysate was then centrifuged (18,000 rpm, 4ºC, 45 min) and the supernatant loaded onto a nickel column (HisTrap HP 5 mL, GE Healthcare Life Sciences), which was then washed in equilibration buffer (40 mM Tris HCl pH 7.5, 10 mM Imidazole, 0.1 mM PMSF, 2 mM TCEP). The eluate was collected over a 30 mL gradient (0-100%) of elution buffer (40 mM Tris-HCl pH 7.5, 200 mM Imidazole, 0.1 mM PMSF, 2 mM TCEP) and loaded directly onto a Source Q column for anion exchange (20 mM Tris HCl pH 8.0, 0.1 mM EDTA, 0.1 mM EGTA, 2 mM TCEP). After elution with an upper gradient of 250 mM NaCl (0-100%), all fractions containing ERK2 were dialyzed overnight into the final storage buffer (20 mM Tris HCl pH 8.0, 0.1 mM EDTA, 0.1 mM EGTA, 200 mM NaCl, 10% glycerol).

Crystallization, Structure Determination, and Analysis. Crystals were grown using the hanging-drop vapor diffusion method with droplets containing 1 µL protein (8-10 mg/ml ERK2 in 20 mM Tris HCl, pH 8.0, with 0.1 mM EDTA, 0.1 mM EGTA, 200 mM NaCl, 10% glycerol) and 1 µL of the reservoir solution (33% PEG 5,000 MME, 0.25 M ammonium sulfate, 0.1 M MES, pH 6.5) in the presence of an arrestin-3 peptide (CH_3CO-AVPETDAPVDTNLIEFE-NH_2) at a molar ratio of 1:2. Droplets were allowed to equilibrate over the reservoir solution at room temperature (approximately 22 ºC). The 2507-8 inhibitor was soaked into the crystals at a molar ratio of 1:3 (ERK2:2507-8) for 24 hours prior to flash cooling. Crystals were cryo-protected with a solution comprised of the reservoir solution and 15% glycerol.

X-ray diffraction data were collected at the Advance Photon Source (APS) beamline 21-ID-F at -173 ºC using a wavelength of 0.9798 Å and a MarMosaic225 CCD detector. Data were processed and scaled using HKL2000(137). The structure was determined using molecular replacement in the program Phaser-MR(138) through the Phenix interface (140), with wild-type ERK2 (PDB entry 1ERK (201)) as the search model. As 1ERK was reported prior to the widespread use of the R_{free} for cross-validation, R_{free} reflections were randomly selected for ERK2. However, because the original model (1ERK) was refined against these reflections, the free-R is of limited utility in this case. Model building was performed in Coot (139) and refinement was conducted using Phenix (140). Residues 328-332 are not included in the final model as the electron density corresponding to these residues was not readily interpretable. Protein-inhibitor interactions were analyzed using the program LigPlot (518), which builds schematic diagrams of protein-ligand interactions using PDB files. All structural figures were made using PyMOL Molecular Graphics System (version 1.5.04, Schrodinger, LLC, New York) unless otherwise indicated. Data collection and refinement statistics are summarized in Table 12.4.

CHAPTER 13

TWO-DOMAIN STRUCTURE OF EVDMO1 OF EVERNINOMICIN BIOSYNTHESIS BY *MICROMONOSPORA CARBONACEA* VAR. *AURANTIACA*

This article was published in Biochemistry (519). Chrystal Starbird was co-first author with **Nicole A. Perry**, and Qiuyan Chen, Sandra Berndt, Izumi Yamakawa, Lioudmila V. Loukachevitch, Emilianne M. Limbrick, Brian O. Bachmann, T.M. Iverson, and Kathryn M. McCulloch contributed to this work. This publication resulted from the Iverson lab experimental section.

13.1 Introduction

Biosynthetic pathways catalyzing the formation of natural products have long been of interest to medicinal and organic chemists. For the medicinal chemist, the potential of a natural product to act as a therapeutic can drive manipulation of the biosynthetic pathway to produce derivatives with more desirable characteristics. Biosynthetic pathways can also be of interest due to the complexity of natural product formation, which can make commercial synthesis inefficient and fermentation of the producing organism more desirable. For the organic chemist or biochemist, unusual structural features found in natural products and the enzymes that catalyze their formation can lead to inspired and novel synthetic strategies.

The orthosomycin natural products, which include avilamycins and everninomicins, are examples of a class of molecules that have been of interest due to their potent antibiotic activity, their unusual structure, and their complex biosynthetic pathways. These compounds are produced by actinomycetes and possess potent antimicrobial activity against Gram-positive bacteria by

targeting protein synthesis on the ribosome (520,521). To date, the most extensively biosynthetically studied orthosomycin is the heptasaccharide avilamycin, which is produced by some strains of *Streptomyces* (522-525). Everninomicin is a related octasaccharide orthosomycin that is produced by *Micromonospora carbonacea* var. *aurantiaca* and has demonstrated efficacy in treating both methicillin-resistant *Staphylococcus aureus* infections and infective endocarditis (526,527). The orthosomycin scaffold contains at least one orthoester linkage (a spirocyclic ortho-δ-lactone group) between carbohydrate moieties that is necessary for antibiotic activity; avilamycin and everninomicin each contain two such linkages. Additionally, both avilamycins and everninomicins possess a terminal eurekanate sugar that contains a methylenedioxy bridge (Figure 13.1A, highlighted in blue).

We recently reported on the mechanism underlying orthoester linkage formation, a crucial step in orthosomycin biosynthesis (528). A set of conserved non-heme iron, α-ketoglutarate (Fe/AKG) dependent oxygenases in the avilamycin and everninomicin gene clusters is proposed to be responsible for catalyzing formation of features requiring oxidation, specifically the orthoester linkages and a methylenedioxy bridge (Figure 13.1A, highlighted in red and blue). This assignment of function is confirmed by the recent demonstration that HygX, the sole oxygenase implicated in hygromycin B biosynthesis, catalyzes the formation of the sole orthoester linkage of that natural product (529). Within avilamycin and everninomicin biosynthetic pathways, however, the assignment of Fe/AKG oxygenases to specific features has been complicated by the presence of multiple orthoester linkages and the highly decorated oligosaccharide scaffold.

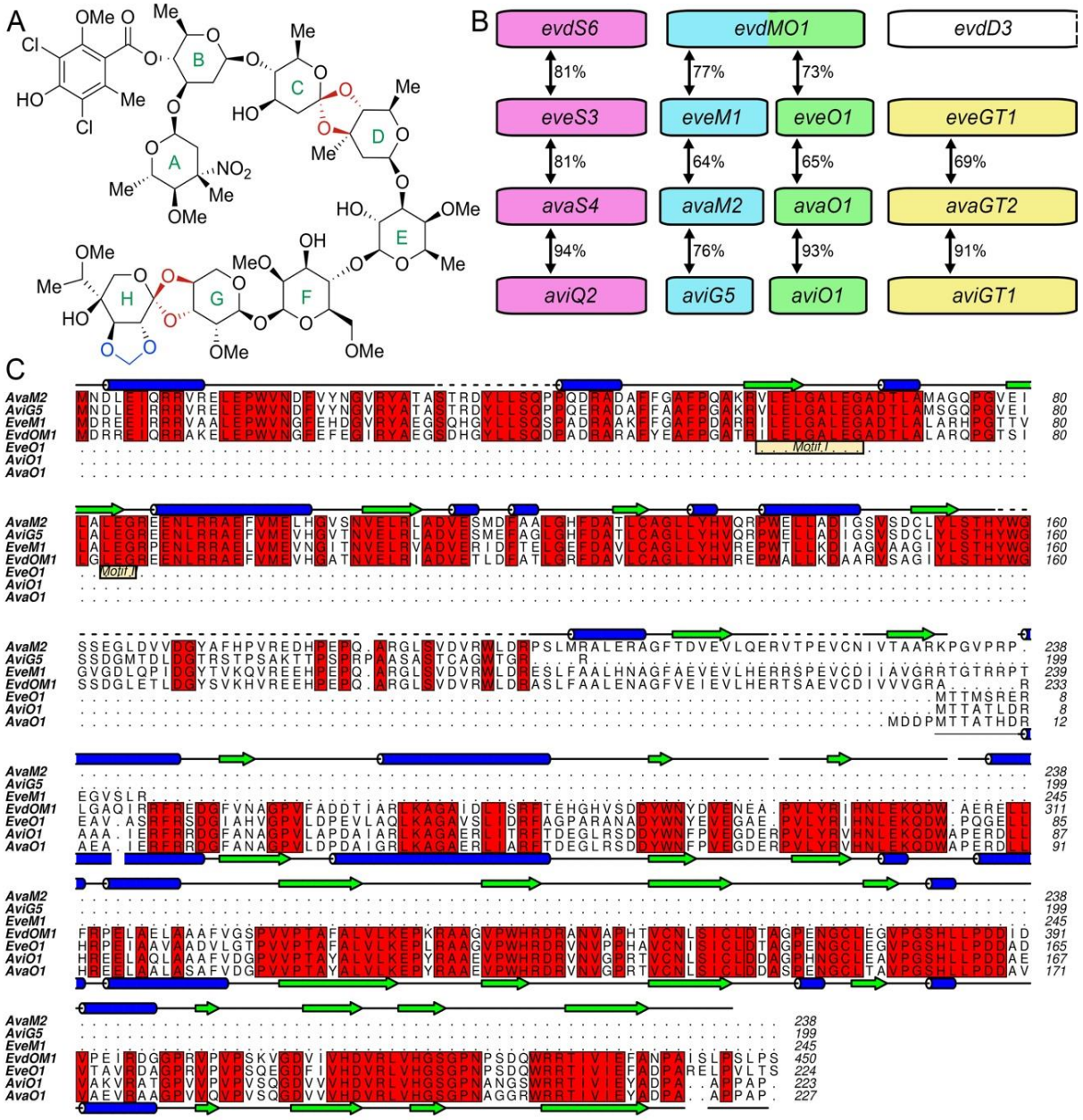

Fig. 13.1. Everninomicin. (A) Chemical structure of everninomicin D with orthoester linkages colored red and the methylenedioxy bridge blue. (B) Gene organization around *evdMO1* and homologous genes of the *eve*, *ava*, and *avi* gene clusters colored by proposed function: epimerase, purple; methyltransferase, blue; oxygenase, green; and glycosyltransferase, yellow. Arrows indicate percent identity. (C) Sequence alignment of EvdMO1 with methyltransferases and oxygenases identified in Fig. 1B reveals large regions of conservation. Secondary structural elements from EvdMO1 are depicted above the alignment and those from AviO1 are below the alignment.

Three putative Fe/AKG oxygenases are encoded in each avilamycin and everninomicin gene cluster (*avi*, *ava*, *eve*, and *evd*). We have structurally characterized EvdO1 and EvdO2, the first two oxygenases encoded in the *evd* gene cluster (528). The third and final oxygenase gene of the *evd* gene cluster, *evdMO1*, is unusual in that it is the only *evd* gene product predicted to have bifunctional activity as a result of gene fusion: the N-terminal domain has homology with *S*-adenosylmethionine (SAM) O-methyltransferases and the C-terminal domain has sequence similarity with the Fe/AKG oxygenases. The implications of this gene fusion are unclear; the corresponding oxygenases and methyltransferases in homologous orthosomycin gene clusters do not have similar gene fusions (Figure 13.1B, 13.1C). However, the organization of these genes in the four orthosomycin biosynthetic gene clusters is conserved (Figure 13.1B, 13.1C) and it remains possible that these orthologues form stable but unfused heterodimers to increase the efficiency of everninomicin biosynthesis. The putative methyltransferases upstream of the oxygenases have not been biochemically characterized.

Here, we used a primarily structural approach to investigate EvdMO1 and its contribution to everninomicin biosynthesis. The full-length structure of EvdMO1 confirmed that this enzyme has two domains and identified fully formed, separate active sites that appear independent and unconnected. As anticipated, the C-terminal Fe/AKG oxygenase domain has strong structural similarities with the Fe/AKG oxygenases found in orthosomycin biosynthetic pathways. The N-terminal domain, while maintaining the SAM-dependent methyltransferase core fold, also has insertions and features not observed in other methyltransferases. To fully characterize the methyltransferase domain, we additionally report here the structure of the resected N-terminal methyltransferase domain (EvdMΔO1) to ultrahigh resolution. This work completes the structural

characterization of the three Fe/AKG oxygenases found in the *evd* gene cluster and offers insight into everninomicin formation.

13.2 Results and Discussion

Structure determination of full-length EvdMO1. EvdMO1 formed square bipyramidal crystals of the $I4_122$ space group with three molecules in the asymmetric. Due to the relatively low resolution, strict noncrystallographic symmetry restraints and NCS-averaged maps were used for refinement and manual model building. The final model, which contains seven residues of the purification tag, is missing residues 30 – 38, 149, 173 – 194, and 443 – 451. Each monomer has one nickel ion at the putative active site of the C-terminal domain. Packing analysis of the contents of the asymmetric unit identifies roughly 1100 $Å^2$ of buried surface area per protein, suggesting that EvdMO1 is likely a monomer (530).

EvdMO1 structure determination was challenging due to a combination of low resolution and a search model that covered only 50% of the molecule (AviO1 is 68% identical to the C-terminal domain). EvdMO1 was initially phased using molecular replacement, but the lack of a good search model for the N-terminal methyltransferase domain resulted in a model containing obvious errors. We thus opted to determine the structure of the methyltransferase domain (consisting of the first 233 residues), hypothesizing that a single domain may pack more tightly. The partial model built from the full-length EvdMO1 structure served as the search model to determine the methyltransferase domain structure. The low resolution EvdMO1 structure could then be confidently refined and analyzed to examine how the domains packed and potentially communicated with each other (Figure 13.2).

The N-terminal, SAM-dependent methyltransferase domain of EvdMO1. The N-terminal domain of EvdMO1 belongs to the SAM-dependent methyltransferase superfamily of proteins. However, the sequence identity of this domain is below 20% and several regions are not structurally conserved. The isolated N-terminal domain (EvdMΔO1) was co-crystallized with SAH and diffracted to 1.15 Å resolution with unambiguous electron density for the entire protein and SAH, producing a final EvdMΔO1 structure consisting of five residues of the purification tag and all 233 residues of the methyltransferase domain. A second ultrahigh resolution structure of EvdM ΔO1 was crystallized in the presence of SAH and 10 mM D-fucose which lacked electron density for residues 33 – 39 and the monosaccharide.

The predominant feature of EvdMΔ01 is a Rossmann-like fold consisting of a seven stranded, mostly parallel β-sheet (↑β11↓β12↑β7↑β6↑β3↑β4↑β5) flanked on either side by three α-helices (green β-strands and blue α-helices, Figure 13.3). EvdMΔO1 has two insertions to this fold: the first 40 residues fold into an α-helix bundled next to a short 2-stranded antiparallel β-sheet leading into a 3_{10}-helix (Figure 13.3, yellow), and a 36 residue insertion (residues 160-196) after the fifth β-strand of the Rossmann fold (β7). This insertion forms a three-stranded antiparallel β-sheet and a 3_{10}-helix before returning to the Rossmann fold (Figure 13.3, red) and contributes to the SAM binding site.

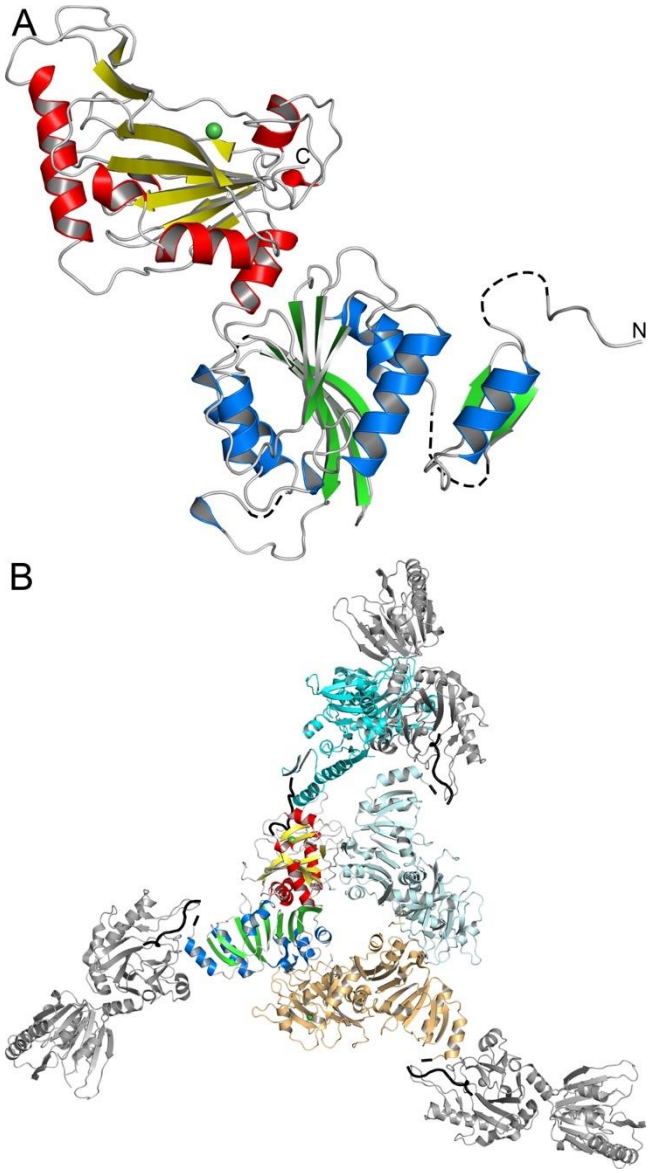

Fig. 13.2. Monomeric structure of EvdMO1 in cartoon representation. (A) Within the N-terminal domain, α-helices are colored blue and β-strands are green. Secondary structural elements within C-terminal domain are colored red for α-helices and yellow for β-strands. The nickel ion is depicted as a green sphere. Regions not included in the final model are indicated by a dashed line. (B) The N-terminal hexahistidine tag (black) extends into the oxygenase domain of symmetry-related molecules (grey). The contents of the asymmetric unit are colored by chain, with the A chain depicted as in (A), the B chain in pale cyan, and the C chain in orange. The hexahistidine tag from the dark cyan molecule, a symmetry mate, enters the oxygenase active site of the A chain.

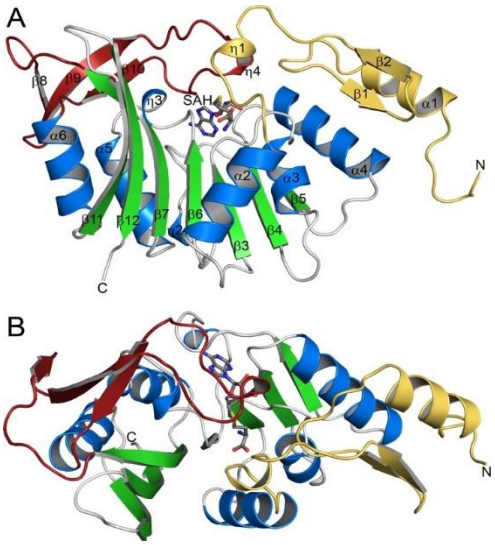

Figure 13.3. Structure of EvdMΔO1 in cartoon representation. SAH is shown in ball-and-stick representation. The modified Rossmann fold has green β-strands and blue α-helices. The N-terminal insertion, not conserved among methyltransferases, is yellow and the second insertion, located after the fifth β-strand of the Rossmann fold, is red. Both insertions contribute to the active site. (A) Side view of EvdMΔO1. (B) View of EvdMΔO1 rotated 90° about the horizontal axis from (A).

The EvdMΔO1 active site is located at the C-terminal end of the central β-sheet and our structure contains unambiguous electron density for SAH (Figure 13.4A). As seen in other SAM-dependent methyltransferases, SAH binds in a pocket composed primarily of residues located on the loops following β6, β3, β4, and β5 with additional contributions from residues preceding α2 and the loop preceding β10. However, only three residues directly interact with SAH: Arg44 hydrogen bonds with the carboxylate group, Glu84 forms a hydrogen bond to each hydroxyl group of the ribose moiety, and Asp111 interacts with the amino group of the adenosine ring (Figure 13.4A). The remaining residues lining the adenosine pocket are hydrophobic. Tyr133, His180, His134, and His157 are located near the sulfur atom of SAH and thus the methyl group transferred from SAM. These residues are likely to be charged or hydrophilic in nature (Figure 13.4B). Hydrophilic and

charged residues found slightly further from SAH (His216, Arg218, Asp225) may bind and orient the substrate.

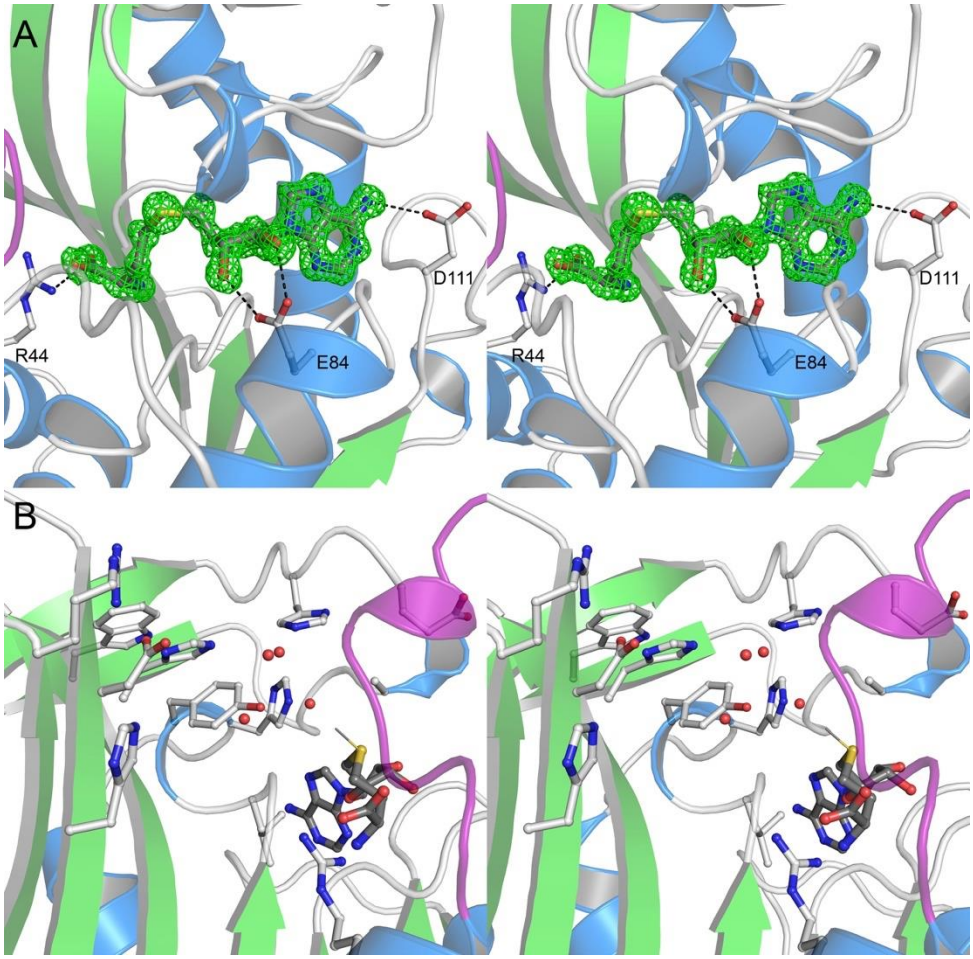

Fig. 13.4. Active site of EvdMΔO1. (A) SAH shown in ball-and-stick representation. Initial $||F_o| - |F_c||$ difference electron density, calculated prior to SAH placement, is contoured at 3 σ. Three residues that interact directly with SAH are also shown in ball-and-stick with hydrogen bonds shown as black dashes. (B) Hydrophilic, charged residues within 5 Å of the theoretical position of the donated methyl group (line projecting from the sulfonium group) are shown lining the EvdMΔO1 active site. Water molecules are shown as red spheres. For clarity, no residues from the loop that becomes disordered in the presence of D-fucose are shown.

EvdMO1 contains two common SAM-dependent methyltransferase sequence motifs (Figure 13.1C). Motif I (GxGxG) is found at the end of β3 leading into α2 (Figure 13.1C, residues 59-65 that encode EL**G**A**L**E**G**), with the middle glycine replaced by a leucine residue. This motif is located at the base of the SAM binding site and provides mostly hydrophobic interactions with the ligand. Motif II in EvdMO1 spans the loop after β4 (Figure 13.1C, residues 83-85). Glu84 is strictly conserved among SAM-dependent methyltransferases and anchors the ribosyl group via two hydrogen bonds to the sugar hydroxyl groups (Figure 13.4A). EvdMO1 also contains a conserved acidic residue in the loop following β5 (Figure 13.1C, residues 110 – 112) that stabilizes the adenosine base of SAM: Asp111 forms a hydrogen bond with N6 and the backbone nitrogen atom of Val112 hydrogen bonds with N1 (Figure 13.4A).

Despite these conserved elements, EvdMO1 shows little additional sequence homology with other members of the SAM-dependent methyltransferase superfamily (531-542). A structural homology search (543) reveals that even the most similar methyltransferases have sequence identities lower than 20% and most have an overall r.m.s. deviation greater than 2 Å when compared to EvdMΔO1. However, the r.m.s. deviation often improves by at least 0.5 Å when the EvdMO1 insertions are excluded. This observation supports the theory that insertion sites allow for a large degree of variability; each insertion was found to have structural homology with only one other protein. CmoB, a carboxymethyltransferase involved in tRNA modification in *E. coli*, has a large N-terminal insertion that is suggested to form a binding platform for the tRNA (537). The latter portion of this insertion, an α-helix and two antiparallel β-strands, is also seen in EvdMO1. In EvdMO1 the insertion results in a second, smaller cleft of roughly 1500 $Å^3$ that is lined with hydrophilic and aromatic residues that may function to bind portions of the bulky orthosomycin substrate further from the position being methylated (Figure 13.5A).

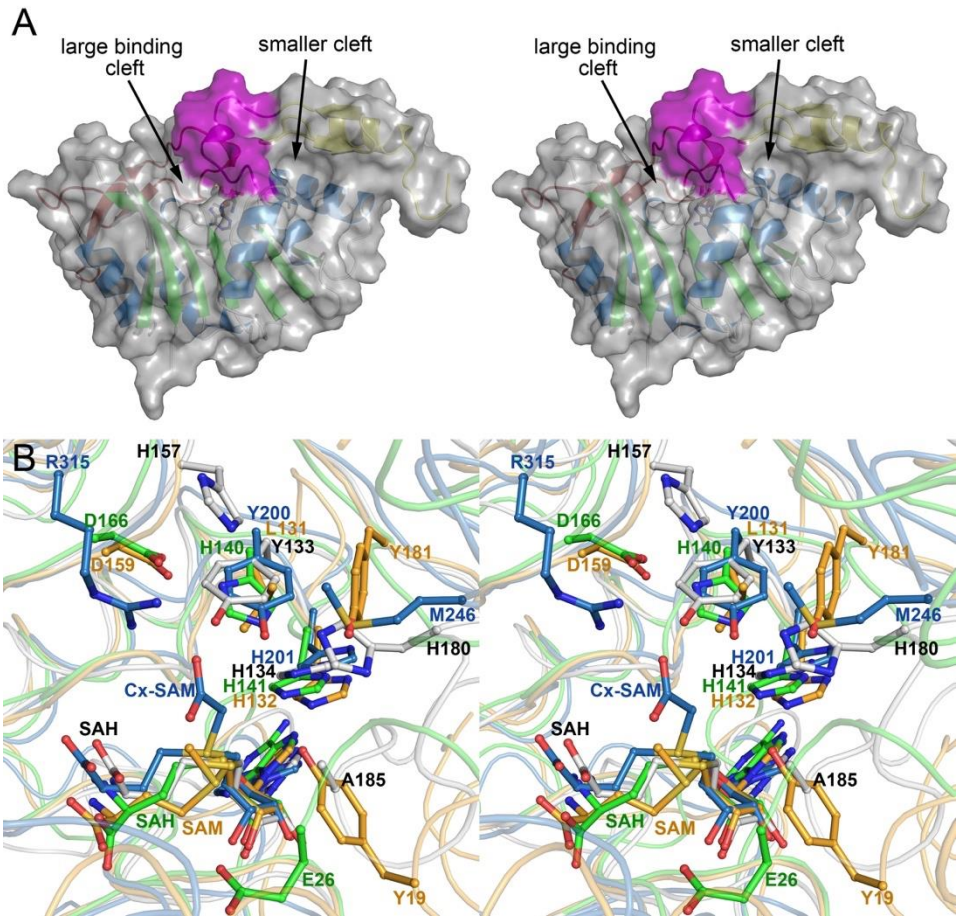
A
large binding cleft
smaller cleft
large binding cleft
smaller cleft
B
R315
H157
D166
Y200
L131
H140
Y133
Y181
D159
M246
H180
H201
H134
H141
H132
Cx-SAM
SAH
A185
SAH
SAM
E26
Y19
R315
H157
D166
Y200
L131
H140
Y133
Y181
D159
M246
H180
H201
H134
H141
H132
Cx-SAM
SAH
A185
SAH
SAM
E26
Y19

Fig. 13.5. Elements of the SAM-dependent methyltransferase that may contribute to mechanism. (A) Stereoview of the EvdMΔO1 surface where the loop region that becomes disordered in the presence of D-fucose is colored purple. The secondary structural elements are otherwise colored as described for Fig. 3. (B) Cartoon and ball-and-stick representation of the EvdMΔO1 active site with residues potentially involved in proton transfer highlighted. EvdMΔO1 active site residues are compared to those of RebM (540) (green carbon atoms, PDB 3BUS), CmoB (537) (blue carbon atoms, PDB 4QNU), and PfPMT (539) (orange carbon atoms, PDB 3UJ7). Notably, the only conserved residue is His134.

Everninomicin and avilamycin biosynthesis share many elements, and the avilamycin *avi* gene cluster has been extensively analyzed by the Bechthold group (522-525). The methyltransferase AviG5 has 63% sequence identity and 72% sequence similarity to the N-terminal domain of EvdMO1. AviG5 is responsible for O-methylation of the E ring of avilamycin, as *aviG5* disruption results in avilamycin derivatives lacking the methyl group on O4. The source sugar for the E ring of both orthosomycins is proposed to be D-mannose, but is extensively modified to form a tailored D-fucose moiety in the final orthosomycin. We thus pursued a ternary complex of EvdMΔO1 with SAH and D-fucose through both soaking and cocrystallization experiments. No electron density appeared for the monosaccharide, but in more than 10 datasets collected in the c superfamily. In EvdMO1, the major sheet has one extra β-strand at the bottom of the DSBH and two additional β-strands at the opening of the DSBH (Figure 13.6). The minor sheet is flanked by two α-helices and two 3_{10}-helices, while the major sheet abuts three α-helices.

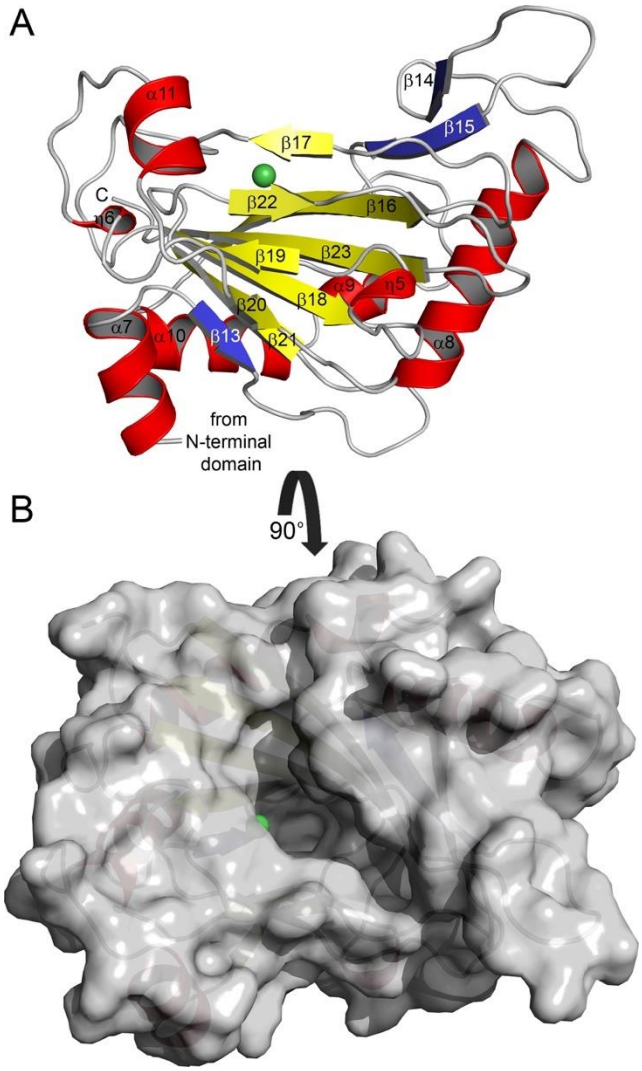

Fig. 13.6. Structure of the C-terminal, Fe/AKG oxygenase domain of EvdMO1. (A) In the cartoon representation, β-strands of the conserved DSBH fold are yellow, α-helices are red, and additional β-strands are blue. (B) Surface representation of EvdMO1 after 90° rotation about the x-axis. This orientation reveals a long and deep binding cleft that leads to the metal ion within the active site.

The C-terminal Fe/AKG oxygenase domain active site is located at the base of a cleft approximately 7 Å wide, 18 Å long, and 10 Å deep that is formed at the interface of the major and minor β-sheets. This cleft is the most striking feature of EvdMO1 and has a volume of roughly 3,000 $Å^3$ (530). Each active site observed in the crystal structure contained a sphere of strong positive $|F_o|-|F_c|$ difference electron density of at least 10 σ where the Fe(II) cofactor is expected to bind. We have modeled a nickel ion into this density, as EvdMO1 was exposed to nickel during protein purification and no metal was added at any other step of purification or crystallization. This metal is coordinated to a triad of conserved residues commonly referred to as the 'facial triad' (His349, Asp351, and His420) that are located on the minor sheet (Figure 13.7). The lower portion of the binding cleft, composed primarily of hydrophobic residues, also contains unanticipated electron density where AKG should bind and is modeled as bis-tris methane (Figure 13.7). EvdMO1 also contains the structurally conserved basic Arg431 and Lys338 that function to orient and hydrogen bond to AKG.

The uppermost solvent exposed portion of the binding cleft is made up of β14, β15, and the loop following β17. These secondary structural elements are rich in hydrophilic and aromatic residues and line the inner face of the DSBH. In EvdMO1, the minor β-sheet contributes Arg352, Asn354, Asn362, and Glu437. From the major β-sheet, Trp283, Tyr285, Tyr295, Arg296, and His298 are likely residues to interact and stabilize the substrate within the EvdMO1 binding cleft. Figure 13.7 illustrates how these residues coordinate a portion of the N-terminal polyhistidine tag (residues prior to the start methionine have negative numbering). Seven residues, including three of the six histidine residues, are visible in the Fe/AKG active site and eventually reach the active site metal where His-11 occupies the nickel coordination site *trans* from His420.

The low 3.35 Å resolution of the EvdMO1 structure would typically make analysis of either domain difficult. However, the EvdMO1 C-terminal domain has very high sequence homology (>75% identical and 80% similar with no gaps in the sequence alignment) with AviO1, an oxygenase from the avilamycin biosynthetic pathway in *S. viridochromogenes* Tü57. In a previous study, we exploited the high degree of similarity between oxygenases of different gene clusters to extend structural findings to enzymes in related pathways (528). This work also showed that disrupting EvdMO1 in the producing organism abolished everninomicin production. As seen in AviO1, EvdMO1 utilizes a conserved facial triad of HxD/E….H to coordinate a metal ion in the active site (Figure 13.7). The large binding cleft in the Fe/AKG oxygenase domain is lined with hydrophilic and aromatic residues, as seen in the active sites of the two other everninomicin-associated oxygenases, EvdO1 and EvdO2. Members of the Fe/AKG oxygenase superfamily rely on AKG as a cosubstrate, and the binding site for AKG is conserved among all members of the family, as represented by the presence of Arg431 for coordinating the 5-carboxylate group of AKG (544).

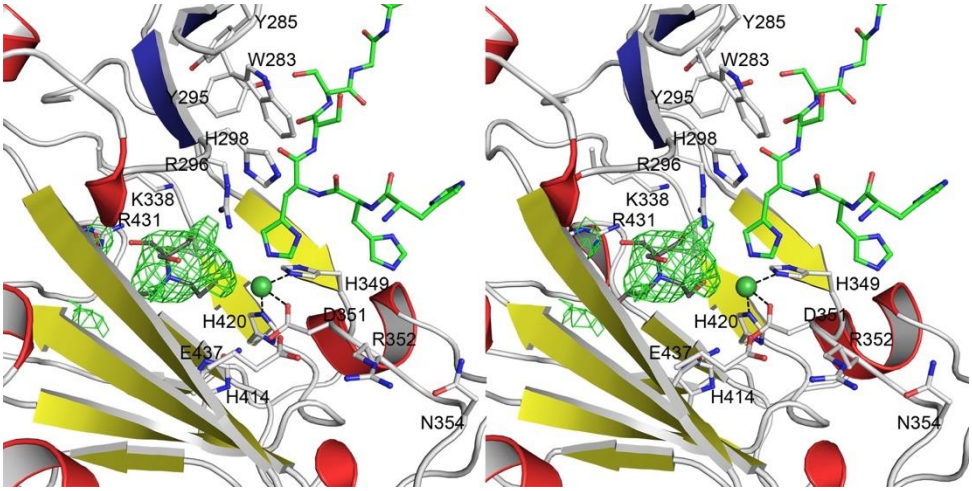

Fig. 13.7. Stereoview of the EvdMO1 Fe/AKG oxygenase domain active site. The facial triad (H349, D351, H42) coordinates the active site nickel ion as shown by dashed lines. Additional hydrophilic residues of the active site are shown in ball-and-stick representation. A mass of unexplained electron density (green mesh, $||F_o| - |F_c||$ map, contoured at 3 σ prior to ligand placement) has been modeled as bis-tris methane (dark gray carbon atoms). The polyhistidine tag from a crystallographically related molecule is shown in ball-and-stick representation with green carbon atoms. For clarity, one β-strand is not shown.

Full-length EvdMO1 structure and implications of EvdMO1 gene fusion for everninomicin biosynthesis. As suggested by primary sequence analysis, EvdMO1 consists of two discrete domains. Figure 13.2 illustrates the modular nature of the domains with respect to each other. Interactions between the domains are minimal and occur between loops leading into β-strands 3, 6, and 8 in the N-terminal domain's Rossmann fold and the first and fourth α-helices (α7 and α10 overall) of the C-terminal domain. While two potential salt bridges between Glu211 - Arg239 and Arg122 - Glu318 are found at the interface, the domains lack hydrophobic or complementary charge surface patches. Lastly, the active sites face the solvent and are oriented away from the other domain, with no channel or tunnel leading between active sites. Together, these elements strongly suggest that the two domains function independently of one another.

The five orthosomycin biosynthetic gene clusters whose sequences are available to date (*eve* and *eve* for everninomicin, *ava* and *avi* for avilamycin, and *hyg* for hygromycin B) encode more than 220 enzymes in total. EvdMO1 is notable as this is the only enzyme that appears to have

bifunctional activity as the result of gene fusion. There is precedence for gene fusion to link enzymatic functions when intermediates are unstable or demands on the organism require rapid production (545,546). While the overall organization of the orthosomycin gene clusters retain a moderate level of conservation with respect to the order open reading frames appear, very few genes are found in the same order in all four gene clusters. Figure 1B, however, shows that the organization of the open reading frames around the *evdMO1* is nearly totally conserved. In three of the four gene clusters, the methyltransferases and oxygenases are flanked by an epimerase and glycosyltransferase, respectively. Sequence identities range from 64% up to 94% for each of the genes, which supports them catalyzing the same reaction on closely related substrates. We wanted to analyze whether the two domains' functions occur sequentially during orthosomycin biosynthesis. If so, it would be tempting to suggest that these two activities could produce the methylenedioxy bridge via consecutive methyl transfer and oxidation (Figure 13.1A), structure highlighted in blue). *In vitro* biochemical characterization of everninomicin biosynthetic enzymes has been complicated by the complexity of the putative substrates; perhaps the structure of EvdMO1 would suggest cooperativity between the methyltransferase and oxygenase functionalities. We found that the active sites of the two domains face away from each other, and interactions at the linker connecting the domains are minimal. Despite the high level of sequence homology between the methyltransferases and oxygenases and EvdMO1, there does not appear to be a channel or any communication between the N- and C-terminal domains. Additionally, when EvdMO1 is aligned with the homologous methyltransferases and oxygenases from the other gene clusters, the sequence between the Rossmann-fold core and DSBH core are conserved. When these elements are taken together, the gene fusion event likely does not indicate that the reactions catalyzed by EvdMO1 produce unstable intermediates that would necessitate immediate shuttling

to the next active site. Nevertheless, both the gene fusion and the possibility of co-translated unfused enzymes allows these two enzymatic activities to be linked temporally.

13.3 Materials and Methods

Cloning, expression, and purification. M. carbonacea var. *aurantiaca* (ATCC 27115) genomic DNA was prepared using the Wizard Genomic DNA Purification kit following manufacturer's instructions for Gram-positive bacteria (Promega Corp). Using primers 5′-CG CAT ATG ATG GAC CGT AGG GAG ATT CA-3′ and 5′-GCG AAG CTT TCA GGA CGG GAG CGT C-3′ *evdMO1* was cloned into the pET28a(+) vector, which encodes an N-terminal hexahistidine tag cleavable by thrombin. To generate *evdMΔO1*, two stop codons were introduced after residue 233 with the following primers: 5′-CCG TGC CCG GTG ACT GGG TGC GCA GAT CCG T-3′ and 5′-CCG GGC ACG GCC G-3′. The resulting plasmids, EvdMO1.pET28a and EvdMΔO1.pET28a, were separately transformed into *E. coli* BL21(*DE3*) cells for protein overexpression.

Cultures (1 L) consisting of LB and 40 mg/L kanamycin were inoculated with 5 mL of overnight culture and grown at 37 °C with shaking until an OD_{600} of 0.3 was reached. The temperature was then lowered to 30 °C and overexpression of the desired protein induced 30 minutes later at an OD_{600} of 0.6 by the addition of 1 mM IPTG. Cultures continued to shake for 4-6 hours, when cells were harvested by centrifugation at 6,000 × *g*. Cell pellets from 2 L of culture were stored frozen at -20°C until purification.

Thawed cell pellets were resuspended in 30 mL of lysis buffer (50 mM NaH_2PO_4, 300 mM NaCl, 10 mM imidazole, pH 8.0) and lysed by 4 cycles of 2 minutes of sonication at 60% duty cycle. Following cell lysis, all purification steps were carried out at 4°C. The crude lysate was then

centrifuged at 38,000 × *g* for one hour and the supernatant applied to 2 mL NiNTA resin pre-equilibrated with lysis buffer. The column was then washed with 50 mL of lysis buffer and 40 mL of lysis buffer containing 20 mM imidazole. The His-tagged protein (EvdMO1 or EvdMΔO1) was eluted from the column using 8 mL of lysis buffer containing 250 mM imidazole. Prior to further purification, EvdMO1 required dialysis against 20 mM Tris, 50 NaCl pH 8.0 for one hour. The final purification step for both EvdMO1 and EvdMΔO1 was size exclusion chromatography (GE Healthcare Superdex S200 10/300 GL) with 20 mM Tris, 50 mM NaCl pH 7.4. EvdMO1 was concentrated to 11 mg/mL and EvdMΔO1 to 20 mg/mL as determined by Bradford assay and then stored frozen at -80 °C.

Crystallization and data collection. Initial crystallization conditions for both EvdMO1 and EvdMΔO1 were identified using commercially available sparse matrix screens and the hanging drop vapor diffusion method. Square bipyramidal crystals of EvdMO1 grew over three days by combining equal volumes (1.5 μL + 1.5 μL) of protein and a reservoir solution of 22% (w/w) PEG3350, 0.2 M Li_2SO_4, and 0.1 M Bis-Tris, pH 7.2. Crystals were cryoprotected by transfer into a drop containing all crystallization components supplemented with 17% ethylene glycol for 30 seconds and then flash cooled by plunging in liquid nitrogen. EvdMΔO1 was buffer exchanged and concentrated to 5 mg/mL in 20 mM sodium malonate, pH 7.0 and pre-incubated with 2 mM S-adenosylhomocysteine (SAH). Initial crystals grew in 50% Tacsimate pH 7. These crystals were microseeded to form diffraction quality crystals, rods approximately 150 μm long. EvdMΔO1 crystals were cryoprotected in a solution containing crystallization components and 15% ethylene glycol, then flash cooled in liquid nitrogen. EvdMΔO1 crystals were additionally soaked overnight or cocrystallized with 10 mM D-fucose.

X-ray diffraction data for EvdMO1 were collected at -180 °C on the LS-CAT 21-ID-D beamline of the Advanced Photon Source using 0.5° frame width over 150° at 0.918 Å with a MAR300 CCD detector. The X-ray diffraction data for both EvdMΔO1 datasets were collected at -180 °C on the LS-CAT 21-ID-F beamline at 0.979 Å using a MarMosaic 225 CCD detector. All data were processed using the HKL2000 suite of programs (547). Data collection statistics are summarized in Table 13.1.

Table 13.1. Crystallographic data collection and refinement statistics for EvdMO1 and EvdMΔO1 structures.

	EvdMO1	**EvdMΔO1**	**EvdMΔO1**
Data Collection			
Wavelength (Å)	0.918	0.979	0.979
Compounds added		AKG, SAH	AKG, SAH, fucose
Ligands modeled	BTB	AKG, SAH	AKG, SAH
Space group	$I\,4_1\,2\,2$	$P\,2_1$	$P\,2_1$
a, *b*, *c* (Å)	191.6, 191.6, 269.6	51.4, 41.3, 56.5	50.2, 41.3, 58.5
α, β, γ (deg)	90, 90, 90	90, 99.8, 90	90, 98.6, 90
Resolution (Å)	45.8 – 3.35	32.0 – 1.15	22.5 – 1.10
No. total reflections	248070	279251	421834
No. unique reflections	34942 (1759)	79855 (2893)	94601 (4550)
Completeness	96.1 (98.8)	96.3 (70.0)	98.5 (95.3)
Multiplicity	7.1 (7.1)	3.5 (2.3)	4.5 (3.7)
Wilson *B* factor	121.87	10.30	10.18
Mean I/σ	31.5 (2.6)	20.2 (2.0)	23.3 (2.7)
R_{sym}	6.3 (92.6)	5.2 (34.7)	6.0 (43.4)
R_{pim}	2.4 (36.1)	3.2 (27.2)	3.1 (25.0)
$CC_{1/2}$	66.9	83.6	86.8
Refinement			
R_{work}/R_{free} (%)	22.1/26.6	15.1/17.0	13.7/15.4
No. protein atoms	9698	1952	1923
No. solvent atoms	0	322	188
No. ligand atoms	45	26	26
RMS for bonds (Å)	0.002	0.006	0.006
RMS for angles (deg)	0.57	0.984	1.009
Average *B* factor (Å^2)			
protein	139.9	15.25	12.95
solvent	n/a	30.48	23.62
ligand	169.1	9.95	9.66
Ramachandran plot			
favored	90.9	99.2	99.2
allowed	8.3	0.8	0.8
outliers	0.8	0	0
Clashscore	5.46	2.34	0.26
PDB ID	6EC3	5T38	5T39

Structure determination and refinement. EvdMO1 crystallized in the space group $I\ 4_122$ with three molecules in the asymmetric unit. The structure was determined using molecular replacement using the program PHASER (548) through the PHENIX (549) interface. Three copies of the C-terminal domain were placed first using the AviO1 structure (528) (PDB ID 4XAA) as the search model. With the positions of the oxygenase domains fixed, the N-terminal methyltransferase domains were located using a methyltransferase from *Methanosarcina mazei* (PDB ID 3MGG)(550) as the search model. Once both domains were successfully placed, manual model building in Coot (551) was alternated with refinement performed using *phenix.refine* (552). Composite omit maps were calculated using CNS (553). Three-fold noncrystallographic symmetry averaging and restraints were enforced throughout model building and refinement. After this treatment, the R-factors remained high and several gaps in the model remained where the protein backbone could not be confidently placed due to ambiguous electron density.

EvdMΔO1 crystallized in the $P2_1$ space group with one molecule in the asymmetric unit and diffracted to ultrahigh resolution (1.15 Å). The structure of EvdMΔO1 was determined through molecular replacement by using the partially built and refined N-terminal domain of the full-length EvdMO1 structure (residues 1 – 30, 40 – 157, and 190 – 233) as the search model in PHASER. Following a round of refinement that included a cycle of rigid body and temperature factor refinement, unambiguous electron density was observed for the missing regions of the model and for the SAH coproduct. Missing loops regions were added to the model by either automated loop fitting in PHENIX or manual placement in Coot. SAH and water molecules were placed during later cycles of refinement.

The final EvdMΔO1 model was then used to correct errors in the full-length EvdMO1 structure. Final refinement statistics for EvdMO1 and EvdMΔO1 are presented in Table 1. The

final models were evaluated using Molprobity (554) and figures prepared with PyMOL (555). All programs were accessed through the SBGrid consortium (556).

CHAPTER 14

CONCLUSIONS

14.1 Introduction

The arrestin proteins were originally discovered for their role in the desensitization and internalization of GPCRs; however, the arrestins have more recently emerged as important regulators of intracellular signaling, which includes acting as scaffold proteins for mitogen-activated protein kinase cascades. The work outlined in this thesis has largely investigated the ability of the nonvisual arrestins, arrestin-2 and arrestin-3, to coordinate MAPK signaling in both a GPCR-dependent and -independent manner. While this thesis provides significant strides in understanding MAPK signaling, more research is needed to determine how arrestins perform their diverse signaling roles at both a conformational and functional level. A thorough understanding of these mechanisms could be beneficial for future drug discovery efforts targeting the arrestin proteins or the pathways they regulate.

14.2 Conformational states of arrestin dictate downstream signaling

The arrestin proteins exist in an equilibrium between cytosolic, microtubule-bound, or GPCR-bound states (557). These states adopt distinct conformations that preferentially associate with certain effectors, i.e., the ASK1-MKK4/7-JNK3 cascade prefers free arrestin (166) (Chapters 5, 6) while the Raf-MEK-ERK1/2 cascade prefers GPCR-bound arrestin (67) (Chapter 7). The nonvisual arrestins have also been shown to self-associate in the presence of small molecules such as heparin (558) or IP_6 (3,103). In fact, IP_6-binding hindered spontaneous nuclear translocation of

arrestin-2 but led to GPCR-independent activation of arrestin-3 (Chapter 4). It is therefore likely that these varied conformational states allow for the diverse cellular functions of arrestins.

Chapters 4-6 of this work closely examined GPCR-independent arrestin-3 activation and the effect of this activation on scaffolding of the ASK1-MKK4/7-JNK3 cascade. In essence, IP_6-mediated activation resulted in a conformation of arrestin-3 that mimicked the GPCR-bound state (3) (Chapter 4). This conformation enhanced inactive JNK3 binding to the arrestin-3 scaffold. In the follow-up study to this work, arrestin-3 acted as a "conveyor belt" for JNK3 activation (2) (Chapter 6). A pre-activated form of arrestin-3 (residues 1-393) exhibited a >15-fold reduction in binding affinity for activated JNK3 over the inactive form. Together these studies suggested that arrestin-3 can facilitate JNK3 activation in a GPCR-independent manner, but the conformational state of arrestin likely resembles its activated form. However, more studies are needed, as arrestin-3-derived peptide T1A (Chapter 5) that facilitates JNK3 activation in vitro and in cells, does not appear to have different conformations in the basal ((92)) and active ((3)) arrestin-3 crystal structure. Our understanding of this mechanism would be greatly enhanced through additional structural studies that can shed light on the arrestin/MAPK interaction.

14.3 Arrestin-2 and arrestin-3 share considerable functional redundancy

Vertebrates have both visual and nonvisual arrestins encoded in their genome (239). Studies in mice have shown that individual knockout of either nonvisual arrestin results in grossly normal phenotypes unless you challenge animals with pharmacologic doses of the agonists of certain GPCRs (189). This suggests that the nonvisual arrestin isoforms have considerable functional redundancy and makes it difficult to study *in vivo* arrestin signaling.

Here, we explored the differences in scaffolding ability of extracellular-regulated signaling

kinase 2 (ERK2) by both arrestin-2 and arrestin-3 (Chapter 8). While the overall interface between the nonvisual arrestins and ERK2 appeared similar, it became clear from the isolated peptide studies that the exact contacts are not. We also completed a comparable analysis of JNK3 interactions with arrestin-3 (Chapters 2,5,6), which provided us with an in-depth understanding of the arrestin-3/JNK3 interaction. While these studies certainly provide clues regarding how nonvisual arrestins mediate MAPK signaling, it is still unknown whether arrestins amplify MAPK signaling using a similar mechanism across all MAPK cascades. For example, does active ERK1/2 lose affinity for the arrestin scaffold in a comparable fashion to activated JNK3? Does the defined mechanism for MAPK amplification (Chapter 6) apply to all protein scaffolds? Additional experiments are needed to investigate these questions, especially to compare JNK3 interaction with arrestin-2, which that does not facilitate activation of JNK3, and continued analysis of the ERK2/nonvisual arrestin interface. It is likely that close examination of these interfaces will help elucidate scaffolding differences between the nonvisual arrestins that could suggest the evolutionary rationale for maintaining both isoforms.

14.4 Modification of the arrestin proteins holds therapeutic potential

The structural elements of the arrestin proteins have been extensively characterized and, consequently, can be engineered to either enhance or remove native functions without compromising the overall function of the protein (559). For example, it is well-established that the concave surfaces of the N and C domains of arrestin are involved in GPCR binding (32,331), while most effectors interact with the outer surfaces. Several modified arrestins have been developed including enhanced arrestins that bind both phosphorylated and non-phosphorylated GPCRs (320,560), self-association deficient mutants (561), and, more relevant to this thesis work, arrestins

where the scaffolding functions have been manipulated (84,96) (Chapter 5). It is also important to consider that binding does not necessarily suggest functionality; for example, the arrestin-3 KNC mutant retains binding to most kinases yet fails to facilitate activation of MAPK cascades. It is therefore necessary to clearly define whether certain arrestin scaffolds can lead to effector activation. As we continue to map out the interaction between the arrestins and MAPK cascades we will get closer to developing small molecule mimetics or novel therapeutics that target these interactions.

14.5 The role of arrestin in disease states

The arrestin proteins are critical for the regulation of several physiological functions including embryologic development (562,563), retinal function (564), cardiovascular regulation (565), and metabolism (377). This thesis contains collaborative work with Dr. Jurgen Wess's lab at the National Institutes of Health that investigated the role of arrestin in Type 2 Diabetes (T2D). The included publications examined the role of arrestin in euglycemia (normal blood sugar levels) and insulin sensitivity (369,424) (Chapters 10, 11).

Chapter 10 focused on conditional knockdown of arrestin-3 in β-cells of adult mice. The β-barr2-KO mice exhibited impaired glucose-stimulated insulin secretion (GSIS) and Ca^{2+} entry, and overexpression of arrestin-3 was able to rescue these metabolic deficits (369). We hypothesized that this effect was due largely to the positive regulation of CAMKII through a direct interaction with arrestin-3. This arrestin-effector interaction did not appear to require input from β-cell GPCRs. Additional work will be required to compare conditional knockdown of arrestin-2 to the results described above, but our findings suggest that modulating arrestin-3 activity in β-cells could provide a novel therapeutic approach for targeting T2D.

Chapter 11 investigated the role of arrestin in T2D from the standpoint of increased hepatic glucose production (HGP) due to enhanced signaling through the glucagon receptor (GCGR) (369). We showed that selective inactivation of arrestin-3 in adult mice hepatocytes lead to an increase in GCGR signaling and deficits in glucose homeostasis. Blood glucose levels were elevated in knockout animals and the mice showed impaired glucose tolerance; therefore, it is likely that arrestin-3 plays a role in the negative regulation of hepatic GCGR signaling. Again, these findings suggest clinical benefits for the modulation of arrestin-3 signaling in the treatment of T2D.

14.6 Conclusion

The arrestins are multifaceted proteins that mediate both signal termination and initiation. This thesis outlines the role of arrestins in facilitating MAPK activation, briefly describes arrestin modulation of G-protein coupled receptors and investigates the function of arrestins in Type 2 Diabetes. While this work represents significant progress in fundamental arrestin processes, more research is necessary to determine exactly how arrestin dictates signaling pathways. After all, arrestin is the heart of it all!

REFERENCES

1. Witzel, F., Maddison, L., and Blüthgen, N. (2012) How scaffolds shape MAPK signaling: what we know and opportunities for systems approaches. *Frontiers in Physiology* **3**, 475
2. Perry, N. A., Kaoud, T. S., Ortega, O. O., Kaya, A. I., Marcus, D. J., Pleinis, J. M., Berndt, S., Chen, Q., Zhan, X., Dalby, K. N., Lopez, C. F., Iverson, T. M., and Gurevich, V. V. (2018) Arrestin-3 scaffolding of the JNK3 cascade suggests a mechanism for signal amplification. *Proceedings of the National Academy of Sciences*, 201819230
3. Chen, Q., Perry, N. A., Vishnivetskiy, S. A., Berndt, S., Gilbert, N. C., Zhuo, Y., Singh, P. K., Tholen, J., Ohi, M. D., Gurevich, E. V., Brautigam, C. A., Klug, C. S., Gurevich, V. V., and Iverson, T. M. (2017) Structural basis of arrestin-3 activation and signaling. *Nature Communications* **8**, 1427
4. Zhan, X., Stoy, H., Kaoud, T. S., Perry, N. A., Chen, Q., Perez, A., Els-Heindl, S., Slagis, J. V., Iverson, T. M., Beck-Sickinger, A. G., Gurevich, E. V., Dalby, K. N., and Gurevich, V. V. (2016) Peptide mini-scaffold facilitates JNK3 activation in cells. *Sci Rep* **6**, 21025
5. Perry, N. A., Zhan, X., Iverson, T. M., Gurevich, E. V., and Gurevich, V. V. (2017) Monofunctional Elements of Multi-functional Proteins. in *The Structural Basis of Arrestin Functions* (Gurevich, V. V. ed.), Springer International Publishing, Cham. pp 255-271
6. Goodman, O. B., Krupnick, J. G., Santini, F., Gurevich, V. V., Penn, R. B., Gagnon, A. W., Keen, J. H., and Benovic, J. L. (1996) [beta]-Arrestin acts as a clathrin adaptor in endocytosis of the [beta]2-adrenergic receptor. *Nature* **383**, 447-450
7. Laporte, S. A., Oakley, R. H., Zhang, J., Holt, J. A., Ferguson, s. S. G., Caron, M. G., and Barak, L. S. (1999) The 2-adrenergic receptor/arrestin complex recruits the clathrin adaptor AP-2 during endocytosis. *Proc Nat Acad Sci USA* **96**, 3712-3717
8. Shukla, A. K., Xiao, K., and Lefkowitz, R. J. (2011) Emerging paradigms of β-arrestin-dependent seven transmembrane receptor signaling. *Trends in Biochemical Sciences* **36**, 457-469
9. Xiao, K., McClatchy, D. B., Shukla, A. K., Zhao, Y., Chen, M., Shenoy, S. K., Yates, J. R., and Lefkowitz, R. J. (2007) Functional specialization of β-arrestin interactions revealed by proteomic analysis. *Proceedings of the National Academy of Sciences* **104**, 12011-12016
10. Good, M., Tang, G., Singleton, J., Reményi, A., and Lim, W. A. (2009) The Ste5 Scaffold Directs Mating Signaling by Catalytically Unlocking the Fus3 MAP Kinase for Activation. *Cell* **136**, 1085-1097
11. Goodman, O. B., Krupnick, J. G., Gurevich, V. V., Benovic, J. L., and Keen, J. H. (1997) Arrestin/clathrin interaction. Localization of the arrestin binding locus to the clathrin terminal domain. *J Biol Chem* **272**, 15017-15022
12. Baillie, George S., Adams, David R., Bhari, N., Houslay, Thomas M., Vadrevu, S., Meng, D., Li, X., Dunlop, A., Milligan, G., Bolger, Graeme B., Klussmann, E., and Houslay, Miles D. (2007) Mapping binding sites for the PDE4D5 cAMP-specific phosphodiesterase to the N- and C-domains of β-arrestin using spot-immobilized peptide arrays. *Biochemical Journal* **404**, 71-80
13. Gurevich, V. V., and Gurevich, E. V. (2015) Analyzing the roles of multi-functional proteins in cells: The case of arrestins and GRKs. *Crit Rev Biochem Mol Biol* **50**, 440-452
14. Pin, J.-P., Galvez, T., and Prézeau, L. (2003) Evolution, structure, and activation mechanism of family 3/C G-protein-coupled receptors. *Pharmacology & Therapeutics* **98**, 325-354
15. Gurevich, E. V., Tesmer, J. J., Mushegian, A., and Gurevich, V. V. (2012) G protein-coupled receptor kinases: more than just kinases and not only for GPCRs. *Pharmacol Ther* **133**, 40-69
16. Wilden, U. (1995) Duration and amplitude of the light-induced cGMP hydrolysis in vertebrate photoreceptors are regulated by multiple phosphorylation of rhodopsin and by arrestin binding. *Biochemistry* **34**, 1446-1454
17. Wilden, U., Hall, S. W., and Kuhn, H. (1986) Phosphodiesterase activation by photoexcited rhodopsin is quenched when rhodopsin is phosphorylated and binds the intrinsic 48-kDa protein

of rod outer segments. *Proc Natl Acad Sci USA* **83**, 1174-1178
18. Krupnick, J. G., Gurevich, V. V., and Benovic, J. L. (1997) Mechanism of quenching of phototransduction. Binding competition between arrestin and transducin for phosphorhodopsin. *J Biol Chem* **272**, 18125-18131
19. Shenoy, S. K., and Lefkowitz, R. J. (2011) β-arrestin-mediated receptor trafficking and signal transduction. *Trends in Pharmacological Sciences* **32**, 521-533
20. Krupnick, J. G., Gurevich, V. V., Schepers, T., Hamm, H. E., and Benovic, J. L. (1994) Arrestin-rhodopsin interaction. Multi-site binding delineated by peptide inhibition. *J Biol Chem* **269**, 3226-3232
21. König, B., Arendt, A., McDowell, J. H., Kahlert, M., Hargrave, P. A., and Hofmann, K. P. (1989) Three cytoplasmic loops of rhodopsin interact with transducin. *Proc Natl Acad Sci U S A* **86**, 6878-6882
22. Hamm, H. E., Deretic, D., Arendt, A., Hargrave, P. A., Koenig, B., and Hofmann, K. P. (1988) Site of G protein binding to rhodopsin mapped with synthetic peptides from the alpha subunit. *Science* **241**, 832
23. Rasmussen, S. G., DeVree, B. T., Zou, Y., Kruse, A. C., Chung, K. Y., Kobilka, T. S., Thian, F. S., Chae, P. S., Pardon, E., Calinski, D., Mathiesen, J. M., Shah, S. T., Lyons, J. A., Caffrey, M., Gellman, S. H., Steyaert, J., Skiniotis, G., Weis, W. I., Sunahara, R. K., and Kobilka, B. K. (2011) Crystal structure of the β2 adrenergic receptor-Gs protein complex. *Nature* **477**, 549-555
24. Carpenter, B., Nehmé, R., Warne, T., Leslie, A. G., and Tate, C. G. (2016) Structure of the adenosine A(2A) receptor bound to an engineered G protein. *Nature* **536**, 104-107
25. Kang, Y., Zhou, X. E., Gao, X., He, Y., Liu, W., Ishchenko, A., Barty, A., White, T. A., Yefanov, O., Han, G. W., Xu, Q., de Waal, P. W., Ke, J., Tan, M. H., Zhang, C., Moeller, A., West, G. M., Pascal, B. D., Van Eps, N., Caro, L. N., Vishnivetskiy, S. A., Lee, R. J., Suino-Powell, K. M., Gu, X., Pal, K., Ma, J., Zhi, X., Boutet, S., Williams, G. J., Messerschmidt, M., Gati, C., Zatsepin, N. A., Wang, D., James, D., Basu, S., Roy-Chowdhury, S., Conrad, C. E., Coe, J., Liu, H., Lisova, S., Kupitz, C., Grotjohann, I., Fromme, R., Jiang, Y., Tan, M., Yang, H., Li, J., Wang, M., Zheng, Z., Li, D., Howe, N., Zhao, Y., Standfuss, J., Diederichs, K., Dong, Y., Potter, C. S., Carragher, B., Caffrey, M., Jiang, H., Chapman, H. N., Spence, J. C., Fromme, P., Weierstall, U., Ernst, O. P., Katritch, V., Gurevich, V. V., Griffin, P. R., Hubbell, W. L., Stevens, R. C., Cherezov, V., Melcher, K., and Xu, H. E. (2015) Crystal structure of rhodopsin bound to arrestin by femtosecond X-ray laser. *Nature* **523**, 561-567
26. Shukla, A. K., Manglik, A., Kruse, A. C., Xiao, K., Reis, R. I., Tseng, W. C., Staus, D. P., Hilger, D., Uysal, S., Huang, L. Y., Paduch, M., Tripathi-Shukla, P., Koide, A., Koide, S., Weis, W. I., Kossiakoff, A. A., Kobilka, B. K., and Lefkowitz, R. J. (2013) Structure of active β-arrestin-1 bound to a G-protein-coupled receptor phosphopeptide. *Nature* **497**, 137-141
27. Gurevich, V. V., and Benovic, J. L. (1993) Visual arrestin interaction with rhodopsin. Sequential multisite binding ensures strict selectivity toward light-activated phosphorylated rhodopsin. *J Biol Chem* **268**, 11628-11638
28. Gurevich, V. V., and Gurevich, E. V. (2006) The structural basis of arrestin-mediated regulation of G-protein-coupled receptors. *Pharmacology & therapeutics* **110**, 465-502
29. Gurevich, V. V., and Gurevich, E. V. (2004) The molecular acrobatics of arrestin activation. *Trends Pharmacol Sci* **25**, 105-111
30. Hanson, S. M., Francis, D. J., Vishnivetskiy, S. A., Kolobova, E. A., Hubbell, W. L., Klug, C. S., and Gurevich, V. V. (2006) Differential interaction of spin-labeled arrestin with inactive and active phosphorhodopsin. *Proc Natl Acad Sci U S A* **103**, 4900-4905
31. Hanson, S. M., and Gurevich, V. V. (2006) The differential engagement of arrestin surface charges by the various functional forms of the receptor. *J Biol Chem* **281**, 3458-3462
32. Vishnivetskiy, S. A., Gimenez, L. E., Francis, D. J., Hanson, S. M., Hubbell, W. L., Klug, C. S., and Gurevich, V. V. (2011) Few residues within an extensive binding interface drive receptor interaction and determine the specificity of arrestin proteins. *J Biol Chem* **286**, 24288-24299

33. Zhuo, Y., Vishnivetskiy, S. A., Zhan, X., Gurevich, V. V., and Klug, C. S. (2014) Identification of receptor binding-induced conformational changes in non-visual arrestins. *J Biol Chem* **289**, 20991-21002
34. Vishnivetskiy, S. A., Hosey, M. M., Benovic, J. L., and Gurevich, V. V. (2004) Mapping the arrestin-receptor interface: structural elements responsible for receptor specificity of arrestin proteins. *J Biol Chem* **279**, 1262-1268
35. Hirsch, J. A., Schubert, C., Gurevich, V. V., and Sigler, P. B. (1999) The 2.8 A crystal structure of visual arrestin: a model for arrestin's regulation. *Cell* **97**, 257-269
36. Vishnivetskiy, S. A., Paz, C. L., Schubert, C., Hirsch, J. A., Sigler, P. B., and Gurevich, V. V. (1999) How does arrestin respond to the phosphorylated state of rhodopsin? *J Biol Chem* **274**, 11451-11454
37. Kim, Y. J., Hofmann, K. P., Ernst, O. P., Scheerer, P., Choe, H. W., and Sommer, M. E. (2013) Crystal structure of pre-activated arrestin p44. *Nature* **497**, 142-146
38. Szczepek, M., Beyrière, F., Hofmann, K. P., Elgeti, M., Kazmin, R., Rose, A., Bartl, F. J., von Stetten, D., Heck, M., Sommer, M. E., Hildebrand, P. W., and Scheerer, P. (2014) Crystal structure of a common GPCR-binding interface for G protein and arrestin. *Nat Commun* **5**
39. Farrens, D. L., Altenbach, C., Yang, K., Hubbell, W. L., and Khorana, H. G. (1996) Requirement of rigid-body motion of transmembrane helices for light activation of rhodopsin. *Science* **274**, 768-770
40. Kim, M., Vishnivetskiy, S. A., Van Eps, N., Alexander, N. S., Cleghorn, W. M., Zhan, X., Hanson, S. M., Morizumi, T., Ernst, O. P., Meiler, J., Gurevich, V. V., and Hubbell, W. L. (2012) Conformation of receptor-bound visual arrestin. *Proc Nat Acad Sci USA* **109**, 18407-18412
41. Vishnivetskiy, S. A., Baameur, F., Findley, K. R., and Gurevich, V. V. (2013) Critical role of the central 139-loop in stability and binding selectivity of arrestin-1. *J Biol Chem* **288**, 11741-11750
42. Ostermaier, M. K., Peterhans, C., Jaussi, R., Deupi, X., and Standfuss, J. (2014) Functional map of arrestin-1 at single amino acid resolution. *Proceedings of the National Academy of Sciences of the United States of America* **111**, 1825-1830
43. Peeler, J. S., Donzell, W. C., and Anderson, R. G. (1993) The appendage domain of the AP-2 subunit is not required for assembly or invagination of clathrin-coated pits. *J Cell Biol* **120**, 47-54
44. Orsini, M. J., and Benovic, J. L. (1998) Characterization of dominant negative arrestins that inhibit beta2-adrenergic receptor internalization by distinct mechanisms. *J Biol Chem* **273**, 34616-34622
45. Goodman, O. B., Krupnick, J. G., Santini, F., Gurevich, V. V., Penn, R. B., Gagnon, A. W., Keen, J. H., and Benovic, J. L. (1996) Beta-arrestin acts as a clathrin adaptor in endocytosis of the beta2-adrenergic receptor. *Nature* **383**, 447-450
46. ter Haar, E., Harrison, S. C., and Kirchhausen, T. (2000) Peptide-in-groove interactions link target proteins to the beta-propeller of clathrin. *Proc Natl Acad Sci U S A* **97**, 1096-1100
47. Kang, D. S., Kern, R. C., Puthenveedu, M. A., von Zastrow, M., Williams, J. C., and Benovic, J. L. (2009) Structure of an arrestin2-clathrin complex reveals a novel clathrin binding domain that modulates receptor trafficking. *J Biol Chem* **284**, 29860-29872
48. Moaven, H., Koike, Y., Jao, C. C., Gurevich, V. V., Langen, R., and Chen, J. (2013) Visual arrestin interaction with clathrin adaptor AP-2 regulates photoreceptor survival in the vertebrate retina. *Proc Natl Acad Sci U S A* **110**, 9463-9468
49. Song, X., Vishnivetskiy, S. A., Seo, J., Chen, J., Gurevich, E. V., and Gurevich, V. V. (2011) Arrestin-1 expression in rods: balancing functional performance and photoreceptor health. *Neuroscience* **174**, 37-49
50. Strissel, K. J., Sokolov, M., Trieu, L. H., and Arshavsky, V. Y. (2006) Arrestin translocation is induced at a critical threshold of visual signaling and is superstoichiometric to bleached rhodopsin. *J Neurosci* **26**, 1146-1153
51. Luttrell, L. M., Ferguson, S. S., Daaka, Y., Miller, W. E., Maudsley, S., Della Rocca, G. J., Lin, F., Kawakatsu, H., Owada, K., Luttrell, D. K., Caron, M. G., and Lefkowitz, R. J. (1999) Beta-

arrestin-dependent formation of beta2 adrenergic receptor-Src protein kinase complexes. *Science* **283**, 655-661
52. Parsons, S. J., and Parsons, J. T. (2004) Src family kinases, key regulators of signal transduction. *Oncogene* **23**, 7906-7909
53. Luttrell, D. K., and Luttrell, L. M. (2004) Not so strange bedfellows: G-protein-coupled receptors and Src family kinases. *Oncogene* **23**, 7969-7978
54. Strungs, E. G., and Luttrell, L. M. (2014) Arrestin-Dependent Activation of ERK and Src Family Kinases. in *Arrestins - Pharmacology and Therapeutic Potential* (Gurevich, V. V. ed.), Springer Berlin Heidelberg, Berlin, Heidelberg. pp 225-257
55. Cohen, G. B., Ren, R., and Baltimore, D. Modular binding domains in signal transduction proteins. *Cell* **80**, 237-248
56. Galet, C., and Ascoli, M. (2008) Arrestin-3 is essential for the activation of Fyn by the luteinizing hormone receptor (LHR) in MA-10 cells. *Cell Signal* **20**, 1822-1829
57. Imamura, T., Huang, J., Dalle, S., Ugi, S., Usui, I., Luttrell, L. M., Miller, W. E., Lefkowitz, R. J., and Olefsky, J. M. (2001) β-Arrestin-mediated Recruitment of the Src Family Kinase Yes Mediates Endothelin-1-stimulated Glucose Transport. *Journal of Biological Chemistry* **276**, 43663-43667
58. McDonald, P. H., Chow, C. W., Miller, W. E., Laporte, S. A., Field, M. E., Lin, F. T., Davis, R. J., and Lefkowitz, R. J. (2000) Beta-arrestin 2: a receptor-regulated MAPK scaffold for the activation of JNK3. *Science* **290**, 1574-1577
59. Luttrell, L. M., Roudabush, F. L., Choy, E. W., Miller, W. E., Field, M. E., Pierce, K. L., and Lefkowitz, R. J. (2001) Activation and targeting of extracellular signal-regulated kinases by β-arrestin scaffolds. *Proceedings of the National Academy of Sciences* **98**, 2449-2454
60. Bruchas, M. R., Macey, T. A., Lowe, J. D., and Chavkin, C. (2006) Kappa Opioid Receptor Activation of p38 MAPK Is GRK3- and Arrestin-dependent in Neurons and Astrocytes. *Journal of Biological Chemistry* **281**, 18081-18089
61. Dhanasekaran, D. N., Kashef, K., Lee, C. M., Xu, H., and Reddy, E. P. (2007) Scaffold proteins of MAP-kinase modules. *Oncogene* **26**, 3185-3202
62. Good, M. C., Zalatan, J. G., and Lim, W. A. (2011) Scaffold proteins: hubs for controlling the flow of cellular information. *Science* **332**, 680-686
63. Gurevich, V. V., and Gurevich, E. V. (2010) Custom-designed proteins as novel therapeutic tools? The case of arrestins. *Expert Reviews in Molecular Medicine* **12**, e13
64. Song, X., Coffa, S., Fu, H., and Gurevich, V. V. (2009) How Does Arrestin Assemble MAPKs into a Signaling Complex? *Journal of Biological Chemistry* **284**, 685-695
65. Seo, J., Tsakem, E. L., Breitman, M., and Gurevich, V. V. (2011) Identification of arrestin-3-specific residues necessary for JNK3 kinase activation. *J Biol Chem* **286**, 27894-27901
66. Breitman, M., Kook, S., Gimenez, L. E., Lizama, B. N., Palazzo, M. C., Gurevich, E. V., and Gurevich, V. V. (2012) Silent scaffolds: inhibition of c-Jun N-terminal kinase 3 activity in the cell by a dominant-negative arrestin-3 mutant. *J Biol Chem* **287**, 19653-19664
67. Coffa, S., Breitman, M., Hanson, S. M., Callaway, K., Kook, S., Dalby, K. N., and Gurevich, V. V. (2011) The Effect of Arrestin Conformation on the Recruitment of c-Raf1, MEK1, and ERK1/2 Activation. *PLoS ONE* **6**, e28723
68. Song, X., Raman, D., Gurevich, E. V., Vishnivetskiy, S. A., and Gurevich, V. V. (2006) Visual and Both Non-visual Arrestins in Their "Inactive" Conformation Bind JNK3 and Mdm2 and Relocalize Them from the Nucleus to the Cytoplasm. *Journal of Biological Chemistry* **281**, 21491-21499
69. Song, X., Gurevich, E. V., and Gurevich, V. V. (2007) Cone arrestin binding to JNK3 and Mdm2: conformational preference and localization of interaction sites. *Journal of Neurochemistry* **103**, 1053-1062
70. Li, X., MacLeod, R., Dunlop, A. J., Edwards, H. V., Advant, N., Gibson, L. C., Devine, N. M., Brown, K. M., Adams, D. R., Houslay, M. D., and Baillie, G. S. (2009) A scanning peptide array

approach uncovers association sites within the JNK/beta arrestin signalling complex. *FEBS Lett* **583**, 3310-3316
71. Meng, D., Lynch, M. J., Huston, E., Beyermann, M., Eichhorst, J., Adams, D. R., Klussmann, E., Houslay, M. D., and Baillie, G. S. (2009) MEK1 Binds Directly to βArrestin1, Influencing Both Its Phosphorylation by ERK and the Timing of Its Isoprenaline-stimulated Internalization. *Journal of Biological Chemistry* **284**, 11425-11435
72. Zhan, X., Perez, A., Gimenez, L. E., Vishnivetskiy, S. A., and Gurevich, V. V. (2014) Arrestin-3 binds the MAP kinase JNK3α2 via multiple sites on both domains. *Cellular signalling* **26**, 766-776
73. Wu, N., Hanson, S. M., Francis, D. J., Vishnivetskiy, S. A., Thibonnier, M., Klug, C. S., Shoham, M., and Gurevich, V. V. (2006) Arrestin binding to calmodulin: a direct interaction between two ubiquitous signaling proteins. *Journal of molecular biology* **364**, 955-963
74. Yang, D. D., Kuan, C.-Y., Whitmarsh, A. J., Rinocn, M., Zheng, T. S., Davis, R. J., Rakic, P., and Flavell, R. A. (1997) Absence of excitotoxicity-induced apoptosis in the hippocampus of mice lacking the Jnk3 gene. *Nature* **389**, 865-870
75. Zhan, X., Stoy, H., Kaoud, T. S., Perry, N. A., Chen, Q., Perez, A., Els-Heindl, S., Slagis, J. V., Iverson, T. M., Beck-Sickinger, A. G., Gurevich, E. V., Dalby, K. N., and Gurevich, V. V. (2016) Peptide mini-scaffold facilitates JNK3 activation in cells. *Scientific Reports* **6**, 21025
76. Sterne-Marr, R., Gurevich, V. V., Goldsmith, P., Bodine, R. C., Sanders, C., Donoso, L. A., and Benovic, J. L. (1993) Polypeptide variants of beta-arrestin and arrestin3. *Journal of Biological Chemistry* **268**, 15640-15648
77. Guo, C., and Whitmarsh, A. J. (2008) The beta-arrestin-2 scaffold protein promotes c-Jun N-terminal kinase-3 activation by binding to its nonconserved N terminus. *J Biol Chem* **283**, 15903-15911
78. Gurevich, E. V., and Gurevich, V. V. (2006) Arrestins are ubiquitous regulators of cellular signaling pathways. *Genome Biol* **7**, 236
79. Xiao, K., McClatchy, D. B., Shukla, A. K., Zhao, Y., Chen, M., Shenoy, S. K., Yates, J. R., and Lefkowitz, R. J. (2007) Functional specialization of beta-arrestin interactions revealed by proteomic analysis. *Proc Natl Acad Sci U S A* **104**, 12011-12016
80. Ostermaier, M. K., Peterhans, C., Jaussi, R., Deupi, X., and Standfuss, J. (2014) Functional map of arrestin-1 at single amino acid resolution. *Proc Natl Acad Sci U S A* **111**, 1825-1830
81. Gimenez, L. E., Babilon, S., Wanka, L., Beck-Sickinger, A. G., and Gurevich, V. V. (2014) Mutations in arrestin-3 differentially affect binding to neuropeptide Y receptor subtypes. *Cell Signal* **26**, 1523-1531
82. Gimenez, L. E., Vishnivetskiy, S. A., Baameur, F., and Gurevich, V. V. (2012) Manipulation of very few receptor discriminator residues greatly enhances receptor specificity of non-visual arrestins. *J Biol Chem* **287**, 29495-29505
83. Meng, D., Lynch, M. J., Huston, E., Beyermann, M., Eichhorst, J., Adams, D. R., Klusmann, E., Houslay, M. D., and Baillie, G. S. (2009) MEK1 binds directly to betaarrestin1, influencing both its phosphorylation by ERK and the timing of its isoprenaline-stimulated internalization. *J Biol Chem* **284**, 11425-11435
84. Coffa, S., Breitman, M., Spiller, B. W., and Gurevich, V. V. (2011) A single mutation in arrestin-2 prevents ERK1/2 activation by reducing c-Raf1 binding. *Biochemistry* **50**, 6951-6958
85. Kook, S., Zhan, X., Kaoud, T. S., Dalby, K. N., Gurevich, V. V., and Gurevich, E. V. (2013) Arrestin-3 binds c-Jun N-terminal kinase 1 (JNK1) and JNK2 and facilitates the activation of these ubiquitous JNK isoforms in cells via scaffolding. *J Biol Chem* **288**, 37332-37342
86. Zhan, X., Kaoud, T. S., Dalby, K. N., and Gurevich, V. V. (2011) Nonvisual arrestins function as simple scaffolds assembling the MKK4-JNK3alpha2 signaling complex. *Biochemistry* **50**, 10520-10529
87. Zhan, X., Kook, S., Kaoud, T. S., Dalby, K. N., Gurevich, E. V., and Gurevich, V. V. (2015) Arrestin-3-Dependent Activation of c-Jun N-Terminal Kinases (JNKs). *Curr Protoc Pharmacol*

68, 1-26
88. Seo, J., Tsakem, E. L., Breitman, M., and Gurevich, V. V. (2011) Identification of arrestin-3-specific residues necessary for JNK3 activation. *J Biol Chem* **286**, 27894-27901
89. Vishnivetskiy, S. A., Zhan, X., Chen, Q., Iverson, T. M., and Gurevich, V. V. (2014) Arrestin expression in E. coli and purification. *Curr Protoc Pharmacol* **67**, 2.11.11-19
90. DeWire, S. M., Ahn, S., Lefkowitz, R. J., and Shenoy, S. K. (2007) β-Arrestins and Cell Signaling. *Annual Review of Physiology* **69**, 483-510
91. Han, M., Gurevich, V. V., Vishnivetskiy, S. A., Sigler, P. B., and Schubert, C. (2001) Crystal structure of beta-arrestin at 1.9 A: possible mechanism of receptor binding and membrane translocation. *Structure* **9**, 869-880
92. Zhan, X., Gimenez, L. E., Gurevich, V. V., and Spiller, B. W. (2011) Crystal structure of arrestin-3 reveals the basis of the difference in receptor binding between two non-visual arrestins. *J Mol Biol* **406**, 467-478
93. Sutton, R. B., Vishnivetskiy, S. A., Robert, J., Hanson, S. M., Raman, D., Knox, B. E., Kono, M., Navarro, J., and Gurevich, V. V. (2005) Crystal Structure of Cone Arrestin at 2.3Å: Evolution of Receptor Specificity. *J Mol Biol* **354**, 1069-1080
94. Gurevich, V. V., and Gurevich, E. V. (2006) The structural basis of arrestin-mediated regulation of G protein-coupled receptors. *Pharm Ther* **110**, 465-502
95. Granzin, J., Stadler, A., Cousin, A., Schlesinger, R., and Batra-Safferling, R. (2015) Structural evidence for the role of polar core residue Arg175 in arrestin activation. *Scientific Reports* **5**, 15808
96. Breitman, M., Kook, S., Gimenez, L. E., Lizama, B. N., Palazzo, M. C., Gurevich, E. V., and Gurevich, V. V. (2012) Silent Scaffolds: INHIBITION OF c-Jun N-TERMINAL KINASE 3 ACTIVITY IN CELL BY DOMINANT-NEGATIVE ARRESTIN-3 MUTANT. *Journal of Biological Chemistry* **287**, 19653-19664
97. Miller, W. E., and Lefkowitz, R. J. (2001) Expanding roles for β-arrestins as scaffolds and adapters in GPCR signaling and trafficking. *Current Opinion in Cell Biology* **13**, 139-145
98. Zhan, X., Kaoud, T. S., Kook, S., Dalby, K. N., and Gurevich, V. V. (2013) JNK3 Enzyme Binding to Arrestin-3 Differentially Affects the Recruitment of Upstream Mitogen-activated Protein (MAP) Kinase Kinases. *Journal of Biological Chemistry* **288**, 28535-28547
99. Zhan, X., Kook, S., Gurevich, E. V., and Gurevich, V. V. (2014) Arrestin-Dependent Activation of JNK Family Kinases. in *Arrestins - Pharmacology and Therapeutic Potential* (Gurevich, V. V. ed.), Springer Berlin Heidelberg, Berlin, Heidelberg. pp 259-280
100. Palczewski, K., Pulvermüller, A., Buczyłko, J., and Hofmann, K. P. (1991) Phosphorylated rhodopsin and heparin induce similar conformational changes in arrestin. *Journal of Biological Chemistry* **266**, 18649-18654
101. Shukla, A. K., Manglik, A., Kruse, A. C., Xiao, K., Reis, R. I., Tseng, W. C., Staus, D. P., Hilger, D., Uysal, S., Huang, L. Y., Paduch, M., Tripathi-Shukla, P., Koide, A., Koide, S., Weis, W. I., Kossiakoff, A. A., Kobilka, B. K., and Lefkowitz, R. J. (2013) Structure of active beta-arrestin-1 bound to a G-protein-coupled receptor phosphopeptide. *Nature* **497**, 137-141
102. Zhan, X., Gimenez, L. E., Gurevich, V. V., and Spiller, B. W. (2011) Crystal structure of arrestin-3 reveals the basis of the difference in receptor binding between two non-visual subtypes. *Journal of molecular biology* **406**, 467-478
103. Milano, S. K., Kim, Y. M., Stefano, F. P., Benovic, J. L., and Brenner, C. (2006) Nonvisual arrestin oligomerization and cellular localization are regulated by inositol hexakisphosphate binding. *J Biol Chem* **281**, 9812-9823
104. Zhan, X., Perez, A., Gimenez, L. E., Vishnivetskiy, S. A., and Gurevich, V. V. (2014) Arrestin-3 binds the MAP kinase JNK3a2 via multiple sites on both domains. *Cellular signalling* **26**, 766-776
105. Bunce, C. M., French, P. J., Allen, P., Mountford, J. C., Moor, B., Greaves, M. F., Michell, R. H., and Brown, G. (1993) Comparison of the levels of inositol metabolites in transformed

haemopoietic cells and their normal counterparts. *Biochemical Journal* **289**, 667
106. Sasakawa, N., Sharif, M., and Hanley, M. R. (1995) Metabolism and biological activities of inositol pentakisphosphate and inositol hexakisphosphate. *Biochemical Pharmacology* **50**, 137-146
107. Scheerer, P., Park, J. H., Hildebrand, P. W., Kim, Y. J., Krauß, N., Choe, H.-W., Hofmann, K. P., and Ernst, O. P. (2008) Crystal structure of opsin in its G-protein-interacting conformation. *Nature* **455**, 497
108. Szczepek, M., Beyriere, F., Hofmann, K. P., Elgeti, M., Kazmin, R., Rose, A., Bartl, F. J., von Stetten, D., Heck, M., Sommer, M. E., Hildebrand, P. W., and Scheerer, P. (2014) Crystal structure of a common GPCR-binding interface for G protein and arrestin. *Nat Commun* **5**, 4801
109. Hirsch, J. A., Schubert, C., Gurevich, V. V., and Sigler, P. B. (1999) The 2.8 A crystal structure of visual arrestin: a model for arrestin's regulation. *Cell* **97**, 257-269
110. Sutton, R. B., Vishnivetskiy, S. A., Robert, J., Hanson, S. M., Raman, D., Knox, B. E., Kono, M., Navarro, J., and Gurevich, V. V. (2005) Crystal structure of cone arrestin at 2.3A: evolution of receptor specificity. *Journal of molecular biology* **354**, 1069-1080
111. Zhuang, T., Chen, Q., Cho, M.-K., Vishnivetskiy, S. A., Iverson, T. I., Gurevich, V. V., and Hubbell, W. L. (2013) Involvement of Distinct Arrestin-1 Elements in Binding to Different Functional Forms of Rhodopsin. *Proc Nat Acad Sci USA* **110**, 942-947
112. Kang, Y., Zhou, X. E., Gao, X., He, Y., Liu, W., Ishchenko, A., Barty, A., White, T. A., Yefanov, O., Han, G. W., Xu, Q., de Waal, P. W., Ke, J., Tan, M. H. E., Zhang, C., Moeller, A., West, G. M., Van Eps, N., Caro, L. N., Vishnivetskiy, S. A., Lee, R. J., Suino-Powell, K. M., Gu, X., Pal, K., Ma, J., Zhi, X., Boutet, S., Williams, G. J., Messerschmidt, M., Gati, C., Zatsepin, N. A., Wang, D., James, D., Basu, S., Roy-Chowdhuty, S., Conrad, S., Coe, J., Liu, H., Lisova, S., Kupitz, C., Grotjohann, I., Fromme, R., Jiang, Y., Tan, M., Yang, H., Li, J., Wang, M., Zheng, Z., Li, D., Zhao, Y., Standfuss, J., Diederichs, K., Dong, Y., Potter, C. S., Carragher, B., Caffrey, M., Jiang, H., Chapman, H. N., Spence, J. C. H., Fromme, P., Weierstall, U., Ernst, O. P., Katritch, V., Gurevich, V. V., Griffin, P. R., Hubbell, W. L., Stevens, R. C., Cherezov, V., Melcher, K., and Xu, H. E. (2015) Crystal structure of rhodopsin bound to arrestin determined by femtosecond X-ray laser. *Nature* **523**, 561-567
113. Krissinel, E., and Henrick, K. (2007) Inference of Macromolecular Assemblies from Crystalline State. *Journal of Molecular Biology* **372**, 774-797
114. Gimenez, L. E., Kook, S., Vishnivetskiy, S. A., Ahmed, M. R., Gurevich, E. V., and Gurevich, V. V. (2012) Role of receptor-attached phosphates in binding of visual and non-visual arrestins to G protein-coupled receptors. *J Biol Chem* **287**, 9028-9040
115. Chen, Q., Zhuo, Y., Kim, M., Hanson, S. M., Francis, D. J., Vishnivetskiy, S. A., Altenbach, C., Klug, C. S., Hubbell, W. L., and Gurevich, V. V. (2014) Self-Association of Arrestin Family Members. in *Arrestins - Pharmacology and Therapeutic Potential* (Gurevich, V. V. ed.), Springer Berlin Heidelberg, Berlin, Heidelberg. pp 205-223
116. Milano, S. K., Pace, H. C., Kim, Y. M., Brenner, C., and Benovic, J. L. (2002) Scaffolding functions of arrestin-2 revealed by crystal structure and mutagenesis. *Biochemistry* **41**, 3321-3328
117. Gimenez, L. E., Babilon, S., Wanka, L., Beck-Sickinger, A. G., and Gurevich, V. V. (2014) Mutations in arrestin-3 differentially affect binding to neuropeptide Y receptor subtypes. *Cellular signalling* **26**, 1523-1531
118. Vey, J. L., Al-Mestarihi, A., Hu, Y., Funk, M. A., Bachmann, B. O., and Iverson, T. M. (2010) Structure and Mechanism of ORF36, an Amino Sugar Oxidizing Enzyme in Everninomicin Biosynthesis. *Biochemistry* **49**, 9306-9317
119. Bruender, N. A., Thoden, J. B., and Holden, H. M. (2010) X-ray Structure of KijD3, a Key Enzyme Involved in the Biosynthesis of d-Kijanose. *Biochemistry* **49**, 3517-3524
120. Vishnivetskiy, S. A., Hirsch, J. A., Velez, M.-G., Gurevich, Y. V., and Gurevich, V. V. (2002) Transition of Arrestin into the Active Receptor-binding State Requires an Extended Interdomain Hinge. *Journal of Biological Chemistry* **277**, 43961-43967

121. Hanson, S. M., Cleghorn, W. M., Francis, D. J., Vishnivetskiy, S. A., Raman, D., Song, X., Nair, K. S., Slepak, V. Z., Klug, C. S., and Gurevich, V. V. (2007) Arrestin Mobilizes Signaling Proteins to the Cytoskeleton and Redirects their Activity. *Journal of Molecular Biology* **368**, 375-387
122. Johnson, E., Nguyen, P. T., Yeates, T. O., and Rees, D. C. (2012) Inward facing conformations of the MetNI methionine ABC transporter: Implications for the mechanism of transinhibition. *Protein Science* **21**, 84-96
123. Renault, L., Guibert, B., and Cherfils, J. (2003) Structural snapshots of the mechanism and inhibition of a guanine nucleotide exchange factor. *Nature* **426**, 525
124. Westblade, L. F., Campbell, E. A., Pukhrambam, C., Padovan, J. C., Nickels, B. E., Lamour, V., and Darst, S. A. (2010) Structural basis for the bacterial transcription-repair coupling factor/RNA polymerase interaction. *Nucleic Acids Research* **38**, 8357-8369
125. Shoemaker, B. A., Portman, J. J., and Wolynes, P. G. (2000) Speeding molecular recognition by using the folding funnel: The fly-casting mechanism. *Proceedings of the National Academy of Sciences* **97**, 8868
126. Sugase, K., Dyson, H. J., and Wright, P. E. (2007) Mechanism of coupled folding and binding of an intrinsically disordered protein. *Nature* **447**, 1021
127. Vishnivetskiy, S. A., Francis, D., Van Eps, N., Kim, M., Hanson, S. M., Klug, C. S., Hubbell, W. L., and Gurevich, V. V. (2010) The Role of Arrestin α-Helix I in Receptor Binding. *Journal of Molecular Biology* **395**, 42-54
128. Vishnivetskiy, S. A., Schubert, C., Climaco, G. C., Gurevich, Y. V., Velez, M.-G., and Gurevich, V. V. (2000) An Additional Phosphate-binding Element in Arrestin Molecule: IMPLICATIONS FOR THE MECHANISM OF ARRESTIN ACTIVATION. *Journal of Biological Chemistry* **275**, 41049-41057
129. Granzin, J., Wilden, U., Choe, H. W., Labahn, J., Krafft, B., and Buldt, G. (1998) X-ray crystal structure of arrestin from bovine rod outer segments. *Nature* **391**, 918-921
130. Kim, J., Ahn, S., Ren, X. R., Whalen, E. J., Reiter, E., Wei, H., and Lefkowitz, R. J. (2005) Functional antagonism of different G protein-coupled receptor kinases for beta-arrestin-mediated angiotensin II receptor signaling. *Proc Natl Acad Sci U S A* **102**, 1442-1447
131. Ren, X. R., Reiter, E., Ahn, S., Kim, J., Chen, W., and Lefkowitz, R. J. (2005) Different G protein-coupled receptor kinases govern G protein and beta-arrestin-mediated signaling of V2 vasopressin receptor. *Proc Natl Acad Sci U S A* **102**, 1448-1453
132. Shukla, A. K., Westfield, G. H., Xiao, K., Reis, R. I., Huang, L.-Y., Tripathi-Shukla, P., Qian, J., Li, S., Blanc, A., Oleskie, A. N., Dosey, A. M., Su, M., Liang, C.-R., Gu, L.-L., Shan, J.-M., Chen, X., Hanna, R., Choi, M., Yao, X. J., Klink, B. U., Kahsai, A. W., Sidhu, S. S., Koide, S., Penczek, P. A., Kossiakoff, A. A., Woods, V. L., Jr., Kobilka, B. K., Skiniotis, G., and Lefkowitz, R. J. (2014) Visualization of arrestin recruitment by a G-protein-coupled receptor. *Nature* **512**, 218-222
133. Sinha, A., Jones Brunette, A. M., Fay, J. F., Schafer, C. T., and Farrens, D. L. (2014) Rhodopsin TM6 Can Interact with Two Separate and Distinct Sites on Arrestin: Evidence for Structural Plasticity and Multiple Docking Modes in Arrestin–Rhodopsin Binding. *Biochemistry* **53**, 3294-3307
134. Yang, F., Yu, X., Liu, C., Qu, C.-X., Gong, Z., Liu, H.-D., Li, F.-H., Wang, H.-M., He, D.-F., Yi, F., Song, C., Tian, C.-L., Xiao, K.-H., Wang, J.-Y., and Sun, J.-P. (2015) Phospho-selective mechanisms of arrestin conformations and functions revealed by unnatural amino acid incorporation and 19F-NMR. *Nature Communications* **6**, 8202
135. Nobles, K. N., Xiao, K., Ahn, S., Shukla, A. K., Lam, C. M., Rajagopal, S., Strachan, R. T., Huang, T. Y., Bressler, E. A., Hara, M. R., Shenoy, S. K., Gygi, S. P., and Lefkowitz, R. J. (2011) Distinct phosphorylation sites on the β(2)-adrenergic receptor establish a barcode that encodes differential functions of β-arrestin. *Sci Signal* **4**, ra51
136. Vishnivetskiy, S. A., Zhan, X., Chen, Q., Iverson, T. M., and Gurevich, V. V. (2014) Arrestin

Expression in E. coli and Purification. *Current protocols in pharmacology / editorial board, S.J. Enna (editor-in-chief) ... [et al.]* **67**, 2.11.11-12.11.19
137. Otwinowski, Z., and Minor, W. (1997) P**rocessing of X-ray Diffraction Data Collected in Oscillation Mode**. Academic Press, *Methods in Enzymology*
138. McCoy, A. J., Grosse-Kunstleve, R. W., Adams, P. D., Winn, M. D., Storoni, L. C., and Read, R. J. (2007) Phaser crystallographic software. *Journal of Applied Crystallography* **40**, 658-674
139. Emsley, P., Lohkamp, B., Scott, W.G. and Cowtan, K. (2010) Features and Development of Coot.
140. Adams, P. D., Afonine, P. V., Bunkóczi, G., Chen, V. B., Davis, I. W., Echols, N., Headd, J. J., Hung, L.-W., Kapral, G. J., Grosse-Kunstleve, R. W., McCoy, A. J., Moriarty, N. W., Oeffner, R., Read, R. J., Richardson, D. C., Richardson, J. S., Terwilliger, T. C., and Zwart, P. H. (2010) PHENIX: a comprehensive Python-based system for macromolecular structure solution. *Acta Crystallographica Section D* **66**, 213-221
141. Donoso, L. A., Gregerson, D. S., Smith, L., Robertson, S., Knospe, V., Vrabec, T., and Kalsow, C. M. (1990) S-Antigen: preparation and characterization of site-specific monoclonal antibodies. *Current Eye Research* **9**, 343-355
142. Zhou, X. E., Gao, X., Barty, A., Kang, Y., He, Y., Liu, W., Ishchenko, A., White, T. A., Yefanov, O., Han, G. W., Xu, Q., de Waal, P. W., Suino-Powell, K. M., Boutet, S., Williams, G. J., Wang, M., Li, D., Caffrey, M., Chapman, H. N., Spence, J. C., Fromme, P., Weierstall, U., Stevens, R. C., Cherezov, V., Melcher, K., and Xu, H. E. (2016) X-ray laser diffraction for structure determination of the rhodopsin-arrestin complex. *Sci Data* **3**, 160021
143. Toledo Warshaviak, D., Khramtsov, V. V., Cascio, D., Altenbach, C., and Hubbell, W. L. (2013) Structure and dynamics of an imidazoline nitroxide side chain with strongly hindered internal motion in proteins. *Journal of Magnetic Resonance* **232**, 53-61
144. Jeschke, G. (2012) DEER Distance Measurements on Proteins. *Annual Review of Physical Chemistry* **63**, 419-446
145. Scheuermann, T. H., Padrick, S. B., Gardner, K. H., and Brautigam, C. A. (2016) On the acquisition and analysis of microscale thermophoresis data. *Analytical Biochemistry* **496**, 79-93
146. Tso, S.-C., Chen, Q., Vishnivetskiy, S. A., Gurevich, V. V., Iverson, T. M., and Brautigam, C. A. (2017) Using two-site binding models to analyze microscale thermophoresis data. *Analytical Biochemistry*
147. Schuck, P. (2000) Size-Distribution Analysis of Macromolecules by Sedimentation Velocity Ultracentrifugation and Lamm Equation Modeling. *Biophysical Journal* **78**, 1606-1619
148. Lim, W. A. (2010) Designing customized cell signalling circuits. *Nat Rev Mol Cell Biol* **11**, 393-403
149. Burack, W. R., and Shaw, A. S. (2000) Signal transduction: hanging on a scaffold. *Curr Opin Cell Biol* **12**, 211-216
150. Dhanasekaran, D. N., Kashef, K., Lee, C. M., Xu, H., and Reddy, E. P. (2007) Scaffold proteins of MAP-kinase modules. *Oncogene*, 3185-3202
151. Keshet, Y., and Seger, R. (2010) The MAP kinase signaling cascades: a system of hundreds of components regulates a diverse array of physiological functions. *Methods Mol Biol* **661**, 3-38
152. Widmann, C., Gibson, S., Jarpe, M. B., and Johnson, G. L. (1999) Mitogen-activated protein kinase: conservation of a three-kinase module from yeast to human. *Physiol Rev* **79**, 143–-180
153. Davis, R. J. (2000) Signal transduction by the JNK group of MAP kinases. *Cell* **103**, 239-252
154. Sabapathy, K. (2012) Role of the JNK pathway in human diseases. *Prog Mol Biol Transl Sci* **106**, 145-169
155. Flemming, A. (2012) Alzheimer's Disease: JNK3 as new target in AD? *Nat Rev Drug Discov* **11**, 829
156. Yoon, S. O., Park, D. J., Ryu, J. C., Ozer, H. G., Tep, C., Shin, Y. J., Lim, T. H., Pastorino, L., Kunwar, A. J., Walton, J. C., Nagahara, A. H., Lu, K. P., Nelson, R. J., Tuszynski, M. H., and Huang, K. (2012) JNK3 perpetuates metabolic stress induced by Aβ peptides. *Neuron* **75**, 824-

837
157. Lawler, S., Fleming, Y., Goedert, M., and Cohen, P. (1998) Synergistic activation of SAPK1/JNK1 by two MAP kinase kinases in vitro. *Curr Biol* **8**, 1387-1390
158. Yasuda, J., Whitmarsh, A. J., Cavanagh, J., Sharma, M., and Davis, R. J. (1999) The JIP group of mitogen-activated protein kinase scaffold proteins. *Mol Cell Biol* **19**, 7245-7254
159. Carman, C. V., and Benovic, J. L. (1998) G-protein-coupled receptors: turn-ons and turn-offs. *Curr Opin Neurobiol* **8**, 335-344
160. McDonald, P. H., Chow, C. W., Miller, W. E., Laporte, S. A., Field, M. E., Lin, F. T., Davis, R. J., and Lefkowitz, R. J. (2000) Beta-arrestin 2: a receptor-regulated MAPK scaffold for the activation of JNK3. *Science* **290**, 1574-1577
161. Kook, S., Zhan, X., Kaoud, T. S., Dalby, K. N., Gurevich, V. V., and Gurevich, E. V. (2013) Arrestin-3 binds JNK1α1 and JNK2α2 and facilitates the activation of these ubiquitous JNK isoforms in cells via scaffolding. *J Biol Chem* **288**, 37332-37342
162. Song, X., Coffa, S., Fu, H., and Gurevich, V. V. (2009) How does arrestin assemble MAPKs into a signaling complex? *J Biol Chem* **284**, 685-695
163. Zhan, X., Kaoud, T. S., Dalby, K. N., and Gurevich, V. V. (2011) Non-visual arrestins function as simple scaffolds assembling MKK4- JNK3α2 signaling complex. *Biochemistry* **50**, 10520-10529
164. Zhan, X., Kaoud, T. S., Kook, S., Dalby, K. N., and Gurevich, V. V. (2013) JNK3 binding to arrestin-3 differentially affects the recruitment of upstream MAP kinase kinases. *J Biol Chem* **288**, 28535-28547
165. Miller, W. E., McDonald, P. H., Cai, S. F., Field, M. E., Davis, R. J., and Lefkowitz, R. J. (2001) Identification of a motif in the carboxyl terminus of beta -arrestin2 responsible for activation of JNK3. *J Biol Chem* **276**, 27770-27777
166. Song, X., Raman, D., Gurevich, E. V., Vishnivetskiy, S. A., and Gurevich, V. V. (2006) Visual and both non-visual arrestins in their "inactive" conformation bind JNK3 and Mdm2 and relocalize them from the nucleus to the cytoplasm. *J Biol Chem* **281**, 21491-21499
167. Zhan, X., Perez, A., Gimenez, L. E., Vishnivetskiy, S. A., and Gurevich, V. V. (2014) Arrestin-3 binds the MAP kinase JNK3α2 via multiple sites on both domains. *Cell Signal* **26**, 766-776
168. Levchenko, A., Bruck, J., and Sternberg, P. W. (2000) Scaffold proteins may biphasically affect the levels of mitogen-activated protein kinase signaling and reduce its threshold properties. *Proc Natl Acad Sci U S A* **97**, 5818-5823
169. Levchenko, A., Bruck, J., and Sternberg, P. W. (2004) Regulatory modules that generate biphasic signal response in biological systems. *Syst Biol (Stevenage)* **1**, 139-148
170. Hirsch, J. A., Schubert, C., Gurevich, V. V., and Sigler, P. B. (1999) The 2.8 A crystal structure of visual arrestin: a model for arrestin's regulation. *Cell* **97**, 257-269
171. Ahmed, M. R., Zhan, X., Song, X., Kook, S., Gurevich, V. V., and Gurevich, E. V. (2011) Ubiquitin ligase parkin promotes Mdm2-arrestin interaction but inhibits arrestin ubiquitination. *Biochemistry* **50**, 3749-3763
172. Hanson, S. M., Cleghorn, W. M., Francis, D. J., Vishnivetskiy, S. A., Raman, D., Song, X., Nair, K. S., Slepak, V. Z., Klug, C. S., and Gurevich, V. V. (2007) Arrestin mobilizes signaling proteins to the cytoskeleton and redirects their activity. *J Mol Biol* **368**, 375-387
173. Kim, M., Vishnivetskiy, S. A., Van Eps, N., Alexander, N. S., Cleghorn, W. M., Zhan, X., Hanson, S. M., Morizumi, T., Ernst, O. P., Meiler, J., Gurevich, V. V., and Hubbell, W. L. (2012) Conformation of receptor-bound visual arrestin. *Proc Nat Acad Sci USA* **109**, 18407-18412
174. Kang, Y., Zhou, X. E., Gao, X., He, Y., Liu, W., Ishchenko, A., Barty, A., White, T. A., Yefanov, O., Han, G. W., Xu, Q., de Waal, P. W., Ke, J., Tan, M. H. E., Zhang, C., Moeller, A., West, G. M., Van Eps, N., Caro, L. N., Vishnivetskiy, S. A., Lee, R. J., Suino-Powell, K. M., Gu, X., Pal, K., Ma, J., Zhi, X., Boutet, S., Williams, G. J., Messerschmidt, M., Gati, C., Zatsepin, N. A., Wang, D., James, D., Basu, S., Roy-Chowdhuty, S., Conrad, S., Coe, J., Liu, H., Lisova, S., Kupitz, C., Grotjohann, I., Fromme, R., Jiang, Y., Tan, M., Yang, H., Li, J., Wang, M., Zheng, Z., Li, D., Zhao, Y., Standfuss, J., Diederichs, K., Dong, Y., Potter, C. S., Carragher, B., Caffrey, M.,

Jiang, H., Chapman, H. N., Spence, J. C. H., Fromme, P., Weierstall, U., Ernst, O. P., Katritch, V., Gurevich, V. V., Griffin, P. R., Hubbell, W. L., Stevens, R. C., Cherezov, V., Melcher, K., and Xu, H. E. (2015) Crystal structure of rhodopsin bound to arrestin determined by femtosecond X-ray laser. *Nature* **523**, 561-567

175. Luttrell, L. M., Roudabush, F. L., Choy, E. W., Miller, W. E., Field, M. E., Pierce, K. L., and Lefkowitz, R. J. (2001) Activation and targeting of extracellular signal-regulated kinases by beta-arrestin scaffolds. *Proc Natl Acad Sci U S A* **98**, 2449-2454
176. Bruchas, M. R., Macey, T. A., Lowe, J. D., and Chavkin, C. (2006) Kappa opioid receptor activation of p38 MAPK is GRK3- and arrestin-dependent in neurons and astrocytes. *J Biol Chem* **281**, 18081-18089
177. Zhan, X., Kook, S., Kaoud, T. S., Dalby, K. N., Gurevich, E. V., and Gurevich, V. V. (2015) Arrestin-3-Dependent Activation of c-Jun N-Terminal Kinases (JNKs). *Curr Protoc Pharmacol* **68**, 2.12.11-12.12.26
178. Els, S., Beck-Sickinger, A. G., and Chollet, C. (2010) Ghrelin receptor: high constitutive activity and methods for developing inverse agonists. *Methods Enzymol* **485**, 103-121
179. Locasale, J. W., Shaw, A. S., and Chakraborty, A. K. (2007) Scaffold proteins confer diverse regulatory properties to protein kinase cascades. *Proceedings of the National Academy of Sciences* **104**, 13307-13312
180. Chol, K.-Y., Satterberg, B., Lyons, D. M., and Elion, E. A. (1994) Ste5 tethers multiple protein kinases in the MAP kinase cascade required for mating in S. cerevisiae. *Cell* **78**, 499-512
181. Brown, M. D., and Sacks, D. B. (2009) Protein scaffolds in MAP kinase signalling. *Cellular Signalling* **21**, 462-469
182. Mayawala, K., Gelmi, C. A., and Edwards, J. S. (2004) MAPK cascade possesses decoupled controllability of signal amplification and duration. *Biophysical journal* **87**, L01-02
183. Turjanski, A. G., Hummer, G., and Gutkind, J. S. (2009) How Mitogen-Activated Protein Kinases Recognize and Phosphorylate Their Targets: A QM/MM Study. *Journal of the American Chemical Society* **131**, 6141-6148
184. Clarke, P. R. (1994) Signal Transduction: Switching off MAP kinases. *Current Biology* **4**, 647-650
185. Kolch, W., Calder, M., and Gilbert, D. (2005) When kinases meet mathematics: the systems biology of MAPK signalling. *FEBS Letters* **579**, 1891-1895
186. Adler, M., Mayo, A., and Alon, U. (2014) Logarithmic and Power Law Input-Output Relations in Sensory Systems with Fold-Change Detection. *PLOS Computational Biology* **10**, e1003781
187. Choi, W. S., Klintworth, H. M., and Xia, Z. (2011) JNK3-mediated apoptotic cell death in primary dopaminergic neurons. *Methods Mol Biol* **758**, 279-292
188. Levchenko, A., Bruck, J., and Sternberg, P. W. (2000) Scaffold proteins may biphasically affect the levels of mitogen-activated protein kinase signaling and reduce its threshold properties. *Proceedings of the National Academy of Sciences* **97**, 5818-5823
189. Luttrell, L. M., and Gesty-Palmer, D. (2010) Beyond Desensitization: Physiological Relevance of Arrestin-Dependent Signaling. *Pharmacological Reviews* **62**, 305
190. Eishingdrelo, H., Sun, W., Li, H., Wang, L., Eishingdrelo, A., Dai, S., McKew, J. C., and Zheng, W. (2015) ERK and β-arrestin interaction: a converging-point of signaling pathways for multiple types of cell-surface receptors. *Journal of biomolecular screening* **20**, 341-349
191. Kook, S., Zhan, X., Cleghorn, W. M., Benovic, J. L., Gurevich, V. V., and Gurevich, E. V. (2013) Caspase-cleaved arrestin-2 and BID cooperatively facilitate cytochrome C release and cell death. *Cell Death And Differentiation* **21**, 172
192. Rusnak, L., and Fu, H. (2017) Regulation of ASK1 signaling by scaffold and adaptor proteins. *Advances in Biological Regulation* **66**, 23-30
193. Kook, S., Zhan, X., Kaoud, T. S., Dalby, K. N., Gurevich, V. V., and Gurevich, E. V. (2013) Arrestin-3 binds c-Jun N-terminal kinase 1 (JNK1) and JNK2 and facilitates the activation of these ubiquitous JNK isoforms in cells via scaffolding. *J Biol Chem* **288**, 37332-37342

194. Tso, S.-C., Chen, Q., Vishnivetskiy, S. A., Gurevich, V. V., Iverson, T. M., and Brautigam, C. A. (2018) Using two-site binding models to analyze microscale thermophoresis data. *Analytical Biochemistry* **540-541**, 64-75
195. Wienken, C. J., Baaske, P., Rothbauer, U., Braun, D., and Duhr, S. (2010) Protein-binding assays in biological liquids using microscale thermophoresis. *Nat Commun* **1**, 100
196. Jerabek-Willemsen, M., Wienken, C. J., Braun, D., Baaske, P., and Duhr, S. (2011) Molecular Interaction Studies Using Microscale Thermophoresis. *Assay and Drug Development Technologies* **9**, 342-353
197. Cuenda, A. (2000) Mitogen-Activated Protein Kinase Kinase 4 (MKK4). *The International Journal of Biochemistry & Cell Biology* **32**, 581-587
198. Gurevich, E. V., Benovic, J. L., and Gurevich, V. V. (2002) Arrestin2 and arrestin3 are differentially expressed in the rat brain during postnatal development. *Neuroscience* **109**, 421-436
199. Gurevich, V. V., and Gurevich, E. V. (2004) The molecular acrobatics of arrestin activation. *Trends in Pharmacological Sciences* **25**, 105-111
200. Lawler, S., Fleming, Y., Goedert, M., and Cohen, P. (1998) Synergistic activation of SAPK1/JNK1 by two MAP kinase kinases in vitro. *Current Biology* **8**, 1387-1391
201. Zhang, F., Strand, A., Robbins, D., Cobb, M. H., and Goldsmith, E. J. (1994) Atomic structure of the MAP kinase ERK2 at 2.3 A resolution. *Nature* **367**, 704-711
202. Canagarajah, B. J., Khokhlatchev, A., Cobb, M. H., and Goldsmith, E. J. (1997) Activation Mechanism of the MAP Kinase ERK2 by Dual Phosphorylation. *Cell* **90**, 859-869
203. Ahmed, M. R., Zhan, X., Song, X., Kook, S., Gurevich, V. V., and Gurevich, E. V. (2011) Ubiquitin Ligase Parkin Promotes Mdm2–Arrestin Interaction but Inhibits Arrestin Ubiquitination. *Biochemistry* **50**, 3749-3763
204. Seo, J., Tsakem, E. L., Breitman, M., and Gurevich, V. V. (2011) Identification of Arrestin-3-specific Residues Necessary for JNK3 Kinase Activation. *Journal of Biological Chemistry* **286**, 27894-27901
205. Lopez, C. F., Muhlich, J. L., Bachman, J. A., and Sorger, P. K. (2013) Programming biological models in Python using PySB. *Mol Syst Biol* **9**, 646
206. Kitano, H., Funahashi, A., Matsuoka, Y., and Oda, K. (2005) Using process diagrams for the graphical representation of biological networks. *Nat Biotechnol* **23**, 961-966
207. Shockley, E. M., Vrugt, J. A., and Lopez, C. F. (2018) PyDREAM: high-dimensional parameter inference for biological models in python. *Bioinformatics* **34**, 695-697
208. Muniyappa, H., and Das, K. C. (2008) Activation of c-Jun N-terminal kinase (JNK) by widely used specific p38 MAPK inhibitors SB202190 and SB203580: A MLK-3-MKK7-dependent mechanism. *Cellular Signalling* **20**, 675-683
209. Lei, K., Nimnual, A., Zong, W.-X., Kennedy, N. J., Flavell, R. A., Thompson, C. B., Bar-Sagi, D., and Davis, R. J. (2002) The Bax Subfamily of Bcl2-Related Proteins Is Essential for Apoptotic Signal Transduction by c-Jun NH₂-Terminal Kinase. *Molecular and Cellular Biology* **22**, 4929
210. Khalid, S., Drasche, A., Thurner, M., Hermann, M., Ashraf, M. I., Fresser, F., Baier, G., Kremser, L., Lindner, H., and Troppmair, J. (2016) cJun N-terminal kinase (JNK) phosphorylation of serine 36 is critical for p66Shc activation. *Scientific Reports* **6**, 20930
211. Alvarez-Curto, E., Inoue, A., Jenkins, L., Raihan, S. Z., Prihandoko, R., Tobin, A. B., and Milligan, G. (2016) Targeted Elimination of G proteins and Arrestins Defines their Specific Contributions to both Intensity and Duration of G protein-Coupled Receptor Signalling. *Journal of Biological Chemistry*
212. Good, M. C., Zalatan, J. G., and Lim, W. A. (2011) Scaffold Proteins: Hubs for Controlling the Flow of Cellular Information. *Science (New York, N.Y.)* **332**, 680-686
213. Miller, W. E., McDonald, P. H., Cai, S. F., Field, M. E., Davis, R. J., and Lefkowitz, R. J. (2001) Identification of a Motif in the Carboxyl Terminus of β-Arrestin2 Responsible for Activation of JNK3. *Journal of Biological Chemistry* **276**, 27770-27777

214. Zhan, X., Kook, S., Kaoud, T. S., Dalby, K. N., Gurevich, E. V., and Gurevich, V. V. (2015) Arrestin-3-dependent activation of c-Jun N-terminal kinases (JNKs). *Current protocols in pharmacology / editorial board, S.J. Enna (editor-in-chief) ... [et al.]* **68**, 2.12.11-12.12.26
215. Zhan, X., Gimenez, L. E., Gurevich, V. V., and Spiller, B. W. (2011) Crystal Structure of Arrestin-3 Reveals the Basis of the Difference in Receptor Binding Between Two Non-visual Subtypes. *Journal of Molecular Biology* **406**, 467-478
216. Sensoy, O., Moreira, I. S., and Morra, G. (2016) Understanding the Differential Selectivity of Arrestins toward the Phosphorylation State of the Receptor. *ACS Chemical Neuroscience* **7**, 1212-1224
217. Tanoue, T., and Nishida, E. (2002) Docking interactions in the mitogen-activated protein kinase cascades. *Pharmacology & Therapeutics* **93**, 193-202
218. Gurevich Eugenia, V., Benovic Jeffrey, L., and Gurevich Vsevolod, V. (2004) Arrestin2 expression selectively increases during neural differentiation. *Journal of Neurochemistry* **91**, 1404-1416
219. Barak, L. S., Ferguson, S. S. G., Zhang, J., and Caron, M. G. (1997) A β-Arrestin/Green Fluorescent Protein Biosensor for Detecting G Protein-coupled Receptor Activation. *Journal of Biological Chemistry* **272**, 27497-27500
220. Namkung, Y., Le Gouill, C., Lukashova, V., Kobayashi, H., Hogue, M., Khoury, E., Song, M., Bouvier, M., and Laporte, S. A. (2016) Monitoring G protein-coupled receptor and β-arrestin trafficking in live cells using enhanced bystander BRET. *Nature Communications* **7**, 12178
221. Milano, S. K., Kim, Y.-M., Stefano, F. P., Benovic, J. L., and Brenner, C. (2006) Nonvisual Arrestin Oligomerization and Cellular Localization Are Regulated by Inositol Hexakisphosphate Binding. *Journal of Biological Chemistry* **281**, 9812-9823
222. Orsini, M. J., and Benovic, J. L. (1998) Characterization of Dominant Negative Arrestins That Inhibit β2-Adrenergic Receptor Internalization by Distinct Mechanisms. *Journal of Biological Chemistry* **273**, 34616-34622
223. Han, M., Gurevich, V. V., Vishnivetskiy, S. A., Sigler, P. B., and Schubert, C. (2001) Crystal Structure of β-Arrestin at 1.9 Å: Possible Mechanism of Receptor Binding and Membrane Translocation. *Structure* **9**, 869-880
224. Bennett, T. A., Foutz, T., Gurevich, V., Sklar, L., and Prossnitz, E. (2002) *Partial Phosphorylation of the N-Formyl Peptide Receptor Inhibits G Protein Association Independent of Arrestin Binding*,
225. Pleinis, J. M., Davis, C. W., Cantrell, C. B., Qiu, D. Y., and Zhan, X. (2017) Purification, auto-activation and kinetic characterization of apoptosis signal-regulating kinase I. *Protein Expression and Purification* **132**, 34-43
226. Vishnivetskiy, S. A., Zhan, X., Chen, Q., Iverson, T. M., and Gurevich, V. V. (2014) Arrestin expression in E. coli and purification. *Curr Protoc Pharmacol* **67**, Unit 2.11.11-19
227. Zhan, X., Kaoud, T. S., Dalby, K. N., and Gurevich, V. V. (2011) Non-visual arrestins function as simple scaffolds assembling the MKK4–JNK3a2 signaling complex. *Biochemistry* **50**, 10520-10529
228. Yan, C., Kaoud, T., Lee, S., Dalby, K. N., and Ren, P. (2011) Understanding the Specificity of a Docking Interaction between JNK1 and the Scaffolding Protein JIP1. *The Journal of Physical Chemistry B* **115**, 1491-1502
229. Bartoschik, T., Galinec, S., Kleusch, C., Walkiewicz, K., Breitsprecher, D., Weigert, S., Muller, Y. A., You, C., Piehler, J., Vercruysse, T., Daelemans, D., and Tschammer, N. (2018) Near-native, site-specific and purification-free protein labeling for quantitative protein interaction analysis by MicroScale Thermophoresis. *Scientific Reports* **8**, 4977
230. Yim, Y. Y., Betke, K., and Hamm, H. (2015) Using Peptide Arrays Created by the SPOT Method for Defining Protein-Protein Interactions. in *Protein-Protein Interactions: Methods and Applications* (Meyerkord, C. L., and Fu, H. eds.), Springer New York, New York, NY. pp 307-320

231. Bar-Even, A., Noor, E., Savir, Y., Liebermeister, W., Davidi, D., Tawfik, D. S., and Milo, R. (2011) The moderately efficient enzyme: evolutionary and physicochemical trends shaping enzyme parameters. *Biochemistry* **50**, 4402-4410
232. Aldridge, B. B., Burke, J. M., Lauffenburger, D. A., and Sorger, P. K. (2006) Physicochemical modelling of cell signalling pathways. *Nature Cell Biology* **8**, 1195
233. Zheng, L.-S., Zhang, Y.-Y., Wu, J.-W., Wu, Z., Zhang, Z.-Y., and Wang, Z.-X. (2012) A continuous spectrophotometric assay for mitogen-activated protein kinase kinases. *Analytical Biochemistry* **421**, 191-197
234. Vrugt, J. A., and C.J.F., t. B. (2011) DREAM(D): An adaptive Markov chain Monte Carlo simulation algorithm to solve discrete, noncontinuous, and combinatorial posterior parameter estimation problems. *Hydrology and Earth System Sciences* **15**, 3701-3713
235. Ho, D. T., Bardwell, A. J., Grewal, S., Iverson, C., and Bardwell, L. (2006) Interacting JNK-docking sites in MKK7 promote binding and activation of JNK mitogen-activated protein kinases. *J Biol Chem* **281**, 13169-13179
236. Bai, H., Yang, K., Yu, D., Zhang, C., Chen, F., and Lai, L. (2010) Predicting kinetic constants of protein–protein interactions based on structural properties. *Proteins: Structure, Function, and Bioinformatics* **79**, 720-734
237. Kennedy, J., and Eberhart, R. (1995) Particle swarm optimization. in *Proceedings of ICNN'95 - International Conference on Neural Networks*
238. Ferguson, S. S. G., Zhang, J., Barak, L. S., and Circ, M. G. (1997) Role of β-Arrestins in the IntracelIular Trafficking of G-Protein-Coupled Receptors. in *Advances in Pharmacology* (Goldstein, D. S., Eisenhofer, G., and McCarty, R. eds.), Academic Press. pp 420-424
239. Ferguson, S. S. (2001) Evolving concepts in G protein-coupled receptor endocytosis: the role in receptor desensitization and signaling. *Pharmacol Rev* **53**, 1-24
240. Chavkin, C., Schattauer, S. S., and Levin, J. R. (2014) Arrestin-Mediated Activation of p38 MAPK: Molecular Mechanisms and Behavioral Consequences. in *Arrestins - Pharmacology and Therapeutic Potential* (Gurevich, V. V. ed.), Springer Berlin Heidelberg, Berlin, Heidelberg. pp 281-292
241. DeFea, K. A. (2011) Beta-arrestins as regulators of signal termination and transduction: How do they determine what to scaffold? *Cellular Signalling* **23**, 621-629
242. Luttrell, L. M., Roudabush, F. L., Choy, E. W., Miller, W. E., Field, M. E., Pierce, K. L., and Lefkowitz, R. J. (2001) Activation and targeting of extracellular signal-regulated kinases by beta-arrestin scaffolds. *Proc Natl Acad Sci U S A* **98**, 2449-2454
243. Jung, S.-R., Kushmerick, C., Seo, J. B., Koh, D.-S., and Hille, B. (2017) Muscarinic receptor regulates extracellular signal regulated kinase by two modes of arrestin binding. *Proceedings of the National Academy of Sciences* **114**, E5579
244. Cassier, E., Gallay, N., Bourquard, T., Claeysen, S., Bockaert, J., Crépieux, P., Poupon, A., Reiter, E., Marin, P., and Vandermoere, F. (2017) Phosphorylation of β-arrestin2 at Thr383 by MEK underlies β-arrestin-dependent activation of Erk1/2 by GPCRs. *eLife* **6**, e23777
245. Bourquard, T., Landomiel, F., Reiter, E., Crépieux, P., Ritchie, D. W., Azé, J., and Poupon, A. (2015) Unraveling the molecular architecture of a G protein-coupled receptor/β-arrestin/Erk module complex. *Scientific Reports* **5**, 10760
246. Srivastava, A., Gupta, B., Gupta, C., and Shukla, A. K. (2015) Emerging Functional Divergence of β-Arrestin Isoforms in GPCR Function. *Trends in Endocrinology & Metabolism* **26**, 628-642
247. Bohn, L. M., Lefkowitz, R. J., Gainetdinov, R. R., Peppel, K., Caron, M. G., and Lin, F. T. (1999) Enhanced morphine analgesia in mice lacking beta-arrestin 2. *Science* **286**, 2495-2498
248. Gong, K., Li, Z., Xu, M., Du, J., Lv, Z., and Zhang, Y. (2008) A Novel Protein Kinase A-independent, β-Arrestin-1-dependent Signaling Pathway for p38 Mitogen-activated Protein Kinase Activation by β2-Adrenergic Receptors. *Journal of Biological Chemistry* **283**, 29028-29036
249. Shenoy, S. K., Drake, M. T., Nelson, C. D., Houtz, D. A., Xiao, K., Madabushi, S., Reiter, E.,

Premont, R. T., Lichtarge, O., and Lefkowitz, R. J. (2006) β-Arrestin-dependent, G Protein-independent ERK1/2 Activation by the β2 Adrenergic Receptor. *Journal of Biological Chemistry* **281**, 1261-1273
250. Ahn, S., Wei, H., Garrison, T. R., and Lefkowitz, R. J. (2004) Reciprocal Regulation of Angiotensin Receptor-activated Extracellular Signal-regulated Kinases by β-Arrestins 1 and 2. *Journal of Biological Chemistry* **279**, 7807-7811
251. Khavrutskii, L., Yeh, J., Timofeeva, O., Tarasov, S. G., Pritt, S., Stefanisko, K., and Tarasova, N. (2013) Protein purification-free method of binding affinity determination by microscale thermophoresis. *J Vis Exp*
252. Douzi, B. (2017) Protein–Protein Interactions: Surface Plasmon Resonance. in *Bacterial Protein Secretion Systems: Methods and Protocols* (Journet, L., and Cascales, E. eds.), Springer New York, New York, NY. pp 257-275
253. Pollard, T. D. (2010) A guide to simple and informative binding assays. *Molecular biology of the cell* **21**, 4061-4067
254. Perry, N. A., Zhan, X., Gurevich, E. V., Iverson, T. M., and Gurevich, V. V. (2019) Using in vitro pull-down and in cell overexpression assays to study protein interactions with arrestins. Springer-Verlag Berlin-Heidelberg, Beta-arrestins
255. Hilpert, K., Winkler, D. F. H., and Hancock, R. E. W. (2007) Peptide arrays on cellulose support: SPOT synthesis, a time and cost efficient method for synthesis of large numbers of peptides in a parallel and addressable fashion. *Nature Protocols* **2**, 1333
256. Schindelin, J., Arganda-Carreras, I., Frise, E., Kaynig, V., Longair, M., Pietzsch, T., Preibisch, S., Rueden, C., Saalfeld, S., Schmid, B., Tinevez, J.-Y., White, D. J., Hartenstein, V., Eliceiri, K., Tomancak, P., and Cardona, A. (2012) Fiji: an open-source platform for biological-image analysis. *Nature Methods* **9**, 676
257. Sommer, M. E., Farrens, D. L., McDowell, J. H., Weber, L. A., and Smith, W. C. (2007) Dynamics of Arrestin-Rhodopsin Interactions: LOOP MOVEMENT IS INVOLVED IN ARRESTIN ACTIVATION AND RECEPTOR BINDING. *Journal of Biological Chemistry* **282**, 25560-25568
258. Oganesyan, I., Lento, C., and Wilson, D. J. (2018) Contemporary hydrogen deuterium exchange mass spectrometry. *Methods* **144**, 27-42
259. Canagarajah, B. J., Khokhlatchev, A., Cobb, M. H., and Goldsmith, E. J. (1997) Activation mechanism of the MAP kinase ERK2 by dual phosphorylation. *Cell* **90**, 859-869
260. Mansoor, S. E., McHaourab, H. S., and Farrens, D. L. (2002) Mapping Proximity within Proteins Using Fluorescence Spectroscopy. A Study of T4 Lysozyme Showing That Tryptophan Residues Quench Bimane Fluorescence. *Biochemistry* **41**, 2475-2484
261. Kikhney, A. G., and Svergun, D. I. (2015) A practical guide to small angle X-ray scattering (SAXS) of flexible and intrinsically disordered proteins. *FEBS Letters* **589**, 2570-2577
262. Rajagopal, S., Kim, J., Ahn, S., Craig, S., Lam, C. M., Gerard, N. P., Gerard, C., and Lefkowitz, R. J. (2010) Beta-arrestin- but not G protein-mediated signaling by the "decoy" receptor CXCR7. *Proc Natl Acad Sci U S A* **107**, 628-632
263. Grundmann, M., Merten, N., Malfacini, D., Inoue, A., Preis, P., Simon, K., Rüttiger, N., Ziegler, N., Benkel, T., Schmitt, N. K., Ishida, S., Müller, I., Reher, R., Kawakami, K., Inoue, A., Rick, U., Kühl, T., Imhof, D., Aoki, J., König, G. M., Hoffmann, C., Gomeza, J., Wess, J., and Kostenis, E. (2018) Lack of beta-arrestin signaling in the absence of active G proteins. *Nature Communications* **9**, 341
264. Gurevich, V. V., and Gurevich, E. V. (2018) Arrestin-mediated signaling: Is there a controversy? *World J Biol Chem* **9**, 25-35
265. Luttrell, L. M., Wang, J., Plouffe, B., Smith, J. S., Yamani, L., Kaur, S., Jean-Charles, P. Y., Gauthier, C., Lee, M. H., Pani, B., Kim, J., Ahn, S., Rajagopal, S., Reiter, E., Bouvier, M., Shenoy, S. K., Laporte, S. A., Rockman, H. A., and Lefkowitz, R. J. (2018) Manifold roles of β-arrestins in GPCR signaling elucidated with siRNA and CRISPR/Cas9. *Sci Signal* **11**

266. Gurevich, E. V., and Gurevich, V. V. (2006) Arrestins: ubiquitous regulators of cellular signaling pathways. *Genome biology* **7**, 236-236
267. Zhang, F., Robbins, D. J., Cobb, M. H., and Goldsmith, E. J. (1993) Crystallization and Preliminary X-ray Studies of Extracellular Signal-regulated Kinase-2/MAP Kinase with an Incorporated His-tag. *Journal of Molecular Biology* **233**, 550-552
268. Kim, D. K., Yun, Y., Kim, H. R., Seo, M.-D., and Chung, K. Y. (2015) Different conformational dynamics of various active states of β-arrestin1 analyzed by hydrogen/deuterium exchange mass spectrometry. *Journal of Structural Biology* **190**, 250-259
269. Kimple, A. J., Muller, R. E., Siderovski, D. P., and Willard, F. S. (2010) A capture coupling method for the covalent immobilization of hexahistidine tagged proteins for surface plasmon resonance. *Methods in molecular biology (Clifton, N.J.)* **627**, 91-100
270. Kim, M., Vishnivetskiy, S. A., Van Eps, N., Alexander, N. S., Cleghorn, W. M., Zhan, X., Hanson, S. M., Morizumi, T., Ernst, O. P., Meiler, J., Gurevich, V. V., and Hubbell, W. L. (2012) Conformation of receptor-bound visual arrestin. *Proceedings of the National Academy of Sciences* **109**, 18407
271. He, T., Gershenson, A., Eyles, S. J., Lee, Y.-J., Liu, W. R., Wang, J., Gao, J., and Roberts, M. F. (2015) Fluorinated aromatic amino acids distinguish cation-π interactions from membrane insertion. *Journal of Biological Chemistry*
272. Yang, F., Xiao, P., Qu, C.-x., Liu, Q., Wang, L.-y., Liu, Z.-x., He, Q.-t., Liu, C., Xu, J.-y., Li, R.-r., Li, M.-j., Li, Q., Guo, X.-z., Yang, Z.-y., He, D.-f., Yi, F., Ruan, K., Shen, Y.-m., Yu, X., Sun, J.-p., and Wang, J. (2018) Allosteric mechanisms underlie GPCR signaling to SH3-domain proteins through arrestin. *Nature Chemical Biology* **14**, 876-886
273. Li, R., Xie, D.-D., Dong, J.-h., Li, H., Li, K.-s., Su, J., Chen, L.-Z., Xu, Y.-F., Wang, H.-M., Gong, Z., Cui, G.-Y., Yu, X., Wang, K., Yao, W., Xin, T., Li, M.-Y., Xiao, K.-H., An, X.-f., Huo, Y., Xu, Z.-g., Sun, J.-P., and Pang, Q. (2014) Molecular mechanism of ERK dephosphorylation by striatal-enriched protein tyrosine phosphatase. *Journal of Neurochemistry* **128**, 315-329
274. Hura, G. L., Menon, A. L., Hammel, M., Rambo, R. P., Poole Ii, F. L., Tsutakawa, S. E., Jenney Jr, F. E., Classen, S., Frankel, K. A., Hopkins, R. C., Yang, S.-j., Scott, J. W., Dillard, B. D., Adams, M. W. W., and Tainer, J. A. (2009) Robust, high-throughput solution structural analyses by small angle X-ray scattering (SAXS). *Nat Meth* **6**, 606-612
275. Ganguly, R., Mohyeldin, A., Thiel, J., Kornblum, H. I., Beullens, M., and Nakano, I. (2015) MELK—a conserved kinase: functions, signaling, cancer, and controversy. *Clinical and Translational Medicine* **4**, 11
276. Lizcano, J. M., Göransson, O., Toth, R., Deak, M., Morrice, N. A., Boudeau, J., Hawley, S. A., Udd, L., Mäkelä, T. P., Hardie, D. G., and Alessi, D. R. (2004) LKB1 is a master kinase that activates 13 kinases of the AMPK subfamily, including MARK/PAR-1. *EMBO J* **23**, 833-843
277. Jung, H., Seong, H.-A., and Ha, H. (2008) Murine Protein Serine/Threonine Kinase 38 Activates Apoptosis Signal-regulating Kinase 1 via Thr838 Phosphorylation. *Journal of Biological Chemistry* **283**, 34541-34553
278. Giuliano, C. J., Lin, A., Smith, J. C., Palladino, A. C., and Sheltzer, J. M. (2018) MELK expression correlates with tumor mitotic activity but is not required for cancer growth. *eLife* **7**, e32838
279. Speers, C., Zhao, S. G., Kothari, V., Santola, A., Liu, M., Wilder-Romans, K., Evans, J., Batra, N., Bartelink, H., Hayes, D. F., Lawrence, T. S., Brown, P. H., Pierce, L. J., and Feng, F. Y. (2016) Maternal Embryonic Leucine Zipper Kinase (MELK) as a Novel Mediator and Biomarker of Radioresistance in Human Breast Cancer. *Clinical Cancer Research* **22**, 5864
280. Gu, C., Banasavadi-Siddegowda, Y. K., Joshi, K., Nakamura, Y., Kurt, H., Gupta, S., and Nakano, I. (2013) Tumor-specific activation of the C-JUN/MELK pathway regulates glioma stem cell growth in a p53-dependent manner. *Stem Cells* **31**, 870-881
281. Joshi, K., Banasavadi-Siddegowda, Y., Mo, X., Kim, S. H., Mao, P., Kig, C., Nardini, D., Sobol, R. W., Chow, L. M., Kornblum, H. I., Waclaw, R., Beullens, M., and Nakano, I. (2013) MELK-

dependent FOXM1 phosphorylation is essential for proliferation of glioma stem cells. *Stem Cells* **31**, 1051-1063
282. Gartel, A. L. (2017) FOXM1 in Cancer: Interactions and Vulnerabilities. *Cancer research* **77**, 3135-3139
283. Seong, H.-A., Gil, M., Kim, K.-T., Kim, S.-J., and Ha, H. (2002) Phosphorylation of a novel zinc-finger-like protein, ZPR9, by murine protein serine/threonine kinase 38 (MPK38). *Biochemical Journal* **361**, 597
284. Cho, Y.-S., Yoo, J., Park, S., and Cho, H.-S. (2014) The structures of the kinase domain and UBA domain of MPK38 suggest the activation mechanism for kinase activity. *Acta Crystallographica Section D: Biological Crystallography* **70**, 514-521
285. Beullens, M., Vancauwenbergh, S., Morrice, N., Derua, R., Ceulemans, H., Waelkens, E., and Bollen, M. (2005) Substrate Specificity and Activity Regulation of Protein Kinase MELK. *Journal of Biological Chemistry* **280**, 40003-40011
286. Amartely, H., Iosub-Amir, A., and Friedler, A. (2014) Identifying Protein-protein Interaction Sites Using Peptide Arrays. *Journal of Visualized Experiments : JoVE*, 52097
287. Katz, C., Levy-Beladev, L., Rotem-Bamberger, S., Rito, T., Rüdiger, S. G. D., and Friedler, A. (2011) Studying protein–protein interactions using peptide arrays. *Chemical Society Reviews* **40**, 2131-2145
288. Granzin, J., Wilden, U., Choe, H. W., Labahn, J., Krafft, B., and Buldt, G. (1998) X-ray crystal structure of arrestin from bovine rod outer segments. *Nature* **391**, 918-921
289. Han, M., Gurevich, V. V., Vishnivetskiy, S. A., Sigler, P. B., and Schubert, C. (2001) Crystal structure of beta-arrestin at 1.9 A: possible mechanism of receptor binding and membrane translocation. *Structure* **9**, 869-880
290. Palczewski, K., Pulvermuller, A., Buczylko, J., and Hofmann, K. P. (1991) Phosphorylated rhodopsin and heparin induce similar conformational changes in arrestin. *J Biol Chem* **266**, 18649-18654
291. Vishnivetskiy, S. A., Francis, D. J., Van Eps, N., Kim, M., Hanson, S. M., Klug, C. S., Hubbell, W. L., and Gurevich, V. V. (2010) The role of arrestin alpha-helix I in receptor binding. *J. Mol. Biol.* **395**, 42-54
292. Canevari, G., Re Depaolini, S., Cucchi, U., Bertrand, J. A., Casale, E., Perrera, C., Forte, B., Carpinelli, P., and Felder, E. R. (2013) Structural Insight into Maternal Embryonic Leucine Zipper Kinase (MELK) Conformation and Inhibition toward Structure-Based Drug Design. *Biochemistry* **52**, 6380-6387
293. Johnson, C. N., Berdini, V., Beke, L., Bonnet, P., Brehmer, D., Coyle, J. E., Day, P. J., Frederickson, M., Freyne, E. J. E., Gilissen, R. A. H. J., Hamlett, C. C. F., Howard, S., Meerpoel, L., McMenamin, R., Patel, S., Rees, D. C., Sharff, A., Sommen, F., Wu, T., and Linders, J. T. M. (2015) Fragment-Based Discovery of Type I Inhibitors of Maternal Embryonic Leucine Zipper Kinase. *ACS Medicinal Chemistry Letters* **6**, 25-30
294. Touré, B. B., Giraldes, J., Smith, T., Sprague, E. R., Wang, Y., Mathieu, S., Chen, Z., Mishina, Y., Feng, Y., Yan-Neale, Y., Shakya, S., Chen, D., Meyer, M., Puleo, D., Brazell, J. T., Straub, C., Sage, D., Wright, K., Yuan, Y., Chen, X., Duca, J., Kim, S., Tian, L., Martin, E., Hurov, K., and Shao, W. (2016) Toward the Validation of Maternal Embryonic Leucine Zipper Kinase: Discovery, Optimization of Highly Potent and Selective Inhibitors, and Preliminary Biology Insight. *Journal of Medicinal Chemistry* **59**, 4711-4723
295. Klaeger, S., Heinzlmeir, S., Wilhelm, M., Polzer, H., Vick, B., Koenig, P.-A., Reinecke, M., Ruprecht, B., Petzoldt, S., Meng, C., Zecha, J., Reiter, K., Qiao, H., Helm, D., Koch, H., Schoof, M., Canevari, G., Casale, E., Depaolini, S. R., Feuchtinger, A., Wu, Z., Schmidt, T., Rueckert, L., Becker, W., Huenges, J., Garz, A.-K., Gohlke, B.-O., Zolg, D. P., Kayser, G., Vooder, T., Preissner, R., Hahne, H., Tõnisson, N., Kramer, K., Götze, K., Bassermann, F., Schlegl, J., Ehrlich, H.-C., Aiche, S., Walch, A., Greif, P. A., Schneider, S., Felder, E. R., Ruland, J., Médard, G., Jeremias, I., Spiekermann, K., and Kuster, B. (2017) The target landscape of clinical

kinase drugs. *Science* **358**
296. Cao, L. S., Wang, J., Chen, Y., Deng, H., Wang, Z. X., and Wu, J. W. (2013) Structural basis for the regulation of maternal embryonic leucine zipper kinase. *PLoS One* **8**, e70031
297. Moravcevic, K., Mendrola, J. M., Schmitz, K. R., Wang, Y.-H., Slochower, D., Janmey, P. A., and Lemmon, M. A. (2010) Kinase Associated-1 Domains Drive MARK/PAR1 Kinases to Membrane Targets by Binding Acidic Phospholipids. *Cell* **143**, 966-977
298. Salic, A., and Mitchison, T. J. (2008) A chemical method for fast and sensitive detection of DNA synthesis in vivo. *Proceedings of the National Academy of Sciences* **105**, 2415
299. Seong, H.-A., Manoharan, R., and Ha, H. (2017) Zinc finger protein ZPR9 functions as an activator of AMPK-related serine/threonine kinase MPK38/MELK involved in ASK1/TGF-β/p53 signaling pathways. *Scientific reports* **7**, 42502
300. Körner, R., Frank-Vaillant, M., Couturier, A., Nigg, E. A., and Tassan, J.-P. (2006) M-phase MELK activity is regulated by MPF and MAPK AU - Badouel, Caroline. *Cell Cycle* **5**, 883-889
301. Beke, L., Kig, C., Linders, J. T. M., Boens, S., Boeckx, A., Van Heerde, E., Parade, M., De Bondt, A., Van Den Wyngaert, I., Bashir, T., Ogata, S., Meerpoel, L., Van Eynde, A., Johnson, C. N., Beullens, M., Brehmer, D., and Bollen, M. (2015) MELK-T1, a small-molecule inhibitor of protein kinase MELK, decreases DNA-damage tolerance in proliferating cancer cells. *Bioscience Reports*, BSR20150194
302. Wang, Y., Begley, M., Li, Q., Huang, H.-T., Lako, A., Eck, M. J., Gray, N. S., Mitchison, T. J., Cantley, L. C., and Zhao, J. J. (2016) Mitotic MELK-eIF4B signaling controls protein synthesis and tumor cell survival. *Proceedings of the National Academy of Sciences* **113**, 9810
303. Jiang, P., and Zhang, D. (2013) Maternal embryonic leucine zipper kinase (MELK): a novel regulator in cell cycle control, embryonic development, and cancer. *Int J Mol Sci* **14**, 21551-21560
304. Seong, H.-A., Manoharan, R., and Ha, H. (2018) Smad proteins differentially regulate obesity-induced glucose and lipid abnormalities and inflammation via class-specific control of AMPK-related kinase MPK38/MELK activity. *Cell Death & Disease* **9**, 471
305. Barlic, J., Andrews, J. D., Kelvin, A. A., Bosinger, S. E., DeVries, M. E., Xu, L., Dobransky, T., Feldman, R. D., Ferguson, S. S. G., and Kelvin, D. J. (2000) Regulation of tyrosine kinase activation and granule release through β-arrestin by CXCR1. *Nature Immunology* **1**, 227
306. Girnita, L., Shenoy, S. K., Sehat, B., Vasilcanu, R., Girnita, A., Lefkowitz, R. J., and Larsson, O. (2005) β-Arrestin Is Crucial for Ubiquitination and Down-regulation of the Insulin-like Growth Factor-1 Receptor by Acting as Adaptor for the MDM2 E3 Ligase. *Journal of Biological Chemistry* **280**, 24412-24419
307. Cho, Y.-S., Kang, Y., Kim, K., Cha, Y.-j., and Cho, H.-S. (2014) The crystal structure of MPK38 in complex with OTSSP167, an orally administrative MELK selective inhibitor. *Biochemical and Biophysical Research Communications* **447**, 7-11
308. Alvarez-Curto, E., Inoue, A., Jenkins, L., Raihan, S. Z., Prihandoko, R., Tobin, A. B., and Milligan, G. (2016) Targeted Elimination of G Proteins and Arrestins Defines Their Specific Contributions to Both Intensity and Duration of G Protein-coupled Receptor Signaling. *J Biol Chem* **291**, 27147-27159
309. Grundmann, M., Merten, N., Malfacini, D., Inoue, A., Preis, P., Simon, K., Rüttiger, N., Ziegler, N., Benkel, T., Schmitt, N. K., Ishida, S., Müller, I., Reher, R., Kawakami, K., Inoue, A., Rick, U., Kühl, T., Imhof, D., Aoki, J., König, G. M., Hoffmann, C., Gomeza, J., Wess, J., and Kostenis, E. (2018) Lack of beta-arrestin signaling in the absence of active G proteins. *Nat Commun* **9**, 341
310. Prokop, S., Perry, N. A., Vishnivetskiy, S. A., Toth, A. D., Inoue, A., Milligan, G., Iverson, T. M., Hunyady, L., and Gurevich, V. V. (2017) Differential manipulation of arrestin-3 binding to basal and agonist-activated G protein-coupled receptors. *Cellular Signalling* **36**, 98-107
311. Schoneberg, T., Schulz, A., Biebermann, H., Hermsdorf, T., Rompler, H., and Sangkuhl, K. (2004) Mutant G-protein-coupled receptors as a cause of human diseases. *Pharmacology &*

therapeutics **104**, 173-206
312. Stoy, H., and Gurevich, V. V. (2015) How genetic errors in GPCRs affect their function: Possible therapeutic strategies. *Genes Dis* **2**, 108-132
313. Russo, D., Arturi, F., Schlumberger, M., Caillou, B., Monier, R., Filetti, S., and Suarez, H. G. (1995) Activating mutations of the TSH receptor in differentiated thyroid carcinomas. *Oncogene* **11**, 1907-1911
314. Hebrant, A., van Staveren, W. C., Maenhaut, C., Dumont, J. E., and Leclere, J. (2011) Genetic hyperthyroidism: hyperthyroidism due to activating TSHR mutations. *Eur J Endocrinol* **164**, 1-9
315. Gurevich, V. V., and Gurevich, E. V. (2004) The molecular acrobatics of arrestin activation. *Trends Pharmacol Sci* **25**, 105-111
316. Kuhn, H., Hall, S. W., and Wilden, U. (1984) Light-induced binding of 48-kDa protein to photoreceptor membranes is highly enhanced by phosphorylation of rhodopsin. *FEBS Lett.* **176**, 473-478
317. Wilden, U., Hall, S. W., and Kühn, H. (1986) Phosphodiesterase activation by photoexcited rhodopsin is quenched when rhodopsin is phosphorylated and binds the intrinsic 48-kDa protein of rod outer segments. *Proceedings of the National Academy of Sciences* **83**, 1174-1178
318. Kim, Y. M., and Benovic, J. L. (2002) Differential roles of arrestin-2 interaction with clathrin and adaptor protein 2 in G protein-coupled receptor trafficking. *J Biol Chem* **277**, 30760-30768
319. Gimenez, L. E., Vishnivetskiy, S. A., and Gurevich, V. V. (2014) Targeting individual GPCRs with redesigned nonvisual arrestins. *Handbook of experimental pharmacology* **219**, 153-170
320. Song, X., Vishnivetskiy, S. A., Gross, O. P., Emelianoff, K., Mendez, A., Chen, J., Gurevich, E. V., Burns, M. E., and Gurevich, V. V. (2009) Enhanced arrestin facilitates recovery and protects rods lacking rhodopsin phosphorylation. *Curr Biol* **19**, 700-705
321. Fredriksson, R., Lagerström, M. C., Lundin, L. G., and Schiöth, H. B. (2003) The G-protein-coupled receptors in the human genome form five main families. Phylogenetic analysis, paralogon groups, and fingerprints. *Mol Pharmacol* **63**, 1256-1272
322. Bockaert, J., and Pin, J. P. (1999) Molecular tinkering of G protein-coupled receptors: an evolutionary success. *EMBO J* **18**, 1723-1729
323. Nikonov, S. S., Brown, B. M., Davis, J. A., Zuniga, F. I., Bragin, A., Pugh, E. N., Jr, and Craft, C. M. (2008) Mouse cones require an arrestin for normal inactivation of phototransduction. *Neuron* **59**, 462-474
324. Gurevich, V. V. (1998) The selectivity of visual arrestin for light-activated phosphorhodopsin is controlled by multiple nonredundant mechanisms. *J Biol Chem* **273**, 15501-15506
325. Celver, J., Vishnivetskiy, S. A., Chavkin, C., and Gurevich, V. V. (2002) Conservation of the phosphate-sensitive elements in the arrestin family of proteins. *J Biol Chem* **277**, 9043-9048
326. Kovoor, A., Celver, J., Abdryashitov, R. I., Chavkin, C., and Gurevich, V. V. (1999) Targeted construction of phosphorylation-independent b-arrestin mutants with constitutive activity in cells. *J Biol Chem* **274**, 6831-6834
327. Barak, L. S., Ferguson, S. S., Zhang, J., and Caron, M. G. (1997) A beta-arrestin/green fluorescent protein biosensor for detecting G protein-coupled receptor activation. *J Biol Chem* **272**, 27497-27500
328. Gurevich, V. V., Dion, S. B., Onorato, J. J., Ptasienski, J., Kim, C. M., Sterne-Marr, R., Hosey, M. M., and Benovic, J. L. (1995) Arrestin interactions with G protein-coupled receptors. Direct binding studies of wild type and mutant arrestins with rhodopsin, beta 2-adrenergic, and m2 muscarinic cholinergic receptors. *J Biol Chem* **270**, 720-731
329. Vishnivetskiy, S. A., Hosey, M. M., Benovic, J. L., and Gurevich, V. V. (2004) Mapping the arrestin-receptor interface. Structural elements responsible for receptor specificity of arrestin proteins. *J Biol Chem* **279**, 1262-1268
330. Vishnivetskiy, S. A., Gimenez, L. E., Francis, D. J., Hanson, S. M., Hubbell, W. L., Klug, C. S., and Gurevich, V. V. (2011) Few residues within an extensive binding interface drive receptor interaction and determine the specificity of arrestin proteins. *J Biol Chem* **286**, 24288-24299

331. Gimenez, L. E., Vishnivetskiy, S. A., Baameur, F., and Gurevich, V. V. (2012) Manipulation of very few receptor discriminator residues greatly enhances receptor specificity of non-visual arrestins. *J Biol Chem* **287**, 29495-29505
332. Han, M., Gurevich, V. V., Vishnivetskiy, S. A., Sigler, P. B., and Schubert, C. (2001) Crystal structure of beta-arrestin at 1.9 A: possible mechanism of receptor binding and membrane Translocation. *Structure* **9**, 869-880
333. Ohguro, H., Palczewski, K., Walsh, K. A., and Johnson, R. S. (1994) Topographic study of arrestin using differential chemical modifications and hydrogen/deuterium exchange. *Protein Sci.* **3**, 2428-2434
334. Pulvermuller, A., Schroder, K., Fischer, T., and Hofmann, K. P. (2000) Interactions of metarhodopsin II. Arrestin peptides compete with arrestin and transducin. *J Biol Chem* **275**, 37679-37685
335. Shukla, A. K., Manglik, A., Kruse, A. C., Xiao, K., Reis, R. I., Tseng, W. C., Staus, D. P., Hilger, D., Uysal, S., Huang, L. Y., Paduch, M., Tripathi-Shukla, P., Koide, A., Koide, S., Weis, W. I., Kossiakoff, A. A., Kobilka, B. K., and Lefkowitz, R. J. (2013) Structure of active β-arrestin-1 bound to a G-protein-coupled receptor phosphopeptide. *Nature* **497**, 137-141
336. Zhuang, T., Chen, Q., Cho, M.-K., Vishnivetskiy, S. A., Iverson, T. I., Gurevich, V. V., and C.R., S. (2013) Involvement of Distinct Arrestin-1 Elements in Binding to Different Functional Forms of Rhodopsin. *Proc Nat Acad Sci USA* **110**, 942-947
337. Vishnivetskiy, S. A., Baameur, F., Findley, K. R., and Gurevich, V. V. (2013) Critical role of the central 139-loop in stability and binding selectivity of arrestin-1. *J Biol Chem* **288**, 11741-11750
338. Henikoff, S., and Henikoff, J. G. (1992) Amino acid substitution matrices from protein blocks. *Proc Nat Acad Sci USA* **89**, 10915-10919
339. Kim, M., Vishnivetskiy, S. A., Van Eps, N., Alexander, N. S., Cleghorn, W. M., Zhan, X., Hanson, S. M., Morizumi, T., Ernst, O. P., Meiler, J., Gurevich, V. V., and Hubbell, W. L. (2012) Conformation of receptor-bound visual arrestin. *Proc Natl Acad Sci U S A* **109**, 18407-18412
340. Gurevich, V. V., and Benovic, J. L. (1992) Cell-free expression of visual arrestin. Truncation mutagenesis identifies multiple domains involved in rhodopsin interaction. *J Biol Chem* **267**, 21919-21923
341. Gurevich, V. V., and Benovic, J. L. (1993) Visual arrestin interaction with rhodopsin: Sequential multisite binding ensures strict selectivity towards light-activated phosphorylated rhodopsin. *J Biol Chem* **268**, 11628-11638
342. Nelson, C. P., Nahorski, S. R., and Challiss, R. A. (2006) Constitutive activity and inverse agonism at the M2 muscarinic acetylcholine receptor. *J Pharmacol Exp Ther* **316**, 279-288
343. Walther, C., and Ferguson, S. S. (20134) Arrestins: role in the desensitization, sequestration, and vesicular trafficking of G protein-coupled receptors. *Prog Mol Biol Transl Sci* **118**, 93-113
344. Luttrell, L. M., and Gesty-Palmer, D. (2010) Beyond desensitization: physiological relevance of arrestin-dependent signaling. *Pharmacological reviews* **62**, 305-330
345. Gurevich, V. V., Hanson, S. M., Song, X., Vishnivetskiy, S. A., and Gurevich, E. V. (2011) The functional cycle of visual arrestins in photoreceptor cells. *Prog Retin Eye Res* **30**, 405-430
346. Lohse, M. J., Benovic, J. L., Codina, J., Caron, M. G., and Lefkowitz, R. J. (1990) beta-Arrestin: a protein that regulates beta-adrenergic receptor function. *Science* **248**, 1547-1550
347. Attramadal, H., Arriza, J. L., Aoki, C., Dawson, T. M., Codina, J., Kwatra, M. M., Snyder, S. H., Caron, M. G., and Lefkowitz, R. J. (1992) Beta-arrestin2, a novel member of the arrestin/beta-arrestin gene family. *J Biol Chem* **267**, 17882-17890
348. Lohse, M. J., Andexinger, S., Pitcher, J., Trukawinski, S., Codina, J., Faure, J. P., Caron, M. G., and Lefkowitz, R. J. (1992) Receptor-specific desensitization with purified proteins. Kinase dependence and receptor specificity of beta-arrestin and arrestin in the beta 2-adrenergic receptor and rhodopsin systems. *J Biol Chem* **267**, 8558-8564
349. Oakley, R. H., Laporte, S. A., Holt, J. A., Caron, M. G., and Barak, L. S. (2000) Differential affinities of visual arrestin, barrestin1, and barrestin2 for G protein-coupled receptors delineate

two major classes of receptors. *J Biol Chem* **275**, 17201-17210
350. DeWire, S. M., Ahn, S., Lefkowitz, R. J., and Shenoy, S. K. (2007) Beta-arrestins and cell signaling. *Annu Rev Physiol* **69**, 483-510
351. Shenoy, S. K., and Lefkowitz, R. J. (2011) β-Arrestin-mediated receptor trafficking and signal transduction. *Trends Pharmacol Sci* **32**, 521-533
352. Gurevich, V. V., and Gurevich, E. V. (2014) Overview of different mechanisms of arrestin-mediated signaling. *Curr Protoc Pharmacol* **67**, 2.10
353. Vishnivetskiy, S. A., Paz, C. L., Schubert, C., Hirsch, J. A., Sigler, P. B., and Gurevich, V. V. (1999) How does arrestin respond to the phosphorylated state of rhodopsin? *J. Biol. Chem.* **274**, 11451-11454
354. Smith, W. C., Milam, A. H., Dugger, D., Arendt, A., Hargrave, P. A., and Palczewski, K. (1994) A splice variant of arrestin. Molecular cloning and localization in bovine retina. *J Biol Chem* **269**, 15407-15410
355. Pulvermuller, A., Maretzki, D., Rudnicka-Nawrot, M., Smith, W. C., Palczewski, K., and Hofmann, K. P. (1997) Functional differences in the interaction of arrestin and its splice variant, p44, with rhodopsin. *Biochemistry* **36**, 9253-9260
356. Vishnivetskiy, S. A., Chen, Q., Palazzo, M. C., Brooks, E. K., Altenbach, C., Iverson, T. M., Hubbell, W. L., and Gurevich, V. V. (2013) Engineering visual arrestin-1 with special functional characteristics. *J Biol Chem* **288**, 11741-11750
357. Elowitz, M., and Lim, W. A. (2010) Build life to understand it. *Nature* **468**, 889-890
358. Peisajovich, S. G., Garbarino, J. E., Wei, P., and Lim, W. A. (2010) Rapid diversification of cell signaling phenotypes by modular domain recombination. *Science* **328**, 368-372
359. Gurevich, E. V., and Gurevich, V. V. (2014) Therapeutic potential of small molecules and engineered proteins. *Handbook of experimental pharmacology* **219**, 1-12
360. Shoemaker, B. A., Portman, J. J., and Wolynes, P. G. (2000) Speeding molecular recognition by using the folding funnel: the fly-casting mechanism. *Proc Natl Acad Sci U S A* **97**, 8868-8873
361. Gurevich, E. V., and Gurevich, V. V. (2015) Beyond traditional pharmacology: new tools and approaches. *Br J Pharmacol* **172**, 3229-3241
362. Song, X., Seo, J., Baameur, F., Vishnivetskiy, S. A., Chen, Q., Kook, S., Kim, M., Brooks, E. K., Altenbach, C., Hong, Y., Hanson, S. M., Palazzo, M. C., Chen, J., Hubbell, W. L., Gurevich, E. V., and Gurevich, V. V. (2013) Rapid degeneration of rod photoreceptors expressing self-association-deficient arrestin-1 mutant. *Cellular signalling* **25**, 2613-2624
363. Kook, S., Zhan, X., Cleghorn, W. M., Benovic, J. L., Gurevich, V. V., and Gurevich, E. V. (2014) Caspase-cleaved arrestin-2 and BID cooperatively facilitate cytochrome C release and cell death. *Cell Death Differ* **21**, 172-184
364. Prossnitz, E. R. (2004) New roles fro arestins in the post-endocytic trafficking of G protein-coupled receptors. *Life Sci.* **75**, 893-899
365. Gurevich, V. V., Pals-Rylaarsdam, R., Benovic, J. L., Hosey, M. M., and Onorato, J. J. (1997) Agonist-receptor-arrestin, an alternative ternary complex with high agonist affinity. *J Biol Chem* **272**, 28849-28852
366. Nobles, K. N., Guan, Z., Xiao, K., Oas, T. G., and Lefkowitz, R. J. The active conformation of beta-arrestin1: direct evidence for the phosphate sensor in the N-domain and conformational differences in the active states of beta-arrestins1 and -2. *J Biol Chem* **282**, 21370-21381
367. Sterne-Marr, R., Gurevich, V. V., Goldsmith, P., Bodine, R. C., Sanders, C., Donoso, L. A., and Benovic, J. L. (1993) Polypeptide variants of beta-arrestin and arrestin3. *J Biol Chem* **268**, 15640-15648
368. Altenhoff, A. M., Skunca, N., Glover, N., Train, C. M., Sueki, A., Pilizota, I., Gori, K., Tomiczek, B., Muller, S., Redestig, H., Gonnet, G. H., and Dessimoz, C. (2015) The OMA orthology database in 2015: function predictions, better plant support, synteny view and other improvements. *Nucleic acids research* **43**, D240-249
369. Zhu, L., Almaça, J., Dadi, P. K., Hong, H., Sakamoto, W., Rossi, M., Lee, R. J., Vierra, N. C.,

Lu, H., Cui, Y., McMillin, S. M., Perry, N. A., Gurevich, V. V., Lee, A., Kuo, B., Leapman, R. D., Matschinsky, F. M., Doliba, N. M., Urs, N. M., Caron, M. G., Jacobson, D. A., Caicedo, A., and Wess, J. (2017) β-arrestin-2 is an essential regulator of pancreatic β-cell function under physiological and pathophysiological conditions. *Nature Communications* **8**, 14295
370. Luttrell, L. M., and Lefkowitz, R. J. (2002) The role of beta-arrestins in the termination and transduction of G-protein-coupled receptor signals. *J Cell Sci* **115**, 455-465
371. Schmid, C. L., and Bohn, L. M. (2009) Physiological and pharmacological implications of beta-arrestin regulation. *Pharmacology & Therapeutics* **121**, 285-293
372. Zhao, J., and Pei, G. (2013) Chapter Sixteen - Arrestins in Metabolic Regulation. in *Progress in Molecular Biology and Translational Science* (Luttrell, L. M. ed.), Academic Press. pp 413-427
373. Pierce, K. L., Premont, R. T., and Lefkowitz, R. J. (2002) Seven-transmembrane receptors. *Nature Reviews Molecular Cell Biology* **3**, 639
374. Beaulieu, J.-M., Gainetdinov, R. R., and Caron, M. G. (2009) Akt/GSK3 Signaling in the Action of Psychotropic Drugs. *Annual Review of Pharmacology and Toxicology* **49**, 327-347
375. Rajagopal, S., Rajagopal, K., and Lefkowitz, R. J. (2010) Teaching old receptors new tricks: biasing seven-transmembrane receptors. *Nature Reviews Drug Discovery* **9**, 373
376. Shukla, A. K., Xiao, K., and Lefkowitz, R. J. (2011) Emerging paradigms of beta-arrestin-dependent seven transmembrane receptor signaling. *Trends Biochem Sci* **36**, 457-469
377. Luan, B., Zhao, J., Wu, H., Duan, B., Shu, G., Wang, X., Li, D., Jia, W., Kang, J., and Pei, G. (2009) Deficiency of a beta-arrestin-2 signal complex contributes to insulin resistance. *Nature* **457**, 1146-1149
378. Zhuang, L.-n., Hu, W.-x., Zhang, M.-l., Xin, S.-m., Jia, W.-p., Zhao, J., and Pei, G. (2011) β-Arrestin-1 Protein Represses Diet-induced Obesity. *Journal of Biological Chemistry* **286**, 28396-28402
379. Kovacs, J. J., Hara, M. R., Davenport, C. L., Kim, J., and Lefkowitz, R. J. (2009) Arrestin development: emerging roles for beta-arrestins in developmental signaling pathways. *Dev Cell* **17**, 443-458
380. Philipp, M., Evron, T., and Caron, M. G. (2013) The role of arrestins in development. *Prog Mol Biol Transl Sci* **118**, 225-242
381. Ravier, M. A., Leduc, M., Richard, J., Linck, N., Varrault, A., Pirot, N., Roussel, M. M., Bockaert, J., Dalle, S., and Bertrand, G. (2014) β-Arrestin2 plays a key role in the modulation of the pancreatic beta cell mass in mice. *Diabetologia* **57**, 532-541
382. Zhang, M., Zhu, Y., Mu, K., Li, L., Lu, J., Zhao, J., Huang, X., Wang, C., and Jia, W. (2013) Loss of β-arrestin2 mediates pancreatic-islet dysfunction in mice. *Biochemical and Biophysical Research Communications* **435**, 345-349
383. Gu, G., Dubauskaite, J., and Melton, D. A. (2002) Direct evidence for the pancreatic lineage: NGN3+ cells are islet progenitors and are distinct from duct progenitors. *Development* **129**, 2447
384. Fu, A., Ng, A. C.-H., Depatie, C., Wijesekara, N., He, Y., Wang, G.-S., Bardeesy, N., Scott, F. W., Touyz, R. M., Wheeler, M. B., and Screaton, R. A. (2009) Loss of Lkb1 in Adult β Cells Increases β Cell Mass and Enhances Glucose Tolerance in Mice. *Cell Metabolism* **10**, 285-295
385. Urs, N. M., Gee, S. M., Pack, T. F., McCorvy, J. D., Evron, T., Snyder, J. C., Yang, X., Rodriguiz, R. M., Borrelli, E., Wetsel, W. C., Jin, J., Roth, B. L., O'Donnell, P., and Caron, M. G. (2016) Distinct cortical and striatal actions of a beta-arrestin-biased dopamine D2 receptor ligand reveal unique antipsychotic-like properties. *Proc Natl Acad Sci U S A*
386. Moosmang, S., Lenhardt, P., Haider, N., Hofmann, F., and Wegener, J. W. (2005) Mouse models to study L-type calcium channel function. *Pharmacology & Therapeutics* **106**, 347-355
387. Yang, S.-N., and Berggren, P.-O. (2006) The Role of Voltage-Gated Calcium Channels in Pancreatic β-Cell Physiology and Pathophysiology. *Endocrine Reviews* **27**, 621-676
388. Scharfmann, R., Pechberty, S., Hazhouz, Y., von Bülow, M., Bricout-Neveu, E., Grenier-Godard, M., Guez, F., Rachdi, L., Lohmann, M., Czernichow, P., and Ravassard, P. (2014) Development of a conditionally immortalized human pancreatic β cell line. *The Journal of Clinical*

Investigation **124**, 2087-2098
389. Matthews, E. K., and Sakamoto, Y. (1975) Electrical characteristics of pancreatic islet cells. *The Journal of Physiology* **246**, 421-437
390. Gautam, D., Han, S.-J., Hamdan, F. F., Jeon, J., Li, B., Li, J. H., Cui, Y., Mears, D., Lu, H., Deng, C., Heard, T., and Wess, J. (2006) A critical role for β cell M3 muscarinic acetylcholine receptors in regulating insulin release and blood glucose homeostasis in vivo. *Cell Metabolism* **3**, 449-461
391. Campbell, Jonathan E., and Drucker, Daniel J. (2013) Pharmacology, Physiology, and Mechanisms of Incretin Hormone Action. *Cell Metabolism* **17**, 819-837
392. Gilon, P., and Henquin, J.-C. (2001) Mechanisms and Physiological Significance of the Cholinergic Control of Pancreatic β-Cell Function. *Endocrine Reviews* **22**, 565-604
393. Dadi, P. K., Vierra, N. C., Ustione, A., Piston, D. W., Colbran, R. J., and Jacobson, D. A. (2014) Inhibition of Pancreatic β-Cell Ca2+/Calmodulin-dependent Protein Kinase II Reduces Glucose-stimulated Calcium Influx and Insulin Secretion, Impairing Glucose Tolerance. *Journal of Biological Chemistry* **289**, 12435-12445
394. Ishida, A., Kameshita, I., Okuno, S., Kitani, T., and Fujisawa, H. (1995) A Novel Highly Specific and Potent Inhibitor of Calmodulin-Dependent Protein Kinase II. *Biochemical and Biophysical Research Communications* **212**, 806-812
395. Ishida, A., Shigeri, Y., Tatsu, Y., Uegaki, K., Kameshita, I., Okuno, S., Kitani, T., Yumoto, N., and Fujisawa, H. (1998) Critical amino acid residues of AIP, a highly specific inhibitory peptide of calmodulin-dependent protein kinase II. *FEBS Letters* **427**, 115-118
396. Ozcan, L., Wong, Catherine C. L., Li, G., Xu, T., Pajvani, U., Park, Sung Kyu R., Wronska, A., Chen, B.-X., Marks, Andrew R., Fukamizu, A., Backs, J., Singer, Harold A., Yates, John R., Accili, D., and Tabas, I. (2012) Calcium Signaling through CaMKII Regulates Hepatic Glucose Production in Fasting and Obesity. *Cell Metabolism* **15**, 739-751
397. Matsumoto, K., Fukunaga, K., Miyazaki, J., Shichiri, M., and Miyamoto, E. (1995) Ca2+/calmodulin-dependent protein kinase II and synapsin I-like protein in mouse insulinoma MIN6 cells. *Endocrinology* **136**, 3784-3793
398. Yamamoto, H., Matsumoto, K., Araki, E., and Miyamoto, E. (2003) New Aspects of Neurotransmitter Release and Exocytosis: Involvement of Ca²⁺/Calmodulin-Dependent Phosphorylation of Synapsin I in Insulin Exocytosis. *Journal of Pharmacological Sciences* **93**, 30-34
399. Yang, E., and Schulman, H. (1999) Structural Examination of Autoregulation of Multifunctional Calcium/Calmodulin-dependent Protein Kinase II. *Journal of Biological Chemistry* **274**, 26199-26208
400. Doliba, N. M., Qin, W., Najafi, H., Liu, C., Buettger, C. W., Sotiris, J., Collins, H. W., Li, C., Stanley, C. A., Wilson, D. F., Grimsby, J., Sarabu, R., Naji, A., and Matschinsky, F. M. (2012) Glucokinase activation repairs defective bioenergetics of islets of Langerhans isolated from type 2 diabetics. *Am J Physiol Endocrinol Metab* **302**, E87-E102
401. Poitout, V., Amyot, J., Semache, M., Zarrouki, B., Hagman, D., and Fontés, G. (2010) Glucolipotoxicity of the pancreatic beta cell. *Biochimica et Biophysica Acta (BBA) - Molecular and Cell Biology of Lipids* **1801**, 289-298
402. Mangmool, S., Shukla, A. K., and Rockman, H. A. (2010) beta-Arrestin-dependent activation of Ca(2+)/calmodulin kinase II after beta(1)-adrenergic receptor stimulation. *The Journal of cell biology* **189**, 573-587
403. Hudmon, A., Schulman, H., Kim, J., Maltez, J. M., Tsien, R. W., and Pitt, G. S. (2005) CaMKII tethers to L-type Ca2+ channels, establishing a local and dedicated integrator of Ca2+ signals for facilitation. *The Journal of cell biology* **171**, 537-547
404. Song, W.-J., Mondal, P., Li, Y., Lee, S. E., and Hussain, M. A. (2013) Pancreatic β-cell response to increased metabolic demand and to pharmacologic secretagogues requires EPAC2A. *Diabetes* **62**, 2796-2807
405. Sonoda, N., Imamura, T., Yoshizaki, T., Babendure, J. L., Lu, J. C., and Olefsky, J. M. (2008)

Beta-Arrestin-1 mediates glucagon-like peptide-1 signaling to insulin secretion in cultured pancreatic beta cells. *Proc Natl Acad Sci U S A* **105**, 6614-6619
406. Boden, G., and Shulman, G. I. (2002) Free fatty acids in obesity and type 2 diabetes: defining their role in the development of insulin resistance and β-cell dysfunction. *European Journal of Clinical Investigation* **32**, 14-23
407. Vasavada, R. C., Cavaliere, C., D'Ercole, A. J., Dann, P., Burtis, W. J., Madlener, A. L., Zawalich, K., Zawalich, W., Philbrick, W., and Stewart, A. F. (1996) Overexpression of Parathyroid Hormone-related Protein in the Pancreatic Islets of Transgenic Mice Causes Islet Hyperplasia, Hyperinsulinemia, and Hypoglycemia. *Journal of Biological Chemistry* **271**, 1200-1208
408. Cabrera, O., Jacques-Silva, M. C., Berman, D. M., Fachado, A., Echeverri, F., Poo, R., Khan, A., Kenyon, N. S., Ricordi, C., Berggren, P.-O., and Caicedo, A. (2007) Automated, High-Throughput Assays for Evaluation of Human Pancreatic Islet Function. *Cell Transplantation* **16**, 1039-1048
409. Cabrera, O., Berman, D. M., Kenyon, N. S., Ricordi, C., Berggren, P.-O., and Caicedo, A. (2006) The unique cytoarchitecture of human pancreatic islets has implications for islet cell function. *Proceedings of the National Academy of Sciences* **103**, 2334
410. Cabrera, O., Jacques-Silva, M. C., Speier, S., Yang, S.-N., Köhler, M., Fachado, A., Vieira, E., Zierath, J. R., Kibbey, R., Berman, D. M., Kenyon, N. S., Ricordi, C., Caicedo, A., and Berggren, P.-O. (2008) Glutamate Is a Positive Autocrine Signal for Glucagon Release. *Cell Metabolism* **7**, 545-554
411. Jain, S., Ruiz de Azua, I., Lu, H., White, M. F., Guettier, J. M., and Wess, J. (2013) Chronic activation of a designer G(q)-coupled receptor improves beta cell function. *J Clin Invest* **123**, 1750-1762
412. Rae, J., Cooper, K., Gates, P., and Watsky, M. (1991) Low access resistance perforated patch recordings using amphotericin B. *Journal of Neuroscience Methods* **37**, 15-26
413. Cai, T., Hirai, H., Zhang, G., Zhang, M., Takahashi, N., Kasai, H., Satin, L. S., Leapman, R. D., and Notkins, A. L. (2011) Deletion of Ia-2 and/or Ia-2β in mice decreases insulin secretion by reducing the number of dense core vesicles. *Diabetologia* **54**, 2347-2357
414. Guofeng, Z., Hiroki, H., Tao, C., Junnosuke, M., Ping, Y., Hanxia, H., Martin, R. S., William, D. S., Richard, D. L., and Abner, L. N. RESP18, a homolog of the luminal domain IA-2, is found in dense core vesicles in pancreatic islet cells and is induced by high glucose. *Journal of Endocrinology* **195**, 313-321
415. Pfeifer, C. R., Shomorony, A., Aronova, M. A., Zhang, G., Cai, T., Xu, H., Notkins, A. L., and Leapman, R. D. (2015) Quantitative analysis of mouse pancreatic islet architecture by serial block-face SEM. *Journal of Structural Biology* **189**, 44-52
416. Shomorony, A., Pfeifer, C. R., Aronova, M. A., Zhang, G., Cai, T., Xu, H., Notkins, A. L., and Leapman, R. D. (2015) Combining quantitative 2D and 3D image analysis in the serial block face SEM: application to secretory organelles of pancreatic islet cells. *Journal of Microscopy* **259**, 155-164
417. Loud, A. V. (1968) A QUANTITATIVE STEREOLOGICAL DESCRIPTION OF THE ULTRASTRUCTURE OF NORMAL RAT LIVER PARENCHYMAL CELLS. *The Journal of Cell Biology* **37**, 27
418. Wenham, R. M., Landt, M., and Easom, R. A. (1994) Glucose activates the multifunctional Ca2+/calmodulin-dependent protein kinase II in isolated rat pancreatic islets. *Journal of Biological Chemistry* **269**, 4947-4952
419. Wang, Z., and Thurmond, D. C. (2010) Differential Phosphorylation of RhoGDI Mediates the Distinct Cycling of Cdc42 and Rac1 to Regulate Second-phase Insulin Secretion. *Journal of Biological Chemistry* **285**, 6186-6197
420. Deng, S., Vatamaniuk, M., Lian, M. M., Doliba, N., Wang, J., Bell, E., Wolf, B., Raper, S., Matschinsky, F. M., and Markmann, J. F. (2003) Insulin gene transfer enhances the function of

human islet grafts. *Diabetologia* **46**, 386-393
421. Deng, S., Vatamaniuk, M., Huang, X., Doliba, N., Lian, M.-M., Frank, A., Velidedeoglu, E., Desai, N. M., Koeberlein, B., Wolf, B., Barker, C. F., Naji, A., Matschinsky, F. M., and Markmann, J. F. (2004) Structural and Functional Abnormalities in the Islets Isolated From Type 2 Diabetic Subjects. *Diabetes* **53**, 624
422. Doliba, N. M., Qin, W., Najafi, H., Liu, C., Buettger, C. W., Sotiris, J., Collins, H. W., Li, C., Stanley, C. A., Wilson, D. F., Grimsby, J., Sarabu, R., Naji, A., and Matschinsky, F. M. (2011) Glucokinase activation repairs defective bioenergetics of islets of Langerhans isolated from type 2 diabetics. *American Journal of Physiology-Endocrinology and Metabolism* **302**, E87-E102
423. Zhu, L., Wang, L., Luo, X., Zhang, Y., Ding, Q., Jiang, X., Wang, X., Pan, Y., and Chen, Y. (2012) Tollip, an Intracellular Trafficking Protein, Is a Novel Modulator of the Transforming Growth Factor-β Signaling Pathway. *Journal of Biological Chemistry* **287**, 39653-39663
424. Zhu, L., Rossi, M., Cui, Y., Lee, R. J., Sakamoto, W., Perry, N. A., Urs, N. M., Caron, M. G., Gurevich, V. V., Godlewski, G., Kunos, G., Chen, M., Chen, W., and Wess, J. (2017) Hepatic β-arrestin 2 is essential for maintaining euglycemia. *The Journal of clinical investigation* **127**, 2941-2945
425. Lam, D. W., and LeRoith, D. (2012) The worldwide diabetes epidemic. *Curr Opin Endocrinol Diabetes Obes* **19**, 93-96
426. Postic, C., Dentin, R., and Girard, J. (2004) Role of the liver in the control of carbohydrate and lipid homeostasis. *Diabetes Metab* **30**, 398-408
427. Lin, H. V., and Accili, D. (2011) Hormonal regulation of hepatic glucose production in health and disease. *Cell Metab* **14**, 9-19
428. Unger, R. H., and Cherrington, A. D. (2012) Glucagonocentric restructuring of diabetes: a pathophysiologic and therapeutic makeover. *J Clin Invest* **122**, 4-12
429. Jiang, G., and Zhang, B. B. (2003) Glucagon and regulation of glucose metabolism. *Am J Physiol Endocrinol Metab* **284**, E671-678
430. Estall, J. L., and Drucker, D. J. (2006) Glucagon and glucagon-like peptide receptors as drug targets. *Curr Pharm Des* **12**, 1731-1750
431. Cho, Y. M., Merchant, C. E., and Kieffer, T. J. (2012) Targeting the glucagon receptor family for diabetes and obesity therapy. *Pharmacol Ther* **135**, 247-278
432. D'Alessio, D. (2011) The role of dysregulated glucagon secretion in type 2 diabetes. *Diabetes Obes Metab* **13 Suppl 1**, 126-132
433. Schmid, C. L., and Bohn, L. M. (2009) Physiological and pharmacological implications of beta-arrestin regulation. *Pharmacol Ther* **121**, 285-293
434. Gurevich, V. V., and Gurevich, E. V. (2006) The structural basis of arrestin-mediated regulation of G-protein-coupled receptors. *Pharmacol Ther* **110**, 465-502
435. Pierce, K. L., Premont, R. T., and Lefkowitz, R. J. (2002) Seven-transmembrane receptors. *Nat Rev Mol Cell Biol* **3**, 639-650
436. Oh, D. Y., Talukdar, S., Bae, E. J., Imamura, T., Morinaga, H., Fan, W., Li, P., Lu, W. J., Watkins, S. M., and Olefsky, J. M. (2010) GPR120 is an omega-3 fatty acid receptor mediating potent anti-inflammatory and insulin-sensitizing effects. *Cell* **142**, 687-698
437. Davidson, J. A., Holland, W. L., Roth, M. G., Wang, M. Y., Lee, Y., Yu, X., McCorkle, S. K., Scherer, P. E., and Unger, R. H. (2016) Glucagon therapeutics, dawn of a new era for diabetes care. *Diabetes Metab Res Rev*
438. Miller, R. A., Chu, Q., Le Lay, J., Scherer, P. E., Ahima, R. S., Kaestner, K. H., Foretz, M., Viollet, B., and Birnbaum, M. J. (2011) Adiponectin suppresses gluconeogenic gene expression in mouse hepatocytes independent of LKB1-AMPK signaling. *J Clin Invest* **121**, 2518-2528
439. Zhang, M., Teng, H., Shi, J., and Zhang, Y. (2011) Disruption of beta-arrestins blocks glucocorticoid receptor and severely retards lung and liver development in mice. *Mech Dev* **128**, 368-375
440. Dunning, B. E., and Gerich, J. E. (2007) The role of alpha-cell dysregulation in fasting and

postprandial hyperglycemia in type 2 diabetes and therapeutic implications. *Endocr Rev* **28**, 253-283
441. Rui, L. (2014) Energy metabolism in the liver. *Compr Physiol* **4**, 177-197
442. Gainetdinov, R. R., Premont, R. T., Bohn, L. M., Lefkowitz, R. J., and Caron, M. G. (2004) Desensitization of G protein-coupled receptors and neuronal functions. *Annu Rev Neurosci* **27**, 107-144
443. Ke, J., Zhang, C., Harikumar, K. G., Zylstra-Diegel, C. R., Wang, L., Mowry, L. E., Miller, L. J., Williams, B. O., and Xu, H. E. (2012) Modulation of beta-catenin signaling by glucagon receptor activation. *PLoS One* **7**, e33676
444. Gurevich, V. V., and Gurevich, E. V. (2014) Extensive shape shifting underlies functional versatility of arrestins. *Curr Opin Cell Biol* **27**, 1-9
445. Baillie, G. S., Sood, A., McPhee, I., Gall, I., Perry, S. J., Lefkowitz, R. J., and Houslay, M. D. (2003) beta-Arrestin-mediated PDE4 cAMP phosphodiesterase recruitment regulates beta-adrenoceptor switching from Gs to Gi. *Proc Natl Acad Sci U S A* **100**, 940-945
446. Neufeld, D. S. (1997) Isolation of rat liver hepatocytes. *Methods Mol Biol* **75**, 145-151
447. Mukund, S., Shang, Y., Clarke, H. J., Madjidi, A., Corn, J. E., Kates, L., Kolumam, G., Chiang, V., Luis, E., Murray, J., Zhang, Y., Hotzel, I., Koth, C. M., and Allan, B. B. (2013) Inhibitory mechanism of an allosteric antibody targeting the glucagon receptor. *J Biol Chem* **288**, 36168-36178
448. Koth, C. M., Murray, J. M., Mukund, S., Madjidi, A., Minn, A., Clarke, H. J., Wong, T., Chiang, V., Luis, E., Estevez, A., Rondon, J., Zhang, Y., Hotzel, I., and Allan, B. B. (2012) Molecular basis for negative regulation of the glucagon receptor. *Proc Natl Acad Sci U S A* **109**, 14393-14398
449. Solloway, M. J., Madjidi, A., Gu, C., Eastham-Anderson, J., Clarke, H. J., Kljavin, N., Zavala-Solorio, J., Kates, L., Friedman, B., Brauer, M., Wang, J., Fiehn, O., Kolumam, G., Stern, H., Lowe, J. B., Peterson, A. S., and Allan, B. B. (2015) Glucagon Couples Hepatic Amino Acid Catabolism to mTOR-Dependent Regulation of alpha-Cell Mass. *Cell Rep* **12**, 495-510
450. Folch, J., Lees, M., and Sloane Stanley, G. H. (1957) A simple method for the isolation and purification of total lipides from animal tissues. *J Biol Chem* **226**, 497-509
451. Conkright, M. D., Guzman, E., Flechner, L., Su, A. I., Hogenesch, J. B., and Montminy, M. (2003) Genome-wide analysis of CREB target genes reveals a core promoter requirement for cAMP responsiveness. *Mol Cell* **11**, 1101-1108
452. Krilov, L., Nguyen, A., Miyazaki, T., Unson, C. G., Williams, R., Lee, N. H., Ceryak, S., and Bouscarel, B. (2011) Dual mode of glucagon receptor internalization: role of PKCalpha, GRKs and beta-arrestins. *Exp Cell Res* **317**, 2981-2994
453. Godlewski, G., Jourdan, T., Szanda, G., Tam, J., Cinar, R., Harvey-White, J., Liu, J., Mukhopadhyay, B., Pacher, P., Ming Mo, F., Osei-Hyiaman, D., and Kunos, G. (2015) Mice lacking GPR3 receptors display late-onset obese phenotype due to impaired thermogenic function in brown adipose tissue. *Sci Rep* **5**, 14953
454. Roskoski, R., Jr. (2012) ERK1/2 MAP kinases: structure, function, and regulation. *Pharmacological research* **66**, 105-143
455. Yoon, S., and Seger, R. (2006) The extracellular signal-regulated kinase: multiple substrates regulate diverse cellular functions. *Growth factors* **24**, 21-44
456. Sheridan, D. L., Kong, Y., Parker, S. A., Dalby, K. N., and Turk, B. E. (2008) Substrate discrimination among mitogen-activated protein kinases through distinct docking sequence motifs. *J Biol Chem* **283**, 19511-19520
457. Fantz, D. A., Jacobs, D., Glossip, D., and Kornfeld, K. (2001) Docking sites on substrate proteins direct extracellular signal-regulated kinase to phosphorylate specific residues. *J Biol Chem* **276**, 27256-27265
458. Callaway, K., Waas, W. F., Rainey, M. A., Ren, P., and Dalby, K. N. (2010) Phosphorylation of the transcription factor Ets-1 by ERK2: rapid dissociation of ADP and phospho-Ets-1.

Biochemistry **49**, 3619-3630
459. Piserchio, A., Warthaka, M., Kaoud, T. S., Callaway, K., Dalby, K. N., and Ghose, R. (2017) Local destabilization, rigid body, and fuzzy docking facilitate the phosphorylation of the transcription factor Ets-1 by the mitogen-activated protein kinase ERK2. *Proceedings of the National Academy of Sciences of the United States of America* **114**, E6287-E6296
460. Rainey, M. A., Callaway, K., Barnes, R., Wilson, B., and Dalby, K. N. (2005) Proximity-induced catalysis by the protein kinase ERK2. *Journal of the American Chemical Society* **127**, 10494-10495
461. Scapin, G. (2006) Protein kinase inhibition: different approaches to selective inhibitor design. *Current drug targets* **7**, 1443-1454
462. Knight, Z. A., and Shokat, K. M. (2005) Features of selective kinase inhibitors. *Chemistry & biology* **12**, 621-637
463. Lawrence, D. S., and Niu, J. (1998) Protein kinase inhibitors: the tyrosine-specific protein kinases. *Pharmacology & therapeutics* **77**, 81-114
464. Breen, M. E., and Soellner, M. B. (2015) Small molecule substrate phosphorylation site inhibitors of protein kinases: approaches and challenges. *ACS chemical biology* **10**, 175-189
465. Roberts, P. J., and Der, C. J. (2007) Targeting the Raf-MEK-ERK mitogen-activated protein kinase cascade for the treatment of cancer. *Oncogene* **26**, 3291-3310
466. Liu, Q. H., Shi, M. L., Sun, C., Bai, J., and Zheng, J. N. (2015) Role of the ERK1/2 pathway in tumor chemoresistance and tumor therapy. *Bioorganic & medicinal chemistry letters* **25**, 192-197
467. Chico, L. K., Van Eldik, L. J., and Watterson, D. M. (2009) Targeting protein kinases in central nervous system disorders. *Nature reviews. Drug discovery* **8**, 892-909
468. Tanti, J. F., and Jager, J. (2009) Cellular mechanisms of insulin resistance: role of stress-regulated serine kinases and insulin receptor substrates (IRS) serine phosphorylation. *Current opinion in pharmacology* **9**, 753-762
469. Kim, E. K., and Choi, E. J. (2010) Pathological roles of MAPK signaling pathways in human diseases. *Biochimica et biophysica acta* **1802**, 396-405
470. Muslin, A. J. (2008) MAPK signalling in cardiovascular health and disease: molecular mechanisms and therapeutic targets. *Clinical science* **115**, 203-218
471. Schnieders, M. J., Kaoud, T. S., Yan, C., Dalby, K. N., and Ren, P. (2012) Computational insights for the discovery of non-ATP competitive inhibitors of MAP kinases. *Current pharmaceutical design* **18**, 1173-1185
472. Garai, A., Zeke, A., Gogl, G., Toro, I., Fordos, F., Blankenburg, H., Barkai, T., Varga, J., Alexa, A., Emig, D., Albrecht, M., and Remenyi, A. (2012) Specificity of linear motifs that bind to a common mitogen-activated protein kinase docking groove. *Science signaling* **5**, ra74
473. Tanoue, T., Maeda, R., Adachi, M., and Nishida, E. (2001) Identification of a docking groove on ERK and p38 MAP kinases that regulates the specificity of docking interactions. *The EMBO journal* **20**, 466-479
474. Burkhard, K., Smith, S., Deshmukh, R., MacKerell, A. D., Jr., and Shapiro, P. (2009) Development of extracellular signal-regulated kinase inhibitors. *Curr Top Med Chem* **9**, 678-689
475. Boston, S. R., Deshmukh, R., Strome, S., Priyakumar, U. D., MacKerell, A. D., Jr., and Shapiro, P. (2011) Characterization of ERK docking domain inhibitors that induce apoptosis by targeting Rsk-1 and caspase-9. *BMC cancer* **11**, 7
476. Cerchietti, L. C., Ghetu, A. F., Zhu, X., Da Silva, G. F., Zhong, S., Matthews, M., Bunting, K. L., Polo, J. M., Fares, C., Arrowsmith, C. H., Yang, S. N., Garcia, M., Coop, A., Mackerell, A. D., Jr., Prive, G. G., and Melnick, A. (2010) A small-molecule inhibitor of BCL6 kills DLBCL cells in vitro and in vivo. *Cancer cell* **17**, 400-411
477. Arkin, M. R., Tang, Y., and Wells, J. A. (2014) Small-molecule inhibitors of protein-protein interactions: progressing toward the reality. *Chemistry & biology* **21**, 1102-1114
478. Tanoue, T., Adachi, M., Moriguchi, T., and Nishida, E. (2000) A conserved docking motif in MAP kinases common to substrates, activators and regulators. *Nature cell biology* **2**, 110-116

479. Bardwell, L., and Thorner, J. (1996) A conserved motif at the amino termini of MEKs might mediate high-affinity interaction with the cognate MAPKs. *Trends in biochemical sciences* **21**, 373-374
480. Xu, B., Wilsbacher, J. L., Collisson, T., and Cobb, M. H. (1999) The N-terminal ERK-binding site of MEK1 is required for efficient feedback phosphorylation by ERK2 in vitro and ERK activation in vivo. *J Biol Chem* **274**, 34029-34035
481. Camps, M., Nichols, A., Gillieron, C., Antonsson, B., Muda, M., Chabert, C., Boschert, U., and Arkinstall, S. (1998) Catalytic activation of the phosphatase MKP-3 by ERK2 mitogen-activated protein kinase. *Science* **280**, 1262-1265
482. Martin, M. C., Allan, L. A., Mancini, E. J., and Clarke, P. R. (2008) The docking interaction of caspase-9 with ERK2 provides a mechanism for the selective inhibitory phosphorylation of caspase-9 at threonine 125. *J Biol Chem* **283**, 3854-3865
483. Dimitri, C. A., Dowdle, W., MacKeigan, J. P., Blenis, J., and Murphy, L. O. (2005) Spatially separate docking sites on ERK2 regulate distinct signaling events in vivo. *Current biology : CB* **15**, 1319-1324
484. Smith, J. A., Poteet-Smith, C. E., Malarkey, K., and Sturgill, T. W. (1999) Identification of an extracellular signal-regulated kinase (ERK) docking site in ribosomal S6 kinase, a sequence critical for activation by ERK in vivo. *J Biol Chem* **274**, 2893-2898
485. Bott, C. M., Thorneycroft, S. G., and Marshall, C. J. (1994) The sevenmaker gain-of-function mutation in p42 MAP kinase leads to enhanced signalling and reduced sensitivity to dual specificity phosphatase action. *FEBS letters* **352**, 201-205
486. Goetz, E. M., Ghandi, M., Treacy, D. J., Wagle, N., and Garraway, L. A. (2014) ERK mutations confer resistance to mitogen-activated protein kinase pathway inhibitors. *Cancer research* **74**, 7079-7089
487. Hancock, C. N., Macias, A., Lee, E. K., Yu, S. Y., Mackerell, A. D., Jr., and Shapiro, P. (2005) Identification of novel extracellular signal-regulated kinase docking domain inhibitors. *Journal of medicinal chemistry* **48**, 4586-4595
488. Kinoshita, T., Sugiyama, H., Mori, Y., Takahashi, N., and Tomonaga, A. (2016) Identification of allosteric ERK2 inhibitors through in silico biased screening and competitive binding assay. *Bioorganic & medicinal chemistry letters* **26**, 955-958
489. Chen, F., Hancock, C. N., Macias, A. T., Joh, J., Still, K., Zhong, S., MacKerell, A. D., Jr., and Shapiro, P. (2006) Characterization of ATP-independent ERK inhibitors identified through in silico analysis of the active ERK2 structure. *Bioorganic & medicinal chemistry letters* **16**, 6281-6287
490. Li, Q., Al-Ayoubi, A., Guo, T., Zheng, H., Sarkar, A., Nguyen, T., Eblen, S. T., Grant, S., Kellogg, G. E., and Zhang, S. (2009) Structure-activity relationship (SAR) studies of 3-(2-amino-ethyl)-5-(4-ethoxy-benzylidene)-thiazolidine-2,4-dione: development of potential substrate-specific ERK1/2 inhibitors. *Bioorganic & medicinal chemistry letters* **19**, 6042-6046
491. Samadani, R., Zhang, J., Brophy, A., Oashi, T., Priyakumar, U. D., Raman, E. P., St John, F. J., Jung, K. Y., Fletcher, S., Pozharski, E., MacKerell, A. D., Jr., and Shapiro, P. (2015) Small-molecule inhibitors of ERK-mediated immediate early gene expression and proliferation of melanoma cells expressing mutated BRaf. *The Biochemical journal* **467**, 425-438
492. Miller, C. J., Muftuoglu, Y., and Turk, B. E. (2017) A high throughput assay to identify substrate-selective inhibitors of the ERK protein kinases. *Biochem Pharmacol*
493. Houghten, R. A. (1994) Combinatorial libraries. Finding the needle in the haystack. *Current biology : CB* **4**, 564-567
494. Ostresh, J. M., Husar, G. M., Blondelle, S. E., Dorner, B., Weber, P. A., and Houghten, R. A. (1994) "Libraries from libraries": chemical transformation of combinatorial libraries to extend the range and repertoire of chemical diversity. *Proceedings of the National Academy of Sciences of the United States of America* **91**, 11138-11142
495. Houghten, R. A., Pinilla, C., Giulianotti, M. A., Appel, J. R., Dooley, C. T., Nefzi, A., Ostresh, J.

M., Yu, Y. P., Maggiora, G. M., Medina-Franco, J. L., Brunner, D., and Schneider, J. (2008) Strategies for the use of mixture-based synthetic combinatorial libraries: Scaffold ranking, direct testing, in vivo, and enhanced deconvolution by computational methods. *J Comb Chem* **10**, 3-19
496. Zhang, J. H., Chung, T. D., and Oldenburg, K. R. (1999) A Simple Statistical Parameter for Use in Evaluation and Validation of High Throughput Screening Assays. *Journal of biomolecular screening* **4**, 67-73
497. Figuera-Losada, M., and LoGrasso, P. V. (2012) Enzyme kinetics and interaction studies for human JNK1beta1 and substrates activating transcription factor 2 (ATF2) and c-Jun N-terminal kinase (c-Jun). *J Biol Chem* **287**, 13291-13302
498. Szafranska, A. E., and Dalby, K. N. (2005) Kinetic mechanism for p38 MAP kinase alpha. A partial rapid-equilibrium random-order ternary-complex mechanism for the phosphorylation of a protein substrate. *FEBS J* **272**, 4631-4645
499. Zhou, T., Sun, L., Humphreys, J., and Goldsmith, E. J. (2006) Docking interactions induce exposure of activation loop in the MAP kinase ERK2. *Structure* **14**, 1011-1019
500. Piserchio, A., Warthaka, M., Devkota, A. K., Kaoud, T. S., Lee, S., Abramczyk, O., Ren, P., Dalby, K. N., and Ghose, R. (2011) Solution NMR insights into docking interactions involving inactive ERK2. *Biochemistry* **50**, 3660-3672
501. Williams, C. J., Headd, J. J., Moriarty, N. W., Prisant, M. G., Videau, L. L., Deis, L. N., Verma, V., Keedy, D. A., Hintze, B. J., Chen, V. B., Jain, S., Lewis, S. M., Arendall Iii, W. B., Snoeyink, J., Adams, P. D., Lovell, S. C., Richardson, J. S., and Richardson, D. C. (2018) MolProbity: More and better reference data for improved all-atom structure validation. *Protein Science* **27**, 293-315
502. Kaoud, T. S., Devkota, A. K., Harris, R., Rana, M. S., Abramczyk, O., Warthaka, M., Lee, S., Girvin, M. E., Riggs, A. F., and Dalby, K. N. (2011) Activated ERK2 is a monomer in vitro with or without divalent cations and when complexed to the cytoplasmic scaffold PEA-15. *Biochemistry* **50**, 4568-4578
503. Yan, C., Kaoud, T., Lee, S., Dalby, K. N., and Ren, P. (2011) Understanding the specificity of a docking interaction between JNK1 and the scaffolding protein JIP1. *The journal of physical chemistry. B* **115**, 1491-1502
504. Waas, W. F., and Dalby, K. N. (2002) Transient protein-protein interactions and a random-ordered kinetic mechanism for the phosphorylation of a transcription factor by extracellular-regulated protein kinase 2. *J Biol Chem* **277**, 12532-12540
505. Waas, W. F., and Dalby, K. N. (2001) Purification of a model substrate for transcription factor phosphorylation by ERK2. *Protein expression and purification* **23**, 191-197
506. Madsen, J. A., Kaoud, T. S., Dalby, K. N., and Brodbelt, J. S. (2011) 193-nm photodissociation of singly and multiply charged peptide anions for acidic proteome characterization. *Proteomics* **11**, 1329-1334
507. Lee, S., Warthaka, M., Yan, C., Kaoud, T. S., Ren, P., and Dalby, K. N. (2011) Examining docking interactions on ERK2 with modular peptide substrates. *Biochemistry* **50**, 9500-9510
508. Zamora-Olivares, D., Kaoud, T. S., Jose, J., Ellington, A., Dalby, K. N., and Anslyn, E. V. (2014) Differential sensing of MAP kinases using SOX-peptides. *Angewandte Chemie* **53**, 14064-14068
509. Shults, M. D., Pearce, D. A., and Imperiali, B. (2003) Modular and tunable chemosensor scaffold for divalent zinc. *Journal of the American Chemical Society* **125**, 10591-10597
510. Kaoud, T. S., Mitra, S., Lee, S., Taliaferro, J., Cantrell, M., Linse, K. D., Van Den Berg, C. L., and Dalby, K. N. (2011) Development of JNK2-selective peptide inhibitors that inhibit breast cancer cell migration. *ACS chemical biology* **6**, 658-666
511. Lee, S., Warthaka, M., Yan, C., Kaoud, T. S., Piserchio, A., Ghose, R., Ren, P., and Dalby, K. N. (2011) A model of a MAPK*substrate complex in an active conformation: a computational and experimental approach. *PloS one* **6**, e18594
512. Devkota, A. K., Kaoud, T. S., Warthaka, M., and Dalby, K. N. (2010) Fluorescent peptide assays for protein kinases. *Current protocols in molecular biology* **Chapter 18**, Unit 18 17
513. Callaway, K., Rainey, M. A., and Dalby, K. N. (2005) Quantifying ERK2-protein interactions by

fluorescence anisotropy: PEA-15 inhibits ERK2 by blocking the binding of DEJL domains. *Biochimica et biophysica acta* **1754**, 316-323
514. Hastie, C. J., McLauchlan, H. J., and Cohen, P. (2006) Assay of protein kinases using radiolabeled ATP: a protocol. *Nature protocols* **1**, 968-971
515. Pervushin, K., Riek, R., Wider, G., and Wuthrich, K. (1997) Attenuated T2 relaxation by mutual cancellation of dipole-dipole coupling and chemical shift anisotropy indicates an avenue to NMR structures of very large biological macromolecules in solution. *Proceedings of the National Academy of Sciences of the United States of America* **94**, 12366-12371
516. Delaglio, F., Grzesiek, S., Vuister, G. W., Zhu, G., Pfeifer, J., and Bax, A. (1995) NMRPipe: a multidimensional spectral processing system based on UNIX pipes. *J Biomol NMR* **6**, 277-293
517. Goddard, T. G. K., D.G. (2008) SPARKY3. University of California, San Francisco
518. Wallace, A. C., Laskowski, R. A., and Thornton, J. M. (1995) LIGPLOT: a program to generate schematic diagrams of protein-ligand interactions. *Protein Eng* **8**, 127-134
519. Starbird, C. A., Perry, N. A., Chen, Q., Berndt, S., Yamakawa, I., Loukachevitch, L. V., Limbrick, E. M., Bachmann, B. O., Iverson, T. M., and McCulloch, K. M. (2018) The Structure of the Bifunctional Everninomicin Biosynthetic Enzyme EvdMO1 Suggests Independent Activity of the Fused Methyltransferase-Oxidase Domains. *Biochemistry* **57**, 6827-6837
520. Arenz, S., Juette, M. F., Graf, M., Nguyen, F., Huter, P., Polikanov, Y. S., Blanchard, S. C., and Wilson, D. N. (2016) Structures of the orthosomycin antibiotics avilamycin and evernimicin in complex with the bacterial 70S ribosome. *Proc. Natl. Acad. Sci. U. S. A.* **113**, 7527-7532
521. Belova, L., Tenson, T., Xiong, L., McNicholas, P. M., and Mankin, A. S. (2001) A novel site of antibiotic action in the ribosome: Interaction of evernimicin with the large ribosomal subunit. *Proc. Natl. Acad. Sci. U. S. A.* **98**, 3726-3731
522. Hofmann, C., Boll, R., Heitmann, B., Hauser, G., Dürr, C., Frerich, A., Weitnauer, G., Glaser, S. J., and Bechthold, A. (2005) Genes Encoding Enzymes Responsible for Biosynthesis of L-Lyxose and Attachment of Eurekanate during Avilamycin Biosynthesis. *Chem. Biol.* **12**, 1137-1143
523. Weitnauer, G., Gaisser, S., Kellenberger, L., Leadlay, P. F., and Bechthold, A. (2002) Analysis of a C-methyltransferase gene (aviG1) involved in avilamycin biosynthesis in Streptomyces viridochromogenes Tü57 and complementation of a Saccharopolyspora erythraea eryBIII mutant by aviG1. *Microbiology* **148**, 373-379
524. Weitnauer, G., Hauser, G., Hofmann, C., Linder, U., Boll, R., Pelz, K., Glaser, S. J., and Bechthold, A. (2004) Novel Avilamycin Derivatives with Improved Polarity Generated by Targeted Gene Disruption. *Chem. Biol.* **11**, 1403-1411
525. Weitnauer, G., Mühlenweg, A., Trefzer, A., Hoffmeister, D., Süßmuth, R. D., Jung, G., Welzel, K., Vente, A., Girreser, U., and Bechthold, A. (2001) Biosynthesis of the orthosomycin antibiotic avilamycin A: deductions from the molecular analysis of the avi biosynthetic gene cluster of Streptomyces viridochromogenes Tü57 and production of new antibiotics. *Chem. Biol.* **8**, 569-581
526. Boucher, H. W., Thauvin-Eliopoulos, C., Loebenberg, D., and Eliopoulos, G. M. (2001) In Vivo Activity of Evernimicin (SCH 27899) against Methicillin-Resistant Staphylococcus aureus in Experimental Infective Endocarditis. *Antimicrobial Agents and Chemotherapy* **45**, 208-211
527. Ganguly, A. K. (2000) Ziracin, a novel oligosaccharide antibiotic. *The Journal of antibiotics* **53**, 1038-1044
528. McCulloch, K. M., McCranie, E. K., Smith, J. A., Sarwar, M., Mathieu, J. L., Gitschlag, B. L., Du, Y., Bachmann, B. O., and Iverson, T. M. (2015) Oxidative cyclizations in orthosomycin biosynthesis expand the known chemistry of an oxygenase superfamily. *Proc. Natl. Acad. Sci. U. S. A.* **112**, 11547-11552
529. Li, S., Zhang, J., Liu, Y., Sun, G., Deng, Z., and Sun, Y. (2018) Direct Genetic and Enzymatic Evidence for Oxidative Cyclization in Hygromycin B Biosynthesis. *ACS Chem. Biol.*
530. Laskowski, R. A. (2009) PDBsum new things. *Nucleic Acids Res.* **37**, D355-D359
531. Bauer, J., Ondrovicova, G., Najmanova, L., Pevala, V., Kamenik, Z., Kostan, J., Janata, J., and

Kutejova, E. (2014) Structure and possible mechanism of the CcbJ methyltransferase from Streptomyces caelestis. *Acta Crystallogr., Sect. D: Biol. Crystallogr.* **70**, 943-957
532. Cakici, O., Sikorski, M., Stepkowski, T., Bujacz, G., and Jaskolski, M. (2010) Crystal Structures of NodS N-Methyltransferase from Bradyrhizobium japonicum in Ligand-Free Form and as SAH Complex. *J. Mol. Biol.* **404**, 874-889
533. Chang, A., Singh, S., Bingman, C. A., Thorson, J. S., and Phillips, G. N., Jr. (2011) Structural characterization of CalO1: a putative orsellinic acid methyltransferase in the calicheamicin-biosynthetic pathway. *Acta Crystallogr., Sect. D: Biol. Crystallogr.* **67**, 197-203
534. Choudhury, Hassanul G., Cameron, Alexander D., Iwata, S., and Beis, K. (2011) Structure and mechanism of the chalcogen-detoxifying protein TehB from Escherichia coli. *Biochem. J.* **435**, 85-91
535. Gómez García, I., Stevenson, C. E. M., Usón, I., Freel Meyers, C. L., Walsh, C. T., and Lawson, D. M. (2010) The Crystal Structure of the Novobiocin Biosynthetic Enzyme NovP: The First Representative Structure for the TylF O-Methyltransferase Superfamily. *J. Mol. Biol.* **395**, 390-407
536. Hagelueken, G., Huang, H., Harlos, K., Clarke, B. R., Whitfield, C., and Naismith, J. H. (2012) Crystallization, dehydration and experimental phasing of WbdD, a bifunctional kinase and methyltransferase from Escherichia coli O9a. *Acta Crystallogr., Sect. D: Biol. Crystallogr.* **68**, 1371-1379
537. Kim, J., Xiao, H., Koh, J., Wang, Y., Bonanno, J. B., Thomas, K., Babbitt, P. C., Brown, S., Lee, Y.-S., and Almo, S. C. (2015) Determinants of the CmoB carboxymethyl transferase utilized for selective tRNA wobble modification. *Nucleic Acids Res.* **43**, 4602-4613
538. Lee, Soon G., and Jez, Joseph M. (2013) Evolution of Structure and Mechanistic Divergence in Di-Domain Methyltransferases from Nematode Phosphocholine Biosynthesis. *Structure* **21**, 1778-1787
539. Lee, S. G., Kim, Y., Alpert, T. D., Nagata, A., and Jez, J. M. (2012) Structure and Reaction Mechanism of Phosphoethanolamine Methyltransferase from the Malaria Parasite Plasmodium falciparum: AN ANTIPARASITIC DRUG TARGET. *J. Biol. Chem.* **287**, 1426-1434
540. Singh, S., McCoy, J. G., Zhang, C., Bingman, C. A., Phillips, G. N., and Thorson, J. S. (2008) Structure and Mechanism of the Rebeccamycin Sugar 4′-O-Methyltransferase RebM. *J. Biol. Chem.* **283**, 22628-22636
541. Tsodikov, O. V., Hou, C., Walsh, C. T., and Garneau-Tsodikova, S. (2015) Crystal structure of O-methyltransferase CalO6 from the calicheamicin biosynthetic pathway: a case of challenging structure determination at low resolution. *BMC Struct. Biol.* **15**, 13
542. Zhu, Y., Wu, B., Zhang, X., Fan, X., Niu, L., Li, X., Wang, J., and Teng, M. (2015) Structural and biochemical studies reveal UbiG/Coq3 as a class of novel membrane-binding proteins. *Biochem. J.* **470**, 105-114
543. Holm, L., and Rosenström, P. (2010) Dali server: conservation mapping in 3D. *Nucleic Acids Res.* **38**, W545-W549
544. Zhou, J., Kelly, W. L., Bachmann, B. O., Gunsior, M., Townsend, C. A., and Solomon, E. I. (2001) Spectroscopic Studies of Substrate Interactions with Clavaminate Synthase 2, a Multifunctional α-KG-Dependent Non-Heme Iron Enzyme: Correlation with Mechanisms and Reactivities. *J. Am. Chem. Soc.* **123**, 7388-7398
545. Maier, T., Leibundgut, M., and Ban, N. (2008) The Crystal Structure of a Mammalian Fatty Acid Synthase. *Science* **321**, 1315-1322
546. An, S., Kumar, R., Sheets, E. D., and Benkovic, S. J. (2008) Reversible Compartmentalization of de Novo Purine Biosynthetic Complexes in Living Cells. *Science* **320**, 103-106
547. Otwinowski, Z., and Minor, W. (1997) Processing of X-ray diffraction data collected in oscillation mode. *Methods Enzymol.* **276**, 307-326
548. McCoy, A. J., Grosse-Kunstleve, R. W., Adams, P. D., Winn, M. D., Storoni, L. C., and Read, R. J. (2007) *Phaser* crystallographic software. *J. Appl. Crystallogr.* **40**, 658-674

549. Adams, P. D., Afonine, P. V., Bunkoczi, G., Chen, V. B., Davis, I. W., Echols, N., Headd, J. J., Hung, L. W., Kapral, G. J., Grosse-Kunstleve, R. W., McCoy, A. J., Moriarty, N. W., Oeffner, R., Read, R. J., Richardson, D. C., Richardson, J. S., Terwilliger, T. C., and Zwart, P. H. (2010) PHENIX: a comprehensive Python-based system for macromolecular structure solution. *Acta Crystallogr., Sect. D: Biol. Crystallogr.* **66**, 213-221
550. Syed Ibrahim, B., Burley, S. K., and Swaminathan, S. (2010) Crystal Structure of Methyl Transferase from *Methanosarcina mazei*. 4/21/2010 Ed., RCSB PDB, Protein Data Bank
551. Emsley, P., Lohkamp, B., Scott, W. G., and Cowtan, K. (2010) Features and development of Coot. *Acta Crystallogr., Sect. D: Biol. Crystallogr.* **D66**, 486-501
552. Afonine, P. V., Grosse-Kunstleve, R. W., Echols, N., Headd, J. J., Moriarty, N. W., Mustyakimov, M., Terwilliger, T. C., Urzhumtsev, A., Zwart, P. H., and Adams, P. D. (2012) Towards automated crystallographic structure refinement with *phenix.refine*. *Acta Crystallogr., Sect. D: Biol. Crystallogr.* **D68**, 352-367
553. Brunger, A. T. (2007) Version 1.2 of the Crystallography and NMR system. *Nat. Protoc.* **2**, 2728-2733
554. Davis, I. W., Leaver-Fay, A., Chen, V. B., Block, J. N., Kapral, G. J., Wang, X., Murray, L. W., Arendall, W. B., 3rd, Snoeyink, J., Richardson, J. S., and Richardson, D. C. (2007) MolProbity: all-atom contacts and structure validation for proteins and nucleic acids. *Nucleic acids research* **35**, W375-383
555. Schrodinger, LLC. (2010) The PyMOL molecular graphics system, version 1.3r1.
556. Morin, A., Eisenbraun, B., Key, J., Sanschagrin, P. C., Timony, M. A., Ottaviano, M., and Sliz, P. (2013) Collaboration gets the most out of software. *eLife* **2**, e01456
557. Peterson, Y. K., and Luttrell, L. M. (2017) The Diverse Roles of Arrestin Scaffolds in G Protein-Coupled Receptor Signaling. *Pharmacol Rev* **69**, 256-297
558. Zhuang, T., Vishnivetskiy, S. A., Gurevich, V. V., and Sanders, C. R. (2010) Elucidation of inositol hexaphosphate and heparin interaction sites and conformational changes in arrestin-1 by solution nuclear magnetic resonance. *Biochemistry* **49**, 10473-10485
559. Gurevich, V. V., and Gurevich, E. V. (2013) Structural determinants of arrestin functions. *Prog Mol Biol Transl Sci* **118**, 57-92
560. Gurevich, V. V., Song, X., Vishnivetskiy, S. A., and Gurevich, E. V. (2014) Enhanced phosphorylation-independent arrestins and gene therapy. *Handb Exp Pharmacol* **219**, 133-152
561. Hanson, S. M., Dawson, E. S., Francis, D. J., Van Eps, N., Klug, C. S., Hubbell, W. L., Meiler, J., and Gurevich, V. V. (2008) A model for the solution structure of the rod arrestin tetramer. *Structure* **16**, 924-934
562. Yu, M.-C., Su, L.-L., Zou, L., Liu, Y., Wu, N., Kong, L., Zhuang, Z.-H., Sun, L., Liu, H.-P., Hu, J.-H., Li, D., Strominger, J. L., Zang, J.-W., Pei, G., and Ge, B.-X. (2008) An essential function for β-arrestin 2 in the inhibitory signaling of natural killer cells. *Nature Immunology* **9**, 898
563. Wilbanks, A. M., Fralish, G. B., Kirby, M. L., Barak, L. S., Li, Y. X., and Caron, M. G. (2004) Beta-arrestin 2 regulates zebrafish development through the hedgehog signaling pathway. *Science* **306**, 2264-2267
564. Li, T., Franson, W. K., Gordon, J. W., Berson, E. L., and Dryja, T. P. (1995) Constitutive activation of phototransduction by K296E opsin is not a cause of photoreceptor degeneration. *Proceedings of the National Academy of Sciences* **92**, 3551
565. Carr, R., Schilling, J., Song, J., Carter, R. L., Du, Y., Yoo, S. M., Traynham, C. J., Koch, W. J., Cheung, J. Y., Tilley, D. G., and Benovic, J. L. (2016) β-arrestin–biased signaling through the β2-adrenergic receptor promotes cardiomyocyte contraction. *Proceedings of the National Academy of Sciences* **113**, E4107-E4116